Analytical and Experimental Investigation of a Controlled Rocking Approach for Seismic Protection of Bridge Steel Truss Piers

by

Michael Pollino and Michel Bruneau

Technical Report MCEER-08-0003
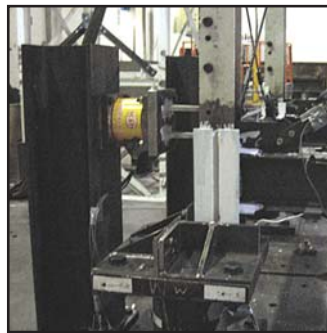
January 21, 2008

NOTICE

Analytical and Experimental Investigation of a Controlled Rocking Approach for Seismic Protection of Bridge Steel Truss Piers

by

Michael Pollino[1] and Michel Bruneau[2]

1   Engineer, Simpson, Gumpertz and Heger, Inc.; Former Graduate Student, Depart-
    ment of Civil, Structural and Environmental Engineering, University at Buffalo,
    State University of New York
2   Professor, Department of Civil, Structural and Environmental Engineering, Univer-
    sity at Buffalo, State University of New York

MCEER
University at Buffalo, The State University of New York
Red Jacket Quadrangle, Buffalo, NY 14261
Phone: (716) 645-3391; Fax (716) 645-3399
E-mail: *mceer@buffalo.edu*; WWW Site: *http://mceer.buffalo.edu*

Preface

The Multidisciplinary Center for Earthquake Engineering Research (MCEER) is a national center of excellence in advanced technology applications that is dedicated to the reduction of earthquake losses nationwide. Headquartered at the University at Buffalo, State University of New York, the Center was originally established by the National Science Foundation in 1986, as the National Center for Earthquake Engineering Research (NCEER).

Comprising a consortium of researchers from numerous disciplines and institutions throughout the United States, the Center's mission is to reduce earthquake losses through research and the application of advanced technologies that improve engineering, pre-earthquake planning and post-earthquake recovery strategies. Toward this end, the Center coordinates a nationwide program of multidisciplinary team research, education and outreach activities.

MCEER's research is conducted under the sponsorship of two major federal agencies, the National Science Foundation (NSF) and the Federal Highway Administration (FHWA), and the State of New York. Significant support is also derived from the Federal Emergency Management Agency (FEMA), other state governments, academic institutions, foreign governments and private industry.

The Center's Highway Project develops improved seismic design, evaluation, and retrofit methodologies and strategies for new and existing bridges and other highway structures, and for assessing the seismic performance of highway systems. The FHWA has sponsored three major contracts with MCEER under the Highway Project, two of which were initiated in 1992 and the third in 1998.

Of the two 1992 studies, one performed a series of tasks intended to improve seismic design practices for new highway bridges, tunnels, and retaining structures (MCEER Project 112). The other study focused on methodologies and approaches for assessing and improving the seismic performance of existing "typical" highway bridges and other highway system components including tunnels, retaining structures, slopes, culverts, and pavements (MCEER Project 106). These studies were conducted to:

- assess the seismic vulnerability of highway systems, structures, and components;
- develop concepts for retrofitting vulnerable highway structures and components;
- develop improved design and analysis methodologies for bridges, tunnels, and retaining structures, which include consideration of soil-structure interaction mechanisms and their influence on structural response; and
- develop, update, and recommend improved seismic design and performance criteria for new highway systems and structures.

The 1998 study, "Seismic Vulnerability of the Highway System" (FHWA Contract DTFH61-98-C-00094; known as MCEER Project 094), was initiated with the objective of performing studies to improve the seismic performance of bridge types not covered under Projects 106 or 112, and to provide extensions to system performance assessments for highway systems. Specific subjects covered under Project 094 include:

- development of formal loss estimation technologies and methodologies for highway systems;
- analysis, design, detailing, and retrofitting technologies for special bridges, including those with flexible superstructures (e.g., trusses), those supported by steel tower substructures, and cable-supported bridges (e.g., suspension and cable-stayed bridges);
- seismic response modification device technologies (e.g., hysteretic dampers, isolation bearings); and
- soil behavior, foundation behavior, and ground motion studies for large bridges.

In addition, Project 094 includes a series of special studies, addressing topics that range from non-destructive assessment of retrofitted bridge components to supporting studies intended to assist in educating the bridge engineering profession on the implementation of new seismic design and retrofitting strategies.

This reports presents the results of an analytical and experimental study on a seismic design (or retrofit) strategy that allows uplift and rocking of steel truss piers on their foundation. Displacement-based steel yielding devices and velocity-dependant viscous dampers, installed at the uplifting location, were used to control system response. The behavior of 2- and 4-legged bridge steel truss piers was considered. Methods to predict their response under multiple components of seismic excitation were evaluated using nonlinear, inelastic time history analyses. The analytical investigation included ground motions typical of far-field rock sites and near-field ground motions with pulse-type characteristics. Also, the response of 4-legged piers that resist transverse and longitudinal demands in bridges was investigated with three components of ground motion. Experimental investigations included shake table testing of a rocking pier with the added devices to verify the analytical methods and further investigate the dynamic response. Response quantities of interest include pier displacements, impact velocity, and maximum developed forces. Overall system behavior and the methods of response prediction were shown to be reasonably accurate.

ABSTRACT

A large number of steel truss bridges were constructed in the U.S. when seismic resistance was not considered. Recent structural analyses of these bridges have revealed that they will likely suffer significant seismic damage and have a risk of collapse during their remaining service life. Contributing significantly to their poor seismic behavior is the built-up, lattice type members used to resist the lateral seismic forces and the pier anchorage connections resulting in very little effective system ductility. Also, these types of bridges may be a vital geographical link to a region and must remain operational following a major earthquake. Therefore, seismic retrofit strategies that enhance the global structural ductility, limit maximum forces transmitted to existing members and the foundation (capacity protect), and prevent residual deformations are needed.

A seismic design (or retrofit) strategy allowing uplift and rocking of steel truss piers on their foundation is investigated both analytically and experimentally. To control system response, the use of displacement-based steel yielding devices and velocity-dependant viscous dampers, implemented at the uplifting location, are considered. The devices can be calibrated to capacity protect the existing vulnerable members and the foundation of the structure. The system provides a significant restoring force that can allow re-centering of the structure with proper selection of device properties. The behavior of 2-legged and 4-legged bridge steel truss piers is considered and methods of predicting response under multiple components of seismic excitation are evaluated using nonlinear, inelastic time history analyses. The analytical investigation of seismic response includes ground motions typical of far-field rock sites and near-field ground motions with pulse-type characteristics. Also, the response of 4-legged piers that resist transverse and longitudinal demands in bridges is investigated with three components of ground motion. Experimental investigations include shake table testing of a rocking pier with the added passive energy dissipation devices to verify analytical methods and further investigate the dynamic response. Response quantities of interest include pier displacements, impact velocity, and maximum developed forces. Overall system behavior and the methods of response prediction are shown to be reasonably accurate using the analytical and experimental techniques.

ACKNOWLEDGMENTS

TABLE OF CONTENTS

TABLE OF CONTENTS

TABLE OF CONTENTS

SECTION	TITLE	PAGE

TABLE OF CONTENTS

LIST OF FIGURES

LIST OF FIGURES

LIST OF FIGURES

LIST OF FIGURES

LIST OF FIGURES

LIST OF FIGURES

LIST OF FIGURES

NOTATIONS

$A_{coupler}$ cross-sectional area of pre-tensioning coupler

A_d cross-sectional area of pier diagonal

A_{dmi} cross-sectional area of diagonal in model specimen

A_L cross-sectional area of pier leg

A_{Lm} cross-sectional area of model specimen leg

A_m area of boundary interface

A_{mcr} cross-sectional area of mass connection rods

$a_{p,max}$ maximum pulse acceleration

A_{ub} cross-sectional area of buckling-restrained brace

a_v general vertical acceleration of pier mass

B_L modification factor for damping in long period range

B_s modification factor for damping in short period range

BS_{SG} base shear force calculated from strain gages

b_T TADAS plate width at fixed support of device

c damping coefficient

c_{bound} damping coefficient of boundary element discrete damper

d pier width

d_{clm} center-to-center distance between pier legs

d_{KD} distance between Krypton diodes

d_m width of model specimen

d_{mcr} distance between mass connection rods

du_z relative differential displacement across the damper

NOTATIONS (CONTINUED)

E	modulus of elasticity
E_m	modulus of elasticity of model specimen
f_{BFMF}	ratio of braced and moment frame stiffness of model specimen
F_d	maximum device force
F_f	horizontal shear force applied to a pier frame
F_{up}	dynamic force effect to a pier leg from the impulsive transfer of loads through the pier during uplift
F_{vd}	viscous damper force
F_{vdo}	maximum viscous damper force
F_{ve}	pier leg force resulting from vertical ground excitation
F_{vo}	pier leg force resulting from impacting of pier leg
F_w	dynamic force effect to a pier leg from the impulsive application of its tributary weight returning during impact
F_x	general shear force in x-direction
F_{xy}	general shear force in -direction
F_y	general shear force in y-direction
F_{yd}	yield force of steel yielding device
F_{yT}	yield stress of steel in TADAS device
F_{yub}	yield stress of buckling-restrained brace core
$F(\ )$	fourier transform of input
$F^*(\ )$	conjugate of $F(\ )$
g	acceleration of gravity

NOTATIONS (CONTINUED)

h	pier height
h_{LC-M}	distance from top of large load cells to center of mass plates
h_m	height of model specimen
h/d	pier aspect ratio
i	leg number index
I_f	moment of inertia of a pier frame
I_{pm}	moment of inertial of model specimen
j	leg number index
k	stiffness of general spring
k_b	steel yielding device influence on rocking stiffness
k_d	device elastic stiffness
KE_1	kinetic energy of controlled rocking pier at position 1
KE_2	kinetic energy of controlled rocking pier at position 2
k_{eT}	elastic stiffness of TADAS device
k_f	horizontal stiffness of a pier frame
k_L	axial stiffness of pier leg
k_o	"fixed-base" horizontal stiffness of pier
k_{oBm}	overturning stiffness of model pier specimen
k_{om}	lateral stiffness of model specimen
k_{oTm}	shear stiffness of model specimen provided by diagonal members
$k_{o,x}$	"fixed-base" horizontal stiffness of pier in x-direction
k_{oXMF}	model specimen lateral horizontal stiffness provided by moment frame in

	x-direction
$k_{o,y}$	"fixed-base" horizontal stiffness of pier in y-direction
k_{oyMF}	model specimen lateral horizontal stiffness provided by moment frame in y-direction
k_{py}	post-yield system stiffness
k_r	rocking stiffness
k_v	vertical shearing stiffness of pier
k_{mc}	rotational stiffness of mass connection in model specimen
L_d	length of pier diagonal
L_{dmi}	length of diagonal in model specimen
L_{mcr}	length of mass connection rods
L_T	length of TADAS plates
L_{ub}	effective length of buckling-restrained brace
m	frame number index
m_h	horizontal tributary mass of pier
M_r	restoring moment
m_v	vertical tributary mass of pier
M_w	earthquake moment magnitude
m_x	tributary pier mass in x-direction
m_y	tributary pier mass in y-direction
n_f	number of frames in a single pier direction
n_p	number of pier panels

NOTATIONS (CONTINUED)

N_T	number of TADAS plates
P_c	horizontal load at the point of steel yielding device reverse yielding
PE_1	potential energy of controlled rocking pier in position 1
PE_2	potential energy of controlled rocking pier in position 2
P_L	pier leg force
p_o	maximum of applied step load
P_r	effective horizontal restoring force
P_u	maximum pier shear force (used for 2-legged piers)
$P_{u,100-40}$	maximum pier shear force using a 100%-40% directional combination rule
P_{uF}	maximum frame shear force
$P_{uF,100-40}$	maximum frame shear force considering bi-directional response and using a 100%-40% directional combination rule
$P_{uF,ABS}$	maximum frame shear force using an absolute sum combination rule
$P_{uF,st}$	maximum frame shear force considering static response
P_{uL}	maximum dynamic force developed in a pier leg
$P_{uL,100-40}$	maximum pier leg axial force considering bi-directional response and using a 100%-40% directional combination rule
$P_{uL,ABS}$	maximum pier leg axial force using an absolute sum combination rule
$P_{uL,st}$	maximum pier leg axial force considering static response
P_{up1}	horizontal base shear at point of uplift during 1st cycle response
P_{up2}	horizontal base shear at point of uplift during 2nd cycle response
$P_{u,st}$	maximum pier shear force considering static response

NOTATIONS (CONTINUED)

P_y	pier yield force for 2-legged controlled rocking pier
$P_{y,uni}$	pier yield force considering uni-directional behavior
$P_{y,xy}$	pier yield force considering bi-directional behavior
q	modification factor for hysteretic energy dissipation
Q	fundamental physical quantities
$Q_{Analytical}$	peak response quantity recorded using an analytical method
Q_{Exp}	peak response quantity from experimental testing
Q_{model}	fundamental physical quantity of model specimen
$Q_{prototype}$	fundamental physical quantity of prototype
R	source-to-site distance
R_d	dynamic amplification factor
R_{dL}	dynamic amplification factor for loading directly down pier leg during impact
R_{dv}	dynamic amplification factor for transfer of loads during uplift
R_f	maximum force developed in foundation beneath pier leg
$R_{f,100-40}$	maximum force developed in foundation beneath pier leg using a 100%-40% directional combination rule
$R_{f,st}$	force developed in foundation beneath pier leg assuming static response
S_1	1-second spectral acceleration value
S_{av}	vertical spectral acceleration value at pier's vertical period
$S_{a,x}$	spectral acceleration value in x-direction
$S_{a,xy}$	bi-directional spectral acceleration value

$S_{a,y}$	spectral acceleration value in y-direction
S_{D1}	design 1-second spectral acceleration
S_{DS}	design short-period spectral acceleration
$S_{ff}(\ )$	power spectrum
$S_{fx}(\ )$	cross spectrum
SG	strain gage recording
S_s	short-period spectral acceleration value
t	time
TF	transfer function
T_L	axial period of vibration of pier leg
T_{Lm}	axial period of vibration of model specimen leg
T_n	period of vibration of elastic SDOF system
T_o	fixed-base period of vibration of pier
T_{om}	fixed-base period of vibration of model specimen
$T_{o,wn}$	fixed-base period of vibration determined from white noise testing
T_p	pulse period
t_r	rise time of step load
t_{r1}	rise time of first load transferred through pier vertically during rocking
t_{r2}	rise time of second load transferred through pier vertically during rocking
t_{rL}	rise time of loading directly down pier leg during impact
t_{rv}	effective rise time of loads transferred through pier vertically during rocking

NOTATIONS (CONTINUED)

T_s	characteristic spectral period
T_{sec}	secant period of vibration
t_T	thickness of single TADAS plate
T_v	period of vertical shearing mode of vibration
T_{vm}	period of vertical shearing mode of vibration of model specimen
u_o	maximum displacement of elastic SDOF system under impulsive loading
$u_{p,max}$	maximum pulse displacement
$(u_{st})_o$	maximum displacement of elastic SDOF system under static loading
$\dot{u}_z$	relative damper velocity
v_m	speed of wave propagation through boundary material
v_o	maximum impact velocity
$v_{o,x}$	maximum impact velocity considering only uni-directional response in x-direction
$v_{o,y}$	maximum impact velocity considering only uni-directional response in y-direction
$v_{p,max}$	maximum pulse velocity
V_{pT}	plastic shear force of TADAS device
w	weight of pier
W_{1-2}	work done by passive energy dissipation devices from position 1 to 2
w_h	horizontal tributary weight of pier
W_k	stored strain energy
w_{mz}	weight of model specimen

NOTATIONS (CONTINUED)

w_v — vertical tributary weight of pier

$X(\ )$ — fourier transform of output

$\quad$ — angle of directional vector measured from x-axis

$_d$ — damping exponent

$_{syd}$ — post-yield stiffness ratio of steel yielding device

$_T$ — TADAS device rotation

$_{ABS,P}$ — absolute displacement of model specimen during testing

$_{br}$ — horizontal displacement resulting from rigid body rotation at the base of the pier

$_{br,Fm}$ — horizontal displacement of frame m resulting from rigid body rotation at the base of the frame

$_c$ — horizontal displacement of pier at point of reverse yielding of steel yielding device

$_G$ — global (deck-level) horizontal pier displacement

$_i$ — incremental horizontal displacement of pier

$_o$ — horizontal pier displacement resulting from deformations of its structural members

$_{REL,P}$ — relative displacement of model specimen during testing

$_t$ — analytical time step

$_T$ — shake table displacement

$_u$ — maximum horizontal displacement in one of the primary orthogonal pier

	directions
$_{u,Fm}$	maximum horizontal displacement of frame m
$_{up1}$	horizontal pier displacement at point of uplift during 1st cycle response
$_{up2}$	horizontal pier displacement at point of uplift during 2nd cycle response
$_{up,100\text{-}40}$	maximum uplifting displacement considering bi-directional response and using a 100%-40% directional combination rule
$_{up,Fm}$	uplifting displacement of frame m
$_{upL}$	uplifting displacement of leg ($_{up}$ in Section 6)
$_{up,Li}$	uplifting displacement of leg i
$_{up,Lj}$	uplifting displacement of leg j
$_{u,x}$	maximum horizontal displacement of pier in x-direction
$_{u,xy}$	maximum horizontal displacement of pier
$_{u,y}$	maximum horizontal displacement of pier in y-direction
$_{x}$	general horizontal displacement in x-direction
$_{xy}$	general horizontal displacement in -direction
$_{y}$	general horizontal displacement in y-direction
$_{y1}$	horizontal pier displacement at point of yield during 1st cycle response
$_{y2}$	horizontal pier displacement at point of yield during 2nd cycle response
$_{yd}$	device yield displacement
$_{y,sc}$	horizontal displacement in smaller displacement component direction at formation of bi-directional yield mechanism

$_{y,uni}$	uni-directional yield displacement
$_{y,x}$	displacement in x-direction at formation of bi-directional yield mechanism
$_{y,xy}$	bi-directional yield displacement
$_{y,y}$	displacement in y-direction at formation of bi-directional yield mechanism
$_{ub}$	maximum strain of buckling-restrained brace
$(_{ub})_{limit}$	limiting strain of a buckling-restrained brace
$_{L}$	local strength ratio
$_{Lv}$	viscous local strength ratio
	pier orientation during Phase I of experimental testing program
$_{d}$	angle diagonal members make with horizontal
$_{T}$	rotation of shake table
	general scale factor for experimental testing
$_{a}$	acceleration scale factor
$_{E}$	modulus scale factor
$_{L}$	length scale factor
$_{t}$	time scale factor
$_{v}$	velocity scale factor
$_{G2}$	global displacement ductility considering 2nd cycle hysteretic properties
$_{G2,uni}$	uni-directional global displacement ductility considering 2nd cycle hysteretic properties
$_{G2,xy}$	bi-directional global displacement ductility considering 2nd cycle hysteretic

NOTATIONS (CONTINUED)

properties

μ_L local displacement ductility ratio

μ_Q mean difference between Q_{Exp} and $Q_{Analytical}$

ξ_{eff} equivalent viscous damping ratio

ξ_{hys} equivalent viscous damping provided from hysteretic energy dissipation

ξ_k viscous damping ratio of kth mode

ξ_o inherent damping ratio of pier

ξ_{PED} equivalent viscous damping provided from passive energy dissipation

devices

ρ_m mass density of boundary material

σ_Q standard deviation of the difference between Q_{Exp} and $Q_{Analytical}$

ω_n natural frequency of general mass-spring system

ABBREVIATIONS

AASHTO	American Association of State Highway and Transportation Officials
AISC	American Institute of Steel Construction
ASTM	American Society for Testing and Materials
ATC	Applied Technology Council
BRB	Buckling-restrained Brace
CQC	Complete Quadratic Combination
CUC	Channel Under Calibration
CUREE	California Universities for Research in Earthquake Engineering
DAQ	Data Acquisition System
EBF	Eccentrically Braced Frame
ESL	Engineering Seismology Laboratory
EU	Engineering Unit
FEA	Finite Element Analysis
FEMA	Federal Emergency Mangagement Agency
FFT	Fast Fourier Transform
LC	Load Cell
LED	Light Emitting Diode
MCE	Maximum Considered Earthquake
MCEER	Multidisciplinary Center for Earthquake Engineering Research
MDOF	Multiple Degree of Freedom
NCHRP	National Cooperative Highway Research Program
NEES	Network for Earthquake Engineering Simulation

ABBREVIATIONS (CONTINUED)

NIST	National Institute of Standards and Technology
PGA	Peak Ground Acceleration
RPI	Rensselaer Polytechnic Institute
SAC	SEAOC-ATC-CUREE
SCBF	Special Concentrically Braced Frames
SDOF	Single Degree of Freedom
SEAOC	Structural Engineers Association of California
SEESL	Structural Engineering and Earthquake Simulation Laboratory
SMRF	Special Moment Resisting Frame
SRSS	Square Root Sum of Squares
TADAS	Triangular Added Damping and Stiffness Device
TARSCTHS	Target Acceleration Spectra Compatible Time Histories
UB	University at Buffalo

SECTION 1

INTRODUCTION

1.1 Motivation

Many of the existing steel bridges in the U.S. were built at a time when seismic resistance was not considered in the design or construction of the bridge (Ritchie et al., 1995). Recent earthquakes such as the 1989 Loma Prieta and 1994 Northridge in California, and the 1995 Kobe earthquake in Japan, as well as recent research, have exposed several deficiencies in the design and detailing of structural elements in steel bridges to resist earthquake excitations. Contributing to the seismic deficiency of existing steel bridges are the steel truss piers that support some bridge superstructures. Such 2-legged and 4-legged truss piers can have poor seismic performance as a result of the limited ductility of built-up lateral load resisting bracing members (Lee and Bruneau 2004). In addition, the bracing members' connections and the pier's anchorage connections are likely seismically inadequate (Pollino 2004). Retrofit of these elements to resist seismic demands elastically is an option, but it can be very costly and gives no assurance of performance beyond the elastic limit.

The required level of seismic performance of a bridge will depend greatly on its use, value as a geographical link for an area, and redundancy of the surrounding transportation system. For "critical" transportation links, a level of performance not necessarily provided by code requirements is required that would allow the structure to remain operational following a major seismic event. Whether for retrofit or new construction, approaches for the seismic design of bridges that provide this increased level of performance, at a reasonable cost, are needed.

Currently, approaches for seismic resistance of steel bridges primarily include the use of a ductility based design and passive control techniques. These approaches can provide varying levels of performance however at different levels of cost, required maintenance, and reliability. Currently, ductility based design approaches are expected to provide satisfactory performance by limiting damage and preventing collapse of the structure. However, damage is expected that would leave the structure with a permanent offset (residual displacement)

1

and would likely require significant repairs before the structure can be re-opened for service. Passive control techniques include the use of metallic or viscous damping devices that are often implemented throughout the structure to absorb earthquake energy and prevent damage to key structural elements. Seismic isolation has been a proven form of passive control for bridges that uses bearings, likely implemented between the bridge deck and its supports, that provides a horizontally flexible layer that elongates the structure's period of vibration, adds energy dissipation, can be very effective at reducing seismically induced forces compared to other techniques. However, implementation of seismic isolation bearings to an existing bridge (retrofit) can be a significant undertaking in terms of cost and labor. Also, isolation bearings implemented on a bridge will likely require a maintenance program to ensure their mechanical properties do not significantly deviate throughout the life of the bridge, from those initially assumed. Each approach to seismic resistance has benefits and drawbacks that would be weighed during the design or retrofit process of a particular bridge to determine the most effective solution. These approaches to seismic resistance and protection have been applied to actual bridges while their behavior continues to be investigated in academic research.

More recently, the reliance on stable rocking to provide satisfactory seismic performance has received a renewed interest: more research is being conducted on this topic and various levels of rocking response have been considered in the retrofit of large bridges (see Section 2). This is in part due to a growing appreciation for the ability of such systems to efficiently withstand seismic demands elastically with little to no damage while providing a self-centering ability. Thus rocking behavior, if properly designed, can meet important seismic performance objectives such as elastic response of the structure while re-centering following an earthquake.

1.2 Objectives and Scope of Work

This study investigates the use of rocking behavior with added passive energy dissipation to control displacements and maximum developed forces such that the structure can be designed to remain elastic and re-center following an earthquake, thus protecting its structural integrity and functionality. Focus is placed here on implementation of controlled

rocking to bridge steel truss piers, however, many of the concepts presented are general enough such that they could be applied to other types of structures, lateral force resisting systems, and materials.

As part of the development of this controlled rocking approach for the seismic protection of bridge steel truss piers, a number of analytical studies and experimental tests were conducted to investigate response of single truss piers such that they could be implemented as a seismic protective "component" in a bridge. Much of the work presented here is an extension of previous research (Pollino 2004). The scope of the work conducted to expand upon previous findings is described below:

1.   Investigate the dynamic response of 2-legged controlled rocking piers subjected to simultaneous horizontal and vertical ground motion components focusing on effects to pier displacements and forces. Develop design equations to predict the forces developed resulting from the combination of horizontal and vertical effects.

2.   Consider the use of both displacement and velocity-dependent passive energy dissipation devices. In particular, the displacement-dependent devices had properties typical of steel yielding devices (i.e. buckling-restrained braces, TADAS devices, shear panels, etc.) that exhibit bi-linear hysteretic behavior and the velocity-dependent devices had properties similar to fluid viscous dampers (linear or nonlinear).

3.   Evaluate the effects of near-fault ground motions containing strong pulse-type excitation using analytical and experimental methods.

4.   Develop the hysteretic and kinematic behavior of controlled rocking 4-legged piers subjected to three components of ground motion. Also, expand upon the simplified method of analysis and the design equations developed for 2-legged piers such that they can be applied to predict response of 4-legged piers. Evaluate the equations

3

developed that describe the hysteretic behavior and the design equations using nonlinear time history analysis.

5. Develop an experimental testing program for earthquake simulation testing to investigate the response of a controlled rocking pier specimen subjected to different forms of seismic excitation and using different passive energy dissipation devices.

6. Evaluate the methods of analysis (simplified and finite element analysis, FEA) and design equations using the results of the experimental testing program.

1.3   Original Contribution of Work

The original contribution of this work to the current state of knowledge in the field of structural and earthquake engineering is as follows:

1. The characterization and quantitative prediction of response resulting from higher vertical mode effects of rocking structures provides additional understanding of the rocking behavior. Both analytical and experimental studies performed in the past by a number of researchers and practicing engineers have recognized the effects of such response however an understanding of the mechanisms causing this behavior and methods to quantify it at a fundamental level were needed.

2. The bi-directional behavior and response of rocking steel braced frame structures subjected to multiple components of seismic excitation expands upon the current state of understanding.

3. A design methodology, based on the developments of the fundamental behavior, has been formulated that provides simple (not requiring advanced analytical models) and reliable (shown through analytical and experimental studies) approach for the prediction of response such that controlled rocking piers could be implemented as a seismic protective "component" in a bridge.

4.   The experimental testing program included investigation of response of a specimen to bi-directional horizontal excitation which has not been performed in the past, to the authors knowledge.

1.4   Organization

This report contains seven sections, a list of references, and four appendices and is organized as follows:

Section 2 provides a brief overview of recent research and applications of rocking for the seismic resistance of structures. It also provides necessary background information of concepts related to the controlled rocking approach described in Pollino (2004).

In Section 3, the response of 2-legged controlled rocking piers to multiple components of excitation is discussed and an energy based formulation for prediction of impact velocity is developed. Also, response to near-fault excitation is investigated. The application of two different types of passive energy dissipation devices are discussed.

Section 4 expands upon the concepts developed for 2-legged controlled rocking piers to provide relevant information on behavior, analysis, and design of 4-legged controlled rocking piers subjected to three components of ground motion. Response of 4-legged piers is then evaluated using 3-dimensional nonlinear time history analysis.

The experimental testing program undertaken is discussed in Section 5. All relevant details pertaining to the similitude scaling, specimen design, passive energy dissipation devices, excitation, and instrumentation is discussed. Specimen design uses concepts presented in Sections 3 and 4.

The results of testing are presented in Section 6. The analytical tools (FEA and simplified analysis method) and developed design equations are evaluated through comparison with the experimental results in terms of key peak response quantities and response history traces (in the case of FEA).

Finally, a summary, conclusions, and recommendations for further research for controlled rocking of structures are provided in Section 7.

SECTION 2

BACKGROUND

2.1 General

Steel truss bridge piers supporting a slab-on-girder or truss bridge exist in nearly every region of the U.S. Lateral load resisting pier elements consisting of built-up lattice type members with riveted connections were prevalent at the time of construction of many of these bridges. These built-up lattice type members can suffer global and local buckling (figure 2-1) resulting in loss of pier lateral strength and major structural damage during an earthquake (Lee and Bruneau, 2004). Another possible non-ductile failure location is the anchorage connection at the pier-to-foundation interface. While strengthening these existing vulnerable elements to resist seismic demands elastically is an option, this method can be expensive and also gives no assurance of performance beyond the elastic limit. Therefore it is desirable to have structures able to deform inelastically, limiting damage to easily replaceable ductile structural "fuses", able to produce stable hysteretic behavior while protecting existing non-ductile elements. Retrofit strategies that include increasing the strength and/or ductility of existing pier members through repair or replacement were investigated by Berman and Bruneau (2005). Ideally, it would also be desirable to prevent residual inelastic deformations and have structural systems that can be self-centering following an earthquake.

Releasing of the pier-to-foundation anchorage connections' tensile capacity (or allowing them to fail) would allow a steel truss pier to rock on its foundation, effectively increasing

| (a) | (b) |
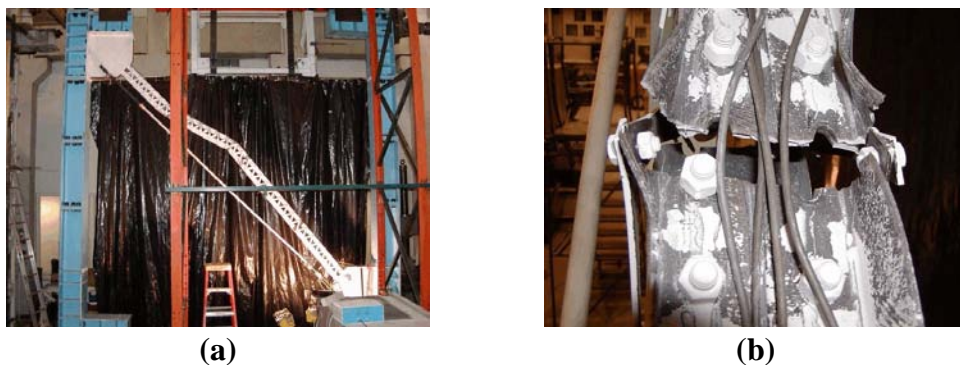
FIGURE 2-1   Specimen By16-120 (Lee and Bruneau, 2004) (a) Buckled Shape and (b) Final Fracture of Member

7

its period of vibration and partially isolating the pier. Such a connection would need to resist translation (sliding) in the two horizontal directions but should allow vertical translation (uplift) from the support. A base connection was designed and implemented as part of the experimental testing program (Section 5.4.1) that developed the necessary boundary conditions and is simple and practical. Adding passive energy dissipation devices at the uplifting location would restrain the uplift displacements while providing additional energy dissipation. This retrofit strategy also is advantageous because the location of the pier anchorage tends to be easily accessible compared to other parts of the bridge. A sketch of a controlled rocking bridge pier is shown in figure 2-2. The rocking system described has
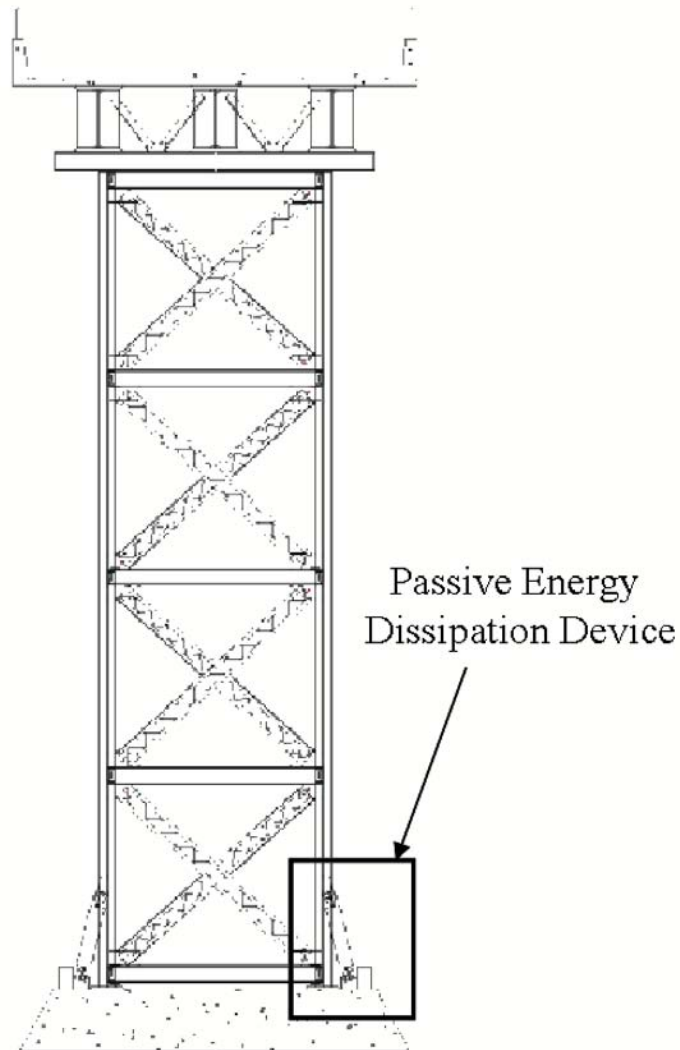
FIGURE 2-2 Sketch of Controlled Rocking Bridge Pier

an inherent restoring force, capable of allowing for automatic re-centering of the tower, leaving the bridge with no residual displacements after an earthquake. The connection at the base of the pier legs to their supports is critically important in developing the boundary conditions that allow the rocking response.

Background information relevant to the continued development of this controlled rocking approach for the seismic protection of bridge steel truss piers is discussed in this section. A review of prior research pertaining to rocking structures, post-tensioned self-centering systems (that exhibit similar behavior to rocking systems), and passive energy dissipation devices is provided in Sections 2.2, 2.3, and 2.4 respectively. A few bridges have been designed or retrofitted using a rocking approach for seismic resistance and are discussed in Section 2.5. Section 2.6 provides necessary information and discussion of concepts developed previously as part of this research project. A simplified method of analysis, used for the prediction of maximum displacements of controlled rocking piers, is presented in Section 2.7 since it is used extensively throughout this report. Finally, the properties of a set of steel truss bridge piers deemed representative of piers in use today are presented in Section 2.8. These properties are used to illustrate or verify concepts later developed.

2.2 Prior Research on Rocking Structures

Evidence of rocking of structures has been observed following major earthquakes and used to explain how very slender and relatively unstable structures may have been able to survive strong earthquakes (Housner, 1963). The study of rocking structures possibly started with investigation of the free-vibration response of rigid rocking blocks, and their response to some simple forms of dynamic loading (such as rectangular and sinusoidal impulses), as well as to earthquake excitations. An expression for an amplitude dependent period of vibration during rocking and a method to determine the amount of kinetic energy lost upon impact (occurring in each half-cycle) was developed assuming an inelastic collision to occur upon impact. Housner (1963) concluded that "the stability of a tall slender block subjected to earthquake motion is much greater than would be inferred from its stability against a constant horizontal force".

From that point some analytical and experimental work was done to predict the response of rocking structures to earthquake motions. Many investigated the response of rigid blocks with emphasis on preventing overturning. Meek (1978) first introduced aspects of structural flexibility to the seismic response of single-degree-of-freedom rocking structures. Psycharis (1982) followed with an analytical study of the dynamic behavior of simplified multi-degree-of-freedom (MDOF) structures supported on flexible foundations free to uplift. Two spring foundations and the Winkler foundation model were both used to study the rocking of rigid blocks, and only the two spring foundation model was used to study MDOF flexible structures. Three different mechanisms were considered to introduce energy dissipation into the foundation attributed to soil radiation damping upon the assumed inelastic impact that occurs during each half-cycle. The energy dissipation mechanisms included spring-dashpot and elastic-plastic spring systems. It was noted that vertical oscillations were introduced to this uplifting system when subjected solely to horizontal excitation. Observations on the benefits of allowing uplifting to occur (opposed to a fixed-base structure) were not conclusive in terms of displacements and stresses, as response varied significantly depending on system parameters and the characteristics of the ground excitations.

Shake-table testing of a rocking frame with energy dissipating devices introduced at the uplift location was performed by Kelley and Tsztoo (1977). An approximately half-scale 3-story steel frame was designed (figure 2-3a), with restraints provided to prevent horizontal movement, and mild steel, torsionally yielding bars used as energy dissipating devices at the uplifting location (figure 2-3b). The test results indicated that the rocking concept with energy dissipating devices provided beneficial response, in terms of base shear, to the same frame with a fixed base, thus preventing uplift.

Priestley et. al. (1978) recognized that following the New Zealand seismic design requirements for buildings at the time would indirectly result in allowing rocking of part or all of some structures during an earthquake. However, rather than characterizing this as an unsafe condition, they recognized this could be advantageous in some instances. In order to

10
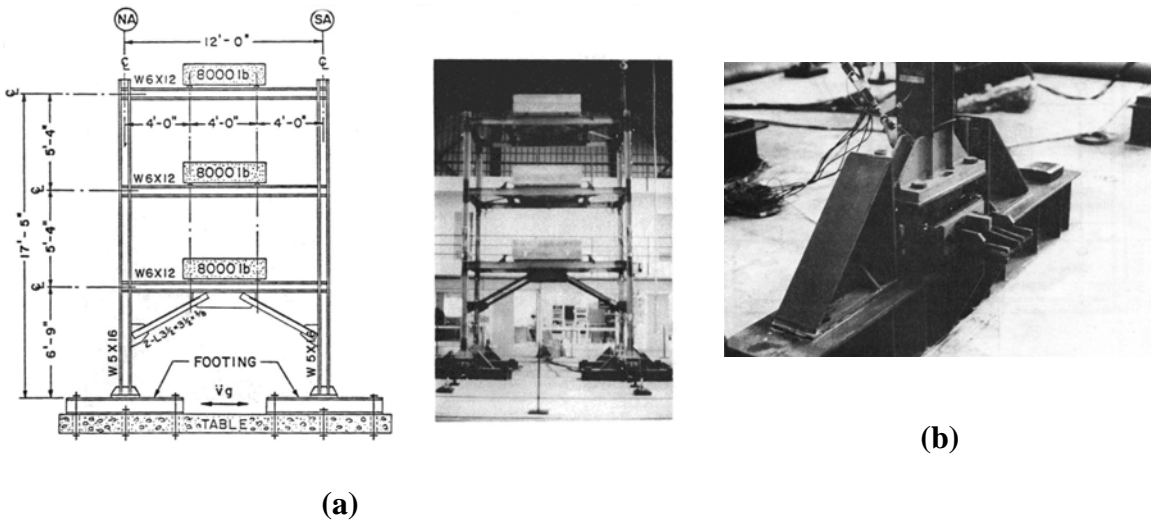
FIGURE 2-3   Uplifting Frame Tested by Kelley and Tsztoo (1997) (a) Elevation View of Steel Frame Specimen and (b) Steel Torsional Yielding Device Introduced at Base of Column

prevent excessive secondary structural damage caused by large rocking displacements, a simple method to predict the maximum displacement of the rocking response during earthquakes was developed. Using the work of Housner (1963), a response spectra design approach was used by transforming the rocking system into an equivalent SDOF linear viscous oscillator. The only energy dissipation in the structural system was assumed to be provided by the inelastic collisions occurring upon each impact. The simple SDOF model tested was subjected to free-vibration response, sinusoidal excitations, and the 1940 –S El Centro record. Results verified Housner's theory on the amplitude dependent frequency assuming inelastic collisions, and the simple method developed by Priestley et. al. (1978) predicted the maximum displacements with reasonable accuracy, especially for design purposes. It was noted during testing that no significant rebound occurred after impact, that large vertical accelerations were induced during impact, and that placing rubber pads underneath the impacting legs to represent a flexible foundation decreased the vertical accelerations significantly.

Roh and Reinhorn (2006) investigated the behavior of rocking concrete columns for buildings that were utilized as part of a weakening and damping strategy for seismic design. The lateral force and deformation behavior was developed from the initial (elastic) response

through the phases of cracking, yielding, crushing, and then rocking. Of particular interest was the stress distribution at the ends of the columns which significantly affect the flexibility of the column and thus the lateral (global) force deformation behavior of the column. The theoretically derived behavior was shown to be in very good agreement with advanced nonlinear finite element analysis.

Toranzo et. al. (2001) proposed a rocking wall system for buildings. Steel flexural yielding elements were placed at the uplifting locations to increase lateral strength and provide hysteretic energy dissipation. With the interest of providing a framework for design, a method for determining the maximum expected displacements was proposed based on the Direct Displacement Method (Priestley and Kowalsky, 2000). Testing of the rocking wall was performed using a uni-axial shake table. A picture of the rocking wall specimen tested, along with the hysteretic energy dissipating devices, is shown in figure 2-4.

FIGURE 2-4   Rocking Wall Specimen with Flexural Steel Yielding Devices at Uplifting Location (Toranzo et. al., 2001)

Midorikawa et. al. (2003) experimentally examined the response of a steel braced frame (figure 2-5a) allowing uplift at the base of columns and yielding of specially designed base plates (figure 2-5b). A 3-story, 2-bay braced frame was subjected to shake table tests using the 1940 El Centro motion, applied in a single horizontal direction. Tests were performed with plate details providing different levels of uplifting strength including a fixed-base case for comparison. It was found that the uplifting base plate yielding system effectively reduced the seismic response of building structures and that the base plates were able to provide
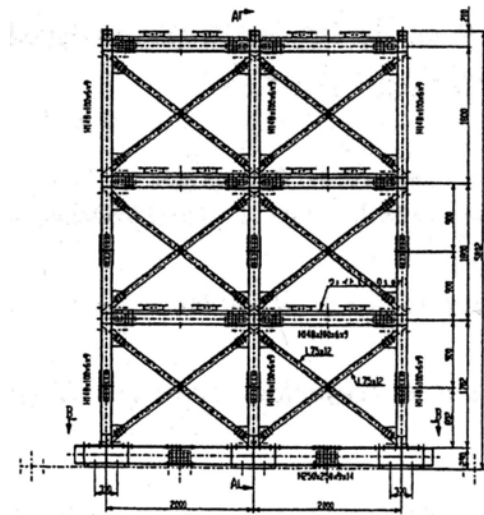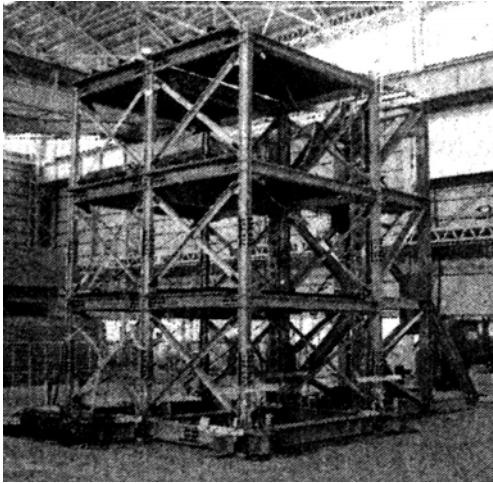
(a)
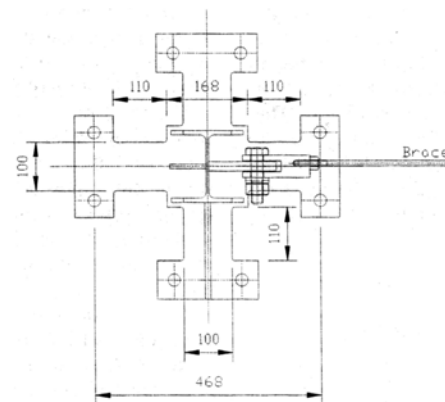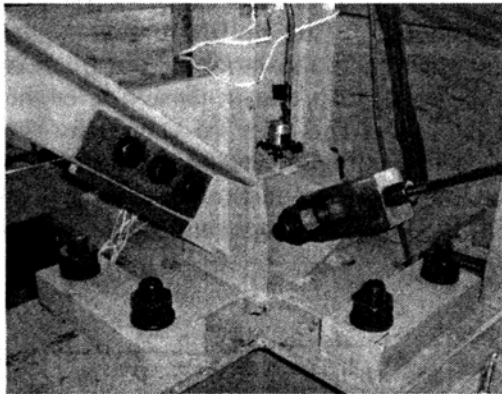
(b)

FIGURE 2-5   Uplifting Braced Frame Tested by Midorikawa et. al. (2003) (a) Frame and (b) Specially Detailed Yielding Base Plate

reliable performance for the uplifting displacements while transferring shear forces. The axial forces observed in the columns during rocking may have been affected by the impacts caused during rocking.

Makris and Konstantinidis (2002) examined the fundamental differences between the response of a SDOF oscillator and the rocking response of a slender rigid block (inverted pendulum structure) and introduced the concept of a rocking spectrum. The rocking spectrum consists of rotation and angular velocity spectra as a function of a "period" defined by:

$$T = \frac{2\pi}{p} = \frac{2\pi}{\sqrt{\dfrac{3g}{4R}}} \tag{2-1}$$

where

$$R = \sqrt{b^2 + h^2} \tag{2-2}$$

where 2b and 2h are the block width and height respectively. The rocking spectrum is generated, assuming no sliding of the block such that only rocking response occurs, by solution of the following nonlinear equation of motion representing the rocking motion under a horizontal ground acceleration:

$$\ddot{\theta}(t) = -p^2 \left[\sin(\alpha \, sgn[\theta(t)]) - \theta(t) \right] + \frac{\ddot{u}_g}{g} \cos(\alpha \, sgn[\theta(t)] - \theta(t)) \tag{2-3}$$

It was found that the rocking spectrum exhibits "noticeable order" until displacements that nearly cause overturning are reached. It was also reported that methods of predicting displacements of rocking blocks using typical response spectrum, such as the method used in Priestley et. al. (1978), may provide acceptable results in some cases, but that there are kinematic characteristics of the rocking system that cannot be reflected in the response spectrum.

More recently, Konstantinidis and Makris (2005) have numerically investigated the seismic response of multi-drum classical columns typical of those found in temples from ancient Greece such as the at the Temple of Zeus at Nemea (figure 2-6). It was found that sliding of each drum was possible even at horizontal force levels lower than the coulomb friction

FIGURE 2-6   Multi-drum Columns Under Repair at Temple of Zeus at Nemea

force due to the impact that occurs during the rocking response. Also, no correlation was found between the peak acceleration of the excitation and peak rotation of the columns however a strong connection was found between the peak rotation and a "length-scale" factor, L_p (Makris and Black, 2004), that is the product of the excitation's dominant pulse period (T_p) and velocity amplitude (v_p).

2.3   Research on Post-tensioned, Self-centering Systems

Exhibiting very similar behavior to the rocking structures discussed in Section 2.2 are post-tensioned (a.k.a. hybrid) structures. Instead of (or in addition to) the restoring force provided by the gravitational weight of the structure, post-tensioning strands can be introduced into the structural framing that provides a significant restoring force that can possibly re-center the structure. The technique of unbonded, post-tensioning of columns, beams, or walls for the seismic resistance of structures has been of considerable interest over the past 15 years and some examples are discussed here.

Stone et. al. (1995) investigated the use of post-tensioned precast concrete beam-column connections and mild steel. Quasi-static testing of ten hybrid connection sub-assemblages was performed and the connections were shown to meet or exceed the performance of

15

conventional monolithic connections in terms of energy dissipation, strength, and drift capacity.

Mander and Cheng (1997) proposed rocking concrete bridge columns as a seismic resistant system consistent with a proposed design methodology called Damage Avoidance Design (DAD). In this concept, each bridge column was allowed to rock individually by making the rebar discontinuous at the column ends thus allowing rocking at the column/cap beam and column/foundation beam interfaces. The columns were subsequently designed as pre-cast elements, post-tensioned vertically to increase and control the lateral strength. A sketch of a deformed bridge pier with the rocking column concept is shown in figure 2-7a. The kinematics of the rocking behavior and force-displacement relationship were established for the rocking columns. The primary energy dissipating mechanism for the system is the lost energy upon impact. A method of converting the lost energy into equivalent viscous damping was established following the assumptions of Housner (1963). In some cases, yielding of the pre-stressing tendons was allowed for increased energy dissipation. Static testing was performed to verify the force-displacement behavior and the effect of the pre-stressing tendons. Shake table testing was also performed (for the specimen shown in figure 2-7b) to verify the concepts presented, along with the simplified design procedure.

(a) (b)
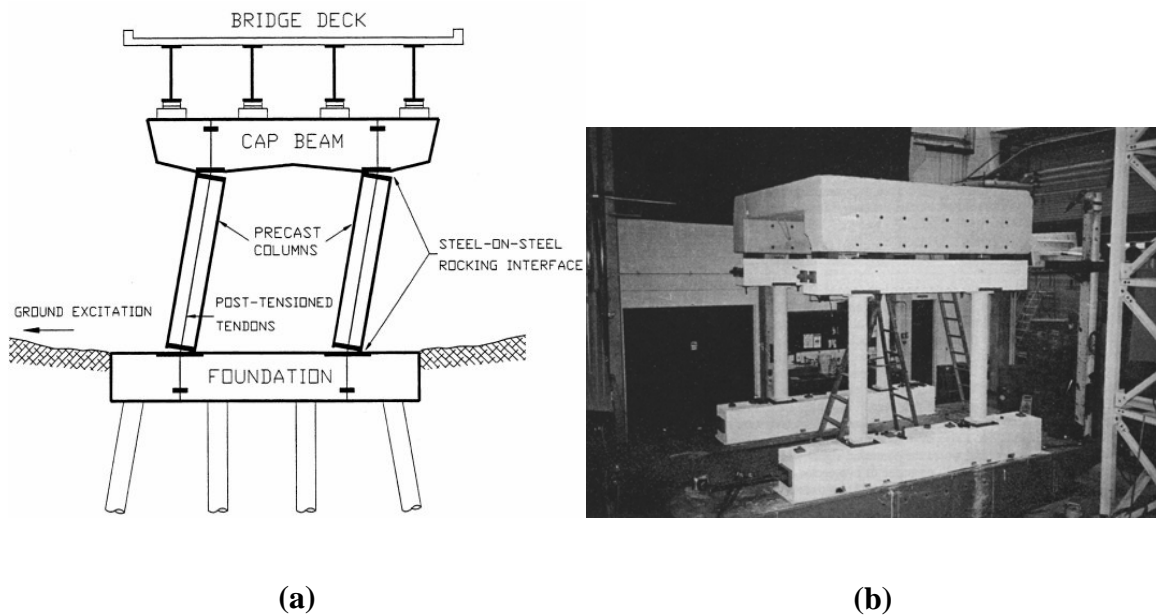
FIGURE 2-7   Rocking Column Concept of Mander and Cheng (1997) (a) Sketch and (b) Specimen Tested on Shake Table

16

Holden et. al. (2003) experimentally compared, using quasi-static testing, the performance of a half-scale, conventional ductile concrete wall with that of a post-tensioned precast concrete (hybrid) wall specimen with hysteretic energy dissipation devices implemented at the base. While the conventional, code-compliant designed ductile wall exhibited very good hysteretic behavior up to drift levels of 2.5%, it incurred significant damage and would have likely been left with a large residual displacement following a seismic event. The hybrid specimen, which required significantly less steel reinforcement due to the force limiting mechanism (base overturning moment), had only minor cracking at the corners of the wall and provided self-centering of the wall.

Perez et. al. (2004) proposed the use of post-tensioned, precast concrete walls (2 or more in the same plane) with ductile shear yielding devices implemented vertically between the two walls to provide energy dissipation to the system. Parametric analytical studies were performed to verify theoretically derived behavior and a proposed design procedure. Key design parameters were identified and recommendations were provided for varying these parameters to meet performance objectives.

Palermo et. al. (2005) has proposed the use of a hybrid system for concrete bridge piers that uses vertical post-tensioning of the concrete bridge columns and different forms of energy dissipation devices (hysteretic, friction, and visco-elastic), as shown in figure 2-8.
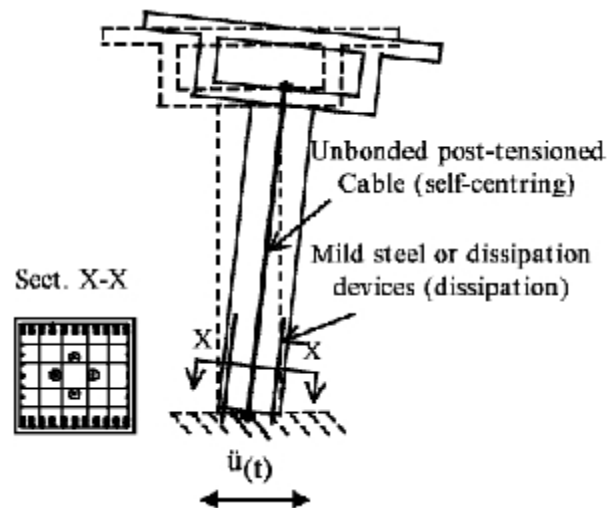
FIGURE 2-8   Hybrid Concrete Bridge Column (Palermo et. al., 2005)

A displacement based approach is discussed for the design of both bridge piers and/or bridge systems. Following on this work, Marriott et. al. (2006) experimentally and analytically investigated these hybrid connections for the seismic resistance of concrete bridges. Quasi-static and pseudo-dynamic testing confirmed the desired performance of the connection that included no "physical" damage and the self-centering ability.

Ricles et. al. (2001) proposed the use of post-tensioned connections for steel frames. The post-tensioning strands were implemented along the length of steel beams and attached at the column flange, clamping the beam ends to the column flange. Angle members were bolted to the beam flange and column flange such that under lateral loading of the frame and following opening of the gap at the beam-column interface, the angle member would yield in flexure. A typical exterior connection is shown in figure 2-9. An analytical model was developed using fiber elements and calibrated based on the results of quasi-static sub-assemblage testing of a connection. Dynamic, time history analyses of a 6-story steel building showed that the steel frames with these types of post-tensioned connections exceeded the performance of a moment-resisting frame with typical welded connections.
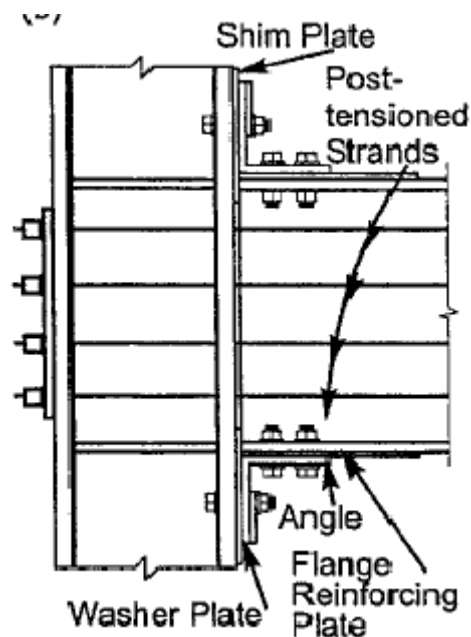
FIGURE 2-9   Post-tensioned Steel Moment-frame Connection with Top and Bottom Angles (Ricles et. al., 2001)

Christopoulos et. al. (2002a) proposed the use of a post-tensioned connection similar to that of Ricles et. al. (2001). Energy dissipating bars that yield in tension and compression are attached to the beam flanges and column. Subjected to lateral loads, the gaps open at the beam-to-column interface activating the energy dissipating bars, as shown in figure 2-10. The hysteretic behavior of the system exhibits a "flag-shaped" response. This flag-shaped hysteretic behavior was investigated numerically by Christopoulos et. al. (2002b). Parametric seismic analyses of SDOF flag-shaped hysteretic systems showed that a flag-shaped system of equal or lesser strength could match or enhance the response of an elasto-plastic (SDOF) system in terms of displacement ductility (while also being able to self-center).

2.4   Existing Rocking Bridges

A limited number of bridges currently exist in which rocking of the piers during earthquakes has been allowed to achieve satisfactory seismic resistance. The South Rangitikei Rail Bridge, located in Mangaweka, New Zealand (figure 2-11a) is such an example bridge, designed and constructed in the 1970's with pier legs allowed to uplift under seismic loads (Priestley et. al., 1996). With pier slenderness ratios of more than 5, large overturning moments would develop at the base of the pier. Allowing pier rocking, significantly reduced moments that needed to be resisted. Instead of allowing free uplift at the base of each pier leg, torsional steel yielding devices, shown in figure 2-11b, were added to control the amount
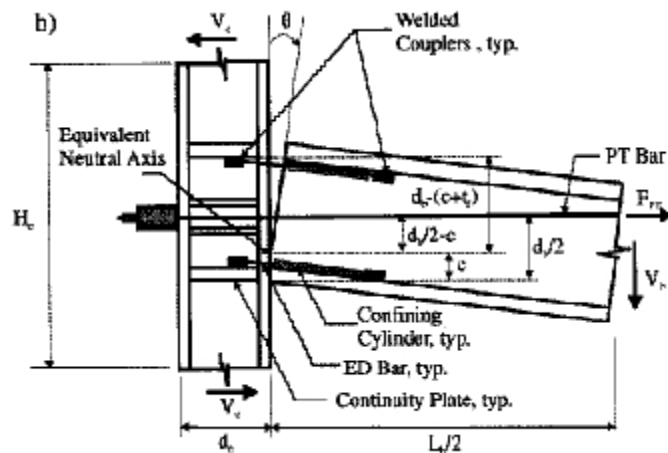
FIGURE 2-10   Post-tensioned Steel Moment-frame Connection with Energy Dissipating Bars (Christopoulos et. al., 2002)
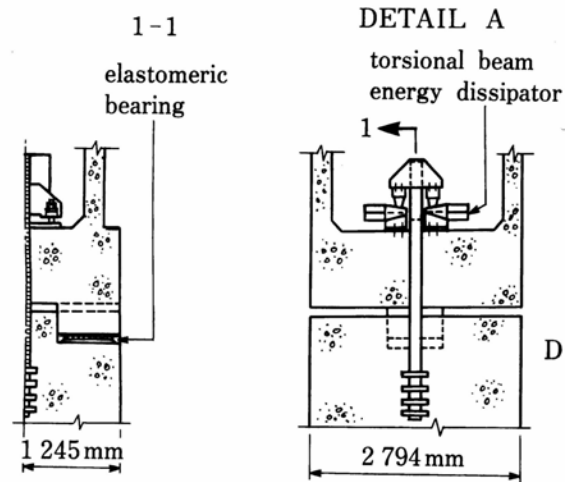
(a)   (b)

FIGURE 2-11   South Rangitikei Rail Bridge (Priestley et. al., 1996) (a) Pier and (b) Torsion Steel Yielding Device at Base of Pier Legs

of uplift while providing energy dissipation (damping). The amount of uplift was limited to 125mm by stopping mechanisms.

The North Approach of the Lions' Gate Bridge, located in Vancouver, British Columbia was seismically upgraded during the 1990's (Dowdell and Hamersley, 2000).   The North Approach Viaduct consists of 25 composite plate girder spans with span lengths ranging from about 25-38 meters (figure 2-12a). Early investigations revealed that many piers would develop large uplifting forces at the foundation. Advantages of using a rocking strategy for seismic retrofit provided a force limiting mechanism, while concentrating retrofit work at the tower bases (a more easily accessible location compared to other parts of the structure).

(a)

(b)

FIGURE 2-12   Lions' Gate Bridge North Approach Viaduct (Dowdell and Hamersley, 2000) (a) Steel, V-braced Piers and (b) Flexural Steel Yielding Devices Implemented at Uplifting Location

Some concerns arose due to the effects of dynamic impacting of a pier leg with the foundation and coupling of vertical and horizontal modes during rocking. Implementation details for the rocking system included removing the nuts of the existing anchor bolts to allow uplift without damage, tying individual foundation pedestals together with tie beams to prevent differential settlement, driving piles through liquefiable soil layers, providing longitudinal and transverse restrainers at deck-level and installing lead core rubber bearings at the abutment. Also, the capacity of some pier diagonals and columns were increased by bolting additional material to the member to increase their elastic buckling capacity. Flexural yielding steel devices (figure 2-12b) were placed at the anchorage interface to provide hysteretic damping and limit the uplifting displacements. Recognizing the increased dynamic force effects resulting from the rocking response, the engineers utilized a 3-dimensional nonlinear dynamic time history model of the approach spans for prediction of maximum forces.

The benefits of allowing partial uplift of the legs of bridge piers has been also recognized by other practicing engineers and the idea has been adopted for the retrofit of some major steel bridges in California. The seismic vulnerability of the Carquinez Bridge was assessed in 1994 and it was determined that the bridge would require retrofitting to meet current seismic

resistance standards. As part of this work, the displacement capacity of the A-frame piers (figure 2-13a), which are expected to carry a significant portion of the seismic loads, was evaluated using nonlinear pushover analysis (Jones et. al., 1997). It was determined that the existing pier was unable to provide the necessary seismic performance for this important transportation link. Three seismic retrofit strategies were investigated which included; rocking of the frames on the concrete foundations, base isolation with friction pendulum bearings, and using viscous dampers in the steel towers. Base isolation and viscous dampers provided a beneficial response, but member and connection retrofit would still have been necessary in both cases and the high costs associated with both of these systems was unattractive. The final retrofit solution was to allow limited rocking of the A-frame towers. A transfer girder, shear keys, restraining beams and elastomeric bearing pads were placed below the tower columns. A schematic of the base connection is shown in figure 2-13b. The restraining beams are allowed to yield during an earthquake, providing energy dissipation, while the elastomeric bearing pads are expected to partially absorb impacts during rocking.
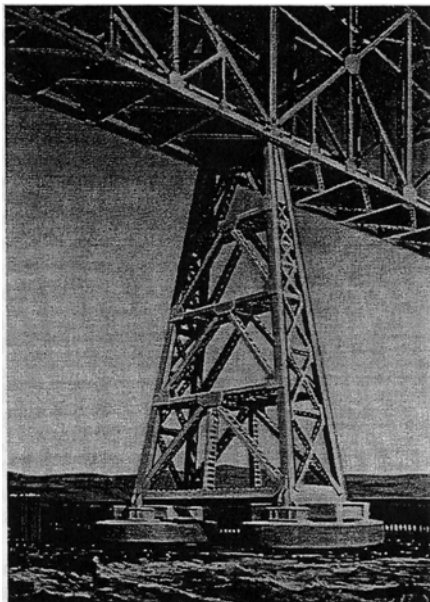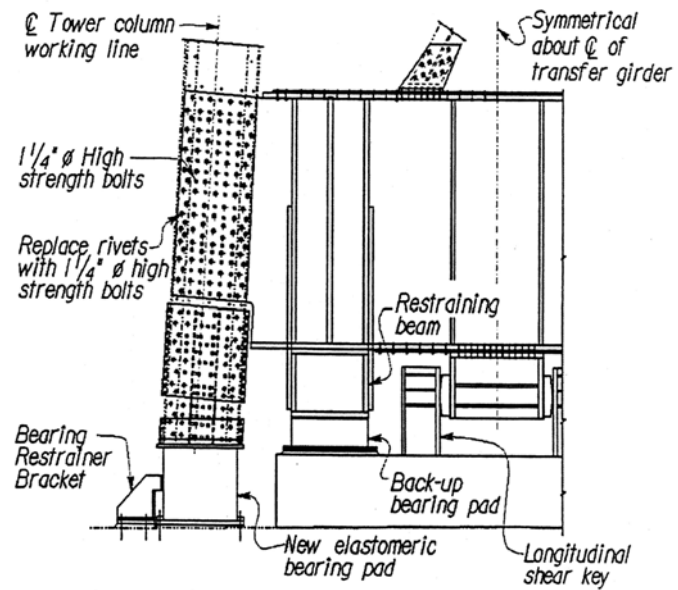
(a)   (b)

FIGURE 2-13   Carquinez Bridge, California (Jones et. al., 1997) (a) A-frame Pier and (b) Uplifting Restraining System Used

The Golden Gate Bridge, completed in 1937, began a seismic retrofit program in the 1990's following the 1989 Loma Prieta earthquake (Ingham et. al., 1997). While the Golden Gate Bridge was not damaged during the earthquake, the San Francisco Bay Bridge was closed for one month due to damage, causing huge economic losses thus prompting a seismic evaluation of all major crossings in California, including the Golden Gate Bridge. The retrofit solution for the bridge's main towers allowed each tower leg to uplift from the foundation by about 2.3 inches, which substantially reduced tower leg stresses compared to the fixed-base alternative. Finite element analysis was used to investigate the nonlinear deformation behavior of the tower leg's multi-cellular riveted steel construction. A picture of the model is shown in figure 2-14. The uplifting caused large axial compressive stresses to develop at the base of the tower legs upon impact requiring the significant stiffening within the multi-cellular construction of the tower leg. Also, the lack of edge distance from the compressive zone of the tower leg to the foundation pedestal's edge required the installation of post-tensioned, high-strength threaded bars through the concrete pedestals to provide confinement and increase the shear resistance near the pedestal edge.

Another major California toll bridge that underwent major rehabilitation following the Loma Prieta earthquake was the San Mateo-Hayward Bridge (Prucz et. al., 1997). The bridge is 7.1 miles long and has a 1.85 mile long main span supported on steel and concrete towers. The steel towers (shown in figure 2-15a) required an increase in overall ductility to satisfy performance objectives. To achieve the desired performance, modifications were made to the column base connections, the columns and the spandrel beams. The column base
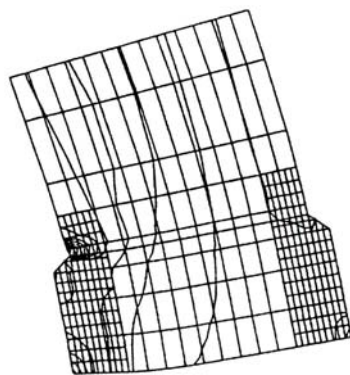
FIGURE 2-14 Uplifting at Base of Tower Leg of Golden Gate Bridge from Finite Element Model (Ingham et. al., 1997)

connections (shown in figure 2-15b) were modified to allow for each tower leg to rock and yield their anchor bolts during uplift. Steel sleeves were placed around the top of the anchor bolts that could resist compression following tensile yielding and was believed to improve cyclic behavior and reduce impact during the rocking motion. Modifications to the column base connections included adding anchor bolts between the existing anchor bolts to increase connection strength, ductility and redundancy. Also, steel pins were added at the column base to transfer the base shear and concrete was added inside the base of the column to increase the stability of its walls.

It is also worth noting that pier E17 of the San Francisco-Oakland Bay Bridge experienced rocking during the Loma Prieta earthquake (Housner, 1990). Pier E17 serves as an anchor pier for the bridge superstructure from pier E11 to pier E17. The concrete bent was not intended to rock however damage following the earthquake provided evidence that rocking of the concrete columns had occurred.

(a)   (b)
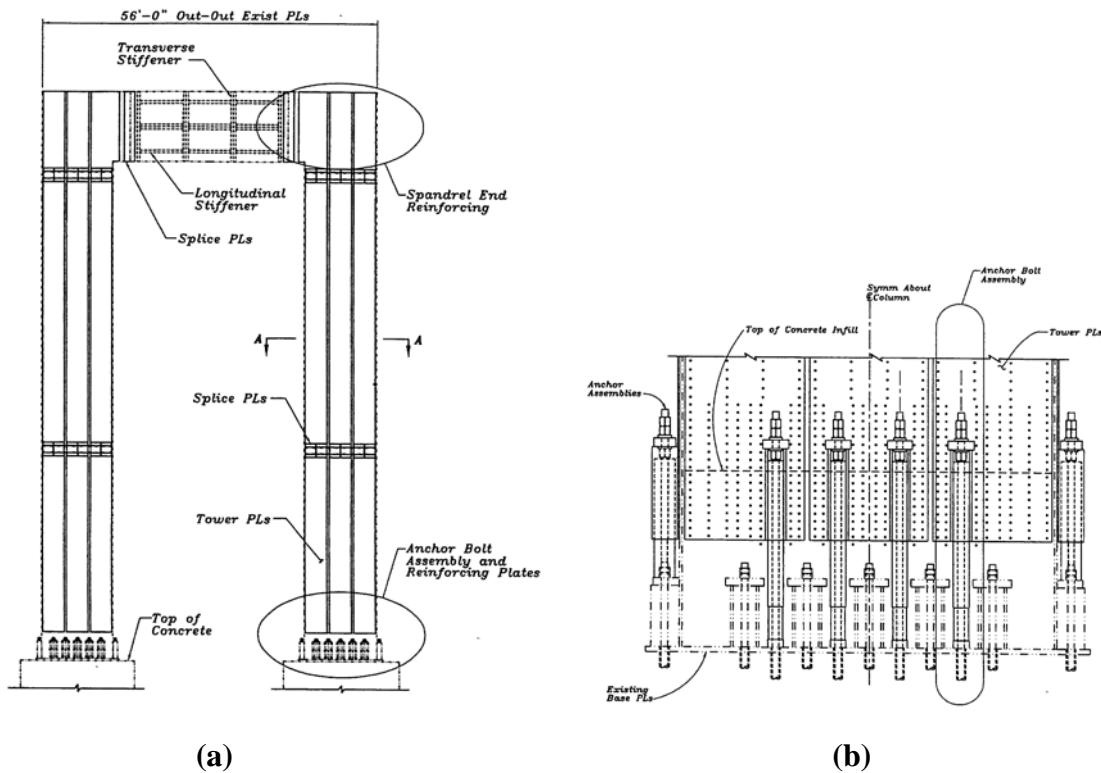
FIGURE 2-15   San Mateo-Hayward Bridge (a) Steel Tower and (b) Modified Anchorage Connection (Prucz et. al., 1997)

24

2.5 Prior Research on Passive Energy Dissipation Devices for Seismic Protection

2.5.1 Steel Yielding Devices

The seismic design of steel lateral force resisting systems, such as special concentrically braced frames (SCBF), eccentrically braced frames (EBF), and special moment resisting frames (SMRF) (AISC, 2005), rely on the inelastic deformations within the structural framing to dissipate seismic energy using capacity design principles. However, damage following an earthquake is expected that would require significant repairs and possible replacement of frame members. More recently, the use of sacrificial steel elements that absorb earthquake energy through non-recoverable plastic work have been used (or considered for use) as passive energy dissipation devices in both buildings (Soong and Spencer, 2002) and bridges (Zahrai and Bruneau, 1998). These steel yielding devices (a.k.a metallic dampers, hysteretic dampers) can be designed to limit or prevent damage to the primary framing system by acting as ductile structural "fuses" (Vargas, 2006). A review of a few such devices are discussed in the following sub-sections, although others exist.

2.5.1.1 Buckling-restrained Braces (BRB)

Buckling-restrained braces, also known as unbonded braces (type of BRB made by Nippon Steel Corporation of Japan), are an emerging seismic device providing, in some cases, supplemental strength, stiffness and energy dissipation to structures. The concept of the buckling-restrained brace behavior contrasts from that of a conventional brace in a significant way. A conventional bracing member subjected to axial loads is able to yield in tension, but typically exhibits global and/or local buckling under compression at a load less than the tensile yield force. Under some circumstances, the buckling of these members within a structural system can provide satisfactory seismic performance (AISC, 2005), even though buckling is not an ideal form of energy dissipation. A buckling-restrained brace is designed to instead allow the brace to reach full yield in tension and compression. It consists of a ductile steel core, carrying axial load, surrounded by a restraining part that prevents global buckling of the core. An "unbonding" material is placed between the steel core and restraining part to limit the shear transfer between the two components, accommodate the lateral expansion of the brace in compression due to the poisson effect, and to ensure that the buckling prevention component will not carry axial load (i.e. will not significantly increase

the strength of the brace). Figure 2-16 shows sketches of the primary components of a buckling-restrained brace.

Several different cross-sections of the steel core and restraining mechanisms have been investigated. Use of a cruciform or rectangular plate as the yielding steel core, wrapped in an unbonding material, and inserted in a rectangular or square HSS steel tube filled with mortar has been a popular configuration that has shown to develop stable hysteretic behavior. Sample specimen dimensions considered in past experimental studies with this type of configuration are shown in figure 2-17.

A number of researchers have investigated the behavior of BRBs. Watanabe et. al. (1988), Wada et. al. (1989) and Watanabe et. al. (1992) investigated the effect of the outer tube configuration, in particular the outer tube flexural capacity, on the performance of the brace. Hasegawa et. al. (1999) performed shake table testing of an unbonded brace subassemblage using the 1995 Kobe Marine Observatory Record and the 1940 El Centro record. The unbonded brace was subjected to a maximum axial strain of 7.2% in one of the tests and stable hysteretic behavior was reported throughout the testing. Iwata et. al. (2000) tested four braces with cross-sections shown in figure 2-18. Specimens 1 and 3 have a soft rubber sheet between the core and restraining part to act as the unbonding layer while specimens 2 and 4 only had a small clearance between the core and restraining part. Hysteretic behavior of the 4 specimens is shown in figure 2-19. It was found that each specimen behaved
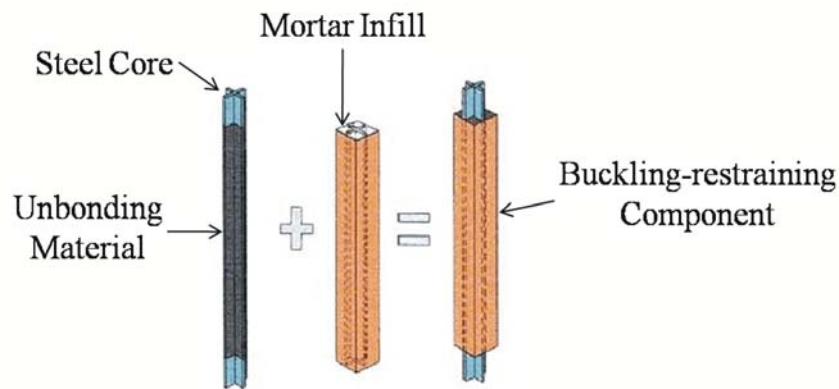
FIGURE 2-16   Primary Components of Buckling-restrained Brace

26
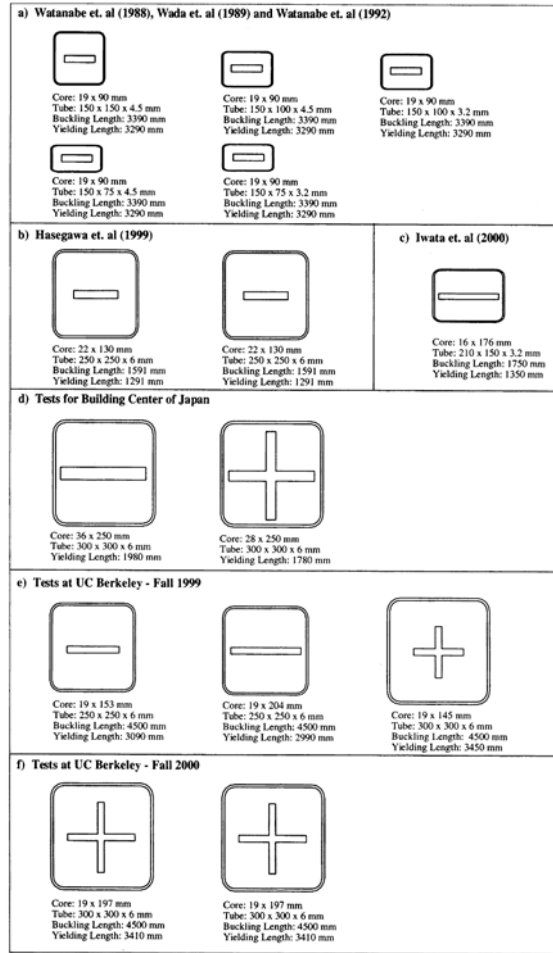
FIGURE 2-17   Experimentally Tested Cross-sections of Buckling-restrained Braces (Black et. al., 2002)
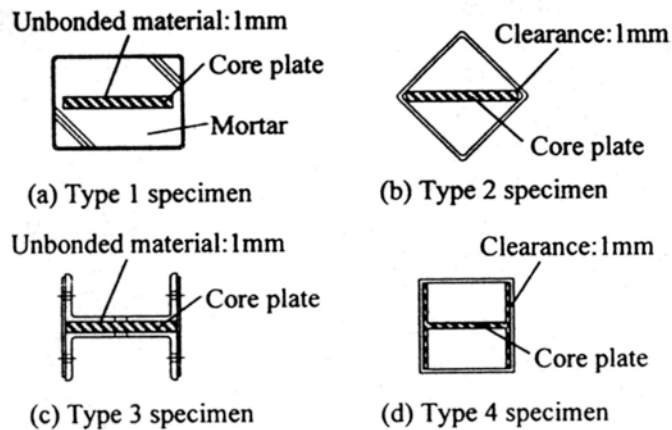
FIGURE 2-18   Cross-sections of Experimentally Tested Unbonded Braces by Iwata et. al. (2000)

27
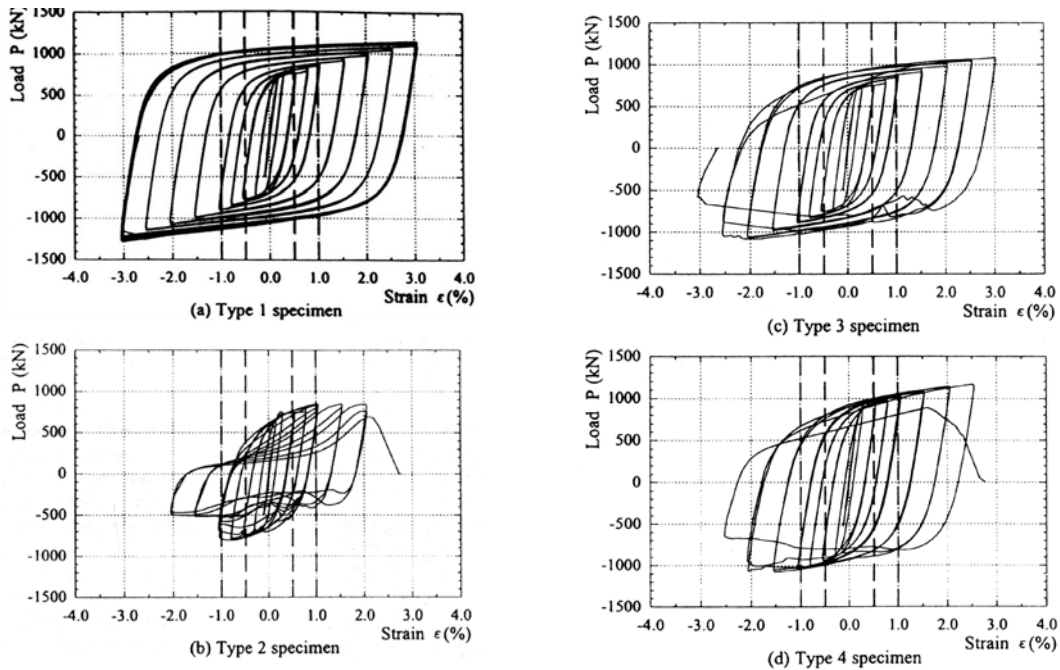
FIGURE 2-19 Hysteretic Response of Unbonded Braces Tested by Iwata et. al. (2000)

satisfactorily up to axial strains of 1% however at higher levels of strain the braces behaved differently. Rapid development of local buckling was observed in the specimens without the unbonding material, resulting in low cycle fatigue and eventual fracture. Black et. al. (2002) tested five specimens with properties representative of braces designed for implementation in two seismic retrofit projects in California. Loading protocols for the testing included the SAC basic loading history, SAC near-field, OSHPD loading history, low-cycle fatigue tests, and displacement histories derived from predicted building response for specific earthquake records. The tested braces exhibited ductile, stable and repeatable hysteretic behavior. A Bouc-Wen analytical brace model (Wen, 1976) was found to model the behavior of the braces "with fidelity".

2.5.1.2 Triangular Added Damping and Stiffness Device (TADAS)

The triangular added damping and stiffness device (TADAS) (shown in figure 2-20) consists of a number of triangular shaped steel plates that allow uniform yielding in flexure along the length of each plate. The device is implemented such that it is fixed at the wide end of the triangular plate and pinned at the tip of the plates such that the plates act as cantilever
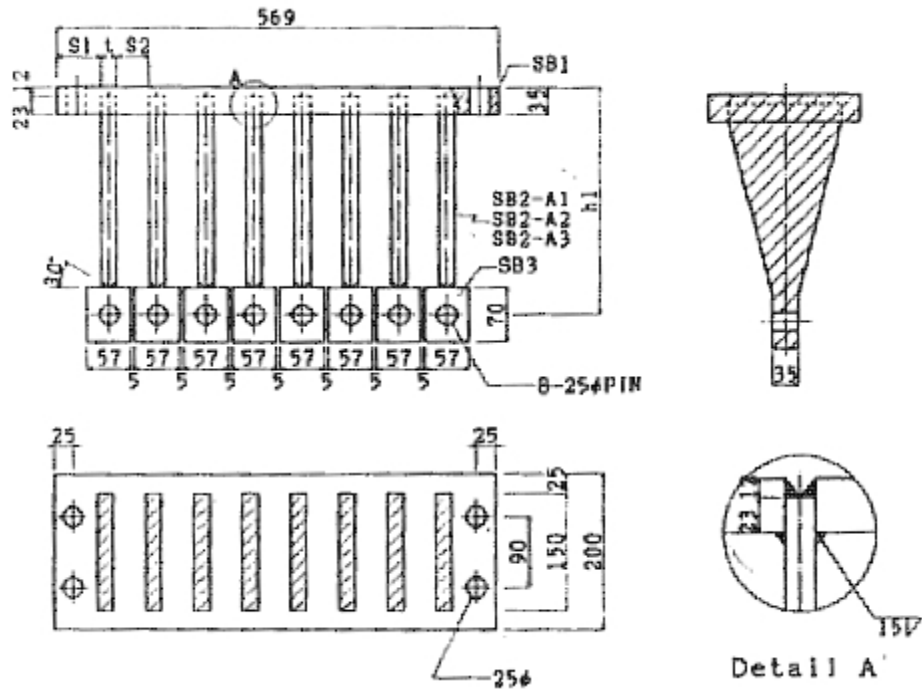
FIGURE 2-20   Sketch of TADAS Device (Tsai et. al., 1993)

members and deform in single curvature. The mechanical properties of the TADAS device and a design procedure was established by Tsai et. al. (1993). Tsai et. al. (1993) also performed quasi-static component tests of TADAS devices and pseudo-dynamic tests of a two-story frame with implemented TADAS devices. Testing revealed that the devices could exceed plastic rotations of 0.25rad. with no strength or stiffness degradation. However, the connections of the devices are critical to developing the desired hysteretic behavior and preventing significant secondary stiffening.

2.5.2   Fluid Viscous Dampers

The use of viscous damping devices in the seismic design of civil engineering structures is relatively new (15-20 years) however they have been used in military applications for many years (Constantinou and Symans, 1992). The fluid viscous damping device discussed here consists of a stainless steel piston rod with a specially shaped head and orifices that passes through an enclosed cylinder filled with a silicone oil. A sketch of the key components of this type of fluid viscous damper is shown in figure 2-21. The orifices and shaping of the piston head significantly affect the characteristics and output response of the device. Fluid
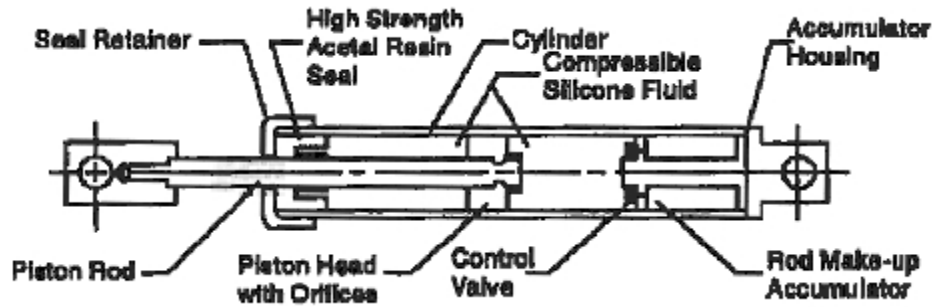
**FIGURE 2-21   Sketch of Internal Components of a Fluid Viscous Damper
(Constantinou et. al., 1998)**

viscous dampers manufactured by Taylor Devices, Inc. of North Tonawanda, NY have been extensively tested and have been implemented in numerous bridges and buildings worldwide (Constantinou et. al., 1998).

Analytical and experimental studies of buildings and bridges with fluid viscous dampers implemented was performed by (Constantinou and Symans, 1992). A number of other studies followed that have investigated the behavior of fluid viscous dampers and their influence on structural response (Reinhorn et. al., 1995; Seleemah and Constantinou, 1997). Also, procedures for the seismic design of structures with supplemental fluid viscous dampers have been proposed by Whittaker et. al. (1993) and Ramirez et. al. (2000). A set of recommended provisions for the seismic design of buildings or other structures with damping systems is provided in FEMA 450 (2004).

2.6   Developments on Controlled Rocking in Pollino (2004)

Relevant fundamental behavior of the controlled rocking approach, presented in Pollino (2004), is reviewed here in order to provide necessary information that will provide clarity in the further developments of this seismic protective approach discussed in this report. Included in this section is the development of the static cyclic hysteretic behavior using step-by-step plastic analysis concepts, a methodology to quantify the dynamic force effects that result from the impact and uplift that occurs during rocking response, and a simplified analysis method that can be used for design.

2.6.1 Static Hysteretic Behavior

The key parameters for the hysteretic response of the rocking bridge pier system considered here include the fixed-base lateral stiffness of the existing steel truss pier (k_o) and the height-to-width aspect ratio of the pier (h/d). The passive energy dissipation device considered is a steel yielding device that is assumed to exhibit elastic-perfectly plastic hysteretic behavior with a yield force, F_{yd}, and an elastic stiffness, k_d. Also, the weight excited by horizontally imposed accelerations (w_h) and the vertical gravity weight carried by a pier (w_v) are assumed equal here and expressed as w.

The simplified model used for static pushover analysis is shown in figure 2-22. The model considers motion of the pier in a direction orthogonal to the bridge deck and assumes there to be no interaction with other piers or abutments through the bridge deck. The various steps and physical behaviors that develop through a typical half-cycle are shown qualitatively in figure 2-23. By symmetry, the process repeats itself for movement in the other direction. Section 2.6.1.1 describes the pier response for the 1st cycle. Transition from 1st to 2nd cycle response occurs when the devices yield and the braces carry a portion of the weight after the
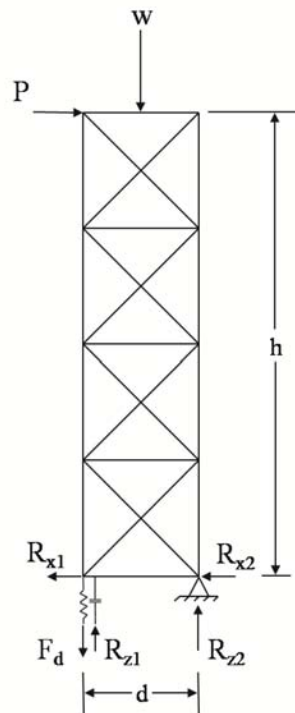
FIGURE 2-22 Model used for Static Pushover Analysis
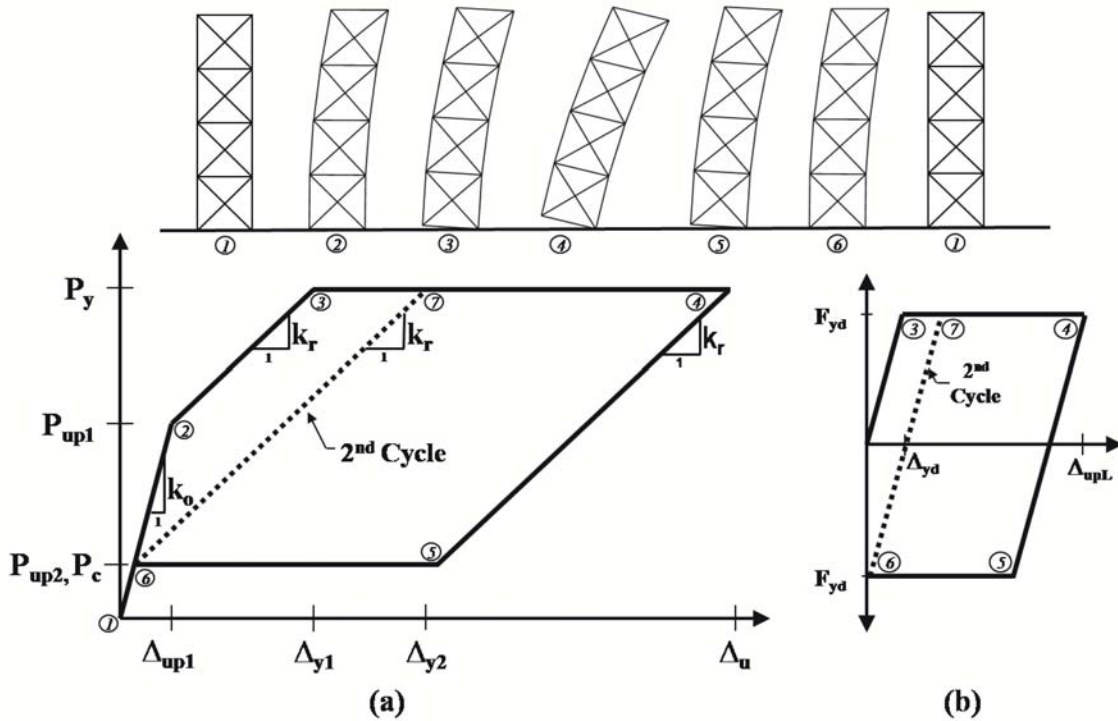
FIGURE 2-23 Cyclic Pushover Response of Rocking Bridge Pier. (a) Global Response and (b) Response of Steel Yielding Device

system comes to rest upon completion of the cycle (a phenomena to be explained later). Section 2.6.1.2 describes how this response differs for the 2nd and subsequent cycles. Section 2.6.1.3 discusses some implications of the rocking response on the post-yield stiffness of the controlled rocking bridge pier system.

2.6.1.1 1st Cycle Response

As the horizontal load applied at the top of the pier is increased, the initial lateral displacement at that location is entirely due to elastic deformations of the pier's structural members. The stiffness of the pier, k_o, is a function of its bending and shear flexibility (step 1 to 2 in figure 2-23). The horizontal force-displacement response at the top of the pier, until uplift begins, is defined by:

$$P = k_o \Delta_G \tag{2-4}$$

where Δ_G="global" horizontal displacement at the top of the pier and k_o is defined above. Uplifting of a tower leg begins when the restoring moment created by the tributary vertical

32

bridge weight is overcome by the applied moment (position 2 in figure 2-23). The horizontal force at the point of uplift is defined by:

$$P_{up1} = \frac{w}{2} \left(\frac{d}{h} \right)$$
(2-5)

where $d/_h$=inverse of the aspect ratio and w was defined previously. The displacement at the point of uplift in the 1st cycle response is defined by:

$$\Delta_{up1} = \frac{P_{up1}}{k_o}$$
(2-6)

The global stiffness is reduced after uplift as the flexibility includes deformations of the pier and base rotations as a tower leg begins to uplift. The horizontal pier stiffness is given by k_o. The base rotational stiffness can be projected to give its effect on the total horizontal flexibility and is controlled by the brace stiffness and the pier aspect ratio as:

$$k_b = k_d \left(\frac{d}{h} \right)^2$$
(2-7)

These deforming mechanisms act as two springs in series as the horizontal load is increased. Thus, the structural stiffness from uplift to the yield point (step 2 to 3 in figure 2-23) is defined here as the elastic rocking stiffness and is expressed by:

$$k_r = \left(\frac{1}{k_o} + \frac{1}{k_b} \right)^{-1} = \left[\frac{1}{k_o} + \frac{1}{k_d \left(\frac{d}{h} \right)^2} \right]^{-1}$$
(2-8)

The pier is then pushed until the device yields, which assumes the device to be the weak link along the lateral load path. The horizontal force at the onset of brace yielding, P_y, and thus the structural system yield strength is defined by:

$$P_y = \left(\frac{w}{2} + F_{yd} \right) \frac{d}{h}$$
(2-9)

The corresponding system yield displacement for the first cycle, $_{y1}$, is defined as:

$$\Delta_{y1} = \left(\frac{w}{2k_o} + \frac{F_{yd}}{k_r} \right) \frac{d}{h}$$
(2-10)

Ignoring strain hardening in the brace and a second order effect to be discussed in Section 2.6.1.3, the system has zero post-elastic stiffness and is deformed to its ultimate displacement

($\ddot{A}_u$). The ultimate displacement is dependent on the seismic demand and a method for calculating the ultimate displacement is discussed in Section 2.7.

As the horizontal load is reduced, the pier first responds elastically with stiffness k_r, the tensile force in the device also reduces per its initial elastic properties. A deformation in the device of 2 $_{yd}$, where $_{yd}$ is the yield displacement of the device equal to F_{yd}/k_d, is required for the device to reach its yield strength in the reverse direction which requires a deck-level displacement of $_{y1}$+ $_{yd}$(h/d) from the undeformed position. The applied lateral load at the top of the pier at the point of reverse yielding of the device, (point 5 in figure 2-23), is defined by:

$$P_c = \left(\frac{w}{2} - F_{yd} \right) \left(\frac{d}{h} \right)$$
(2-11)

The corresponding displacement at this point is defined as:

$$\Delta_c = \Delta_u - \frac{2\,F_{yd}\dfrac{d}{h}}{k_o} - 2\,\Delta_{yd}\frac{h}{d}$$
(2-12)

The device displaces plastically in compression and again is assumed to yield with no significant stiffness until the uplifted pier leg returns in contact to its support (step 5 to 6 in figure 2-23). At this point of contact, system stiffness is again defined by k_o.

It can be seen from (2-11) that if the device yield strength (F_{yd}) is greater than half of the bridge deck weight tributary to the pier ($^w/_2$) then the horizontal force required at yielding in the reverse direction is negative. Thus the restoring moment provided by the vertical tributary weight is not enough to yield the device upon unloading, leaving a pier leg slightly elevated above the foundation and not allowing for self-centering of the pier. By limiting the device strength to $^w/_2$, the plastic rotations accommodated at the pier base can be returned to the undeformed position leaving the pier with no residual deformations.   A local strength ratio, $_L$, is defined here as:

$$\eta_L = \frac{F_{yd}}{w/2}$$
(2-13)

Parameters that give $_L$ less than one allow for pier self-centering.

2.6.1.2 2nd Cycle Response

As a device yields in compression and the pier settles back to its support, the device effectively carries a portion of the bridge weight equal to its yield strength (assumed to be F_{yd}). The corresponding free-body diagram of a pier in an undeformed shape after the 1st cycle is shown in figure 2-24. As a result of this transfer of the gravity load path, a smaller horizontal force is required to initiate uplift causing an earlier transition from stiffness k_o to the rocking stiffness k_r thus increasing the flexibility and system yield point from the 1st cycle response as can be seen by the 2nd cycle curve in figure 2-23. The horizontal force at the onset of uplift can be shown equal to P_c (defined by 2-11) and is defined for the 2nd and subsequent cycles as:

$$P_{up2} = P_c = (1 - \eta_L)\frac{w}{2}\frac{d}{h} < P_{up1} \tag{2-14}$$

The corresponding displacement at the point of uplift in the 2nd and subsequent cycles is equal to:

$$\Delta_{up2} = \frac{P_{up2}}{k_o} < \Delta_{up1} \tag{2-15}$$
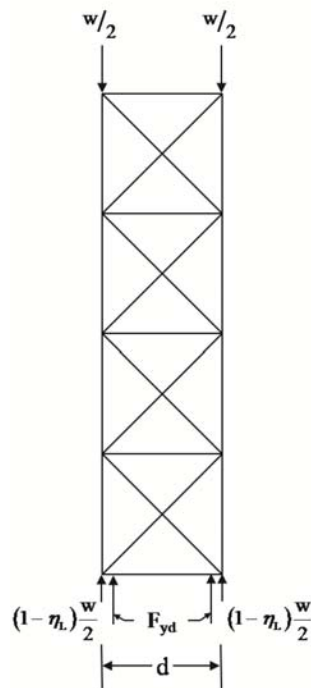
FIGURE 2-24   Free-Body Diagram of Pier, at Rest, after 1st Cycle

The yield displacement can be expressed as:

$$\Delta_{y2} = \frac{(1-\eta_L)\dfrac{w}{2}\dfrac{d}{h} + 2 F_{yd}\dfrac{d}{h}}{k_o} + \frac{2 F_{yd}\dfrac{d}{h}}{k_r} > \Delta_{y1} \qquad (2\text{-}16)$$

The yield strength of the system, P_y, is unchanged. The force in the device changes from its compressive strength (F_{yd}) to tension yielding (F_{yd}) for the 2nd and subsequent cycles that exceed deck level displacement of $_{y2}$. Hysteretic behavior in the 1st and subsequent cycles, for a given magnitude of inelastic deformation in the devices, are shown together on a single plot in figure 2-25. Note that the controlled rocking bridge pier considered develops a flag-shaped hysteresis. This is due to the combination of pure rocking response from the restoring moment, provided by the bridge deck weight, and energy dissipation provided by yielding of the devices.

2.6.1.3 Influence of Second Order Effects on Hysteretic Response

The proposed rocking bridge pier system has characteristics of both a linear-elastic oscillator and a rigid rocking system. The restoring force for the pier flexibility is provided by
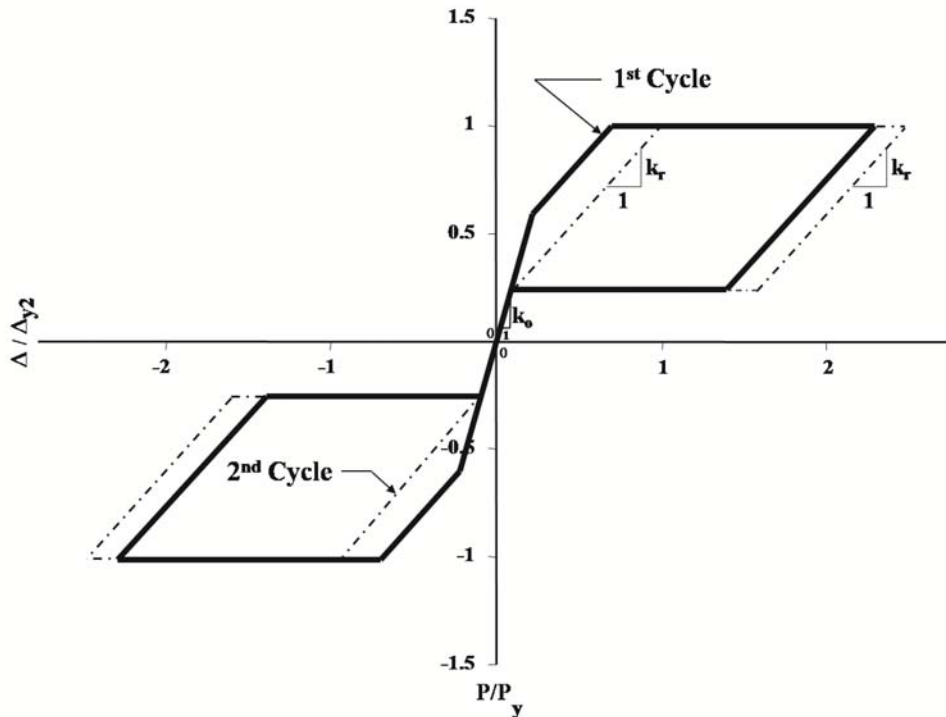
FIGURE 2-25 Hysteretic Behavior of 1st and 2nd Cycles

elasticity while the restoring moment, M_r, for base rocking is provided by gravity and equal to:

$$M_r = w\frac{d}{2}$$ (2-17)

As the center of mass displaces, the restoring moment provided by gravity is reduced. The reduction of the restoring moment is dependent on the ratio of the horizontal seismically induced displacement of the bridge deck to pier width (d) such that the restoring moment can be defined in terms of the induced displacement as:

$$M_r(\Delta_i) = w\left(\frac{d}{2} - \Delta_i\right)$$ (2-18)

This loss in restoring moment can be written in terms of the loss in horizontal base shear as:

$$P_r(\Delta_i) = \frac{w}{h}\left(\frac{d}{2} - \Delta_i\right) = \frac{w}{2}\frac{d}{h} - \frac{w}{h}\Delta_i = P_{up1} - \frac{w}{h}\Delta_i$$ (2-19)

Thus from (2-19) it can be seen that there effectively exists a negative stiffness of -w/h in the hysteretic response. The loss of restoring moment becomes more pronounced at larger displacements and is therefore examined further for the post-yield response. Considering this effect along with the strain hardening of the devices, in the form of a post-yield stiffness ratio ($_{syd}=k_h/k_d$), results in a global post-yield stiffness of:

$$k_{py} = \alpha_{syd} k_d \left(\frac{d}{h}\right)^2 - \frac{w}{d}\left(\frac{d}{h}\right)$$ (2-20)

where k_d is the initial, elastic stiffness of the device equal to:

$$k_d = \frac{F_{yd}}{\Delta_{yd}}$$ (2-21)

Therefore, under some circumstances the strain hardening of the devices can negate the effective negative stiffness due to the nonlinear geometric effect, thus resulting in a positive global post-yield stiffness, k_{py}.

For pier widths and aspect ratios considered herein (representing bridge piers), a modestly sized device can result in a positive global post-yield stiffness. However in some cases where the base width of a bridge pier is not of this magnitude, this effect may be more

critical. Due to the fact that the restoring moment is lost with increasing displacement, the self-centering ability is also affected.

2.6.2 Excitation of Vertical Modes During Rocking Response

Some of the past analytical and experimental studies investigating systems that allow a rocking response, discussed in Section 2.2, have observed an increase in demands beyond that explained through the static behavior as a result of impacting and uplift of the pier legs with the foundation. However, they have not provided significant insight into the possible mechanisms causing these additional demands. The passive energy dissipating devices (buckling-restrained braces, viscous dampers, etc.) can be calibrated to control the rocking response to within certain limits, however, as part of a capacity-based design philosophy, these additional demands must be accounted for in order to capacity protect the primary structural elements of the system during seismic excitation.

A methodology to quantify the dynamic force effects has been developed considering a simple steel bridge braced frame. However, the concepts presented are general and could be extended to include different materials and structural systems. The steel braced frame considered is illustrated in figure 2-26 and has a number of square panels (n_p) with a height (h) and a width ($d=h/n_p$) with the bracing members in a concentric X-configuration. The
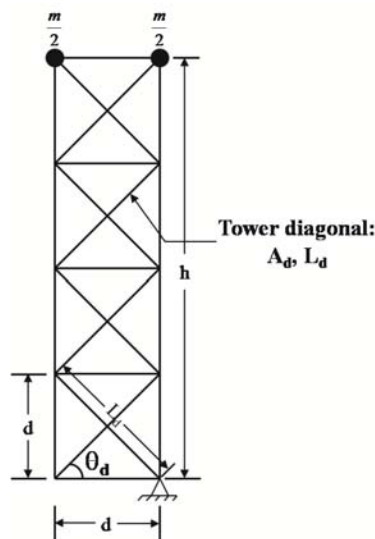
FIGURE 2-26   Representative Piers for Calculation of Vertical Stiffness of X-braced Piers

concept will be presented here for a controlled rocking pier with a steel yielding device that has the general properties discussed previously (F_{yd}, k_d, $_{yd}$).

2.6.2.1 Discussion of Dynamic Response of Controlled Rocking Frame

If the system is designed to allow for frame rocking and self-centering, then after a leg uplifts from the foundation, it eventually returns to its support with a certain velocity upon impact (position 2 in figure 2-27). Without a more sophisticated analysis of the impact that occurs between the frame leg and the foundation, an elastic impact is assumed to occur resulting in no loss of system energy thus providing an upper bound on the forces developed within the frame. As the frame leg begins the impacting process, the weight tributary to that leg is also suddenly (impulsively) returned to the impacting leg forcing the leg to remain in contact with the foundation. As the motion continues, the frame shifts its axis of rotation from the base
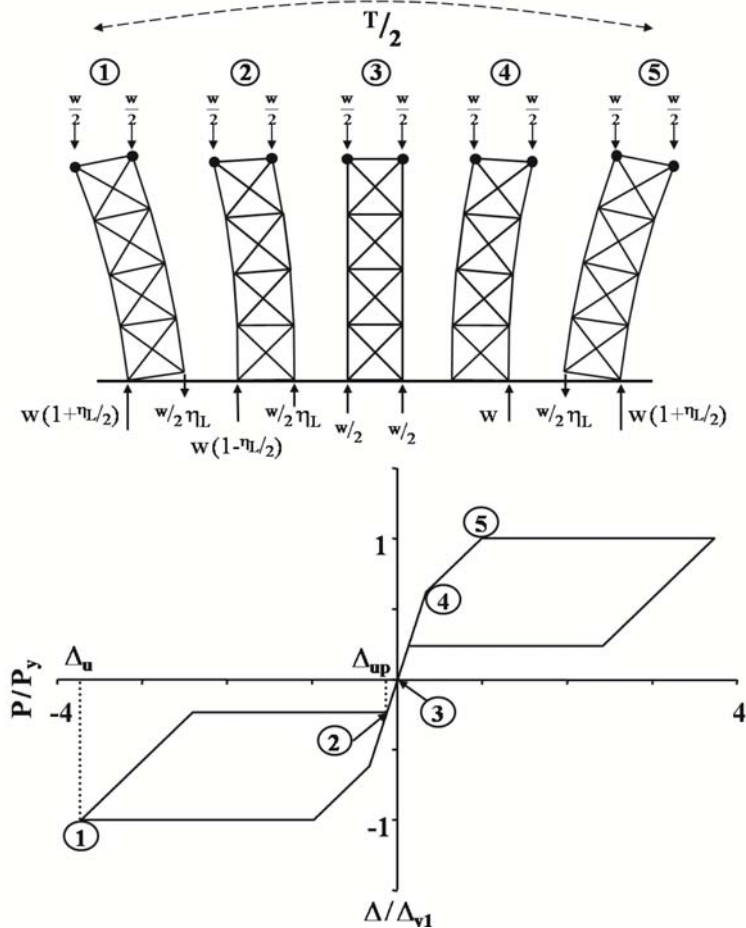
FIGURE 2-27   Static Free-Body Diagrams and Hysteretic Response of Frame through Half-cycle of Rocking Motion

of one leg to another and the weight and device forces are suddenly transferred through the frame vertically to the frame leg that is now being compressed. Beginning with the initial velocity upon impact and followed by the transfer of impulsive forces, a number of dynamic effects are occurring that need to be considered to capacity protect the frame. A fundamental structural dynamics approach is used here that identifies the vertical modes of vibration that are excited and calculates the response from each dynamic effect when the frame is subjected to horizontal excitation. As will be shown, the forces developed due to the vertical accelerations of the mass can be quite significant and need to be accounted for to achieve capacity protection of the frame.

2.6.2.2 Static Transfer of Vertical Loads

Before addressing the dynamic response of rocking steel braced frames, it is worthwhile to briefly review their static behavior. The transfer of loads statically through the braced frame during rocking response is described for a half-cycle of motion (shown in figure 2-27) starting from a displacement of $-\Delta_u$ (position 1 in figure 2-27), a point at which one side of the frame has uplifted from the foundation and yielded the steel device. The free body diagram of the frame in five different positions while rocking (assuming static response) from left to right, is also shown in figure 2-27. As the frame travels from position 1 to 2, the force in the steel device is reversed and the steel device yields until the uplifted leg returns to its support at position 2. In position 2, half of the weight, $^W/_2$, is being transferred directly down the left leg while a portion of the weight, $^W/_2(1-\alpha_L)$, is transferred through the frame diagonals also to this leg. From 2 to 3 the portion of the weight, $^W/_2(1-\alpha_L)$, is transferred to the impacting leg on the right. From 3 to 4 the frame begins to move in the other direction and the other half of the weight, $^W/_2$, is transferred to the leg on the compressive side through the diagonals. At position 4, the frame is on the verge of uplift and then from 4 to 5 the frame uplifts, activating the steel device until it reaches its yield force ($\alpha_L {}^W/_2$) at point 5. This force is transferred through the frame vertically to the compressive side.

2.6.2.3 Review of SDOF Linear Mass-Spring Systems Subjected to Impulsive Load

The response of simplified linear mass-spring systems subjected to a step force with finite rise time is first reviewed to provide the relevant theory to determine the dynamic amplification during the rocking response.

A general solution for the displacement response of a linear dynamic system, based on an impulse-momentum formulation, known as the convolution integral, can be found in Clough and Penzien (1975) expressed as:

$$u(t) = \int_0^t p(\tau)\, h(t-\tau)\, d\tau \tag{2-22}$$

where $p(\tau)d\tau$ is the magnitude of the impulse at time τ and $h(t-\tau)$ is defined as the unit impulse-response function. More specifically, the form of loading can be described as a step force with finite rise time (t_r) defined as:

$$p(t) = p_o \frac{t}{t_r} \quad (t \le t_r) \tag{2-23}$$

$$p(t) = p_o \quad (t \ge t_r)$$

The undamped displacement response for this type of loading (assuming zero initial conditions), for time greater than t_r, can be shown to equal:

$$u(t) = (u_{st})_o \left(1 - \frac{1}{\omega_n t_r} \left[\sin \omega_n t - \sin \omega_n (t - t_r) \right] \right) \tag{2-24}$$

where ω_n is the natural frequency of the mass-spring system, $(u_{st})_o$ is the static displacement response of the system subjected to the same maximum force, p_o, and is defined as:

$$(u_{st})_o = \frac{p_o}{k} \tag{2-25}$$

where k is the stiffness of the spring in the simple mass-spring system. A dynamic amplification factor, R_d, defined as the ratio of maximum displacement response over time, u_o (maximum of 2-24), to the static displacement response (2-25) can be shown to equal:

$$R_d = \frac{u_o}{(u_{st})_o} = 1 + \frac{\left| \sin\left(\dfrac{\pi t_r}{T_n}\right) \right|}{\dfrac{\pi t_r}{T_n}} \qquad (2\text{-}26)$$

Therefore the dynamic amplification factor is dependent only on the rise time of the applied load (t_r) and natural period of the mass-spring system (T_n). These values will be determined in the next section. Since the system is linear, forces are directly proportional to deformation thus R_d also defines the ratio of maximum force response to the static force response. In other words, the maximum force can be determined by amplifying the static force by R_d.

If the same linear mass-spring system were subjected solely to an initial velocity, v_o, the time varying displacement response could simply be defined as:

$$u(t) = \frac{T_n v_o}{2\pi} \sin\left(2\pi \frac{t}{T_n} \right) \qquad (2\text{-}27)$$

2.6.2.4   Simplified Mass-Spring Systems

Axial Mode of Frame legs

As described above, as the frame steps from one leg to another, a series of loads are transferred through the frame vertically. A number of behaviors described in this section start when the leg impacts the foundation with a vertical velocity, v_o, and a portion of its tributary weight, $^w/_2(1-\text{}_L)$, is re-applied to the leg. Thus, the first simple mass-spring system investigated represents the axial vibration of a leg with mass concentrated at the top of the leg, as shown in figure 2-28(a). The stiffness of this system can be taken as:

$$k_L = \frac{EA_L}{h} \qquad (2\text{-}28)$$

where A_L is the cross-sectional area of a leg and h is the total height of the leg. The system mass is assumed to only consist of the concentrated mass, $^m/_2$, at the top of the leg, therefore the period of vibration can be taken as:

$$T_L = 2\pi \sqrt{\frac{m}{2k_L}} \qquad (2\text{-}29)$$
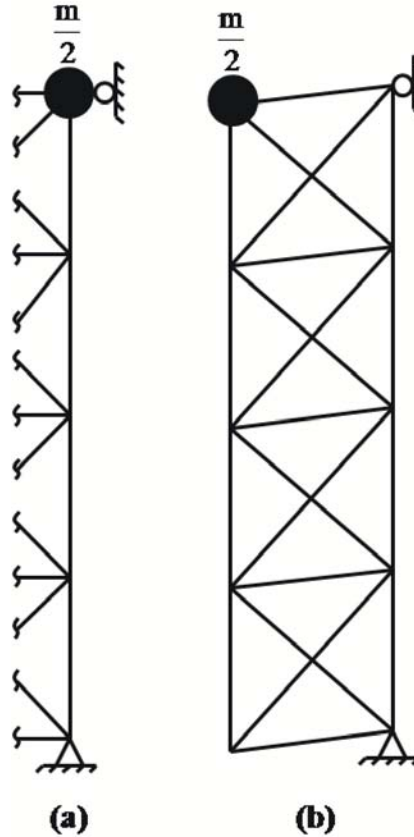
FIGURE 2-28 Vertical Modes of Vibration Excited During Rocking. (a) Axial Vibration of Pier Leg and (b) Vertical Shearing Mode of Pier Panels

As the motion continues from position 2 to 3 (figure 2-27), half of the frame's tributary vertical weight is transferred directly down the frame leg. This impulsive load can be defined by (2-23). To determine the effect of the impulsive load, an approach to approximate the rise time of the impulsive load is required. The approach is based on free-vibration response of the frame approximating its primary horizontal rocking mode as a linear elastic system and assuming equivalent response times between the two systems and is illustrated in figure 2-29. The response of the equivalent linear elastic system with respect to time can be expressed as:

$$\Delta(t) = \Delta_u \sin\left(2\pi\frac{t}{T_{sec}} \right)$$

(2-30)

where Δ_u=maximum global horizontal displacement of the frame (and could be determined using methods described in Section 2.7) and T_{sec}=secant period of vibration taken at the maximum system displacement such that:

43

$$T_{sec} = 2\pi \sqrt{\frac{m\, \Delta_u}{P_y}} \qquad (2\text{-}31)$$

where P_y is the horizontal yield force of the controlled rocking system defined by (2-9). Therefore the time it takes the system to travel from position 2 to 3 (figure 2-27) is defined as the rise time for the load applied directly down a leg, t_{rL}, and can be approximated by the expression:

$$t_{rL} = \frac{T_{sec}}{2\pi}\, \sin^{-1}\left(\frac{\Delta_{up2}}{\Delta_u}\right) \qquad (2\text{-}32)$$

where $_{up2}$ is the horizontal displacement of the frame at the point of uplift during 2nd cycle response (2-15). Finally, the dynamic amplification factor for this load, R_{dL}, can be defined by:

$$R_{dL} = 1 + \frac{\left| \sin\left(\dfrac{\pi t_{rL}}{T_L}\right) \right|}{\dfrac{\pi t_{rL}}{T_L}} \qquad (2\text{-}33)$$

Since this load acts through the new axis of rotation, it does not affect the base overturning moment. However, it will affect the maximum axial force developed in the leg as shown in the sample pier axial force response from dynamic finite element analysis in figure 2-30(a).
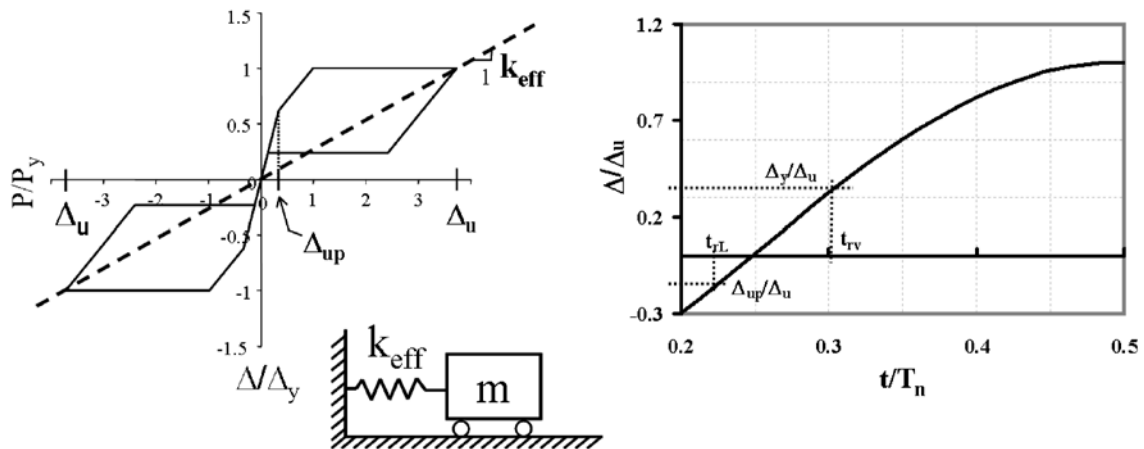
FIGURE 2-29   Illustration of Linear-Elastic System used for Determination of System Rise Times

44

(a)   **(b)**
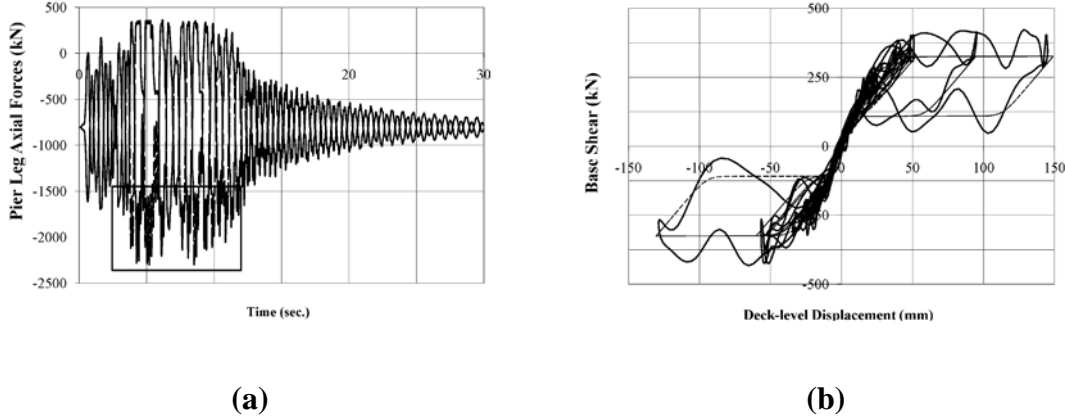
FIGURE 2-30 Fluctuation of Force Response Resulting from Vertical Mode Participation (a) Pier Leg Axial Forces and (b) Base Shear Force

Vertical shear mode of frame

As the rocking motion continues, vertical loads are transferred through the frame vertically to the other side as the frame uplifts. During uplift the simple mass-spring system is assumed to be subjected to zero initial conditions unlike during impact. Two loads are applied in series during uplifting (positions 3 to 5, figure 2-27). First, a load of $^w/_2$ is transferred through the frame vertically as the gravitational restoring moment is overcome followed by the yield force of the device.

The vertical stiffness in shear of the system for frames with panel heights equal to the frame width and diagonals in an X-braced configuration could be taken as:

$$k_v = \left(\frac{5h}{8EA_L} + \frac{\sqrt{2}d^2}{2hEA_d\cos^2\theta} \right)^{-1} \tag{2-34}$$

where E=modulus of elasticity of steel, A_d=cross-sectional area of the frame diagonals, =angle the diagonals make with the horizontal, and all other terms have already been defined. For the vertical shearing mode of vibration shown in figure 2-28(b), the effective mass is taken equal to $^m/_2$. The period of vibration of this simplified system is therefore:

$$T_v = 2\pi\sqrt{\frac{m}{2k_v}} \tag{2-35}$$

45

This expression does not account for the minor participation of the mass from the remaining vertical tributary mass of the frame. Performing elastic modal analysis of a system as depicted in figure 2-28(b) including mass from both sides would more accurately determine the period of this mode however this difference does not significantly change the maximum developed forces. For simplicity in design, (2-34) could be used.

As the frame moves from position 3 to 5, the two uplifting forces ($^w/_2$ and P_{yd}) are transferred through the frame vertically with rise times t_{r1} and t_{r2} respectively. It can be shown that t_{r2} is greater than t_{r1}, assuming free-vibration response, while both forces vibrate at the same frequency. Looking at a sample response of figure 2-31, the motions tend to be somewhat out of phase. They will become in-phase as t_{r2} approaches T_v however the amplification factor approaches 1 as t_{r2} approaches T_v. Consideration of the two separate loads and superposition of their individual dynamic amplification considering phase differences can become complex. The complexity of considering the two separate loads and superposition of their individual dynamic amplification including phase differences is not warranted with the simplified systems used. Therefore an approach is taken to obtain a single amplification factor for the two uplifting loads. Following that approach, a rise time, t_{rv}, is defined for the
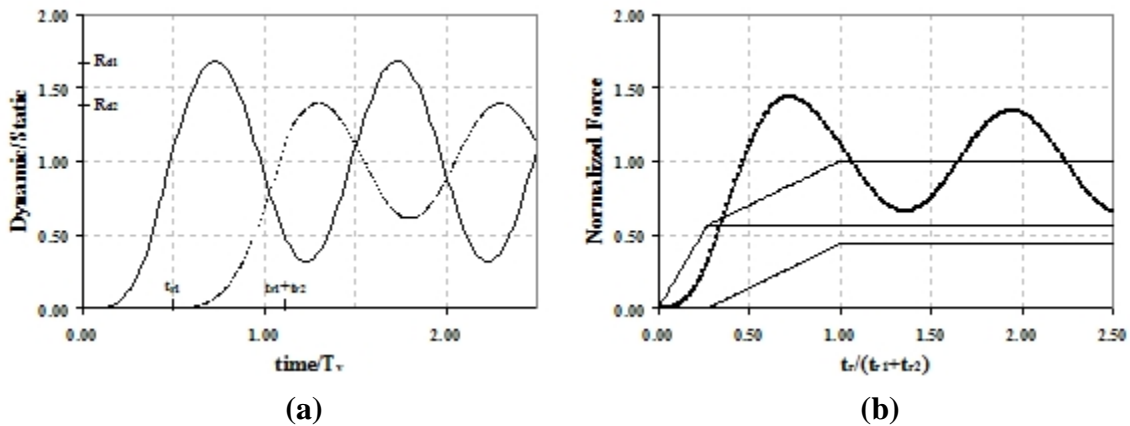
FIGURE 2-31   Dynamic and Static Response of Loads Through Truss Pier Vertically. (a) Dynamic Response of Each Load (w/2, F_{yd}) and (b) Normalized Total Dynamic and Static Response

two loads during uplift as:

$$t_{rv} = \frac{T_{sec}}{2\pi} \sin^{-1}\left(\frac{\frac{1}{2}\Delta_{y1}}{\Delta_u}\right)$$

(2-36)

where $_{y1}$=frame displacement at the point of yield assuming 1st cycle response. Therefore the dynamic amplification factor for the sum of these two loads is taken as:

$$R_{dv} = 1 + \frac{\left|\sin\left(\frac{\pi t_{rv}}{T_v}\right)\right|}{\frac{\pi t_{rv}}{T_v}}$$

(2-37)

Note that both 1st and 2nd cycle response parameters are being considered that yield conservative amplification factors. The influence of this dynamic effect is illustrated in the sample response shown in figure 2-30(b) with the dynamic base shear response overlaid on the static cyclic hysteretic curve defined previously. The dynamic amplification factors for the impulsive loads (R_{dL} and R_{dv}) applied during rocking will be used in the capacity protection design equations presented in later sections.

2.7 Simplified Method of Analysis

A simplified method for the prediction of maximum displacements a controlled rocking pier is discussed that is evaluated throughout this report. The method proposed in the FEMA 450 (2004) document for the design of passive energy dissipation systems uses spectral capacity (pushover) and demand curves and can represent the response in a graphical format. Conversion of the demand and capacity (pushover) curve to spectral ordinates is based on modal analysis theory. The bridge piers are assumed here to behave as a single degree of freedom system representing the dominant horizontal mode of vibration. The added energy dissipation from the passive energy dissipation devices is converted to equivalent viscous damping and the seismic demand curve reduced from the 2% damped spectrum (assumed inherent damping for this steel structure). For the flag-shaped hysteretic behavior of the controlled rocking system, the equivalent viscous damping can be determined by:

$$\xi_{eff} = \xi_o + \xi_{PED}$$

(2-38)

47

where ξ_o=inherent structural damping (assumed to be 2%) and ξ_{PED}=damping provided by passive energy dissipation devices during rocking response. For example, the hysteretic damping of the controlled rocking system with steel yielding devices (ξ_{hys}) can be approximated by modifying the equivalent damping of a bi-linear system (with no strain hardening) by a factor q:

$$\xi_{hys} = q \cdot \xi_{bi} = \frac{\eta_L}{1 + \eta_L} \cdot \frac{2}{\pi} \cdot \left(1 - \frac{1}{\mu_{G2}}\right) \qquad (2\text{-}39)$$

where μ_{G2}=displacement ductility ratio considering 2nd cycle properties such that:

$$\mu_{G2} = \frac{\Delta_u}{\Delta_{y2}} \qquad (2\text{-}40)$$

Factors for reducing the spectrum in the short (B_s) and long period ranges (B_L), for the effective damping (ξ_{eff}) from (2-38), are given in the FEMA 274 document. This method is briefly illustrated in figure 2-32. Further discussion on simple methods for calculating the response of passive energy dissipation systems can be found in Ramirez et al. (2000).

Rocking structures also dissipate energy through the radiation of stress waves into the soil (or assumed as an inelastic impact) that occurs during each half-cycle. Conversion of this form of energy dissipation into equivalent viscous damping has been considered by Housner
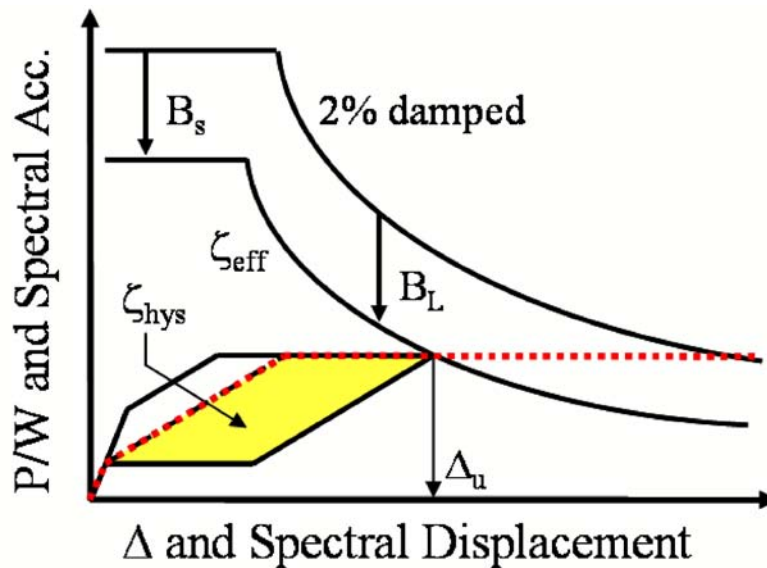
FIGURE 2-32   Simplified Method of Analysis Procedure Plot

(1963), Priestley et. al. (1978) and Mander and Cheng (1997). The amount of energy dissipation, in the form of equivalent viscous damping, has been shown to be in the range of 2-6% and decreases with increasing aspect ratio of the rocking element. The energy dissipated by the yielding steel elements or viscous dampers is much more significant and ignoring this effect is conservative.

2.8 Discussion of Pier Properties Used

A range of parameters assumed representative of steel truss bridge piers were established to investigate the response of self-centering, flag-shaped hysteretic systems. The parameters related to existing steel truss bridge piers are largely dependent on the pier aspect ratio ($^h/_d$). Inspection of drawings of a few existing steel truss bridges revealed some consistent details. They include:

- aspect ratios generally ranging from 1 to 4, although other values also exist
- pier diagonals of constant cross-section over pier height
- pier legs continuous over height
- pier diagonals and legs of similar sizes for different aspect ratios

These particular details reflect design practice at the time of construction. The piers carry their own tributary vertical gravity load. If vertical loads are assumed to be the same for all pier aspect ratios then pier legs would all be the same size. Similarly, if the design base shear is assumed identical for all piers (uniform design wind load) then the lateral load resisting elements may also be similar for all pier aspect ratios.

A set of pier properties, assumed to be representative, were adopted and some of their relevant dynamic properties for both horizontal and vertical vibrations are given in table 2-1 for rocking truss piers. More details of the piers used are given in Appendix A.

TABLE 2-1   Relevant Horizontal and Vertical Dynamic Properties of Representative Piers

h/d	h (m)	d (m)	w (kN)	k_o (kN/mm)	T_o (sec)	k_L (kN/mm)	T_L (sec)	k_v (kN/mm)	T_v (sec)
4	29.26	7.32	1730	12.5	0.74	213	0.128	290	0.155
3	21.95	7.32	1730	23.1	0.55	283	0.111	350	0.141
2	14.63	7.32	1730	47.5	0.38	425	0.091	360	0.139

SECTION 3

FURTHER DEVELOPMENT OF 2D CONTROLLED ROCKING FRAMES

3.1 General

The controlled rocking approach for seismic resistance of 2-legged bridge steel truss piers is investigated to further add to the developments of Pollino (2004). Some important concepts for the behavior of controlled rocking 2-legged piers were derived in that document and the essential information from it is reviewed briefly in Section 2. The influence on the key response parameters of controlled rocking 2-legged piers, subjected to both vertical and horizontal ground motion is discussed here and a method is proposed for combining the effects of horizontal and vertical excitation along with the dynamic effects that occur as a result of impact and uplift during rocking. These results are then compared with the results of nonlinear time history analysis for a few cases.

The response of controlled rocking piers to near-fault seismic excitation is then investigated using analytical techniques. Ground motions at a site close to fault rupture (<15km, i.e. near-fault) often have a strong pulse-type characteristic in the fault-normal direction that is capable of significant structural response. Also, the structural response can be different from that typically resulting from far-field excitation due to the strong concentration of seismic energy near the frequency of the pulse. The response of the controlled rocking system to such excitation is investigated using a set of near-fault ground motions used as part of the SAC Steel Project (Somerville, 1997) along with a number of simple pulse excitations. Focus is placed on the displacement response and dynamic analysis results are compared with the simplified method of analysis discussed in Section 2.

The use of viscous dampers implemented at the base of the structure is then considered as the passive energy dissipating control device. Relevant concepts are presented for use of the simplified methods of analysis and design incorporating viscous dampers to controlled rocking piers. The behavior of 2-legged piers with added viscous damping devices to sinusoidal displacement controlled loading and seismic input is then presented for a few cases.

51

3.2   Response of Controlled Rocking Piers to Horizontal and Vertical Seismic Excitation

The response of controlled rocking piers to both horizontal and vertical excitation is discussed in this section. Response to solely horizontal excitation was presented in past research (Pollino 2004). However, in an actual earthquake, the vertical component of excitation should also be considered for the design or retrofit of such structures. While the site and structural properties will dictate how significant the influence of the vertical component (or horizontal) is, a general methodology is proposed here for the combination of effects. The results predicted using this methodology are then compared to results of nonlinear time history analyses that include both horizontal and vertical excitations.

3.2.1   Prediction of Response Quantities

3.2.1.1   Maximum Pier Displacements

The maximum pier horizontal displacement ($_u$) of a controlled rocking pier can be predicted using the simplified method of analysis discussed in Section 2.7. It is assumed that the vertical component of excitation does not influence this displacement. The pier leg uplifting displacement ($_{upL}$) thus remains determined from the maximum pier displacement as was done previously in Section 2 and is equal to:

$$\Delta_{upL} = \left[\Delta_u - \frac{\left(\dfrac{w_v}{2} + F_d \right) \dfrac{d}{h}}{k_o} \right] \frac{d}{h} \tag{3-1}$$

where F_d=maximum device force at the maximum displacement of the pier and all other terms have been defined in Section 2.

3.2.1.2   Base Shear Force

The base shear response is influenced by the vertical acceleration of mass. The resulting base shear force, P_u, obtained from equilibrium of the pier forces shown in figure 3-1, is equal to:

$$P_u = \left[\frac{w_v}{2} \left(1 + \eta_L \right) \cdot R_{dv} + \frac{1}{2} m_v \cdot a_v \right] \cdot \frac{d}{h} \tag{3-2}$$

where w_v=vertical tributary weight of pier, m_v=vertical tributary mass of pier, R_{dv}=dynamic amplification factor during rocking as a result of uplift (defined in Section 2.6.2), a_v=vertical acceleration of mass. The other variable in the equation, η_L, is the local strength ratio of the controlled rocking system defined as the ratio of the maximum device force to the vertical tributary weight of the leg to which it is attached. For 2-legged piers it could be taken equal to:

$$\eta_L = \frac{F_d}{w_v/2} \tag{3-3}$$

Figure 3-1 and the base shear force defined in (3-2), shows how the base shear force is affected by the vertical acceleration of the mass. Upon rocking, the forces resulting from the vertical acceleration of the mass on the uplifting side of the pier (left side in figure 3-1) are transferred to the leg in contact with the support (right pier leg in figure 3-1).
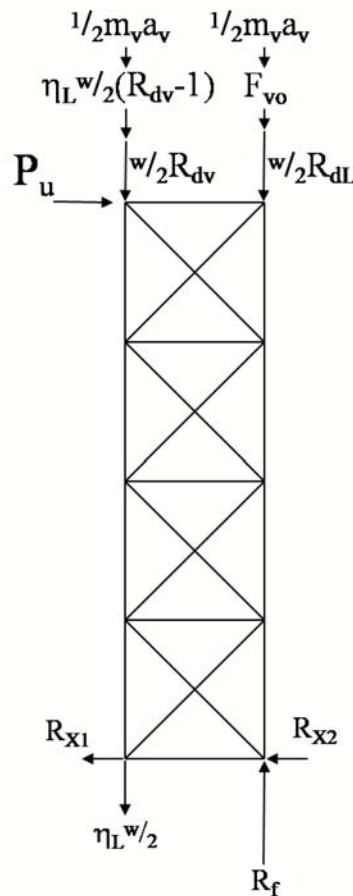
FIGURE 3-1 Free-body Diagram of 2-legged Pier Including Dynamic Effects

53

There is a substantial difference in behavior and load path between a pier prevented from uplifting from its support (restrained pier) and a rocking pier. The load path for forces generated as a result of vertical acceleration of the mass changes from being directed down a pier leg into the support (or reducing the uplifting force) for a restrained pier, to transferring through the pier diagonals to the leg in contact with the support for a rocking pier. There are some assumptions made in the previous statement regarding the relative stiffness of each load path however this would be the general case and that which is typically assumed for design. For the case of the restrained pier, no change in the base shear force would be observed due to the vertical excitation of the mass because it would be offset by the equal and opposite support reaction beneath the same leg. For the case of the controlled rocking pier, the lack of an equal and opposite support reaction results in fluctuation of the base shear response (seen in moment equilibrium about the base of the pier leg in contact).

In (3-2), the vertical acceleration of the mass (a_v) could be set equal to the vertical spectral acceleration value (S_{av}) at the vertical period of the pier (T_L), where the vertical period of the pier is taken equal to:

$$T_L = 2 \cdot \pi \sqrt{\frac{m_v/2}{k_L}} = 2 \cdot \pi \sqrt{\frac{m_v}{2\,EA_L/h}} \tag{3-4}$$

where A_L=cross-sectional area of a pier leg and h=height of the pier. The vertical spectral acceleration value, S_{av}, would be determined based on the vertical design spectrum for the site of interest. This would be the maximum expected vertical acceleration of the pier resulting from the vertical excitation. Therefore, when combining with the effects of horizontal excitation, a directional combination rule should be applied. For the design of bridges, a 100%-40% directional combination rule is often applied to combine the effects of multiple components of earthquake ground motion (ATC/MCEER 2004) to account for the non-simultaneity of the response of each component. It may seem reasonable to simply apply this combination rule to (3-2) where the first term is the result of horizontal excitation and the second term resulting from vertical excitation. However, for a nonlinear elasto-plastic system designed for maximum displacement greater than 2.5 times its yield displacement (μ_G>2.5), as shown in figure 3-2, 40% of the displacement response would still result in
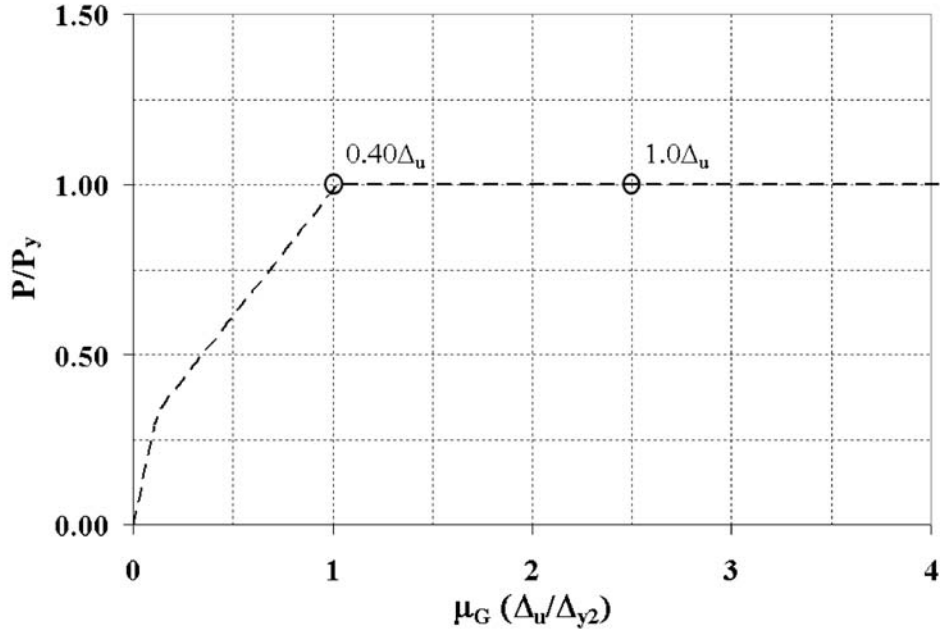
FIGURE 3-2 Normalized Pushover Curve Showing Base Shear Forces Using 100-40 Directional Combination Rule for μ_G<2.5

formation of a plastic mechanism. Therefore, even when using the combination rule, the forces generated from formation of the plastic mechanism should be considered in the design of this nonlinear system regardless of whether the 100% or 40% is applied to the horizontal response. However the factor R_{dv} in (3-2) that accounts for vertical excitation of the mass resulting from the horizontal rocking response (as discussed in Section 2.6.2) is included in the combination rule since this is a force resulting from a linear-elastic mode. Therefore, the base shear force including the effect of vertical ground motion and applying a directional combination rule is defined as:

$$P_{u,100-40} = \max \begin{cases} P_{u,st} + 1.0 \cdot P_{u,st} \cdot \left(R_{dv} - 1\right) + 0.4 \cdot \left(\frac{1}{2} m_v \cdot S_{av} \cdot \frac{d}{h}\right) \\ P_{u,st} + 0.4 \cdot P_{u,st} \cdot \left(R_{dv} - 1\right) + 1.0 \cdot \left(\frac{1}{2} m_v \cdot S_{av} \cdot \frac{d}{h}\right) \end{cases} \tag{3-5}$$

where $P_{u,st}$=static base shear resulting from formation of the plastic mechanism and is equal to:

$$P_{u,st} = \frac{w_v}{2} \cdot \left(1 + \eta_L\right) \cdot \frac{d}{h}$$

<div align="right">(3-6)</div>

3.2.1.3 Foundation Reaction and Pier Leg Axial Force

The maximum foundation reaction can also be determined from the free-body diagram of figure 3-1 and as such is equal to:

$$R_f = R_{f,st} + m_v \cdot a_v + F_{vo} + \frac{w_v}{2} \cdot \left(R_{dL} - 1\right) + \frac{w_v}{2} \left(1 + \eta_L\right) \cdot \left(R_{dv} - 1\right)$$

<div align="right">(3-7)</div>

where $R_{f,st}$=force generated statically as a result of uplifting and yielding of the device and is simply equal to:

$$R_{f,st} = \frac{w_v}{2} \cdot \left(2 + \eta_L\right)$$

<div align="right">(3-8)</div>

F_{vo}=force resulting from the mass tributary to a pier leg impacting the foundation with velocity v_o and can be calculated as:

$$F_{vo} = v_o \cdot \sqrt{\frac{m_v k_L}{2}}$$

<div align="right">(3-9)</div>

where k_L=axial stiffness of a pier leg and v_o=velocity upon impact of the pier leg with the foundation and a method to predict this velocity is presented in Section 3.2.1.4. The fourth and fifth terms in (3-7) are the dynamic effect of the weight tributary to a single pier leg being suddenly applied as the leg returns to the support and the dynamic effect of the remaining pier tributary weight and device force sudden transfer to the compressed pier leg during uplift. The factors R_{dL} and R_{dv} are the dynamic amplification factors resulting from the excitation of vertical modes of vibration and can be determined using concepts presented in Section 2.

Similarly to the combination of forces for prediction of the base shear force, a directional combination rule should be applied to (3-7) to account for the non-simultaneity in the response due to multiple components of excitation. However, some of the forces in (3-7) develop as a result simply from the horizontal rocking response (such as F_{vo} and the terms with factors R_{dv} and R_{dL}) and their dynamic effects are combined using an SRSS modal combination rule also in accordance with ATC/MCEER (2004) for multiple modal effects

in a single direction. Using the 100-40 directional combination rule, the foundation reaction could be determined as:

$$R_{f,100-40} = \max \begin{bmatrix} R_{f,st} + 0.4 \cdot (m_v \cdot S_{av}) + 1.0 \cdot \sqrt{F_{vo}^2 + F_w^2 + F_{up}^2} \\ R_{f,st} + 1.0 \cdot (m_v \cdot S_{av}) + 0.4 \cdot \sqrt{F_{vo}^2 + F_w^2 + F_{up}^2} \end{bmatrix} \qquad (3\text{-}10)$$

The second term $(m_v S_{av})$ is the force resulting from vertical excitation using the vertical spectral acceleration as done for the maximum base shear force. The fourth (F_w) and fifth (F_{up}) terms are equal to the fourth and fifth terms in (3-7).

The maximum pier leg axial force could conservatively be taken as the foundation reaction force or could be reduced by accounting for the lower panel diagonal member's force that is directed into the foundation (not applied to the lower panel leg). For a pier in an X-braced configuration (as shown in figure 3-1) the maximum pier leg axial force could be taken equal to:

$$P_{uL,100-40} = \max \begin{bmatrix} P_{uL,st} + 0.4 \cdot \left(\dfrac{m_v}{2} \cdot \left(2 - \dfrac{d}{2h} \right) \cdot S_{av} \right) + 1.0 \cdot \sqrt{F_{vo}^2 + F_w^2 + F_{up}^2} \\ P_{uL,st} + 1.0 \cdot \left(\dfrac{m_v}{2} \cdot \left(2 - \dfrac{d}{2h} \right) \cdot S_{av} \right) + 0.4 \cdot \sqrt{F_{vo}^2 + F_w^2 + F_{up}^2} \end{bmatrix} \qquad (3\text{-}11)$$

where the statically generated pier leg axial force, $P_{uL,st}$ is equal to:

$$P_{uL,st} = \frac{w_v}{2} + \frac{w_v}{2} (1 + \eta_L) \cdot \left(1 - \frac{d}{2h} \right) \qquad (3\text{-}12)$$

The terms F_{vo} and F_w are the same as defined for the foundation reaction and the fifth term, F_{up} is equal to:

$$F_{up} = \frac{w_v}{2} (1 + \eta_L) \cdot (R_{dv} - 1) \cdot \left(1 - \frac{d}{2h} \right) \qquad (3\text{-}13)$$

3.2.1.4 Maximum Impact Velocity

A method to calculate the impact velocity was presented in Pollino (2004) that calculates the impact velocity from the pseudo-velocity of the structure and uses a correction factor from Ramirez et. al. (2000) to account for the difference between relative and pseudo-velocity for damped structures. However, this approach to estimate the impact velocity does not have

57

a rigorous theoretical basis for this type of structural system. Another method is proposed here in which the velocity upon impact is determined using an energy balance approach where the energy is equated at the point of maximum deformation (position 1, as seen in figure 2-27) and just before the point of leg impact with the support (position 2 of figure 2-27) with the energy dissipated by the passive energy dissipation devices included as work done between these two points. Use of an elasto-plastic bi-linear yielding device is used in the derivation presented here, but other types of energy dissipating devices could be considered by equating their work done between these two points.

The energy balance in this case is defined as:

$$PE_1 + KE_1 + W_{1-2} = PE_2 + KE_2 \tag{3-14}$$

where the kinetic energy at position 1 (KE_1) is equal to zero since the frame is at the maximum deformation and has zero velocity. The potential energy at position 1 (PE_1) includes the internal strain energy developed in the frame members, gravitational potential energy of the mass as the leg is uplifted, and strain energy in the steel yielding device such that:

$$PE_1 = \frac{1}{2}\frac{P_y^{\,2}}{k_o} + \Delta_{upL}\frac{w_v}{2} + \frac{1}{2}\left(\frac{w_v}{2}\eta_L\right)\Delta_{yd} \tag{3-15}$$

where k_o=frame lateral stiffness, $_{upL}$=maximum uplift displacement of a leg and is related to the maximum displacement of the frame by (3-1), and $_{yd}$=yield displacement of the steel yielding device. The work done by the steel yielding device from position 1 to 2 is equal to:

$$W_{1-2} = \eta_L\frac{w_v}{2}\left(\Delta_{upL} - 2\Delta_{yd}\right) \tag{3-16}$$

The potential energy at position 2 (PE_2) includes a smaller amount of strain energy in the frame members (as opposed to position 1) and no gravitational potential energy as the leg has returned to the support such that:

$$PE_2 = \frac{1}{2}\frac{\left[(1-\eta_L)\frac{w_v}{2}\frac{d}{h}\right]^2}{k_o} \tag{3-17}$$

Finally, the kinetic energy at position 2 (KE_2) can be related to the vertical leg velocity as:

$$KE_2 = \frac{1}{2} m v_o{}^2 \left[\left(\frac{h}{d} \right)^2 + \frac{1}{4} \right] \tag{3-18}$$

Placing (3-15)-(3-18) into (3-14) and solving for v_o results in:

$$v_o = \sqrt{ g \left(\frac{1}{\frac{1}{4} \left(\frac{h}{d} \right)^2 + \frac{1}{2}} \right) \cdot \left[\frac{w_v}{2} \frac{\eta_L{}^2 - 1}{k_o} \left(\frac{d}{h} \right)^2 + 2 \eta_L \Delta_{yd} + \Delta_u \frac{d}{h} \left(1 - \eta_L \right) \right] } \tag{3-19}$$

This approach does not take into account work done by the ground motion during the time the frame displaces from position 1 to 2. This could be considered the inelastic pseudo-velocity of the controlled rocking system as is similarly defined for elasto-plastic systems (Newmark and Hall, 1982).

3.2.2 Response History Analysis of 2-legged Piers to Horizontal and Vertical Excitation

A few cases of controlled rocking piers are considered to evaluate the response under horizontal and vertical seismic excitation. The representative pier properties of Section 2 with aspect ratios of 4 and 3 are used along with steel yielding devices that have yield forces corresponding to $_L$=0.50 and 1.0. The elastic stiffness of these devices are designed for a local displacement ductility ($_L$) of 10 where:

$$\mu_L = \frac{\Delta_{upL}}{\Delta_{yd}} \tag{3-20}$$

The case of free rocking ($_L$=0) is also considered. The resulting device properties are shown in table 3-1 along with the predicted response from the equations derived in Section 3.2.1.

3.2.2.1 Ground Motions

Spectra compatible ground acceleration time histories were used for the base excitation of the analytical model and are generated using the Target Acceleration Spectra Compatible Time Histories (TARSCTHS) software developed by the Engineering Seismology Laboratory (ESL) at the University at Buffalo (http://civil.eng.buffalo.edu/users_ntwk/index.htm). Synthetic ground motions were generated by TARSCTHS to match the elastic horizontal

response spectrum for a site with the following arbitrary 5% damped spectral demand parameters (S_1=0.75g, S_s=1.875g). The vertical spectrum was assumed to have a magnitude of 2/3 the horizontal and the motions had less, low frequency content in the record and had a shape similar to that shown in figure 4-13.

3.2.2.2 Analytical Model

The dynamic response of the structure was predicted analytically using the program SAP2000 (Wilson 2000). The model mass is lumped equally at the two nodes at the top of each pier leg and acts in the horizontal and vertical translation DOFs. The pier's structural members are assumed to remain elastic and are modeled with elastic frame elements. The diagonal braces are modeled by members that can only resist axial forces (in tension and compression).

Compression-only gap elements were attached to the base of the legs in the vertical direction that provided no resistance to movement vertically upward at the base of the leg. The gap elements in compression, however, were essentially rigid compared to the specimen itself, as the gap elements were provided with an elastic stiffness of 1750kN/mm, compared to the axial stiffness of the pier leg of 116kN/mm.

The steel yielding devices were modeled using the Wen (1976) plasticity property that is defined by the elastic stiffness, yield force, post-yield stiffness ratio, and a parameter that controls the smoothing of the transition to yield. The elastic stiffness and yield force were assigned corresponding to the device properties stated in table 3-1. The post-elastic stiffness was assumed to be 2% of its elastic value and the yielding parameter was set equal to 2.

Damping was assigned to the model in the form of a Rayleigh damping matrix with 2% of critical damping assigned to periods of 2.5sec and 0.05sec. The upper limit of 2.5sec was chosen to limit the influence of the mass proportional damping term on the structure after it has uplifted from its base and the period of the rocking structure exceeds significantly the fixed-base period (0.74sec for h/d=4 and 0.55sec for h/d=3). The lower limit is chosen such

that the important higher modes of vibration are not over-damped but spurious high frequencies modes of no significance are numerically damped out.

The gravitation weight of the specimen is modeled by statically applying these forces at the top of each leg before conducting the dynamic analysis. The analytical model was excited dynamically by applying the synthetic acceleration histories to the fixed supports.

Solution of the nonlinear equations of motion is performed using Newmark's average acceleration method (Newmark 1959). To ensure accuracy in the solution, a convergence study was undertaken decreasing the size of the solution time step (t) and convergence tolerance (defined in the program as the magnitude of the force error over the magnitude of the force on the structure). Some of the key response quantities monitored were the pier leg forces, gap forces, pier displacements, and uplifting displacements. Following a few iterations, a time step of 0.0001sec and force convergence tolerance of 1E-10 was found to provide accurate results and was used for all analyses.

3.2.2.3 Results and Discussion

The maximum response of each analysis was recorded and the average response to the seven synthetic records presented in table 3-1 as $_{u,TH}$, $_{upL,TH}$, $P_{u,TH}$, and $P_{uL,TH}$. The results show the response is predicted reasonably well for the cases of $_L$=0.50 and 1.0 with the displacements predicted reasonably closely and the forces predicted with more conservatism. However, for the case of free-rocking ($_L$=0), the pier forces from the time history analysis can be significantly greater than that predicted using the concepts presented above. As will be discussed in more detail in Section 6, along with direct comparison with experimental response traces, the analytical model has significant sensitivity to the damping model used.

3.3 Response to Seismic Excitation with Near-Fault Characteristics and Simple Pulse-Type Excitation

The response of controlled rocking piers subjected to ground excitation with near-fault characteristics is investigated in this section using analytical methods. Ground motions at sites located close to a fault may contain a large pulse that can significantly influence the

TABLE 3-1 Design and Analysis Results Considering Horizontal and Vertical Seismic Excitation

h/d	L	k_d (kN/mm)	u (mm)	upL (mm)	P_u (kN)	P_{uL} (kN)	u,TH (mm)	upL,TH (mm)	$P_{u,TH}$ (kN)	P_{uL} (kN)
4	0	-	680	168	569	-4319	716	177	728	-5000
	0.5	290	365	84.8	686	-4880	288	67.7	616	-4300
	1.0	1080	218	45.9	904	-5500	212	45.5	662	-4410
3	0	-	620	202	762	-4490	468	154	1130	-4960
	0.5	300	264	81.8	958	-5060	245	79.2	983	-4490
	1.0	1100	160	45.0	1260	-5800	172	52.9	1020	-4500

response of structures (Alavi and Krawinkler 2004). The behavior is first investigated using a set of recorded and synthetically generated records with this type of excitation and then using simple pulse-type excitation. Focus here is placed on maximum developed pier displacements for the representative piers with aspect ratios of 4 and 3. The analytical model discussed in Section 3.2.2.2. is used here. However, large displacement analysis was also performed such that solution of the equilibrium equations are performed in the structure's deformed configuration and uses an updated Lagrangian approach (Bathe 1996) for updating nodal positions. The influence of the large displacement analysis on a sample static pushover curve of a controlled rocking system is seen in figure 3-3.

3.3.1 SAC Steel Project Near Fault Motions

A set of 20 near-fault ground motions were used that were developed as a part of the SAC Steel Project (Somerville 1997). Details of each of the motions are seen in table 3-2. Ten of the motions (nf01-19) were recorded from actual earthquakes and ten were synthetically generated (nf21-39). These probability of exceedance associated with these records is a 2% in 50 year (MCE) earthquake event. Only the fault-normal component of the recorded or generated records were used in the analyses. The component of ground motion parallel to the fault is not considered here since it does not contain the pulse (or fling) characteristic that is a result of the fault rupture process and source-to-site wave propagation and is typically observed only in the direction normal to the fault. The motions were not scaled to achieve
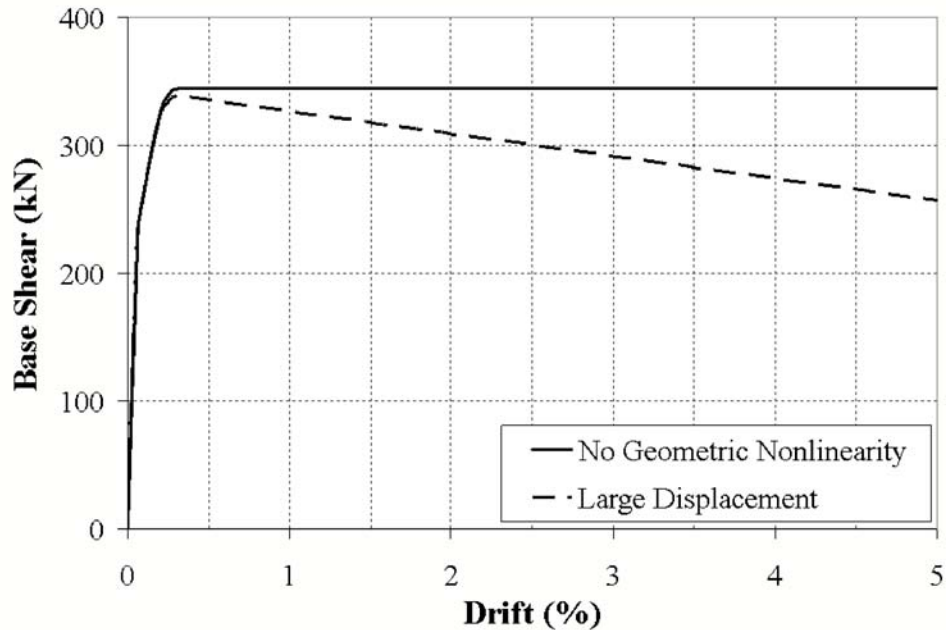
FIGURE 3-3   Static Pushover Curve Showing Influence of Geometric Nonlinearity in Analysis

a target spectrum however the intensity and variability of the motions were representative of a magnitude 7 earthquake at a distance of 5km predicted by empirical models (Abrahamson and Silva, 1997). Response spectra of each ground motion along with the average, and average plus and minus a standard deviation is seen in figure 3-4. The last column of table 3-2 is the period at the global maximum of the velocity spectrum of the motion which is assumed to be related to the dominant period of the pulse (Alavi and Krawinkler, 2004).

Analysis was performed for the representative piers with aspect ratios of 4 and 3 that had steel yielding devices with strength ratios ($_L$) of 0.50 and 1.0 and had an elastic stiffness of 46.4kN/mm and 92.8kN/mm respectively. The maximum displacement response was predicted for each of the 20 ground motions using the simplified analysis procedure discussed in Section 2.7 and uses each individual spectrum (nf01-39) for determination of the maximum displacement from each ground motion. For reference, the average predicted uplifting displacement would result in an axial strain of approximately 3.0% for buckling-restrained braces sized to achieve the above properties.

TABLE 3-2 SAC Near-fault Ground Motions Properties

EQ	Description	EQ Magnitude	Distance (km)	PGA (g)	PGV (cm/sec)	$T_p{}^1$ (sec)
nf01	fn Tabas, 1978	7.4	1.2	0.90	110	0.74
nf03	fn Loma Prieta, 1989, Los Gatos	7.0	3.5	0.72	173	0.72
nf05	fn Loma Prieta, 1989, Lex. Dam	7.0	6.3	0.69	178	1.01
nf07	fn C. Mendocino, 1992, Petrolia	7.1	8.5	0.64	125	0.72
nf09	fn Erzincan, 1992	6.7	2.0	0.43	120	2.26
nf11	fn Landers, 1992	7.3	1.1	0.71	136	3.97
nf13	fn Nothridge, 1994, Rinaldi	6.7	7.5	0.89	174	1.30
nf15	fn Nothridge, 1994, Olive View	6.7	6.4	0.73	123	2.38
nf17	fn Kobe, 1995	6.9	3.4	1.09	160	0.89
nf19	fn Kobe, 1995, Takatori	6.9	4.3	0.79	174	1.23
nf21	fn Elysian Park 1	7.1	17.5	0.86	96	1.31
nf23	fn Elysian Park 2	7.1	10.7	1.80	310	1.27
nf25	fn Elysian Park 3	7.1	11.2	1.01	155	1.76
nf27	fn Elysian Park 4	7.1	13.2	0.92	287	2.15
nf29	fn Elysian Park 5	7.1	13.7	1.16	251	2.03
nf31	fn Palos Verdes 1	7.1	1.5	0.97	274	2.38
nf33	fn Palos Verdes 2	7.1	1.5	0.97	288	2.59
nf35	fn Palos Verdes 3	7.1	1.5	0.87	263	1.82
nf37	fn Palos Verdes 4	7.1	1.5	0.79	195	1.63
nf39	fn Palos Verdes 5	7.1	1.5	0.92	265	2.67

[1]Pulse Period Taken as the Period at Maximum Value of Spectral Velocity
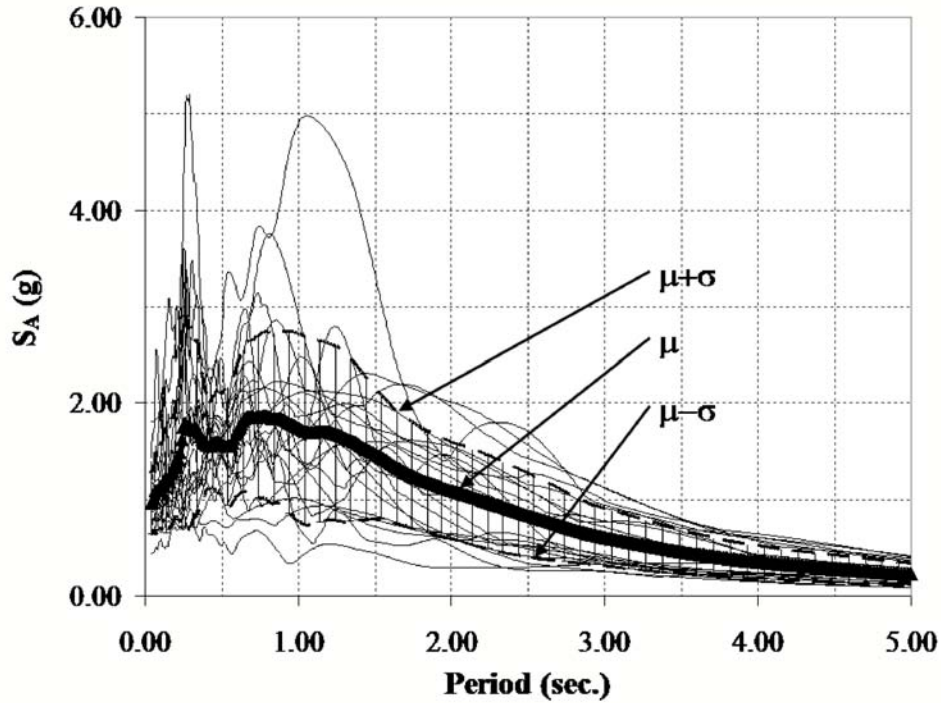
FIGURE 3-4   Response Spectra of SAC Near-fault Ground Motions

The results of the dynamic analyses are shown in figure 3-5 for each case. It is observed that even with the pulse type characteristics of the ground motions considered, the simplified analysis method provides reasonable prediction of response in terms of maximum displacements. In general, it appears that as the intensity of the motions increases, larger scatter in the prediction of response is present.

3.3.2 Simple Pulse-Type Excitation

A series of simple pulses were used to represent the fault-normal component of near-fault ground motions and are based on the work of Alavi and Krawinkler (2004). This type of excitation was used to hopefully provide trends in controlled rocking response subjected to simple pulses with varying pulse periods. The pulses used can be completely defined by their shape, pulse period (T_p), and the maximum pulse velocity ($v_{p,max}$). The intensity of the pulse, measured in terms of maximum pulse velocity ($v_{p,max}$), is determined based on
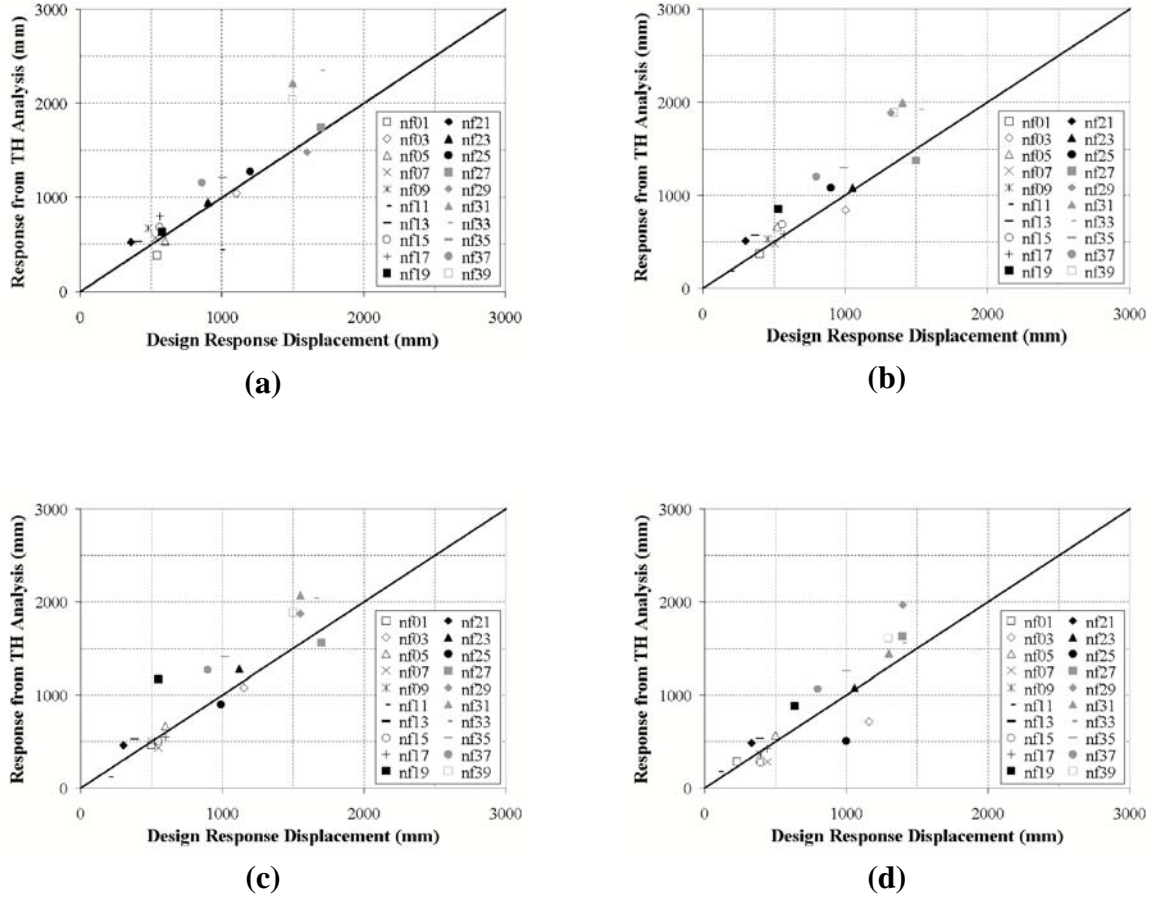
FIGURE 3-5 Analysis Results of SAC Near-fault Ground Motions (a) h/d=4, ρ_L=0.50, (b) h/d=4, ρ_L=1.0, (c) h/d=3, ρ_L=0.50, (d) h/d=3, ρ_L=1.0

regression analysis performed by Alavi and Krawinkler (2004) that relates the earthquake moment magnitude (M_w) and source-to-site distance (R) such that:

$$v_{p,\max} = 10^{\left(-2.03 + 0.65 M_w - 0.47 \log_{10} R\right)} \ (cm/\sec) \tag{3-21}$$

The magnitude and distance were arbitrarily set in this study as 7.0 and 10km respectively resulting in a maximum pulse velocity of 1122mm/sec. The two pulse shapes acceleration histories considered are shown in figure 3-6 normalized by each maximum pulse acceleration on the vertical axis and normalized by the pulse period (T_p) on the horizontal axis. For pulse P2, the maximum pulse acceleration ($a_{p,\max}$) is related to the maximum pulse velocity by:

$$a_{p,\max} = \frac{4 \cdot v_{p,\max}}{T_p} \tag{3-22}$$

66
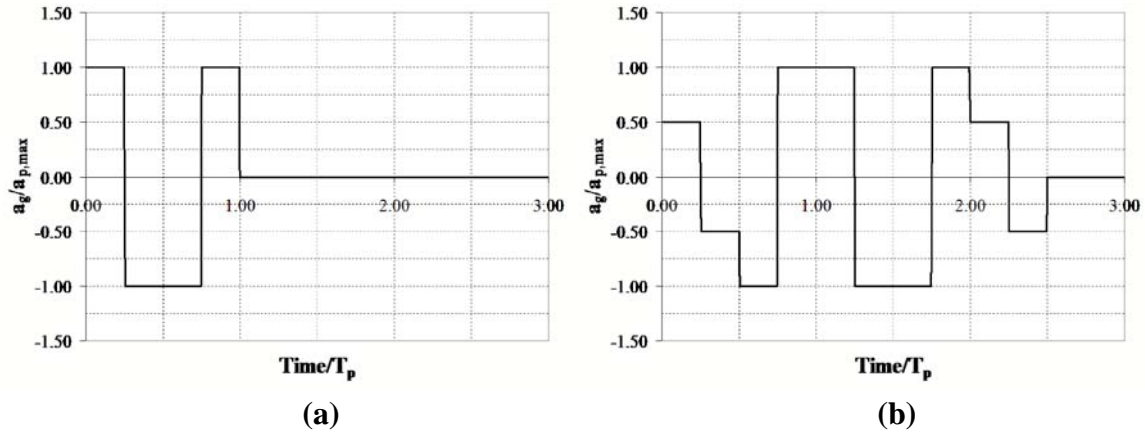
FIGURE 3-6   Simple Pulse Acceleration Shapes (a) Pulse P2 and (b) Pulse P3

and the maximum pulse displacement ($u_{p,max}$) is then equal to:

$$u_{p,\max} = \frac{v_{p,\max} \cdot T_p}{4} \tag{3-23}$$

The maximum pulse displacement of pulse P3 is half of P2 given by (3-23). The response of controlled rocking piers was investigated for pulses with pulse periods (T_p) ranging from 0.25sec to 5.0sec in increments of 0.25sec. For each analysis, the peak pier displacement was recorded and is shown in figure 3-7 plotted with the pulse period normalized by the pier's fixed base period of vibration (T_o) on the horizontal axis (T_o=0.74sec for h/d=4 and T_o=0.55sec for h/d=3). For each case considered, the maximum displacement is reached at pulse periods equal to approximately 3 to 5 times the fixed base period of vibration for pulse P2 and P3. However, for pulse P3 and the cases with $_L$=0, displacements exceeding half
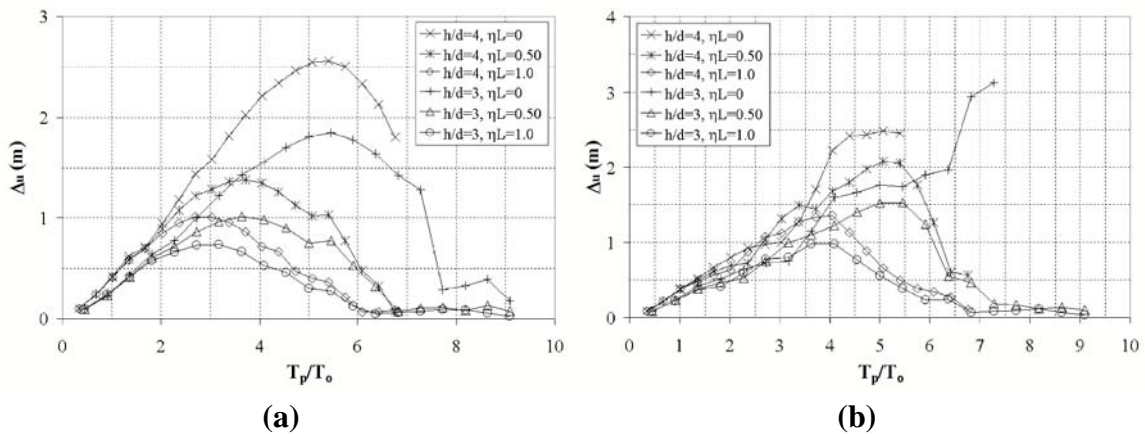
FIGURE 3-7   Analysis Results of Simple Pulse-type Excitation (a) Pulse P2 and (b) Pulse P3

the base width of the structure (d/2) were reached and the displacements beyond this point were not recorded since the analytical model would likely not be able to capture structural behavior during overturning. Note that for pulse P3 with T_p=5.0sec, the pulse displacement is over 70cm (a very rare event).

3.4   Use of Viscous Damping Devices as Passive Control Device

The use of fluid viscous damping devices (viscous dampers) as the passive energy dissipating control device was investigated in addition to the steel yielding devices which have been discussed exclusively to this point. Such devices produce a force response dependent on the relative velocity across its two ends such that:

$$F_{vd} = c \cdot sgn(v_d) \, |v_d|^{\alpha_d} \tag{3-24}$$

where c=damping coefficient, α_d=damping exponent, v_d=relative velocity across the damper, and sgn=sign function. Damping exponents in the range of 0.30 to 1.0 are common for seismic applications and the value of the damping coefficient will depend largely on the application. Many concepts related to the use of viscous dampers as the passive control device in this application are presented here that can be applied to the procedures for the use of controlled rocking discussed previously.

3.4.1   Calculation of Work Done by Viscous Dampers

Inclusion of viscous dampers to a controlled rocking pier will influence the cyclic hysteretic curve (considering dynamic response) and the amount of energy dissipation of the system. The calculation of the energy dissipated by viscous dampers implemented into building structures has been derived previously (Constantinou et. al., 1998) however the formulation of the work done for the case in which the dampers are implemented at the uplifting location (base of the structure) is performed here for completeness. For a controlled rocking 2-legged pier undergoing a quarter cycle of motion (from point of maximum displacement and returning back to the support, point 1 to 2 in figure 2-27), the work done by a viscous damper is equal to:

$$W_{1-2,vd} = \int F_{vd} \cdot du_z \tag{3-25}$$

where F_d=damper force and du_z=relative differential displacement across the damper. The damper is assumed to be implemented vertically (parallel with a pier leg) such that the relative damper displacement and velocity are in the vertical or z-direction. The damper relative differential displacement and velocity are related by:

$$du_z = \dot{u}_z \, dt \qquad (3\text{-}26)$$

Placing (3-26) and (3-24) into (3-25), the work done is equal to:

$$W_{1-2,vd} = \int c \cdot \dot{u}_z^{\alpha_d} \cdot \dot{u}_z \, dt = \int c \cdot \dot{u}_z^{(\alpha_d+1)} \, dt \qquad (3\text{-}27)$$

Assuming sinusoidal motion between these two positions, the velocity can be described by:

$$\dot{u}_z = \Delta_{upL} \left(\frac{2\pi}{T_{sec}} \right) \cdot \sin\left(\frac{2\pi t}{T_{sec}} \right) \qquad (3\text{-}28)$$

where $_{upL}$=maximum pier leg uplifting displacement defined by (3-1) and T_{sec}=secant period of vibration defined by (2-31). Placing (3-28) into (3-27), the work done is equal to:

$$W_{1-2,vd} = c \, \Delta_{upL}^{(\alpha_d+1)} \cdot \left(\frac{2\pi}{T_{sec}} \right)^{(\alpha_d+1)} \cdot \int_0^{T_{sec}/4} \left[\sin\left(\frac{2\pi t}{T_{sec}} \right) \right]^{(\alpha_d+1)} dt \qquad (3\text{-}29)$$

Evaluating this expression results in:

$$W_{1-2,vd} = \frac{1}{4} \cdot \left[\left(\frac{2\pi}{T_{sec}} \right)^{\alpha_d} c \, \lambda \, \Delta_{upL}^{(\alpha_d+1)} \right] \qquad (3\text{-}30)$$

where   is equal to:

$$\lambda = 4 \cdot 2^{\alpha_d} \cdot \frac{\Gamma^2\left(1 + \dfrac{\alpha_d}{2}\right)}{\Gamma(2 + \alpha_d)} \qquad (3\text{-}31)$$

and   =gamma function and is equal to:

$$\Gamma(\alpha_d) = \int_0^\infty t^{\alpha_d-1} \cdot e^{-1} \, dt \qquad (3\text{-}32)$$

For a damping exponent ($_d$) value of 1.0 (linear viscous damper),   (3-31) is equal to   and the work done by the damper from (3-30) is equal to:

$$W_{1-2,lvd} = c \, \Delta_{upL}^2 \, \frac{\pi^2}{2 \, T_{sec}} \qquad (3\text{-}33)$$

For reference, a damping exponent ( ) value of 0.50 results in   equal to 3.496.

3.4.2 Maximum Impact Velocity and Damper Force

The expression for the work done by the viscous dampers of (3-30) can be used to determine the maximum impact velocity similarly to that done previously for steel yielding devices. The maximum impact velocity is important for prediction of maximum pier leg forces and is also used to determine the maximum viscous damper force (using (3-24)). Using the energy balance approach discussed in Section 3.2.1.4, the potential energy at position 1 (PE$_1$) is equal to (3-15) with $_L$=0 since the viscous damper force will equal zero at the maximum displacement (position 1). The work done from position 1 to 2 is equal to (3-30). The potential energy at position 2 is solely due to the strain energy of the pier's members and is dependent on the force in the viscous damper at this position. However the influence of the damper force on the internal strain energy of the pier is negligible such that the potential energy at position 2 (PE$_2$) could simply be determined from (3-17) with $_L$=0. Finally, the maximum impact velocity could be taken equal to:

$$v_o = \sqrt{\frac{2}{m\left[\left(\dfrac{h}{d}\right)^2 + \dfrac{1}{2}\right]} \cdot \left(\Delta_{upL}\frac{w}{2} - W_{1-2,vd}\right)}$$

(3-34)

The maximum nominal viscous damper force output could then simply be determined combining (3-24) and (3-34) such that:

$$F_{vdo} = c \cdot v_o^{\alpha_d}$$

(3-35)

Note that as was done previously, the calculation of v_o in (3-34) is of the pseudo-velocity. The difference between pseudo and relative velocity and potential influence of the vertical component of motion should be included in some manner to ensure capacity protection of the pier, device connections, etc. The use of nonlinear viscous dampers with $_d$<1.0 will help alleviate the sensitivity in output damper force with the uncertainty of maximum relative damper velocity compared to that of a linear viscous damper ($_d$=1.0). For this reason, damping exponent values around 0.50 are commonly used in seismic applications.

A local strength ratio is defined here similarly for the use of viscous damping devices as:

$$\eta_{Lv} = \frac{c\, v_o^{\alpha_d}}{w_v/2}$$

(3-36)

3.4.3 Prediction of Response Quantities

3.4.3.1 Maximum Displacements

The simplified analysis method used previously for the prediction of maximum pier displacements can also be used when viscous damping devices are implemented. The primary difference in the use of this method for viscous dampers is the work done by the viscous dampers defined by (3-30) to equate the energy loss per cycle provided by the viscous dampers and the equivalent damping for the controlled rocking system. The equivalent viscous damping of the controlled rocking system can be determined as:

$$\xi_{eff} = \xi_o + \xi_{vd} = \xi_o + \frac{4 \cdot W_{1-2,vd}}{4 \pi W_k} \tag{3-37}$$

where W_k=stored strain energy in the system at the maximum displacement (Δ_u) and is taken as:

$$W_k = \frac{1}{2} P_y \Delta_u \tag{3-38}$$

The maximum uplifting displacement can be determined using (3-1) with F_d=0 since at maximum displacement the controlled rocking system has zero velocity thus the viscous dampers provide no force.

Note that since the device force is dependent on velocity, the controlled rocking system's ability to self-center is not affected by the properties of the device used. Once the earthquake has ceased, the structure can "slowly" re-center. This property of the controlled rocking system with viscous dampers is an advantage over the steel yielding devices, allowing more freedom on the selection of device capacity while still maintaining the self-centering ability of the structure.

3.4.3.2 Pier Forces

The maximum base shear force is predicted using (3-5) and replacing μ_L by μ_{Lv} (3-36). The maximum pier leg axial force can be predicted using (3-11), replacing μ_L by μ_{Lv}, and calculating the impact velocity with (3-34).

3.4.4 Example Behavior of Controlled Rocking Pier with Viscous Dampers

The analytical response of a controlled rocking pier with viscous dampers implemented vertically at the uplifting location is presented in this section. The same analytical model discussed in Section 3.2.2.2 is used here for the representative pier with an aspect ratio of 4. The behavior is first investigated by subjecting the pier to a sinusoidal displacement controlled input at the top of the pier to show the primary differences in the hysteretic behavior compared to the controlled rocking pier with steel yielding devices attached (discussed in Section 2.6.1). The amplitude of the sinusoidal input is 585mm (2% pier drift) and the period of input is set equal to the secant period (T_{sec}) for this displacement amplitude such that:

$$T_{sec} = 2\pi \sqrt{\frac{m_h \Delta_u}{P_y}} = 2\pi \sqrt{\frac{w_h \, 0.02 \, h}{g \, \dfrac{w_v}{2} \, \dfrac{d}{h}}} = 2\pi \sqrt{\frac{1730\,kN\,(0.02 \cdot 29.26\,m)}{\left(9.81\,\dfrac{m}{sec^2}\right)\dfrac{1730\,kN}{2}\dfrac{1}{4}}} = 4.34\,sec \tag{3-39}$$

The maximum pier horizontal velocity with this input is equal to 847mm/sec resulting in maximum uplifting velocity of 212mm/sec (assuming rigid body rotation of the pier). The viscous dampers properties were chosen to provide a local strength ratio ($_{Lv}$) of 0.67 with a damping exponent of 0.50. Therefore the damping coefficient was set equal to:

$$c = \frac{\eta_{Lv} \cdot \dfrac{w_v}{2}}{v^{\alpha_d}} = \frac{0.67 \cdot \dfrac{1730\,kN}{2}}{(212\,mm/\text{sec})^{0.50}} = 39.8\,kN\left(\frac{\text{sec}}{mm}\right)^{0.50} \tag{3-40}$$

The viscous damper was modeled with the *damper* element in SAP2000 that uses a Maxwell model (Malvern 1969) and has an elastic spring in series with a nonlinear dashpot. To achieve purely viscous behavior, the elastic spring is arbitrarily assigned a stiffness of 1750kN/mm to make it sufficiently stiff and to limit the spring deformations to approximately 0.25% of the damper stroke. Using a spring stiffness excessively exceeding the above value would have resulted in numerical problems and the analysis would not run.

The results are shown in figure 3-8 and are provided for an analytical model with zero vertical mass assigned at the top two nodes (dotted line), such that the higher vertical modes cannot participate and the hysteretic curve from the primary rocking mode is more easily

72

(a)   **(b)**
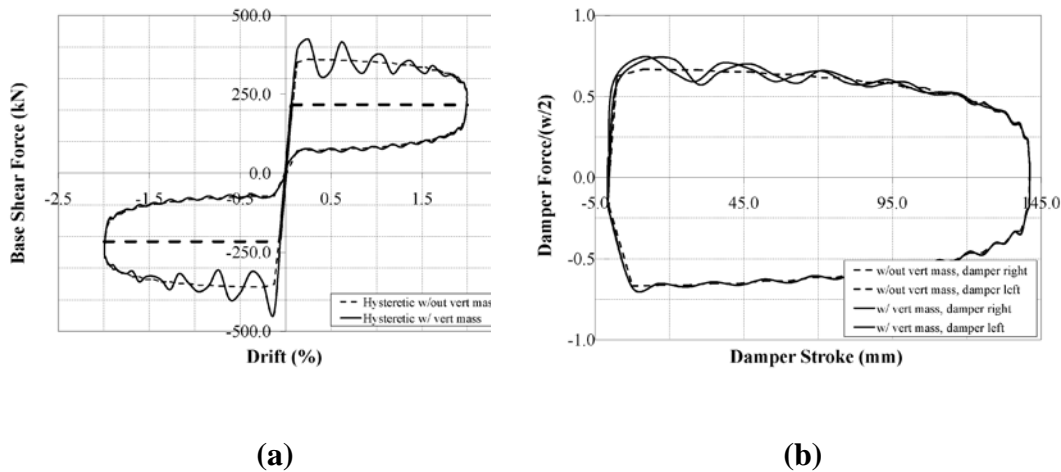
FIGURE 3-8   Controlled Rocking Behavior with Viscous Damping Devices, Sinusoidal Displacement Controlled Excitation (a) Global Hysteretic Response and (b) Damper Force-Displacement Response

seen. The same analysis is run with the vertical tributary mass of the pier and the fluctuation in the hysteretic curve due to the higher mode participation also shown (solid line). The static backbone curve is also shown in the figure (thick dotted line) for reference. The static behavior is equivalent to that of a free-rocking system since the velocity-dependent viscous devices do not participate statically.

Dynamic, time history analysis is also performed for the two representative piers (h/d=4 and 3), the set of viscous damper properties just discussed, along with the set of synthetically generated horizontal ground motions discussed in Section 3.2.2. to provide some dynamic analysis results of the controlled rocking system with viscous dampers. Note that only horizontal excitation is used in the analyses here. The results of analysis are presented in table 3-3 in a very similar manner to those discussed in Section 3.2.2. The displacement response is predicted well while the pier force response is predicted with a significant amount of conservatism. This is in part due to the conservative prediction of the viscous damper force.

TABLE 3-3 Design and Analysis Results for Controlled Rocking System with Viscous Damping Devices

h/d	u (mm)	upL (mm)	F_{vdo} (kN)	P_u (kN)	P_{uL} (kN)	u,TH (mm)	upL,TH (mm)	F_{vdo} (kN)	$P_{u,TH}$ (kN)	P_{uL} (kN)
4	360	85.7	423	630	-3400	326	76.9	328	415	-2640
3	265	84.2	465	875	-3470	259	81.8	392	737	-2990

Further analytical results and discussion are provided as part of the experimental testing program (discussed in Sections 5 and 6) which included testing with a set of viscous dampers. The analytical results are also compared with experimental test results that includes a controlled rocking specimen subjected to 3 components of seismic excitation. A detailed set of response prediction calculations are presented in Appendix D for the properties of the experimental specimen and viscous dampers used there and consider bi-directional response of the pier.

3.5 Summary

Further development and investigation of the response of the controlled rocking approach for the seismic protection of bridge steel truss piers is provided in this section. A method for the combination of key response parameters for a pier subjected to horizontal and vertical excitation is discussed that builds on concepts from past research discussed in Section 2. Nonlinear time history dynamic analysis is used to assess response of a pier subjected to horizontal and vertical seismic excitation and then response of controlled rocking piers to near-fault type of input is presented. For the bin of SAC near-fault ground motions, it is shown that the simplified analysis method can predict the maximum displacements with reasonable accuracy even with the significant pulse contained in the records. Finally, the use of viscous dampers as the passive control device was discussed and some important aspects of behavior derived to allow implementation and design with such devices into the controlled rocking approach.

SECTION 4

ANALYSIS AND DESIGN OF 4-LEGGED CONTROLLED ROCKING PIERS TO THREE COMPONENTS OF EXCITATION

4.1 General

Bridges supported on steel truss piers often have many 2-legged piers primarily designed to support gravity loads, that also resist transverse lateral loads but do not provide any significant resistance to longitudinal lateral loads. Where 4-legged piers are used, they provide support for gravity loads, transverse loads, and are the primary elements for resisting longitudinal lateral loads (together with abutments) in some instances. Expanding the controlled rocking concept developed earlier to make it applicable for the seismic resistance of 4-legged piers requires the development of design equations considering ground motions in two horizontal directions in addition to the vertical direction.

A typical 4-legged truss pier is shown in figure 4-1 along with a defined coordinate system. Also shown is a directional vector that lies in the x-y plane at an angle from the x-axis and which will be used throughout this section. The kinematic and hysteretic behavior of a controlled rocking 4-legged pier is developed and then investigated using nonlinear static and dynamic analyses and the observed results are used to establish rules and methods for the design of controlled rocking 4-legged piers.

4.2 Cyclic Hysteretic Behavior of 4-legged Pier Considering Uni-directional Motion

The cyclic hysteretic curve for a 2-legged pier was developed "step-by-step" in Pollino (2004) and the key variables are defined in Section 2. The cyclic hysteretic curve for a 4-legged pier, displaced along the x- or y-axis ($=n/2$, n=0,1,2,...) can be defined in a very similar manner and are provided in Appendix B for reference. The primary difference between the uni-directional hysteretic behavior of 2-legged and 4-legged piers is the use of four steel yielding devices (one at the base of each leg) and two pier frames in each direction. The cyclic hysteretic curve defined in the appendix for 4-legged piers is only valid for structural motion along one of the pier's primary axes. Note that the uni-directional response is not path dependent beyond the 2nd cycle.
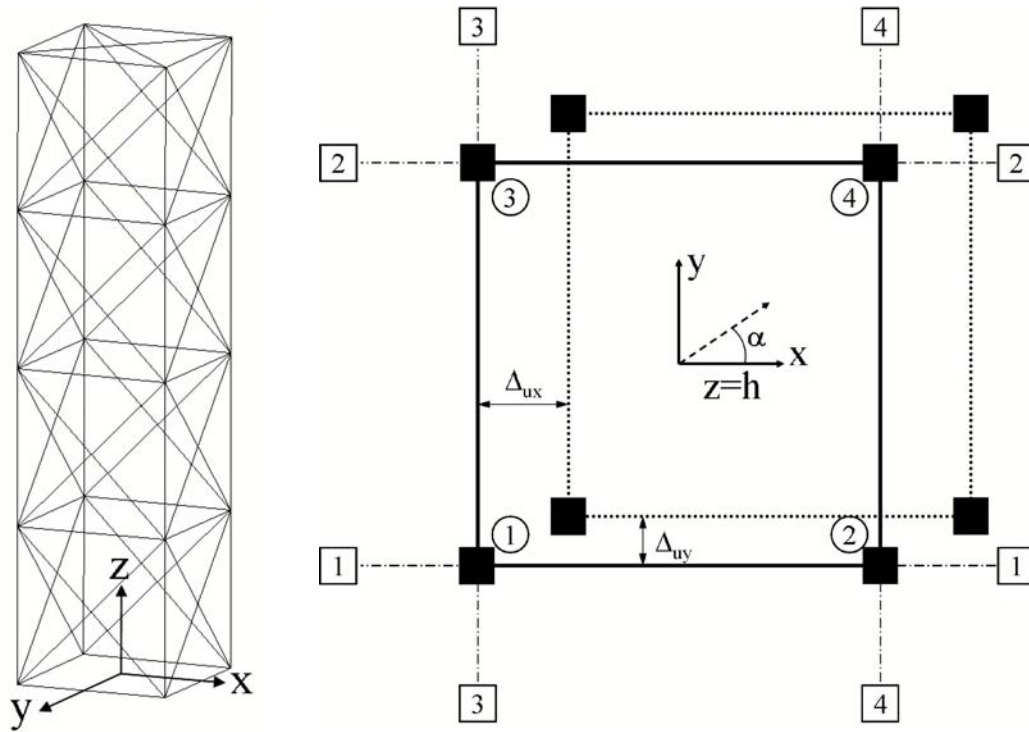
FIGURE 4-1   Typical 4-legged Pier and Defined Coordinate System

On the contrary, as will be shown in the next section, the bi-directional hysteretic behavior is path dependent and therefore can only be defined for the path considered. As the structure moves in both directions in the horizontal plane, the changes in stiffness and sequence of yielding of the devices depends on the path of the motion undergone. It is possible for the structure to uplift and yield three of the devices such that it is supported on a single leg. While it is not possible to know the path of the structure for design purposes, it is important to understand the bi-directional behavior in order to predict bounds on its response in terms of displacements and forces.

4.3   Bi-directional Kinematic and Hysteretic Pier Properties

Compatibility, equilibrium, and force-deformation relationships for a 4-legged pier are derived below to assist in the design of controlled rocking piers. For earthquake excitation in two horizontal directions, it is possible for the pier to uplift such that it is at times supported vertically on only one of its legs. In that case, three of the steel yielding devices

located at the base of the pier could yield, depending on the magnitude of their respective uplifting displacements and the device properties. Assuming that rotation of the pier about a vertical axis does not occur (i.e. neglecting torsional response), the top of parallel frames undergo the same horizontal deformations. In other words, using the notation illustrated in figure 4-1, the top of frames along lines 1-1 and 2-2 experience the same horizontal displacements while frames along lines 3-3 and 4-4 experience the same displacements. The displacement of the top of each frame (Δ_u) is the sum of deformations due to flexibility of frame's structural members (Δ_o) and rigid body rotation at the base of the frame (Δ_{br}) (see figure 4-2) such that:

$$\Delta_u = \Delta_o + \Delta_{br} \tag{4-1}$$

where the displacement due to deformation of the frame's structural members (Δ_o) can be determined using methods of structural analysis. For a frame with a number (n_p) of square panels with diagonal members of equal cross-sectional area along its height and in an X-braced configuration, this displacement can be defined as:

$$\Delta_o = \frac{F_f}{k_f} = F_f\left(\frac{h^3}{3EI_f} + \frac{L_d^3}{2Ed^2A_d}n_p \right) \tag{4-2}$$

where k_f=horizontal stiffness of the frame expressed in terms of the lateral displacement at the top of the frame, F_f=horizontal shear force applied to top of the frame, E=modulus of elasticity of steel, I_f=moment of inertia of the frame, L_d=length of truss diagonal, A_d=cross-sectional area of truss diagonal and n_p=number of pier panels along height. The displacement due to rigid body rotation of frame m ($\Delta_{br,Fm}$) is related to the uplifting displacement of the frame ($\Delta_{up,Fm}$), which is defined as the difference of the uplifting displacement of the two legs (i and j) of the frame such that:

$$\Delta_{br,Fm} = \Delta_{up,Fm}\cdot\frac{h}{d} = \left(\Delta_{up,Li} - \Delta_{up,Lj}\right)\cdot\frac{h}{d} \tag{4-3}$$

where $\Delta_{up,Li}$ and $\Delta_{up,Lj}$ are the larger and smaller uplifting displacements of the frame legs respectively, as shown in figure 4-2.

Since each pier leg "belongs" to two frames (one in each of the x- and y-direction), the uplifting displacement of any given pier leg is dependent on the pier lateral displacement in the x- and y-direction. For example, considering a global displacement in the +x- and y-
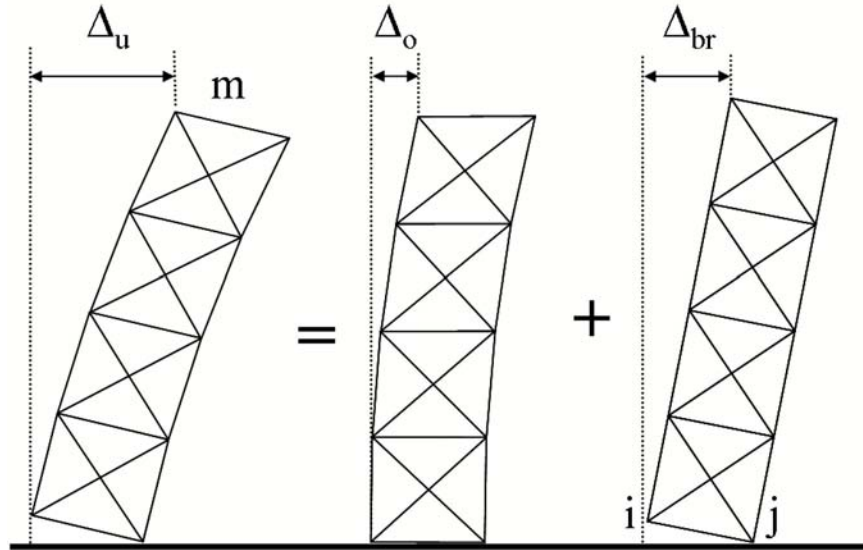
FIGURE 4-2   Kinematics of Controlled Rocking Truss Pier

directions such that pier leg 4 is the only one remaining in contact with its support, the uplifting displacement of pier leg 1 (see figure 4-1 for pier leg numbers) can be determined by summing the uplifting displacements of frames 4 and 1 or frames 2 and 3 (where frame "X" here is defined as the frame located along line X-X in figure 4-1). Using frames 4 and 1, the uplifting displacement of pier leg 1 is determined using (4-1) to (4-3) where i=1, j=2, and m=1 such that:

$$\Delta_{up,L1} = \Delta_{up,L2} + \left(\Delta_{u,F1} - \frac{F_{F1}}{k_f} \right) \cdot \frac{d}{h} \tag{4-4}$$

where $\Delta_{up,L2}$ can be determined using (4-1) to (4-3) with i=2, j=4, and m=4 such that:

$$\Delta_{up,L2} = \Delta_{up,L4} + \left(\Delta_{u,F4} - \frac{F_{F4}}{k_f} \right) \cdot \frac{d}{h} \tag{4-5}$$

where F_{F1} and F_{F4} are the horizontal shear applied to frames 1 and 4 respectively. If the top of pier displacements are in the positive x- and y-directions, and ignoring torsion as indicated earlier, then $\Delta_{u,F1} = \Delta_{u,F2} = \Delta_{u,x}$, $\Delta_{u,F3} = \Delta_{u,F4} = \Delta_{u,y}$, and $\Delta_{up,L4}=0$. The corresponding uplifting displacement of legs 1, 2, and 3 respectively is given by:

$$\Delta_{up,L1} = \left(\Delta_{u,x} + \Delta_{u,y} - \frac{F_{F1} + F_{F4}}{k_f} \right) \cdot \frac{d}{h} \tag{4-6}$$

78

$$\Delta_{up,L2} = \left(\Delta_{u,y} - \frac{F_{F4}}{k_f} \right) \cdot \frac{d}{h} \tag{4-7}$$

$$\Delta_{up,L3} = \left(\Delta_{u,x} - \frac{F_{F2}}{k_f} \right) \cdot \frac{d}{h} \tag{4-8}$$

If the hysteretic path to reach $_{u,x}$ and $_{u,y}$ results in the formation of the pier's plastic mechanism defined as any pier displacement resulting in yield of three steel yielding devices, the pier static free body diagram shown in figure 4-3a is obtained. From that diagram, it is possible to separate each frame from the pier and draw free body diagrams of each frame as shown in figure 4-3b (note columns from adjacent frames are shown twice). Through the equilibrium of forces, the horizontal shear force to frames 1 and 3 is:

$$F_{F1,3} = \left(\frac{w_v}{8} + \frac{1}{2} F_d \right) \cdot \frac{d}{h} \tag{4-9}$$

and the shear force applied to frames 2 and 4 is:

$$F_{F2,4} = \left(\frac{3w_v}{8} + \frac{3}{2} F_d \right) \cdot \frac{d}{h} \tag{4-10}$$

Note the larger shear force on the frames attached to the pier leg that remains in contact with its support (frames 2 and 4 for the motion considered).
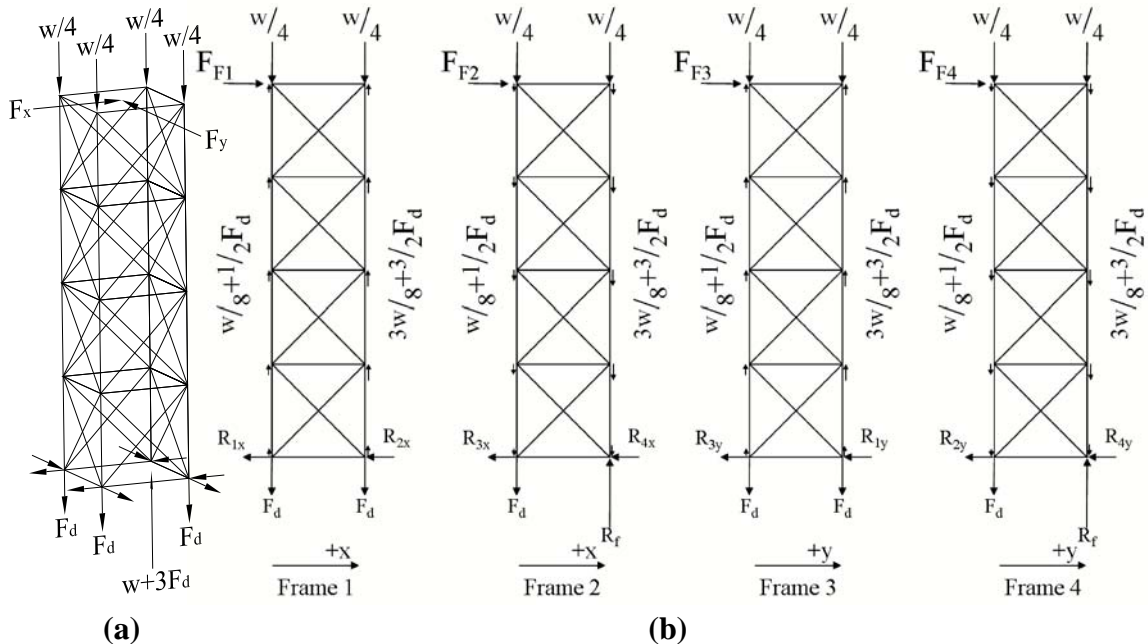
FIGURE 4-3   Free-body Diagrams of Frames at Formation of Plastic Mechanism

4.3.1. Yield Displacements and Plastic Capacity Surfaces

The hysteretic behavior of controlled rocking 4-legged piers, considering bi-directional response, is dependent on the pier's displacement path. An infinite number of paths is possible. The hysteretic properties of the system are investigated here considering a continuous linear horizontal displacement path in the α-direction for all possible values of α (0-2π rad.) and are presented in the form of force and displacement interaction plots.

The bi-directional yield displacement ($\Delta_{y,xy}$) is defined as the vectorial displacement at the top of the pier in the x-y plane when the last device yields such that:

$$\Delta_{y,xy} = \sqrt{\Delta_{y,x}^{2} + \Delta_{y,y}^{2}} \tag{4-11}$$

where $\Delta_{y,x}$ and $\Delta_{y,y}$ are the displacements in the x- and y-direction when the bi-directional yield mechanism forms. For a pier displacement in a direct linear path, a simple geometric relationship exists between the x- and y-displacements and the displacement direction angle, α:

$$\tan \alpha = \frac{\Delta_{y}}{\Delta_{x}} \tag{4-12}$$

Depending on the value of α, the pier is displacing more in either the x- or y-direction (or the same if $\alpha = \pi/4$) and controls the sequence of device yielding. For example, if the pier is assumed to travel in a direct path from zero pier displacements (x=y=0) to $\Delta_{u,x}$ and $\Delta_{u,y}$ ($\Delta_{u,y} = \Delta_{u,x} \tan \alpha$, 0rad.$< \alpha < \pi/4$ rad.) then device 1 will yield first, followed by device 3 and then device 2. When $\alpha = \pi/4$rad., device 1 yields first then devices 2 and 3 yield simultaneously. When $\alpha = 0, \pi/2, \pi, 3\pi/2$ rad., only two of the devices yield and they will yield simultaneously (uni-directional response) and the yield displacement is defined as in Appendix B. Figure 4-4 shows the sequence of device yielding for each $\pi/4$ interval of α.

The pier displacement, in the smaller displacement component direction, when the 3rd device yields ($\Delta_{y,sc}$) can be determined from the kinematic frame behavior defined by (4-1) where i and j are equal to the last number in the yielding sequence (figure 4-4) and the number of the compressed leg (number not shown) respectively, such that:

$$\Delta_{y,sc} = \Delta_o + \Delta_{br} = \frac{F_F}{k_f} + \Delta_{up,Li} \cdot \frac{h}{d} \tag{4-13}$$

where F_F=frame shear force with leg in contact with support (4-10) and $_{up,Li}$ is equal to the uplifting displacement at yield of the steel device considering 2nd cycle properties (2 $_{yd}$). Finally, using (4-11) and the geometric relationship of (4-12), the bi-directional yield displacement ($_{y,xy}$) is defined as:

$$\Delta_{y,xy} = \sqrt{\Delta_{y,sc}^2 + \left(\frac{1}{\tan\alpha}\cdot\Delta_{y,sc}\right)^2} = \Delta_{y,sc}\sqrt{1 + \frac{1}{\tan^2\alpha}} \quad \left(-\frac{\pi}{4} < \alpha < \frac{\pi}{4}, \ \frac{3\pi}{4} < \alpha < \frac{5\pi}{4}\right) \tag{4-14}$$

$$\Delta_{y,xy} = \Delta_{y,sc}\sqrt{1 + \tan^2\alpha} \quad \left(\frac{\pi}{4} < \alpha < \frac{3\pi}{4}, \ \frac{5\pi}{4} < \alpha < \frac{7\pi}{4}\right)$$

Once the pier has reached the displacement defined in (4-14) to form the bi-directional yield mechanism, the maximum static forces can be determined from the equilibrium diagrams for the pier shown in figure 4-3. It can be shown that the maximum shear forces in each
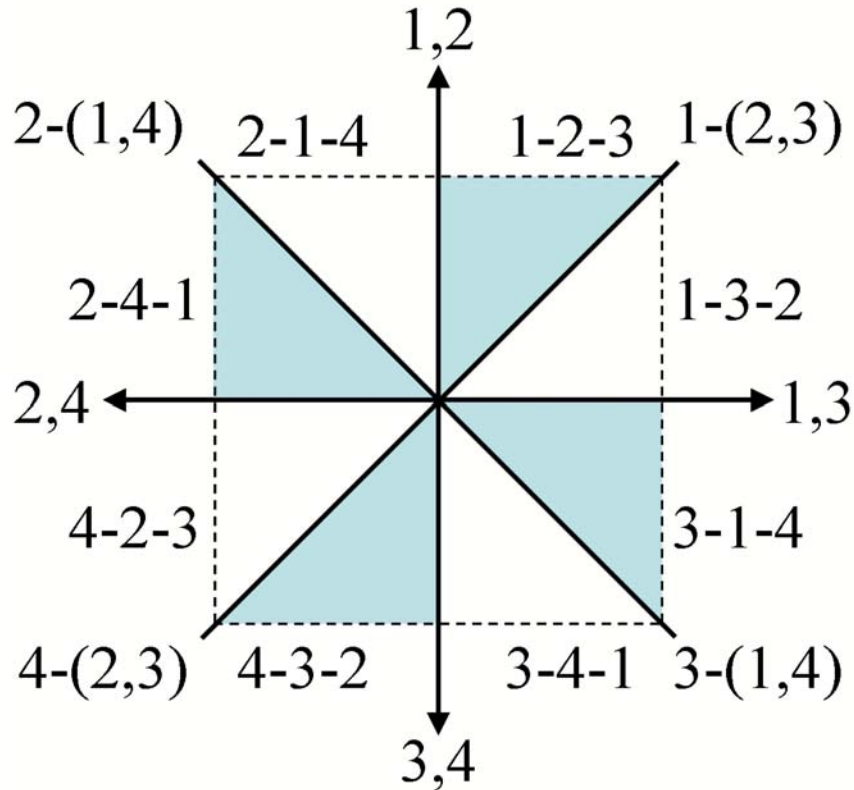
FIGURE 4-4 Sequence of Device Yielding for each Value of

direction is equal to the uni-directional yield force, $P_{y,uni}$, thus, $F_x = F_y = P_{y,uni}$ and the bi-directional yield force is:

$$P_{y,xy} = \sqrt{F_x^2 + F_y^2} = \sqrt{2 \cdot F_x^2} = \sqrt{2} \cdot P_{y,uni} \quad \left(\alpha \neq \frac{n\pi}{2} rad., n = 0, 1, 2, ... \right) \quad (4\text{-}15)$$

To illustrate the physical implications of the above equations, bi-directional force and displacement interaction plots are presented here for the representative pier from Pollino (2004) with h/d=4, $_L$=0.5, and k_d=36.9kN/mm. These types of plots are developed considering the structure to be subjected to displacement controlled and force controlled loading in the -direction. Following the structural response as it is subjected to each form of loading and developing the force and displacement interaction curves will provide insight into the bi-directional structural behavior and its path dependent hysteretic response.

In the case of applying a constantly increasing displacement vector (or assuming a direct linear path in the -direction as done previously), the applied shear force vector changes magnitude and direction to satisfy equilibrium and compatibility relationships. Considering a constant displacement vector applied in the directions of =atan(0.4/1.0)=21.8deg., =atan(1.0/0.3)=73.3deg., and =atan(1.0/1.5)=45deg. results in force and displacement response of the controlled rocking system shown in figure 4-5. Note that the force and displacement plots are normalized by the uni-directional yield force ($P_{y,uni}$) and uni-

(a)   (b)
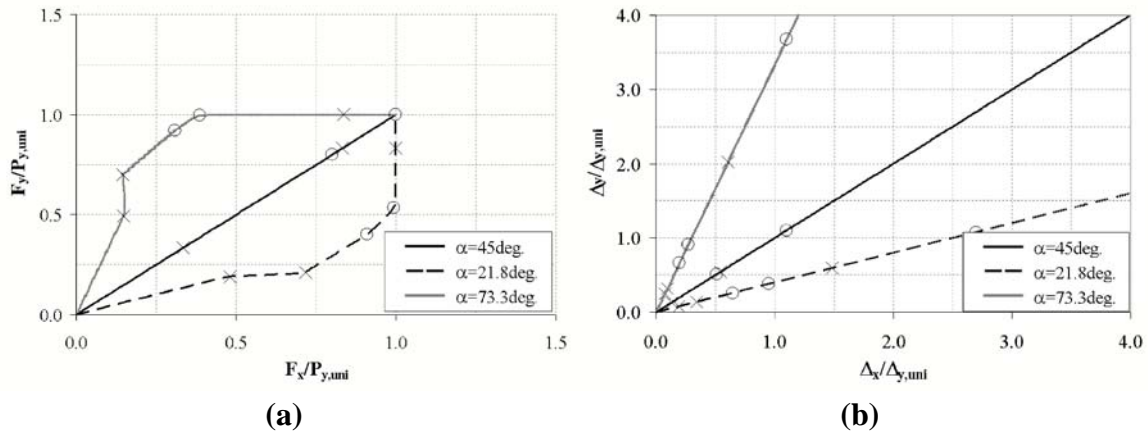
FIGURE 4-5 Pier Response for Displacement Controlled Loading (a) Base Shear Force and (b) Global Pier Displacement

82

directional yield displacement ($\Delta_{y,uni}$) respectively (defined in Section 2). Under this type of loading, the bi-directional yield mechanism will eventually be reached for all values of α (except α=nπ/2, uni-directional response). Considering the path with α=atan(0.4/1.0)=21.8deg., the bi-directional yield mechanism is developed when $\Delta_x \cong$ (1.0/0.4) $\Delta_{y,uni}$=2.5 $\Delta_{y,uni}$ (or $\Delta_{G:} \cong$ 2.5). Or similarly, for the path with α=atan(1.0/0.3)=73.3deg., $\Delta_y \cong$ (1.0/0.3) $\Delta_{y,uni}$=3.33 $\Delta_{y,uni}$ (or $\Delta_{G:} \cong$ 3.33) when the bi-directional yield mechanism forms.

On the other hand, applying a constant shear force vector requires changes in the displacement path such that equilibrium and compatibility relationships are satisfied as the magnitude of the force is increased. Force and displacement response is shown for the same directions (α=21.8, 73.3, 45deg.) in figure 4-6. The force response shows that the structure will only undergo bi-directional yielding when α=45deg. For any other value of α, once the yield force is reached in either direction it will continue to displace in that direction.

Considering every case of α, bi-directional yield interaction curves could be plotted using polar coordinates with α as the angular coordinate and the bi-directional yield force ($P_{y,xy}$) or yield displacement ($\Delta_{y,xy}$) as the radial coordinate. Both of the radial coordinate quantities are defined as the magnitude of the vector formed by the x- and y-components of the respective quantity at the point when the bi-directional yield mechanism develops. For the

(a)   (b)
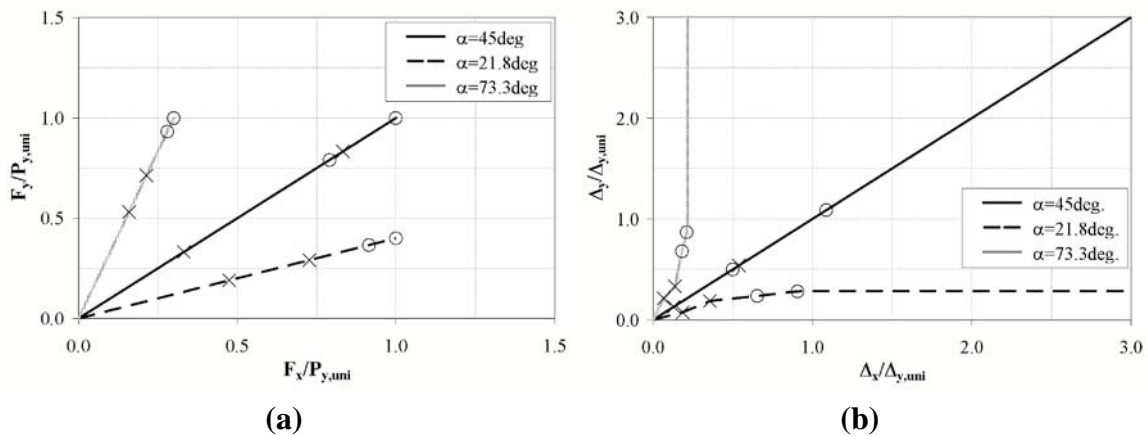
FIGURE 4-6   Pier Response for Force Controlled Loading (a) Base Shear Force and (b) Global Pier Displacement

case of an applied constant shear force, the yield force interaction surface is seen in figure 4-7a. The corresponding bi-directional yield displacement interaction plot is shown in figure 4-7b where $_{y,xy}$ has been defined by (4-14). The resulting yield displacement interaction plot is shown considering both pier flexibility and rigid pier members. For the case considered here, with identical pier stiffness in each direction and properties of devices attached to each leg, an axis of symmetry exists in each plot every /4 rad., as would be expected due to the physical symmetry of the system.

Again, while this information does not provide the path expected to be taken during response of a controlled rocking pier, it will provide insight into bounds of expected response that can be used for design.

4.3.2 Example and Verification of Static Kinematic/Hysteretic Behavior

Nonlinear static pushover analysis is used to verify and illustrate the analytical expressions defined above. The representative pier with aspect ratio of 4 (Pollino 2004) and device properties used in the previous section are also considered here. An elasto-plastic model is used for the steel yielding devices for comparison with the expressions derived above although a more sophisticated model will be used for the dynamic analyses presented later.

(a)   (b)
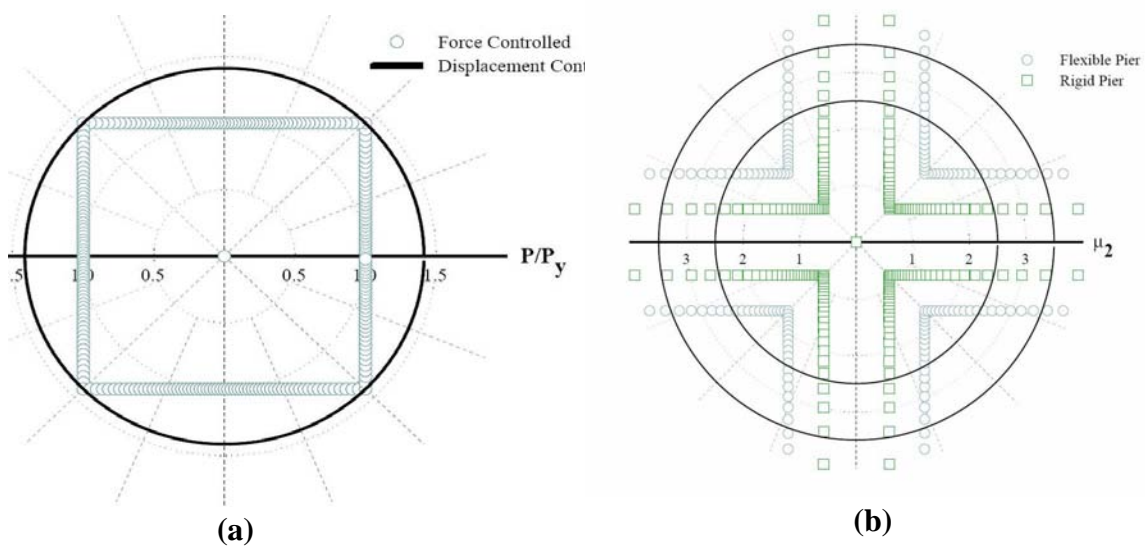
FIGURE 4-7   Yield Interaction Surfaces. (a) Yield Force and (b) Yield

Displacement

84

This example considers a progressively increasing displacement applied in the α-direction such that α=atan(0.4/1.0)=21.8deg. This direction of α was chosen to achieve a maximum displacement following the 100%-40% directional combination rule that is often applied for the seismic design of bridges (ATC/MCEER 2004). The pier is pushed until a displacement equivalent to 2.0% drift is reached in one of the principal directions. The pushover curve is defined as the resulting shear in the α-direction (F_{xy}) versus the displacement along the α-direction (Δ_{xy}). The resulting pushover curve is shown in figure 4-8. The pushover curve changes slope 6 times as each of the three legs uplift from the foundation and each of the steel devices yield. Results of the pushover analysis are compared in table 4-1 with the response parameters derived earlier in this section. The maximum developed base shear is equal to the pier's plastic capacity defined by (4-15). As can be seen from the table, the derived values of uplifting displacements and frame forces are in very good agreement with the results of nonlinear pushover analysis, as expected. The largest discrepancy is with the pier displacement in the smaller component direction when the 3rd device yields ($\Delta_{y,sc}$). The difference is about 4.7% and likely due to interaction between frames 2 and 4 (in this case) since the additional axial deformation of leg 4 due to demands coming from frame 2 is not included in the derivation of (4-13). The difference in the bi-directional yield displacement ($\Delta_{y,xy}$) is a direct result of the discrepancy of $\Delta_{y,sc}$ since the analysis results show the relationship between these two quantities defined by (4-14).
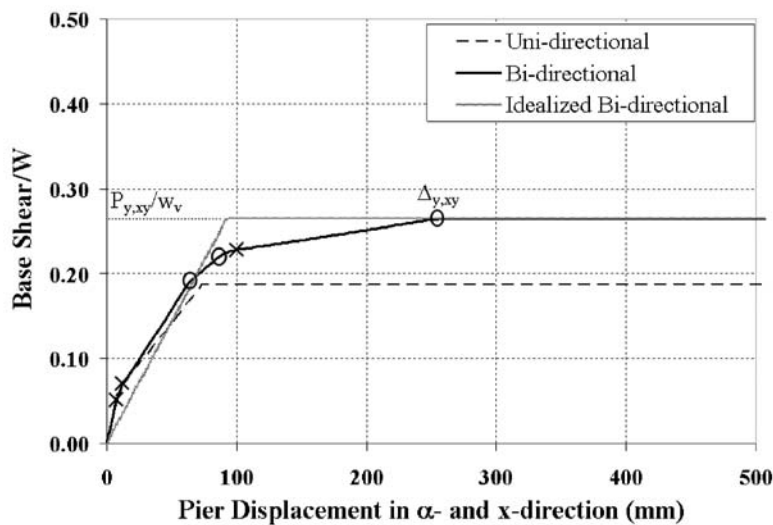
FIGURE 4-8 Bi-directional and Uni-directional Pushover Curves (2nd Cycle Properties)

85

TABLE 4-1 Results of Nonlinear, Static Pushover Analysis and Values from Developed Kinematic/Hysteretic Properties

	Action	Eq. #	Value	Analysis Result
$_{up,L1}$	Uplift Disp. of Leg 1	4-6	193	193
$_{up,L2}$	Uplift Disp. of Leg 2	4-7	49.0	48.0
$_{up,L3}$	Uplift Disp. of Leg 3	4-8	137	136
F_{F1}	Shear of Frame 1	4-9	81.0	81.0
F_{F3}	Shear of Frame 3	4-9	81.0	81.0
F_{F2}	Shear of Frame 2	4-10	243	243
F_{F4}	Shear of Frame 4	4-10	243	243
$_{y,xy}$	Pier Displacement when 3rd Device Yields	4-14	231	239.6
$_{y,sc}$	Pier Displacement in Smaller Component Direction when 3rd Device Yields	4-13	85.7	88.9
$P_{y,xy}$	Bi-directional Pier Yield Force	4-15	459	459

*all units in kN and mm

4.4 Use of Simplified Analysis Method Considering Bi-directional Horizontal Input

To determine maximum pier displacements, the capacity spectrum analysis method (ATC/MCEER 2004) was evaluated previously for 2-legged piers subjected to controlled rocking (Pollino 2004) and shown to predict the maximum seismic displacements of the pier with reasonable accuracy for design. This method of analysis characterizes a MDOF nonlinear system by a linear-viscous SDOF system. The simplification to the SDOF system is done by developing the structural capacity (pushover) curve of the MDOF system, in a particular direction, using a loading profile corresponding to the first mode of vibration (assuming this to be the dominant mode). The hysteretic energy dissipated through nonlinear behavior is then converted to an assumed equivalent amount of viscous damping per cycle. The seismic demand spectrum is then reduced as a function of this increased amount of energy dissipation.

However, questions arise using this simplified analysis method for bi-directional horizontal response such as, what path to consider in the development of the structural capacity curves, and what should be the corresponding demand curves. Due to the path dependency of the hysteretic behavior, the spectral capacity curve can vary for any path with θ=0 to θ=45deg. The case of θ=0 (uni-directional behavior) provides a lower bound on the structural force capacity ($P_{y,uni}$) and on the energy dissipated per cycle since only 2 of the steel yielding devices are activated. The path with θ=45deg. provides an upper bound on the structural force capacity ($P_{y,xy}$ of (4-15)) and energy dissipated per cycle since all 3 devices are activated at the smallest displacements compared to other paths as seen in figure 4-7b. The corresponding demand curve for uni-directional response can be derived from the design spectrum in one of the principal pier directions. However, use of the bi-directional capacity curve requires some form of a bi-directional demand curve that has a larger spectral acceleration values in order to predict the bi-directional response. These concepts will be presented in an example using two sets of spectral capacity and demand curves, one considering uni-directional and the other bi-directional properties. A flow chart is shown in figure 4-9 that illustrates the procedure of the simplified analysis method when considering the two sets of properties.

4.4.1 Example Simplified Analysis (Uni-directional Behavior)

The same pier (h/d=4, h=29.26m, k_f=6.25kN/mm, w_v=1730kN, m_x=m_y=w_v/g) and steel yielding device properties (β_L=0.5, k_d=36.9kN/mm) that were used previously in this section are used here. In an actual design scenario, the devices would be calibrated to satisfy a number of design constraints and pier properties (strength, stiffness) and in some cases the pier may need to be strengthened or stiffened to satisfy the performance objectives (namely, elastic response of the pier). This process has been detailed for 2-legged piers in Pollino (2004).

The uni-directional spectral capacity curve is developed using the variables in Section 2 (P_{up2}=109kN, Δ_{up2}=8.7mm, $P_{y,uni}$=324kN, Δ_{y2}=94.5mm). The 5% damped demand spectrum corresponding to this capacity curve could simply be taken as the design spectrum defined in ATC/MCEER (2004). A site located in Northridge, CA and seismic event with 3%
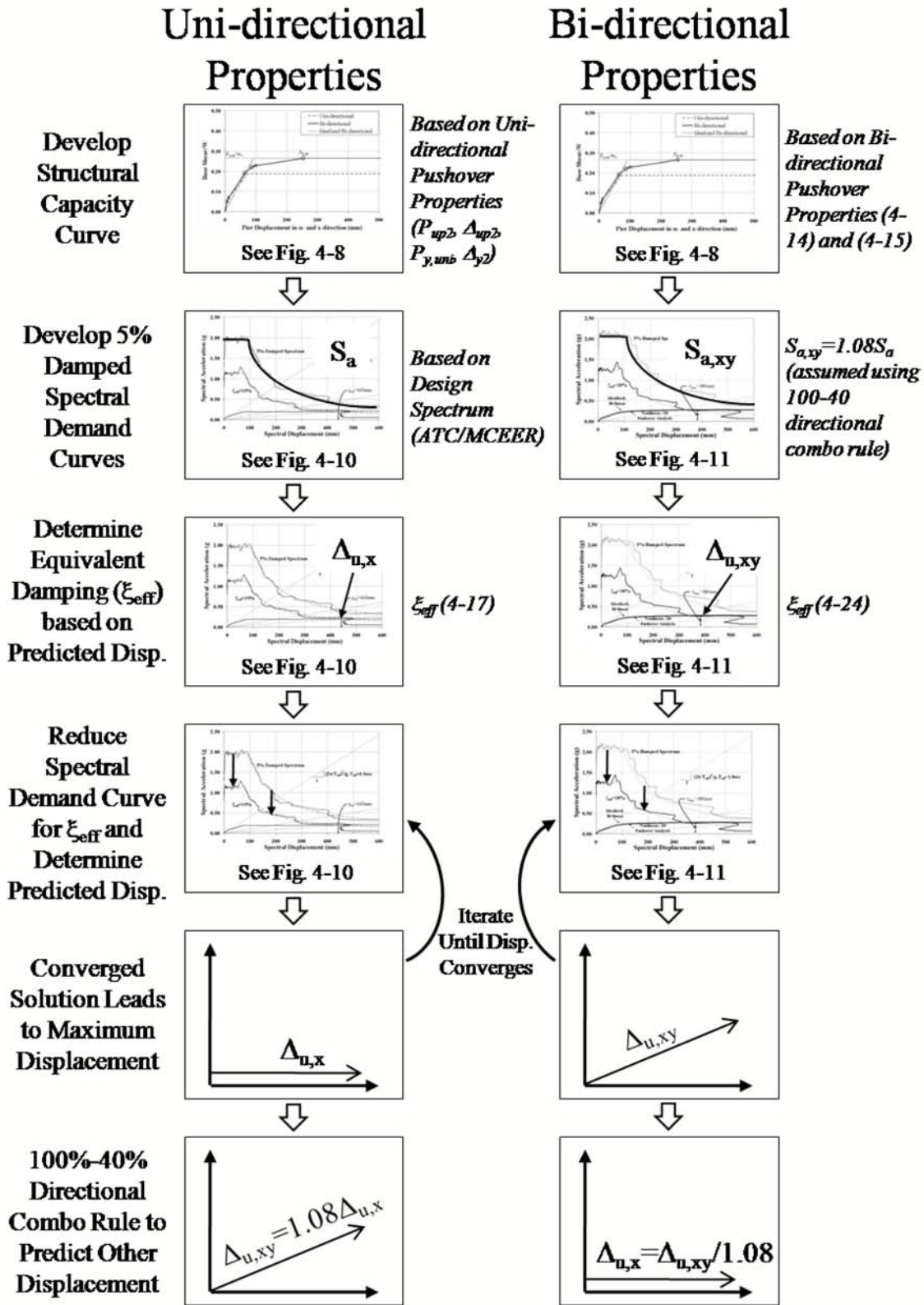
FIGURE 4-9   Simplified Analysis Method Flow Chart Considering Uni-directional and Bi-directional Properties

88

probability of exceedence in 75 years is considered here. The spectral acceleration values are taken from the USGS with a short period (0.2sec) spectral acceleration, S_s, of 1.95g and one-second spectral acceleration, S_1, of 0.87g. The resulting spectral demand curve and uni-directional capacity curve for the pier are shown in figure 4-10.

The spectral demand curve is then reduced to account for the energy dissipation that occurs due to the plastic work of the devices, expressed as an equivalent amount of viscous damping. The system's equivalent viscous damping is determined using the following expression:

$$\xi_{eff} = \xi_o + \xi_{hys} \tag{4-16}$$

where ξ_o=inherent structural damping (assumed to be 2%) and ξ_{hys}=hysteretic damping provided by the steel yielding devices during rocking response and is taken as:

$$\xi_{hys} = \frac{\eta_L}{1+\eta_L} \cdot \frac{2}{\pi} \cdot \left(1 - \frac{1}{\mu_{G2,uni}}\right) \tag{4-17}$$

where $\mu_{G2,uni}$=displacement ductility ratio considering 2nd cycle properties such that:

$$\mu_{G2,uni} = \frac{\Delta_u}{\Delta_{y2}} \tag{4-18}$$

and where Δ_{y2} is the system yield displacement considering 2nd cycle properties. Damping modification factors (ATC/MCEER 2004) are then used to reduce the demand spectrum for
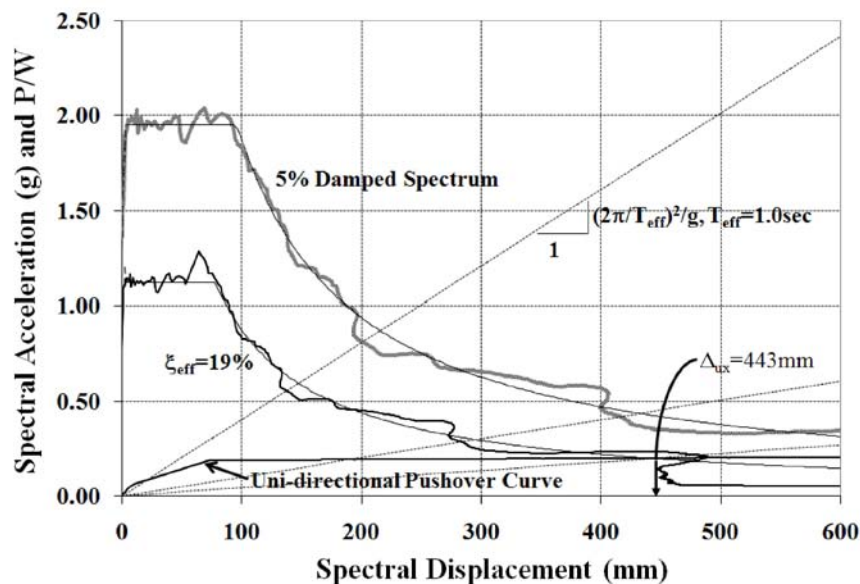
FIGURE 4-10 Uni-directional Spectral Analysis Plot

the amount of equivalent viscous damping. However, since the amount of hysteretic damping is dependent on the unknown displacement ($\Delta_{G2,uni}$ in (4-17)), the process is iterative until a displacement is converged upon.

Following a few iterations, the final spectral capacity and demand curves are also shown in figure 4-10. It can be seen that a displacement of 443mm is predicted using this approach. This pier displacement resulted in an equivalent damping ratio of:

$$\xi_{eff} = 0.02 + \frac{0.5}{1+0.5} \cdot \frac{2}{\pi} \cdot \left(1 - \frac{1}{\dfrac{443\,mm}{94.5\,mm}}\right) = 0.02 + 0.17 = 0.19\ (19\%) \tag{4-17}$$

Typically, the design seismic demand can be assumed equal in each orthogonal direction; however the maximum structural response does not occur simultaneously. If the uni-directional pier properties considered are identical in each direction then the predicted displacement in the x- and y-direction will be equal ($\Delta_{u,x} = \Delta_{u,y}$). Using a 100-40 directional combination rule to account for the non-simultaneity of the maximum displacement response would result in a displacement magnitude of:

$$\Delta_{u,xy} = \sqrt{1.0^2 + 0.4^2} \cdot \Delta_{u,x} = 1.08 \cdot \Delta_{u,x} \tag{4-18}$$

Therefore, applying a 100-40 directional combination rule suggests an increase in the uni-directional displacement demand by a factor of 1.08 and the maximum bi-directional displacement predicted considering uni-directional capacity and demand curves is equal to:

$$\Delta_{u,xy} = 1.08 \cdot 443\,mm = 478\,mm \tag{4-19}$$

4.4.2 Example Simplified Analysis (Bi-directional Behavior)

For comparison and further discussion, the bi-directional capacity and demand curves are developed. The bi-directional capacity curve is defined by the bi-directional yield force, $P_{y,xy}$ of (4-15), such that:

$$P_{y,xy} = \sqrt{2} \cdot P_{y,uni} = \sqrt{2} \cdot \frac{w_v}{2}\left(1 + \eta_L\right) \cdot \frac{d}{h} = \sqrt{2} \cdot \frac{1730\,kN}{2}\left(1 + 0.5\right)\frac{1}{4} = 458\,kN \tag{4-20}$$

and the yield displacement, $_{y,xy}$, is given by (4-14). This yield displacement depends largely on the displacement direction angle, . The angle considered here for design is based on the 100%-40% directional combination rule such that:

$$\alpha = \tan^{-1}\left(\frac{0.4}{1.0}\right) = 0.38\,rad.$$ (4-21)

Using (4-13) and (4-14), the yield displacement is equal to:

$$\Delta_{y,xy} = \left(38.9\,mm + 2 \cdot 8.55\,mm \cdot \frac{4}{1}\right) \cdot \sqrt{1 + \frac{1}{[\tan(0.38\,rad.)]^2}} = 289\,mm$$ (4-22)

The bi-directional spectral demand curve considers the seismic demand in the two orthogonal directions. In most cases the seismic demand is assumed equal in the two orthogonal directions and taken in the form of a site design spectrum. While this demand is assumed the same in each direction ($S_{a,x}=S_{a,y}=S_a$), each motion can be assumed to be uncorrelated in each direction (i.e. not in-phase). Considering a 100-40 directional combination rule, the bi-direction design spectrum is formed from the uni-directional design spectrum by increasing its magnitude by 1.08 such that:

$$S_{a,xy} = \sqrt{(1.0 \cdot S_{a,x})^2 + (0.4 \cdot S_{a,y})^2} = 1.08\,S_a$$ (4-23)

The equivalent viscous damping is obtained similarly to that for uni-directional response, such that:

$$\xi_{eff} = \xi_o + \frac{\eta_L}{1+\eta_L} \cdot \frac{2}{\pi} \cdot \left(1 - \frac{1}{\mu_{G2,xy}}\right)$$ (4-24)

except that the displacement ductility, $_{G2,xy}$, is taken as:

$$\mu_{G2,xy} = \frac{\Delta_{u,xy}}{0.40 \cdot \Delta_{y,xy}}$$ (4-25)

using a 100-40 directional combination rule. This results in an idealized bi-linear capacity curve with =0.38rad. as seen in figure 4-11. The actual bi-directional capacity curve is also shown in that figure. It is observed that the two curves have the same maximum base shear force and have an approximately equal amount of energy dissipation (area beneath capacity curve). Note that the final bi-directional spectral demand curves (i.e. the ones obtained after iterating upon the displacement until a solution converges), are shown in figure 4-11 and the
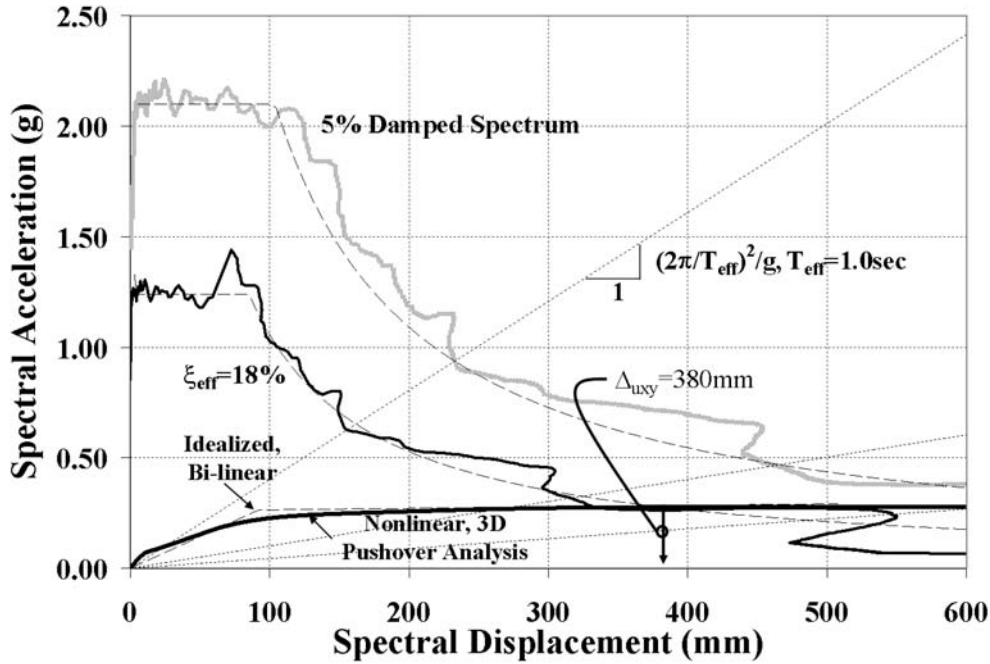
FIGURE 4-11 Bi-directional Spectral Analysis Plot

predicted bi-directional displacement ($\Delta_{u,xy}$) is shown to be equal to 380mm. Thus the resulting maximum displacement in the x-direction is equal to:

$$\Delta_{u,x} = \Delta_{u,xy} \cdot \sqrt{\frac{1}{1 + \tan^2 \alpha_d}} = 380\,mm \cdot \sqrt{\frac{1}{1 + \tan^2(0.38\,rad)}} = 353\,mm \qquad (4\text{-}26)$$

Thus the predicted displacement considering bi-directional behavior is less than that predicted using uni-directional behavior.

4.5 Design Applications

The design of a controlled rocking pier for seismic design (or retrofit) requires limiting pier displacements and ductility demands to the device while capacity design principles are applied to the pier and superstructure. The design process for 2-legged piers has been illustrated in detail in Pollino (2004). Here, those concepts are expanded upon to discuss the key design constraints to achieve the performance objectives for controlled rocking 4-legged piers. Also, simplified methods of predicting the key response quantities to satisfy the design constraints are discussed. More explicitly, these response quantities include pier

displacements (or pier drift), uplifting displacements, and maximum pier forces (frame shear, pier leg axial force).

4.5.1 Pier Displacements

Pier displacement limits will vary from bridge-to-bridge and should be met to achieve the desired seismic performance of the bridge. Since the design intent requires the pier to remain elastic and all inelastic action is to occur through rotations at the base of the structure, limits on structural drift typically set to prevent excessive damage are not relevant for a controlled rocking pier. Limits on the pier displacements may be set to ensure pier stability or to prevent excessive movement of the bridge deck at abutments or other piers. For instance, longitudinal bridge deck movement must be limited to prevent potential unseating of spans where it is connected with roller supports for thermal expansion. Maximum displacements of a controlled rocking pier can be predicted using the capacity spectrum analysis method discussed on Section 4.4.

4.5.2 Uplifting Displacements

The design of the steel yielding devices requires limiting the pier leg uplifting displacements such that the devices behave in a stable, predictable manner during the design level of excitation. Provided the maximum pier displacements are known, the maximum uplifting displacement under bi-directional response is determined from (4-6) and using a 100-40 directional combination rules such that:

$$\Delta_{up,100-40} = \left[\max\left(\begin{array}{c} 1.0\Delta_{u,x} + 0.40\Delta_{u,y} \\ 0.40\Delta_{u,x} + 1.0\Delta_{u,y} \end{array} \right) - \frac{F_{F1} + F_{F4}}{k_f} \right] \cdot \frac{d}{h} \qquad (4\text{-}27)$$

Many types of steel yielding devices exist that could be used in this application to provide bi-linear hysteretic behavior and dissipate energy through plastic deformations of steel. Limiting of the uplifting displacement is presented here for the use of buckling-restrained braces (AISC, 2005). For this type of steel yielding device, the limit on the uplifting displacement can be expressed in terms of a limiting axial strain on the BRB's inner steel core through the following relationship:

$$\Delta_{up,100-40} \le \left(\varepsilon_{ub} \right)_{limit} \cdot L_{ub} \qquad (4\text{-}28)$$

where $(\varepsilon_{ub})_{limit}$=limit on the maximum steel axial strain. The limit should be set based on experimental test data and behavior of such devices under qualified cyclic testing with a loading protocol representative of expected response under earthquake loading and at displacements exceeding the strain limit set here. The AISC Seismic Provisions for Structural Steel Buildings (2005) can provide guidance on the qualification testing of such braces. Based on available literature on the behavior of such devices, a well-detailed BRB can successfully sustain repeated cycling at axial strain levels of 3% or greater (Iwata et. al. 2000). The maximum uplifting displacements can be controlled by limiting the displacements at the top of the pier and using (4-27).

4.5.3 Maximum Pier Forces

Maximum pier forces developed during rocking response need to be predicted conservatively, such that the pier can remain elastic during a seismic event (capacity protection), and with reasonable accuracy for an economical design. For the case of 4-legged piers, the structure needs to be designed for its response under 3 components of earthquake excitation. Maximum forces are determined using directional and modal combination rules to combine the effects of bi-directional rocking of a pier subjected to 3 components of ground motion including the dynamic forces that result from activation of higher vertical modes from impact and uplift of the pier. The 100%-40% directional combination rule (ATC/MCEER 2004) is used for combining horizontal and vertical excitation effects and the SRSS modal combination rule is used for the dynamic forces (a CQC modal combination rule could also be used in place of the SRSS rule). During the rocking response, the impacting and uplift of pier legs causes the excitation of vertical modes of vibration as discussed in Pollino (2004). The dynamic amplification factors determined for 2-legged piers (R_{dv} and R_{dL}) are also applied to controlled rocking 4-legged piers.

First, consider force demands generated by the bi-directional horizontal response of a pier. For this nonlinear earthquake resisting system, the maximum generated static forces are limited by the development of the plastic mechanism. Applying the 100%-40% directional combination rule, forces are calculated as a result of the simultaneous pier displacements in each direction (1.0 $\Delta_{u,x}$ and 0.4 $\Delta_{u,y}$; or vice versa) since the structure is nonlinear. Referring

back to the discussion in Section 4.3.1, assuming a displacement along a path with =atan(0.4/1.0)=21.8deg. results in development of the bi-directional yield mechanism (3 devices yielding) if the larger direction has a global uni-directional displacement ductility greater than 2.5 (1.0/0.4=2.5, $_{G2,uni}$=2.5). In other words, if the controlled rocking pier is designed for at least a global displacement ductility of 2.5 in a single direction, then the bi-directional yield mechanism is expected to form, resulting in static forces as shown in the free-body diagram in figure 4-3. Therefore, under these assumptions, regardless whether the 100-40, 40-100, or 40-40 combination of the two horizontal demands is used, the forces resulting from development of the bi-directional yield mechanism should be considered.

The effect of the vertical excitation is included by determining the design vertical spectral acceleration value at the vertical period of the pier, T_L, which is taken equal to:

$$T_L = 2 \cdot \pi \sqrt{\frac{m_v/4}{k_L}} = 2 \cdot \pi \sqrt{\frac{m_v}{4\,EA_L/h}} \tag{4-29}$$

where A_L=cross-sectional area of a pier leg and m_v=vertical tributary mass of the pier. This is the "fixed-base" period of the pier since the pier is intended to remain elastic during an earthquake. However, one could argue that the vertical period increases as the pier uplifts from its supports and becomes more flexible vertically, and the spectral acceleration value could decrease as a result of this phenomenon. However, for simplicity and conservatism, the "fixed-base" spectral acceleration value is used here. The maximum vertical force applied to the pier as a result of the vertical excitation is thus simply equal to $m_v S_{av}$.

Including the dynamic forces caused during impact and uplift along with the effects of vertical excitation, the free body diagram of each pier frame is shown in figure 4-12. The dynamic forces are all shown in figure 4-12 with their maximum values and all applied in the same direction (downward).

Using these free-body diagrams forces in critical members, connections, and other components can be determined by applying appropriate combination rules to these demands (since the forces shown are the maximums of each effect). Use of the combination rules to
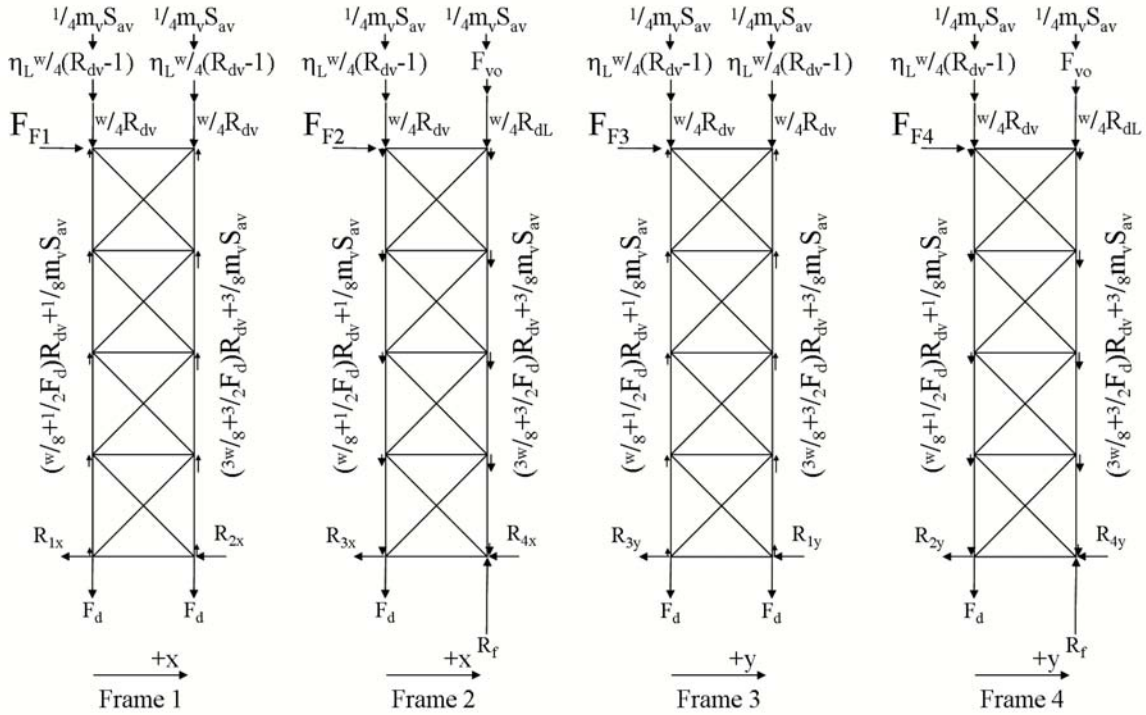
FIGURE 4-12 Free-body Diagrams of Frames Including Forces due to Dynamic Effects

determine critical pier forces, such as frame shear forces and pier leg axial forces, will be presented in the next two subsections.

4.5.3.1 Maximum Frame Shear

The maximum frame shear (P_{uF}) that develops, including dynamic effects, can be determined using the free-body diagram of figure 4-12 applying the appropriate combination rules. The maximum frame shear includes a term from the uplift of the pier and yielding of the devices times the dynamic amplification factor during uplift (R_{dv}) and the effect of vertical excitation. Using an absolute sum combination rule, the maximum frame shear can be determined directly from equilibrium of forces shown in figure 4-12 such that:

$$P_{uF,ABS} = P_{uF,st} \cdot R_{dv} + \frac{3\,m_v}{8} \cdot S_{av} \cdot \frac{d}{h} \tag{4-30}$$

where $P_{uF,st}$=maximum frame shear considering static response and is equal to (4-10).

96

As discussed previously, application of the 100-40 directional combination rule to the 2 horizontal components of motion results in development of the bi-directional yield mechanism for $_{G2,uni}$>2.5. However, when the third (vertical) component is included in the combination rule, the dynamic effect resulting during uplifting (R_{dv}) is combined with the vertical excitation using the combination rule due to their non-simultaneity and the design frame shear force is taken as:

$$P_{uF,100-40} = \max \begin{cases} P_{uF,st} + 1.0 \cdot P_{uF,st} \cdot (R_{dv} - 1) + 0.4 \cdot \left(\dfrac{3\,m_v}{8} \cdot S_{av} \cdot \dfrac{d}{h} \right) \\[2ex] P_{uF,st} + 0.4 \cdot P_{uF,st} \cdot (R_{dv} - 1) + 1.0 \cdot \left(\dfrac{3\,m_v}{8} \cdot S_{av} \cdot \dfrac{d}{h} \right) \end{cases} \qquad (4\text{-}31)$$

4.5.3.2 Maximum Pier Leg Axial Force

The maximum developed axial force in a pier leg (P_{uL}) can be determined by equating vertical equilibrium from figure 4-12. Applying an absolute sum combination rule, the foundation reaction (R_f) beneath the pier leg is equal to:

$$R_f = m_v \cdot S_{av} + v_o \cdot \sqrt{\frac{m_v k_L}{4}} + \frac{w_v}{4} \cdot R_{dL} + \left(\frac{3 \cdot w_v}{4} + 3 F_d \right) \cdot R_{dv} \qquad (4\text{-}32)$$

Considering that two pier diagonals connect to the base of the compressed pier leg, such that their load is applied directly into the support, the maximum load on the pier leg is less than the support reaction. Considering equilibrium at the base of the pier leg in figure 4-12 and applying an absolute sum combination rule (both directional and modal), the force developed in the pier leg, P_{uL}, is defined by:

$$P_{uL,ABS} = \begin{aligned} & P_{uL,st} + \left[\frac{1}{4} m_v \cdot S_{av} + \frac{3}{4} m_v \cdot S_{av} \cdot \left(1 - \frac{d}{2h} \right) \right] + v_o \cdot \sqrt{\frac{m_v k_L}{4}} + \dots \\ & \dots + \frac{w_v}{4} \cdot (R_{dL} - 1) + \left(\frac{3 \cdot w_v}{4} + 3 F_d \right) \cdot (R_{dv} - 1) \cdot \left(1 - \frac{d}{2h} \right) \end{aligned} \qquad (4\text{-}33)$$

The five terms are a result of uplifting and yielding devices, vertical excitation, and the dynamic effects that occur during pier rocking. The first term, $P_{uL,st}$, is the axial force generated statically in the pier leg as a result of development of the bi-directional yield mechanism and is equal to:

$$P_{uL,st} = \left(\frac{3w}{4} + 3 \cdot F_d \right) \cdot \left(1 - \frac{d}{2h} \right) + \frac{w}{4} \qquad (4\text{-}34)$$

The second term is the pier leg force resulting from vertical excitation and will be noted as F_{ve}. The third term results from the initial impacting of the pier leg after it has uplifted and is returning to its support (F_{vo}) with an impact velocity v_o. The fourth term is the dynamic effect of the weight tributary to a single pier leg being suddenly applied as the leg returns to the support (F_w). The fifth term is the dynamic effect of the remaining pier tributary weight and devices' forces sudden transfer to the compressed pier leg during uplift (F_{up}). The dynamic amplification factors, R_{dv} and R_{dL}, are used to account for the vertical modes of vibration activated as a result of the rocking behavior and are discussed in Section 2.

To account for the fact that all of these forces are not occurring at the same instance in time, directional and modal combination rules are applied to (4-33). As was the case for using the directional combination rule maximum frame shear forces, it is assumed that applying the 100-40 directional combination rule results in development of the bi-directional yield mechanism such that the first term, $P_{uL,st}$, exists in all combinations. Terms 3, 4, and 5 in (4-33) are a result of horizontal motion and excite different modes and are combined using an SRSS modal combination rule. Finally, the second term (resulting from vertical excitation), is combined using a 100-40 directional combination rule with the SRSS combination of terms 3, 4, and 5 such that the maximum pier leg force is equal to:

$$P_{uL,\,100\text{-}40} = \max \begin{pmatrix} P_{uL,st} + 0.4 \cdot F_{ve} + 1.0 \cdot \sqrt{F_{vo}^{\;2} + F_w^{\;2} + F_{up}^{\;2}} \\ P_{uL,st} + 1.0 \cdot F_{ve} + 0.4 \cdot \sqrt{F_{vo}^{\;2} + F_w^{\;2} + F_{up}^{\;2}} \end{pmatrix} \qquad (4\text{-}35)$$

The impact velocity of the pier leg, v_o, can be determined using the energy balance approach developed in Section 3 where energy is equated at the point of maximum deformation and just before the point of leg impact with the support with the non-conservative work done by the energy dissipation devices included between these two points. This approach does not take into account work done by the ground motion during the time the frame moves between

these two positions. Considering uni-directional motion (i.e. in the x-direction) and the use of an elasto-plastic steel yielding device, the impact velocity could be taken as:

$$v_{o,x} = \sqrt{g \left(\frac{1}{\frac{1}{4}\left(\frac{h}{d}\right)^2 + \frac{1}{2}} \right) \cdot \left[\frac{w}{2} \frac{\eta_L^2 - 1}{k_{o,x}} \left(\frac{d}{h}\right)^2 + 2\eta_L \Delta_{yd} + \Delta_{u,x} \frac{d}{h}\left(1 - \eta_L\right) \right]} \qquad (4\text{-}36)$$

However, in this case, the impact velocity depends on the pier's motion in two directions. The maximum impact velocity is taken as the sum of the impact velocity as a result of the of the pier's motion in the two horizontal directions (v_{ox}, v_{oy}) such that the total impact velocity, v_o, is equal to:

$$v_o = v_{o,x} + v_{o,y} \qquad (4\text{-}37)$$

Using a 100%-40% directional combination rule, the velocity in one direction (say, the x-direction) is calculated using (4-36) with 1.0 $_{u,x}$ and in the other direction with 0.4 $_{u,y}$, whichever produces the larger velocity.

4.6 Dynamic Analysis Example

A set of dynamic time history analyses are conducted to further investigate the bi-directional response and to compare with the simplified analysis approach of Section 4.4 and the design equations presented in Section 4.5. The pier properties, energy dissipating devices, and seismic demand parameters used are the same as those discussed in Section 4.4.1 and have been used throughout the section. In that section, a generic set of steel yielding device properties are used ($_L$=0.5, k_d=36.9kN/mm). Buckling-restrained brace dimensions that provide these properties are A_{ub}=9.23cm^2, L_{ub}=5.00m, and F_{yub}=234MPa. The same horizontal demand spectrum (shown in figure 4-13) is considered and the vertical spectrum is determined by shifting the characteristic period of the horizontal spectrum, T_s (defined in ATC/MCEER 2004), to a shorter period range and reducing the amplitude of the horizontal spectrum. For the case considered, the characteristic period is reduced by a factor of 1.55 and the amplitude is reduced by a factor of 1.25 resulting in the vertical design spectrum in figure 4-13.
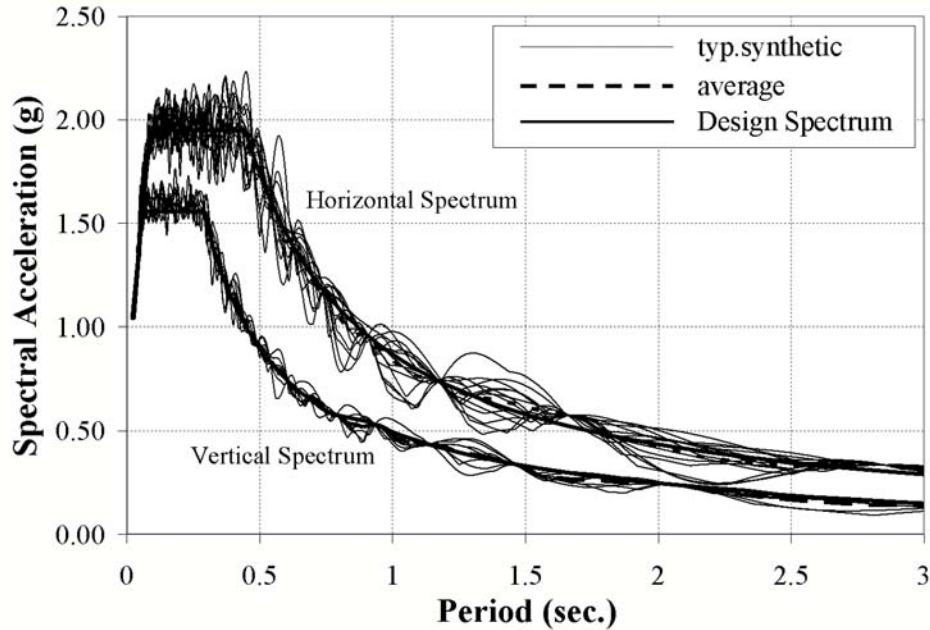
FIGURE 4-13   Horizontal and Vertical Synthetic Spectrum

4.6.1   Simplified Analysis and Design Response Predictions

The maximum pier displacement in one of the primary directions considering uni-directional pier properties is predicted using the simplified analysis procedure and was shown equal to 443mm in Section 4.4.1 resulting in a total bi-direction displacement (using 100-40 directional combination rule) of 478mm. The maximum uplifting displacement can then be calculated from (4-27), (4-9), and (4-10) and is equal to:

$$\Delta_{up,100-40} = \left[1.0 \cdot (443\,mm) + 0.40 \cdot (443\,mm) - \frac{81.1\,kN + 243\,kN}{6.25\,kN/mm} \right] \cdot \frac{1}{4} = 142\,mm \quad (4\text{-}38)$$

which results in a maximum buckling-restrained brace strain of:

$$\varepsilon_{ub} = \frac{\Delta_{up,100-40}}{L_{ub}} = \frac{142\,mm}{5000\,mm} = 0.028 \quad (2.8\%) \tag{4-39}$$

The dynamic amplification factors (R_{dv} and R_{dL}) are determined using the methods presented in Section 2 and are equal to 1.84 and 1.97 respectively. The vertical spectral acceleration value is determined from the vertical spectrum of figure 4-13 at the vertical period of the pier (4-29) which is equal to:

$$T_L = 2 \cdot \pi \sqrt{\frac{(1730\,kN) \cdot (29.26\,m)}{4 \cdot g \cdot (200\,GPa) \cdot (171\,cm^2)}} = 0.12\,\text{sec} \qquad (4\text{-}40)$$

The vertical period lies in the constant acceleration region of the spectrum and the vertical spectral acceleration value is equal to 1.56g as seen in figure 4-13. The maximum frame shear, from (4-31), is equal to 548kN and the maximum pier leg axial force is determined from (4-35) and is equal to 4290kN.

4.6.2 Ground Motions

Spectra compatible ground acceleration time histories were used for the base excitation of the analytical model and are generated using the Target Acceleration Spectra Compatible Time Histories (TARSCTHS) software developed by the Engineering Seismology Laboratory (ESL) at the University at Buffalo (http://civil.eng.buffalo.edu/users_ntwk/index.htm). Synthetic ground motions were generated by TARSCTHS to match the elastic response spectrum for the Northridge, CA site discussed in Section 4.4.1. Seven ground motions are made for each direction (x, y, and z) matching the target design spectrum as shown in figure 4-13. Since the design spectrum is assumed equal in the two horizontal directions, 14 acceleration histories were randomly generated to match the horizontal design spectrum.

4.6.3 Analytical Model

The dynamic response of the structure was predicted analytically using the program SAP2000 and is very similar to the model used in Section 3 (with a large displacement formulation) however a 3-dimensional analysis is performed for the 4-legged pier. The model mass is lumped in a single node at the assumed center of mass (geometric center at the top of the pier) and acts in the 3 translation DOF. This node is then constrained to move as a rigid diaphragm with the nodes at the top of the pier legs. The pier's structural members are assumed to remain elastic and are modeled with elastic frame elements with rigid end offsets at the connection points. The diagonal braces are modeled by members that can only resist axial forces (in tension and compression).

Compression-only gap elements were attached to the base of the legs in the vertical and two horizontal directions to simulate a base connection that relied on bearing to resist forces in these three directions (similar to a connection used for the experimental test specimen discussed in Section 5.4.1). The gap elements provided no resistance to movement vertically upward at the base of the leg, or horizontally towards the inside of the pier (directions that would otherwise apply tension to the elements) and were assigned an elastic stiffness of 1750kN/mm.

A set of general steel yielding devices were modeled using the Wen (1976) plasticity property and an elastic stiffness and yield force were assigned corresponding to the device properties stated above ($_L$=0.5, k_d=36.9kN/mm). A post-elastic stiffness was assumed to be 2% of its elastic value and the yielding parameter was set equal to 2.

All other relevant details of the analytical model are discussed in Section 3.2.2.2 and 3.3.

4.6.4 Results and Discussion

The results of the seven time history analyses are shown in figure 4-14. All plots are presented with the value of the design response quantity (calculated in Section 4.6.1) on the horizontal axis (single value, x-coordinate) and the peak result from each time history analysis shown on the vertical axis (y-coordinate). The result of each time history analysis is shown as a data point, along with the mean (large solid horizontal bar), mean+ , and mean- response (smaller horizontal bars connected to mean bar) of all results. Also, a solid diagonal line on each plot divides the range of conservative and unconservative prediction of response (y=x). Data points below this line represent conservative prediction of response for which the result of time history analysis was less than the predicted response, and points above the line represent unconservative predictions. Both uni-directional and bi-directional pier displacements ($_{u,x}$, $_{u,y}$, and $_{u,xy}$) are shown in figure 4-14a since the simplified methods of analysis predict each of these quantities. The maximum of the uplifting displacement of the 4 pier legs, frame shear force of the 4 pier frames, and axial force of the 4 pier legs are presented in figure 4-14b, c, and d respectively.

The uni-directional displacement values in the x-direction are predicted conservatively by approximately 12% with respect to the mean result of the time history analyses and the y-direction displacement predicted almost exactly. However, the bi-directional displacement prediction is slightly unconservative (~8% difference) using the 100-40 directional combination rule. The uplifting displacement results deviate from the predicted response by approximately the same percentage as the bi-directional displacement, $\Delta_{u,xy}$ (~9%), as would be expected since the uplifting displacement is primarily dependent on prediction of the maximum bi-directional pier displacement and uses the 100-40 combination rule. The maximum frame shear force and pier leg axial force are predicted more conservatively (14% and 16% difference, respectively).

4.7. Summary

The uni-directional and bi-directional kinematic and hysteretic properties of controlled rocking, 4-legged steel truss piers have been investigated. Key variables for the cyclic hysteretic behavior of controlled rocking piers have been identified considering bi-directional horizontal response and analytical expressions have been developed for their calculation. Results of nonlinear static pushover analysis are presented and compared with results obtained from these analytically derived expressions, and shown to be in good agreement. A simplified method of analysis has been proposed for prediction of maximum pier displacements considering the path dependent hysteretic behavior of 4-legged controlled rocking piers. Design rules have been established to determine maximum displacement demands on the energy dissipating devices and to achieve capacity protection of the pier. The design rules account for three components of ground excitation and dynamic effects caused by impacting and uplifting during the rocking response. It was proposed that uni-directional hysteretic properties be used for prediction of displacements since these properties would provide a lower bound on the pier's force and energy dissipating capacity thus providing an upper bound on prediction of the maximum displacement. On the other hand, bi-directional hysteretic behavior is considered for prediction of maximum forces to provide an upper-bound and conservative estimate of the force response. This could be considered a type of bounding analysis for design. Nonlinear dynamic time history analyses were performed to assess the effectiveness of the proposed design rules. Results of the

analyses found the design rules to conservatively predict response with respect to the mean response, except that results were slightly unconservative when using the 100-40 directional combination rule for prediction of displacement response (bi-directional pier displacement and uplifting displacement).
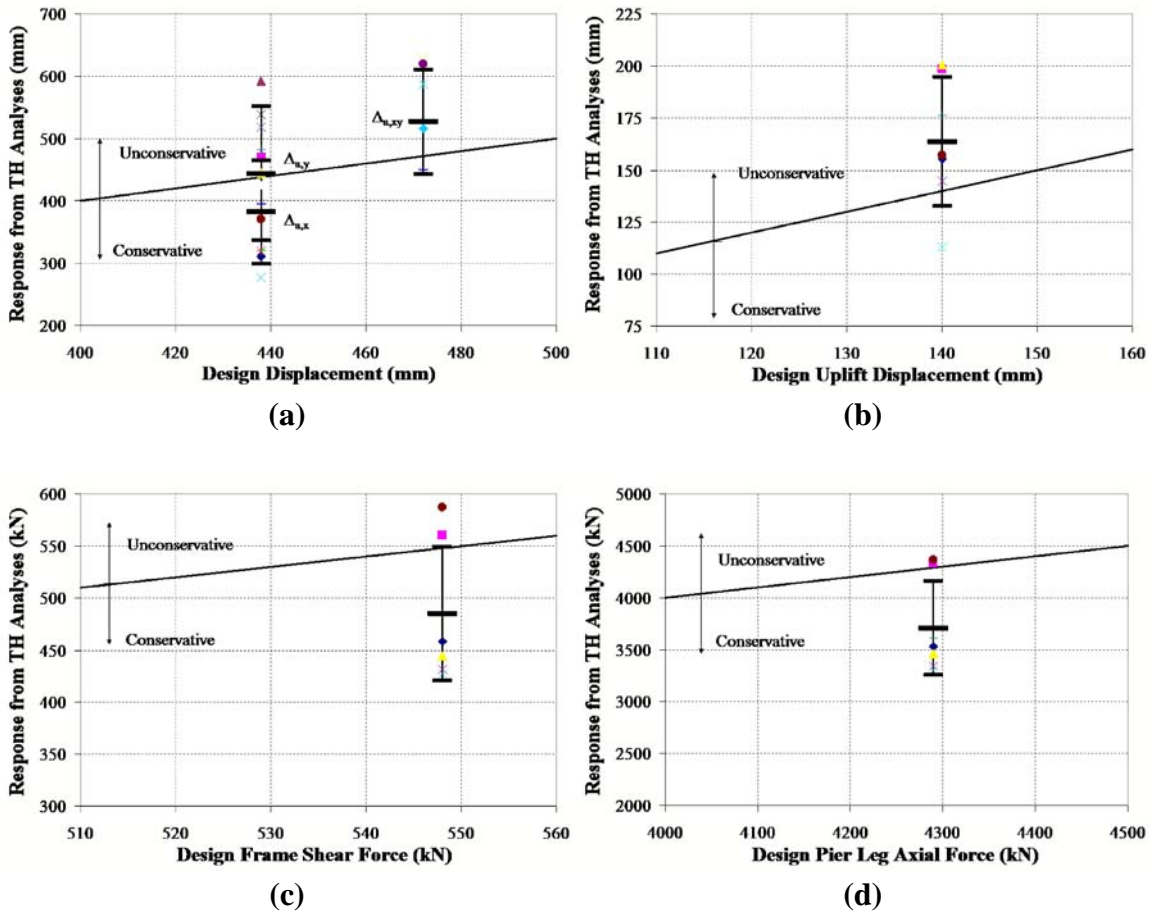
FIGURE 4-14   Results of Dynamic Analyses and Design Response Values (a) Max. Pier Displacements; x-, y-, and x-y directions, (b) Max. Uplifting Displacements, (c) Max. Frame Shear, and (d) Max. Pier Leg Axial Force

SECTION 5

SEISMIC TESTING OF A 1/5-LENGTH SCALE 4-LEGGED BRIDGE PIER- DESIGN OF SPECIMEN AND TESTING PROGRAM

5.1 General

The experimental testing program of this research was conducted in two phases in the Structural Engineering and Earthquake Simulation Laboratory (SEESL) at the University at Buffalo (UB). The primary differences between the two phases of testing were the earthquake simulators and energy dissipating devices used during testing. Phase I tests were conducted on a 5 degree-of-freedom (DOF) shake table that could not apply input motion to one of the horizontal translation DOF. The experimental specimen was attached to the table in two different orientations for testing during Phase I. In the first orientation (=0), the specimen was attached with two of its frames parallel to the direction of horizontal shaking and in the second orientation (=45) the specimen was rotated (in plan) by 45deg. The specimen is seen on the 5DOF shake table in each orientation in figure 5-1. The purpose for this was to first investigate the uni-directional response of the controlled rocking system under solely horizontal and horizontal and vertical motions. The specimen was then rotated to investigate behavior that would be associated with bi-directional response using the 5DOF table. Phase II of testing was performed on a 6DOF shake table that allowed investigation of true bi-directional controlled rocking response.

The scaled model considered for testing is based on a prototype bridge steel truss pier which is discussed in Section 5.2. The prototype pier is considered to be representative of a typical 2-lane highway bridge supported on such piers. Following similitude scaling requirements and based on the available laboratory resources, a 1/5-length scale model was used in this study. The experimental specimen utilized was a steel structure that has been used for previous testing at UB (Yao 1991). Modifications were made to the existing structure to satisfy similitude requirements deemed most relevant, and for connection of the steel yielding devices and artificial mass. The similitude scaling laws and factors are discussed in Section 5.3. Section 5.4 provides the important properties of the model specimen and the passive energy dissipation devices used during each phase of testing. The experimental

testing facilities in the SEES Laboratory and instrumentation used are discussed in Sections 5.5 and 5.6 respectively. Finally, the model base excitation used is presented in Section 5.7 and the testing program described in Section 5.8.

5.2 Discussion of Prototype Pier

Prototype pier properties are based on a brief review of drawings of existing bridges supported on steel truss piers that was the basis for the analytical work in previous sections. The prototype bridge pier is assumed to support a segment of a 2-lane highway bridge deck between the bridge's abutments. The pier is assumed to have a tributary inertial mass in the longitudinal and transverse directions equal to its vertical mass. In general, steel truss pier diagonals tend to have a constant cross-section in each pier panel and pier legs are continuous over its height. Connection of beam members to pier legs typically were such that they could be considered pin-connected however moment resisting connection details were observed in some cases. Connection of the bridge deck to pier varies considerably depending on the type of bridge bearing used. For the purpose of this study, the connection of the bridge deck to pier is assumed to be pin-connected near the top of each pier leg. Prototype pier properties deemed relevant for dynamic testing are given in table 5-1

5.3 Similitude Scaling and Artificial Mass Simulation

The design, construction, and testing of any structural model must follow a set of similitude requirements in order for the behavior of the model to truly replicate that of the prototype structure. The fundamental quantities (Q) relevant for modeling of dynamic behavior are length (L), force(F), and time (T). Due to limitations of available materials to replicate the inelastic response expected to occur as a result of earthquake loading and the requirement of constant acceleration scaling (gravitational acceleration exists in both the prototype and model), an artificial mass simulation scaling law is often used. This scaling law has been used in many experimental tests investigating response of structures to earthquakes (Harris and Sabnis 1999).

It was desired to have the largest scaled model reasonably possible given the available resources in the laboratory (table size, capacity; vertical clearance). Model scale was

ultimately controlled by the vertical distance from the shake table to a workable crane clearance height (~7m). This led to a model height of approximately 6m and a length scale factor of 5 based on the prototype height of 29.3m.

The important quantity scale factors required following the artificial mass simulation scaling law are given in table 5-2. The scale factors, , are defined as the ratio of the prototype quantity to the model quantity such that:

$$\lambda = \frac{Q_{prototype}}{Q_{model}} \qquad (5\text{-}1)$$

For constant acceleration scaling and since the model is made of the same material as the prototype (steel), the acceleration scale factor, $_a$, and the elastic modulus scale factor, $_E$, are equal to one. The length scale factor, $_L$, is taken to be 5. Based on the scale factors in table 5-2, the required model properties and properties provided after modifications discussed in Section 5.4 are shown in table 5-1.

It was discovered that an existing slender steel specimen in the laboratory, that has been used in past testing, was available and provided most of the required relevant model properties reasonably well. Additional details of the specimen can be found in Yao (1991). A photograph of the specimen is shown in figure 5-1 on the 5DOF shake table. However, some modifications were made to the existing structure to better satisfy similitude requirements as well as for strength purposes. The primary similitude requirements targeted were the "fixed-base" lateral and vertical period of vibration of the model (T_{om} and T_{Lm}), the shearing mode period of vibration (T_{vm}), and the applied and restoring forces of the model, which would be controlled primarily by the added mass. The specimen modifications required are discussed in more detail in Section 5.4.

Although an added mass of 69.2kN/g is required by similitude, steel plates totaling 80.1kN/g were used since they were readily available in the laboratory. Influence of the connection of the added mass to the pier specimen on possibly engaging the steel plates was investigated to ensure that the added mass did not artificially stiffen the specimen and is discussed in Section 5.4.3.

5.4 Specimen Properties

The experimental model specimen is discussed in detail in this section. The specimen had an aspect ratio of 4.0 thus matching the prototype aspect ratio. However, the specimen had five truss panels along it height unlike the prototype structure that had square panels (thus four panels along the height). Where appropriate, modifications are made to previously developed equations to account for this difference in structural properties. To meet similitude and strength requirements and to develop the desired rocking response, modifications were required primarily at the base of the structure (Section 5.4.1). The truss diagonal members also needed special consideration (Section 5.4.2). Forces used to design the specimen were determined using concepts presented in Section 4 that consider bi-directional yielding and dynamic amplification resulting from the excitation of the vertical modes of vibration. Connection of the mass to the pier is discussed in Section 5.4.3. Design of the passive energy dissipation devices and their connections are discussed in Section 5.4.4.

5.4.1 Base Modifications

Modifications made to the base of the pier specimen included removing existing base plates, attaching new plates to the base of the columns; adding column flange cover plates, column web doubler plates, beam-column transverse stiffeners, and a base perimeter beam (collector beam). Dimensions and weld details of these modifications are shown in figure 5-2.

The connection at the base of the pier legs to their supports is critically important in developing the boundary conditions that allow the rocking response. As has been discussed previously, the connection needs to resist translation (sliding) in the two horizontal directions but should allow vertical translation (uplift) from the support. First, load cells were placed beneath the base of each pier leg to record pier base reactions during testing. Connection of the pier base to the load cells is done through a horizontal bearing "pit" connection using angle members that are bolted to the top of each load cell as shown in figure 5-3. No resistance is provided vertically through this connection except for friction that may occur along an angle's leg as the pier leg uplifts from the load cell. The angles were only placed on the two outer sides of the load cells in contact with the two outer sides of the column base plates such the horizontal shear force of the pier would not be transferred at the base of the

uplifting pier legs. Such placement of the angle members limited the amount of contact the base of the pier legs would have with the base connection during uplifting while resisting horizontal shear at the base of the other legs and thus preventing sliding. Shown in figure 5-4 is the assumed shear transfer at the base of the structure. The base connection is also capable of transferring torsion in the pier that may develop as a result of accidental eccentricities.

5.4.2 Pier Diagonals

Pier diagonals were designed in order to meet similitude and strength requirements. The existing specimen had moment-resisting beam-column connections such that when the pier diagonals were added, the specimen acted as a braced moment frame. The lateral flexural stiffness of the existing moment frame could be determined using a portal frame method of analysis (Hibbeler 1999) to make the indeterminate system determinant by assuming points of inflection at mid-span of the beams and mid-height of the columns, ignoring shear and axial deformations, and resolving internal forces. The lateral flexural stiffness of the pier is different considering whether bending of the pier legs occurs about their larger (k_{oXMF}) or smaller (k_{oYMF}) moment of inertia and shown to be equal to 0.52 and 0.34kN/mm respectively. The bending (overturning) stiffness of the pier, k_{oBm}, is calculated simply as:

$$k_{oBm} = \frac{3E_m I_{pm}}{h_m^3} = \frac{3E_m \left(n_f 2A_{Lm} \dfrac{d_{clm}^2}{2} \right)}{h_m^3} \qquad (5\text{-}2)$$

where n_f=number of frames acting in the direction of interest, A_{Lm}=cross-sectional area of the pier leg, d_{clm}=center-to-center distance between the pier legs, and h_m=height of the model. The shear stiffness of the pier specimen from the added diagonals in an X-braced configuration can be calculated as:

$$k_{oTm} = 2 \cdot \left[\sum_{i=1}^{n_p} \frac{L_{dmi}}{2A_{dmi}E_m \cos^2\theta_{di}} \right]^{-1} \qquad (5\text{-}3)$$

where n_P=total number of panels (i) along the height of the specimen, A_{dmi}=cross-sectional area of the diagonal in panel i, $_{di}$=angle the diagonal in panel i makes with the horizontal, L_{dmi}=length of the diagonals in panel i. The two in the front of the bracketed term is due to

the fact that the four legged specimen pier has two frames that act in each direction. The total pier stiffness is equal to:

$$k_{om} = \left(\frac{1}{k_{oTm} + k_{oMFm}} + \frac{1}{k_{oBm}} \right)^{-1}$$ (5-4)

since the moment frame and diagonal members act in parallel to resist the shear deformations and the pier legs resist the pier's overturning deformations.

The cross-sectional area of the diagonal members (A_{dmi}) were sized such that the fixed-base and vertical periods of the specimen were close to that required by similitude and would have the required strength to resist demands resulting from formation of the bi-directional yield mechanism and the dynamic effects (discussed in Section 4.5). Considering an X-braced configuration, resulted in the use of high-strength circular threaded rod (ASTM A193 B7, $_y$=869MPa) diagonal bracing members with a 9.5mm diameter. Such members have essentially no buckling capacity thus could not be relied on in compression. These members would have likely undergone elastic buckling during testing creating a tension-only bracing system. The prototype was not designed as a tension-only system and it was undesirable to have the dynamic effects, generally associated with such a system, participate in the response. Therefore, all diagonal bracing members were pre-tensioned to a prescribed axial force level such that these members would have a net tension force during testing and not develop compressive forces. The pre-tensioning was achieved by using right and left-handed threaded rod for the bracing members and connecting them with a reverse threaded hex coupler as seen in figure 5-5. A strain gauge was attached on one face of the hex coupler to measure strain and determine pre-tensioning force during installation and to measure force in the bracing member during testing.

From the specimen properties in table 5-1, the overturing specimen of the pier, k_{oBm}, is equal to:

$$k_{oBm} = \frac{3(200GPa)\left[2 \cdot 2\left(15.5cm^2\right)\frac{(132cm)^2}{2}\right]}{(609cm)^3} = 14.3\,kN/mm$$ (5-5)

The shear stiffness of the frame from the added diagonal members is:

$$k_{oTm} = 2 \cdot \left[\frac{L_{dm1}}{2A_{dm1}E_m\cos^2\theta_1} + 4 \cdot \frac{L_{dm25}}{2A_{dm25}E_m\cos^2\theta_{25}} \right]^{-1} = 3.46 \, kN/mm \qquad (5\text{-}6)$$

Finally, the use of these diagonal members results in a total pier lateral stiffness of:

$$k_{om} = \left(\frac{1}{3.46\dfrac{kN}{mm} + 0.34\dfrac{kN}{mm}} + \frac{1}{14.3\dfrac{kN}{mm}} \right)^{-1} = 3.00 \, kN/mm \qquad (5\text{-}7)$$

With the added mass of 80.1kN/g, the theoretical lateral period of the pier specimen could be taken as:

$$T_{om} = 2 \cdot \pi \sqrt{\frac{80.1 \, kN}{(9810 \, mm/\text{sec}^2) \cdot (3.00 \, kN/mm)}} = 0.33 \, \text{sec} \qquad (5\text{-}8)$$

Using these properties the vertical modes discussed in Section 2 can be characterized by the vertical pier stiffness, k_L=51.1kN/mm (2-28), vertical shearing stiffness, k_v=42.5kN/mm (2-34), vertical period, T_L=0.040sec (2-29), and vertical shearing period, T_v=0.062sec (2-35).

5.4.3 Mass Connection

Connection of the bridge deck to its piers is typically achieved through the use of some form of bearing (rocker, pot, elastomeric, cylindrical, spherical; AASHTO 1998). Each type of bearing transfers loads between the deck and pier by different mechanisms. For this study, a semi-rigid connection of the mass plates to the truss pier is used.

The connection of the model's mass is designed to transfer shear force in the horizontal plane, vertical forces, and moments between the mass and pier. The connection (figure 5-6) uses 16-9.5mm diameter, fully tensioned high-strength threaded rods (ASTM A193 B7) through the 2-90mm thick steel mass plates, a double concave hardened steel bearing, mild-steel connection plate, and 2-19.1mm plate washers. The shear force was assumed to be transferred through friction between each piece. Using four fully-tensioned rods per connection point could easily transfer the shear force demand however created a semi-rigid connection that allows moment transfer through the connection and could potentially engage the rigid mass, affecting the specimen's dynamic response and artificially stiffen the

111

structure. Also, additional moments would be applied at the top of the pier that need to be designed for. The rotational rigidity of the connection, can be determined using methods of virtual work and shown to equal:

$$k_{\theta mc} = \frac{EA_{mcr}}{L_{mcr}} \frac{d_{mcr}^{2}}{rad.} = 665 \frac{kN \cdot m}{rad.} \qquad (5\text{-}9)$$

where E=elastic modulus of the steel threaded rods (200GPa), A_{mcr}=cross-sectional area of the mass-connection rods (~53.2mm^2), L_{mcr}=length of the mass connection rods (~250mm), d_{mcr}=distance separating the mass connection rods (125mm) as seen in figure 5-6.

The influence of the rotational rigidity of the connection was assessed by including the connection in the analytical structural model of the specimen and performing eigenvalue analysis. The connection was modeled with an elastic element that was rigid in translation and had a rotational stiffness, k_{mc}, about the x- and y-axis. No torsional stiffness was assigned to the connection. The eigenvalue analysis was performed for models for the "fixed-base" and "shearing" modes of vibration to determine the level of stiffening the connection and mass added the specimen. The mode shapes resulting from these analyses are shown in figure 5-7. The lateral period is equal to 0.33sec and the vertical "shearing" modal period is equal to 0.061sec and thus the mass connection did not affect the lateral or shearing periods of vibration.

Therefore, the connection considered here, representing the connection of the bridge deck to the pier does not appear to affect the response compared to the idealized model considered in this research. However, connection between the deck and pier is important in transferring the deck inertia forces.

5.4.4 Passive Energy Dissipation Devices

Steel yielding devices were designed and fabricated for both Phase I and II of the testing. The differences between the devices used in each phase will be discussed later in this section. Also, as part of Phase II, a set of viscous dampers were implemented as the passive energy dissipation devices in the controlled rocking system.

Steel yielding devices with bi-linear hysteretic behavior were designed with connections to provide only a vertical force to the base of the pier legs. The important design quantities for the devices are the plastic device force, elastic stiffness, and maximum allowable vertical displacement. Different steel yielding devices were considered for experimental testing including buckling-restrained braces (AISC 2005) and shear panel devices (Zahrai and Bruneau 1999). However, scaling both the braces and shear panels resulted in devices that were not easily and reliably manufactured or fabricated at this scale.

The number of design parameters for TADAS devices (Tsai et. al. 1993) resulted in dimensions of a device that could be fabricated at this scale. TADAS devices consist of triangular plates that yield in flexure uniformly along its length when a shear force is applied on one end and the plates are bent about their minor axis. The plastic shear force of the device, V_{pT}, can be shown to equal:

$$V_{pT} = \frac{N_T t_T^2 b_T F_{yT}}{4 L_T}$$

(5-10)

where N_T=number of plates, t_T=plate thickness, b_T=plate width at fixed support of device, F_{yT}=yield stress of steel (50ksi, ASTM A572 Gr. 50), and L_T=length of plates from fixed support to point of loading. The elastic stiffness is equal to:

$$k_{eT} = \frac{E b_T N_T}{6} \left(\frac{t_T}{L_T} \right)^3$$

(5-11)

Results of component and sub-assemblage testing (Tsai et. al. 1993) has shown the devices able to easily withstand rotations of 0.15rad.

5.4.4.1 Phase I

For Phase I of testing, three sets of devices were designed and fabricated with local strength ratios ($_L$=V_{pT}/w_{mz}/4) of 1.0, 0.67, and 0.33. Device dimensions were designed to limit rotations on the device to 0.15rad. for the maximum level of shaking prescribed during testing where the device rotation, $_T$, is defined as:

$$\gamma_T = \frac{\Delta_{upL}}{L_T}$$

(5-12)

Fabrication drawings of each set of devices are shown in figure 5-8a. The ball bearing end connections were used to ensure that only the vertical shear force would be transferred between the device and pier leg as it uplifted from its base.

A side view of the connection into the pier leg is shown in figure 5-9. A "slider mechanism" was designed that would allow easy installation and removal of devices between set-ups. The slider utilizes slotted holes and a slip critical connection to allow the mechanism to slide down and bear onto to the devices ball bearing.

5.4.4.2 Phase II

For Phase II of the experimental testing, new sets of devices with local strength ratios ($_L$) of 0.67 and 0.33 were re-designed and fabricated. The design intent for the steel yielding devices in Phase I were to develop a specific plastic shear force and limit the rotation to 0.15rad. (a conservative design rotation). However this led to flexible devices that did not undergo significant ductility demands during testing especially after the devices were on their "2nd cycle" of response and required a larger uplifting displacement prior to yielding. New devices were designed to maximize their elastic stiffness within practical limits while limiting device design rotations to 0.30, thus allowing a larger ductility demand on the devices. A new set of devices were not made for the case of $_L$=1.0 as it was found that its elastic stiffness was already nearly maximized within the practical constraints. Dimensions of the two new sets of devices ($_L$=0.67, 0.33) are shown in figure 5-8b. For comparison, the static hysteretic pushover curve of the experimental specimen with each set of steel yielding devices attached, considering 2nd cycle response and P- effects is shown in figure 5-10. It is seen in the figure that the re-design of these two sets of devices allowed global yielding of the specimen at a much smaller displacement compared to the initial design. Table 5-3 lists the key dimensions and nominal properties of each set of the devices used during testing.

Also, as a part of the Phase II testing program, the controlled rocking response with viscous dampers was investigated to verify analytical methods presented previously and to compare with the response with displacement-based steel yielding devices. A single set of nonlinear

viscous dampers were implemented in a very similar manner as the TADAS devices as seen in figure 5-11. The nonlinear viscous dampers used were manufactured and graciously donated by Taylor Devices of North Tonawanda, NY and were initially used as part of the NEESWood Project by Dr. Michael Symans from Rensselaer Polytechnic Institue (RPI). The nonlinear dampers had a force output, dependent on the velocity across the damper equal to:

$$F_{vdm} = c_m \cdot sgn(v) \ |v|^{\alpha_{dm}} \tag{5-13}$$

where c_m=damping coefficient of 1.32kN(sec/mm) , v=relative velocity across the two ends of the damper, sgn=sign function, and $_{dm}$=damping exponent of 0.50. The dampers had a stroke of $\pm$ 31.75mm. These damper properties were the prescribed values however component tests were not performed due to the limited time the dampers were available. With the dampers implemented to a controlled rocking system as described, the dampers would only primarily have a stroke in a single direction as the pier legs uplifted from their base. However, as depicted in figure 5-12, dampers connected to compressed (non-uplifting) would undergo some amount of stroke as the base of pier rotates. In an attempt to prevent the damper from reaching is stroke limit, the installation procedure called for attaching the dampers in a position that allowed for 9.53mm of stroke in the other direction. However, as will be shown in Section 6, this stroke limit was reached during testing and will be discussed further there.

5.5   Experimental Testing Facilities and Loading System

5.5.1   Phase I

Phase I of the experimental testing program was performed on the 5DOF shake table in the SEES Laboratory at UB. The table can achieve a nominal acceleration performance of 1.15g and 2.30g in the horizontal and vertical directions respectively with a 20-ton rigid specimen. A photograph and dimensions of the shake table is shown in figure 5-13. The table is driven by 2 horizontal and 4 vertical hydraulic actuators that are programmable with feedback control to simultaneously control displacement, velocity, and acceleration. The horizontal actuators have a stroke of $\pm$ 150mm and the vertical ones have a stroke o $\pm$ 75mm. The actuators have the ability to control table movement in all DOF except translation in the E-W direction.

5.5.2 Phase II

Phase II of the experimental testing component was performed on one of the two 6-DOF relocatable shake tables (shown in figure 5-14a) available in SEESL. A table extension was attached to the table during testing that is 7x7m in plan. The table can achieve a nominal acceleration performance of 1.15g and 1.15g in each of the horizontal directions and the vertical direction respectively with a 20-ton rigid specimen (not including mass of the table extension). The table is driven in each horizontal direction by 2 hydraulic actuators, as seen in figure 5-14b (without table extension). Each horizontal actuator is an MTS Model 244.4 hydraulic actuator with a dynamic force rating of 21 metric ton with a dynamic stroke of $\pm$ 150mm. The table is driven vertically by 4 MTS Model 206.S with a dynamic force rating of 25 metric ton and a dynamic stroke of $\pm$ 75mm.

5.6 Instrumentation

The instrumentation used for both phases of experimentation included accelerometers, string potentiometers, 8 strain gauge based load cells, and strain gauges that were attached within the specimen. A Krypton K600 high performance dynamic mobile coordinate measurement machine was used to measure displacements near the base of the structure. The accelerometers used have a peak acceleration range of $\pm$ 10g and a frequency range of 0-400Hz. The string potentiometers used have a total stroke of 1092mm and use a high-resolution digital output with a nominal resolution of 37pulses/mm. Two sets of strain gage based load cells were used during testing, a set of larger capacity (black) load cells and smaller capacity (yellow) load cells. Calibration of the set of black load cells is discussed in Appendix C. The calibration procedure for the yellow load cells is very similar. The black load cells were calibrated for 454kN axial (A), 89kN shear (Sx,Sy), and 24.9kN-mm moment (Mx,My). Yellow load cells were calibrated for 133.6kN axial (A), 22.3kN shear (Sx,Sy), and 3.4kN-mm moment (Mx,My). However, the mechanical capacity of the load cells are larger and shown in the capacity spectrum in Appendix C. Electrical resistance strain gages made by the Vishay Corporation were used. These gages can measure strain in the range of $\pm$ 3%, thus able to easily measure within the elastic range of steel. The Krypton K600 coordinate measurement machine (shown in figure 5-15a) uses light emitting diodes (LEDs) that can measure translation in 3 dimensions at a rate of 3000samples/sec/LED with

116

an accuracy of approximately 190 µm for the LEDs at a distance between 5-6m (furthest distance of LEDs used during testing).

5.6.1 Phase I

During Phase I of testing, a portable Pacific Instruments™ 6000 series data acquisition (DAQ) system was used to manage and record all digital instrumentation signals except for the data recorded from the Krypton machine that used its own proprietary acquisition system. The portable Pacific allowed a total of 64 channels to be recorded. The Pacific system supplied an excitation voltage to the various transducers (accelerometers, load cells, string potentiometers, strain gages), amplified the transducer output signal, and low-pass filtered the amplified signals at a cut-off frequency of 50Hz. All data was sampled at a rate of 128Hz and recorded to PC hard disk in ASCII format.

The instrumentation layout for Phase I of the experimental testing is shown in figure 5-16 and the instrumentation list is given in table 5-4. Accelerometers were positioned on the outer edges of the mass plates to measure horizontal mass accelerations in the N-S and E-W directions and an accelerometer added to the center of the plates to measure vertical acceleration. Accelerometers were attached to the shake table to measure acceleration in the horizontal and vertical directions. They were also attached near the base of the specimen's columns to measure vertical accelerations upon impact. Two string potentiometers were attached to the reference frame and one edge of the mass plates (as seen in figure 5-16) to measure the total displacement in the N-S direction and rotation of the mass plates. Similarly in the E-W direction, string potentiometers were attached to the crane rail and edge of the mass plates to measure total displacement in this direction and rotation of the mass plates. However, significant displacements in the E-W direction were not observed (as expected) since the 5DOF table is not designed to move in this direction. The black load cells were positioned beneath the legs of the pier specimen to measure the axial and shear forces (x- and y-directions) at the base of each column during testing. Moments (Mx, My) were also recorded during every test. The smaller capacity, yellow, load cells were attached between the support column and fixed end of the TADAS device to measure the TADAS shear force and moment. Only the relevant shear and moment channel from these load cells were

117

recorded due to the limitation of available channels on the portable Pacific DAQ system. As discussed previously, stain gages were attached to each specimen diagonal to measure the pre-tensioning force. During testing, only strains in the 1st panel diagonal members were recorded due to limitation of the number of channels on the DAQ system. Strain gages were also attached and oriented on the flanges of the collector beams such that axial forces and moments about its major axis, at each end, could be determined. The Krypton diodes were attached to the base of the specimen legs and the top end plate of black load cells to determine the uplifting displacements of each leg. Diodes were also attached and oriented on the shake table to determine horizontal and vertical translation of the table, and also rotation of the table. More diodes are attached than absolutely necessary to determine these quantities for redundancy. Note that the Krypton machine has its own DAQ system thus did not occupy channels on the portable Pacific system.

5.6.2 Phase II

Instrumentation for Phase II of the testing was very similar to the previous phase of testing with some minor changes since the number of data acquisition channels was significantly increased with the use of the Pacific Instruments^{TM} 6000 Mainframe. This DAQ system functioned nearly identical to the portable Pacific DAQ system used in Phase I however it allowed for a significant increase in the number of channels. The significant changes in instrumentations were the addition of 4 string potentiometers that were attached to the table (1 in X-direction, 1 Y-direction, 2 Z-direction), additional redundant accelerometers to the table in the X- and Y-direction, all pier diagonal member strain gages in the 1st panel were recorded, and 3 accelerometers were added on top of the mass to measure vertical acceleration. During testing with the viscous dampers, load cells that were attached in-line with the damper shaft (as seen in figure 5-11) were used to measure damper force. These load cells were designed to only measure axial forces with a capacity of $\pm$ 44.5kN. These load cells were graciously provided by Dr. Michael Symans of RPI.

5.7 Base Excitation

5.7.1 Phase I, =0deg.

The input excitation to the shake table included banded white noise excitation, three seismic ground motion histories, and a series of pulses. The banded acceleration controlled, flat-spectrum, white noise excitation had frequency content in the range of 0-40Hz and had a PGA of approximately 0.05g. A sample white noise acceleration history is shown in figure 5-17. Horizontal, vertical, and combined horizontal-vertical white noise tests were performed.

The seismic ground motions included the 1940 El Centro earthquake (array #9), the Newhall record from the 1994 Northridge earthquake, and a synthetically generated record. Under similitude scaling laws, the acceleration of the record is scaled by a factor, $_a$, which is equal to one and the time of the record scaled by the factor, $_t$, which is taken equal to 2.24 in these tests. The target acceleration histories of each motion, in prototype and model scale, are shown in figure 5-18. The target pseudo-acceleration response spectrums from these three motions, in prototype and model scale are shown in figure 5-19. For each set of test results in Section 6, the target and achieved spectrums in model scale are presented to display the actual base input to the specimen.

The series of pulses used were based on the simplified pulses used on Section 3.3 which were generated to represent the fault-normal component of near-fault ground motions. The pulses are completely defined by their shape, pulse period (T_p), and the maximum pulse velocity ($v_{p,max}$). The intensity of the pulse, measured in terms of the maximum pulse velocity, is based on regression analysis performed by Alavi and Krawinkler (2004) that relates the earthquake moment magnitude (M_w) and source-to-site distance (R). The magnitude and distance were arbitrarily set in this study as 7.0 and 10km respectively, resulting in a maximum prototype pulse velocity of 1122mm/sec. This pulse velocity was scaled for the experimental study by the velocity scale factor, $_v$ from table 5-2 (=2.24), and thus equal to 468mm/sec. Three pulse periods were used during testing to investigate the controlled rocking system's response to this type of input: 0.5, 1.0, and 1.5$T_{o,wn}$, where $T_{o,wn}$

is the fixed-base period actually determined from white noise testing (=0.40sec). The three pulses are shown in figure 5-20 along with their resulting pseudo-acceleration spectrum.

5.7.2 Phase I, =45deg.

With the pier in the second orientation (=45deg.), the same table input discussed in Section 5.7.1 was used except the horizontal component of excitation was amplitude scaled by a factor of 1.4. The intent of this portion of phase I was to investigate the type of behavior that would be expected from bi-directional shaking however using the 5DOF shake table. Amplitude scaling the horizontal table input by a factor of 1.4 was assumed to effectively apply 100% of the motion to the two orthogonal directions of the pier. One major difference between this and actual bi-directional input is the that these motions would be applied in-phase to the two orthogonal directions which does not occur during a real earthquake where it is typically assumed that these two motions are uncorrelated.

5.7.3 Phase II

Testing during phase II used 3 components of table input since testing was performed on one of the 6DOF shaking tables at UB. The motions used during these tests used a time scale factor of 1.85 opposed to the value of 2.24 required by similitude and used in phase I. The time scale factor was changed since the actual, observed period of the specimen was 0.4sec and the prototype period was 0.74sec (0.74/0.40=1.85). The Newhall record (H+V) from phase I was used again but included its other horizontal component of motion. The synthetically generated motion (H+V) from phase I was also used again and another randomly generated motion with the same target spectrum as S1X was used for the additional horizontal component. The target acceleration histories of the additional component of each motion (Y-component), in prototype and model scale, are shown in figure 5-21. The target pseudo-acceleration response spectrums of all three components for each record, in prototype and model scale, are shown in figure 5-22.

5.8 Testing Program

5.8.1 Phase I

As discussed previously, Phase I included tests with the specimen oriented orthogonal to the direction of shaking and rotated in-plan at an angle of 45deg. to the direction of shaking. For each orientation, tests were run with the three sets of steel yielding devices ($_L$=0.33, 0.67, and 1.0) attached and tests of the free-rocking pier ($_L$=0) for a total of 8 set-ups. Table 5-5 lists all of the tests performed during each orientation and set-up of Phase I. Testing of the controlled rocking specimen began with the series of 3 white noise tests followed by the seismic input and then the pulses. The three white noise tests were run following each full-scale input. For the first set of devices tested in each orientation, the seismic motions were initially run with 1/3 and 2/3 amplitude scaled inputs then the full-scale and similarly, the pulses were run with ½ amplitude scaled inputs followed by the full-scale input. This was done for the initial set-up to verify instrumentation functionality, table performance, and specimen behavior. As testing continued, some of the lower-level seismic tests and white noise tests were omitted.

5.8.2 Phase II

The test set-ups for phase II included 3 sets of steel yielding devices ($_L$=0.33, 0.67, and 1.0, two of which were re-designed as discussed previously), a set of nonlinear viscous dampers, and tests on the free-rocking pier. Each test set-up began with a white noise test followed by an earthquake record amplitude scaled to 35% of the target value simply to verify instrumentation functionality, table performance, and specimen behavior. The Newhall record was run at 100% amplitude followed by the Synthetic record at 100%. Following completion of the two 100% amplitude tests, different records were run at higher amplitude (150%+) for different set-ups. Table 5-6a lists all tests performed during Phase II with the TADAS devices attached and for the free-rocking specimen. Table 5-6b lists all tests performed with the nonlinear viscous dampers attached.

5.9 Summary

Details pertaining to the design, set-up, instrumentation, and testing program of the experimental portion of this research was presented in this section. In particular, the use of

an artificial mass simulation scaling procedure and the level to which the scaling laws were met were discussed. The connection at the base of the pier legs is critical in developing the desired type of response and its details were presented. A number of different set-ups with two types of passive energy dissipation devices was considered and subjected to many forms of excitation to investigate its response. Recorded response quantities are discussed in the following section and compared with different analytical procedures.

TABLE 5-1 Prototype and Model Pier Properties

Quantity	Prototype	Model	
		Required[a]	Provided[b]
Pier Height, h	29.3m	5.86m	6.09m
Pier Width, d	7.32m	1.46m	1.52m
Pier Aspect Ratio, h/d	4.0	4.0	4.0
Inertial Mass, m_x (and m_y)	1730 kN/g	69.2 kN/g	80.1 kN/g
Gravitational Weight, w_{mz}	1730 kN	69.2 kN	80.1 kN
Material Elastic Modulus, E	200GPa	200GPa	200GPa
Pier Lateral Stiffness, k_{ox} (and k_{oy})	12.6 kN/mm	2.52 kN/mm	3.00 kN/mm
"Fixed-base" Lateral Period of Vibration, T_{ox} (and T_{oy})	0.74 sec.	0.33 sec.	0.33 sec.
"Fixed-base" Vertical Period of Vibration, T_{ov}	0.13 sec.	0.058 sec.	0.040 sec.
Vertical "Shearing" Period of Vibration, T_v	0.12 sec.	0.054 sec.	0.062 sec.
A_L	155cm^2	6.2cm^2	15.5cm^2
d_{cl}	732cm	146cm	132cm
L_d	1035cm	207cm	157cm[c] 178cm[d]
i	45deg	45deg	35deg[c] 43deg[d]
A_d	35.5cm^2	1.42cm^2	0.45cm^2

[a]Required model properties determined from the prototype properties and "required" scale factors from table 5-2
[b]Theoretical model properties provided by the specimen
[c]Properties in panel 1 of specimen
[d]Properties in panels 2-5 of specimen

TABLE 5-2 Model Scale Factors for Dynamic Behavior Using Artificial Mass Simulation Scaling Procedure

Scaling Quantity	Dimensional Scale Requirements	Required Scale Factor
Geometric Length, L	$\lambda_L = 5^a$	5.00
Area, A	$\lambda_A = \lambda_L^2$	25.0
Second Moment of Area, I	$\lambda_I = \lambda_L^4$	625
Gravitational Acceleration, g	$\lambda_g = \lambda_E/(\lambda_\rho \lambda_L) = 1.0^b$	1.00
Acceleration, a	$\lambda_a = \lambda_E/(\lambda_\rho \lambda_L)$	1.00
Time, t	$\lambda_t = \sqrt{\lambda_L/\lambda_a}$	2.24
Frequency,	$\lambda_\omega = \left(\sqrt{\lambda_E/\lambda_\rho}\right)/\lambda_L$	0.447
Velocity, v	$\lambda_v = \sqrt{\lambda_L \cdot \lambda_a}$	2.24
Elastic Modulus, E	$\lambda_E = 1.0^c$	1.0
Force, F	$\lambda_F = \lambda_E \lambda_L^2$	25.0
Stiffness, k	$\lambda_k = \lambda_F/\lambda_L$	5.00
Stress,	$\lambda_\sigma = \lambda_E$	1.00
Strain,	$\lambda_\varepsilon = 1.0$	1.00
Mass Density,	$\lambda_\rho = \lambda_E/(\lambda_L \lambda_A)$	0.200
Mass, m	$\lambda_m = \lambda_\rho \lambda_L^3$	25.0
Energy, e	$\lambda_e = \lambda_E \lambda_L^3$	125
Impulse, I	$\lambda_i = \lambda_L^3 \cdot \sqrt{\lambda_\rho \lambda_E}$	55.9

[a]Geometric length scale limited by laboratory resources
[b]Acceleration scale factors equal to one due to model tested in 1-g acceleration field
[c]Elastic modulus scale factor equal to one due use of same material (steel) used for prototype and model

TABLE 5-3 TADAS and Viscous Damper Properties used in Experimental Testing[a]

TADAS, Phase I

L	N_T	L_T	t_T	b_T	k_T	$_{pT}$	design	design
1.0	4	88.9	9.53	50.8	8.34	2.13	0.15	6.3
0.67	2	133	12.7	60.5	3.47	3.63	0.15	5.5
0.33	1	159	14.3	57.2	1.38	4.57	0.15	5.2

Phase II

L	N_T	L_T	t_T	b_T	k_T	$_{pT}$	design	design
0.67	2	88.9	11.1	54.0	7.02	1.83	0.30	14.6
0.33	1	88.9	11.1	54.0	3.52	1.83	0.30	14.6

Viscous Dampers

c		$_{d,max}$	$F_{d,max}$
1.32	0.50	63.5	44.5

[a]All units in kN,mm

TABLE 5-4a Instrumentation during Phase I of Experimental Testing Acquired on Portable Pacific DAQ System

Channel #	Descriptor	Gage Location	Units
1	LC1N	SE Tower Leg	kips
2	LC1Sx		kips
3	LC1Sy		kips
4	LC1Mx		kips
5	LC1My		kips
6	LC2N	NE Tower Leg	kips
7	LC2Sx		kips
8	LC2Sy		kips
9	LC2Mx		kips
10	LC2My		kips
11	LC3N	SW Tower Leg	kips
12	LC3Sx		kips
13	LC3Sy		kips
14	LC3Mx		kips
15	LC3My		kips
16	LC4N	NW Tower Leg	kips
17	LC4Sx		kips
18	LC4Sy		kips
19	LC4Mx		kips
20	LC4My		kips
21	LC5Sx	SE Tower Leg	kips
22	LC5Mx		kips
23	LC6Sx	NE Tower Leg	kips
24	LC6Mx		kips
25	LC7Sx	SW Tower Leg	kips
26	LC7Mx		kips
27	LC8Sx	NW Tower Leg	kips
28	LC8Mx		kips

TABLE 5-4a Instrumentation during Phase I of Experimental Testing Acquired on Portable Pacific DAQ System (Cont.)

Channel #	Descriptor	Gage Location	Units
29	SP1	Top of Tower, X-direction (N-S)	inches
30	SP2	Top of Tower, X-direction (N-S)	inches
31	SP3	Top of Tower, Y-direction (E-W)	inches
32	SP4	Top of Tower, Y-direction (E-W)	inches
33	A1	Top of Tower, X-direction (N-S)	g
34	A2	Top of Tower, X-direction (N-S)	g
35	A3	Top of Tower, Y-direction (E-W)	g
36	A4	Top of Tower, Y-direction (E-W)	g
37	A5	Base of SE Tower Leg, Z-direction	g
38	A6	Base of NE Tower Leg, Z-direction	g
39	A7	Base of SW Tower Leg, Z-direction	g
40	A8	Base of NW Tower Leg, Z-direction	g
41	A9	Table 0, X-direction (N-S)	g
42	A10	Table 0, Y-direction (E-W)	g
43	A11	Table 0, South End, Z-direction	g
44	A12	Table 0, North End, Z-direction	g
45	SG1	Panel 1 Diagonal, East X-direction Frame	-
46	SG2	Panel 1 Diagonal, West X-direction Frame	-
47	SG3	Panel 1 Diagonal, South Y-direction Frame	-
48	SG4	Panel 1 Diagonal, North Y-direction Frame	-
49	SG5	Collector Beam (CB), East X-direction Frame, South End 1	-
50	SG6	CB, East X-direction Frame, South End 2	-
51	SG7	CB , East X-direction Frame, North End 1	-
52	SG8	CB , East X-direction Frame, North End 2	-
53	SG9	CB, West X-direction Frame, South End 1	-
54	SG10	CB, West X-direction Frame, South End 2	-
55	SG11	CB, West X-direction Frame, North End 1	-

TABLE 5-4a Instrumentation during Phase I of Experimental Testing Acquired on Portable Pacific DAQ System (Cont.)

Channel #	Descriptor	Gage Location	Units
56	SG12	CB, West X-direction Frame, North End 2	-
57	SG13	CB, South Y-direction Frame, East End 1	-
58	SG14	CB, South Y-direction Frame, East End 2	-
59	SG15	CB, South Y-direction Frame, West End 1	-
60	SG16	CB, South Y-direction Frame, West End 2	-
61	SG17	CB , North Y-direction Frame, East End 1	-
62	SG18	CB , North Y-direction Frame, East End 2	-
63	SG19	CB, North Y-direction Frame, West End 1	-
64	SG20	CB, North Y-direction Frame, West End 2	-

TABLE 5-4b Instrumentation during Phase I of Experimental Testing Acquired on Krypton Machine

Channel #	Descriptor	Gage Location	Units
k1	KD1x	SE Tower Leg, X-direction (N-S)	mm
k2	KD1y	SE Tower Leg, Y-direction (E-W)	mm
k3	KD1z	SE Tower Leg, Z-direction	mm
k4	KD2x	NE Tower Leg, X-direction (N-S)	mm
k5	KD2y	NE Tower Leg, Y-direction (E-W)	mm
k6	KD2z	NE Tower Leg, Z-direction	mm
k7	KD3x	SW Tower Leg, X-direction (N-S)	mm
k8	KD3y	SW Tower Leg, Y-direction (E-W)	mm
k9	KD3z	SW Tower Leg, Z-direction	mm
k10	KD4x	NW Tower Leg, X-direction (N-S)	mm
k11	KD4y	NW Tower Leg, Y-direction (E-W)	mm
k12	KD4z	NW Tower Leg, Z-direction	mm
k13	KD5x	Table 0, SE, X-direction (N-S)	mm
k14	KD5y	Table 0, SE, Y-direction (E-W)	mm

TABLE 5-4b Instrumentation during Phase I of Experimental Testing Acquired on Krypton Machine (Cont.)

Channel #	Descriptor	Gage Location	Units
k15	KD5z	Table 0, SE, Z-direction	mm
k16	KD6x	Table 0, NE, X-direction (N-S)	mm
k17	KD6y	Table 0, NE, Y-direction (E-W)	mm
k18	KD6z	Table 0, NE, Z-direction	mm
k19	KD7x	Table 0, SW, X-direction (N-S)	mm
k20	KD7y	Table 0, SW, Y-direction (E-W)	mm
k21	KD7z	Table 0, SW, Z-direction	mm
k22	KD8x	Table 0, NW, X-direction (N-S)	mm
k23	KD8y	Table 0, NW, Y-direction (E-W)	mm
k24	KD8z	Table 0, NW, Z-direction	mm
k25	KD9x	Table, NW, X-direction (E-W)	mm
k26	KD9y	Table, NW, Y-direction (N-S)	mm
k27	KD9z	Table, NW, Z-direction	mm
k28	KD10x	Table, NE, X-direction (E-W)	mm
k29	KD10y	Table, NE, Y-direction (N-S)	mm
k30	KD10z	Table, NE, Z-direction	mm
k31	KD11x	SW Load Cell Top Plate, W, X-direction (E-W)	mm
k32	KD11y	SW Load Cell Top Plate, W, Y-direction (N-S)	mm
k33	KD11z	SW Load Cell Top Plate, W, Z-direction	mm
k34	KD12x	SW Load Cell Top Plate, E, X-direction (E-W)	mm
k35	KD12y	SW Load Cell Top Plate, E, Y-direction (N-S)	mm
k36	KD12z	SW Load Cell Top Plate, E, Z-direction	mm
k37	KD13x	SE Load Cell Top Plate, W, X-direction (E-W)	mm
k38	KD13y	SE Load Cell Top Plate, W, Y-direction (N-S)	mm
k39	KD13z	SE Load Cell Top Plate, W, Z-direction	mm
k40	KD14x	SE Load Cell Top Plate, E, X-direction (E-W)	mm
k41	KD14y	SE Load Cell Top Plate, E, Y-direction (N-S)	mm
k42	KD14z	SE Load Cell Top Plate, E, Z-direction	mm

TABLE 5-5 Experimental Testing Program (Phase I)

TADAS Strength Ratio L	Orientation	Test Type	Excitation Name	Intensity Direction		
				X	Y	Z
0.67	0	w hite noise	wnh	0.05g	-	-
0.67	0	white noise	wnv	-	-	0.05g
0.67	0	white noise	wnc	0.05g	-	0.05g
0.67	0	seismic	EC33	33%	-	-
0.67	0	w hite noise	wnh	0.05g	-	-
0.67	0	white noise	wnv	-	-	0.05g
0.67	0	white noise	wnc	0.05g	-	0.05g
0.67	0	seismic	EC67	67%	-	-
0.67	0	w hite noise	wnh	0.05g	-	-
0.67	0	white noise	wnv	-	-	0.05g
0.67	0	white noise	wnc	0.05g	-	0.05g
0.67	0	seismic	EC100	100%	-	-
0.67	0	w hite noise	wnh	0.05g	-	-
0.67	0	white noise	wnv	-	-	0.05g
0.67	0	white noise	wnc	0.05g	-	0.05g
0.67	0	seismic	NH33	33%	-	-
0.67	0	w hite noise	wnh	0.05g	-	-
0.67	0	white noise	wnv	-	-	0.05g
0.67	0	white noise	wnc	0.05g	-	0.05g
0.67	0	seismic	NH67	67%	-	-
0.67	0	w hite noise	wnh	0.05g	-	-
0.67	0	white noise	wnv	-	-	0.05g
0.67	0	white noise	wnc	0.05g	-	0.05g
0.67	0	seismic	NH100	100%	-	-
0.67	0	w hite noise	wnh	0.05g	-	-
0.67	0	white noise	wnv	-	-	0.05g
0.67	0	white noise	wnc	0.05g	-	0.05g

TABLE 5-5 Experimental Testing Program (Phase I) (Cont.)

TADAS Strength Ratio $_L$	Orientation	Test Type	Excitation Name	Intensity Direction		
				X	Y	Z
0.67	0	seismic	Syn33	33%	-	-
0.67	0	white noise	wnh	0.05g	-	-
0.67	0	white noise	wnv	-	-	0.05g
0.67	0	white noise	wnc	0.05g	-	0.05g
0.67	0	seismic	Syn67	67%	-	-
0.67	0	white noise	wnh	0.05g	-	-
0.67	0	white noise	wnv	-	-	0.05g
0.67	0	white noise	wnc	0.05g	-	0.05g
0.67	0	seismic	Syn100	100%	-	-
0.67	0	white noise	wnh	0.05g	-	-
0.67	0	white noise	wnv	-	-	0.05g
0.67	0	white noise	wnc	0.05g	-	0.05g
0.67	0	seismic	NH67hv	67%	-	67%
0.67	0	white noise	wnh	0.05g	-	-
0.67	0	white noise	wnv	-	-	0.05g
0.67	0	white noise	wnc	0.05g	-	0.05g
0.67	0	seismic	NH100hv	100%	-	100%
0.67	0	white noise	wnh	0.05g	-	-
0.67	0	white noise	wnv	-	-	0.05g
0.67	0	white noise	wnc	0.05g	-	0.05g
0.67	0	pulse	p2tp020-50	50%	-	-
0.67	0	pulse	p2tp020-100	100%	-	-
0.67	0	white noise	wnh	0.05g	-	-
0.67	0	white noise	wnv	-	-	0.05g
0.67	0	white noise	wnc	0.05g	-	0.05g
0.67	0	pulse	p2tp040-50	50%	-	-
0.67	0	pulse	p2tp040-100	100%	-	-

TABLE 5-5 Experimental Testing Program (Phase I) (Cont.)

TADAS Strength Ratio $_L$	Orientation	Test Type	Excitation Name	Intensity Direction		
				X	Y	Z
0.67	0	white noise	wnh	0.05g	-	-
0.67	0	white noise	wnv	-	-	0.05g
0.67	0	white noise	wnc	0.05g	-	0.05g
0.67	0	seismic	Syn50hv	50%	-	50%
0.67	0	seismic	Syn100hv	100%	-	100%
0.67	0	white noise	wnh	0.05g	-	-
0.67	0	white noise	wnv	-	-	0.05g
0.67	0	white noise	wnc	0.05g	-	0.05g
0.67	0	seismic	Syn125	125%	-	-
0.67	0	white noise	wnh	0.05g	-	-
0.67	0	white noise	wnv	-	-	0.05g
0.67	0	white noise	wnc	0.05g	-	0.05g
0.67	0	pulse	p2tp060-50	50%	-	-
0.67	0	pulse	p2tp060-100	100%	-	-
0.67	0	white noise	wnh	0.05g	-	-
0.67	0	white noise	wnv	-	-	0.05g
0.67	0	white noise	wnc	0.05g	-	0.05g
0.67	0	seismic	Syn150	150%	-	-
0.67	0	white noise	wnh	0.05g	-	-
0.67	0	white noise	wnv	-	-	0.05g
0.67	0	white noise	wnc	0.05g	-	0.05g
0.33	0	white noise	wnh	0.05g	-	-
0.33	0	white noise	wnv	-	-	0.05g
0.33	0	white noise	wnc	0.05g	-	0.05g
0.33	0	seismic	EC33	33%	-	-
0.33	0	white noise	wnh	0.05g	-	-
0.33	0	white noise	wnv	-	-	0.05g

132

TABLE 5-5 Experimental Testing Program (Phase I) (Cont.)

TADAS Strength Ratio $_L$	Orientation	Test Type	Excitation Name	Intensity Direction		
				X	Y	Z
0.33	0	seismic	EC100	100%	-	-
0.33	0	white noise	wnh	0.05g	-	-
0.33	0	white noise	wnv	-	-	0.05g
0.33	0	white noise	wnc	0.05g	-	0.05g
0.33	0	seismic	NH67	67%	-	-
0.33	0	white noise	wnh	0.05g	-	-
0.33	0	white noise	wnv	-	-	0.05g
0.33	0	white noise	wnc	0.05g	-	0.05g
0.33	0	seismic	NH100	100%	-	-
0.33	0	white noise	wnh	0.05g	-	-
0.33	0	white noise	wnv	-	-	0.05g
0.33	0	white noise	wnc	0.05g	-	0.05g
0.33	0	seismic	Syn67	67%	-	-
0.33	0	white noise	wnh	0.05g	-	-
0.33	0	white noise	wnv	-	-	0.05g
0.33	0	white noise	wnc	0.05g	-	0.05g
0.33	0	seismic	Syn100	100%	-	-
0.33	0	white noise	wnh	0.05g	-	-
0.33	0	white noise	wnv	-	-	0.05g
0.33	0	white noise	wnc	0.05g	-	0.05g
0.33	0	pulse	p2tp020-100	100%	-	-
0.33	0	white noise	wnh	0.05g	-	-
0.33	0	white noise	wnv	-	-	0.05g
0.33	0	white noise	wnc	0.05g	-	0.05g
0.33	0	pulse	p2tp040-100	100%	-	-
0.33	0	white noise	wnh	0.05g	-	-
0.33	0	white noise	wnv	-	-	0.05g

TABLE 5-5 Experimental Testing Program (Phase I) (Cont.)

TADAS Strength Ratio $_L$	Orientation	Test Type	Excitation Name	Intensity Direction		
				X	Y	Z
0.33	0	white noise	wnc	0.05g	-	0.05g
0.33	0	pulse	p2tp060-50	50%	-	-
0.33	0	white noise	wnh	0.05g	-	-
0.33	0	white noise	wnv	-	-	0.05g
0.33	0	white noise	wnc	0.05g	-	0.05g
0.33	0	seismic	Syn100hv	100%	-	100%
0.33	0	white noise	wnh	0.05g	-	-
0.33	0	white noise	wnv	-	-	0.05g
0.33	0	white noise	wnc	0.05g	-	0.05g
0.33	0	seismic	NH100hv	100%	-	100%
0.33	0	white noise	wnh	0.05g	-	-
0.33	0	white noise	wnv	-	-	0.05g
0.33	0	white noise	wnc	0.05g	-	0.05g
0.33	0	pulse	p2tp060-100	100%	-	-
0.33	0	white noise	wnh	0.05g	-	-
0.33	0	white noise	wnv	-	-	0.05g
0.33	0	white noise	wnc	0.05g	-	0.05g
0.33	0	seismic	NH125	125%	-	-
0.33	0	white noise	wnh	0.05g	-	-
0.33	0	white noise	wnv	-	-	0.05g
0.33	0	white noise	wnc	0.05g	-	0.05g
0.33	0	seismic	Syn150	150%	-	-
0.33	0	white noise	wnh	0.05g	-	-
0.33	0	white noise	wnv	-	-	0.05g
0.33	0	white noise	wnc	0.05g	-	0.05g
1.0	0	white noise	wnh	0.05g	-	-
1.0	0	white noise	wnv	-	-	0.05g

TABLE 5-5 Experimental Testing Program (Phase I) (Cont.)

TADAS Strength Ratio $_L$	Orientation	Test Type	Excitation Name	Intensity Direction		
				X	Y	Z
1.0	0	white noise	wnc	0.05g	-	0.05g
1.0	0	seismic	EC67	67%	-	-
1.0	0	white noise	wnh	0.05g	-	-
1.0	0	white noise	wnv	-	-	0.05g
1.0	0	white noise	wnc	0.05g	-	0.05g
1.0	0	seismic	EC100	100%	-	-
1.0	0	white noise	wnh	0.05g	-	-
1.0	0	white noise	wnv	-	-	0.05g
1.0	0	white noise	wnc	0.05g	-	0.05g
1.0	0	seismic	NH67	67%	-	-
1.0	0	white noise	wnh	0.05g	-	-
1.0	0	white noise	wnv	-	-	0.05g
1.0	0	white noise	wnc	0.05g	-	0.05g
1.0	0	seismic	NH100	100%	-	-
1.0	0	white noise	wnh	0.05g	-	-
1.0	0	white noise	wnv	-	-	0.05g
1.0	0	white noise	wnc	0.05g	-	0.05g
1.0	0	seismic	Syn67	67%	-	-
1.0	0	white noise	wnh	0.05g	-	-
1.0	0	white noise	wnv	-	-	0.05g
1.0	0	white noise	wnc	0.05g	-	0.05g
1.0	0	seismic	Syn100	100%	-	-
1.0	0	white noise	wnh	0.05g	-	-
1.0	0	white noise	wnv	-	-	0.05g
1.0	0	white noise	wnc	0.05g	-	0.05g
1.0	0	pulse	p2tp020-100	100%	-	-
1.0	0	white noise	wnh	0.05g	-	-

TABLE 5-5 Experimental Testing Program (Phase I) (Cont.)

TADAS Strength Ratio L	Orientation	Test Type	Excitation Name	Intensity Direction		
				X	Y	Z
1.0	0	white noise	wnv	-	-	0.05g
1.0	0	white noise	wnc	0.05g	-	0.05g
1.0	0	pulse	p2tp040-100	100%	-	-
1.0	0	white noise	wnh	0.05g	-	-
1.0	0	white noise	wnv	-	-	0.05g
1.0	0	white noise	wnc	0.05g	-	0.05g
1.0	0	pulse	p2tp060-50	50%	-	-
1.0	0	white noise	wnh	0.05g	-	-
1.0	0	white noise	wnv	-	-	0.05g
1.0	0	white noise	wnc	0.05g	-	0.05g
1.0	0	seismic	EC100hv	100%	-	100%
1.0	0	white noise	wnh	0.05g	-	-
1.0	0	white noise	wnv	-	-	0.05g
1.0	0	white noise	wnc	0.05g	-	0.05g
1.0	0	seismic	Syn100hv	100%	-	100%
1.0	0	white noise	wnh	0.05g	-	-
1.0	0	white noise	wnv	-	-	0.05g
1.0	0	white noise	wnc	0.05g	-	0.05g
1.0	0	seismic	NH100hv	100%	-	100%
1.0	0	white noise	wnh	0.05g	-	-
1.0	0	white noise	wnv	-	-	0.05g
1.0	0	white noise	wnc	0.05g	-	0.05g
1.0	0	pulse	p2tp060-100	100%	-	-
1.0	0	white noise	wnh	0.05g	-	-
1.0	0	white noise	wnv	-	-	0.05g
1.0	0	white noise	wnc	0.05g	-	0.05g
1.0	0	seismic	Syn125	125%	-	-

136

TABLE 5-5 Experimental Testing Program (Phase I) (Cont.)

TADAS Strength Ratio $_L$	Orientation	Test Type	Excitation Name	Intensity Direction		
				X	Y	Z
1.0	0	white noise	wnh	0.05g	-	-
1.0	0	white noise	wnv	-	-	0.05g
1.0	0	white noise	wnc	0.05g	-	0.05g
0	0	white noise	wnh	0.05g	-	-
0	0	white noise	wnv	-	-	0.05g
0	0	white noise	wnc	0.05g	-	0.05g
0	0	seismic	EC33	33%	-	-
0	0	white noise	wnh	0.05g	-	-
0	0	white noise	wnv	-	-	0.05g
0	0	white noise	wnc	0.05g	-	0.05g
0	0	seismic	EC67	67%	-	-
0	0	white noise	wnh	0.05g	-	-
0	0	white noise	wnv	-	-	0.05g
0	0	white noise	wnc	0.05g	-	0.05g
0	0	seismic	EC100	100%	-	-
0	0	white noise	wnh	0.05g	-	-
0	0	white noise	wnv	-	-	0.05g
0	0	white noise	wnc	0.05g	-	0.05g
0	0	seismic	Syn67	67%	-	-
0	0	white noise	wnh	0.05g	-	-
0	0	white noise	wnv	-	-	0.05g
0	0	white noise	wnc	0.05g	-	0.05g
0	0	seismic	Syn100	100%	-	-
0	0	white noise	wnh	0.05g	-	-
0	0	white noise	wnv	-	-	0.05g
0	0	white noise	wnc	0.05g	-	0.05g
0	0	seismic	NH33	33%	-	-

TABLE 5-5 Experimental Testing Program (Phase I) (Cont.)

TADAS Strength Ratio L	Orientation	Test Type	Excitation Name	Intensity Direction		
				X	Y	Z
0	0	white noise	wnh	0.05g	-	-
0	0	white noise	wnv	-	-	0.05g
0	0	white noise	wnc	0.05g	-	0.05g
0	0	seismic	NH67	67%	-	-
0	0	white noise	wnh	0.05g	-	-
0	0	white noise	wnv	-	-	0.05g
0	0	white noise	wnc	0.05g	-	0.05g
0.67	45	white noise	wnh	0.05g	-	-
0.67	45	white noise	wnv	-	-	0.05g
0.67	45	white noise	wnc	0.05g	-	0.05g
0.67	45	seismic	EC33[1]	46%	-	-
0.67	45	white noise	wnh	0.05g	-	-
0.67	45	white noise	wnv	-	-	0.05g
0.67	45	white noise	wnc	0.05g	-	0.05g
0.67	45	seismic	EC67	94%	-	-
0.67	45	white noise	wnh	0.05g	-	-
0.67	45	white noise	wnv	-	-	0.05g
0.67	45	white noise	wnc	0.05g	-	0.05g
0.67	45	seismic	EC100	140%	-	-
0.67	45	white noise	wnh	0.05g	-	-
0.67	45	white noise	wnv	-	-	0.05g
0.67	45	white noise	wnc	0.05g	-	0.05g
0.67	45	seismic	NH33	46%	-	-
0.67	45	white noise	wnh	0.05g	-	-
0.67	45	white noise	wnv	-	-	0.05g
0.67	45	white noise	wnc	0.05g	-	0.05g
0.67	45	seismic	NH67	94%	-	-

TABLE 5-5 Experimental Testing Program (Phase I) (Cont.)

TADAS Strength Ratio L	Orientation	Test Type	Excitation Name	Intensity Direction		
				X	Y	Z
0.67	45	white noise	wnh	0.05g	-	-
0.67	45	white noise	wnv	-	-	0.05g
0.67	45	white noise	wnc	0.05g	-	0.05g
0.67	45	seismic	NH100	140%	-	-
0.67	45	white noise	wnh	0.05g	-	-
0.67	45	white noise	wnv	-	-	0.05g
0.67	45	white noise	wnc	0.05g	-	0.05g
0.67	45	seismic	Syn33	46%	-	-
0.67	45	seismic	Syn67	94%	-	-
0.67	45	white noise	wnh	0.05g	-	-
0.67	45	white noise	wnv	-	-	0.05g
0.67	45	white noise	wnc	0.05g	-	0.05g
0.67	45	seismic	Syn100	140%	-	-
0.67	45	white noise	wnh	0.05g	-	-
0.67	45	white noise	wnv	-	-	0.05g
0.67	45	white noise	wnc	0.05g	-	0.05g
0.67	45	seismic	Syn67hv	94%	-	67%
0.67	45	white noise	wnh	0.05g	-	-
0.67	45	white noise	wnv	-	-	0.05g
0.67	45	white noise	wnc	0.05g	-	0.05g
0.67	45	seismic	Syn100hv	140%	-	100%
0.67	45	pulse	p2tp020-100	140%	-	-
0.67	45	pulse	p2tp040-100	140%	-	-
0.67	45	pulse	p2tp060-100	140%	-	-
0.67	45	white noise	wnh	0.05g	-	-
0.67	45	white noise	wnv	-	-	0.05g
0.67	45	white noise	wnc	0.05g	-	0.05g

TABLE 5-5 Experimental Testing Program (Phase I) (Cont.)

TADAS Strength Ratio $_L$	Orientation	Test Type	Excitation Name	Intensity Direction		
				X	Y	Z
0.33	45	white noise	wnh	0.05g	-	-
0.33	45	white noise	wnv	-	-	0.05g
0.33	45	white noise	wnc	0.05g	-	0.05g
0.33	45	seismic	NH67	94%	-	-
0.33	45	seismic	NH100	140%	-	-
0.33	45	white noise	wnh	0.05g	-	-
0.33	45	white noise	wnv	-	-	0.05g
0.33	45	white noise	wnc	0.05g	-	0.05g
0.33	45	seismic	NH67hv	94%	-	67%
0.33	45	seismic	NH100hv	140%	-	100%
0.33	45	white noise	wnh	0.05g	-	-
0.33	45	white noise	wnv	-	-	0.05g
0.33	45	white noise	wnc	0.05g	-	0.05g
0.33	45	seismic	Syn67	94%	-	-
0.33	45	seismic	Syn100	140%	-	-
0.33	45	white noise	wnh	0.05g	-	-
0.33	45	white noise	wnv	-	-	0.05g
0.33	45	white noise	wnc	0.05g	-	0.05g
0.33	45	pulse	p2tp020-100	140%	-	-
0.33	45	pulse	p2tp040-100	140%	-	-
0.33	45	pulse	p2tp060-100	140%	-	-
0.33	45	white noise	wnh	0.05g	-	-
0.33	45	white noise	wnv	-	-	0.05g
0.33	45	white noise	wnc	0.05g	-	0.05g
1.0	45	white noise	wnh	0.05g	-	-
1.0	45	white noise	wnv	-	-	0.05g
1.0	45	white noise	wnc	0.05g	-	0.05g

TABLE 5-5 Experimental Testing Program (Phase I) (Cont.)

TADAS Strength Ratio L	Orientation	Test Type	Excitation Name	Intensity Direction		
				X	Y	Z
1.0	45	seismic	NH67	94%	-	-
1.0	45	seismic	NH100	140%	-	-
1.0	45	white noise	wnh	0.05g	-	-
1.0	45	white noise	wnv	-	-	0.05g
1.0	45	white noise	wnc	0.05g	-	0.05g
1.0	45	seismic	Syn67	94%	-	-
1.0	45	seismic	Syn100	140%	-	-
1.0	45	white noise	wnh	0.05g	-	-
1.0	45	white noise	wnv	-	-	0.05g
1.0	45	white noise	wnc	0.05g	-	0.05g
1.0	45	seismic	Syn67hv	94%	-	67%
1.0	45	seismic	Syn100hv	140%	-	100%
1.0	45	white noise	wnh	0.05g	-	-
1.0	45	white noise	wnv	-	-	0.05g
1.0	45	white noise	wnc	0.05g	-	0.05g
1.0	45	pulse	p2tp020-100	140%	-	-
1.0	45	pulse	p2tp040-100	140%	-	-
1.0	45	pulse	p2tp060-100	140%	-	-
1.0	45	white noise	wnh	0.05g	-	-
1.0	45	white noise	wnv	-	-	0.05g
1.0	45	white noise	wnc	0.05g	-	0.05g
1.0	45	seismic	NH67hv	94%	-	67%
1.0	45	seismic	NH100hv	140%	-	100%
1.0	45	white noise	wnh	0.05g	-	-
1.0	45	white noise	wnv	-	-	0.05g
1.0	45	white noise	wnc	0.05g	-	0.05g

TABLE 5-5 Experimental Testing Program (Phase I) (Cont.)

TADAS Strength Ratio L	Orientation	Test Type	Excitation Name	Intensity Direction		
				X	Y	Z
0	45	white noise	wnh	0.05g	-	-
0	45	white noise	wnv	-	-	0.05g
0	45	white noise	wnc	0.05g	-	0.05g
0	45	seismic	EC67	94%	-	-
0	45	seismic	EC100	140%	-	-
0	45	white noise	wnh	0.05g	-	-
0	45	white noise	wnv	-	-	0.05g
0	45	white noise	wnc	0.05g	-	0.05g
0	45	seismic	Syn67	94%	-	-
0	45	seismic	Syn100	140%	-	-
0	45	white noise	wnh	0.05g	-	-
0	45	white noise	wnv	-	-	0.05g
0	45	white noise	wnc	0.05g	-	0.05g
0	45	seismic	NH67	94%	-	-
0	45	seismic	NH84	118%	-	-
0	45	seismic	NH100	140%	-	-
0	45	white noise	wnh	0.05g	-	-
0	45	white noise	wnv	-	-	0.05g
0	45	white noise	wnc	0.05g	-	0.05g
0	45	pulse	p2tp020-100	140%	-	-
0	45	pulse	p2tp040-100	140%	-	-
0	45	pulse	p2tp060-100	140%	-	-
0	45	white noise	wnh	0.05g	-	-
0	45	white noise	wnv	-	-	0.05g
0	45	white noise	wnc	0.05g	-	0.05g

TABLE 5-6a Experimental Testing Program (Phase II)

TADAS Strength Ratio L	Test Type	Excitation Name	Intensity Direction		
			X	Y	Z
0.67	white noise	wnc	0.05g	0.05g	0.05g
0.67	seismic	NH35	35%	35%	35%
0.67	seismic	Syn35	35%	35%	35%
0.67	seismic	Syn100	100%	100%	100%
0.67	seismic	NH100	100%	100%	100%
0.67	seismic	Syn150	150%	150%	150%
0.67	white noise	wnc	0.05g	0.05g	0.05g
1.0	white noise	wnc	0.05g	0.05g	0.05g
1.0	seismic	NH35	35%	35%	35%
1.0	seismic	Syn35	35%	35%	35%
1.0	white noise	wnc	0.05g	0.05g	0.05g
1.0	seismic	NH100	100%	100%	100%
1.0	seismic	Syn100	100%	100%	100%
1.0	seismic	NH150	150%	150%	150%
1.0	seismic	Syn150	150%	150%	150%
1.0	white noise	wnc	0.05g	0.05g	0.05g
0.33	white noise	wnc	0.05g	0.05g	0.05g
0.33	seismic	NH35	35%	35%	35%
0.33	seismic	Syn35	35%	35%	35%
0.33	seismic	NH100	100%	100%	100%
0.33	seismic	Syn100	100%	100%	100%
0.33	seismic	Syn150	150%	150%	150%
0.33	white noise	wnc	0.05g	0.05g	0.05g
0	white noise	wnc	0.05g	0.05g	0.05g
0	seismic	NH100	100%	100%	100%
0	seismic	Syn100	100%	100%	100%
0	seismic	NH150	150%	150%	150%

TABLE 5-6a Experimental Testing Program (Phase II) (Cont.)

TADAS Strength Ratio $_L$	Test Type	Excitation Name	Intensity Direction		
			X	Y	Z
0	seismic	Syn150	150%	150%	150%
0	white noise	wnc	0.05g	0.05g	0.05g

TABLE 5-6b Experimental Testing Program (Phase II, Viscous Dampers)

Test Type	Excitation Name	Intensity Direction		
		X	Y	Z
white noise	wnc	0.05g	0.05g	0.05g
seismic	NH35	35%	35%	35%
seismic	Syn35	35%	35%	35%
seismic	NH100	100%	100%	100%
seismic	Syn100	100%	100%	100%
seismic	NH150	150%	150%	150%
seismic	Syn150	150%	150%	150%
seismic	NH175	175%	175%	175%
seismic	Syn175	175%	175%	175%
seismic	NH200	200%	200%	200%
white noise	wnc	0.05g	0.05g	0.05g
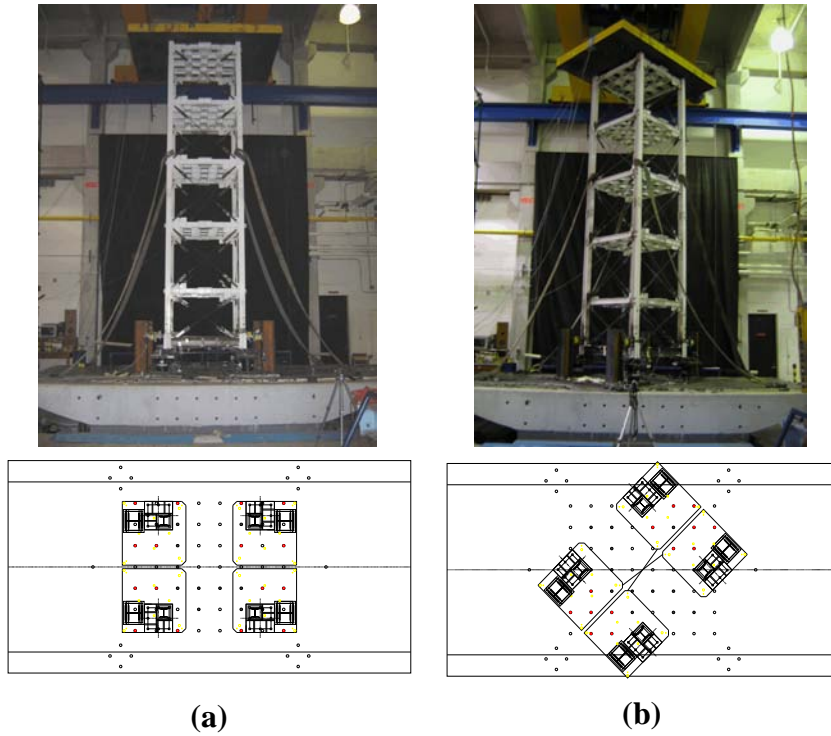
FIGURE 5-1 Experimental Pier Specimen on 5DOF Shake Table (a) Orientation =0deg. and (b) =45deg.
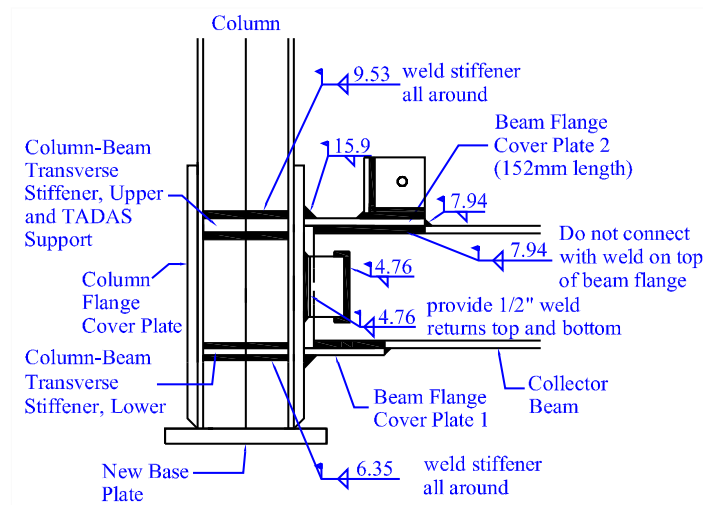
FIGURE 5-2 Column Base Modifications (weld dimensions, mm)
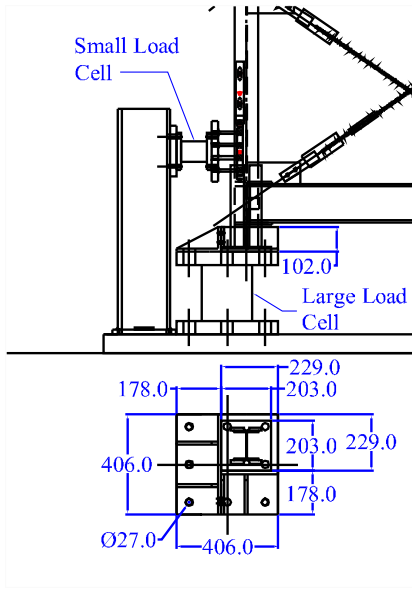
FIGURE 5-3 Pier Base Connection
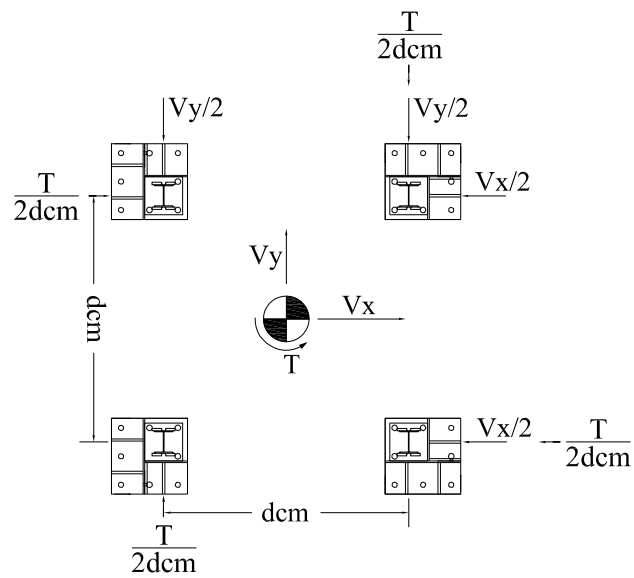
FIGURE 5-4 Shear Transfer at Base of Pier Using "Pit" Connection

146
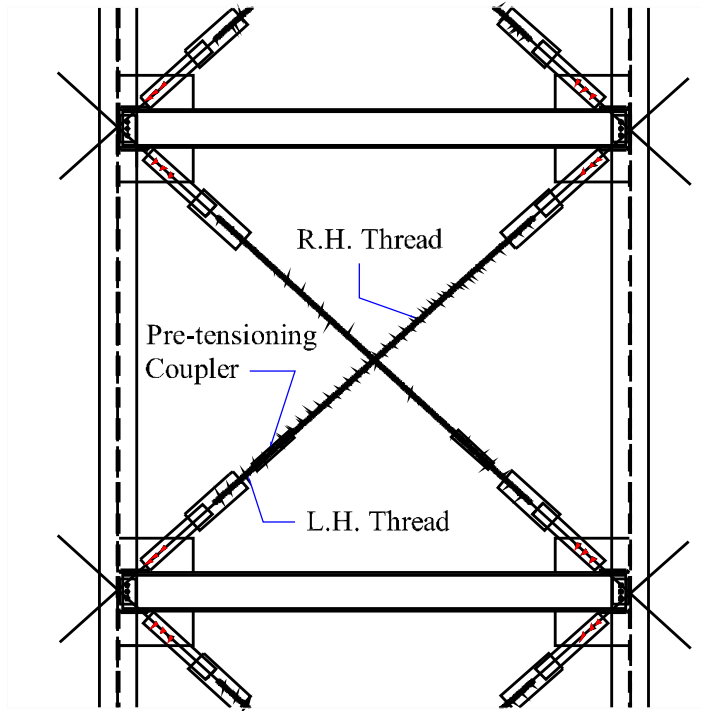
FIGURE 5-5 Pre-tensioned Diagonal Members
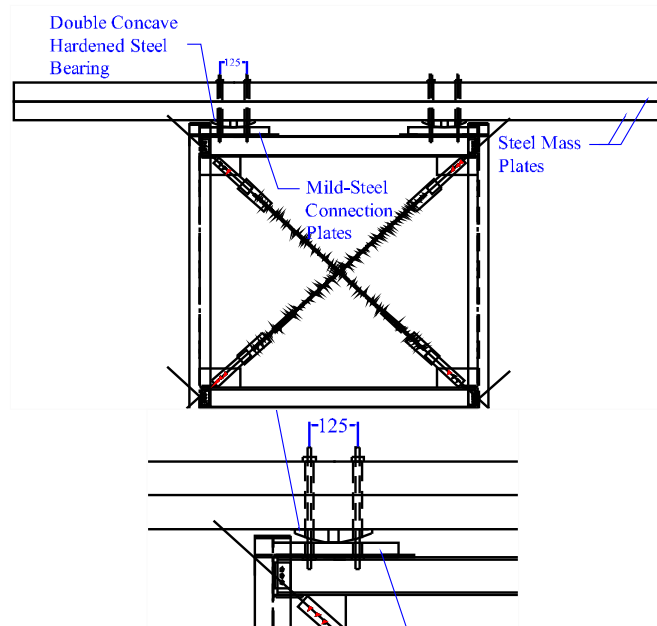
FIGURE 5-6 Mass Connection Details

(a) **(b)**
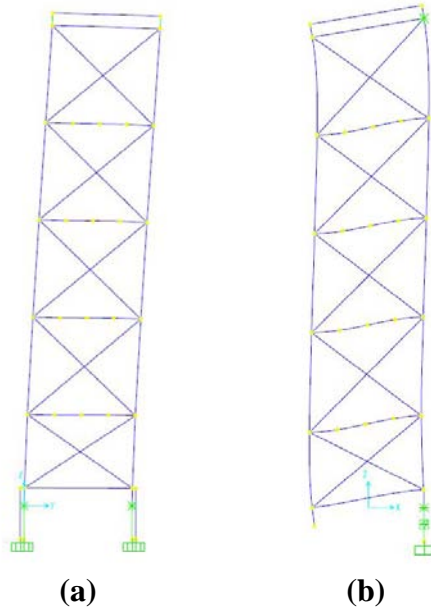
FIGURE 5-7 Mode Shapes of Experimental Specimen Including Rotational Stiffness of Mass Connection (a) Lateral and (b) Vertical Shearing Mode

(a) **(b)**
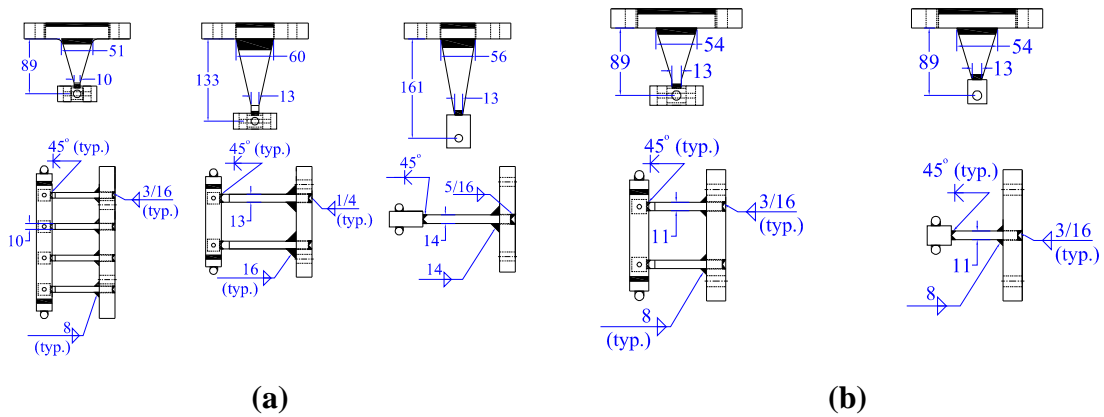
FIGURE 5-8 TADAS Dimensions and Weld Details (a) Phase I (γ_L=1.0, 0.67, 0.33) and (b) Phase II (γ_L=0.67, 0.33)

148
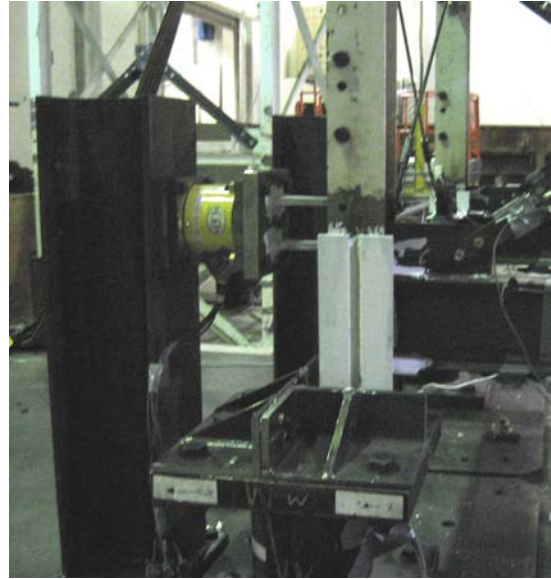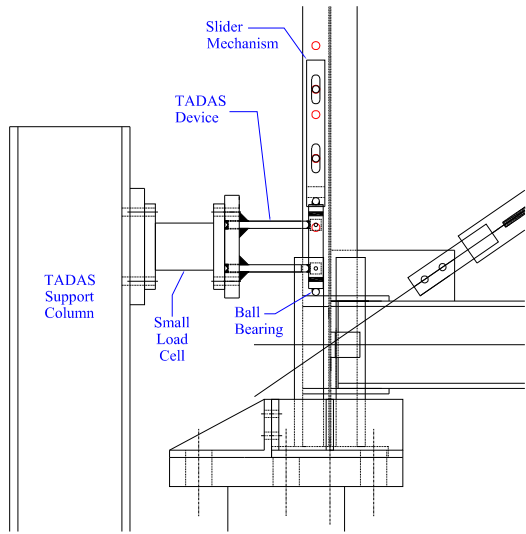
FIGURE 5-9 TADAS-to-Pier Leg Connection
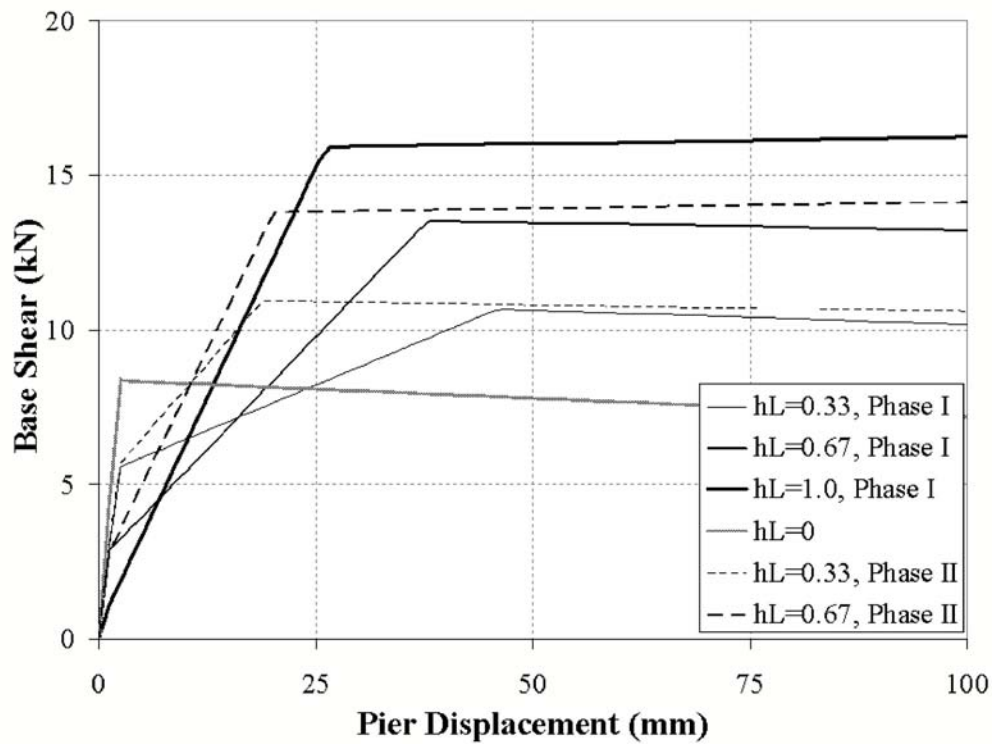
FIGURE 5-10 Uni-directional Static Pushover Curves for Experimental Specimen with Steel Yielding Devices for Phase I and II of Testing

149
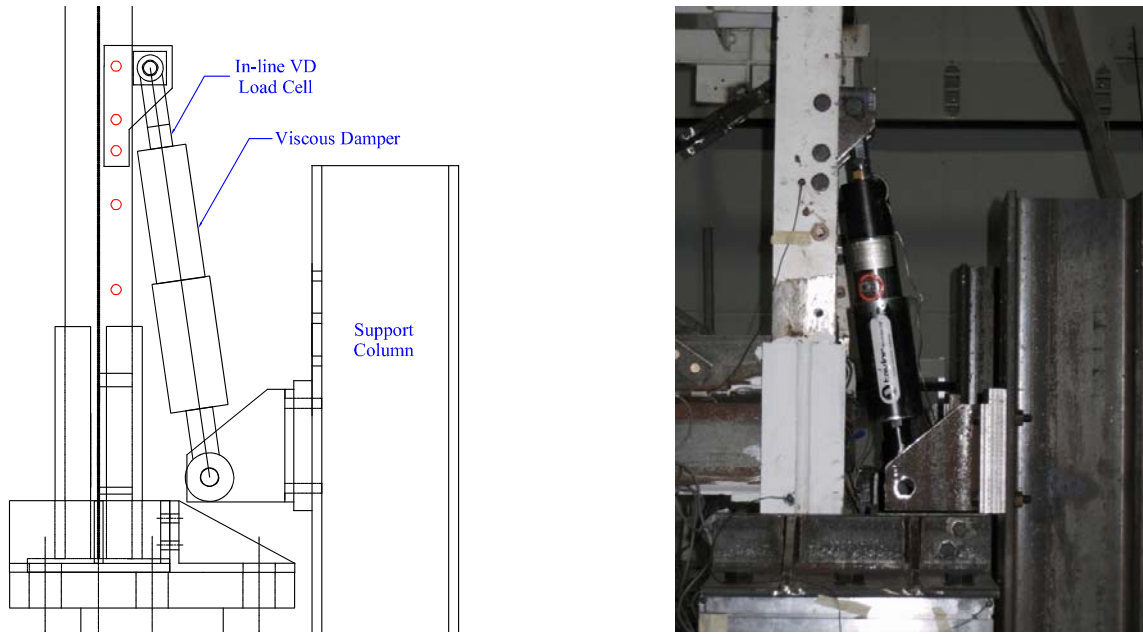
FIGURE 5-11 Connection of Nonlinear Viscous Damper to Leg of Experimental Pier Specimen
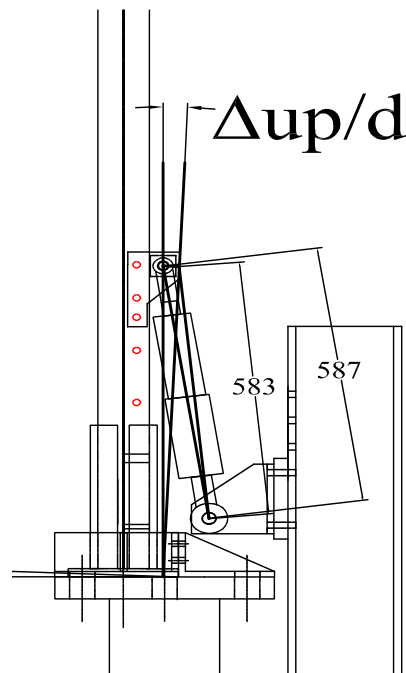
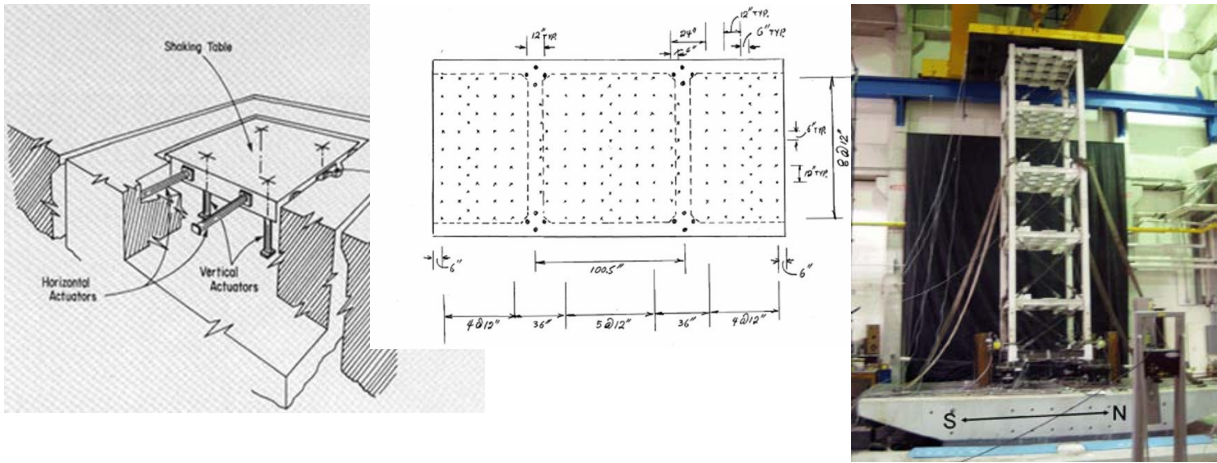**FIGURE 5-12 Damper Stroke Resulting from Rotation of Compressed Pier Leg**
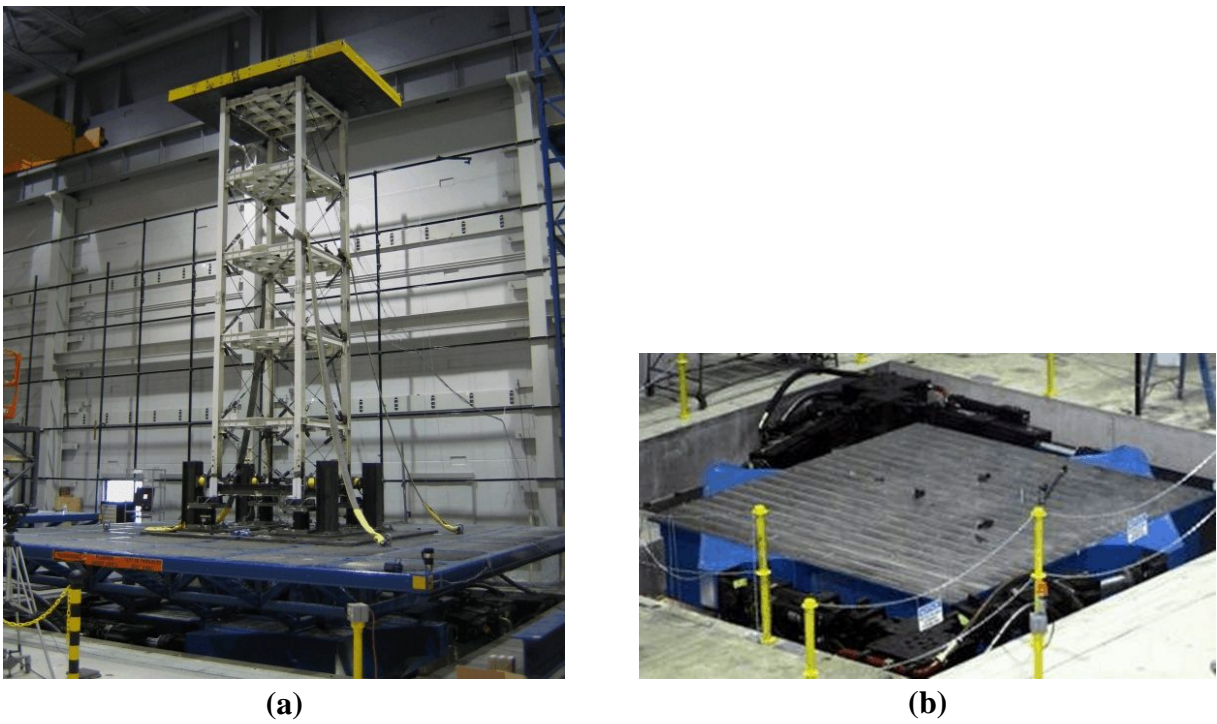
FIGURE 5-13 5DOF Shake Table in SEESL

(a)	**(b)**

FIGURE 5-14 6-DOF Shake Table in SEESL (a) With Extension Platform and (b) Without Extension Platform showing Horizontal Actuators

FIGURE 5-15 Krypton K600 Coordinate Measurement Machine (a) Front View and (b) Position in Front of Specimen during Testing
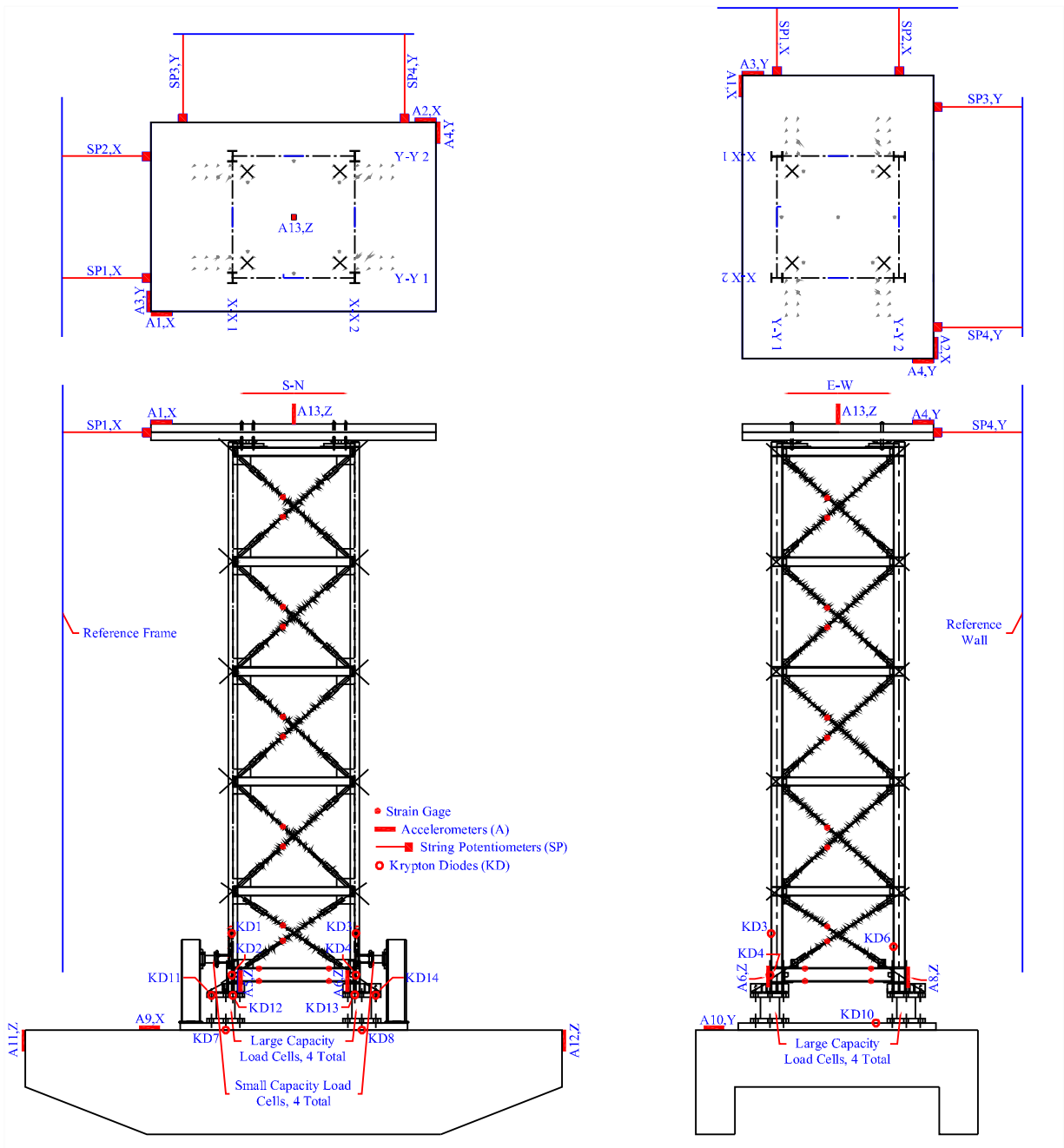
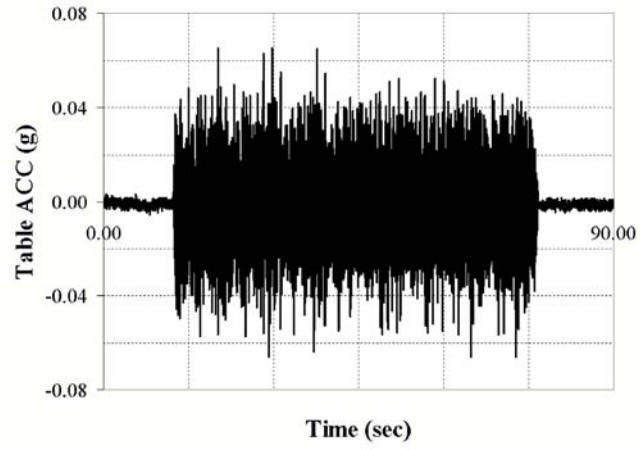**FIGURE 5-16 Instrumentation Layout for Phase I of Testing**

FIGURE 5-17 Banded White Acceleration History

Prototype Scale   **Model Scale**

(a)
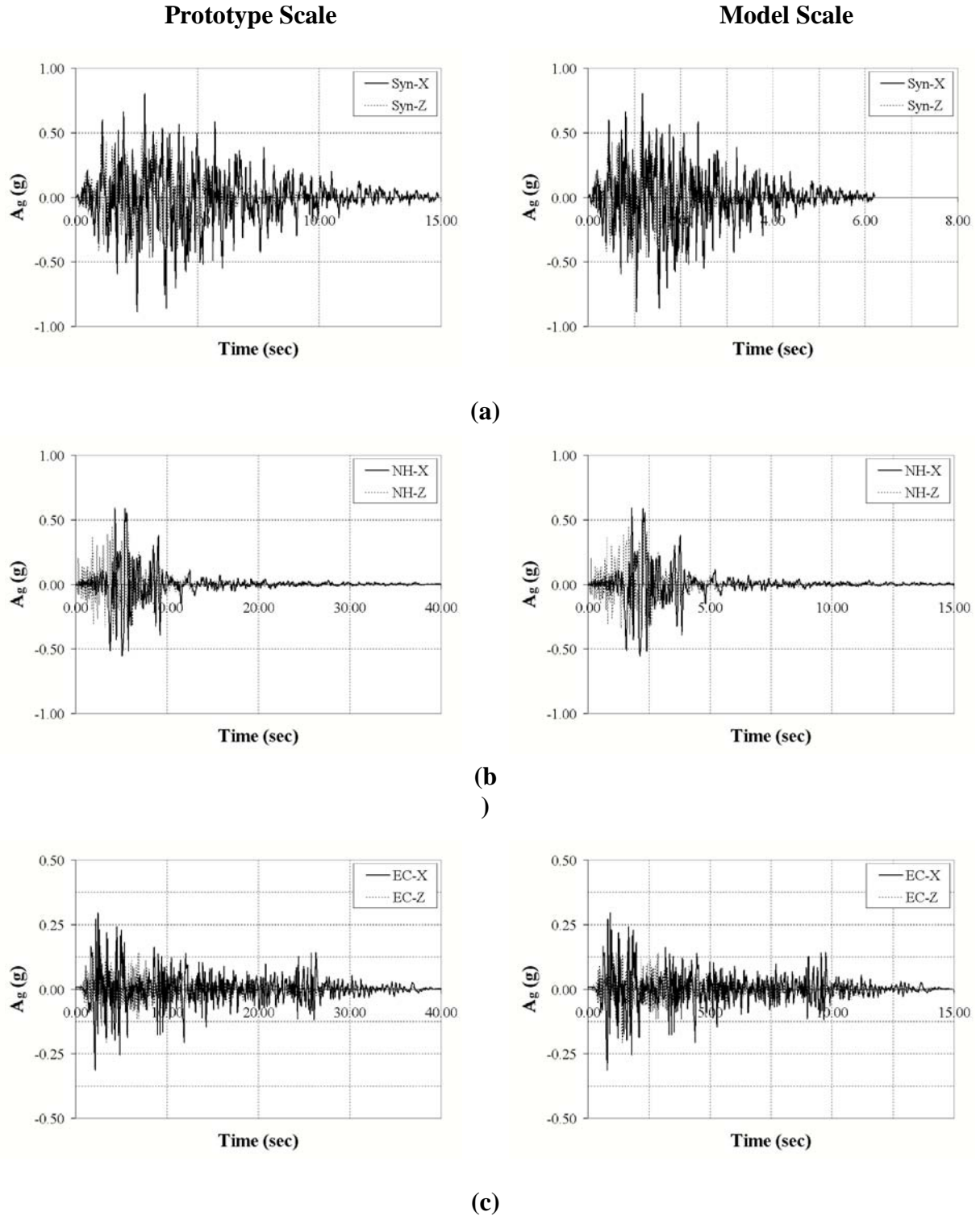

**(b
)**

(c)

**FIGURE 5-18 Target Ground Motion Acceleration Histories (Phase I) in Prototype and
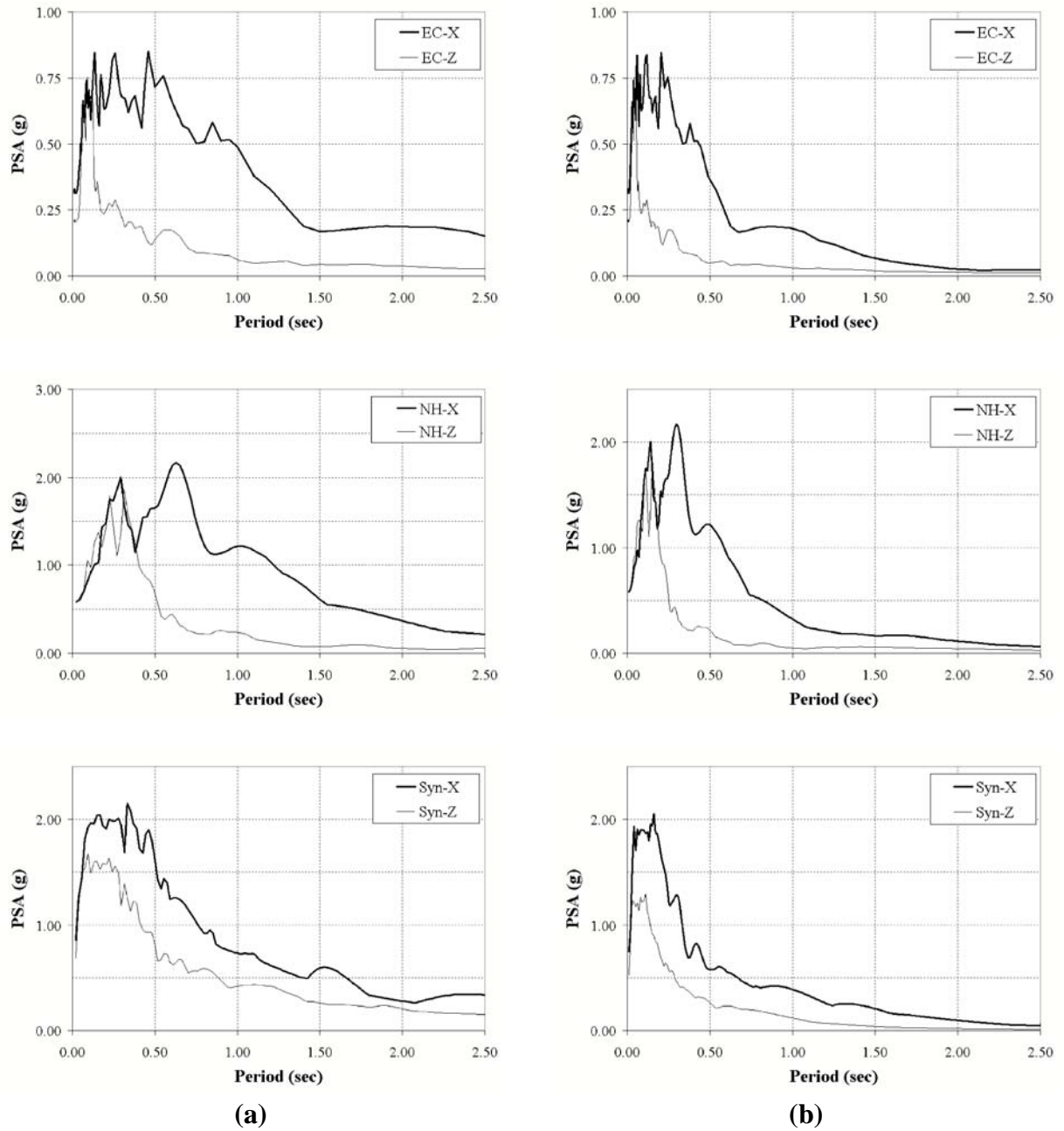Model Scale (a) Synthetic Motion, (b) Newhall, and (c) El Centro**

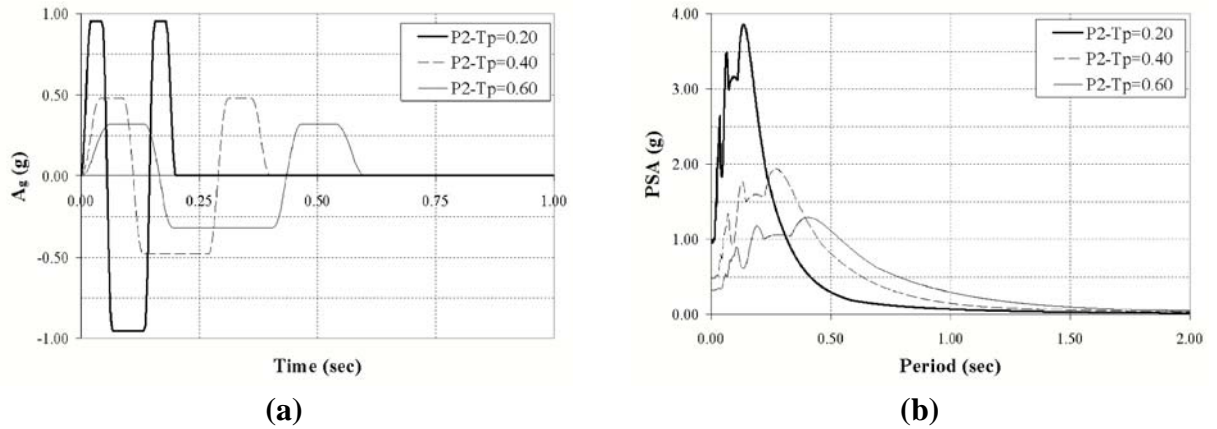**FIGURE 5-19 Target Ground Motion Pseudo-Acceleration Spectra in (a) Prototype and (b) Model Scale**

156

(a)   **(b)**

**FIGURE 5-20 Experimental Testing Input Pulses (a) Pulse P2 Acceleration Histories
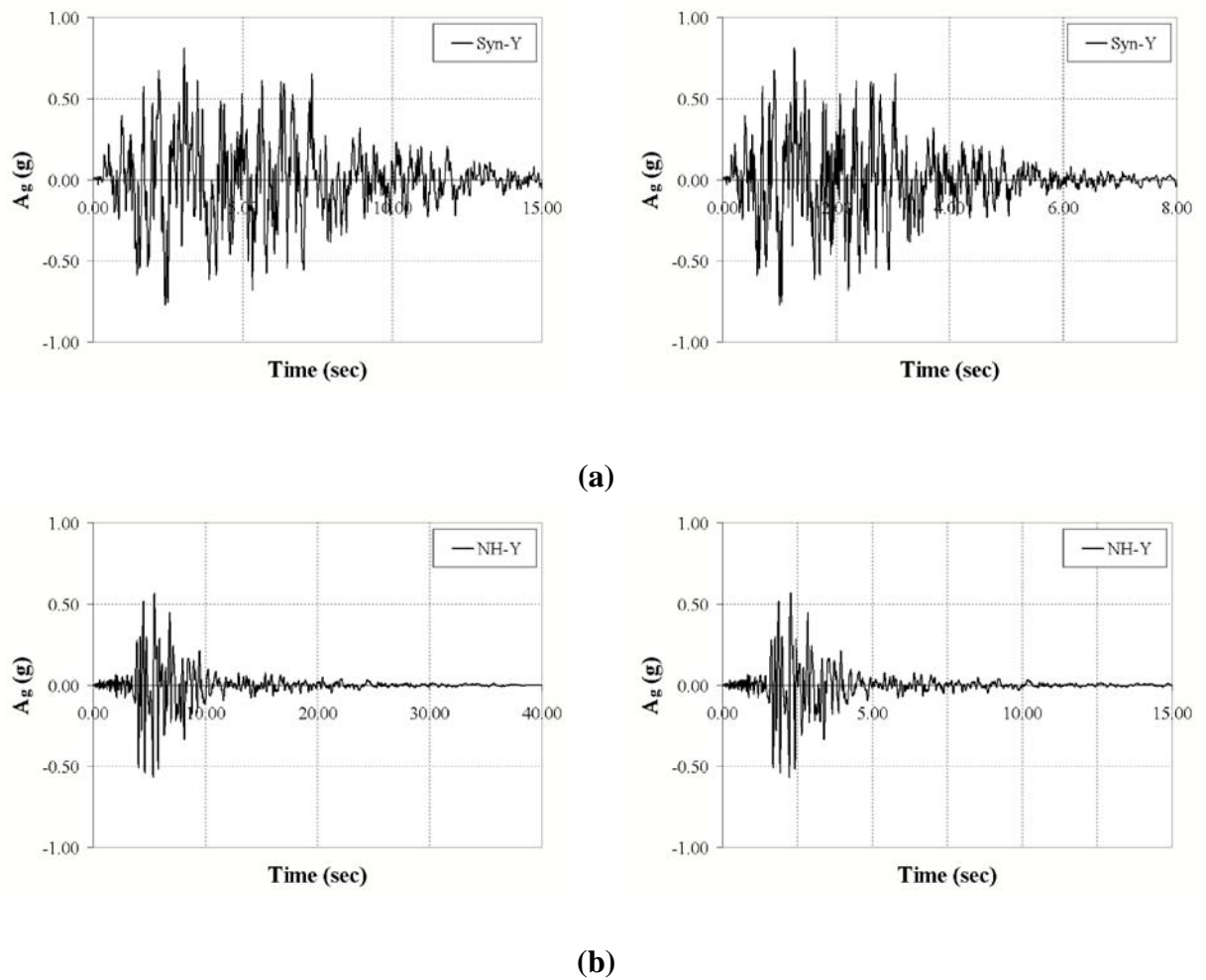and (b) Pseudo-Acceleration Spectra of Each Pulse**

(a)

(b)

**FIGURE 5-21 Target Ground Motion Acceleration Histories (Phase II, Y-component
only) in Prototype and Model Scale (a) Synthetic and (b) Newhall**

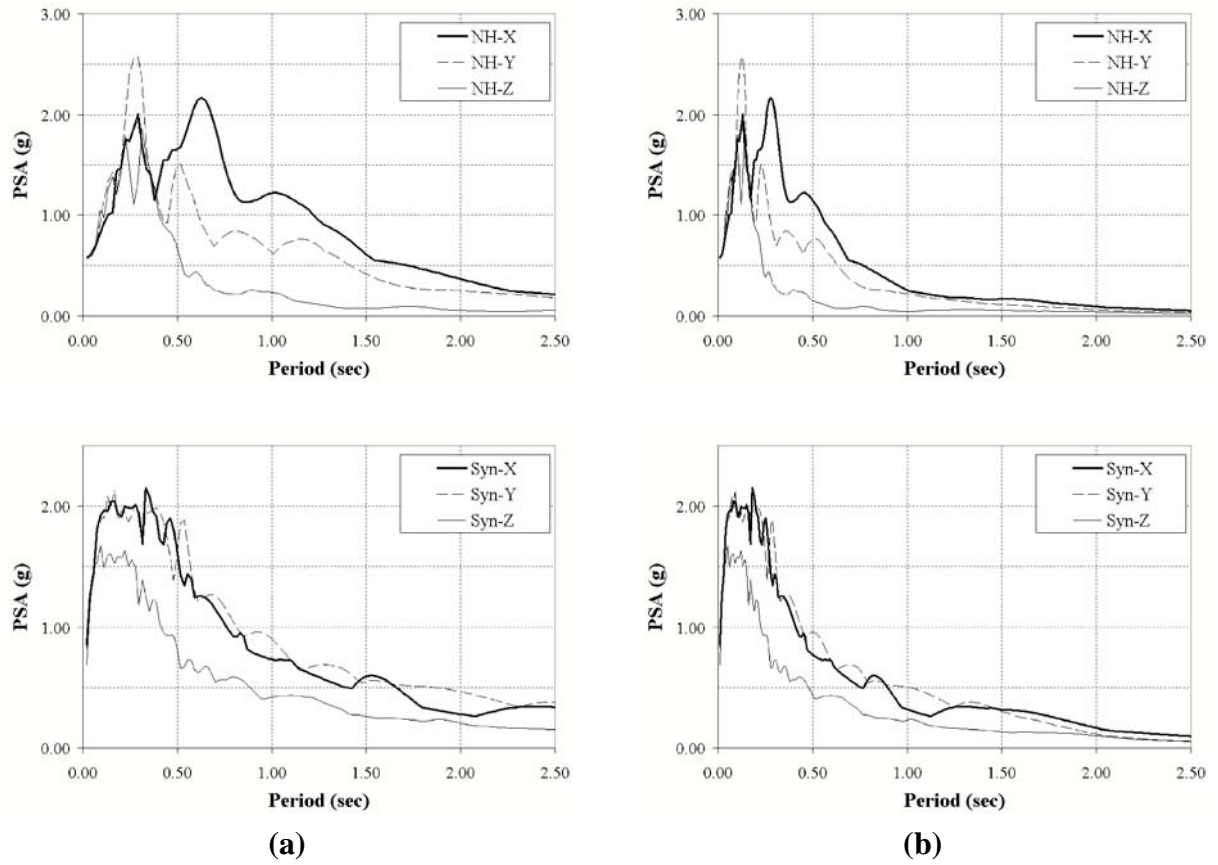**FIGURE 5-22 Target Ground Motion Pseudo-Acceleration Spectra in (a) Prototype and (b) Model Scale**

SECTION 6

TESTING RESULTS AND COMPARISON WITH ANALYTICAL METHODS

6.1 General

Results of the testing program are presented in this section. The dynamic characteristics of the specimen are determined using banded white noise acceleration input during the testing history. The method for calculating the structure's modal frequency and damping ratio is discussed in Section 6.2. The properties of the model do not change significantly throughout the testing program since the structure is designed to remain elastic. Therefore following discussion of the method used to of calculate these quantities, the dynamic characteristics obtained from all the white noise tests conducted throughout the course of this experimental program are not individually discussed, but are nonetheless provided in a series of figures.

The following sections discuss the reduction of experimental data recorded from various instruments and compares this data with advanced and simplified analytical methods. Section 6.3 explicitly describes the methods of processing the data recorded from instruments and calculation of important response quantities such as: relative pier displacement, horizontal base shear forces, pier leg axial forces, uplifting displacements, device forces, and device deformations. Also presented in this section are the results of tests conducted with an input table acceleration amplitude of 100% or greater of the target. Section 6.4 compares testing results with results of nonlinear time history analysis in terms of peak response and time history traces of each response quantity. Differences in results are discussed and a refined analytical model is developed based on the results obtained. Section 6.5 compares the experimental results to the simplified analysis method and design equations developed in Sections 3 and 4.

6.2 Identification of Dynamic Characteristics

6.2.1 Modal Frequencies

As discussed in Section 5.7, banded white noise excitation was used for identification of the model structure's dynamic properties. Response of the model structure during white noise excitation was limited to the elastic range of response thus providing the fixed base pier

properties, and could not capture the system behavior after uplift. The mode shapes, frequencies, and damping ratios of the structure were determined using a modal identification technique based on pier transfer function response. The transfer functions are defined as the ratio of the cross and power spectrum between the top of pier and table accelerations in a particular direction. This definition of the transfer function has been termed in the past as the H_1 estimator (Bendat and Piersol, 1980). Calculation of the transfer function consists of processing of the raw acceleration records by first zeroing the record to remove any initial offset, filtering the acceleration record in the frequency domain using a trapezoidal filtering window, and applying a Hanning windowing function to the record to reduce the effect of energy "leakage" (Yao, 1991) by forcing the beginning and end of the time record to zero and making the function appear periodic. The fourier transform of the processed acceleration records were then calculated using the Fast Fourier Transform (FFT) function implemented in the program DADisp (DSP Development Corporation) which uses a mixed radix FFT. The transfer function is explicitly defined as:

$$TF = H_1(\omega) \;=\; \frac{X(\omega)\,F^*(\omega)}{F(\omega)\,F^*(\omega)} \;=\; \frac{S_{fx}(\omega)}{S_{ff}(\omega)} \tag{6-1}$$

where X( )=fourier transform of output (acceleration at top of pier), F( )=fourier transform of input (acceleration of table), F^*( )=conjugate of F( ), S_{fx}( )=cross spectrum, and S_{ff}( )=power spectrum.

For the model specimen considered, only two horizontal modes and a vertical mode were expected to significantly contribute to the fixed-base response. For Phase I of testing only a single horizontal mode would contribute since base excitation could not be provided in one of the horizontal directions on the 5DOF table. Therefore, to determine the modal frequency for the horizontal mode in the X-direction, the average of accelerometers A1 and A2 along with A9 are used in the modal identification technique. Similarly, A3, A4, and A10 are used for the horizontal mode in the Y-direction and A13, A11, and A12 for the vertical "fixed-base" mode (Z-direction).

Many white noise tests were run to first identify the structure's initial dynamic properties and then to ensure that these properties did not change during the course of testing, likely

indicating damage to the model specimen. An example is provided here to illustrate the modal identification technique and then simple, numerical results are presented for every other test. Figure 6-1 shows the power and cross spectrum plots for a horizontal white noise excitation. The transfer function plot is shown in figure 6-2 and is smoothed using a 7 point moving average to reduce noise. As seen in this figure, the peak of the transfer function plot occurs at approximately 2.5Hz indicating that the model structure has a "fixed-base" horizontal frequency of 2.5Hz (T_{oxm}=0.40sec).

The variation of the fixed-base frequency of the structure throughout Phase I, =0deg. testing history is shown in figure 6-3 and Phase I, =45deg. is shown in figure 6-4. The figures are presented in the sequence of tests listed in tables 5-5 on the horizontal axis and the vertical axis has the frequency calculated from the white noise test (f_i) normalized by the frequency calculated from the first test in that particular orientation (f_1). As seen in each figure, the frequency changes very little (approximately 5% or less) from the initial test in each set-up. There is an initial drop in the structural frequency within the first few tests, a flat portion of the curve, followed by a few rises and flattening of the curve throughout the testing history. The rises typically occur when a new set of devices is attached to the structure, creating a bit of "re-stiffening" near the base. After a few tests following attachment of the new devices, the frequency drops slightly but quickly levels off indicating no changes in structural frequency.

Results of white noise tests run during Phase II are presented in figure 6-5a. The sequence of tests for this phase are given in table 5-6. Similar results are seen for Phase II testing with the exception of white noise test 5 which exhibits a significant drop in frequency relative to the initial test. White noise test 5 was performed following the seismic tests of the set-up with $_L$=1.0. Since the strength of the devices in this set-up is nearly equal to or greater than the structures tributary weight, the structure may have ended-up being partially supported on the devices following the tests with $_L$=1.0. Although, upon close examination, no residual uplift or relative pier displacement was observed following these tests. To investigate this hypothesis, consider that as the structure is cycled with this set of devices, it no longer has a "fixed-base" response. Rather, its period shifts to the 2nd cycle response and increases. If

this is the case, the structure's period obtained from the white noise tests should nearly be equal to the "rocking" period of vibration determined using the rocking stiffness defined in Appendix B (for 4-legged piers), which for the specimen and device properties considered is equal to 0.73sec. This would correspond to a ratio of $f_i/f_1 = 0.55$. With the observed reduction being substantially less (with $f_i/f_1 \cong 0.70$), one could assume that a few of the legs are not completely supported by the devices. After these devices were removed and the devices with $\mu_L = 0.33$ were attached for the next set-up, the following white noise test performed showed the initial trend, with approximately 93% of its initial frequency.

The mode shape corresponding to the "fixed-base" lateral period of vibration with period $T_{oxm} = 0.40$sec is shown in figure 6-5b.

6.2.2 Modal Damping Characteristics

The equivalent viscous damping characteristics of each mode is determined from the frequency response analysis described using the half-power (bandwidth) method and then using the logarithmic decrement method (Clough and Penzien 1975).

Using the half-power (bandwidth) method, the damping ratio (ξ_k) can be determined from the frequency response curves by determining the frequencies (f) at which the maximum response (TF_k) is reduced by $1/\sqrt{2}$. Following this approach, the kth modal damping ratio can be defined as:

$$\xi_k = \frac{f_2 - f_1}{2 f_k} \tag{6-2}$$

Thus, figure 6-6a shows that the peak transfer function amplitude of 11.7 occurs at a horizontal frequency of 2.5Hz and the frequencies at which the transfer function (TF) is equal to $1/\sqrt{2}$ of its maximum occurs at 2.42Hz and 2.56Hz. Therefore, the equivalent viscous damping ratio of the model structure's horizontal mode in the X-direction, using this method, is equal to:

$$\xi_X = \frac{2.56\,Hz - 2.42\,Hz}{2 \cdot (2.5 Hz)} = 0.028 = 2.8\% \tag{6-3a}$$

Using the logarithmic decrement method, the equivalent viscous damping ratio can be determined by considering the free-vibration decay of motion. For lightly damped structures, the equivalent damping can be determined by:

$$\xi_{logdec} = \frac{\Delta_n - \Delta_{n+m}}{2\,m\,\pi\,\Delta_{n+m}}$$

(6-3)b

Observing the free-vibration, "fixed-base" ($_{up2}$) response of the specimen following the completion of a seismic or pulse test can provide the necessary information to calculate the equivalent damping using this method. A sample set of response data is shown in figure 6-6b and ten cycles of free-vibration response is considered such that:

$$\xi_{logdec} = \frac{3.15\,mm - 1.3\,mm}{2 \cdot 10 \cdot \pi \cdot (1.3\,mm)} = 0.023 = 2.3\%$$

(6-3)c

6.3 Data Reduction and Presentation of Results

6.3.1 Calculation of Response Quantities

The instrumentation described in Section 5.6 is used to calculate the following key response quantities: table acceleration (horizontal and vertical), table displacement (horizontal and vertical), pier relative displacement, pier horizontal base shear force, pier leg axial forces, uplift displacements, and device forces. This section describes the procedures for processing the raw instrumentation data and converting it into response quantities that can be compared to results from the analytical methods that will be presented in Sections 6.4 and 6.5.

The raw table accelerations are recorded from accelerometers A9 and A14 (X-direction), A10 and A15 (Y-direction), and A11 and A12 (Z-direction). The acceleration records are first zero-corrected then filtered in the frequency domain using a trapezoidal filtering window with corner frequencies of 0.20, 0.25, 30, and 38Hz to remove low frequency errors and high frequency noise in the signal. The absolute maximum of the filtered acceleration history was taken as the maximum table acceleration in the particular direction. All table displacements were determined from Krypton diodes KD7, 8, 9, and 10 since each diode measured translational movement in 3 dimensions. In each translational direction, the corresponding values recorded from each instrument were averaged to determine the table translational displacement history. The absolute maximum for each of the average recorded displacement

histories are presented along with each maximum table acceleration in tables 6-1 to 6-3 to provide a gage of the intensity of each actual excitation used during the testing program.

The pier relative displacement was calculated from the string potentiometers attached to the pier mass in each direction and the Krypton diodes attached on or near the load cells. The relative pier displacement ($\Delta_{REL,P}$) was calculated as:

$$\Delta_{REL,P} = \Delta_{ABS,P} - \Delta_T - h_{LC-M} \cdot \theta_T \qquad (6\text{-}4)$$

where $\Delta_{ABS,P}$=absolute pier mass displacement measured relative to a stationary reference frame using SP1 and SP2 (X-direction) or SP3 and SP4 (Y-direction), Δ_T=table displacement measured by KD7, 8, 9, and 10 (X- and Y-direction), h_{LC-M}=distance from top of large load cells to center of mass plates (6.09m), and θ_T=rotation of the table. All channels are first zero-corrected to remove any initial offset. Rotation of the table about it's Y-axis was calculated as:

$$\theta_{T,Y} = \tan^{-1}\left(\frac{KD7z - KD8z}{d_{KD7\text{-}8}}\right) \qquad (6\text{-}5)$$

where $d_{KD7\text{-}8}$=horizontal distance between KD 7 and 8 (1.47m). Rotation of the table about it's X-axis was calculated as:

$$\theta_{T,X} = \tan^{-1}\left(\frac{KD7z - KD9z}{d_{KD7\text{-}9}}\right) \qquad (6\text{-}6)$$

where $d_{KD7\text{-}9}$=horizontal distance between KD 7 and 9 (1.27m).

Using SP1 and SP2 (or SP3 and SP4) and the geometry of the pier, the rotation of the mass could be measured during each test. The largest observed rotation during testing was approximately 0.10deg. This level of rotation results in 1.1mm of deformation to each frame or approximately 1/5 of the deformation of a frame to induce uplift of the free-rocking set-up. This small amount of rotation was ignored for any calculation of experimental response quantities.

The total horizontal base shear force could be determined by three different approaches: from the large capacity load cells, from strain gages on the 1st panel diagonals, or using data from accelerometers attached to the specimen mass. In the results presented here, the base shear

was calculated from the strain recorded on the 1st panel diagonals. This approach was used, as opposed to the others, due to electrical problems with one of the load cells leading to unreliable recordings and the acceleration records appeared rather sensitive to localized vibrations. However, in most cases, the base shear results calculated from all sources were comparable. Each strain recording was first zero-corrected to remove any initial offset. For Phase I test results with =0deg., for example, base shear was calculated as:

$$BS_{SG} = f_{BFMF} \cdot 2\,E\,A_{coupler} \cdot \cos\theta_{d1} \cdot \left(SG_1 + SG_2\right) \tag{6-7}$$

where f_{BFMF}=factor to account for the braced frame and moment frame acting in parallel, E=modulus of elasticity of steel, $A_{coupler}$=cross-sectional area of the pre-tensioning coupler to which the strain gage was attached (1.94cm^2), $_{d1}$=angle the 1st panel diagonal makes with the horizontal (35deg.), and SG_1 and SG_2=recordings from the strain gages on 1st panel diagonals on the east and west side of the pier respectively. The factor f_{BFMF} is determined from elastic analysis of the specimen as the ratio of lateral shear force transferred through the diagonal members (braced frame action) to the total shear force transferred through the specimen (braced frame and moment frame action) and is equal to approximately 1.6. During Phase II of testing, strain gages attached to all 1st panel diagonals are recorded and used in the calculation of base shear in the X- and Y-directions in a very similar manner.

Pier leg axial force is calculated by summing the axial channel of the large capacity load cells and shear channel from the smaller capacity load cells. For example, the total axial force for pier leg 1 is calculated as:

$$P_{L1} = LC1N + LC5X \tag{6-8}$$

Thus, it is calculating the axial force in the leg above the connection point with the energy dissipation device. No zero-correction was applied to these channels since the starting value during each test should be equal to the gravitational weight.

Uplifting displacements were determined from Krypton diodes attached to the top of the large capacity load cells, shake table, and to the base of the specimen's columns. For example, during Phase I of testing the uplifting displacement of the NE column was calculated as:

$$\Delta_{upNE} = KD4z - KD13z \tag{6-9}$$

Maximum device forces are measured directly from the load cells that are attached to them. For the TADAS devices used in both Phase I and Phase II of testing, the device force is measured directly from the shear recording of the small capacity (yellow) load cells since the devices were designed to only apply a vertical shear force where they connected to the pier leg. For the viscous dampers tested during Phase II, load cells were attached in-line with the piston rod of the damper that directly measured the damper's force. The damper was attached at an angle of approximately 8deg. from the vertical such that the damper force was nearly equal to the vertical component of the force applied to the pier leg.

The TADAS rotation demands defined by (5-12) is calculated using the uplifting displacement from (6-9) and the device length given in table 5-3. The damper stroke is, for all practical purposes, equal to the uplifting displacement (6-9).

Some of the results in this section are presented normalized by important quantities of the controlled rocking system such as the uni-directional yield force ($P_{y,uni}$) and 2nd cycle yield displacement ($_{y2}$). These quantities are defined in Appendix B and can be seen in figure 5-10 that presents the backbone curves for each experimental set-up. These static backbone curves are also overlaid on the dynamic hysteretic curves of the experimental results discussed in the following sections.

Some other information from the experiments that may be of interest to other researchers is the raw normal channel data from the large capacity load cells (LC1N, LC2N, LC3N, and LC4N) and the uplifting displacements (calculated from (6-9) and from which the uplifting velocities could be determined). This data has been uploaded to the UB NEES (http://www.nees.org/) repository at \\nas.nees.buffalo.edu\repository\AllProjects\MCEER\Controlled rocking pier\NormalForceUpliftDispData.

6.3.2 Experimental Results of Phase I, =0deg.

The important response quantities described in the previous section are presented here for each test that was conducted with an excitation that had an acceleration amplitude of at least 100% of the target base excitation (Section 5.7).

Note that there are differences, both in amplitude and frequency content, between the target and achieved seismic motions during testing due to shake table fidelity in reproducing the desired (target) motions. For comparison, the 5% damped target pseudo-acceleration spectrum and spectra calculated from the recorded table accelerations during testing are presented in figures 6-7 to 6-12 for Phase I tests with the specimen in an orientation with =0deg. In general the achieved motion of the table undershot the target motion in terms of pseudo-acceleration for the three seismic motions. After amplitude scaling the input signal to 125% to 150% of its initial values, the spectra generally reached or slightly exceeded the target spectrum in the primary period range of interest which is from approximately 0.40sec (fixed-base) to 1.2sec (accounting for the elongated period during rocking). The spectra for the pulse excitations with pulse periods (T_p) of 0.20 and 0.40sec matched well with the target spectrum, however the pulse with period of 0.60sec did not match well. This may be in large part due to the significant uplift and rocking response of the structure when subjected to this pulse, as expected, resulting in more table-structure interaction compared to the other two pulses. Fewer tests were conducted with the pulses (see table 5-5) and thus fewer iterations were performed that correct the table's drive signal for the interaction.

Figures 6-13 to 6-45 show, combined on each figure for a given test, time history plots of the pier relative displacement, defined by (6-4) with $_T = _{T,Y}$ (6-5), base shear force (6-7) normalized by the added weight (W_m=77kN) and specimen weight (W_p=18.7kN), global pier hysteretic behavior in terms of normalized base shear force and pier relative displacement, overlaid with static backbone curves for 1st and 2nd cycle properties (dotted lines), pier leg axial forces (6-8), and devices' hysteretic response, in terms of device force versus device rotation. In the case of $_L$=0 (free rocking), the uplifting displacement (6-9) is shown in place of the devices' hysteresis. Pier leg axial force histories are presented for the two south legs on the left plot and the two north legs in the right plot. The TADAS hysteretic behavior

167

and leg uplifting displacements (for the cases with $_L$=0) are presented in the same manner. For uni-directional response (=0deg.), it is expected that the leg forces, TADAS behavior, and uplifting displacements on the south and north sides, respectively, should be nearly the same for a perfectly symmetric and balanced specimen.

Maximums of the key response parameters are tabulated in table 6-1 for tests conducted during Phase I with =0deg. These values are provided for reference and will be compared later with the values from time history analysis, and with those obtained from the simplified methods of analysis used for design.

6.3.3 Experimental Results of Phase I, =45deg.

The important response quantities described in Section 6.3.1 are presented here for each test that was conducted with an excitation that had an acceleration amplitude of at least 100% of the target base excitation (Section 5.7).

The target 5% damped pseudo-acceleration spectrum, together with the corresponding spectra calculated from the recorded table accelerations during testing are presented in figures 6-46 to 6-51 for Phase I tests with the specimen oriented at =45deg. As discussed in Section 5, the motions are scaled in amplitude to 140% of their target for these set of tests. Similar to what was observed for the prior tests series, (with the tower oriented at =0deg.), the achieved motion of the table undershot the target motion in terms of pseudo-acceleration. However, successive increases in the amplitude of the motions were not performed because the purpose of this set-up and set of tests was to observe a "pseudo" bi-directional behavior (simultaneous uplift and yielding of three of the devices, resulting in the pier supported on a single leg) using the 5DOF shake table and this goal was achieved with the motions with spectra slightly less than 140% of the target.

For the orientation with =45deg., calculation of some of the key response quantities is slightly changed. Pier relative displacement is still measured and calculated in the global X-direction (N-S) the same way as before since the string pots and Krypton diodes still measure

with respect to a fixed reference system. The base shear, calculated using strain gages on the first panel diagonals, is now equal to:

$$BS_{SG, \theta=45} = f_{BFMF} \cdot 2\, E\, A_{coupler} \cdot \cos \theta_{dl} \cdot \left(SG_1 + SG_2 + SG_3 + SG_4 \right) \cdot \cos 45^{o} \qquad (6\text{-}10)$$

where all terms have been defined previously. The other two strain gages and the cos(45º) is added to account for the rotated specimen. The base shear force is calculated in the global X-direction from data measured on the diagonal braces in all panels which are oriented 45deg. from the X-direction. The static backbone curve overlaid on the hysteretic plots is from the hysteretic properties presented in Section 4, with the pier displaced along the path with =45deg. and thus has a yield strength of $\sqrt{2}$ $P_{y,uni}$. The pier leg axial forces, TADAS hysteretic behavior, and uplifting displacements are calculated the same as described in Section 6.3.1 since they can be calculated from the same instruments, independent of the orientation of the specimen. Finally, plots showing time history traces of these quantities are shown in figures 6-52 to 6-77 for Phase I tests with the specimen oriented at =45deg.

Maximums of the key response parameters are tabulated in table 6-2 for tests conducted during Phase I with =45deg.

6.3.4 Experimental Results of Phase II

The important response quantities described in Section 6.3.1 are presented here for each test of Phase II that was conducted with an excitation that had an acceleration amplitude of at least 100% of the target base excitation (Section 5.7).

The target 5% damped pseudo-acceleration spectrum and spectra calculated from the recorded table accelerations during testing are presented in figures 6-78 to 6-83 for Phase II tests. Spectra are presented for each of the motions (Newhall and Synthetic) for each excitation direction (X, Y, and Z). In the two horizontal directions (X and Y), it can be seen in the figures that the achieved spectra is slightly less than the target spectrum beyond a period of approximately 0.25sec for the case of the Newhall record and beyond approximately 0.40sec for the case of the Synthetic record. In the period range less than these values, the table begins to overshoot the target spectrum. This was achieved at the best possible controller settings of the table actuators. The differences in the horizontal spectral

169

values for this range of periods was deemed acceptable since it was not expected that the response of the structure would be significantly affected by frequency content much higher than the fixed-base lateral period of vibration (0.40sec). The vertical spectra also overshoot the target spectrum in the range of the vertical period of the specimen (~0.06sec). The differences between the target and achieved spectra for both horizontal and vertical excitations will be accounted for when comparing experimental results with prediction from the analytical methods.

Calculation of the key response quantities is very similar to the case during Phase I with θ=0deg. The pier relative displacement is calculated from (6-4) with $\theta_T=\theta_{T,Y}$ (6-5) for displacement in the X-direction (Δ_x) and equal to (6-4) with $\theta_T=\theta_{T,X}$ (6-6) for displacement in the Y-direction. The base shear in the X-direction is calculated as:

$$BSX_{SG} = f_{BFMF} \cdot E\,A_{coupler} \cdot \cos\theta_{dl} \cdot \left(SG_1 + SG_2 - SG_{21} - SG_{22} \right) \qquad (6\text{-}11)$$

For this phase of testing, all 4 diagonal member strain gages in the 1st panel, in each direction were recorded. Similarly, for base shear in the Y-direction:

$$BSY_{SG} = f_{BFMF} \cdot E\,A_{coupler} \cdot \cos\theta_{dl} \cdot \left(SG_3 + SG_4 - SG_{23} - SG_{24} \right) \qquad (6\text{-}12)$$

The static backbone curve overlaid in the hysteretic plots for the X- and Y-direction is the uni-directional curves shown in figure 5-10 for each set of devices considered . The pier leg axial forces, TADAS hysteretic behavior, uplifting displacements, and viscous damper forces and displacements are calculated per the procedure presented in Section 6.3.1.

Also shown in these figures for Phase II tests are plane plots that display the bi-directional displacement and force response traces for each test. In these plots, the pier relative displacement is shown normalized by the uni-directional yield displacement and the base shear force normalized by the uni-directional yield force. These figures provide a sense of the bi-directional displacement path in the plane of the added mass (top of pier) and bi-directional shear force history. Note, in the shear force plots, most of the response is in a box from -1 to 1 ($P_{y,uni}$) due to the limitation in the "static" force in each direction. Of course, force response exceeding $P_{y,uni}$ is observed and is mostly due to the dynamic rocking effects.

Plots showing time history traces of the above quantities are shown in figures 6-84 to 6-104 for Phase II.

Maximums of the key response parameters are tabulated in table 6-3 for tests conducted during Phase II.

6.4 Results Comparison Between Experimental and Nonlinear Time History Analysis

The response of the experimental specimen was predicted analytically using nonlinear time history analysis. Discussion of the analytical model, used for the time history analysis, is provided in Section 6.4.1 followed by comparison of the key response parameters with the experimental results (Section 6.4.2). First, comparison is made between the peak experimental response quantities (from tables 6-1 to 6-3) and peak response results from time history analysis. Then, response history traces are compared for a selected number of cases in Section 6.4.3 followed by discussion of differences between predicted and observed response in Section 6.4.4.

6.4.1 Mathematical Model and Analysis Results

The analytical modeling is very similar to that which has been discussed throughout this report. The analytical model of the 4-legged experimental specimen included 3-dimensional analysis as was done in Section 4. Many of the relevant properties of the specimen which were applied to elements in the analytical model are tabulated in table 5-1. The model mass is lumped in a single node at the geometric centroid of the steel mass plates that acts in the 3 translation DOF. The mass moments of inertia of the steel plates about each axis is also accounted for at this single node (thus the effects of torsion are accounted for). This node is then constrained to move as a rigid diaphragm with the nodes at the four connection points of the mass and specimen. The pier specimen's structural members are assumed to remain elastic and are modeled with elastic frame elements with rigid end offsets at the connection points. The diagonal braces are modeled by members that can only resist axial forces (in tension and compression). The pre-tensioning force in the members is applied in the model using a temperature loading on the members to match the prescribed axial force applied on the specimen by pre-tensioning (using reverse threaded couplers). Since the diagonal

171

members could resist both tension and compression forces (without buckling) in the analytical model, the temperature loading was applied only to achieve the correct internal forces in the specimen (not required otherwise analytically to prevent buckling).

Compression-only gap elements were attached to the base of the legs in the vertical and two horizontal directions to simulate the base connection that relied on bearing to resist forces in these three directions. The gap elements provided no resistance to movement vertically upward at the base of the leg, or horizontally towards the inside of the specimen (directions that would otherwise apply tension to the elements). The elements in compression, however, were essentially rigid compared to the specimen itself, as the gap elements were provided with an elastic stiffness of 850kN/mm, compared to the axial stiffness of the pier leg of 52.1kN/mm.

The TADAS elements were modeled using the Wen (1976) plasticity property that is defined by the elastic stiffness, yield force, post-yield stiffness ratio, and a parameter that controls the smoothing of the transition to yield. The elastic stiffness and yield force for each set of devices tested is given in table 5-3. For TADAS devices tested in past research, the post-elastic stiffness was assumed to be 2% of its elastic value and the yielding parameter was set equal to 2. The viscous damper was modeled with the *damper* element in SAP2000 that uses a Maxwell model (Malvern 1969) and has an elastic spring in series with a nonlinear dashpot. The properties of the dashpot element are those given in table 5-3. To achieve purely viscous behavior, the elastic spring is assigned a stiffness of 880kN/mm to make it sufficiently stiff.

Damping was assigned to the model in the form of a Rayleigh damping matrix with 2% of critical damping assigned to periods of 1.5sec and 0.04sec. The upper limit of 1.5sec was chosen to limit the influence of the mass proportional damping term on the structure after it has uplifted from its base and the period of the rocking structure exceeds significantly the fixed-base period of 0.40sec. The lower limit is chosen such that the important higher modes of vibration are not over-damped but spurious high frequencies modes of no significance are

numerically damped out. The variation of modal damping ratios assigned to the model using this approach is plotted in figure 6-105.

The gravitation weight of the specimen is modeled by statically applying these forces at the top of each leg before conducting the dynamic analysis. The analytical model was excited dynamically by applying acceleration histories to the fixed supports. In light of the aforementioned discrepancies observed between the target and achieved motions during testing on the shaking tables, the acceleration of the table recorded during each test (X, Y, and Z) was supplied to the analytical model as the base input (as opposed to the target motion).

Solution of the nonlinear equations of motion is performed using Newmark's average acceleration method (Newmark 1959). Large displacement analysis is performed such that solution of the equilibrium equations are performed in the structure's deformed configuration and uses an updated Lagrangian approach (Bathe 1996) for updating nodal positions (in hindsight, for the problem considered here, it was probably not necessary to use large displacement analysis). To ensure accuracy in the solution, a convergence study was undertaken decreasing the size of the solution time step (t) and convergence tolerance (defined in the program as the magnitude of the force error over the magnitude of the force on the structure). The case with $_L$=0 subjected to the 3 components of the synthetic record was deemed the most critical case due to the significant amount of deformation and impact velocity within the rigid gap elements. Some of the key response quantities monitored were the pier leg forces, gap forces, pier displacements, and uplifting displacements. Following a few iterations, a time step of 0.0001sec and force convergence tolerance of 1E-10 was found to provide accurate results and was used for all analyses.

Maximum response parameters for all analyses are tabulated in table 6-4. Results include tests from both Phase I and II of the experimental testing program.

6.4.2 Comparison of Peak Response

The experimental and time history analytical results for Phase I tests are compared in terms of peak relative displacement, peak base shear force, peak pier leg axial force, and peak uplift displacement in figures 6-106 to 6-109 where subscripts "Exp" refers to the experimental results from table 6-1 to 6-3 and "TH" refers to the values in table 6-4. Separate data points are shown on the figures for each set-up considered in Phase I. A solid, dark line is plotted for $Q_{Exp}=Q_{Analytical}$ (Q referring in general to a peak response quantity). This line defines a boundary for each data point that represents conservative (below line) and unconservative (above line) prediction of response. The second solid line represents the average difference of the data from this boundary and is defined in general as:

$$Q_{Exp} = Q_{Analytical} + \mu_{\Delta Q}$$ (6-13)

where μ_Q=mean difference between the experimental and analytical data points and is defined as:

$$\mu_{\Delta Q} = \frac{\sum\limits_{i=1}^{n} \left[Q_{Exp}(i) - Q_{Analaytical}(i) \right]}{n}$$ (6-14)

where n=total number of tests run for the cases considered. Two dotted lines are also shown on the plots, corresponding to the mean difference of the data plus and minus one standard deviation of the data, σ_Q, and defined as:

$$Q_{Exp} = Q_{Analytical} + \mu_{\Delta Q} \pm \sigma_{\Delta Q}$$ (6-15)

where σ_Q is defined as:

$$\sigma_{\Delta Q} = \sqrt{\frac{\sum\limits_{i=1}^{n} \left[Q_{Exp}(i) - Q_{Analaytical}(i) - \mu_{\Delta Q} \right]^2}{n-1}}$$ (6-16)

Figures 6-106 and 6-109 show a good correlation between the experimental and time history analysis results in terms of maximum relative and uplifting displacement. More scatter in the data exists for the maximum force demands with some points that deviate significantly from the predicted force.

Similar comparison between experimental and analytical results is presented for Phase II tests in figures 6-110 to 6-115. Since this phase of testing included bi-directional horizontal input in addition to vertical input, the same response quantities considered previously for the Phase I tests are presented along with relative displacement and base shear in the other horizontal direction (Y). Again, good correlation is seen for the displacement quantities, however, with more variability for the force quantities. Note the good correlation of base shear results for cases with viscous dampers attached vertically at the base (circle data points in figure 6-112). Interestingly, the same figure shows that the analytical results for other cases (especially free rocking) can exceed the experimental values by 150% to 200%.

6.4.3 Comparison of Selected Time History Traces

To better understand the differences between the theoretical and experimental responses, selected data points were chosen for which complete traces of responses were plotted. Comparison of the experimental and analytical time history responses of the specimen is presented in terms of response history traces of some of the key response parameters. The following cases are presented in figures 6-116 to 6-124:

- Phase I, =0deg., $_L$=0, Synthetic 100%
- Phase I, =0deg., $_L$=0.33, Newhall 125%
- Phase I, =0deg., $_L$=0.67, Synthetic 150%
- Phase I, =0deg., $_L$=0, Pulse P2 T_p=0.60sec 100%
- Phase II, $_L$=0, Synthetic 150%
- Phase II, $_L$=0.33, Synthetic 100%
- Phase II, $_L$=1.0, Newhall 150%
- Phase II, $_{LV}$, Newhall 200%
- Phase II, $_{LV}$, Synthetic 175%

For the Phase I tests, results of the relative pier displacement, base shear force, and pier leg axial force of leg 1 (SE leg) are presented. For the Phase II tests, the relative pier displacement is both X- and Y-directions, base shear (X & Y), and pier leg axial force of leg 1 (SW leg) are presented. To investigate the causes of the observed differences between these results, a number of analytical parameters were varied, as described in the next section.

6.4.4 Potential Sources for Response Variability

6.4.4.1 Force Response

Looking at the base shear results of Phase II (figures 6-112 and 6-113), there exists significant variability between the experimental and predicted response in terms of peak response. This is especially true for cases without viscous dampers. The time history traces of the cases of free rocking (figure 6-120) and with TADAS devices attached (figures 6-121 and 6-122) show significant overshooting of the force response in the analysis compared to the experimental results. Also, many of these overshoots appear to be a result of higher frequency mode participation. However, the analyses with viscous dampers attached to the base (figures 6-123 and 6-124) provide a much better match with the experimental results. Thus it appears that the model has some rather severe sensitivity to the damping, at least in the calculation of the force response.

Some analyses were re-run with increasing levels of damping in the higher frequency range by changing the stiffness proportional damping term in the Rayleigh damping matrix to levels of 3, 5, and 10% of critical at 25Hz (0.04sec). The changes in the modal damping ratios from the initially assigned value of 2% at this frequency is shown in figure 6-125. New traces for the case of $_L=0$, Syn 150% (Phase II) are presented in figure 6-126 to 6-128 to show the sensitivity of the response to these changes in damping.

Using increased levels of damping in the higher frequency range eliminates some of the higher mode response (which is present in the analytical results but not observed experimentally). However, there still exists significant spikes in the force response (even with 10% damping), especially in the base shear response (figure 6-128c and d). In investigating the cause of these high frequency modes, it was found that removing mass attributed to the specimen's structural members (the member self-weight not the added mass) in the analytical model eliminated some of the localized higher modes within the structure, as seen by comparing results in figure 6-129 with the results of figure 6-128 where each case has 10% critical damping at 25Hz in the Rayleigh damping model. However, these large increases in damping in the higher frequency range and removal of mass are not physically

justifiable at this time. It is suspected to be a numerical issue possibly introduced by the participation of higher and unrealistic modes of vibration.

Another source of energy loss in reality (experimentally) and one of the major differences between the analytical model and experimental specimen is at the boundary conditions at the base of the specimen. The use of elastic gap elements at the base do not allow for attenuation of stress waves out of the structure and into the supports rather they require dissipation of the waves within the structural damping model. In reality, and in the tests, these waves could travel out from the base of the columns and into the shaking table, hydraulic actuators, and eventually into table support and laboratory foundation providing radiation damping. Modeling of this wave propagation problem was beyond the scope of this research. Other researchers (Wolf, 1991) have proposed using assemblages of discrete springs and dashpots to more accurately model the boundary conditions and account for this effect. Using one-dimensional wave propagation theory with the following assumptions: harmonic stress waves propagate out of the base of the specimen's columns when in contact with the supports, that these waves are not affected by the boundary (i.e. there is no reflection of the waves), and the waves are not reflected off of another boundary and return to the column; then the required linear damping coefficient of an added discrete damper to remove these stress waves at this boundary should be set equal to:

$$c_{bound} = \rho_m v_m A_m \qquad (6\text{-}17)$$

where ρ_m=mass density of the boundary material, v_m=speed of wave propagation through the material at the boundary, and A_m=area of boundary interface.

To investigate this hypothesis, analysis was re-run for the case of ζ_L=0, Syn 150% (Phase II), modifying the boundary conditions at the base of the column leg to that shown in figure 6-130. Thus a Maxwell damping element was placed in series with another gap element which was added to the existing gap element. Adding the gap element in series with the damper element would only allow the damping element to be activated when the base of the leg was in contact with the support. It was hoped that this would model the radiation damping and eliminate "trapping" of the stress waves that was possibly causing the higher frequency response. For the case considered here, the boundary material was steel (ρ_m=7849kg/m^3) and

177

the boundary interface was the base of the column, thus $A_m=A_{Lm}=15.5cm^2$. Implementing the discrete dampers vertically at the base would dissipate the p-waves from the column therefore the wave speed would be the p-wave speed of steel ($v_m=5960m/sec$). This resulted in a discrete damping coefficient from (6-17) equal to 0.0725kN*sec/m. The results of the analysis of this case are shown in figure 6-131. Adding the discrete dampers at the base removed a significant amount of the higher frequency oscillations, but not completely, as high spikes are still visible in the base shear response in the X-direction compared to the experimental results.

6.4.4.2 Force Response with Revised Damping Model

A second set of analyses were performed that included the Rayleigh damping matrix with 10% of critical damping in the higher frequency range and with the pier specimen's mass removed as was the case of the analysis results shown in figure 6-129. These analyses were assumed to provide a set of results for the "calibrated" damping model to match the conditions of the experimental specimen. Each test presented in Section 6.4.4.1 was re-run and the peak response results presented in figures 6-132 to 6-141 for both Phase I and II tests. Comparing the force results from the analytical model with the revised damping model to the previous results, a significant reduction in the scatter of results is evident. This is especially clear comparing the base shear force in the X-direction for Phase II tests (figures 6-112 and 6-138). However, the same figure also shows that the increased damping reduces the force response below that observed, on average, during the experimental tests. Little difference is seen in the peak displacement results, as expected, since the increased damping is only applied in the high frequency range.

The same cases for the time history traces presented in Section 6.4.3 are presented for the analyses run with the revised damping model and are presented in figures 6-142 to 6-150. The response traces show a better match of the force results, removing much of the higher frequency participation. However, it appears that the damping model may be reducing the effect of the vertical modes discussed in past sections (quantified in the design equations by R_{dv} and R_{dL}) as is more clearly seen in figure 6-143.

6.4.4.3 Displacement Response

Looking at the comparison of peak displacement response (figures 6-106, 6-110, and 6-111), there exist few outliers. One potential source of variability could be due to the differences in the applied base excitation between experimental and analytical results. The input for the time history analyses used the actual recorded table accelerations for each test however these recordings only captured the table's motion in the translation degrees of freedom. In some cases, the table's rotational motion could have affected response of the specimen more significantly. Accelerometers were not placed on the table to capture all of the rotational motions however data from the Krypton diodes (measuring displacement in 3D) that were placed on the table did capture the table's rotational motion. As described in Section 6.3, the component of pier relative displacement due to table rotation was removed from the experimental results during its calculation.

To consider the rotational component of input motion, displacement data from the Krypton diodes was applied as displacement loading at the base of the structure in the analytical model and a few analyses were re-run for cases which the displacement response significantly deviated from the predicted response. The following tests were re-run with this type of base excitation:

- Syn100, $_L$=0, =0, PI (**162mm**, 185mm)
- NH125, $_L$=0.33, =0, PI (**117mm**, 170mm)
- Syn100, $_L$=0.33, =45, PI (**140mm**, 145mm)
- NH150, $_L$=0, PII (**146mm**, 81.4mm)

The results of peak relative pier displacement for these analyses are given in parentheses and bold type in the list above along with the previous values. In all cases considered, the results are closer to that seen in the experimental results. The difference in the results is substantial in some cases (NH125, $_L$=0.33, =0, PI and NH150, $_L$=0, PII) and not that substantial in the other cases (Syn100, $_L$=0, =0, PI and Syn100, $_L$=0.33, =45, PI).

179

6.5   Results Comparison Between Experimental and Simplified Analysis and Design Methods

The simplified method of analysis and design equations developed and presented in Sections 3 and 4 are used to predict the dynamic response of the 4-legged controlled rocking experimental specimen and its results are compared with that from testing (tables 6-1 to 6-3). Use of this type of analysis method is more useful for design purposes as it doesn't require time history analysis. The relative pier displacement is predicted using this simplified method of analysis ($\Delta_{rel,Design}$) and is based on the capacity spectrum analysis method that is used throughout this report. Other relevant response quantities ($P_{u,Design}$, $P_{uL,Design}$, $\Delta_{up,Design}$) are predicted using the design equations derived from fundamental research presented in Sections 3 and 4.

6.5.1 Discussion of the Simplified Analysis Method

Due to the differences in the target spectrum and achieved spectra during testing, the horizontal spectra actually achieved by the table are used here and converted to the spectral demand curves when using this simplified method of analysis. In reality, the spectral demand would not be known this accurately for design purposes. The objective here, however, is not to evaluate the variability between design (target) and actual (achieved) spectra inherent in the design process, but rather to assess the method of analysis and design equations.   Therefore, using the achieved spectra eliminated this potential source of difference that is beyond the scope of this study.

A structural capacity curve is also needed for use of the simplified analysis method and is derived from the relevant structural pushover curve as discussed in Section 4. The pushover curve used for both Phase I, θ=0deg. and Phase II tests was the uni-directional pushover curve defined generally in Appendix B for 4-legged piers. The pushover curves for each of specific experimental set-up are presented in figure 5-10. For the tests of Phase I with θ=45deg., however, the structure is undergoing a "pseudo" bi-directional behavior due to its orientation on the 5DOF shake table. For this phase and orientation, the hysteretic path described in Section 4 is known with θ=45deg. Therefore, the structural capacity curve used for the simplified analysis in predicting displacement response of these tests is derived from

the bi-directional hysteretic properties discussed in Section 4.3 with θ=45deg. (π/4). The demand curve is the achieved spectral values calculated from the table acceleration history from each test as done for every other test.

Other relevant details for the use of this method of analysis has been discussed in Section 4 such as calculation of the equivalent damping.

6.5.2 Discussion of Application of Design Equations

6.5.2.1 Displacements

The maximum uplifting displacement is calculated using (4-6). For Phase I with θ=0deg., this equation simplifies to:

$$\Delta_{up,Design} = \left(\Delta_{rel,Design} - \frac{\frac{w_{mz}}{2}(1+\eta_L)\frac{d_m}{h_m}}{k_{om}} \right) \cdot \frac{d_m}{h_m} \tag{6-18}$$

where $\Delta_{rel,Design}$=maximum pier displacement calculated from the simplified method of analysis. For Phase I with θ=45deg., this equation is equal to:

$$\Delta_{up,Design} = \left(\Delta_{rel,Design} - \frac{\frac{w_{mz}}{2}(1+\eta_L)\frac{d_m}{h_m}}{k_{fm}} \cdot \cos 45^\circ \right) \cdot \frac{d_m}{h_m} \tag{6-19}$$

For Phase II, which used two different horizontal inputs, the maximum relative displacement was determined for each direction separately using the corresponding spectrum for the particular direction. The uplifting displacement could then be determined from (4-27) as:

$$\Delta_{up} = \left[\max \left(\begin{array}{c} 1.0\Delta_{rel,DesignX} + 0.40\Delta_{rel,DesignY} \\ 0.40\Delta_{rel,DesignX} + 1.0\Delta_{rel,DesignY} \end{array} \right) - \frac{\frac{w_{mz}}{2}(1+\eta_L)\frac{d_m}{h_m}}{k_{fm}} \right] \cdot \frac{d_m}{h_m} \tag{6-20}$$

where the 1.0 and 0.4 are applied to the maximum relative displacements in each direction following a directional combination rule described in Section 4 to account for the fact that the maximums do not occur in each direction simultaneously. For the tests with the viscous dampers, the uplifting displacement could be calculated with (6-20) with η_L equal to zero since the velocity of each damper force should be nearly zero when the pier is at its maximum displacement.

6.5.2.2 Forces

Predictions of the maximum forces are calculated using concepts presented in past sections. The predicted base shear force is calculated including the effects of vertical excitation and the dynamic forces that develop during rocking. The maximum frame shear force resulting from bi-directional rocking of 4-legged piers was discussed in Section 4.5 and the design equation given by (4-31). Some modifications need to be made to this equation such that it could be used for each testing phase and orientation. For the tests that only considered uni-directional response of the 4-legged pier specimen (Phase I tests, =0deg.), the base shear force prediction is calculated as:

$$P_u = 2 \cdot P_{uF} = 2 \cdot \left[\max \left\{ \begin{array}{l} P_{uF,st} + 1.0 \cdot P_{uF,st} \cdot \left(R_{dv} - 1\right) + 0.4 \cdot \left(\dfrac{m_v}{4} \cdot S_{av} \cdot \dfrac{d}{h} \right) \\[2ex] P_{uF,st} + 0.4 \cdot P_{uF,st} \cdot \left(R_{dv} - 1\right) + 1.0 \cdot \left(\dfrac{m_v}{4} \cdot S_{av} \cdot \dfrac{d}{h} \right) \end{array} \right\} \right] \tag{6-21}$$

where the maximum static frame force is taken equal to:

$$P_{uF,st} = \left(\frac{w_v}{4} + F_{yd} \right) \cdot \frac{d}{h} \tag{6-22}$$

The maximum frame shear force is multiplied by two since two pier frames are acting in parallel in this orientation and the distribution of base shear to each frame is depicted in figure 6-151a. The base shear distribution to each frame for Phase I tests with =45deg. is shown in figure 6-151b. For this case the base shear considered is along the axis of shaking, not orthogonal to the pier frames and therefore is predicted as:

$$P_u = 2\frac{2}{3} \cdot \cos45° \cdot \left[\max \left\{ \begin{array}{l} P_{uF,st} + 1.0 \cdot P_{uF,st} \cdot \left(R_{dv} - 1\right) + 0.4 \cdot \left(\dfrac{3\,m_v}{8} \cdot S_{av} \cdot \dfrac{d}{h} \right) \\[2ex] P_{uF,st} + 0.4 \cdot P_{uF,st} \cdot \left(R_{dv} - 1\right) + 1.0 \cdot \left(\dfrac{3\,m_v}{8} \cdot S_{av} \cdot \dfrac{d}{h} \right) \end{array} \right\} \right] \tag{6-23}$$

where the maximum static frame force is equal to:

$$P_{uF,st} = \left(\frac{3\,w_v}{8} + \frac{3}{2} F_{yd} \right) \cdot \frac{d}{h} \tag{6-24}$$

For Phase II tests, that included bi-directional shaking, the base shear distribution is shown in figure 6-151c and the maximum base shear force, in either direction (X or Y), is calculated as:

$$P_u = 1\frac{1}{3} \cdot P_{uF} = 1\frac{1}{3} \cdot \left[\max \begin{cases} P_{uF,st} + 1.0 \cdot P_{uF,st} \cdot \left(R_{dv} - 1 \right) + 0.4 \cdot \left(\frac{3 m_v}{8} \cdot S_{av} \cdot \frac{d}{h} \right) \\ P_{uF,st} + 0.4 \cdot P_{uF,st} \cdot \left(R_{dv} - 1 \right) + 1.0 \cdot \left(\frac{3 m_v}{8} \cdot S_{av} \cdot \frac{d}{h} \right) \end{cases} \right] \quad (6\text{-}25)$$

where $P_{uF,st}$ is equal to (6-24).

The maximum pier leg axial force is determined using (4-35) for both Phase I with =45deg. and Phase II tests since the specimen is undergoing bi-directional rocking and supported on a single leg, as was discussed in Section 4. For the tests of Phase I with =0deg., the maximum pier leg axial force is predicted by modifying (4-35) to recognize that uni-directional rocking of a 4-legged pier is occurring. The modifications to that equation include the following:

$$F_{ve} = \frac{m_v \cdot S_{av}}{2} \cdot \left(1 - \frac{d}{2h} \right) \quad (6\text{-}26)$$

$$F_{up} = \left(\frac{w_v}{4} + F_{yd} \right) \cdot \left(R_{dv} - 1 \right) \cdot \left(1 - \frac{d}{h} \right) \quad (6\text{-}27)$$

$$P_{uL,st} = \left(\frac{w_v}{4} + F_{yd} \right) \cdot \left(1 - \frac{d}{2h} \right) + \frac{w_v}{4} \quad (6\text{-}28)$$

These equations were derived for the controlled rocking system assuming that the corresponding yield mechanism has formed and includes the dynamic rocking effects and the additional demands from the vertical component of motion. For any tests run without a vertical component of acceleration (Phase I), the vertical spectral acceleration value (S_{av}) that appears in these equations can simply be set equal to zero. For tests conducted with viscous dampers attached at the base (Phase II), the peak forces can be determined using the above equations with F_{yd} replaced by F_{vdo} (3-35).

A set of example calculations that present use of the simplified method of analysis and design equations for use of both the steel yielding devices (TADAS) and viscous dampers are provided in Appendix D for reference.

Finally, results of all peak response values using the simplified method of analysis and design equations are provided in table 6-5.

6.5.3 Comparison of Peak Response

Comparison of the experimental and the simplified methods of analysis are made in an identical manner as was done for the time history results. The response quantity predicted by the simplified analysis and design equations (design quantity) is plotted on the horizontal axis while the experimental response quantity is the vertical coordinate. Figures 6-152 to 6-155 compare results from Phase I tests while figures 6-156 to 6-161 presents results of Phase II tests.

6.5.3.1 Force Response

The maximum force response shown in figures 6-153, 6-154, 6-158, 6-159, and 6-160 is predicted reasonably accurately and conservative in most cases by the simplified methods of analysis. The base shear and pier leg axial force results of Phase I in figures 6-153 and 6-154 show that the design equations predict an increase in force response for increasing strength ratio ($_L$), however, much smaller increases were observed in the experimental results especially for the orientation with =0deg. For the set-ups with =0deg. and low strength ratios, the experimental results match closely with the predicted response.

For the Phase II tests shown in figures 6-158 to 6-160, similar trends of results are seen. However, with increasing prediction in forces, more of a corresponding increase was observed in the experimental results. For instance, the pier leg axial force results for Phase II (figure 6-160) show this trend (even though the predictions are nearly all conservative) compared to the results of Phase I (figure 6-154).

Some of the conservatism observed can be explained. For example, following the derivation of (4-31) and (4-35), that predicts the maximum developed base shear and pier leg axial force, the dynamic effects due to impact, uplift, and vertical excitation are combined with a modal combination rule and added to the forces developed assuming the plastic yield mechanism has formed (uplift and yielding of devices). The energy dissipating devices were designed such that the design level motion would lead to development of the plastic mechanism and the maximum uplifting displacements were limited by deformations to the devices. However not all tests reached the design level thus the displacement response may not have been large enough to develop the plastic mechanism. It is also conservative to assume that the combination of the dynamic effects are occurring simultaneously to when the structure is in the state at which the yield mechanism has formed. This is especially true for the cases with a higher strength ratio (η_L), for which the structure spends less time in a position in which the yield mechanism has developed. In the case of bi-directional response (Phase I, θ=45deg. and Phase II), the structure spends even less time in the state of the bi-directional yielding. On the other hand, the re-designed TADAS devices used in Phase II allowed more device ductility (thus yielded at smaller uplifting displacements) and the input excitation for more of these tests exceeded the design input thus leading to development of the bi-directional yield mechanism sooner and more often.

If these hypotheses are correct, then one would expect the differences between forces observed during experimental testing and the response predictions to decrease as the controlled rocking specimen spent more time in the yielded state. By gaging the amount of yielding by the global displacement ductility ($\mu_{G2}=\Delta_u/\Delta_{y2}$) and comparing it with the percent difference between the base shear force predicted using the design equations and that observed during experiments would provide some verification. Results for the tests performed during Phase I are presented in this manner in figure 6-162 where ΔQ_{Pu} is the difference between the predicted and experimental base shear force and $Q_{exp,Pu}$ is the experimentally observed base shear force. The figure shows the difference between predicted and observed, to reduce for increasing displacement ductility. The figure also shows that the reduction in the differences occurs much faster (with increasing μ_{G2}) for systems with smaller strength ratios (η_L) and for tests with θ=0deg.

6.5.3.2 Displacement Response

For the Phase I tests, the simplified method of analysis predict maximum pier displacements and uplifting displacements with good accuracy as seen in figures 6-152 and 6-155 where the mean difference between experimental and analytical is approximately 10mm on the conservative side and the standard deviation of the difference is approximately 20mm for the case of $_{rel}$.

For the Phase II tests seen in figures 6-156, 6-157, and 6-161, the simplified analysis method yields displacement results that compare closely to the experimental results until the predicted relative pier displacements exceeded approximately 100mm where the experimental results were larger than the predicted by 150% to 200%. With exception of two data points, all of these outlier points for the relative displacement are for $_L$=0 or the viscous damper tests. Taking a closer look at the use of the capacity spectrum method for these cases, it was found that for those systems, having large secant periods, low yield strength, and very low or negative post-yield stiffness (due to P- effect), the intersection of the spectral capacity and demand curves occurs in a range of the spectrum that does not match the target spectrum well. This is illustrated in figure 6-163, which shows the spectral capacity and demand curves for the case of $_L$=0, Syn150%. In this figure, the spectral demand curve does not match the target spectrum beyond a displacement of approximately 260mm and the intersection with the spectral capacity curve occurs at a displacement of 150mm. While the predicted response depends on the intersection of these two curves, the behavior of the system is not completely dependent on this range of the response spectrum and will also depend on the frequency content of the motion prior to uplift and yield which is not considered in this analysis method.

6.6 Summary

The results of the experimental testing program were presented and compared with analytical methods in this section. Reduction of the raw recorded instrument data to relevant response quantities is discussed. The "fixed-base" dynamic properties of the pier specimen were found and the primary horizontal period of vibration was found to be higher (T_{om}=0.40sec) than that determined theoretically in Section 5 (0.33sec). The pier specimen's damping ratio

under horizontal motion was found to be 2.8% of critical however this was believed to be of little significance in the overall response of the controlled rocking pier specimen.

The experimental results were compared to time history analysis; first, in terms peak response of each test and secondly in terms of response traces for selected number of tests. The results showed good correlation of results in terms of displacements however more scatter and in a few cases significant deviation of the force response was observed. The time history results showed significant high frequency spikes in excess of that observed during testing. The force response in the analytical model was shown to be sensitive to the damping model and this was investigated by assigning increasing levels of damping in the high frequency range of the Rayleigh damping model and further comparing discussing results. The advanced analytical model provided a means for investigating the response of controlled rocking piers, however, it appears from the trace comparisons that significant challenges still remain in the modeling of this problem. Some sensitivity studies were conducted with respect to the level of damping provided in the model however a more reliable and physically based method to assign the damping properties are needed.

The peak response from the experimental tests were then compared with the simplified method of analysis and design equations developed in past sections that included uni-directional and bi-directional response with both steel yielding devices and viscous dampers used as the passive control devices. The methods for response predictions were shown to provide conservative and reasonably accurate results compared to the experimental tests. Some significant deviation between the experimental and predicted peak relative pier displacement was observed for a small number of tests.

TABLE 6-1 Experimental Testing Peak Response Results (Phase I, θ=0deg.)

Test	Excitation	Table Motion					Pier Response			
		ACC^H	Δ^H	ACC^V	Δ^V	$\Delta_{REL,P}$	P_u	P_{uL}	Δ_{up}	P_{ud}
η_L000EC100	El Centro - 100%	0.28	13.5	0.15	8.46	9.30	0.13	75.2	1.42	-
η_L000NH67	Newhall - 67%	0.49	34.2	0.35	4.57	41.3	0.18	103.1	8.71	-
η_L000Syn100	Synthetic - 100%	1.16	50.3	1.03	9.38	111.0	0.27	100.0	22.7	-
η_L3300EC100	El Cento - 100%	0.38	16.0	0.27	6.33	13.6	0.15	82.1	2.21	3.64
η_L3300NH100	Newhall - 100%	0.84	52.6	0.41	6.27	65.2	0.22	87.0	12.8	6.95
η_L3300NH125	Newhall - 125%	1.08	66.6	0.71	7.99	116.9	0.28	104.2	24.8	7.15
η_L3300NH100hv	Newhall -100%, H+V	0.88	41.5	0.68	5.08	46.8	0.26	96.3	9.41	5.22
η_L3300Syn100	Synthetic - 100%	0.71	36.1	0.60	7.46	48.3	0.23	93.5	10.2	5.46
η_L3300Syn150	Synthetic - 150%	2.03	67.5	1.17	102	114.7	0.34	131.9	25.0	7.07
η_L3300Syn100hv	Synthetic - 100%, H+V	0.87	28.1	0.52	2.59	33.4	0.20	87.1	7.12	3.83
η_L3300p2tp20100	Pulse P2, T_p=0.20sec - 100%	1.04	17.1	0.71	5.07	15.4	0.19	84.1	2.70	0
η_L3300p2tp40100	Pulse P2, T_p=0.40sec - 100%	0.83	32.5	0.41	4.29	44.3	0.23	97.7	9.32	5.28
η_L3300p2tp60100	Pulse P2, T_p=0.60sec - 100%	0.68	55.5	0.50	2.28	83.6	0.32	102.4	18.1	5.96

*All units in g, mm, or kN

TABLE 6-1 (cont.) Experimental Testing Peak Response Results (Phase I, θ=0deg.)

Test	Excitation	Table Motion						Pier Response		
		ACC^H	Δ^H	ACC^V	Δ^V	$\Delta_{REL,P}$	P_u	P_{uL}	Δ_{up}	P_{ud}
η_L6700EC100	El Centro - 100%	0.45	18.3	0.24	0.40	14.9	0.20	91.5	2.26	11.4
η_L6700NH100	Newhall - 100%	0.73	44.1	0.44	5.28	51.3	0.29	117.4	10.7	17.4
η_L6700NH100hv	Newhall - 100%, H+V	0.85	41.3	1.55	4.99	51.6	0.34	134.0	10.4	16.6
η_L6700Syn100	Synthetic - 100%	0.78	37.4	1.56	8.07	46.6	0.29	116.1	9.53	16.7
η_L6700Syn125	Synthetic - 125%	1.21	42.3	0.64	0.95	60.2	0.29	92.7	12.5	17.9
η_L6700Syn150	Synthetic - 150%	1.29	50.5	0.83	0.81	100.3	0.34	122.1	21.8	19.8
η_L6700Syn100hv	Synthetic -100%, H+V	0.90	34.3	5.99	10.82	52.8	0.39	161.2	12.4	18.7
η_L6700p2tp20100	Pulse P2, T_p=0.20sec - 100%	1.03	17.3	0.79	5.99	15.0	0.16	82.1	2.85	1.30
η_L6700p2tp40100	Pulse P2, T_p=0.40sec - 100%	0.97	33.2	0.33	4.85	45.4	0.25	104.9	8.48	16.2
η_L6700p2tp60100	Pulse P2, T_p=0.60sec - 100%	0.58	42.5	0.45	2.79	70.9	0.26	119.8	14.3	18.3
η_L10000EC100	El Centro - 100%	0.26	12.1	0.12	1.95	8.29	0.16	76.0	1.20	6.38
η_L10000EC100hv	El Centro - 100%, H+V	0.42	14.1	0.38	5.44	12.2	0.17	80.9	2.07	0.40

*All units in g, mm, or kN

189

TABLE 6-1 (cont.) Experimental Testing Peak Response Results (Phase I, θ=0deg.)

Test	Excitation	Table Motion						Pier Response		
		ACC^H	Δ^H	ACC^V	Δ^V	$\Delta_{REL,P}$	P_u	P_{uL}	Δ_{up}	P_{ud}
η_L10θ0NH100	Newhall - 100%	0.71	47.3	0.50	3.35	63.2	0.32	123.2	12.5	31.4
η_L10θ0NH100hv	Newhall - 100%, H+V	0.72	43.9	0.45	4.70	63.8	0.26	116.5	12.3	30.6
η_L10θ0Syn100	Synthetic - 100%	0.71	41.4	0.86	8.12	51.4	0.32	133.6	9.53	29.9
η_L10θ0Syn125	Synthetic - 125%	0.94	50.8	1.71	9.86	70.0	0.40	132.1	13.5	32.0
η_L10θ0Syn100hv	Synthetic - 100%, H+V	1.37	37.0	0.78	3.43	60.1	0.39	115.6	12.2	30.4
η_L10θ0p2tp20100	Pulse P2, T_p=0.20sec - 100%	1.08	16.9	0.52	5.92	14.5	0.12	83.7	2.82	0.51
η_L10θ0p2tp40100	Pulse P2, T_p=0.40sec - 100%	0.59	31.5	0.27	2.99	38.2	0.24	98.9	6.61	21.0
η_L10θ0p2tp60100	Pulse P2, T_p=0.60sec - 100%	1.02	81.1	0.56	2.33	134.3	0.36	132.5	28.0	45.6

*All units in g, mm, or kN

TABLE 6-2 Experimental Testing Peak Response Results (Phase I, θ=45deg.)

Test	Excitation	Table Motion					Pier Response			
		ACC^H	Δ^H	ACC^V	Δ^V	$\Delta_{REL.P}$	P_u	P_{uL}	Δ_{up}	P_{ud}
$\eta_L\_0045NH100$	Newhall - 100%	1.05	73.7	1.08	2.67	99.5	0.26	160.6	31.5	-
$\eta_L\_0045Syn100$	Synthetic - 100%	1.03	63.7	0.90	1.05	129.7	0.27	141.6	40.5	-
$\eta_L\_0045p2tp20100$	Pulse P2, T_p=0.20sec - 100%	1.40	16.9	0.49	0.85	15.3	0.23	98.4	2.49	-
$\eta_L\_0045p2tp40100$	Pulse P2, T_p=0.40sec - 100%	0.58	30.3	0.28	0.74	40.1	0.24	120.0	11.6	-
$\eta_L\_0045p2tp60100$	Pulse P2, T_p=0.60sec - 100%	0.37	41.5	0.45	0.55	77.0	0.23	126.2	23.2	-
$\eta_L\_33045NH100$	Newhall - 100%	1.30	59.1	0.59	1.87	73.0	0.30	138.9	20.3	7.52
$\eta_L\_33045NH100hv$	Newhall - 100%, H+V	1.08	57.4	1.84	16.0	77.1	0.60	224.7	24.4	7.57
$\eta_L\_33045Syn100$	Synthetic - 100%	0.98	56.8	0.99	0.97	89.6	0.30	140.8	26.8	7.56
$\eta_L\_33045p2tp20100$	Pulse P2, T_p=0.20sec - 100%	1.49	16.8	0.47	0.85	14.9	0.23	95.5	2.45	0
$\eta_L\_33045p2tp40100$	Pulse P2, T_p=0.40sec - 100%	0.66	29.6	0.27	0.47	38.8	0.23	117.7	11.2	2.06
$\eta_L\_33045p2tp60100$	Pulse P2, T_p=0.60sec - 100%	0.55	39.9	0.37	0.64	76.2	0.25	129.3	22.3	6.86

*All units in g, mm, or kN

TABLE 6-2 (cont.) Experimental Testing Peak Response Results (Phase I, θ=45deg.)

Test	Excitation	Table Motion					Pier Response			
		ACC^H	Δ^H	ACC^V	Δ^V	$\Delta_{REL.P}$	P_u	P_{uL}	Δ_{up}	P_{ud}
η_L67θ45EC67	El Centro - 67%, $\lambda_t=1$	0.35	43.2	0.42	1.05	68.1	0.31	161.8	17.6	18.5
η_L67θ45EC100	El Centro - 100%	0.60	17.7	0.31	0.52	22.5	0.27	106.6	4.57	0.92
η_L67q45NH100	Newhall - 100%	1.10	59.1	0.43	1.75	74.5	0.35	167.9	19.3	18.5
η_L67θ45Syn100	Synthetic - 100%	1.07	49.3	0.68	1.11	80.4	0.41	138.6	22.9	19.4
η_L67θ45Syn100hv	Synthetic - 100%, H+V	1.20	44.0	2.26	10.2	80.5	0.40	141.1	22.6	18.9
η_L67θ45p2tp20100	Pulse P2, T_p=0.20sec - 100%	1.27	18.5	0.45	0.41	17.6	0.20	98.3	3.72	0
η_L67θ45p2tp40100	Pulse P2, T_p=0.40sec - 100%	1.18	34.7	0.38	0.55	47.7	0.26	118.8	13.9	9.95
η_L67θ45p2tp60100	Pulse P2, T_p=0.60sec - 100%	0.71	40.2	0.37	0.70	67.0	0.29	128.9	19.2	16.2
η_L100θ45NH100	Newhall - 100%	1.32	74.8	0.79	1.87	102.0	0.51	245.1	23.7	35.1
η_L100θ45NH100hv	Newhall - 100%, H+V	0.93	61.6	3.0	17.2	82.1	0.60	240.8	18.5	33.7
η_L100θ45Syn100	Synthetic - 100%	1.00	60.7	1.19	1.31	74.2	0.53	139.7	19.8	36.2

*All units in g, mm, or kN

TABLE 6-2 (cont.)   Experimental Testing Peak Response Results (Phase I, θ=45deg.)

Test	Excitation	Table Motion						Pier Response		
		ACC^H	Δ^H	ACC^V	Δ^V	$\Delta_{REL,P}$	P_u	P_{uL}	Δ_{up}	P_{ud}
η_L100θ45Syn100hv	Synthetic - 100%, H+V	0.86	41.1	2.15	8.31	60.1	0.41	132.9	14.9	28.4
η_L100θ45p2tp20100	Pulse P2, T_p=0.20sec - 100%	1.28	16.4	0.39	0.97	15.9	0.19	90.4	2.73	0
η_L100θ45p2tp40100	Pulse P2, T_p=0.40sec - 100%	0.60	30.1	0.30	0.94	35.8	0.29	126.5	9.45	17.3
η_L100θ45p2tp60100	Pulse P2, T_p=0.60sec - 100%	0.39	40.9	0.34	0.85	63.8	0.40	149.8	16.9	32.5

*All units in g, mm, or kN

TABLE 6-3 Experimental Testing Peak Response Results (Phase II)

Test	Excitation	Table Motion								Pier Response				
		ACC			Δ			$\Delta_{REL,P}$		P_u		P_{uL}	Δ_{up}	P_{ud}
		X	Y	Z	X	Y	Z	X	Y	X	Y			
η_L0NH100	Newhall - 100%	1.17	0.96	0.93	32.8	19.7	10.8	65.4	52.8	0.44	0.20	193	17.2	-
η_L0NH150	Newhall - 150%	1.83	1.49	1.12	48.1	29.9	15.8	193	68.1	0.44	0.29	193	48.9	-
η_L0Syn100	Synthetic - 100%	1.01	1.09	1.23	45.1	43.2	26.7	202	174	0.41	0.42	305	60.9	-
η_L0Syn150	Synthetic - 150%	1.61	2.05	1.46	67.8	64.6	40.3	236	212	0.55	0.40	315	81.9	-
η_L33NH100	Newhall - 100%	1.17	0.93	0.80	32.6	19.9	10.6	54.8	45.9	0.38	0.20	166	15.4	9.41
η_L33Syn100	Synthetic - 100%	1.02	1.14	1.27	45.0	43.2	26.6	97.9	90.7	0.34	0.29	194	22.6	8.69
η_L33Syn150	Synthetic - 150%	1.48	1.88	1.37	68.2	64.4	40.3	153	208	0.38	0.20	314	53.7	19.2
η_L67NH100	Newhall - 100%	1.03	0.88	0.73	31.5	20.1	10.6	55.6	39.4	0.35	0.23	175	11.5	17.1
η_L67Syn100	Synthetic - 100%	1.15	1.18	1.16	44.2	43.6	26.6	67.4	92.3	0.33	0.36	199	20.9	22.7
η_L67Syn150	Synthetic - 150%	1.79	1.84	1.64	68.1	65.5	36.0	159	192	0.43	0.39	314	47.1	29.2
η_L100NH100	Newhall - 100%	1.27	1.02	0.78	32.0	19.4	11.1	57.8	41.4	0.34	0.29	205	14.3	39.2
η_L100NH150	Newhall - 150%	2.07	1.56	1.47	50.1	30.1	16.2	84.1	62.5	0.37	0.25	230	22.4	37.9
η_L100Syn100	Synthetic - 100%	1.00	1.10	1.12	44.9	43.7	26.6	64.6	88.5	0.40	0.36	206	18.1	39.8
η_L100Syn150	Synthetic - 150%	1.57	1.86	1.60	68.4	65.1	35.7	116	189	0.44	0.50	263	39.0	57.2

*All units in g, mm, or kN

194

TABLE 6-3 (cont.) Experimental Testing Peak Response Results (Phase II)

Test	Excitation	Table Motion						Pier Response						
		ACC			Δ			$\Delta_{REL,P}$		P_u		P_{uL}	Δ_{up}	P_{ud}
		X	Y	Z	X	Y	Z	X	Y	X	Y			
η_{Lv}NH100	Newhall - 100%	1.09	0.95	0.74	32.5	19.7	10.8	53	42.1	0.31	0.23	149	11.3	16.6
η_{Lv}NH150	Newhall - 150%	1.86	1.47	1.15	49.7	30.0	16.1	76.5	59.4	0.40	0.27	189	17.9	19.4
η_{Lv}NH175	Newhall - 175%	2.27	1.81	1.35	57.5	35.4	18.7	100	66	0.37	0.32	205	23.3	21.9
η_{Lv}NH200	Newhall - 200%	2.49	2.00	1.84	64.6	41.0	21.6	124	69.9	0.36	0.30	259	35.8	25.7
η_{Lv}Syn100	Synthetic - 100%	1.06	1.16	1.11	44.7	43.8	26.7	71.1	79.2	0.28	0.26	169	17.7	22.5
η_{Lv}Syn150	Synthetic - 150%	1.51	1.81	1.47	68.3	64.7	40.9	170	167	0.40	0.34	245	41.0	26.1
η_{Lv}Syn175	Synthetic - 175%	1.67	2.10	1.89	79.1	75.1	47.9	198	193	0.42	0.36	296	59.8	29.2

*All units in g, mm, or kN

TABLE 6-4 Time History Analysis Peak Response Results (Phase I, θ=0deg.)

Test	Excitation	Pier Response				
		$\Delta_{REL,P}$	P_u	P_{uL}	Δ_{up}	P_{ud}
η_L0θ0EC100	El Centro - 100%	34.0	0.25	85.4	6.87	-
η_L0θ0NH67	Newhall - 67%	46.7	0.27	84.3	9.62	-
η_L0θ0Syn100	Synthetic - 100%	131.7	0.34	87.3	28.1	-
η_L33θ0EC100	El Cento - 100%	34.5	0.25	85.1	6.80	4.82
η_L33θ0NH100	Newhall - 100%	53.6	0.31	82.6	10.70	6.35
η_L33θ0NH125	Newhall - 125%	75.8	0.34	91.0	15.6	6.59
η_L33θ0NH100hv	Newhall -100%, H+V	52.8	0.59	140.6	11.2	6.21
η_L33θ0Syn100	Synthetic - 100%	98.0	0.34	93.4	20.2	6.69
η_L33θ0Syn150	Synthetic - 150%	159.5	0.51	95.9	34.1	6.93
η_L33θ0Syn100hv	Synthetic - 100%, H+V	119.5	0.31	118.5	25.9	6.72
η_L33θ0p2tp20100	Pulse P2, T_p=0.20sec - 100%	16.1	0.22	82.4	3.26	3.87
η_L33θ0p2tp40100	Pulse P2, T_p=0.40sec - 100%	49.8	0.33	91.7	10.5	6.29
η_L33θ0p2tp60100	Pulse P2, T_p=0.60sec - 100%	93.4	0.31	89.5	19.7	6.68
η_L67θ0EC100	El Centro - 100%	23.9	0.23	84.0	3.96	9.81
η_L67θ0NH100	Newhall - 100%	60.9	0.36	84.9	12.1	13.1
η_L67θ0NH100hv	Newhall - 100%, H+V	52.4	1.03	111.2	10.8	13.0
η_L67θ0Syn100	Synthetic - 100%	84.9	0.49	87.5	17.4	13.5
η_L67θ0Syn125	Synthetic - 125%	101.3	0.40	106.0	20.9	13.7
η_L67θ0Syn150	Synthetic - 150%	120.1	0.46	105.7	24.8	13.9
η_L67θ0Syn100hv	Synthetic -100%, H+V	93.0	0.96	98.9	19.8	13.6
η_L67θ0p2tp20100	Pulse P2, T_p=0.20sec - 100%	16.5	0.27	80.8	3.0	8.5
η_L67θ0p2tp40100	Pulse P2, T_p=0.40sec - 100%	53.0	0.37	94.4	10.7	13.0

*All units in g, mm, or kN

TABLE 6-4 (cont.) Time History Analysis Peak Response Results (Phase I, θ=0deg., θ=45deg.)

Test	Excitation	Pier Response				
		$\Delta_{REL,P}$	P_u	P_{uL}	Δ_{up}	P_{ud}
$\eta_L6\theta0p2tp60100$	Pulse P2, T_p=0.60sec - 100%	94.1	0.31	92.1	19.3	13.6
$\eta_L10\theta0EC100$	El Centro - 100%	18.5	0.24	87.8	3.0	13.9
$\eta_L10\theta0EC100hv$	El Centro - 100%, H+V	23.4	0.55	89.2	3.56	16.8
$\eta_L10\theta0NH100$	Newhall - 100%	59.5	0.36	92.6	11.7	19.4
$\eta_L10\theta0NH100hv$	Newhall - 100%, H+V	52.0	0.44	124.2	11.1	18.9
$\eta_L10\theta0Syn100$	Synthetic - 100%	71.6	0.39	88.7	14.0	19.8
$\eta_L10\theta0Syn125$	Synthetic - 125%	90.8	0.34	96.3	18.5	20.5
$\eta_L10\theta0Syn100hv$	Synthetic - 100%, H+V	79.1	0.54	112.9	16.4	20.1
$\eta_L10\theta0p2tp20100$	Pulse P2, T_p=0.20sec - 100%	17.4	0.26	87.7	2.8	14.9
$\eta_L10\theta0p2tp40100$	Pulse P2, T_p=0.40sec - 100%	55.0	0.30	92.1	10.7	19.3
$\eta_L10\theta0p2tp60100$	Pulse P2, T_p=0.60sec - 100%	92.8	0.37	94.6	18.7	20.5
$\eta_L0\theta45NH100$	Newhall - 100%	84.0	0.28	138	25.5	-
$\eta_L0\theta45Syn100$	Synthetic - 100%	164.8	0.31	132	49	-
$\eta_L0\theta45p2tp20100$	Pulse P2, T_p=0.20sec - 100%	22.9	0.27	139.4	6.75	-
$\eta_L0\theta45p2tp40100$	Pulse P2, T_p=0.40sec - 100%	65.1	0.25	125.7	18.4	-
$\eta_L0\theta45p2tp60100$	Pulse P2, T_p=0.60sec - 100%	128.4	0.26	128.5	38.1	-
$\eta_L33\theta45NH100$	Newhall - 100%	73.4	0.35	138.3	21.1	6.72
$\eta_L33\theta45NH100hv$	Newhall -100%, H+V	71.7	0.58	130.3	20.9	6.71
$\eta_L33\theta45Syn100$	Synthetic - 100%	122.8	0.38	152.2	35.8	7.0
$\eta_L33\theta45p2tp20100$	Pulse P2, T_p=0.20sec - 100%	22.8	0.32	131.8	6.15	5.52

*All units in g, mm, or kN

TABLE 6-4 (cont.) Time History Analysis Peak Response Results (Phase I, θ=45deg.)

Test	Excitation	Pier Response				
		$\Delta_{REL,P}$	P_u	P_{uL}	Δ_{up}	P_{ud}
$\eta_L33\theta45p2tp40100$	Pulse P2, T_p=0.40sec - 100%	68.8	0.29	144.5	19.0	6.66
$\eta_L33\theta45p2tp60100$	Pulse P2, T_p=0.60sec - 100%	128.5	0.36	132.9	37.3	7.01
$\eta_L67\theta45EC67$	El Centro - 67%, λ_t=1	104.4	0.31	148.2	29.3	14.1
$\eta_L67\theta45EC100$	El Centro - 100%	33.6	0.24	130.7	7.93	12.5
$\eta_L67q45NH100$	Newhall - 100%	83.1	0.32	154.2	23.3	13.8
$\eta_L67\theta45Syn100$	Synthetic - 100%	113.2	0.35	147.3	32.1	14.2
$\eta_L67\theta45Syn100hv$	Synthetic - 100%, H+V	126.5	0.46	147.4	37.0	14.4
$\eta_L67\theta45p2tp20100$	Pulse P2, T_p=0.20sec - 100%	22.6	0.31	133.1	5.51	11.4
$\eta_L67\theta45p2tp40100$	Pulse P2, T_p=0.40sec - 100%	71.6	0.28	158.9	19.6	13.6
$\eta_L67\theta45p2tp60100$	Pulse P2, T_p=0.60sec - 100%	130.6	0.30	156.0	38.0	14.4
$\eta_L100\theta45NH100$	Newhall - 100%	84.4	0.43	166.7	22.5	20.9
$\eta_L100\theta45NH100hv$	Newhall - 100%, H+V	79.5	0.74	164.5	22.8	20.9
$\eta_L100\theta45Syn100$	Synthetic - 100%	101.1	0.39	170.9	27.8	21.5
$\eta_L100\theta45Syn100hv$	Synthetic - 100%, H+V	113.0	0.51	173.9	33.1	22.1
$\eta_L100\theta45p2tp20100$	Pulse P2, T_p=0.20sec - 100%	23.4	0.31	137.9	4.7	17.8
$\eta_L100\theta45p2tp40100$	Pulse P2, T_p=0.40sec - 100%	73.0	0.28	167.1	19.8	20.5
$\eta_L100\theta45p2tp60100$	Pulse P2, T_p=0.60sec - 100%	129.6	0.31	176.4	37.4	22.5

*All units in g, mm, or kN

TABLE 6-4 (cont.) Time History Analysis Peak Response Results (Phase II)

Test	Excitation	Pier Response						
		$\Delta_{REL,P}$		P_u		P_{uL}	Δ_{up}	P_{ud}
		X	Y	X	Y			
$\eta_L0NH100$	Newhall - 100%	62.7	49.6	0.45	0.24	169	19.5	-
$\eta_L0NH150$	Newhall - 150%	81.4	94.7	0.75	0.48	302	33.5	-
$\eta_L0Syn100$	Synthetic - 100%	178	154	0.86	0.40	243	58.4	-
$\eta_L0Syn150$	Synthetic - 150%	227	202	0.74	0.66	390	90.6	-
$\eta_L33NH100$	Newhall - 100%	59.4	38.1	0.84	0.26	174	14.6	7.29
$\eta_L33Syn100$	Synthetic - 100%	90.1	113	0.53	0.38	237	42.5	8.45
$\eta_L33Syn150$	Synthetic - 150%	187	198	0.58	0.47	313	66.4	9.20
$\eta_L67NH100$	Newhall - 100%	54.5	35.8	0.40	0.28	173	13.7	14.2
$\eta_L67Syn100$	Synthetic - 100%	79.1	86.7	0.45	0.40	195	19.9	15.0
$\eta_L67Syn150$	Synthetic - 150%	198	188	0.68	0.48	266	58.1	17.9
$\eta_L100NH100$	Newhall - 100%	50.6	37.3	0.34	0.28	158	11.3	19.3
$\eta_L100NH150$	Newhall - 150%	79.5	49.7	0.71	0.29	231	19.6	20.5
$\eta_L100Syn100$	Synthetic - 100%	58.7	82.3	0.55	0.34	208	18.1	19.9
$\eta_L100Syn150$	Synthetic - 150%	120	196	0.75	0.57	282	50.5	23.0
$\eta_{LV}NH100$	Newhall - 100%	52.8	34.2	0.29	0.19	161	11.0	16.2
$\eta_{LV}NH150$	Newhall - 150%	62.6	49.4	0.44	0.28	206	15.5	18.4
$\eta_{LV}NH175$	Newhall - 175%	84.3	64.1	0.42	0.39	214	19.2	23.0
$\eta_{LV}NH200$	Newhall - 200%	105	78.2	0.45	0.49	247	34.1	26.2
$\eta_{LV}Syn100$	Synthetic - 100%	78.4	72.8	0.25	0.31	173	19.2	19.7
$\eta_{LV}Syn150$	Synthetic - 150%	174	175	0.37	0.38	195	49.9	22.2
$\eta_{LV}Syn175$	Synthetic - 175%	207	185	0.48	0.37	227	58.8	24.6

*All units in g, mm, or kN

TABLE 6-5   Simplified Analysis Peak Response Values (Phase I, θ=0deg.)

Test	Excitation	Pier Response				
		$\Delta_{REL,P}$	P_u	P_{uL}	Δ_{up}	P_{ud}
$\eta_L 0\theta 0EC100$	El Centro - 100%	49.5	0.19	68.2	10.1	-
$\eta_L 0\theta 0NH67$	Newhall - 67%	94.0	0.19	74.2	19.9	-
$\eta_L 0\theta 0Syn100$	Synthetic - 100%	107	0.19	75.5	22.8	-
$\eta_L 33\theta 0EC100$	El Cento - 100%	53.3	0.24	81.4	10.7	9.65
$\eta_L 33\theta 0NH100$	Newhall - 100%	102	0.24	88.1	21.3	9.96
$\eta_L 33\theta 0NH125$	Newhall - 125%	121	0.24	89.9	25.7	10.1
$\eta_L 33\theta 0NH100hv$	Newhall -100%, H+V	102	0.33	125	21.3	9.96
$\eta_L 33\theta 0Syn100$	Synthetic - 100%	85.1	0.24	85.9	17.8	9.88
$\eta_L 33\theta 0Syn150$	Synthetic - 150%	108	0.24	88.5	22.9	10.0
$\eta_L 33\theta 0Syn100hv$	Synthetic - 100%, H+V	85.1	0.35	133	17.8	9.88
$\eta_L 33\theta 0p2tp20100$	Pulse P2, T_p=0.20sec - 100%	21.6	0.24	76.6	3.56	9.47
$\eta_L 33\theta 0p2tp40100$	Pulse P2, T_p=0.40sec - 100%	43.2	0.24	79.9	8.35	9.61
$\eta_L 33\theta 0p2tp60100$	Pulse P2, T_p=0.60sec - 100%	61.0	0.24	82.8	12.3	9.72
$\eta_L 67\theta 0EC100$	El Centro - 100%	45.7	0.32	95.6	8.62	19.2
$\eta_L 67\theta 0NH100$	Newhall - 100%	71.1	0.32	99.5	14.3	19.6
$\eta_L 67\theta 0NH100hv$	Newhall - 100%, H+V	71.1	0.39	136	14.3	19.6
$\eta_L 67\theta 0Syn100$	Synthetic - 100%	86.4	0.32	102	17.7	19.8
$\eta_L 67\theta 0Syn125$	Synthetic - 125%	94.0	0.32	102	19.3	20.0
$\eta_L 67\theta 0Syn150$	Synthetic - 150%	107	0.32	104	22.2	20.2
$\eta_L 67\theta 0Syn100hv$	Synthetic -100%, H+V	86.4	0.41	144	17.7	19.8
$\eta_L 67\theta 0p2tp20100$	Pulse P2, T_p=0.20sec - 100%	21.6	0.32	91.4	3.27	18.8

*All units in g, mm, or kN

200

TABLE 6-5 (cont.) Simplified Analysis Peak Response Values (Phase I, θ=0deg.)

Test	Excitation	Pier Response				
		$\Delta_{REL,P}$	P_u	P_{uL}	Δ_{up}	P_{ud}
η_L67θ0p2tp40100	Pulse P2, T_p=0.40sec - 100%	41.9	0.32	95.0	7.78	19.2
η_L67θ0p2tp60100	Pulse P2, T_p=0.60sec - 100%	57.2	0.32	97.5	11.2	19.4
η_L100θ0EC100	El Centro - 100%	34.3	0.38	107	5.84	27.4
η_L100θ0EC100hv	El Centro - 100%, H+V	34.3	0.42	121	5.84	27.4
η_L100θ0NH100	Newhall - 100%	50.8	0.38	110	9.50	28.0
η_L100θ0NH100hv	Newhall - 100%, H+V	50.8	0.44	144	9.50	28.0
η_L100θ0Syn100	Synthetic - 100%	82.6	0.38	114	16.6	29.2
η_L100θ0Syn125	Synthetic - 125%	96.5	0.38	116	19.7	29.7
η_L100θ0Syn100hv	Synthetic - 100%, H+V	82.6	0.46	154	16.6	29.2
η_L100θ0p2tp20100	Pulse P2, T_p=0.20sec - 100%	21.6	0.38	104	3.02	27.0
η_L100θ0p2tp40100	Pulse P2, T_p=0.40sec - 100%	34.3	0.38	107	5.84	27.4
η_L100θ0p2tp60100	Pulse P2, T_p=0.60sec - 100%	50.8	0.38	110	9.50	28.0

*All units in g, mm, or kN

TABLE 6-5 (cont.) Simplified Analysis Peak Response Values (Phase I, θ=45deg.)

Test	Excitation	Pier Response				
		$\Delta_{REL,P}$	P_u	P_{uL}	Δ_{up}	P_{ud}
$\eta_L0\theta45NH100$	Newhall - 100%	171	0.27	147	51.7	-
$\eta_L0\theta45Syn100$	Synthetic - 100%	158	0.27	145	47.8	-
$\eta_L0\theta45p2tp20100$	Pulse P2, T_p=0.20sec - 100%	28.7	0.24	129	7.15	-
$\eta_L0\theta45p2tp40100$	Pulse P2, T_p=0.40sec - 100%	53.9	0.26	136	15.1	-
$\eta_L0\theta45p2tp60100$	Pulse P2, T_p=0.60sec - 100%	82.6	0.26	140	24.1	-
$\eta_L33\theta45NH100$	Newhall - 100%	89.8	0.30	159	25.7	10.1
$\eta_L33\theta45NH100hv$	Newhall -100%, H+V	89.8	0.44	244	25.7	10.1
$\eta_L33\theta45Syn100$	Synthetic - 100%	108	0.30	160	31.4	10.2
$\eta_L33\theta45p2tp20100$	Pulse P2, T_p=0.20sec - 100%	21.6	0.30	155	4.30	9.49
$\eta_L33\theta45p2tp40100$	Pulse P2, T_p=0.40sec - 100%	39.5	0.30	156	9.94	9.65
$\eta_L33\theta45p2tp60100$	Pulse P2, T_p=0.60sec - 100%	68.2	0.30	157	19.0	9.90
$\eta_L67\theta45EC67$	El Centro - 67%, λ_t=1	79.0	0.38	189	21.8	20.1
$\eta_L67\theta45EC100$	El Centro - 100%	61.1	0.38	188	16.1	19.7
$\eta_L67q45NH100$	Newhall - 100%	71.8	0.38	189	19.5	20.0
$\eta_L67\theta45Syn100$	Synthetic - 100%	89.8	0.38	190	25.2	20.4
$\eta_L67\theta45Syn100hv$	Synthetic - 100%, H+V	75.4	0.52	283	20.6	20.0
$\eta_L67\theta45p2tp20100$	Pulse P2, T_p=0.20sec - 100%	25.1	0.38	186	4.84	19.0
$\eta_L67\theta45p2tp40100$	Pulse P2, T_p=0.40sec - 100%	53.9	0.38	188	13.9	19.6
$\eta_L67\theta45p2tp60100$	Pulse P2, T_p=0.60sec - 100%	64.7	0.38	188	17.3	19.8
$\eta_L100\theta45NH100$	Newhall - 100%	71.8	0.44	215	19.0	29.6

*All units in g, mm, or kN

TABLE 6-5 (cont.) Simplified Analysis Peak Response Values (Phase I, θ=45deg.)

Test	Excitation	Pier Response				
		$\Delta_{REL,P}$	P_u	P_{uL}	Δ_{up}	P_{ud}
η_L100θ45NH100hv	Newhall - 100%, H+V	64.7	0.54	287	16.8	29.2
η_L100θ45Syn100	Synthetic - 100%	79.0	0.44	216	21.3	30.0
η_L100θ45Syn100hv	Synthetic - 100%, H+V	64.7	0.57	303	16.8	29.2
η_L100θ45p2tp20100	Pulse P2, T_p=0.20sec - 100%	21.6	0.44	212	3.21	27.0
η_L100θ45p2tp40100	Pulse P2, T_p=0.40sec - 100%	43.1	0.44	213	9.98	28.1
η_L100θ45p2tp60100	Pulse P2, T_p=0.60sec - 100%	53.9	0.44	214	13.4	28.7

*All units in g, mm, or kN

Table 6-5 (cont.) Simplified Analysis Peak Response Values (Phase II)

Test	Excitation	Pier Response						
		$\Delta_{REL,P}$		P_u		P_{uL}	Δ_{up}	P_{ud}
		X	Y	X	Y			
$\eta_L 0NH100$	Newhall - 100%	76.2	53.3	0.28	0.28	228	19.8	-
$\eta_L 0NH150$	Newhall - 150%	91.4	71.1	0.38	0.38	309	24.8	-
$\eta_L 0Syn100$	Synthetic - 100%	117	99.1	0.33	0.33	270	32.9	-
$\eta_L 0Syn150$	Synthetic - 150%	150	125	0.43	0.43	352	42.5	-
$\eta_L 33NH100$	Newhall - 100%	43.2	38.1	0.31	0.31	245	10.5	10.3
$\eta_L 33Syn100$	Synthetic - 100%	102	88.9	0.36	0.36	288	28.0	11.5
$\eta_L 33Syn150$	Synthetic - 150%	125	109	0.46	0.46	371	34.9	12.0
$\eta_L 67NH100$	Newhall - 100%	43.2	35.6	0.35	0.35	269	9.67	20.5
$\eta_L 67Syn100$	Synthetic - 100%	48.3	88.9	0.40	0.40	311	20.9	22.1
$\eta_L 67Syn150$	Synthetic - 150%	135	114	0.50	0.50	397	37.0	24.3
$\eta_L 100NH100$	Newhall - 100%	45.7	35.6	0.38	0.38	288	9.76	28.1
$\eta_L 100NH150$	Newhall - 150%	53.3	48.3	0.48	0.48	369	12.6	28.5
$\eta_L 100Syn100$	Synthetic - 100%	53.3	73.7	0.43	0.43	330	17.5	29.4
$\eta_L 100Syn150$	Synthetic - 150%	130	117	0.53	0.53	415	35.6	32.4
$\eta_{LV}NH100$	Newhall - 100%	33.0	30.5	0.33	0.33	254	8.16	11.5
$\eta_{LV}NH150$	Newhall - 150%	50.8	40.6	0.43	0.43	338	13.0	12.6
$\eta_{LV}NH175$	Newhall - 175%	63.5	48.3	0.44	0.44	341	16.5	13.1
$\eta_{LV}NH200$	Newhall - 200%	71.1	50.8	0.44	0.44	343	18.4	13.4
$\eta_{LV}Syn100$	Synthetic - 100%	81.3	71.1	0.40	0.40	307	22.5	14.1
$\eta_{LV}Syn150$	Synthetic - 150%	96.5	86.4	0.50	0.50	390	27.2	14.6
$\eta_{LV}Syn175$	Synthetic - 175%	104	91.4	0.50	0.50	392	29.4	14.8

*All units in g, mm, or kN
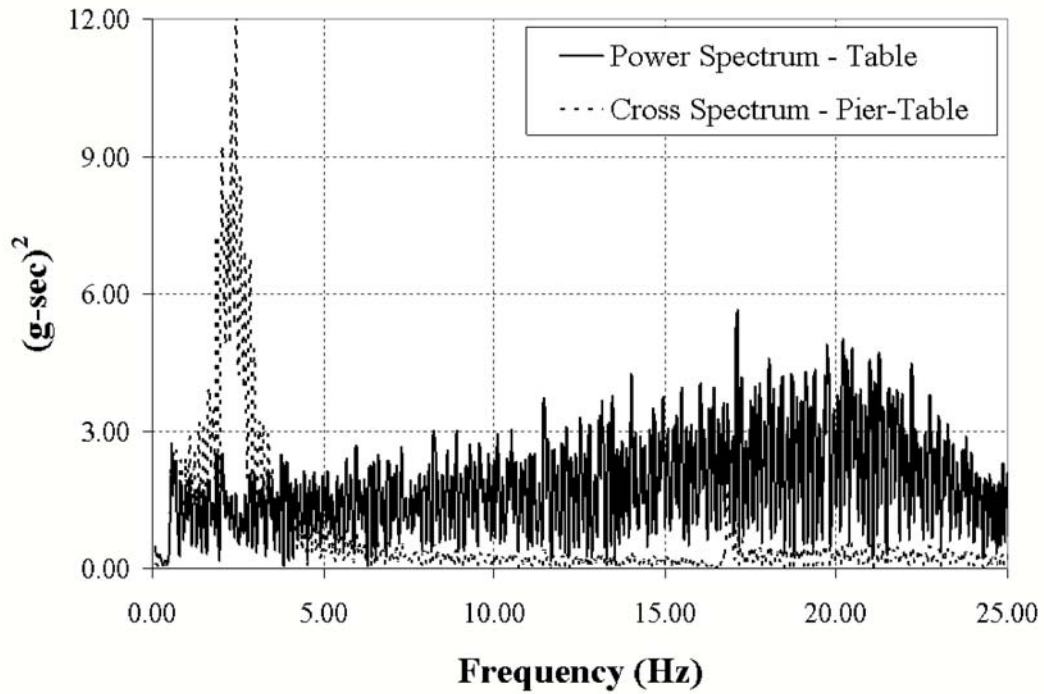
FIGURE 6-1 Example Power and Cross Spectrum Plot for Development of Transfer Function
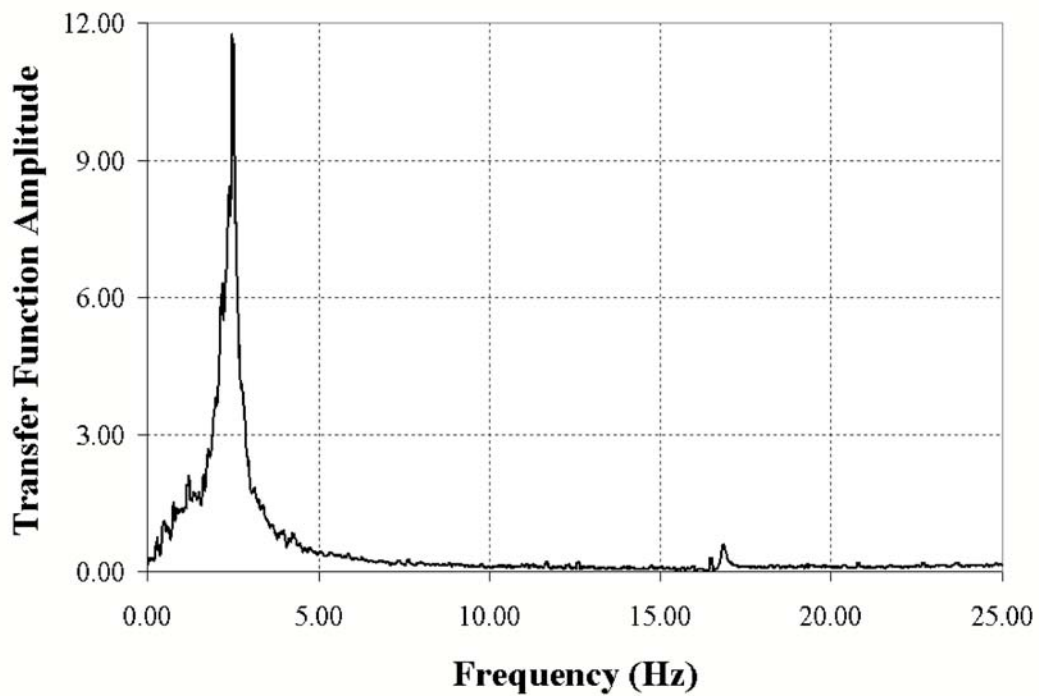
FIGURE 6-2 Example Transfer Function Plot

205
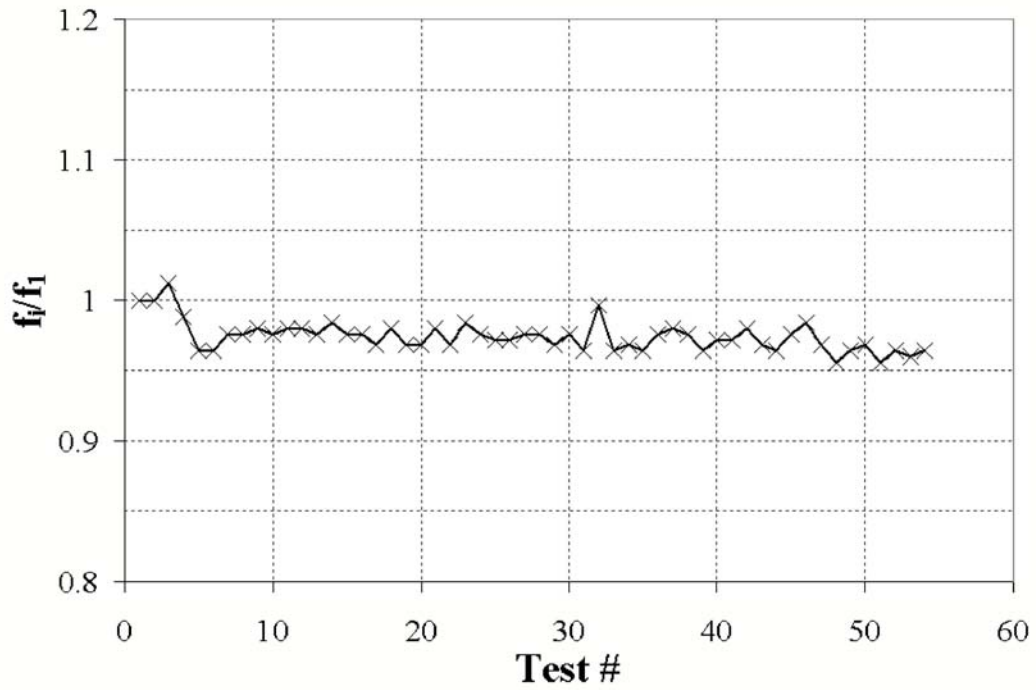
FIGURE 6-3 Specimen Fixed-base Frequency throughout Phase I Testing History

(=0deg.)
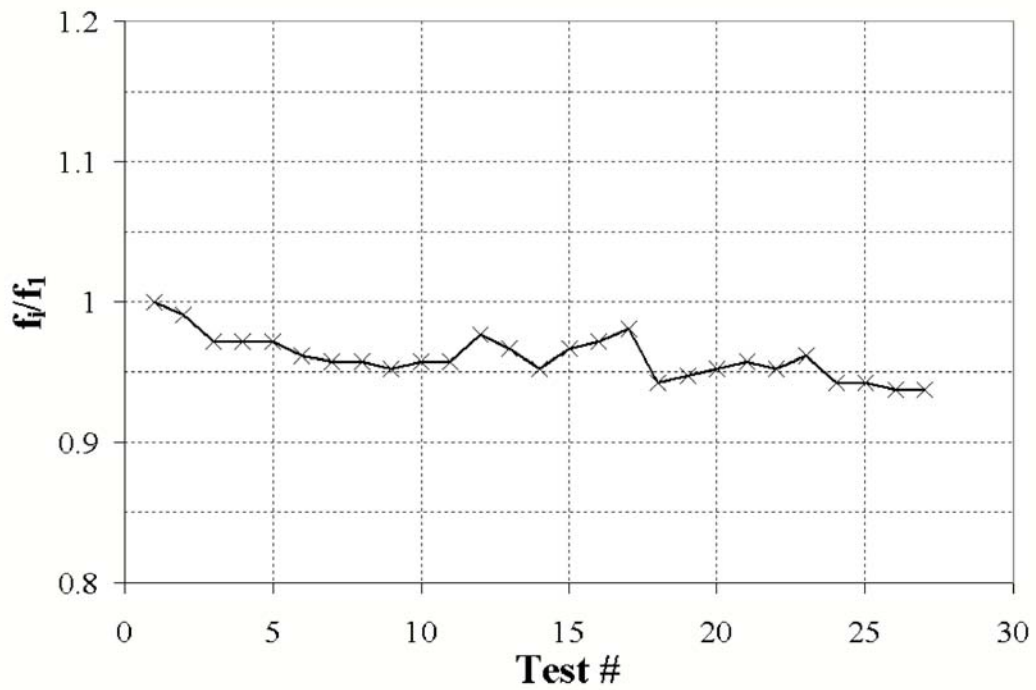
FIGURE 6-4 Specimen Fixed-base Frequency throughout Phase I Testing History

(=45deg.)
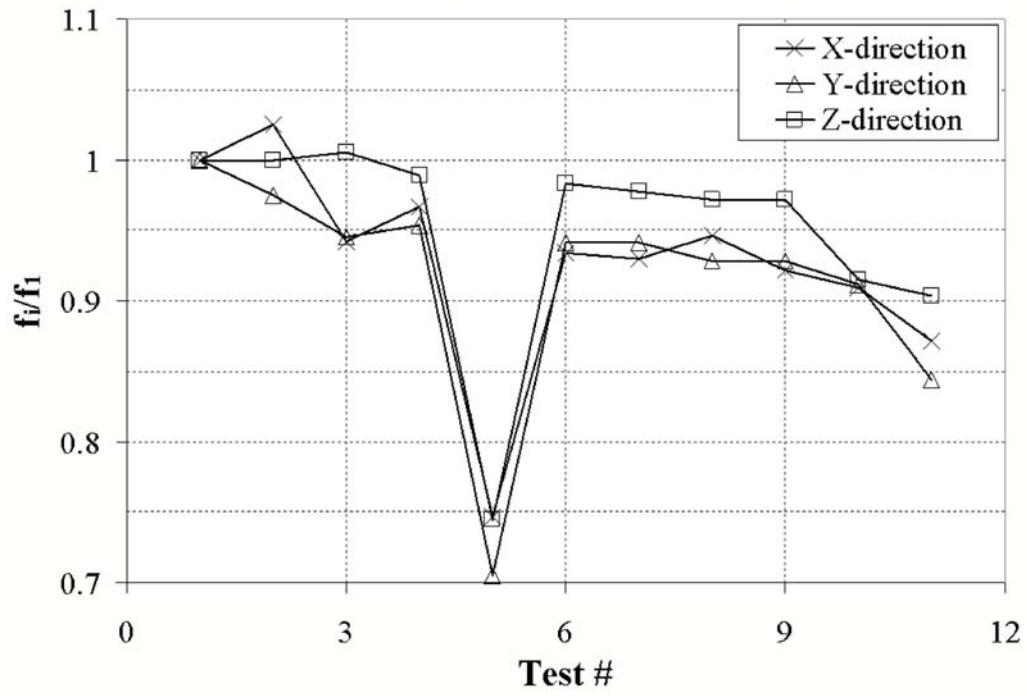
(a)
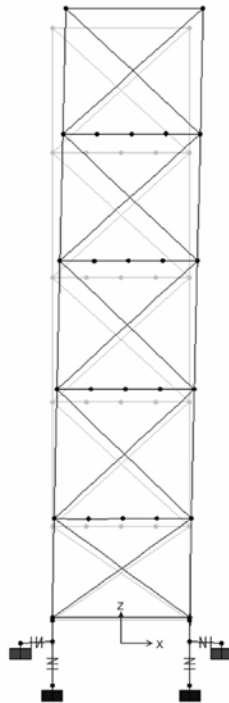
(b)

FIGURE 6-5 (a) Specimen Fixed-base Frequency throughout Phase II Testing History and (b) Specimen Lateral Mode Shape
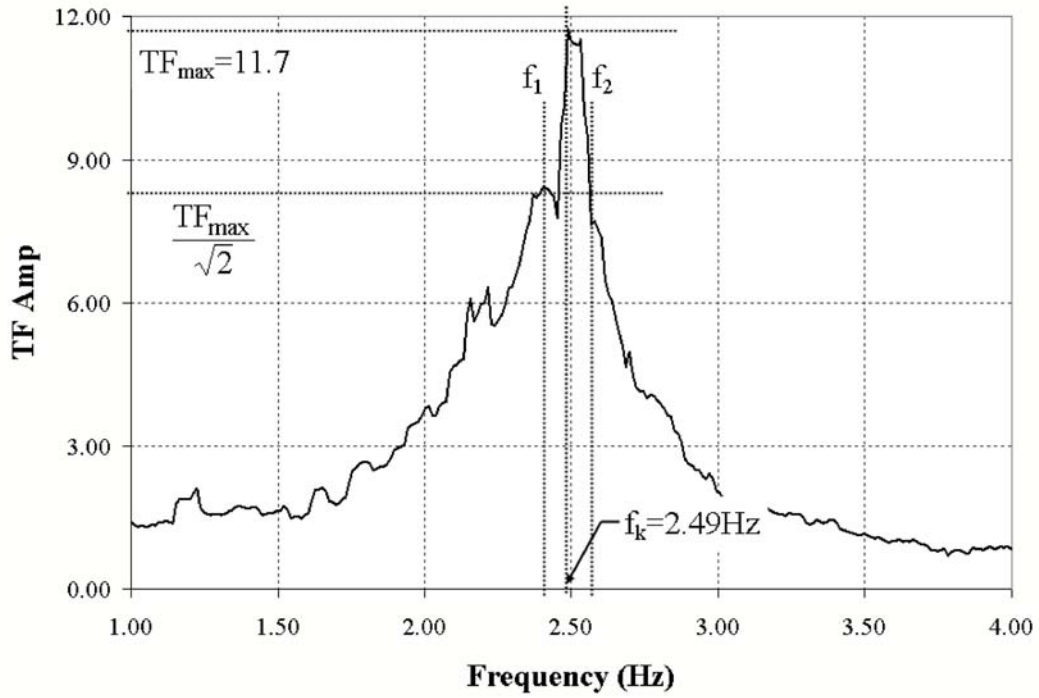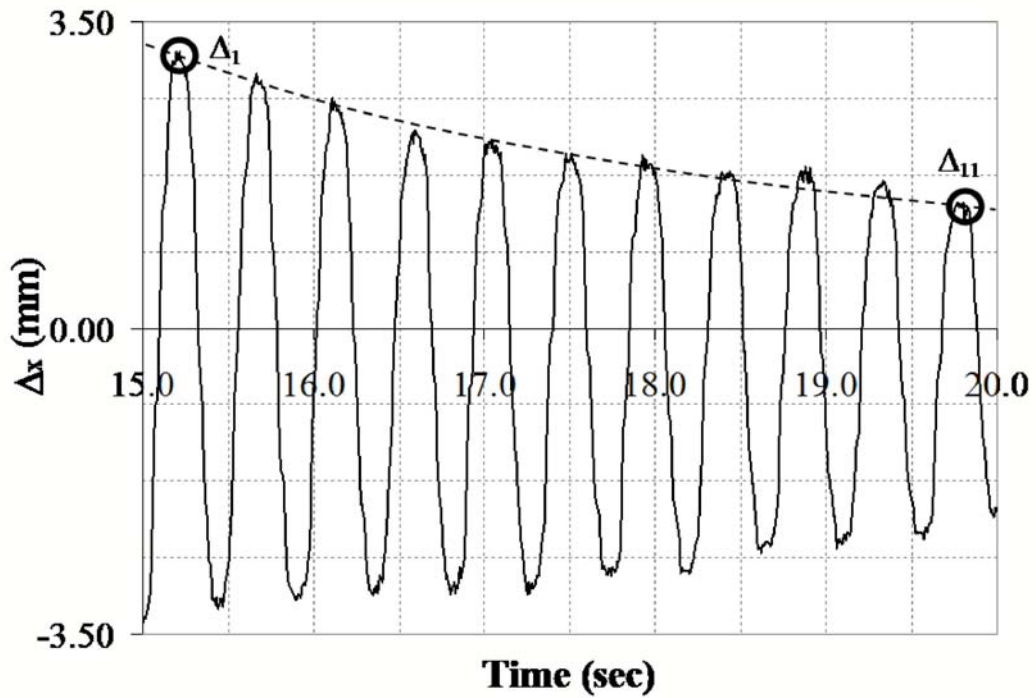
FIGURE 6-6 Illustrations of Damping Calculations Using (a) Half-power

(bandwidth) Method and (b) Logarithmic Decrement Method
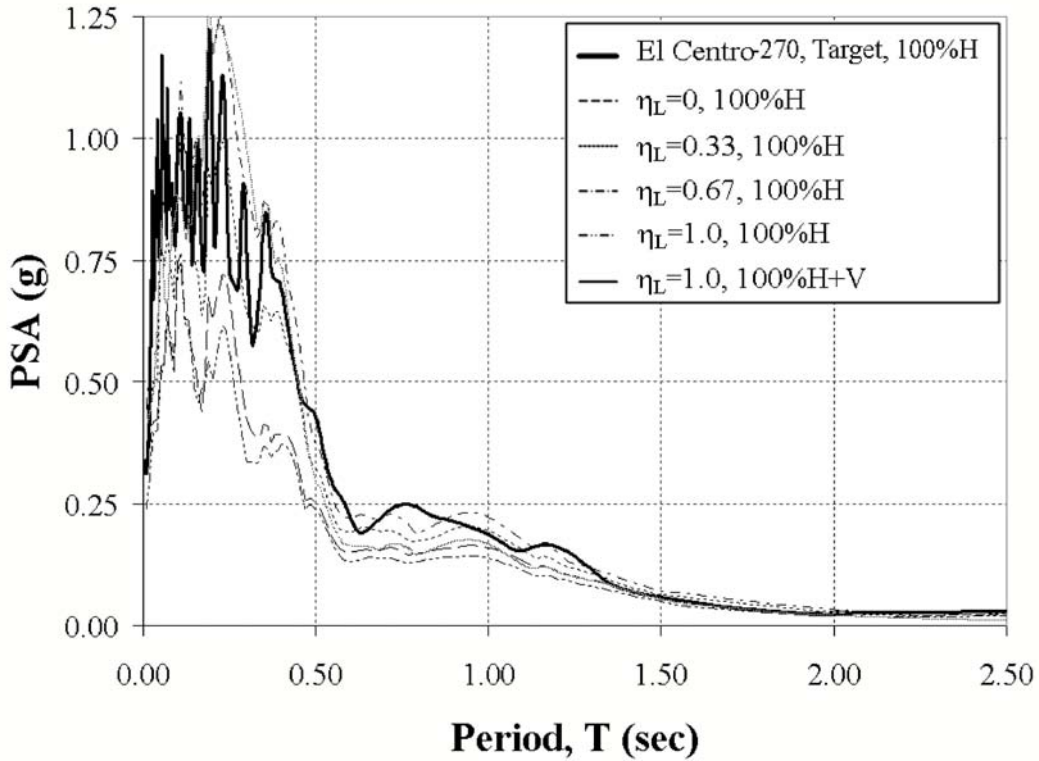
FIGURE 6-7 Actual Table Spectra for El Centro - 100%, 5% Damping (=0deg.)
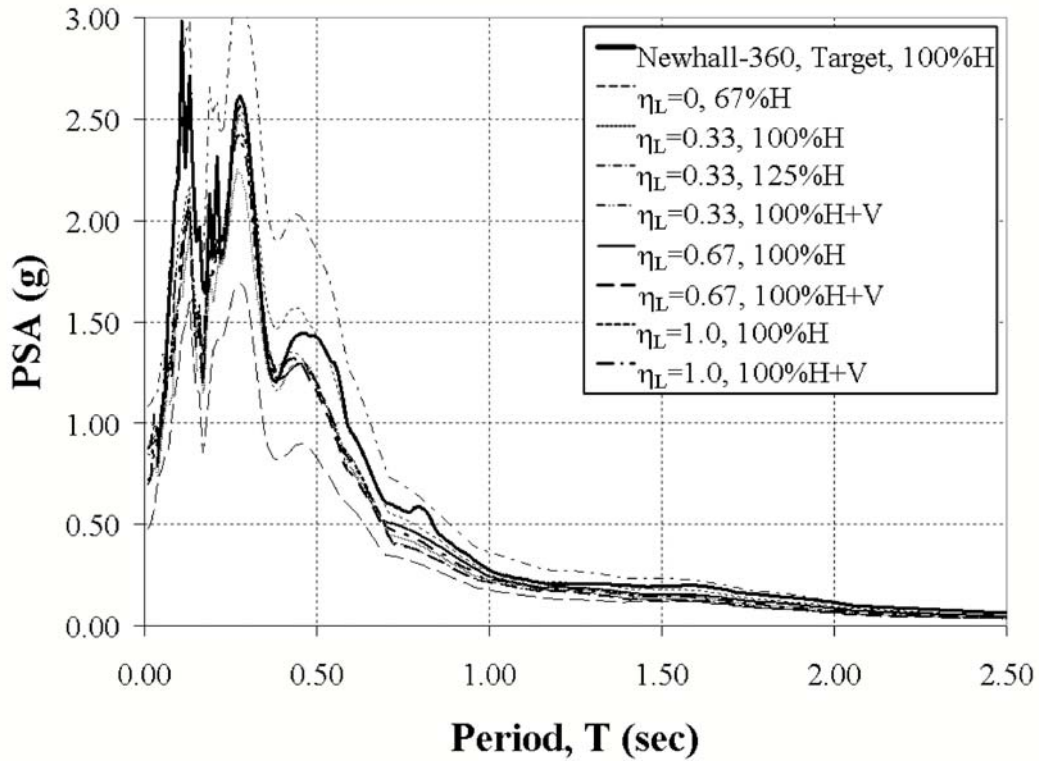
FIGURE 6-8 Actual Table Spectra for Newhall - 100%, 5% Damping (=0deg.)
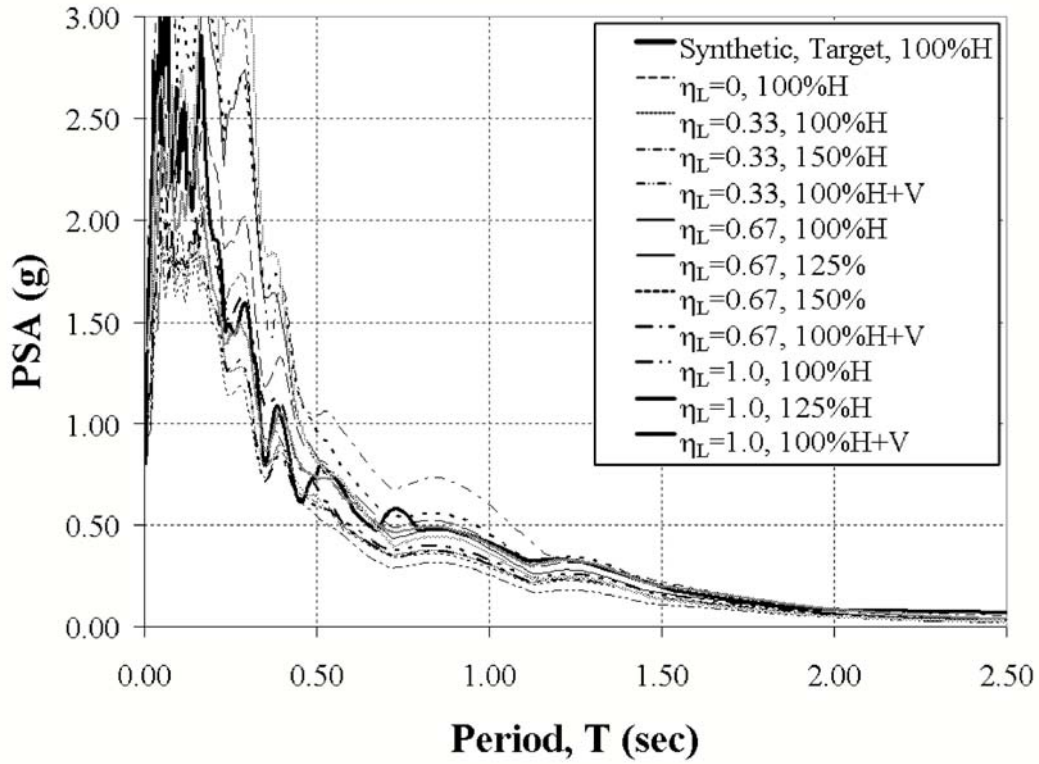
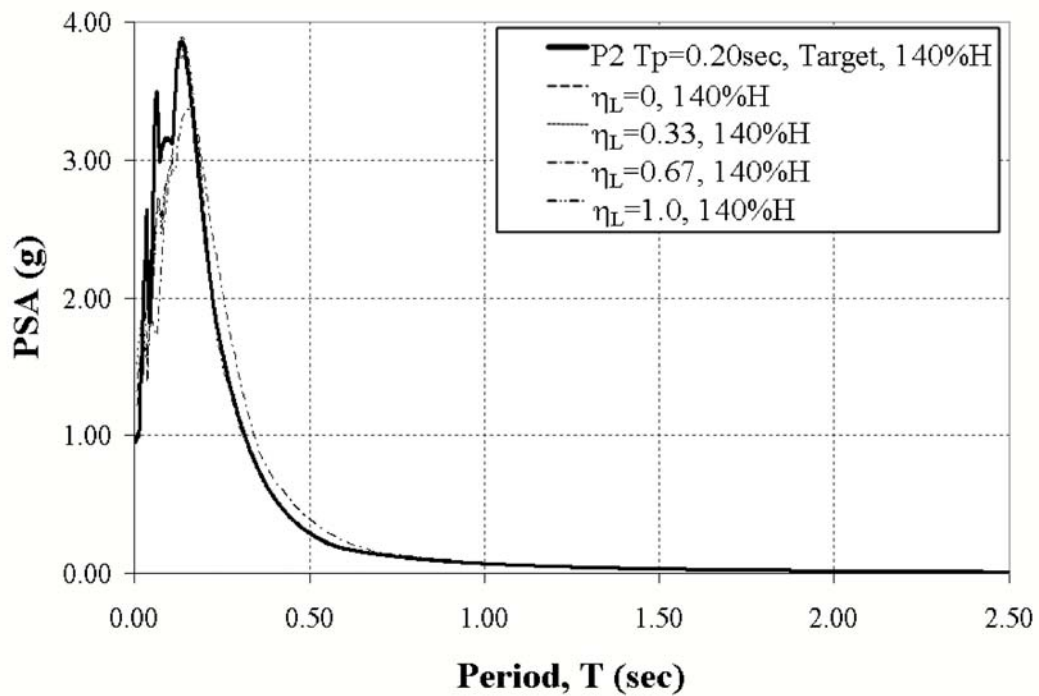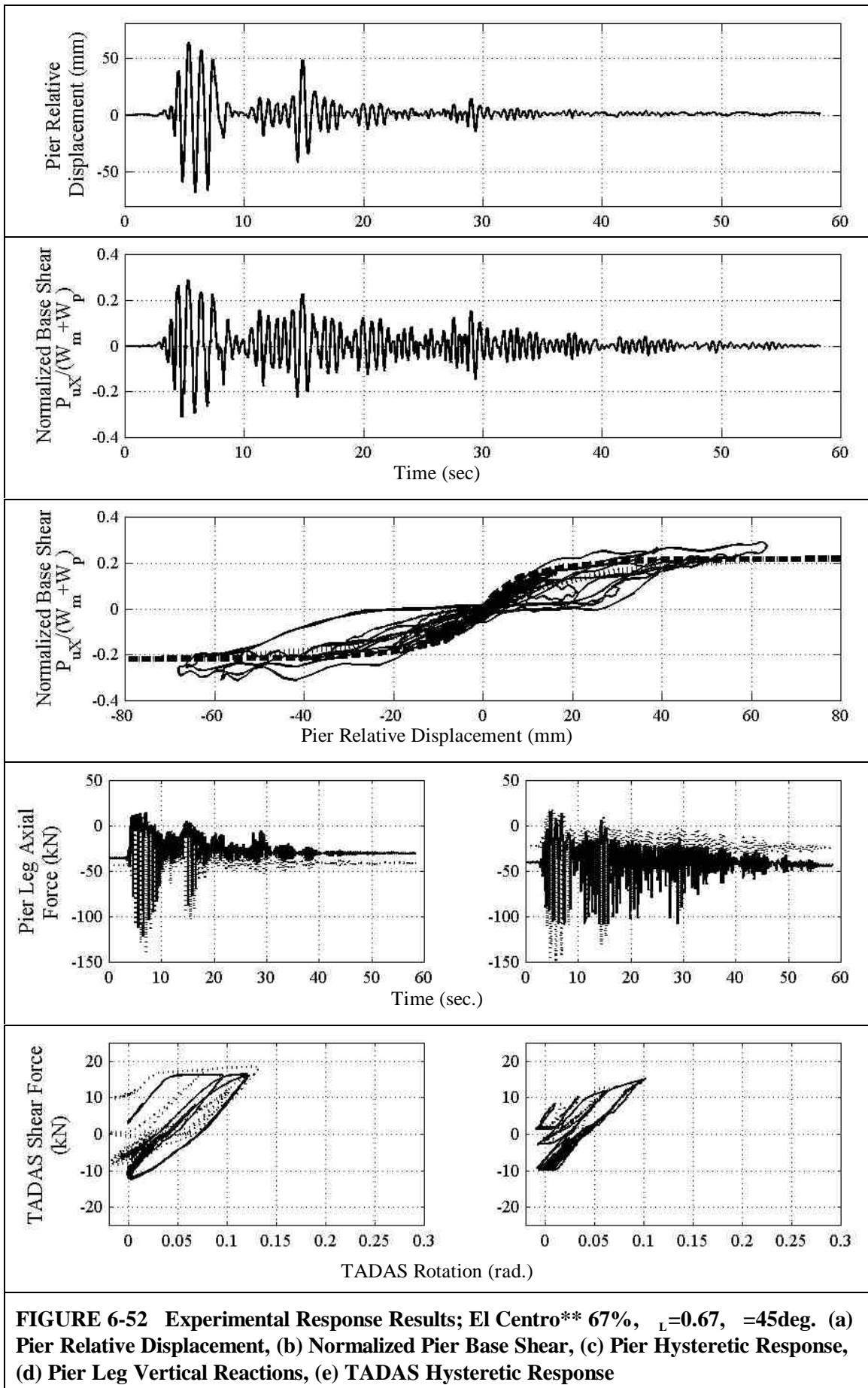**FIGURE 6-9 Actual Table Spectra for Synthetic - 100%, 5% Damping (=0deg.)**
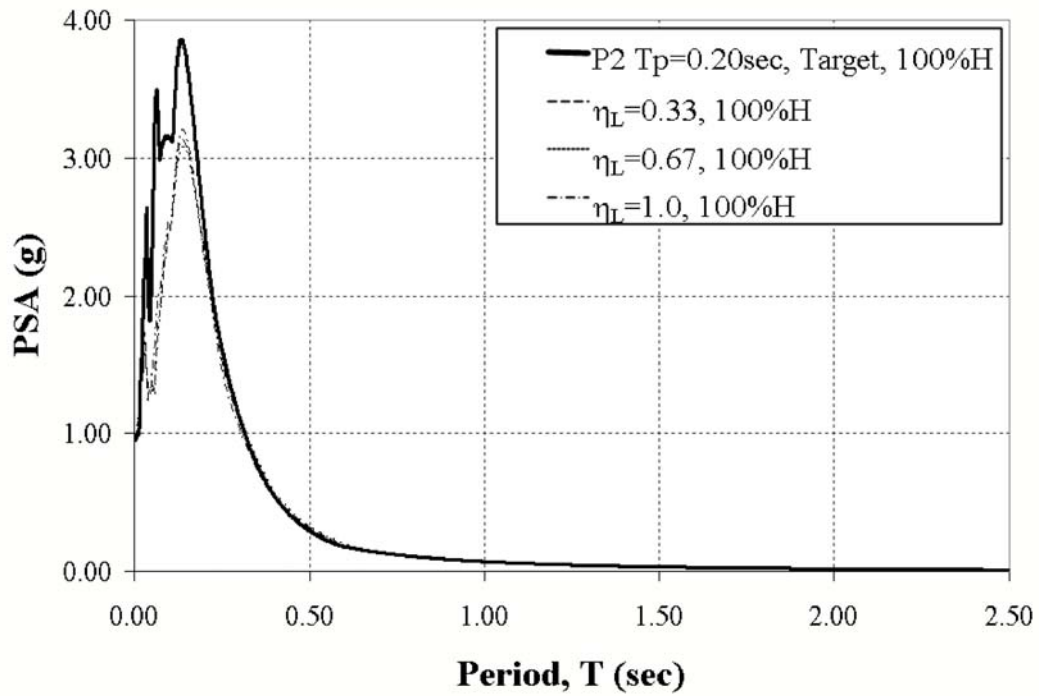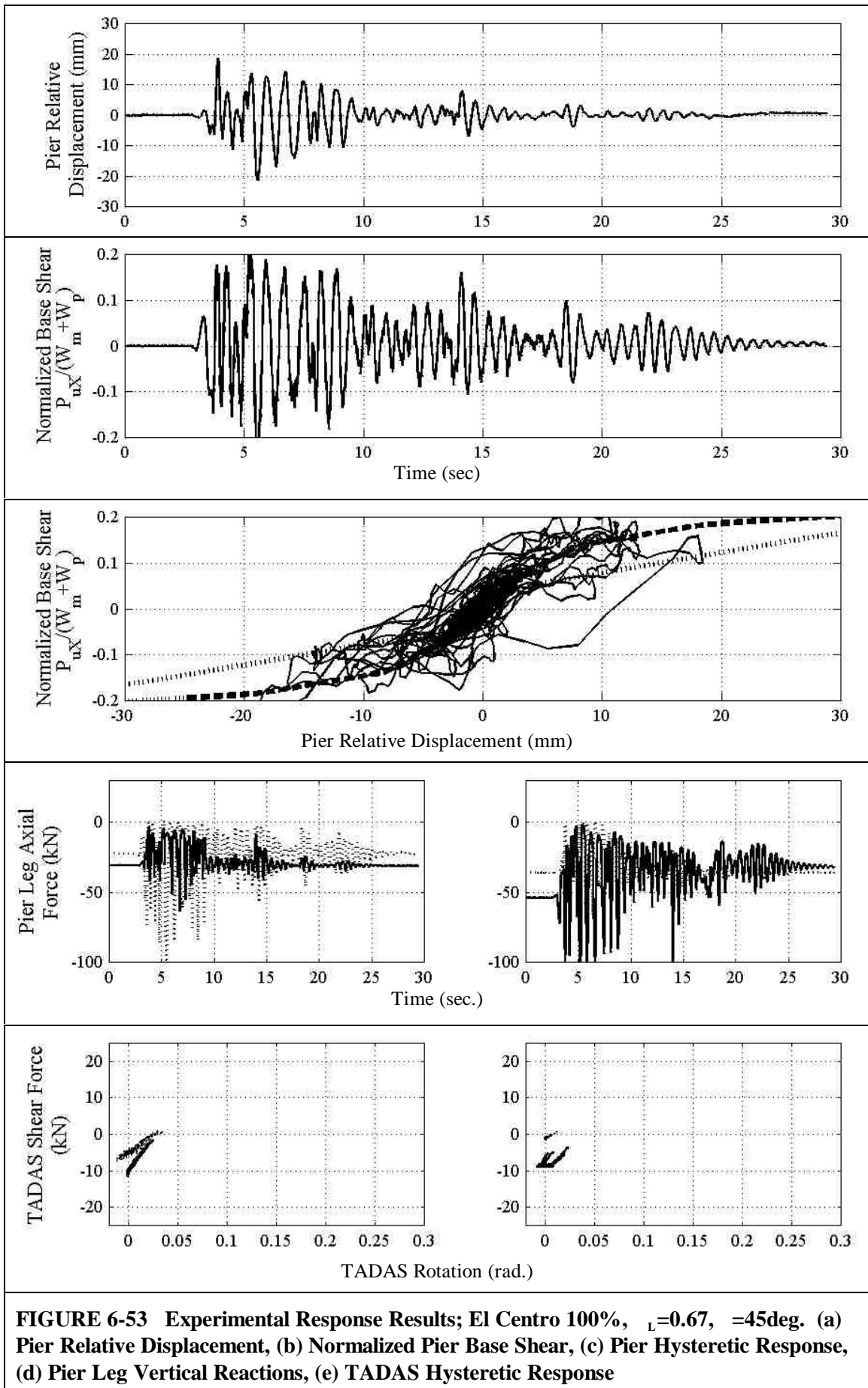

FIGURE 6-10 Actual Table Spectra for Pulse P2, T_p=0.20sec - 100%, 5% Damping
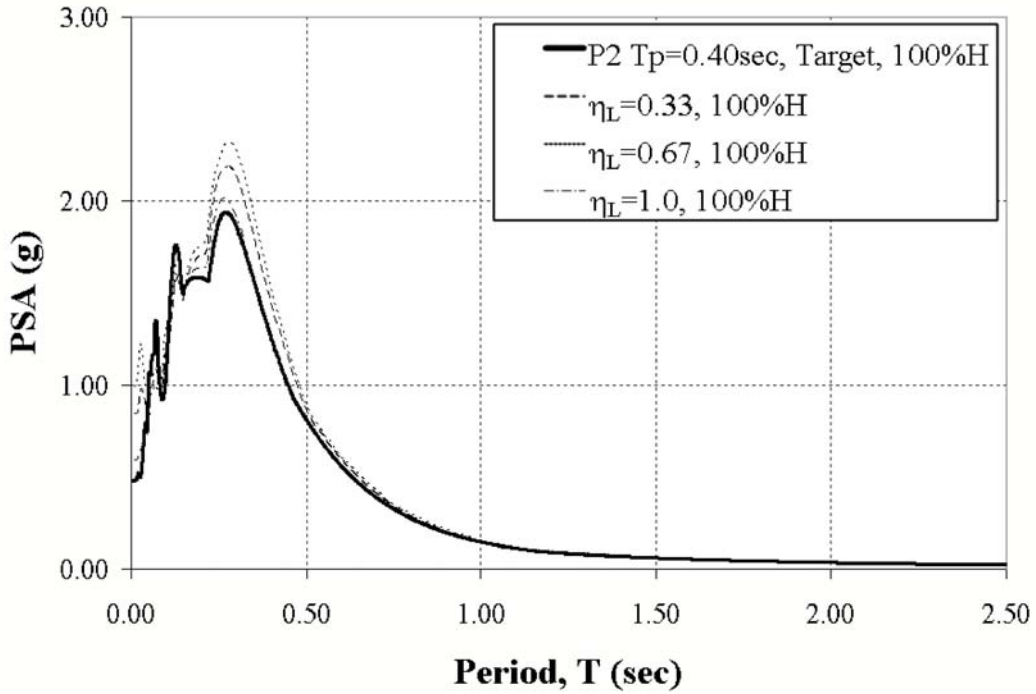
(=0deg.)

FIGURE 6-11 Actual Table Spectra for Pulse P2, T_p=0.40sec - 100%, 5% Damping
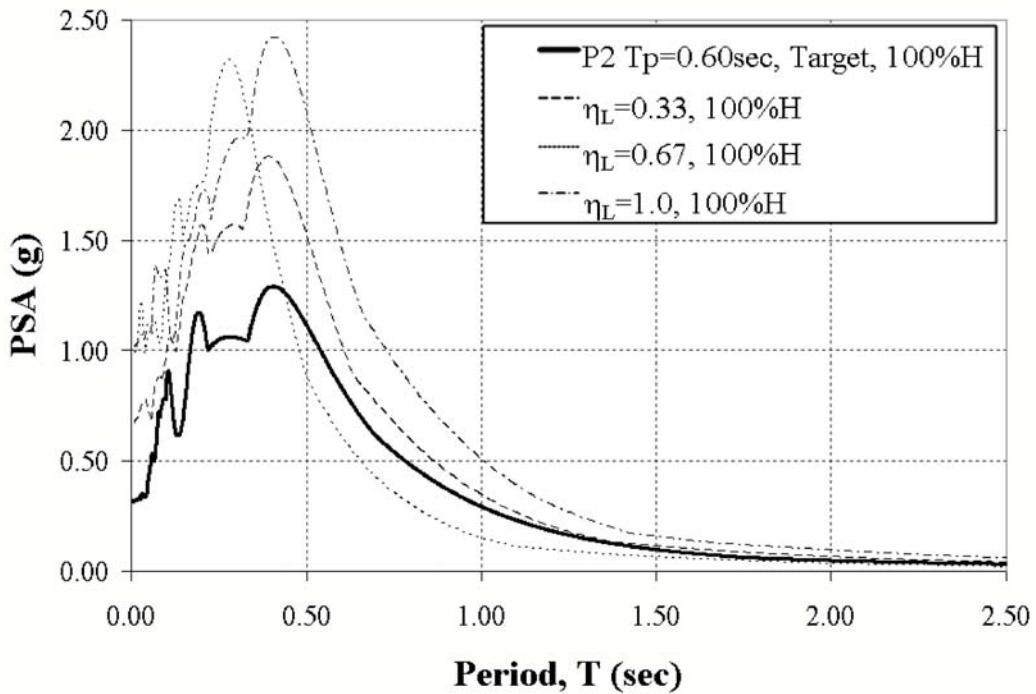
(=0deg.)

FIGURE 6-12 Actual Table Spectra for Pulse P2, T_p=0.60sec - 100%, 5% Damping

(=0deg.)

211
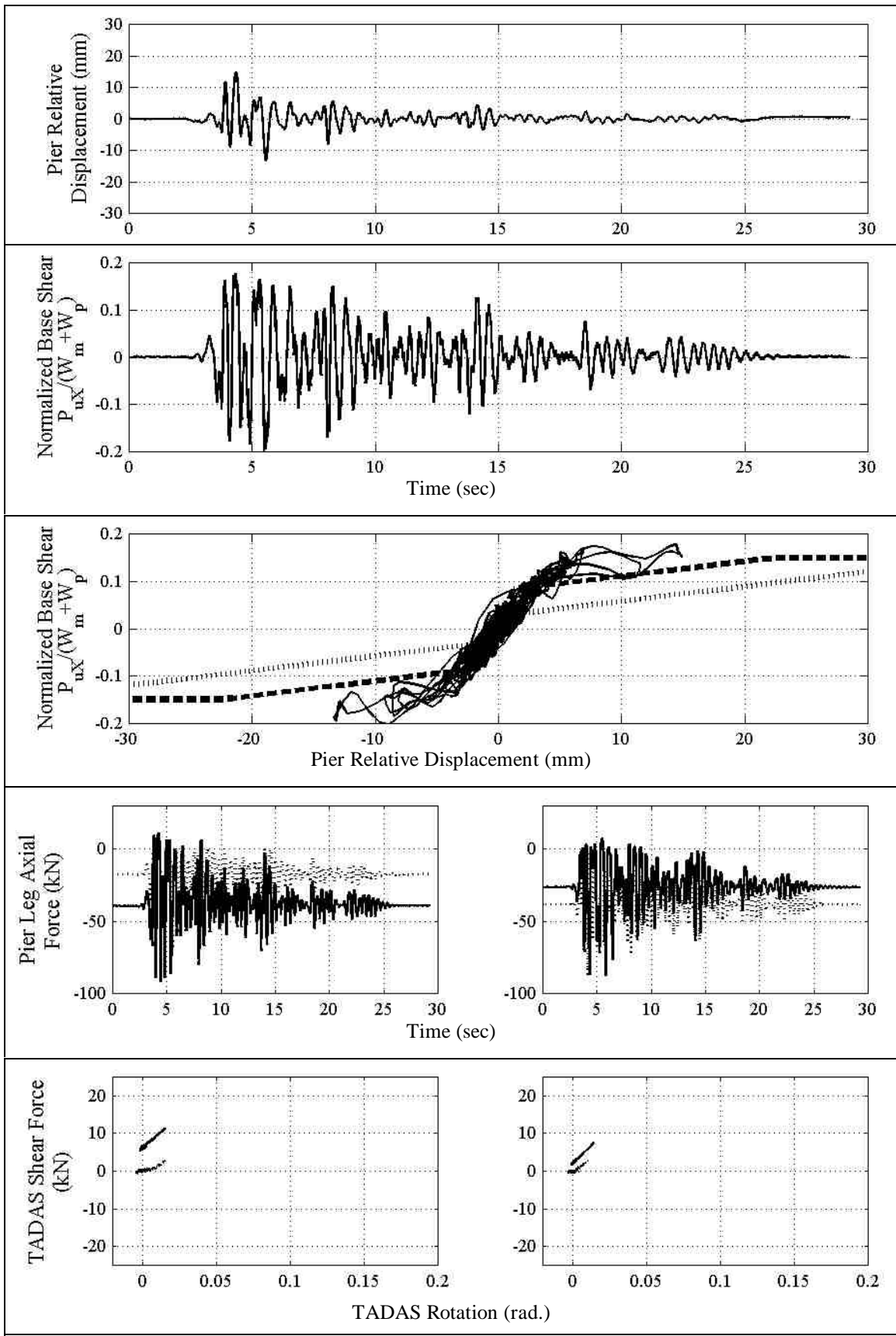
FIGURE 6-13   Experimental Response Results; El Centro, 100%, ₗ=0.67, =0deg. (a) Pier Relative Displacement, (b) Normalized Pier Base Shear, (c) Pier Hysteretic Response, (d) Pier Leg Vertical Reactions, (e) TADAS Hysteretic Response
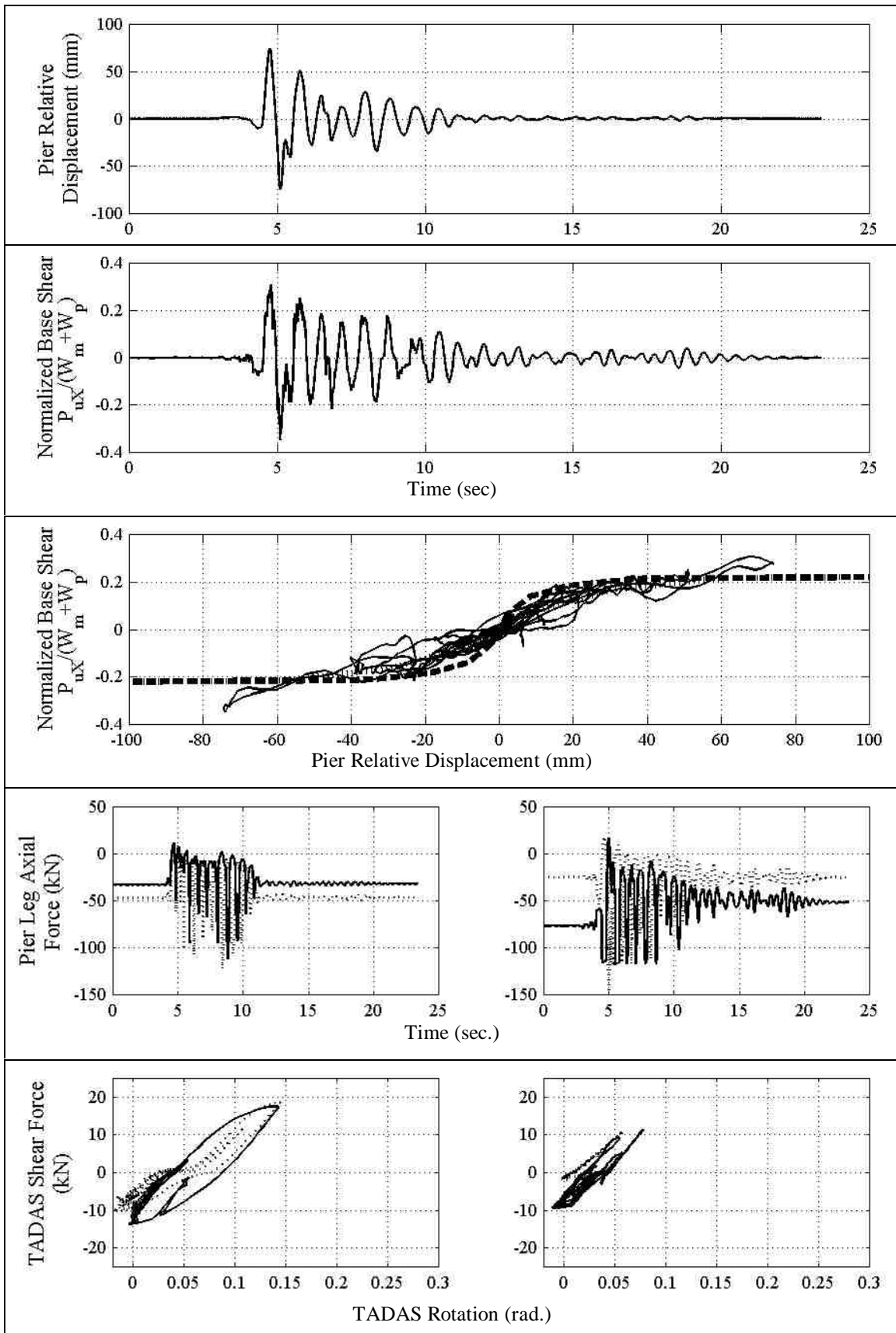
FIGURE 6-14 Experimental Response Results; Newhall, 100%, $_L$=0.67, =0deg. (a) Pier Relative Displacement, (b) Normalized Pier Base Shear, (c) Pier Hysteretic Response, (d) Pier Leg Vertical Reactions, (e) TADAS Hysteretic Response
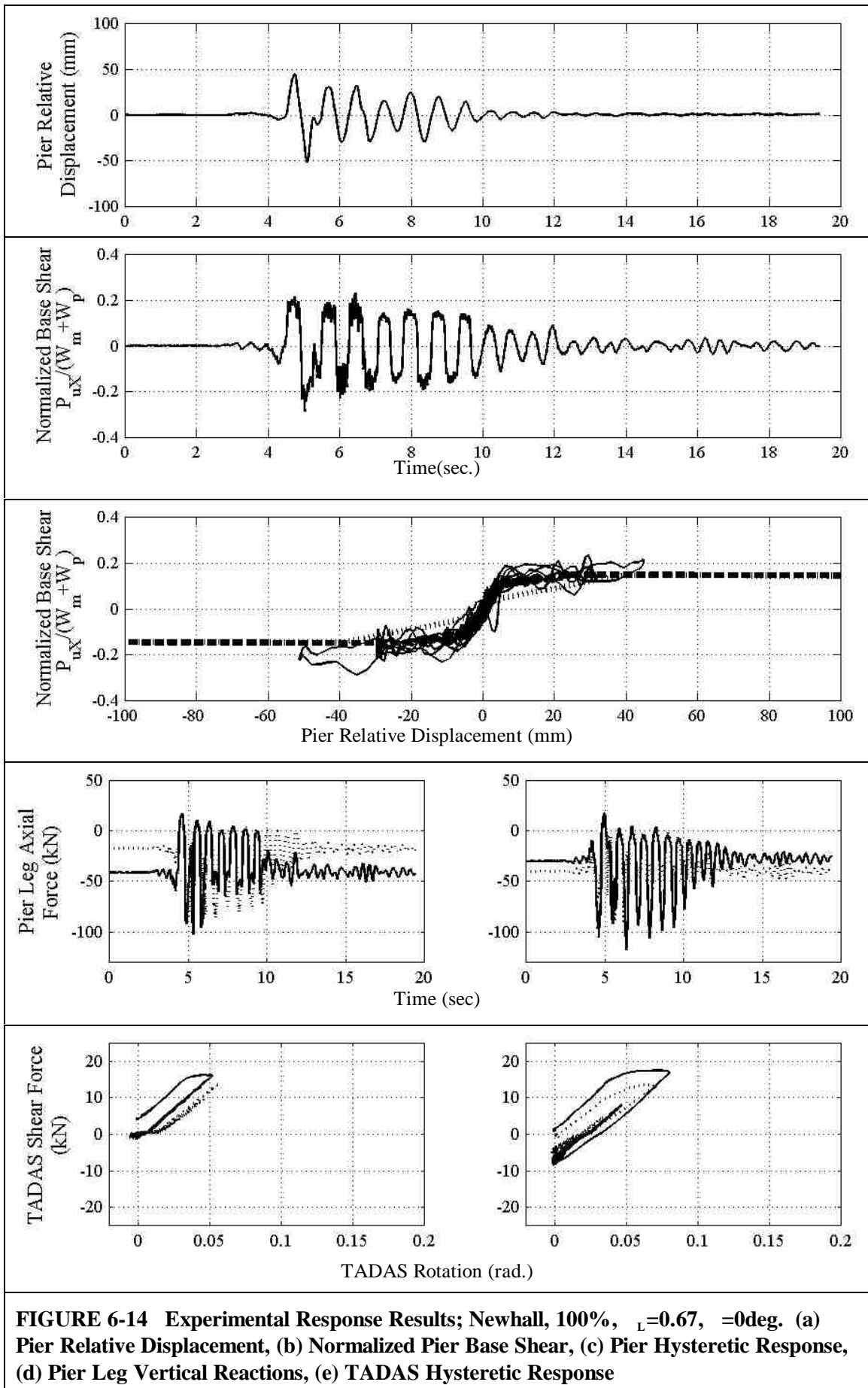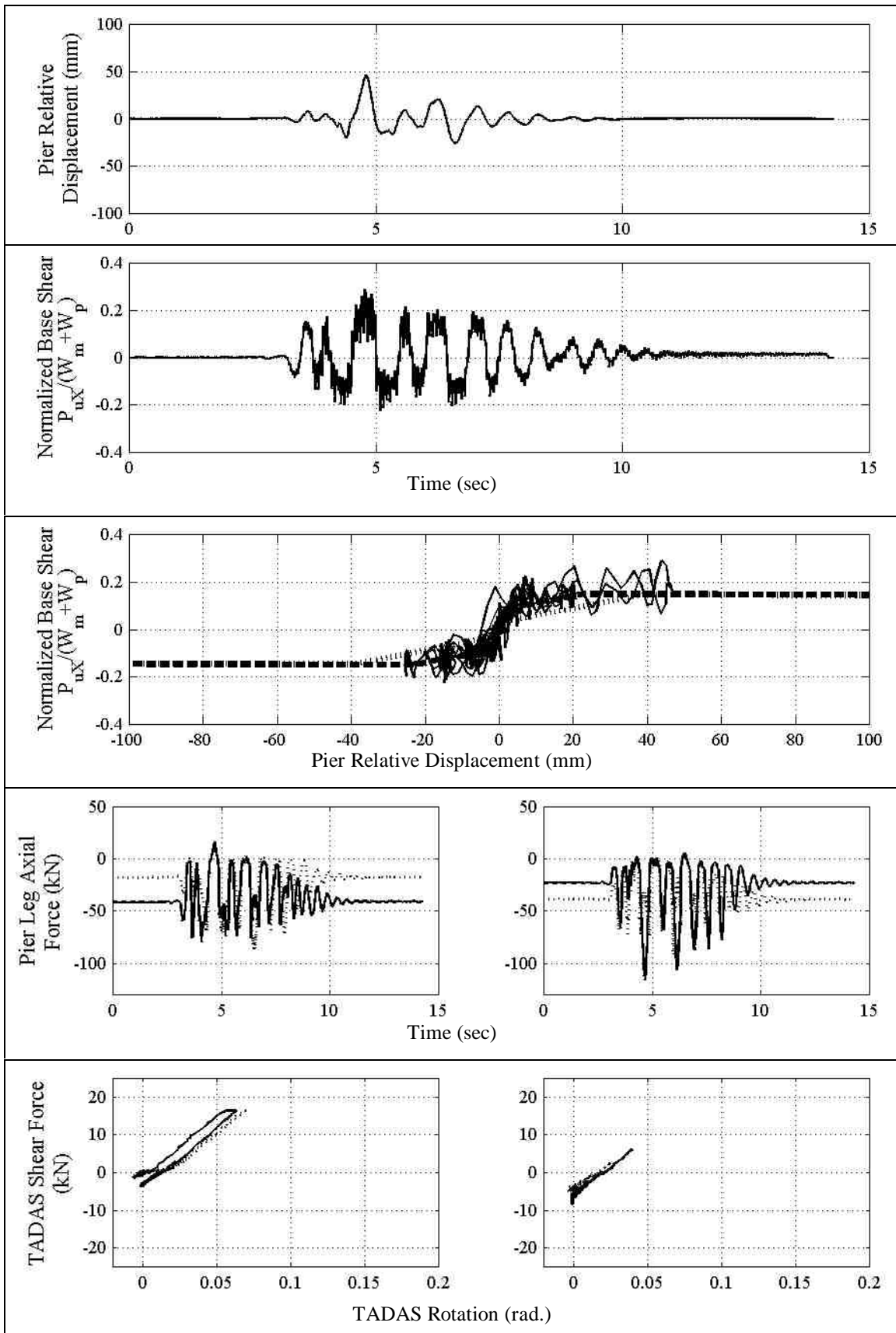
FIGURE 6-15   Experimental Response Results; Synthetic, 100%, $_L$=0.67, =0deg. (a) Pier Relative Displacement, (b) Normalized Pier Base Shear, (c) Pier Hysteretic Response, (d) Pier Leg Vertical Reactions, (e) TADAS Hysteretic Response

**FIGURE 6-16   Experimental Response Results; Newhall, 100% H+V, $_L$=0.67, =0deg.
(a) Pier Relative Displacement, (b) Normalized Pier Base Shear, (c) Pier Hysteretic
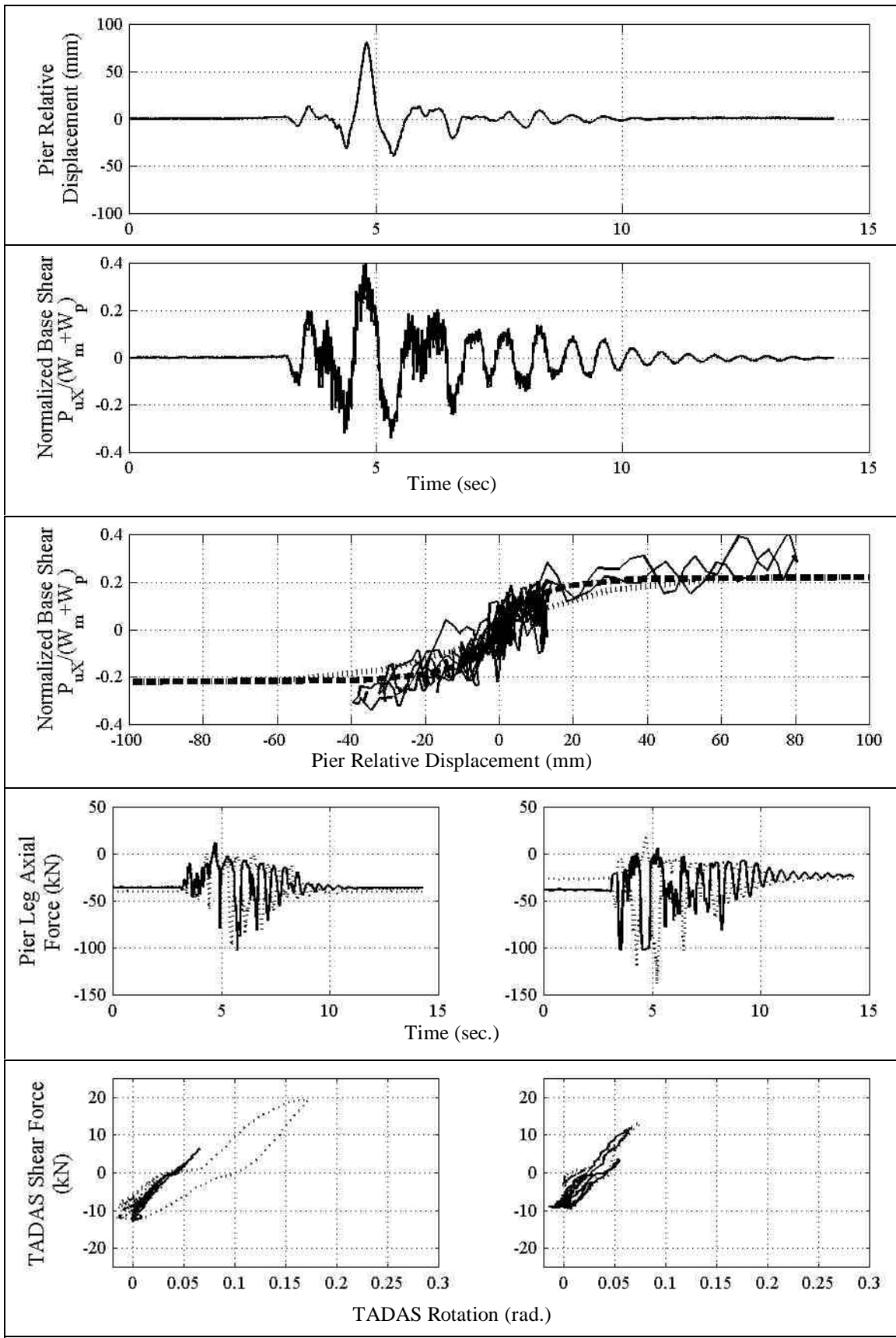Response, (d) Pier Leg Vertical Reactions, (e) TADAS Hysteretic Response**

215
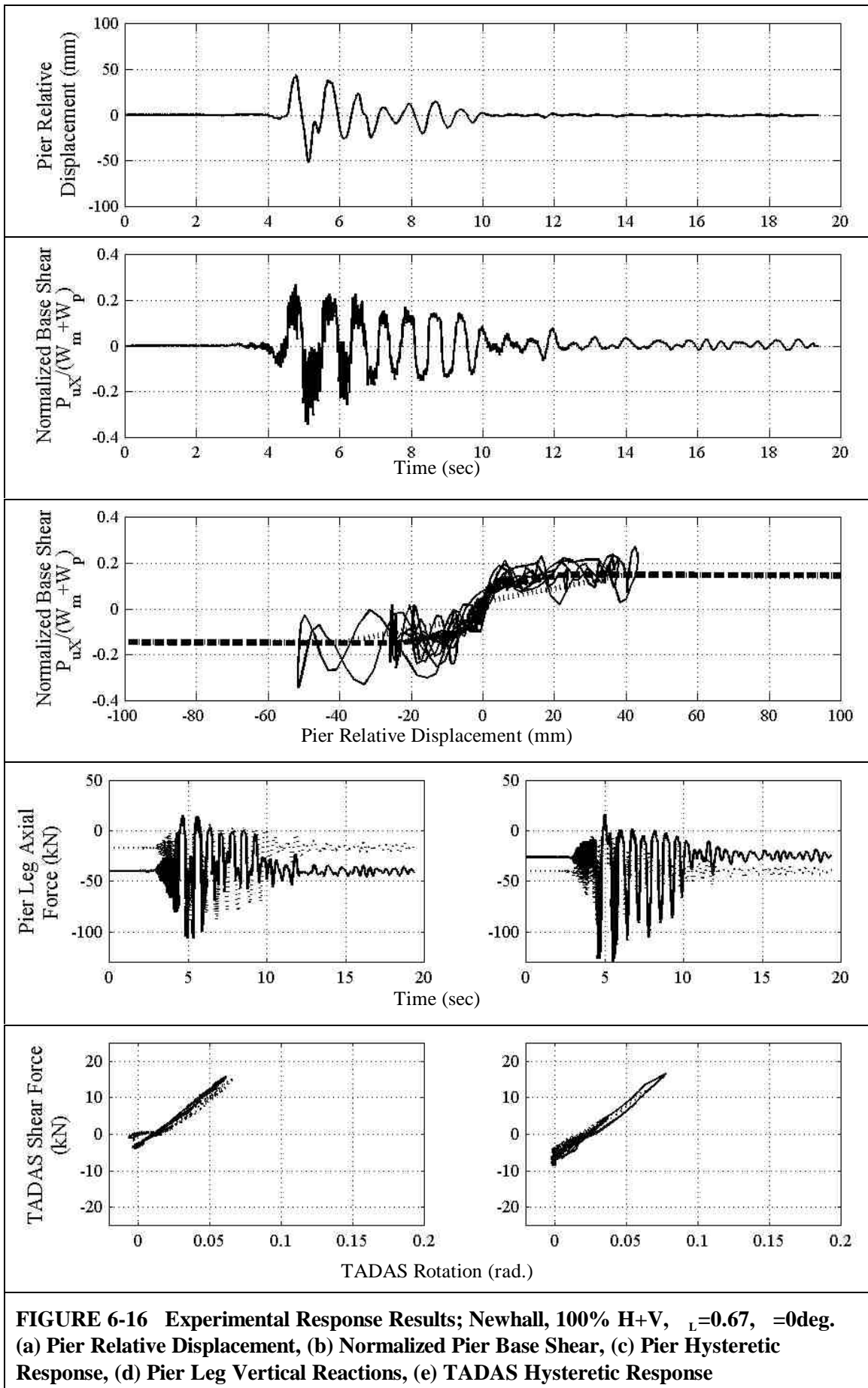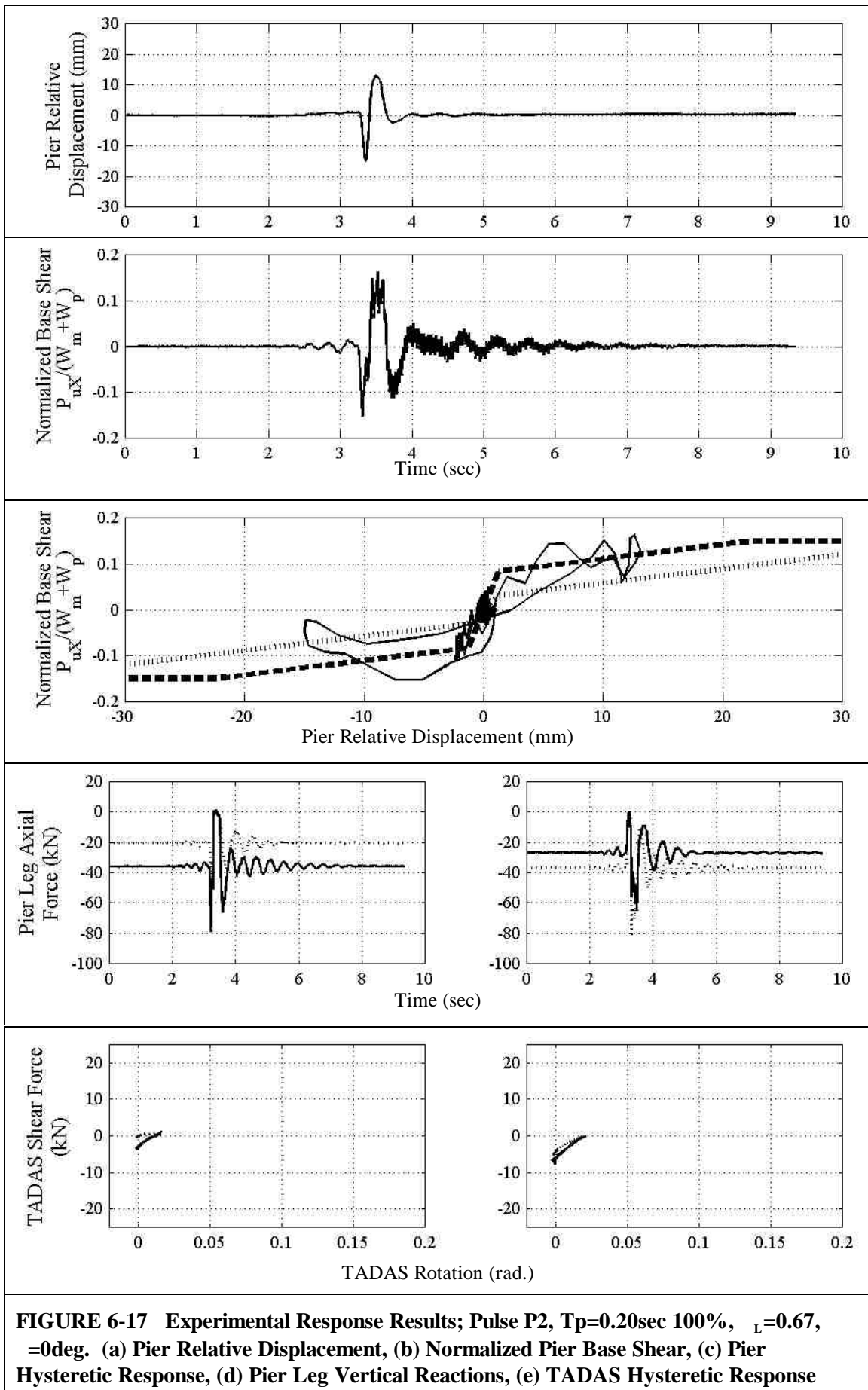
FIGURE 6-17 Experimental Response Results; Pulse P2, Tp=0.20sec 100%, $_L$=0.67, =0deg. (a) Pier Relative Displacement, (b) Normalized Pier Base Shear, (c) Pier Hysteretic Response, (d) Pier Leg Vertical Reactions, (e) TADAS Hysteretic Response
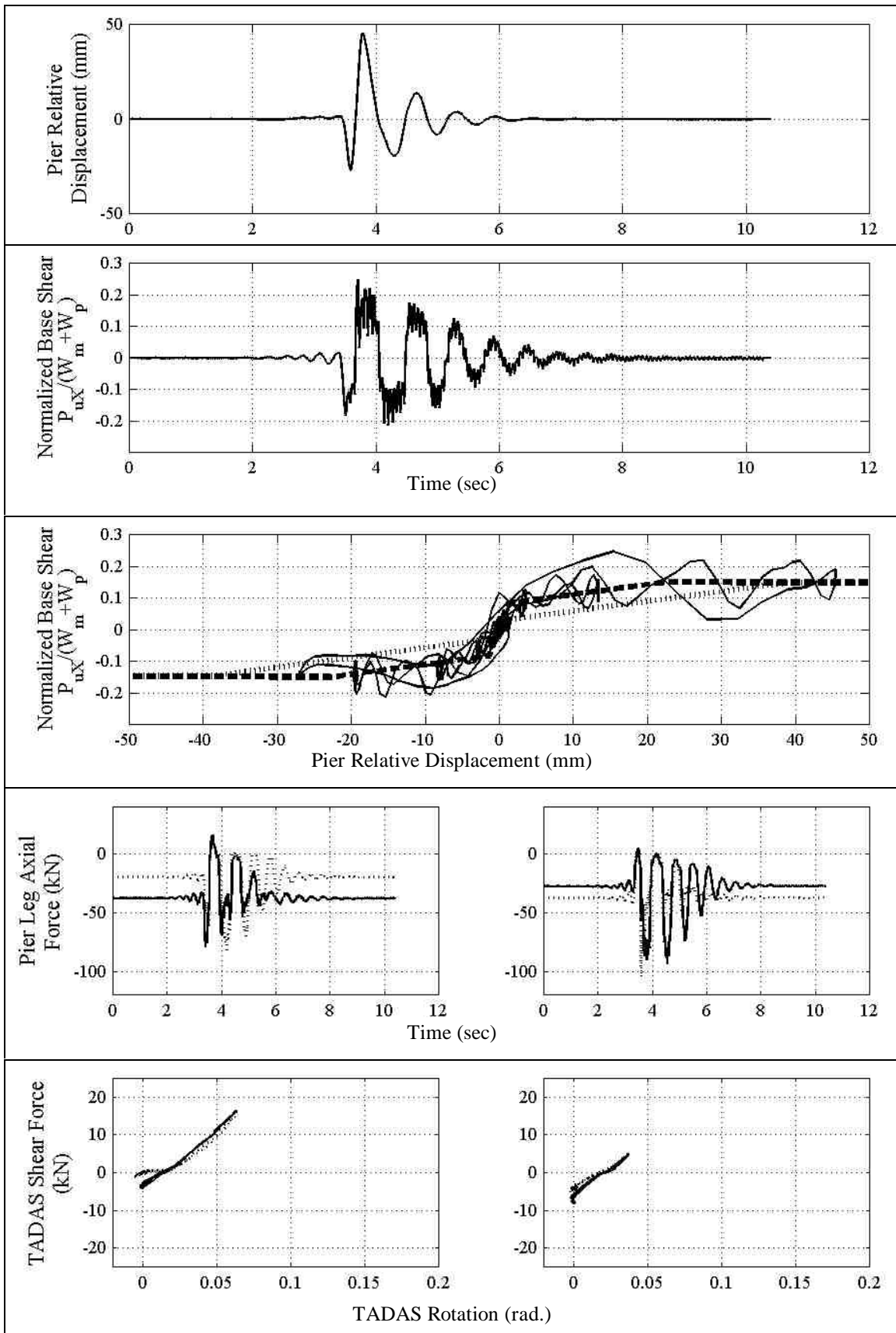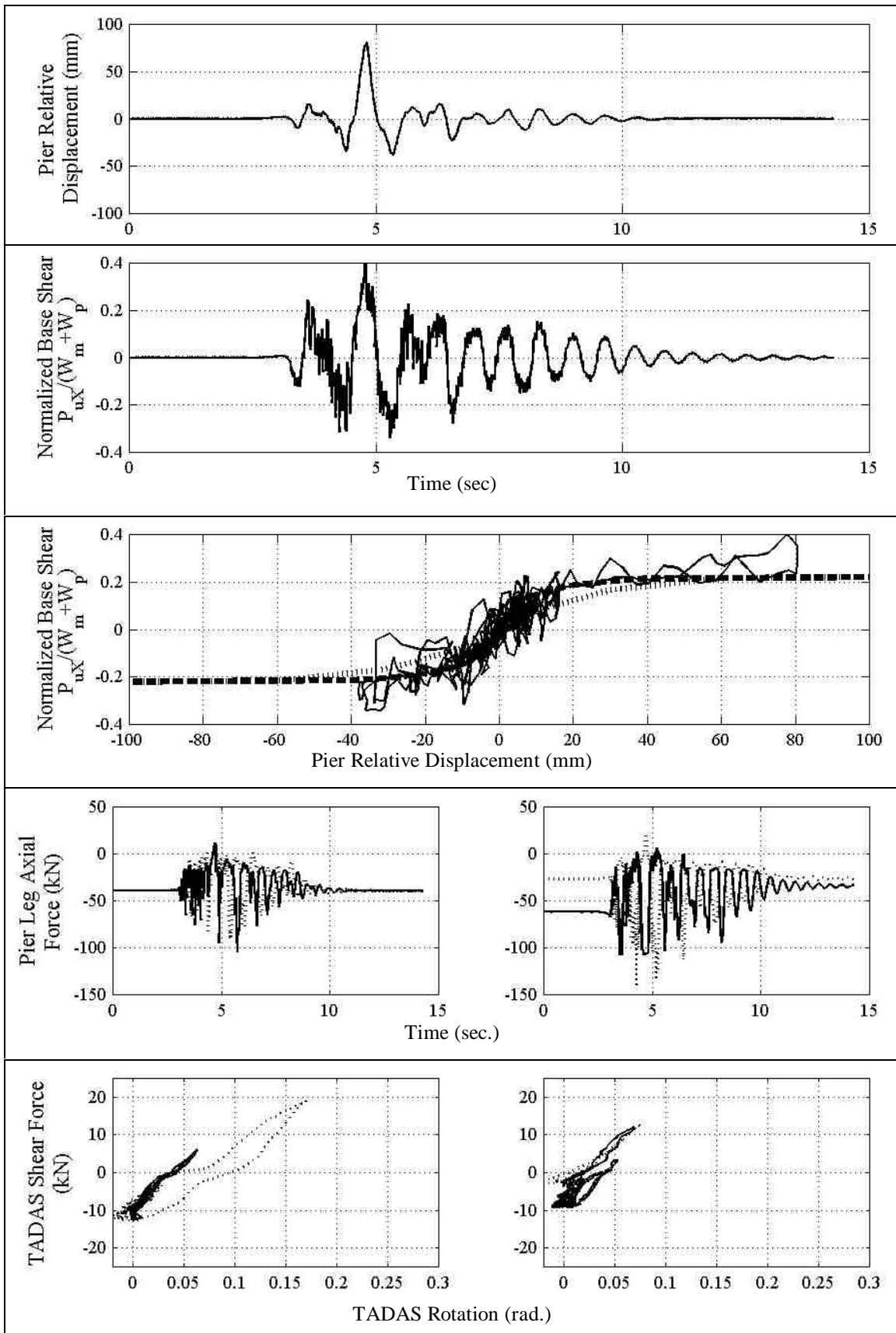
FIGURE 6-18   Experimental Response Results; Pulse P2, Tp=0.40sec 100%, ₗ=0.67, =0deg. (a) Pier Relative Displacement, (b) Normalized Pier Base Shear, (c) Pier Hysteretic Response, (d) Pier Leg Vertical Reactions, (e) TADAS Hysteretic Response

**FIGURE 6-19 Experimental Response Results; Synthetic, 100% H+V, $_L$=0.67, =0deg.
(a) Pier Relative Displacement, (b) Normalized Pier Base Shear, (c) Pier Hysteretic
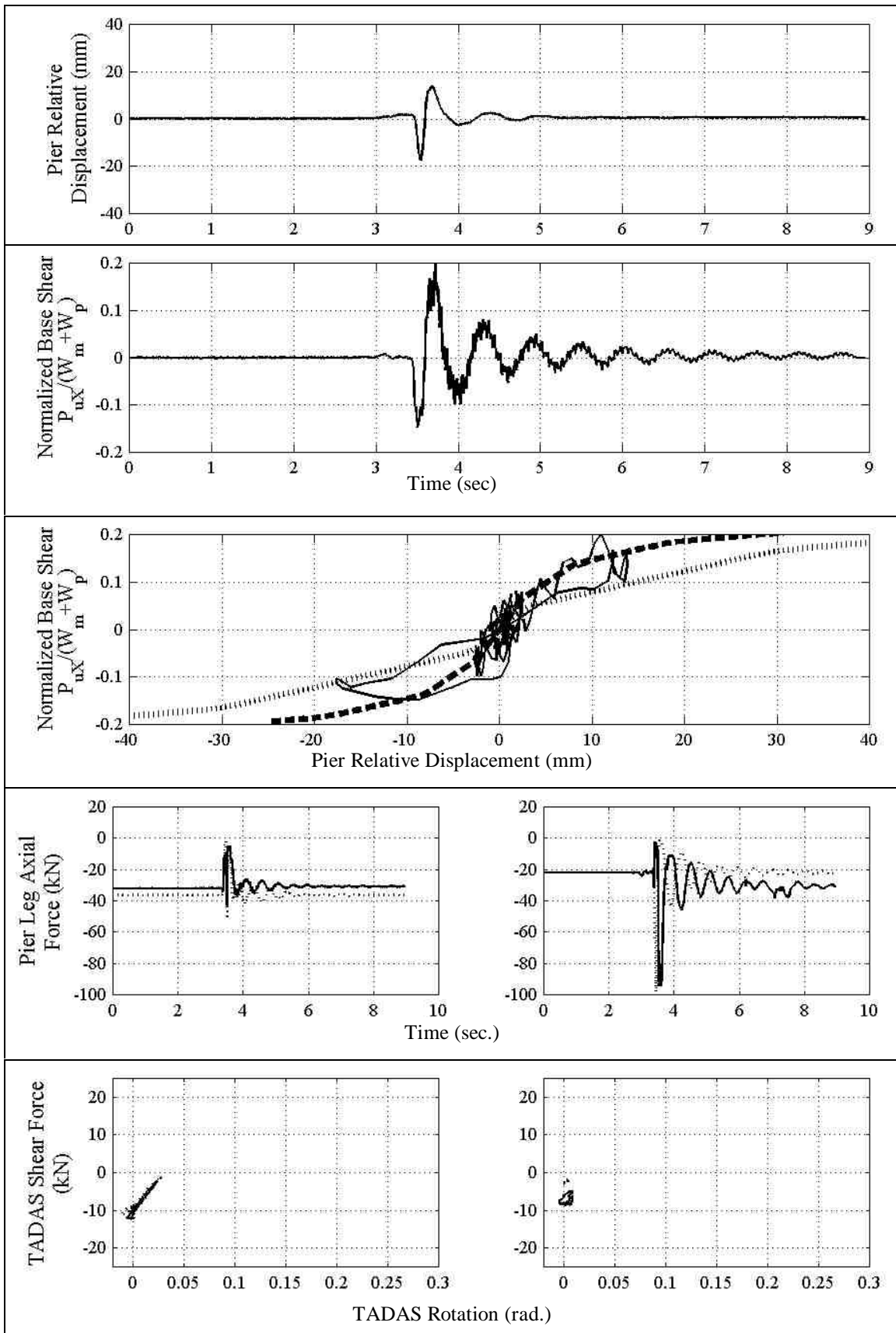Response, (d) Pier Leg Vertical Reactions, (e) TADAS Hysteretic Response**

FIGURE 6-20 Experimental Response Results; Synthetic, 125%, ₗ=0.67, =0deg. (a) Pier Relative Displacement, (b) Normalized Pier Base Shear, (c) Pier Hysteretic Response, (d) Pier Leg Vertical Reactions, (e) TADAS Hysteretic Response
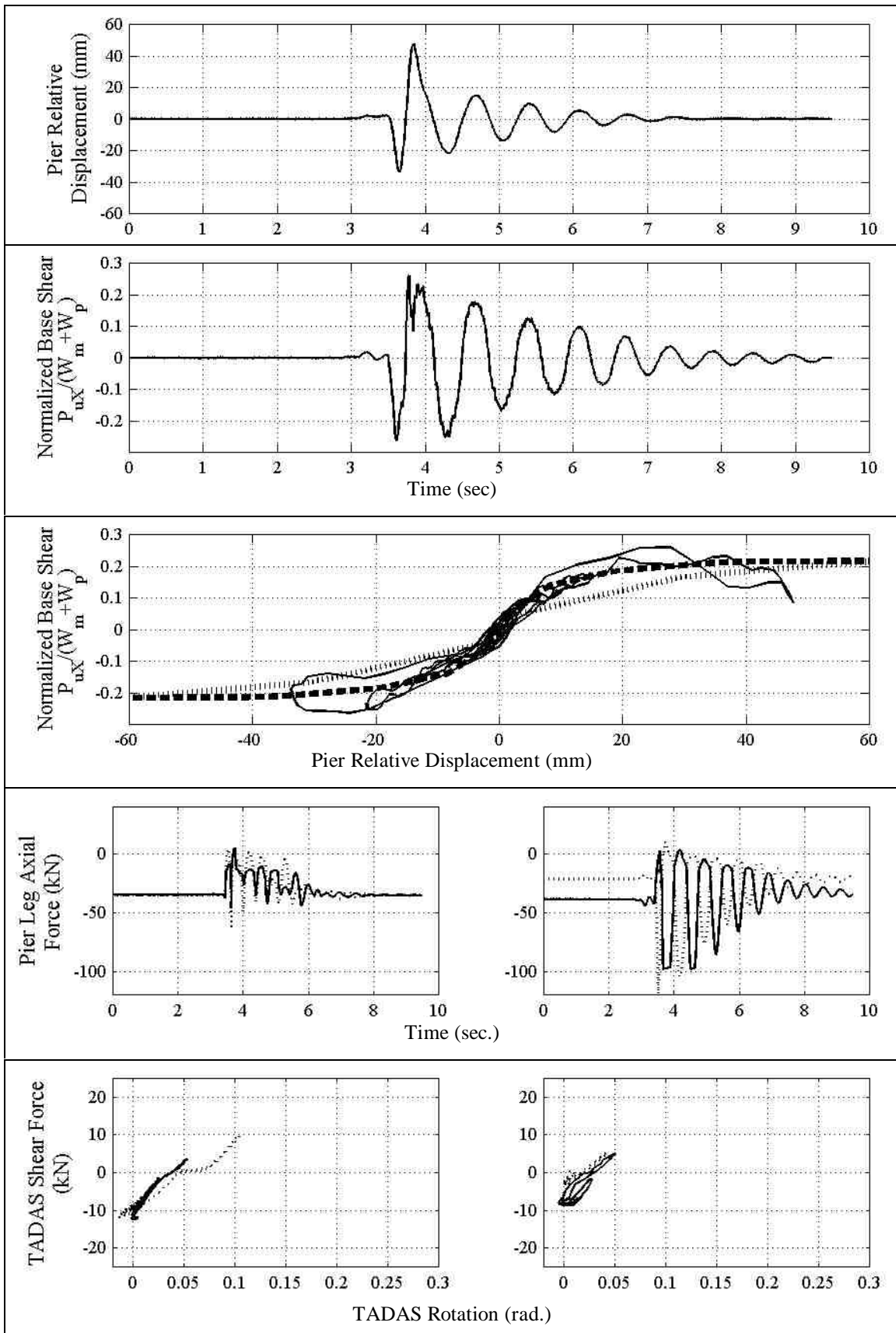
219
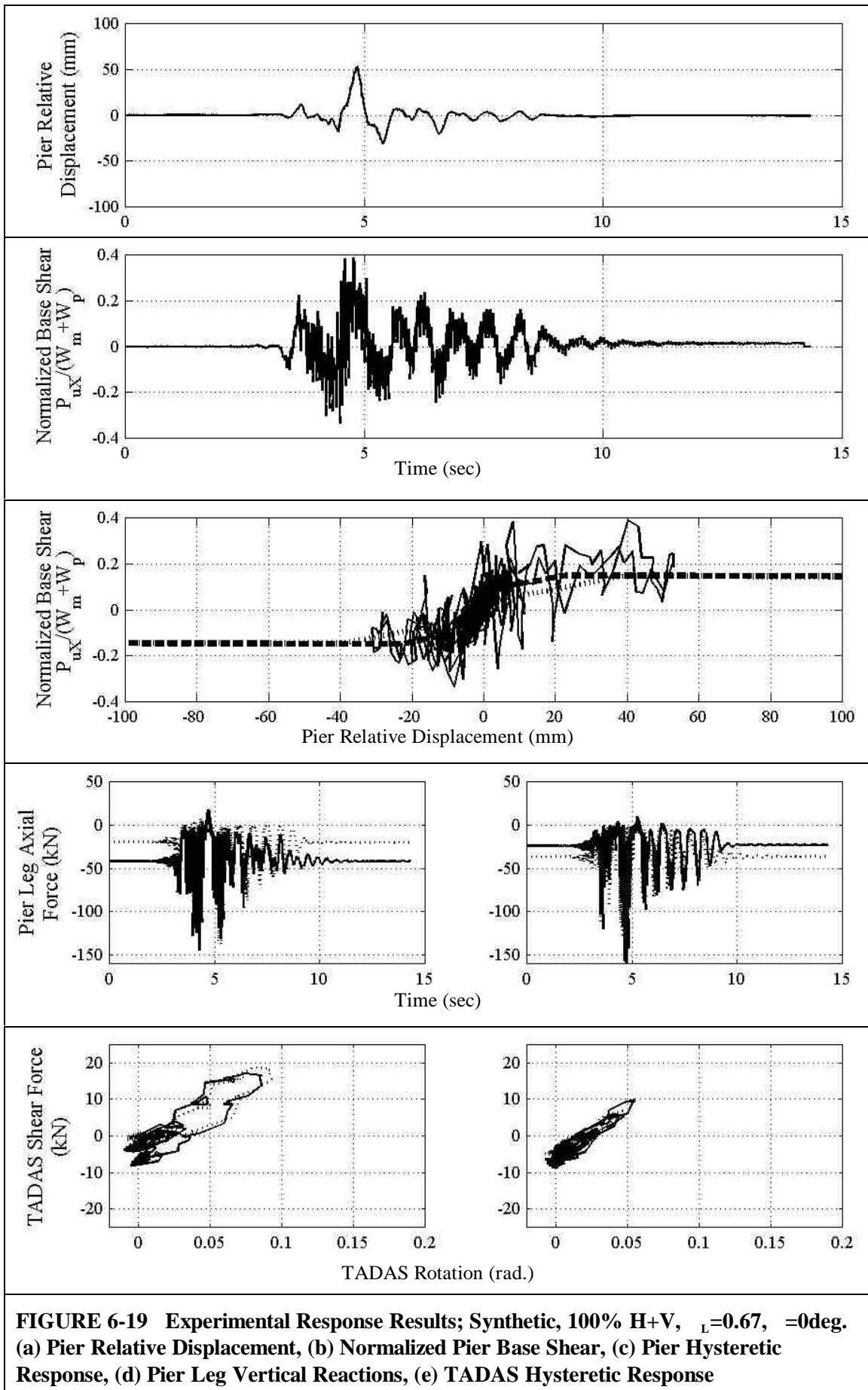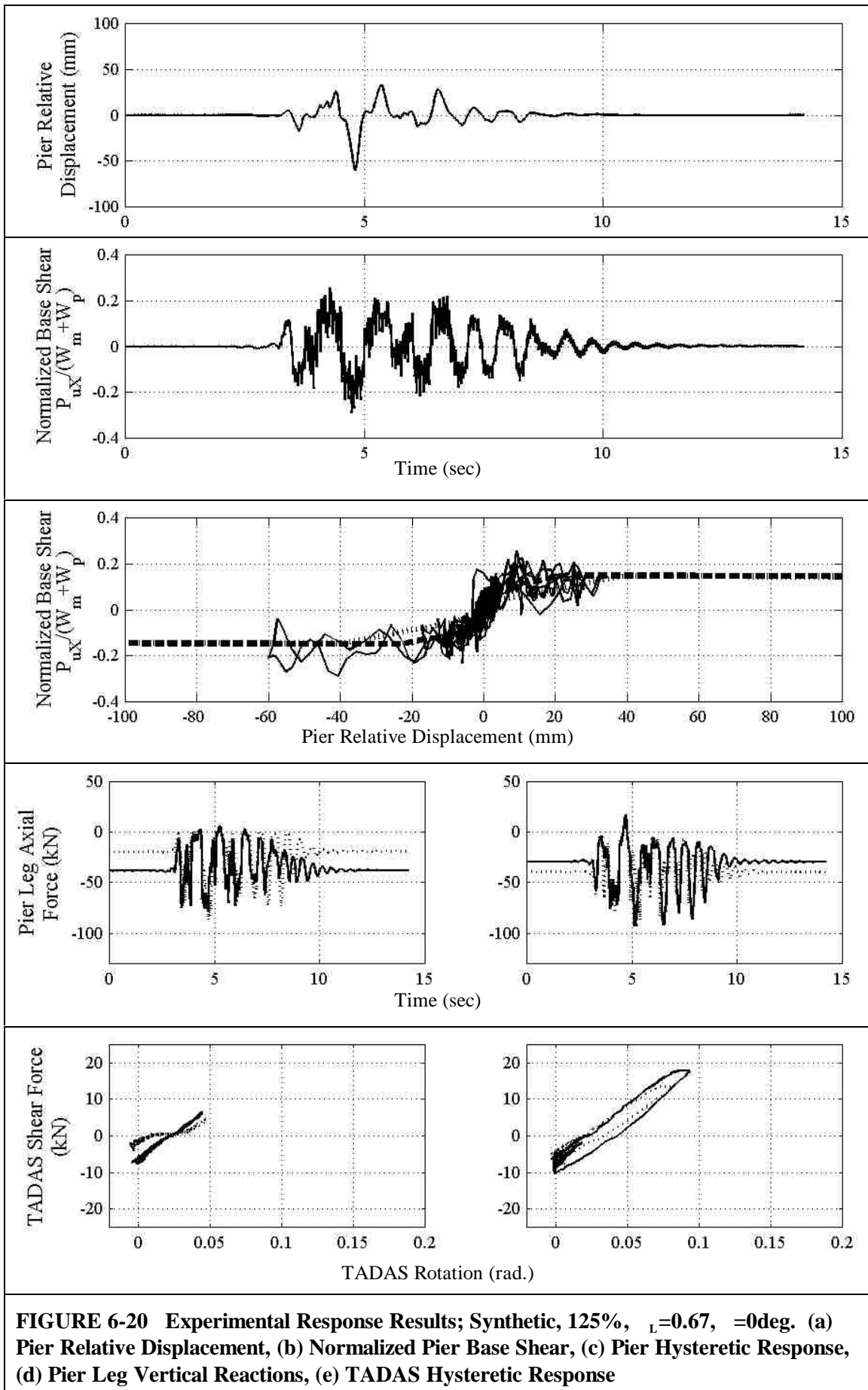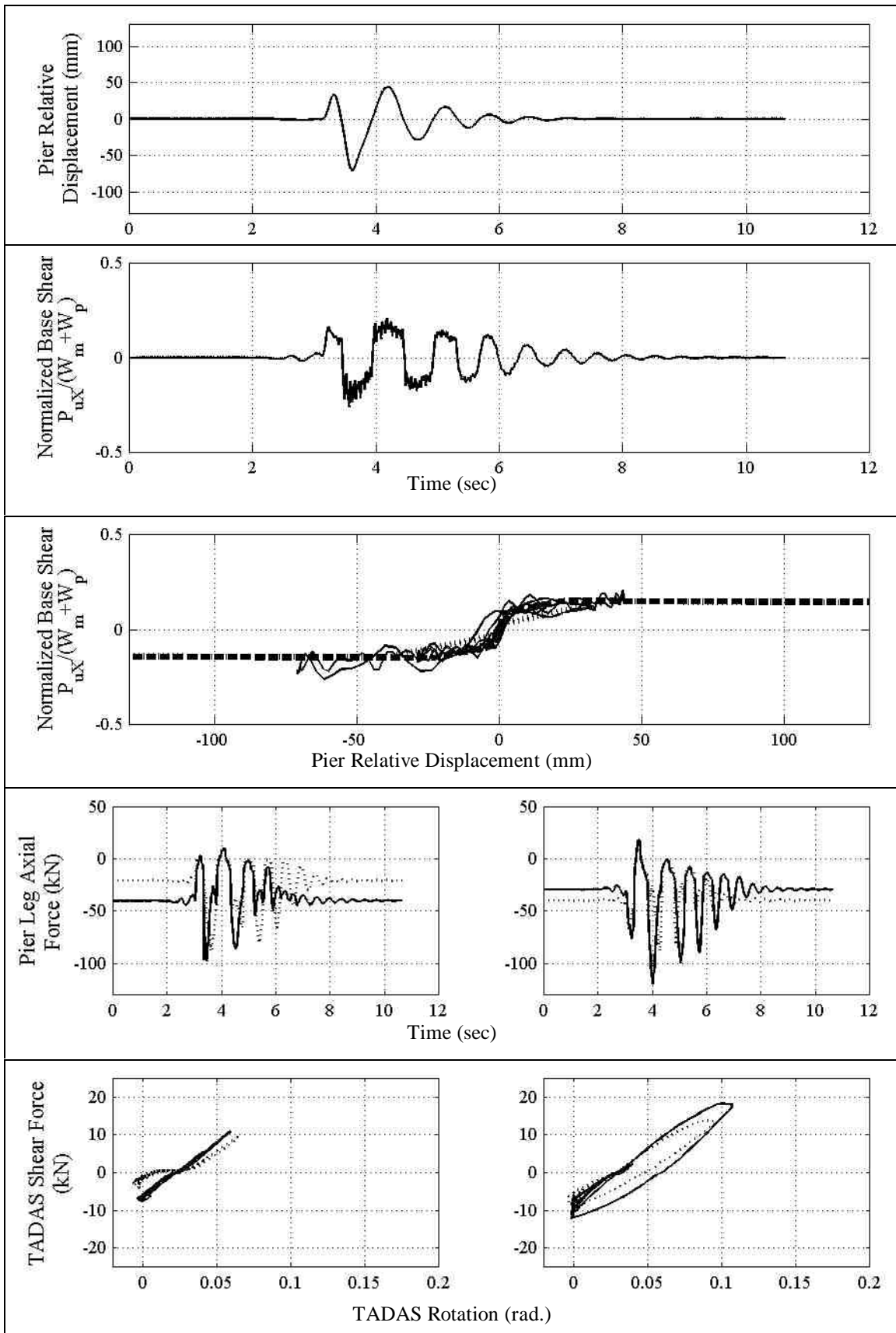
FIGURE 6-21   Experimental Response Results; Pulse P2, Tp=0.60sec 100%, $_L$=0.67,
 =0deg. (a) Pier Relative Displacement, (b) Normalized Pier Base Shear, (c) Pier
Hysteretic Response, (d) Pier Leg Vertical Reactions, (e) TADAS Hysteretic Response

220

FIGURE 6-22   Experimental Response Results; Synthetic, 150%, ₍L₎=0.67, =0deg. (a) Pier Relative Displacement, (b) Normalized Pier Base Shear, (c) Pier Hysteretic Response, (d) Pier Leg Vertical Reactions, (e) TADAS Hysteretic Response
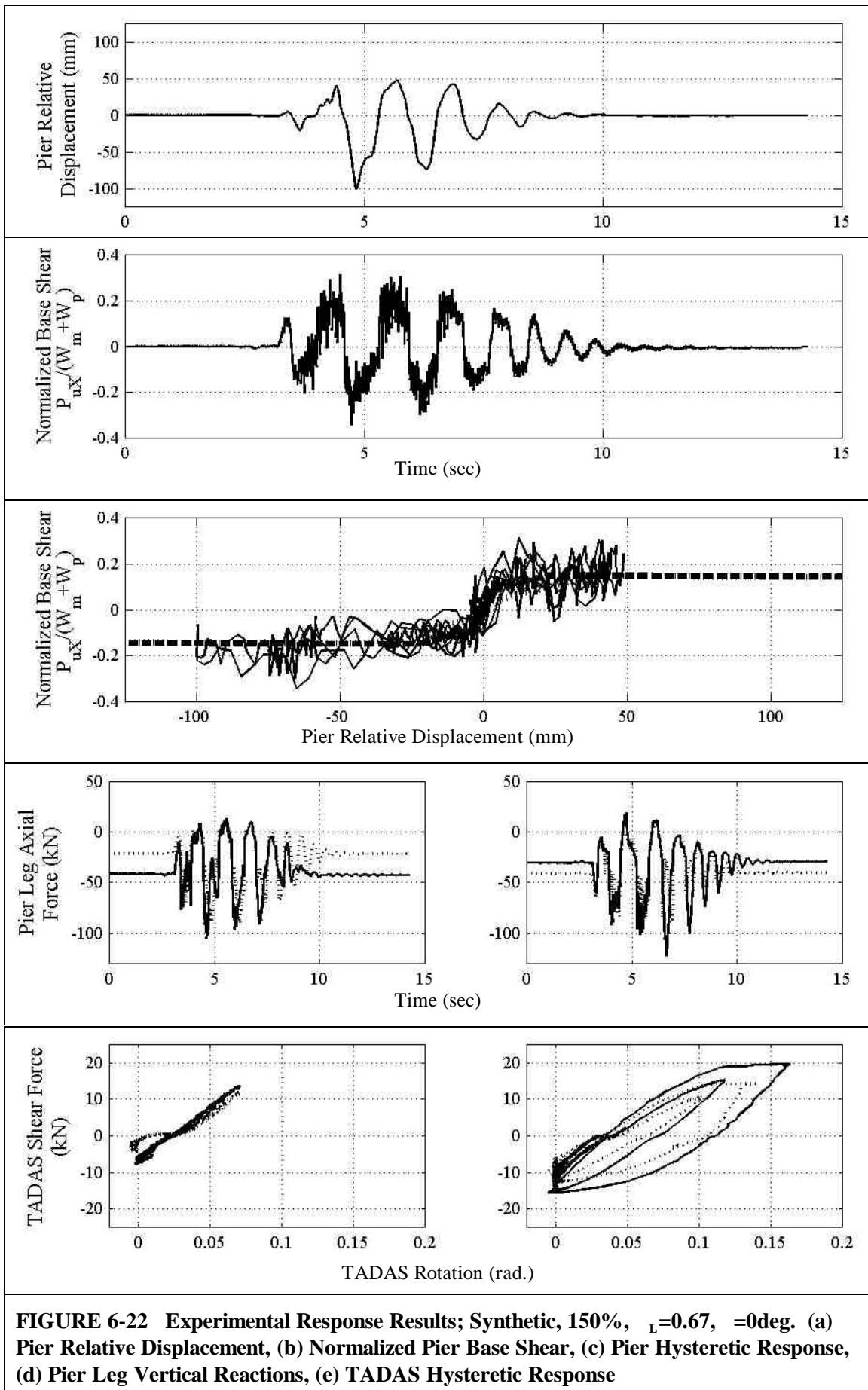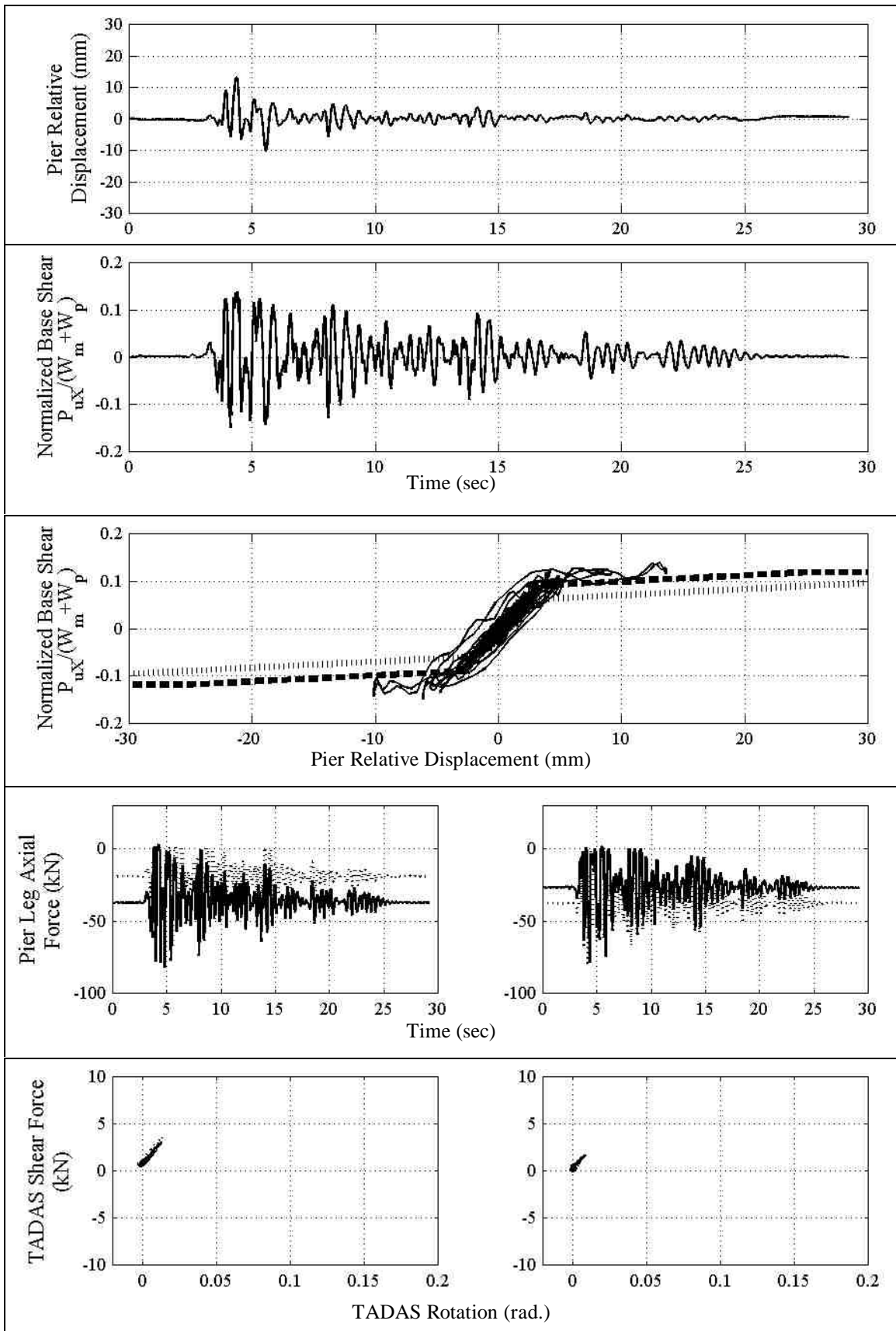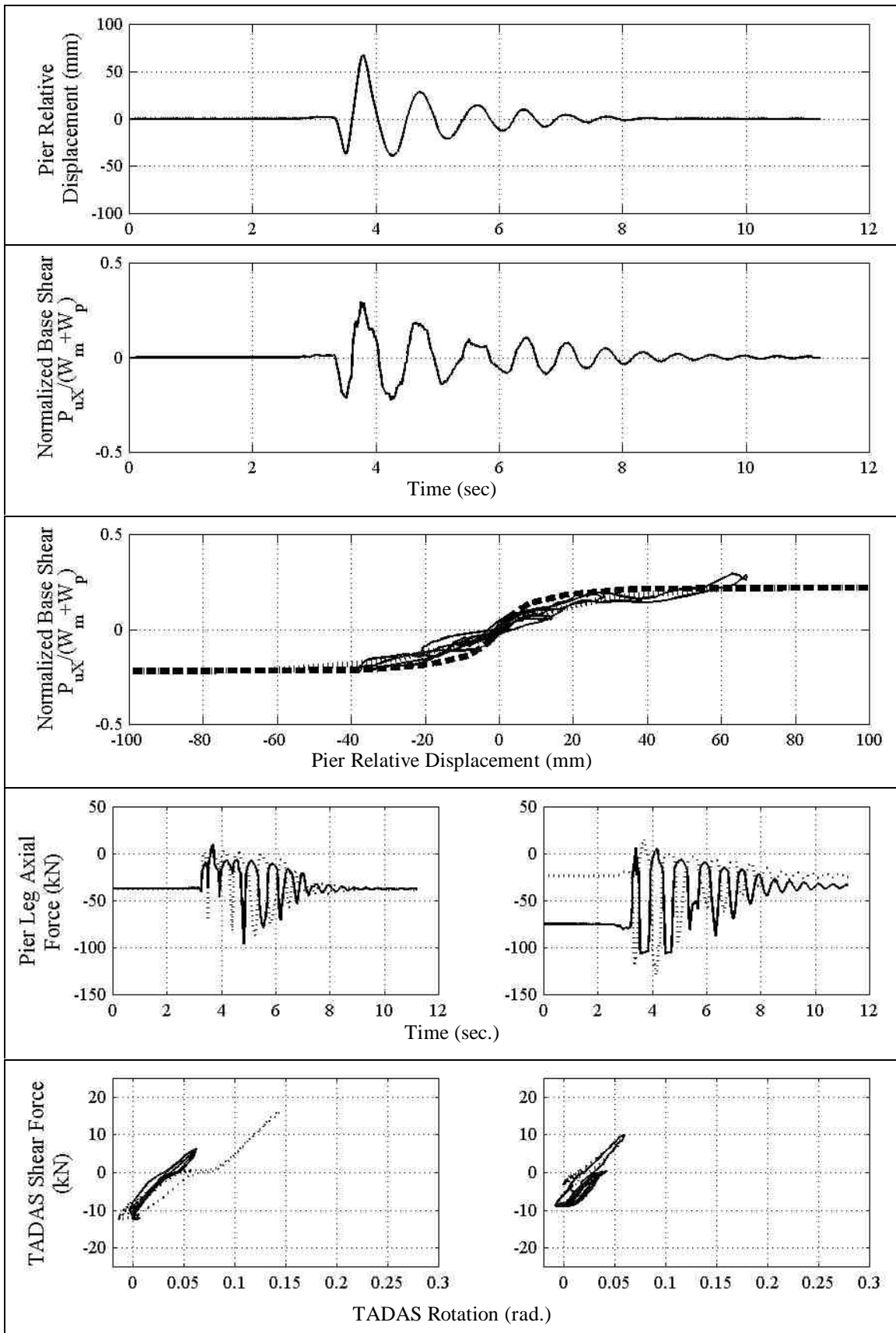
FIGURE 6-23   Experimental Response Results; El Centro 100%, $_L$=0.33, =0deg. (a) Pier Relative Displacement, (b) Normalized Pier Base Shear, (c) Pier Hysteretic Response, (d) Pier Leg Vertical Reactions, (e) TADAS Hysteretic Response
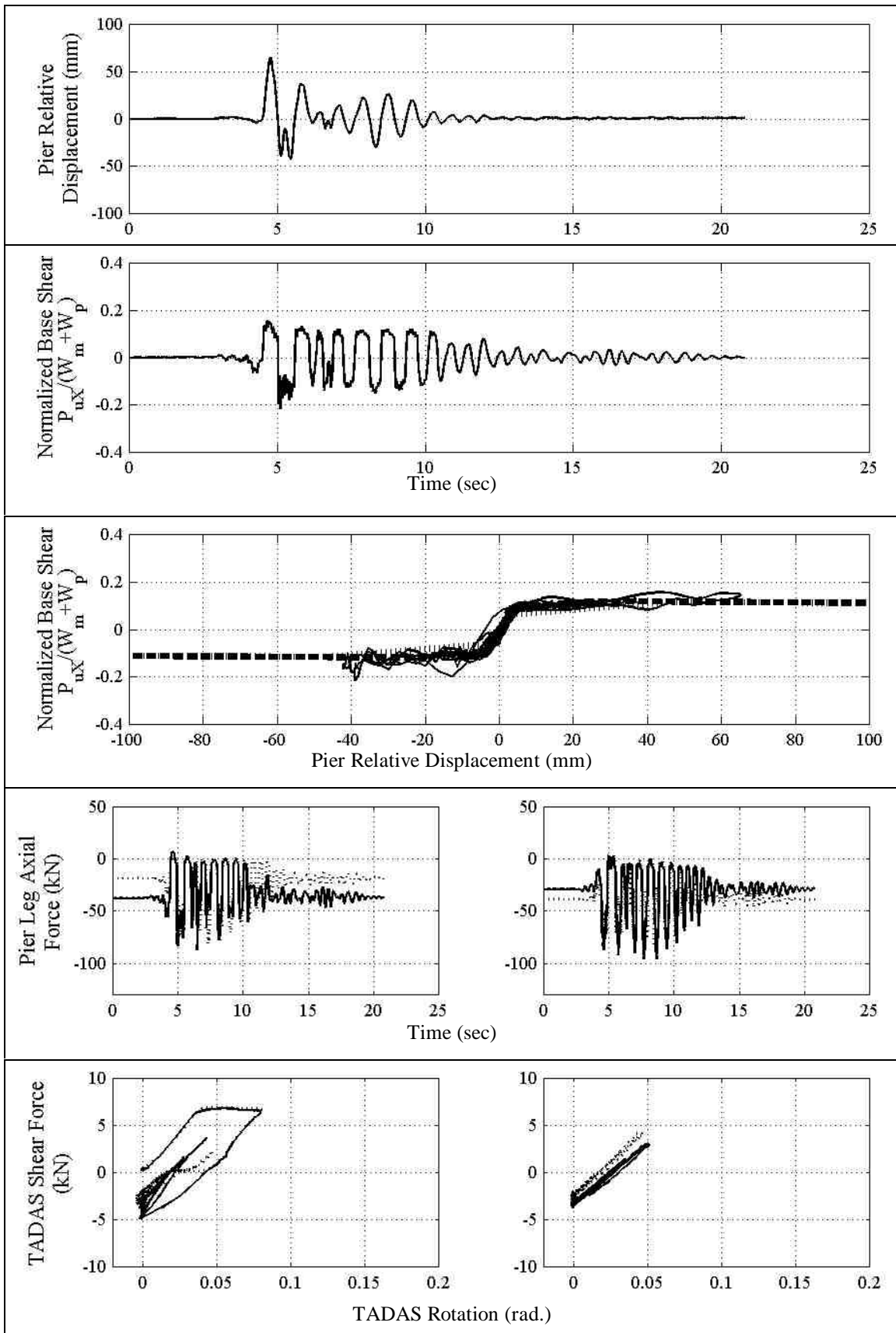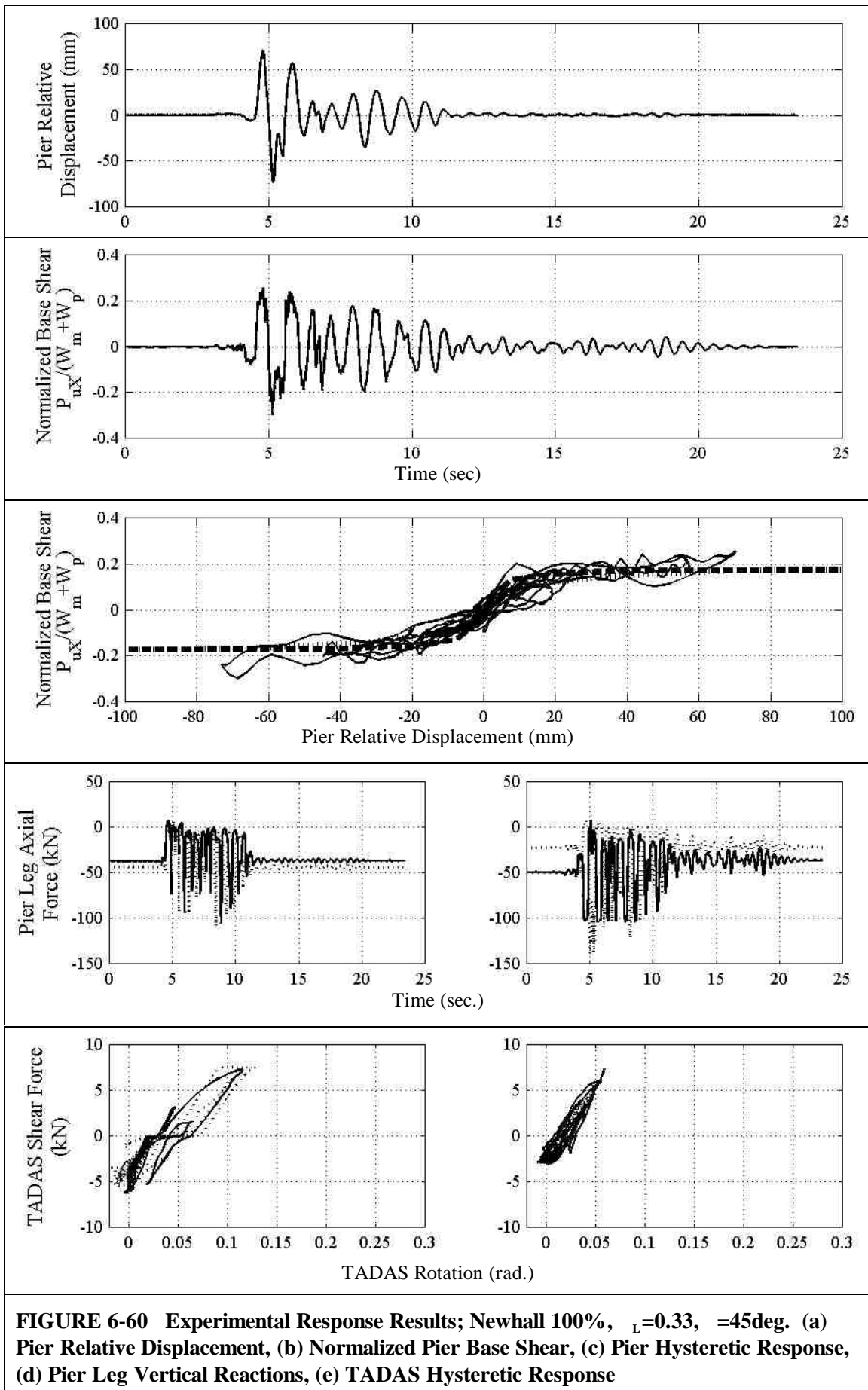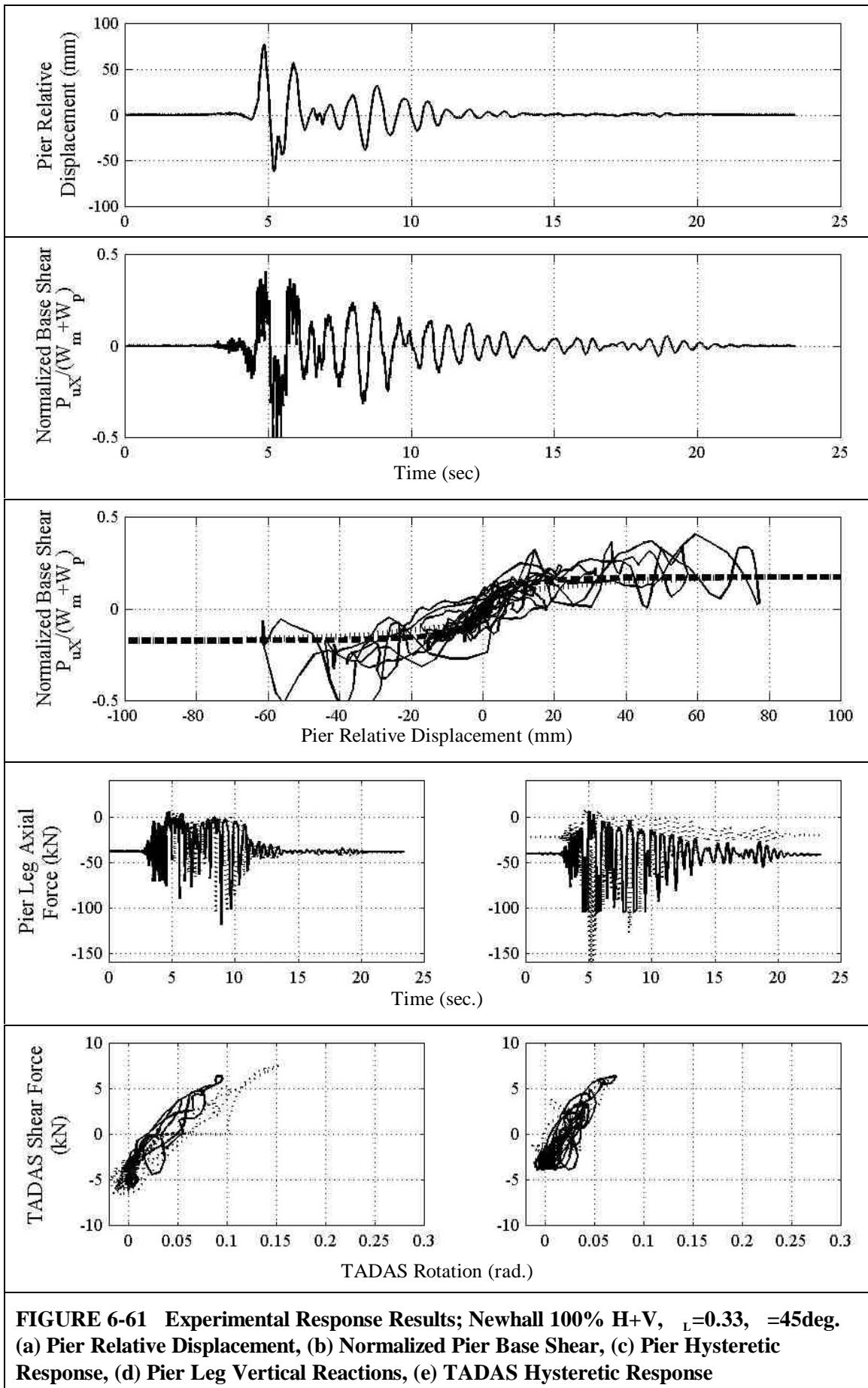
FIGURE 6-24 Experimental Response Results; Newhall 100%, $_L$=0.33, =0deg. (a) Pier Relative Displacement, (b) Normalized Pier Base Shear, (c) Pier Hysteretic Response, (d) Pier Leg Vertical Reactions, (e) TADAS Hysteretic Response

FIGURE 6-25 Experimental Response Results; Synthetic 100%, $_L$=0.33, =0deg. **(a) Pier Relative Displacement, (b) Normalized Pier Base Shear, (c) Pier Hysteretic Response, (d) Pier Leg Vertical Reactions, (e) TADAS Hysteretic Response**
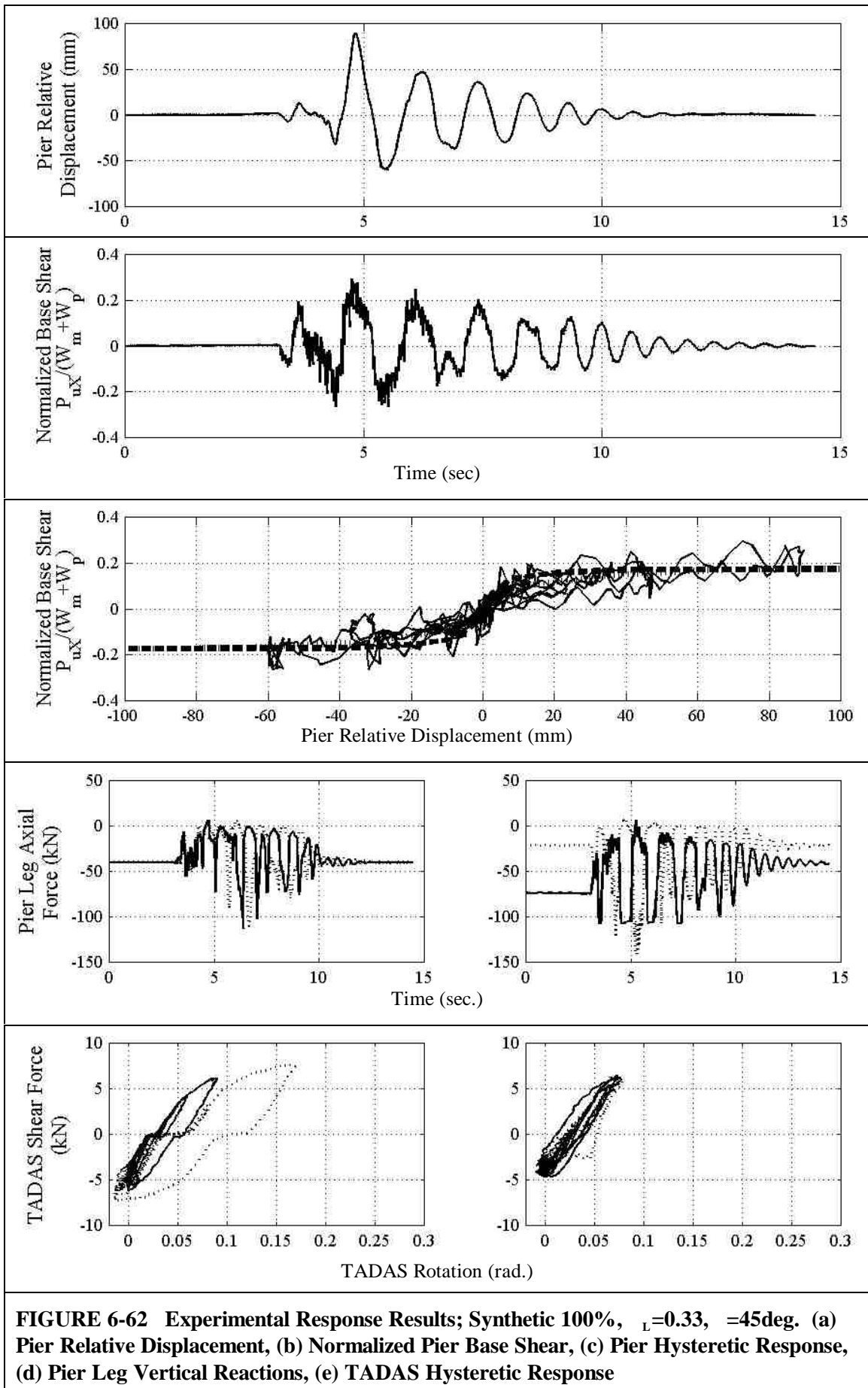
224
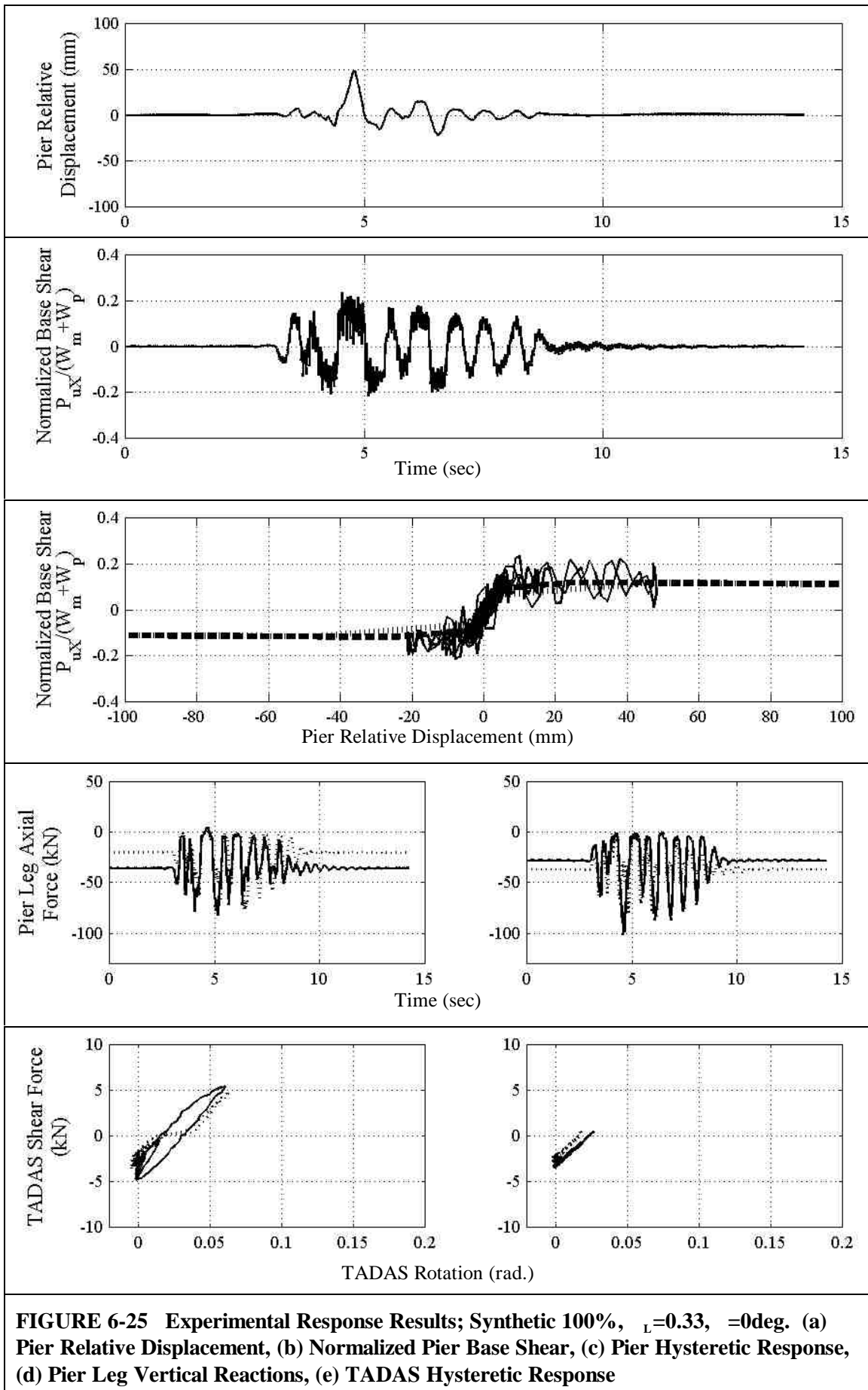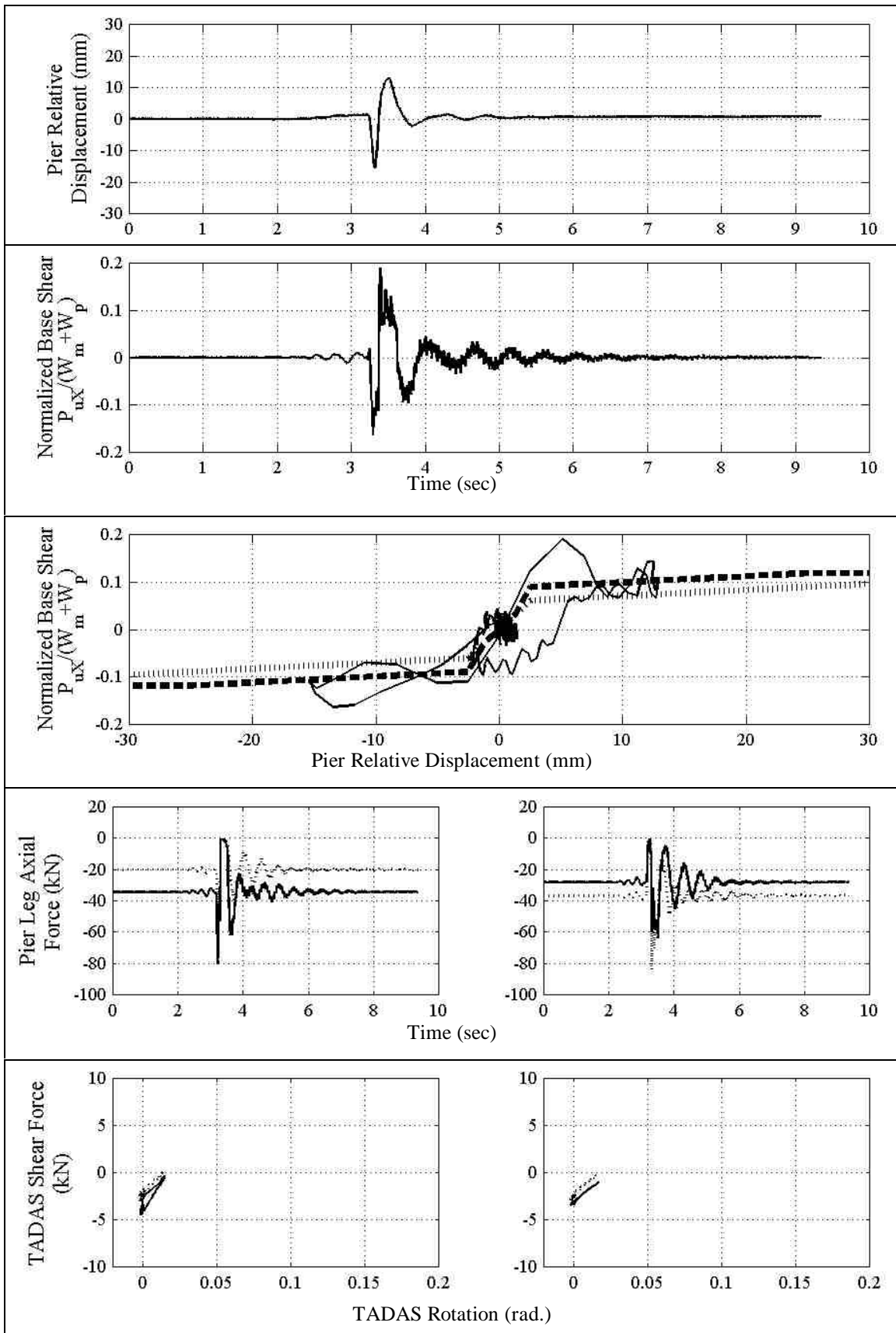
FIGURE 6-26   Experimental Response Results; Pulse P2, Tp=0.20sec 100%, $_L$=0.33, =0deg. (a) Pier Relative Displacement, (b) Normalized Pier Base Shear, (c) Pier Hysteretic Response, (d) Pier Leg Vertical Reactions, (e) TADAS Hysteretic Response
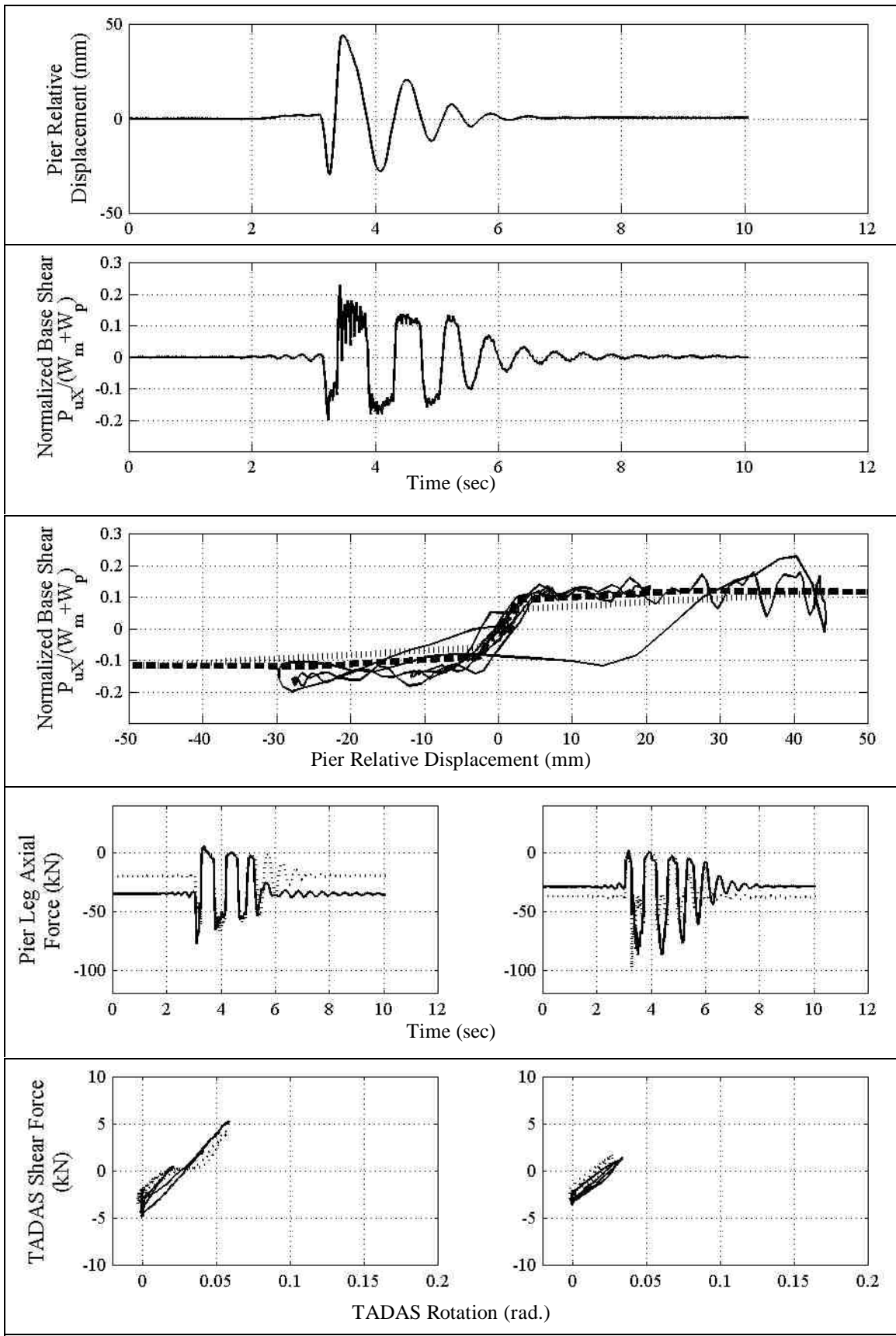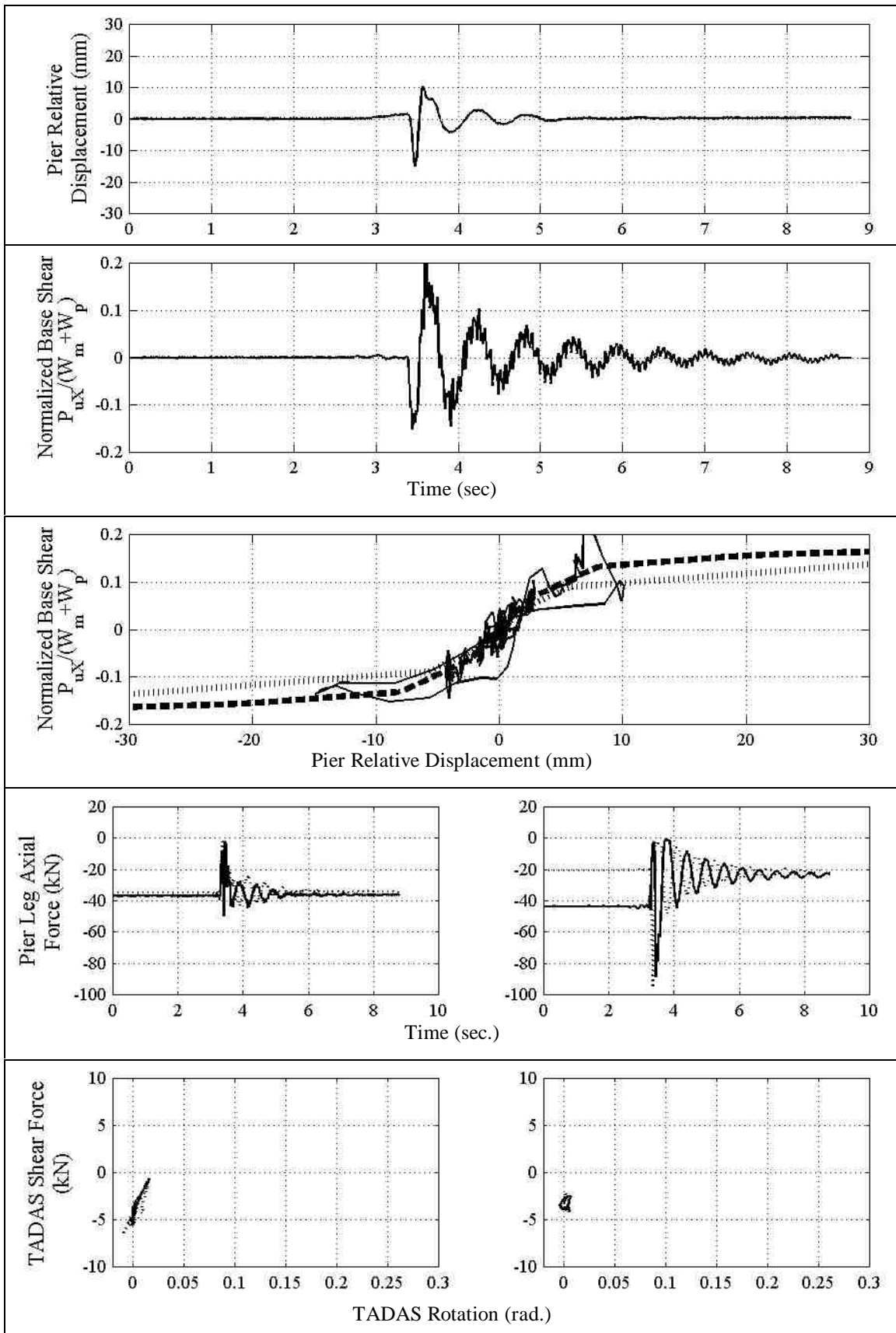
FIGURE 6-27   Experimental Response Results; Pulse P2, Tp=0.40sec 100%, ρ_L=0.33, θ=0deg. (a) Pier Relative Displacement, (b) Normalized Pier Base Shear, (c) Pier Hysteretic Response, (d) Pier Leg Vertical Reactions, (e) TADAS Hysteretic Response
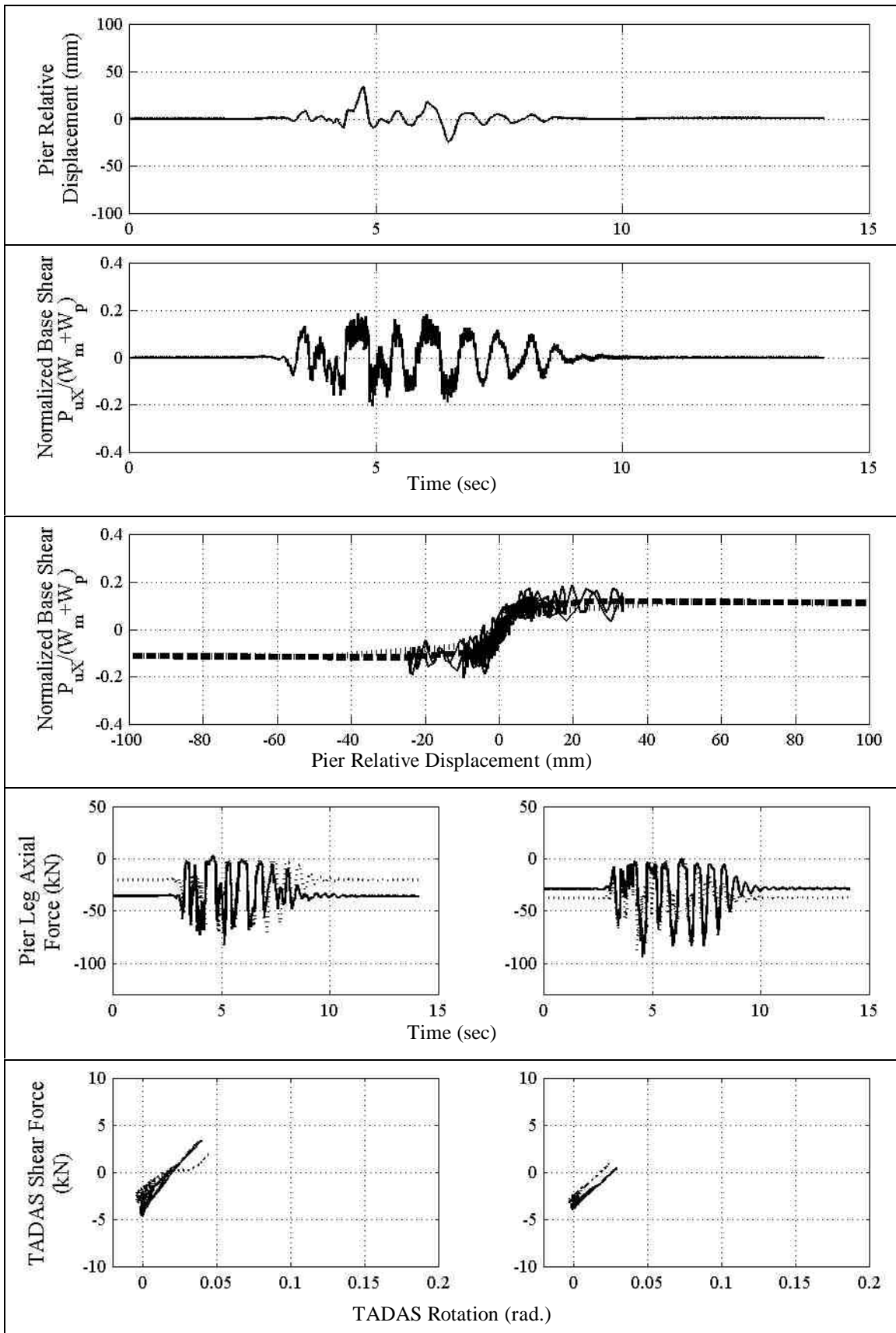
FIGURE 6-28   Experimental Response Results; Synthetic 100% H+V, $_L$=0.33, =0deg. (a) Pier Relative Displacement, (b) Normalized Pier Base Shear, (c) Pier Hysteretic Response, (d) Pier Leg Vertical Reactions, (e) TADAS Hysteretic Response
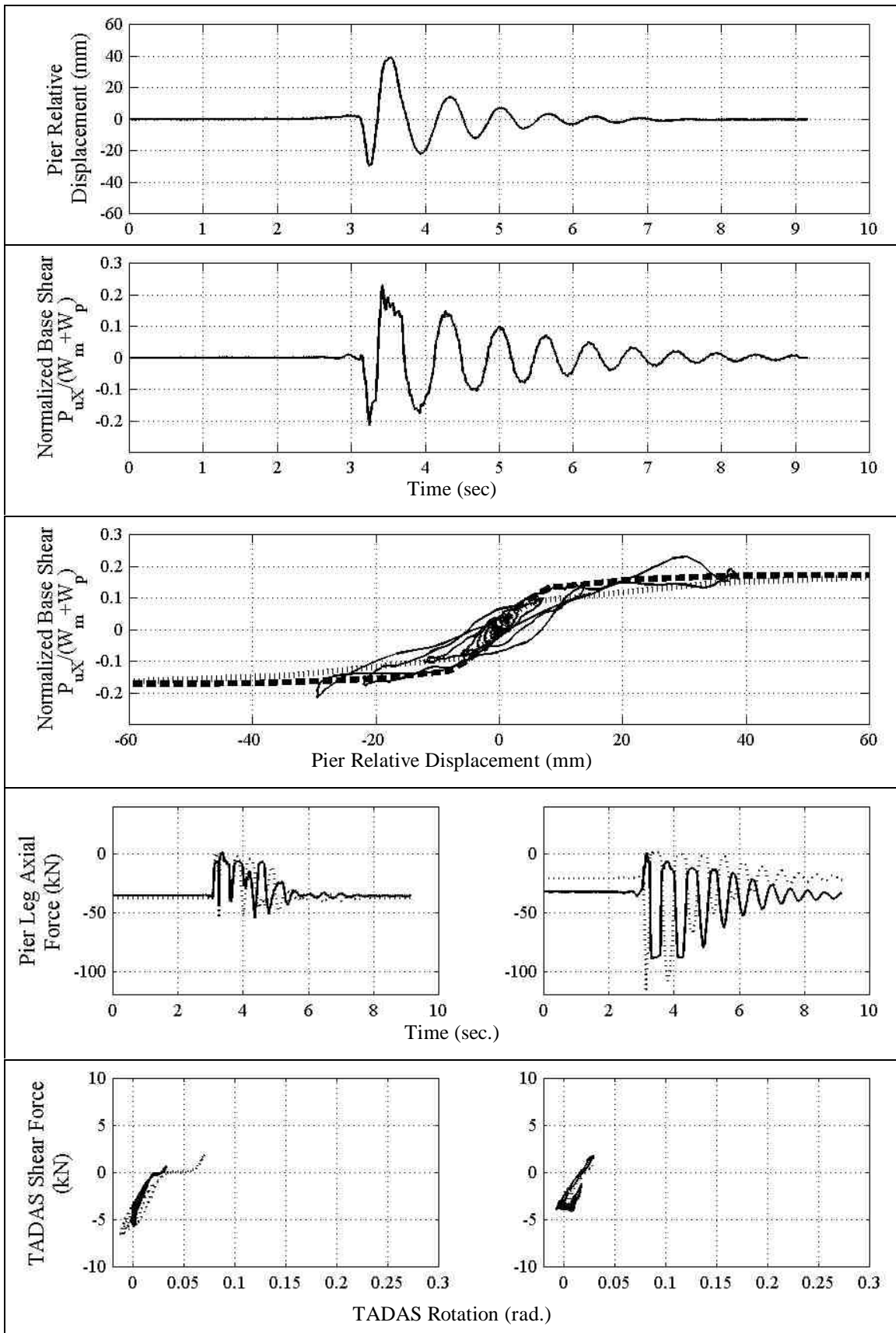
227
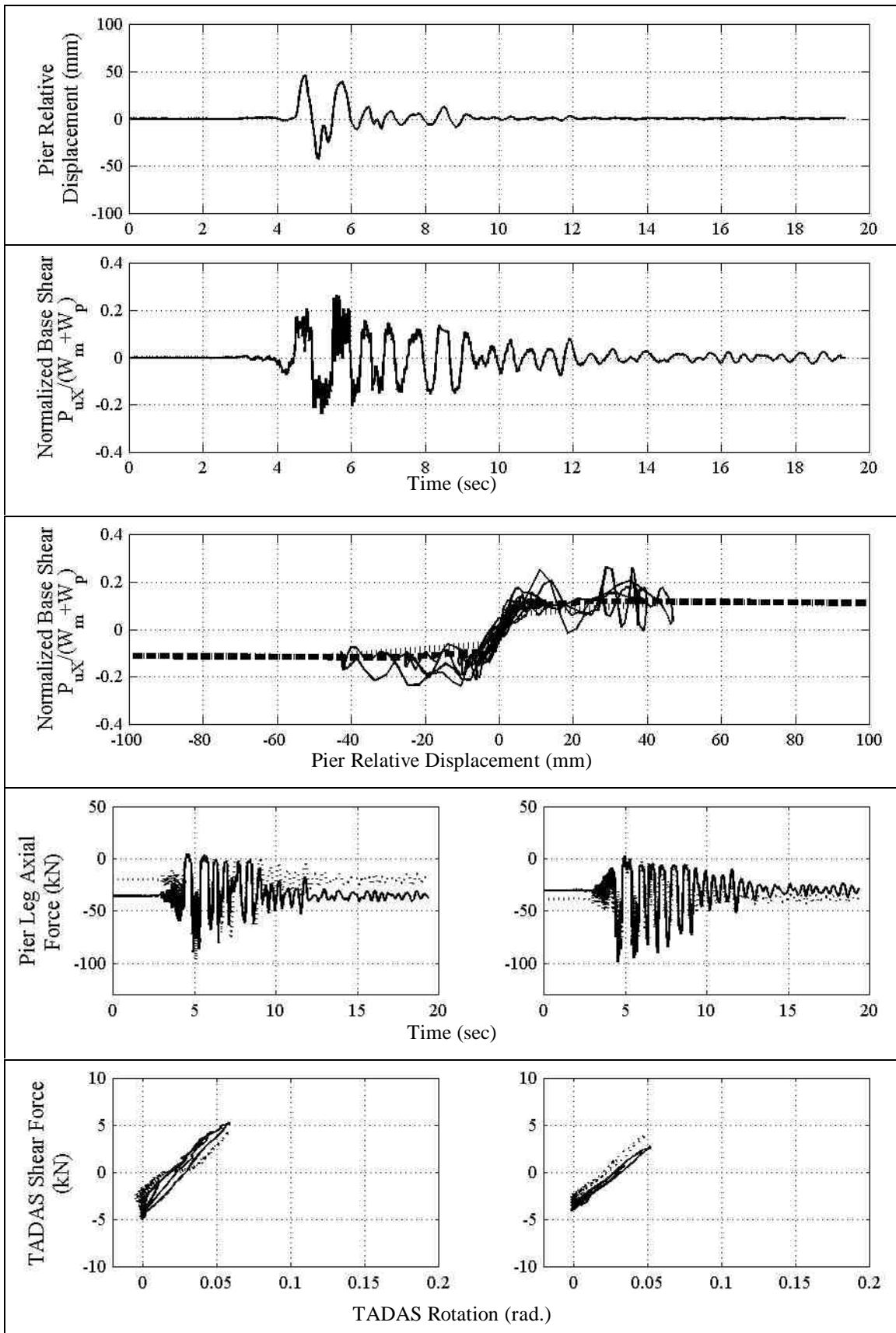
FIGURE 6-29   Experimental Response Results; Newhall 100% H+V, $_L$=0.33, =0deg.
(a) Pier Relative Displacement, (b) Normalized Pier Base Shear, (c) Pier Hysteretic
Response, (d) Pier Leg Vertical Reactions, (e) TADAS Hysteretic Response
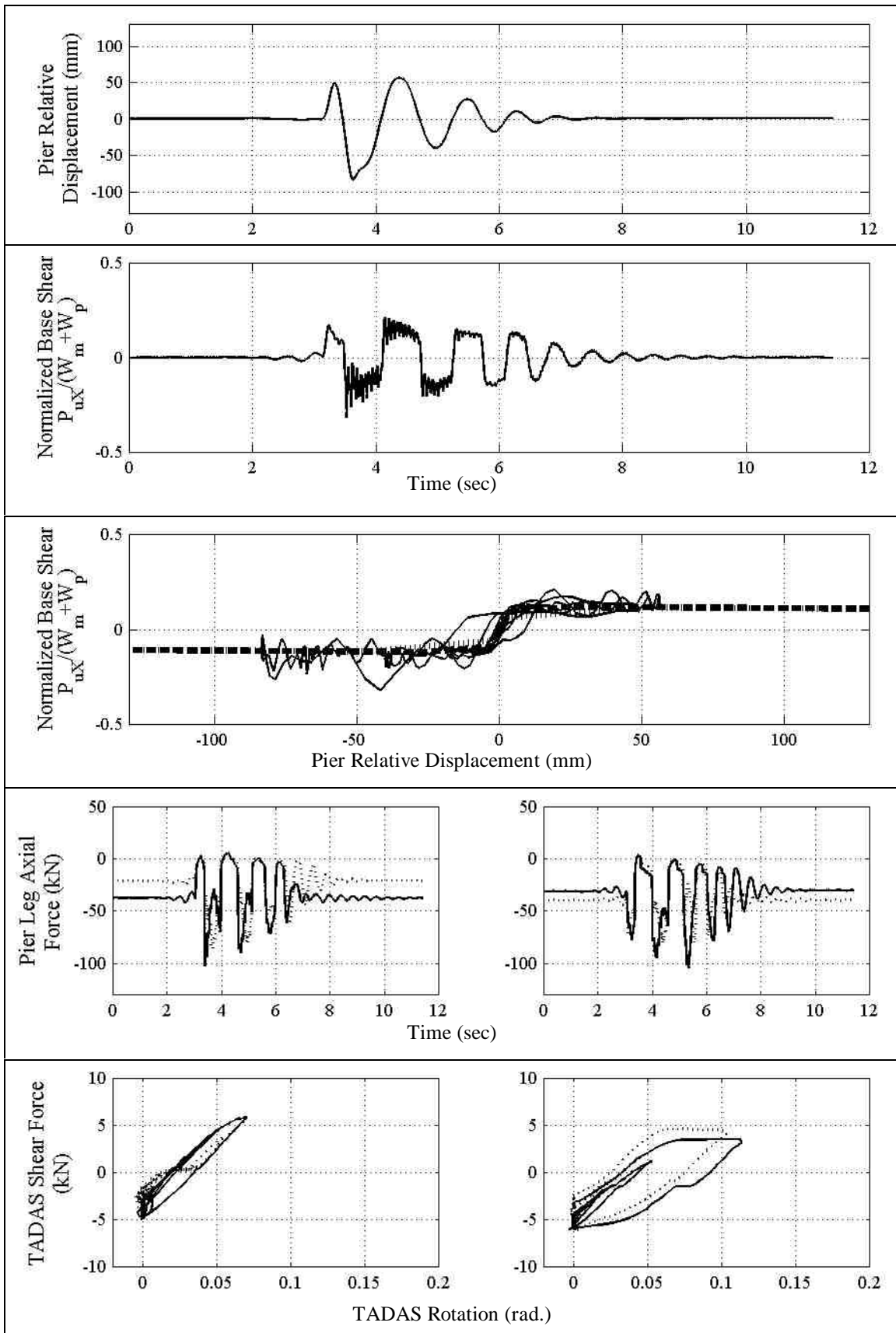
FIGURE 6-30   Experimental Response Results; Pulse P2, Tp=0.60sec 100%, L=0.33, =0deg. (a) Pier Relative Displacement, (b) Normalized Pier Base Shear, (c) Pier Hysteretic Response, (d) Pier Leg Vertical Reactions, (e) TADAS Hysteretic Response
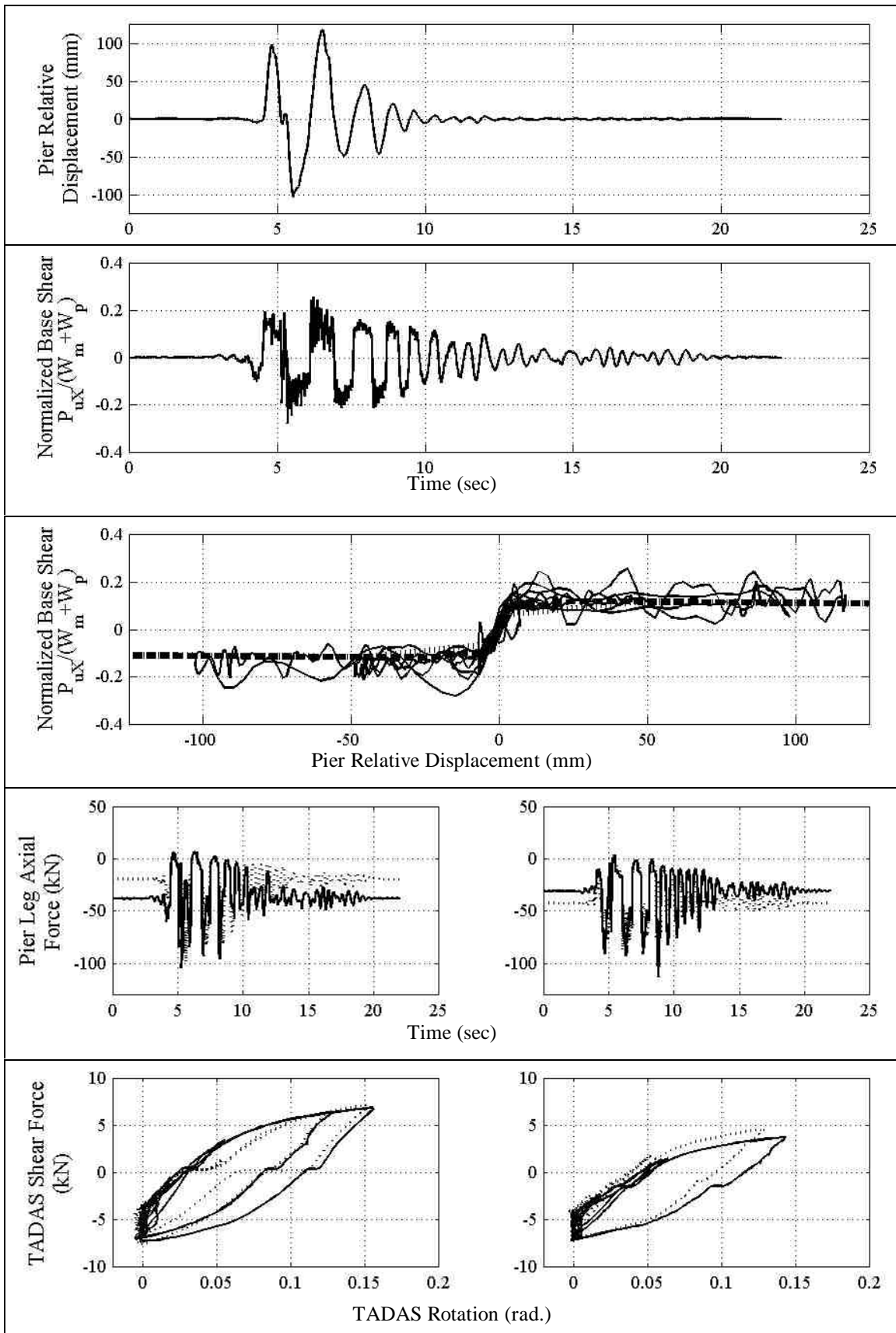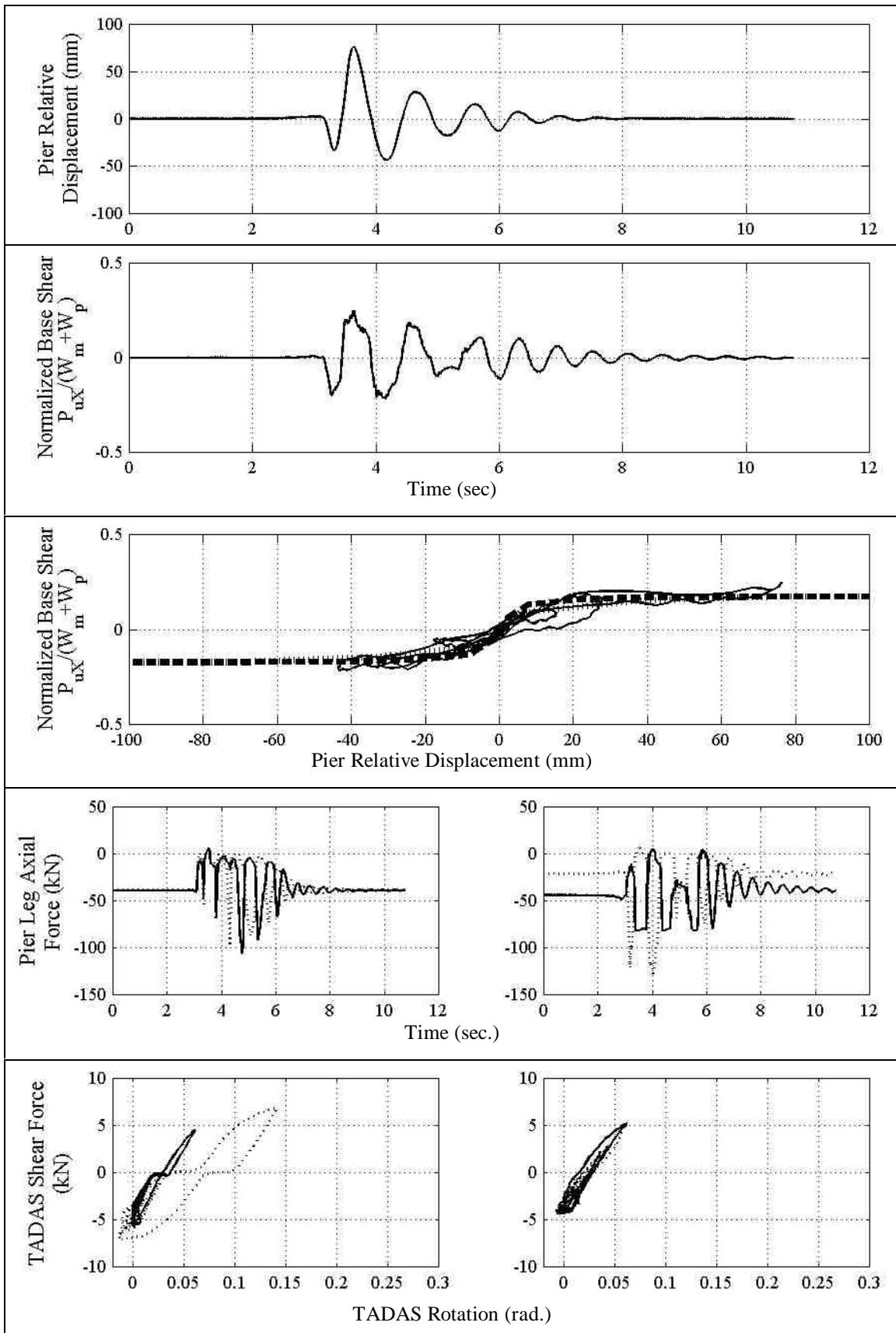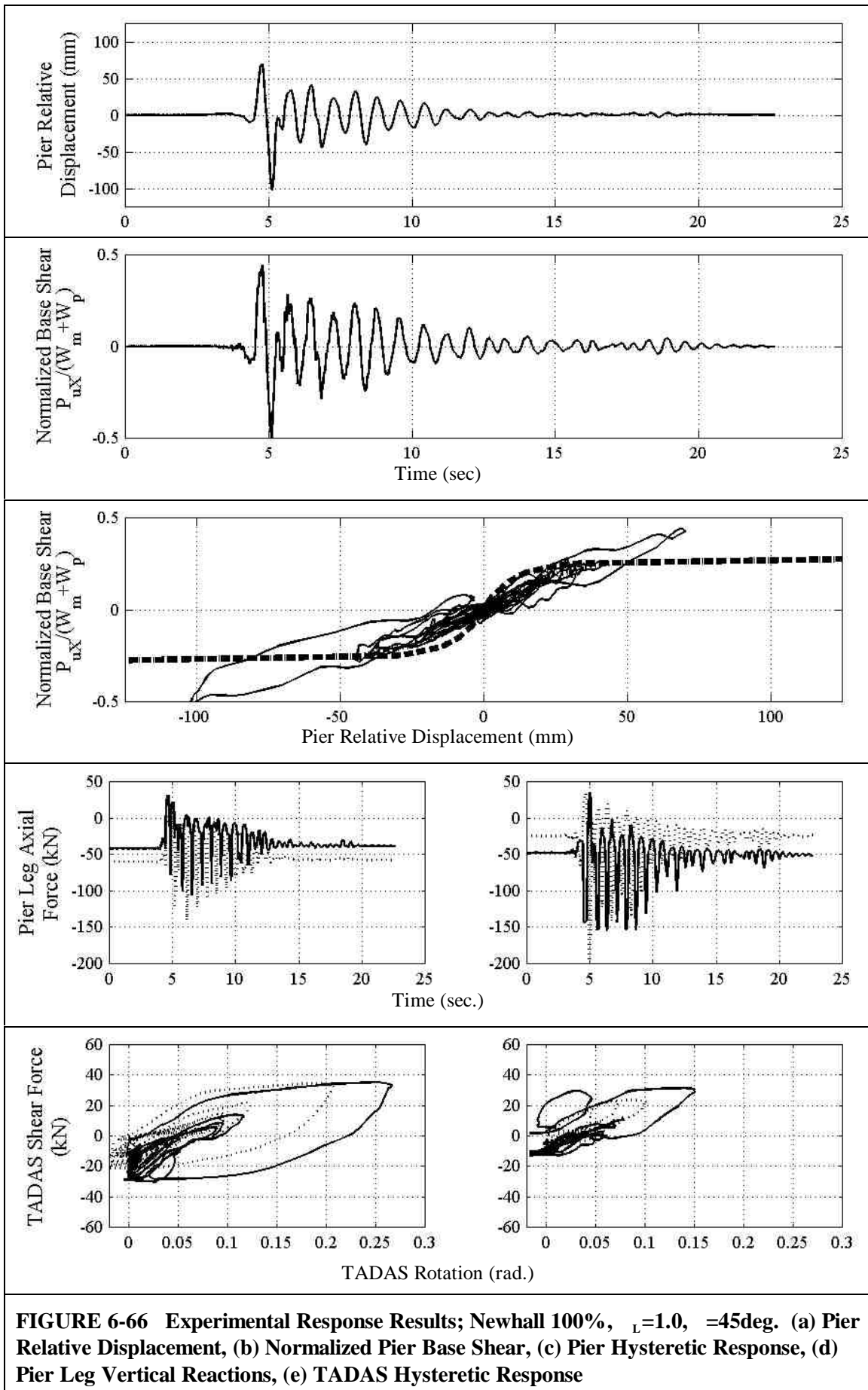
FIGURE 6-31   Experimental Response Results; Newhall 125%, $_L$=0.33, =0deg. (a) Pier Relative Displacement, (b) Normalized Pier Base Shear, (c) Pier Hysteretic Response, (d) Pier Leg Vertical Reactions, (e) TADAS Hysteretic Response
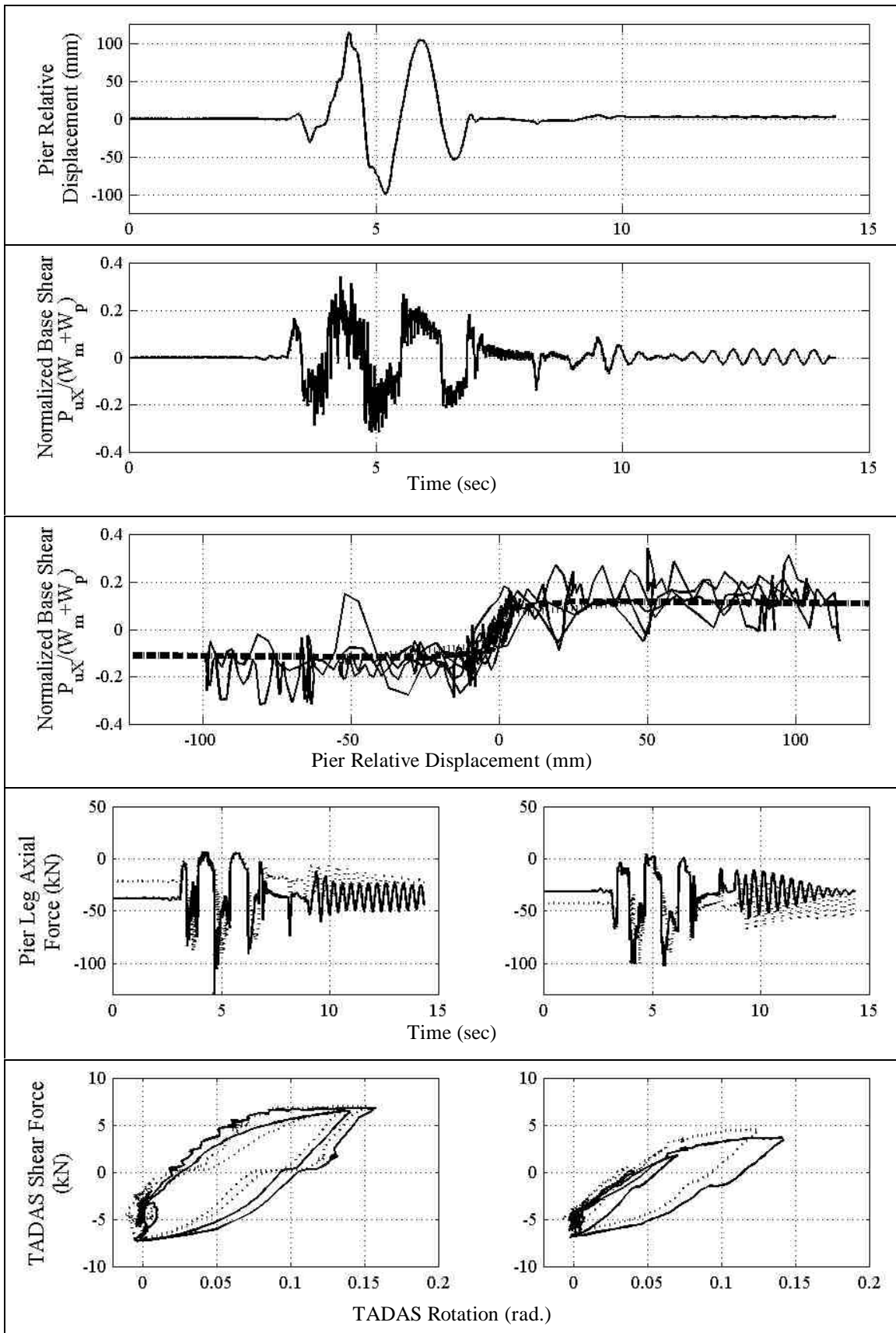
FIGURE 6-32 Experimental Response Results; Synthetic 150%, $_L$=0.33, =0deg. (a) Pier Relative Displacement, (b) Normalized Pier Base Shear, (c) Pier Hysteretic Response, (d) Pier Leg Vertical Reactions, (e) TADAS Hysteretic Response
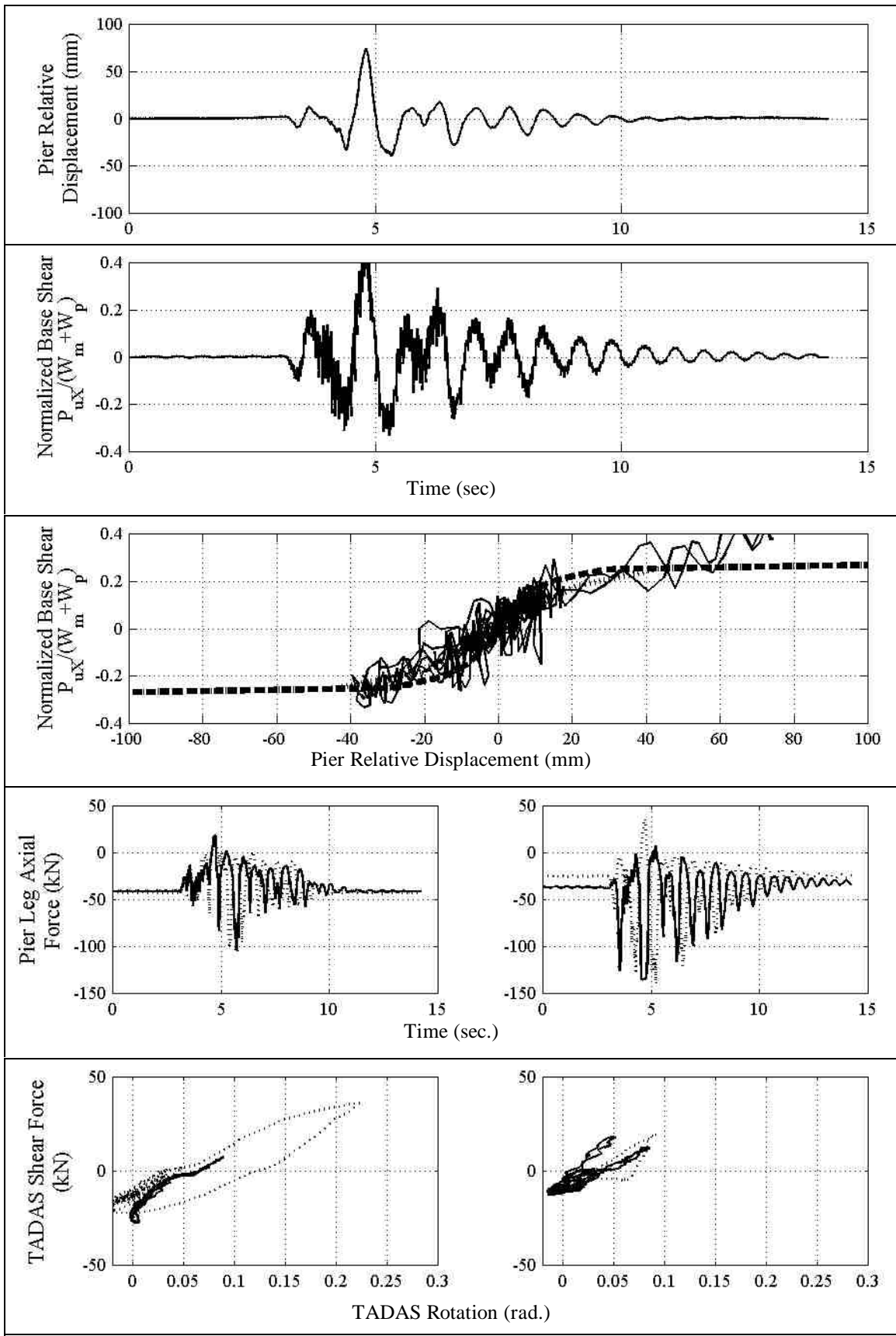
231
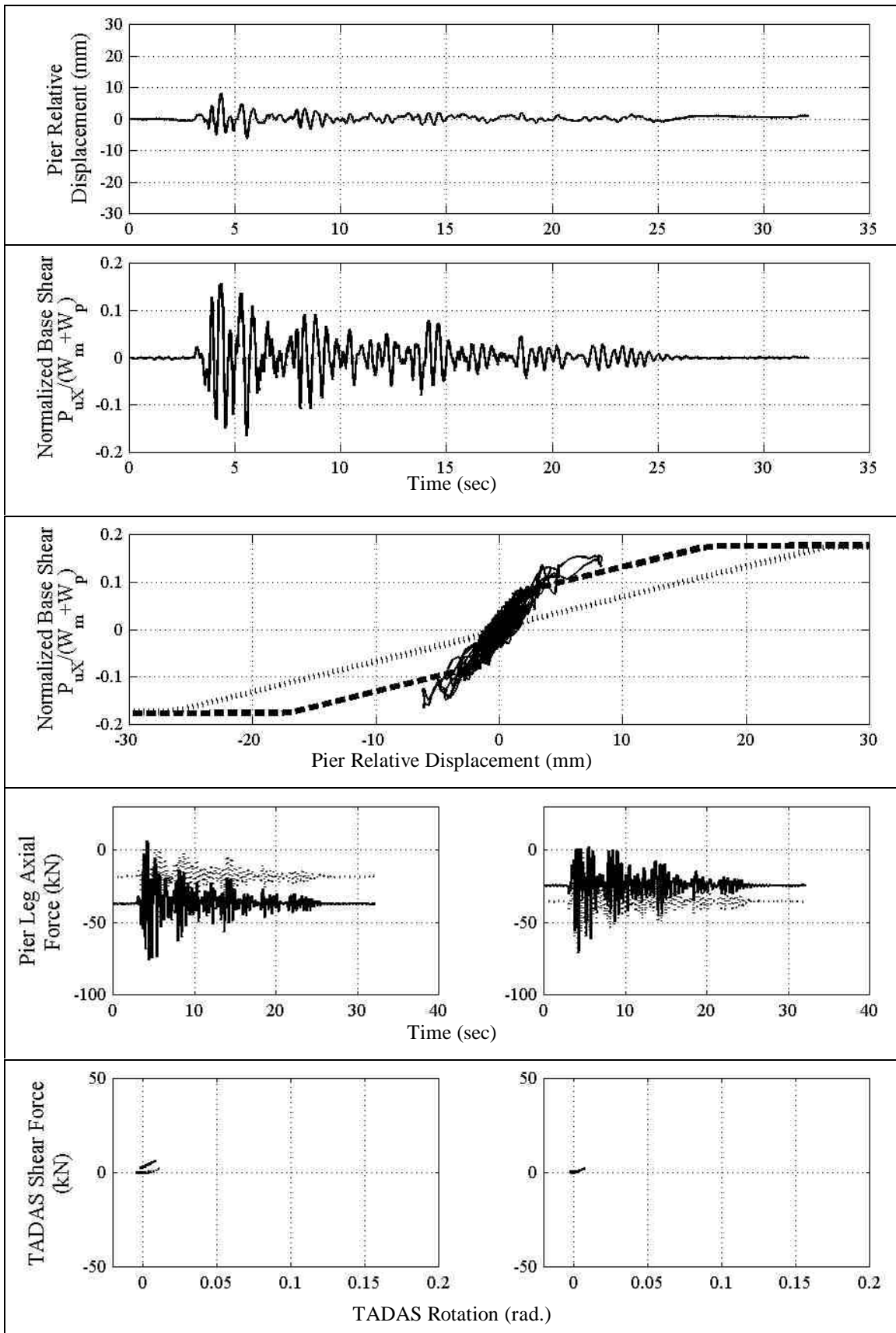
FIGURE 6-33 Experimental Response Results; El Centro 100%, λ_L=1.0, θ=0deg. (a) Pier Relative Displacement, (b) Normalized Pier Base Shear, (c) Pier Hysteretic Response, (d) Pier Leg Vertical Reactions, (e) TADAS Hysteretic Response
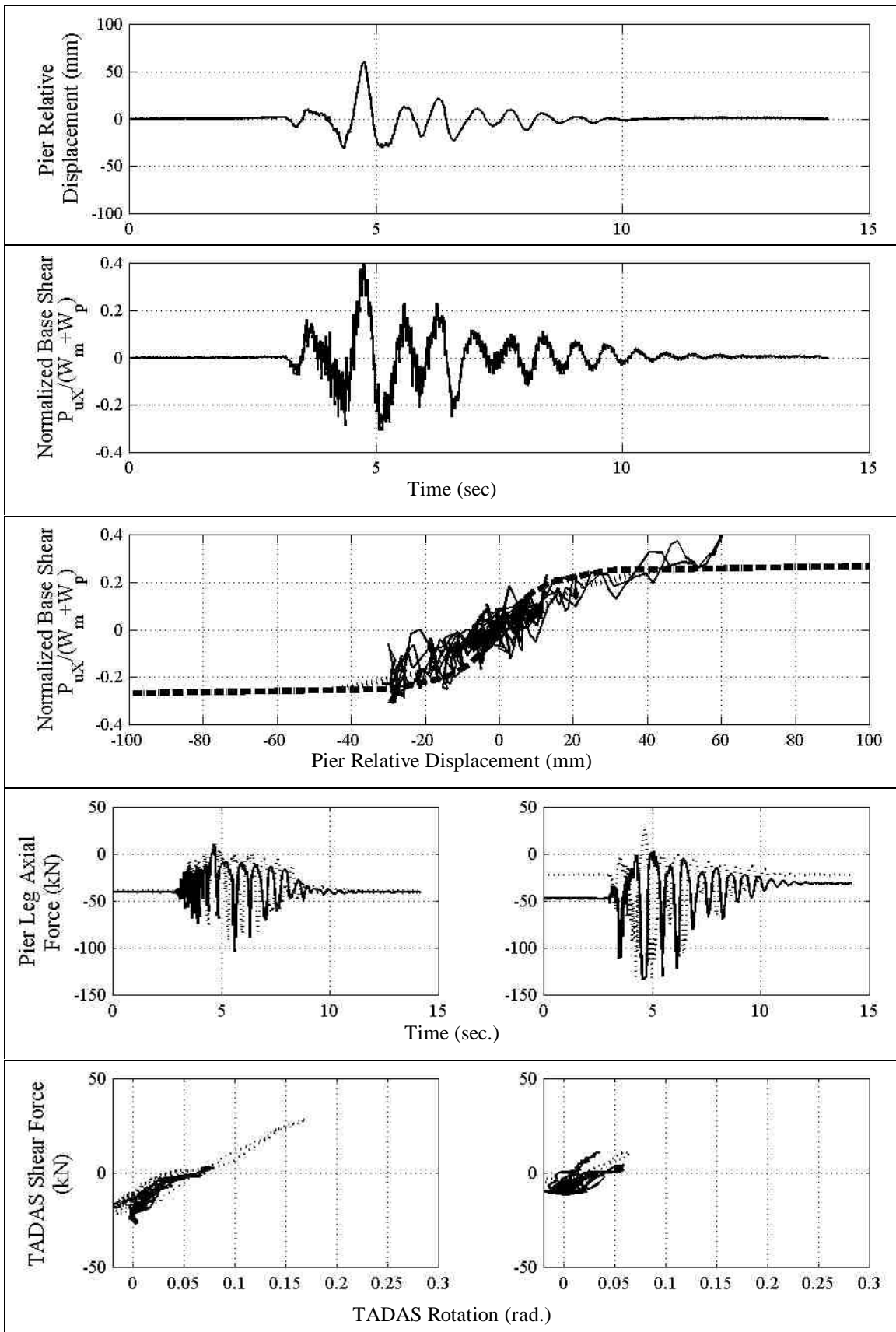
232

FIGURE 6-34 Experimental Response Results; Newhall 100%, ₗ=1.0, =0deg. (a) Pier Relative Displacement, (b) Normalized Pier Base Shear, (c) Pier Hysteretic Response, (d) Pier Leg Vertical Reactions, (e) TADAS Hysteretic Response

233
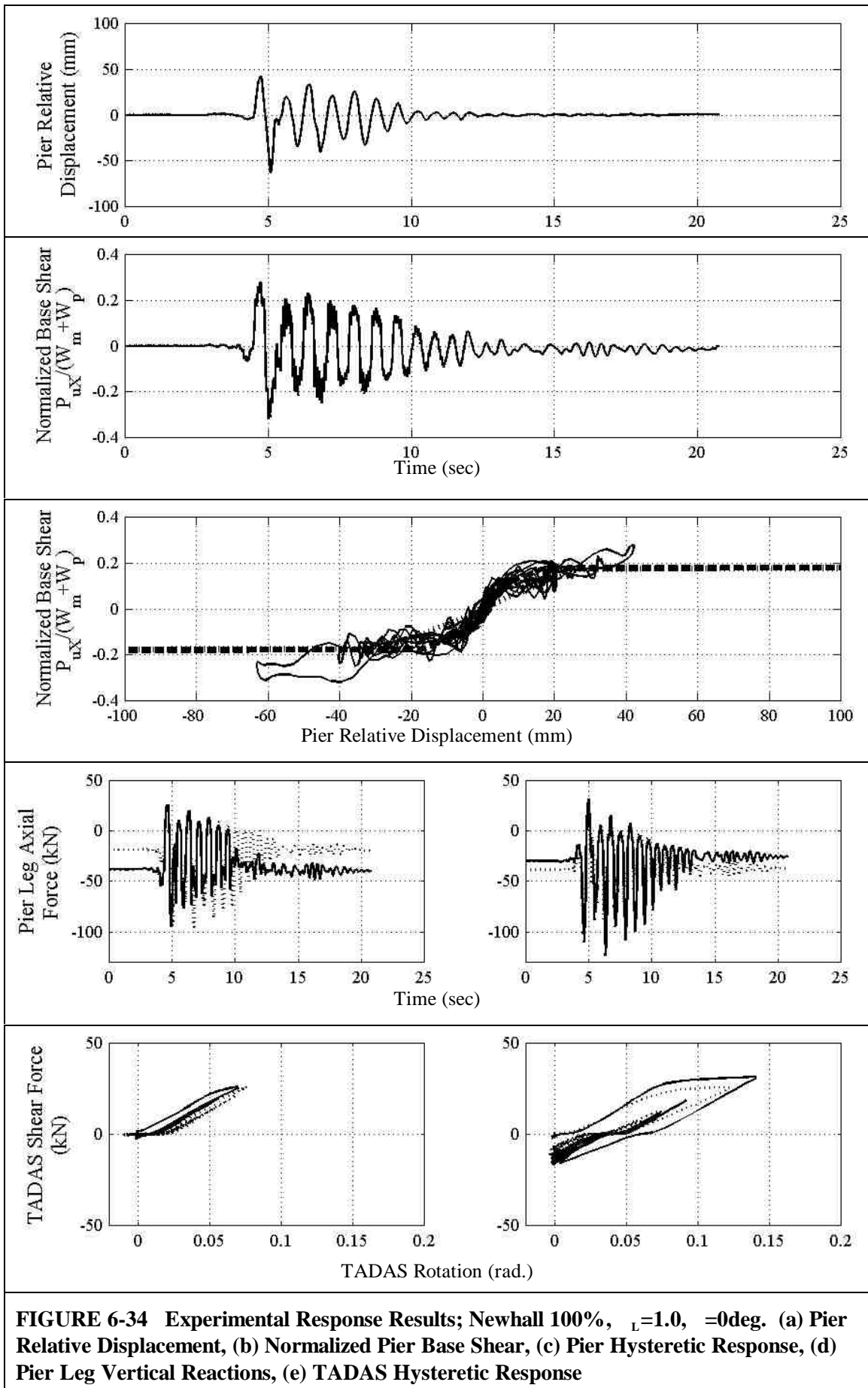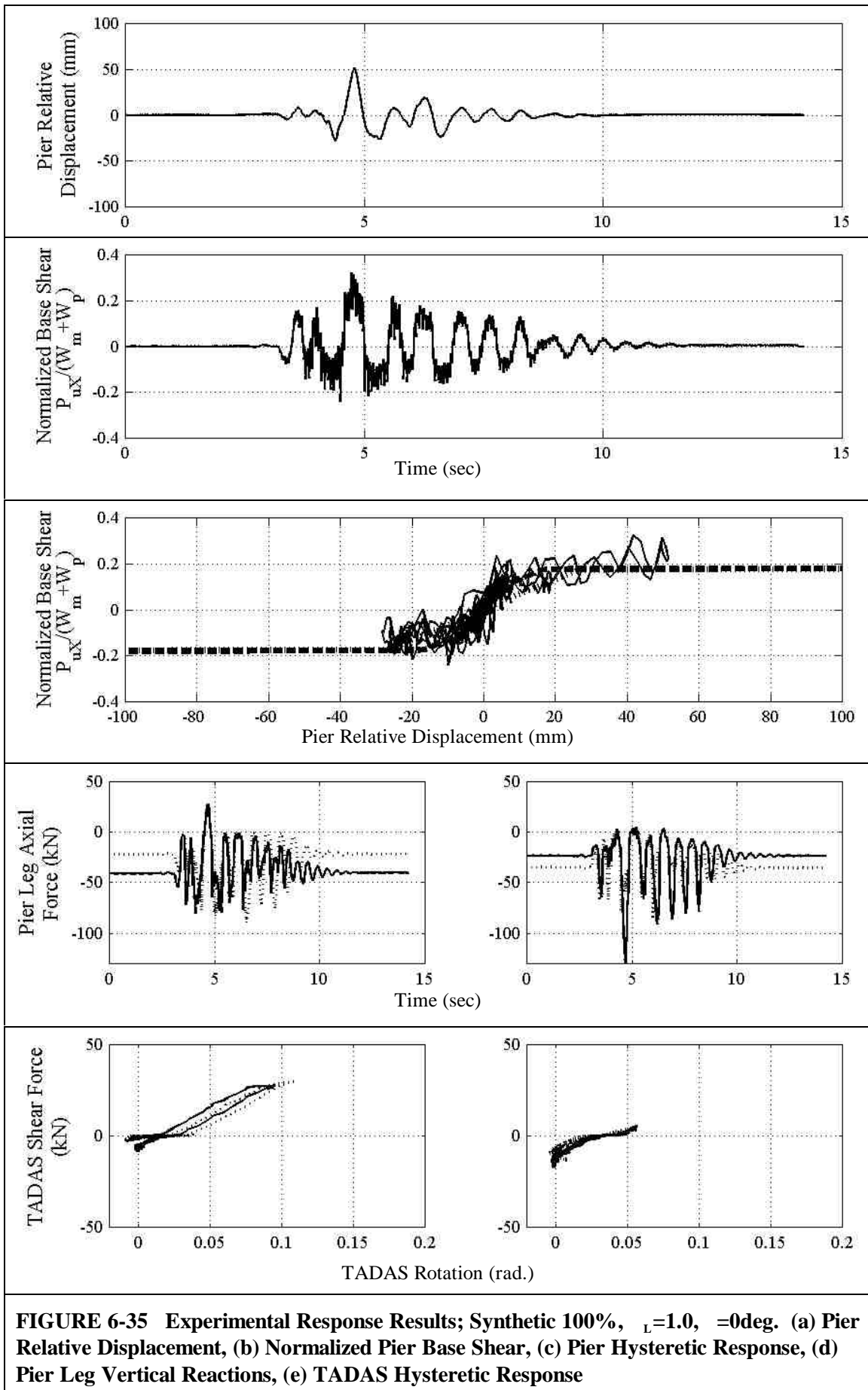
FIGURE 6-35 Experimental Response Results; Synthetic 100%, $_L$=1.0, =0deg. (a) Pier Relative Displacement, (b) Normalized Pier Base Shear, (c) Pier Hysteretic Response, (d) Pier Leg Vertical Reactions, (e) TADAS Hysteretic Response
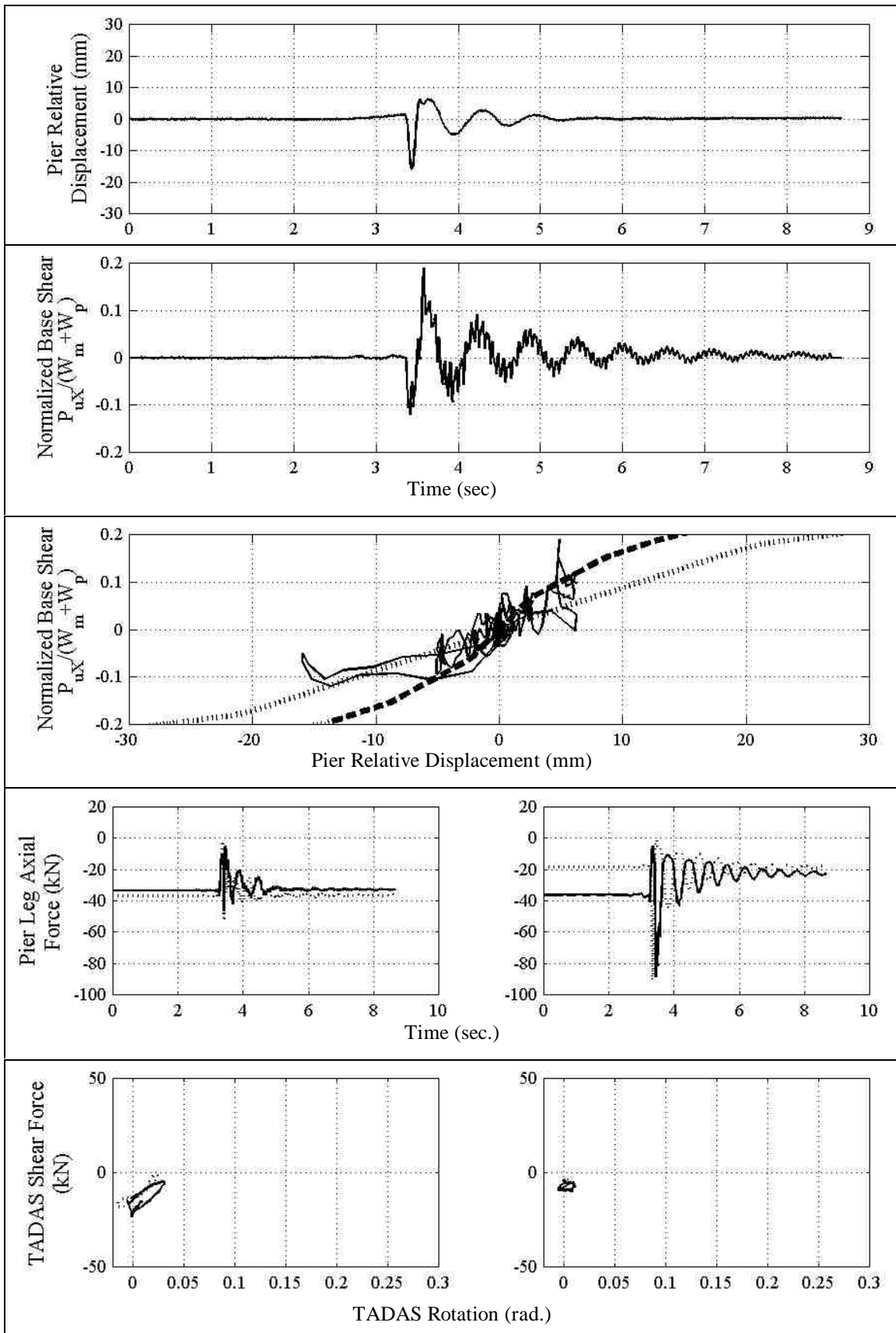
234
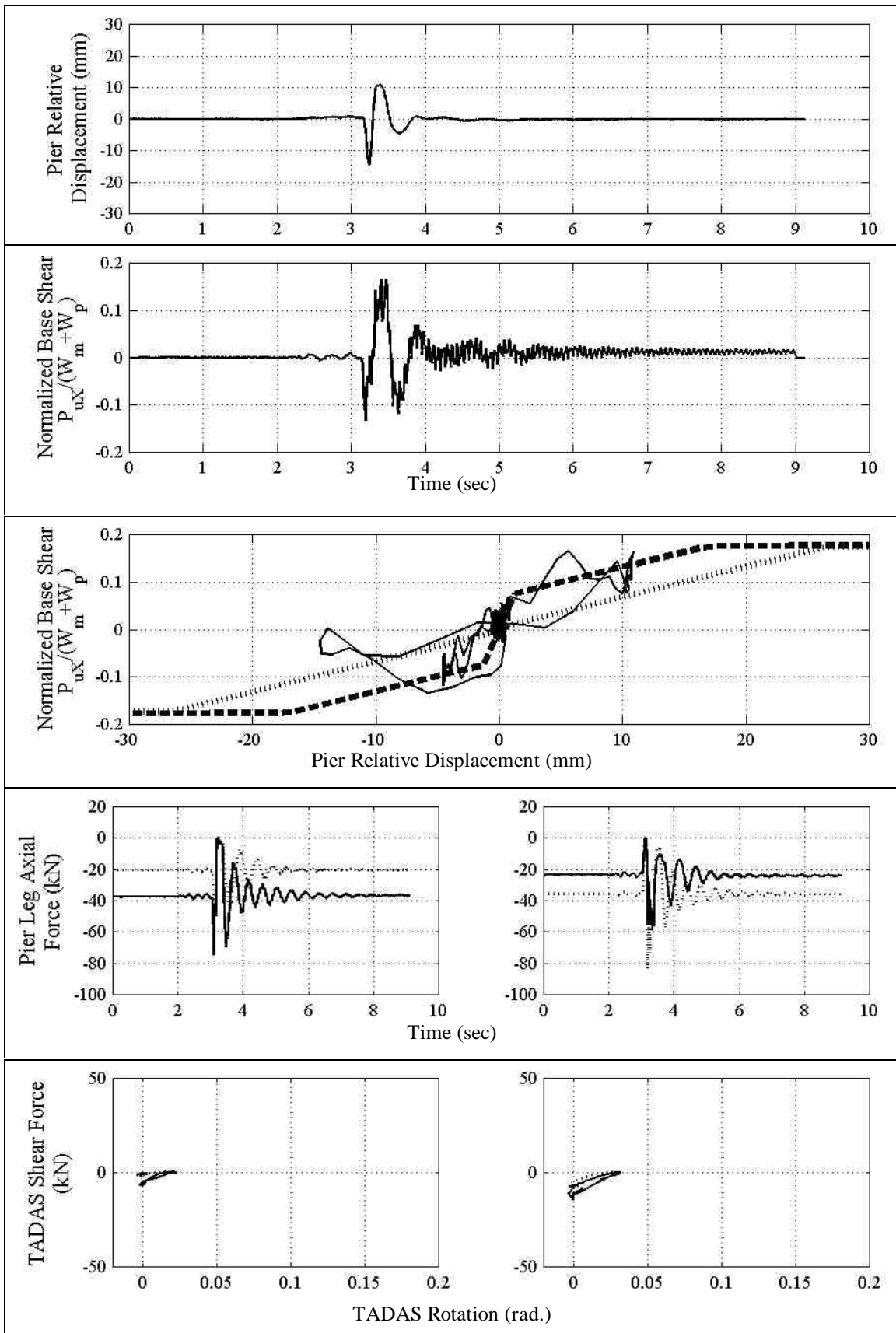
FIGURE 6-36 **Experimental Response Results; Pulse P2, Tp=0.20sec, 100%, $\_L$=1.0, Θ=0deg.** **(a) Pier Relative Displacement, (b) Normalized Pier Base Shear, (c) Pier Hysteretic Response, (d) Pier Leg Vertical Reactions, (e) TADAS Hysteretic Response**
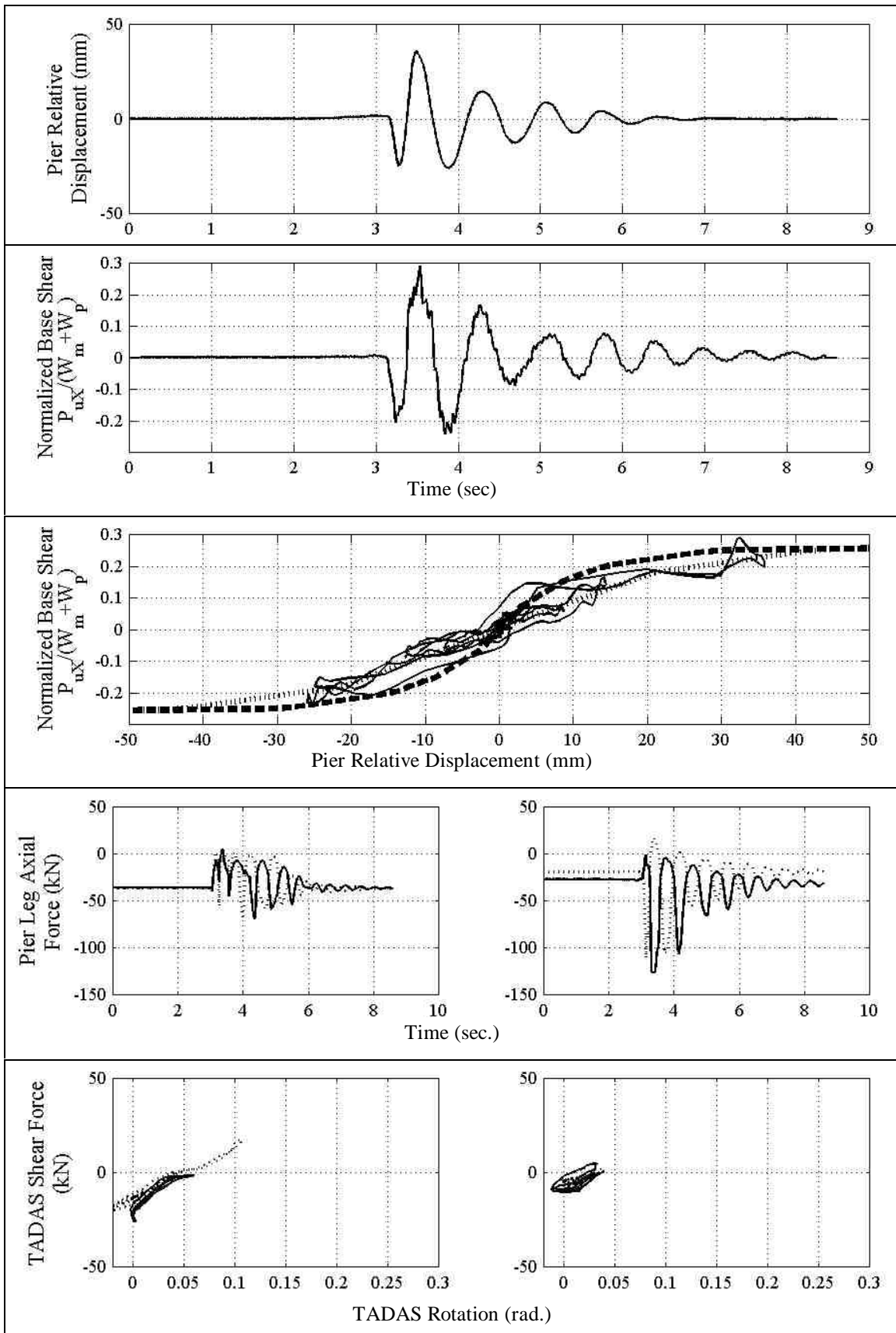
235
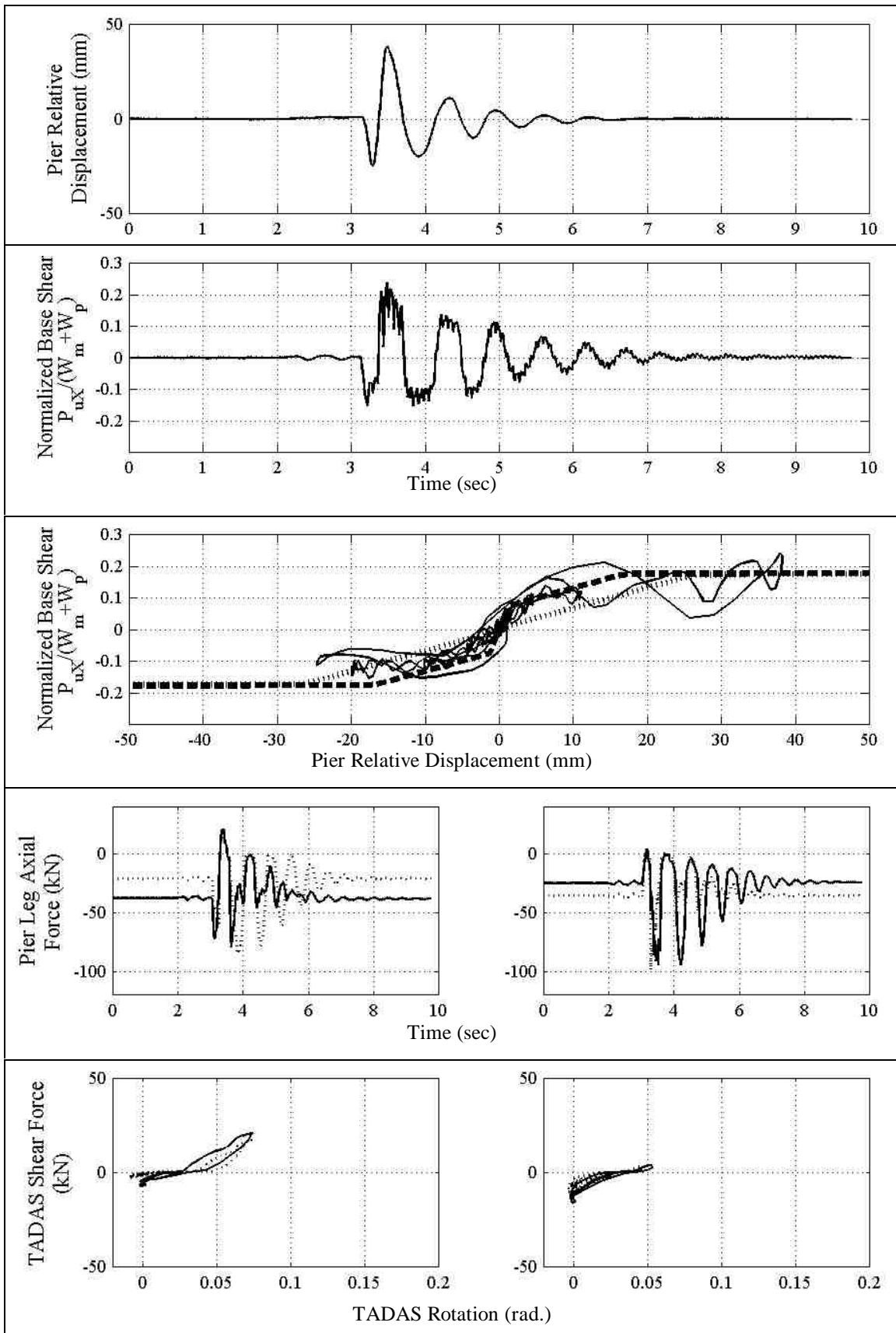
FIGURE 6-37 Experimental Response Results; Pulse P2, Tp=0.40sec, 100%, $_L$=1.0, =0deg. (a) Pier Relative Displacement, (b) Normalized Pier Base Shear, (c) Pier Hysteretic Response, (d) Pier Leg Vertical Reactions, (e) TADAS Hysteretic Response

236
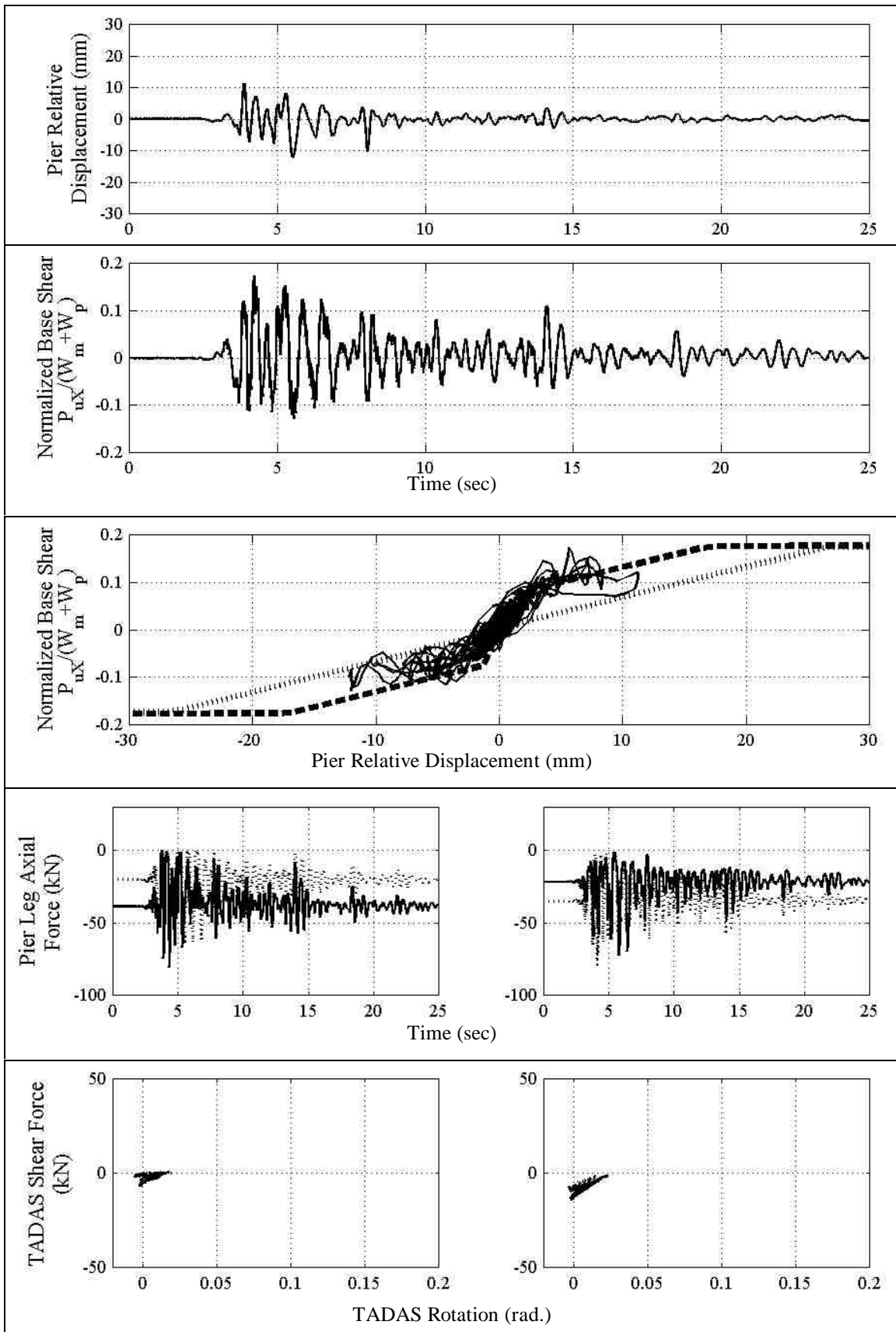
FIGURE 6-38 Experimental Response Results; El Centro, 100% H+V, μ_L=1.0, θ=0deg. (a) Pier Relative Displacement, (b) Normalized Pier Base Shear, (c) Pier Hysteretic Response, (d) Pier Leg Vertical Reactions, (e) TADAS Hysteretic Response
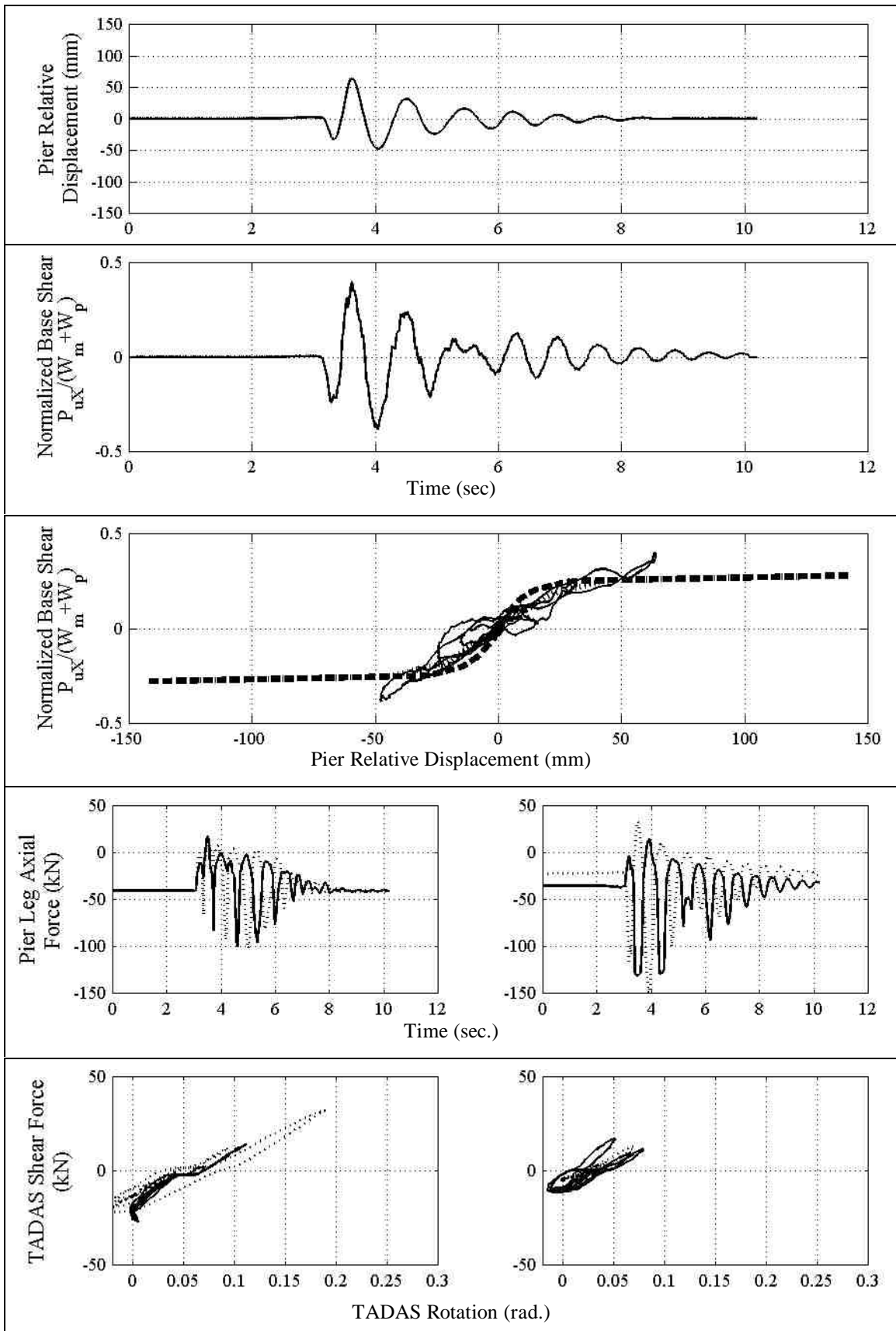
237
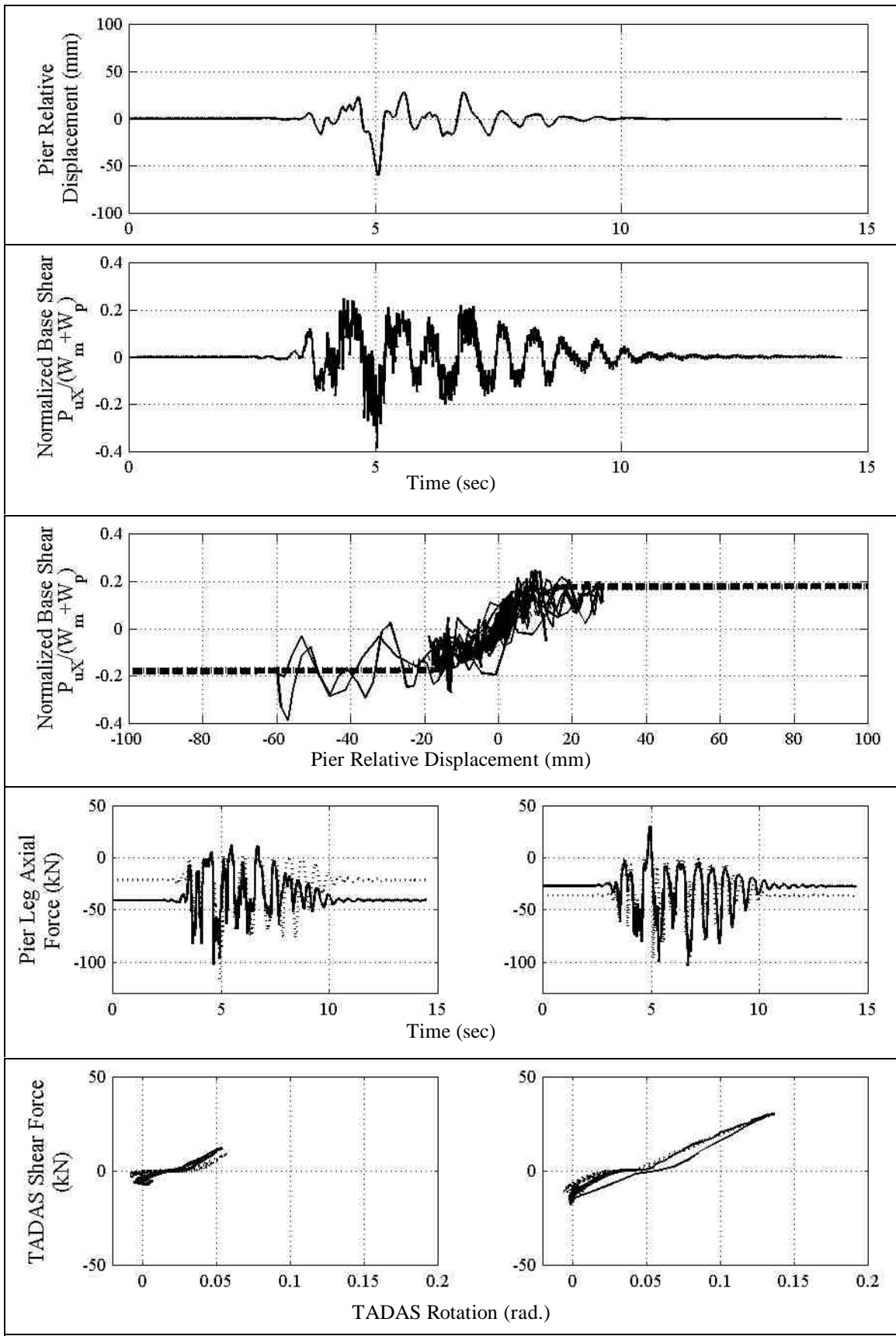
FIGURE 6-39 **Experimental Response Results; Synthetic, 100% H+V, $_L$=1.0, =0deg.**
(a) Pier Relative Displacement, (b) Normalized Pier Base Shear, (c) Pier Hysteretic
Response, (d) Pier Leg Vertical Reactions, (e) TADAS Hysteretic Response

FIGURE 6-40 Experimental Response Results; Newhall, 100% H+V, γ_L=1.0, θ=0deg. (a) Pier Relative Displacement, (b) Normalized Pier Base Shear, (c) Pier Hysteretic Response, (d) Pier Leg Vertical Reactions, (e) TADAS Hysteretic Response
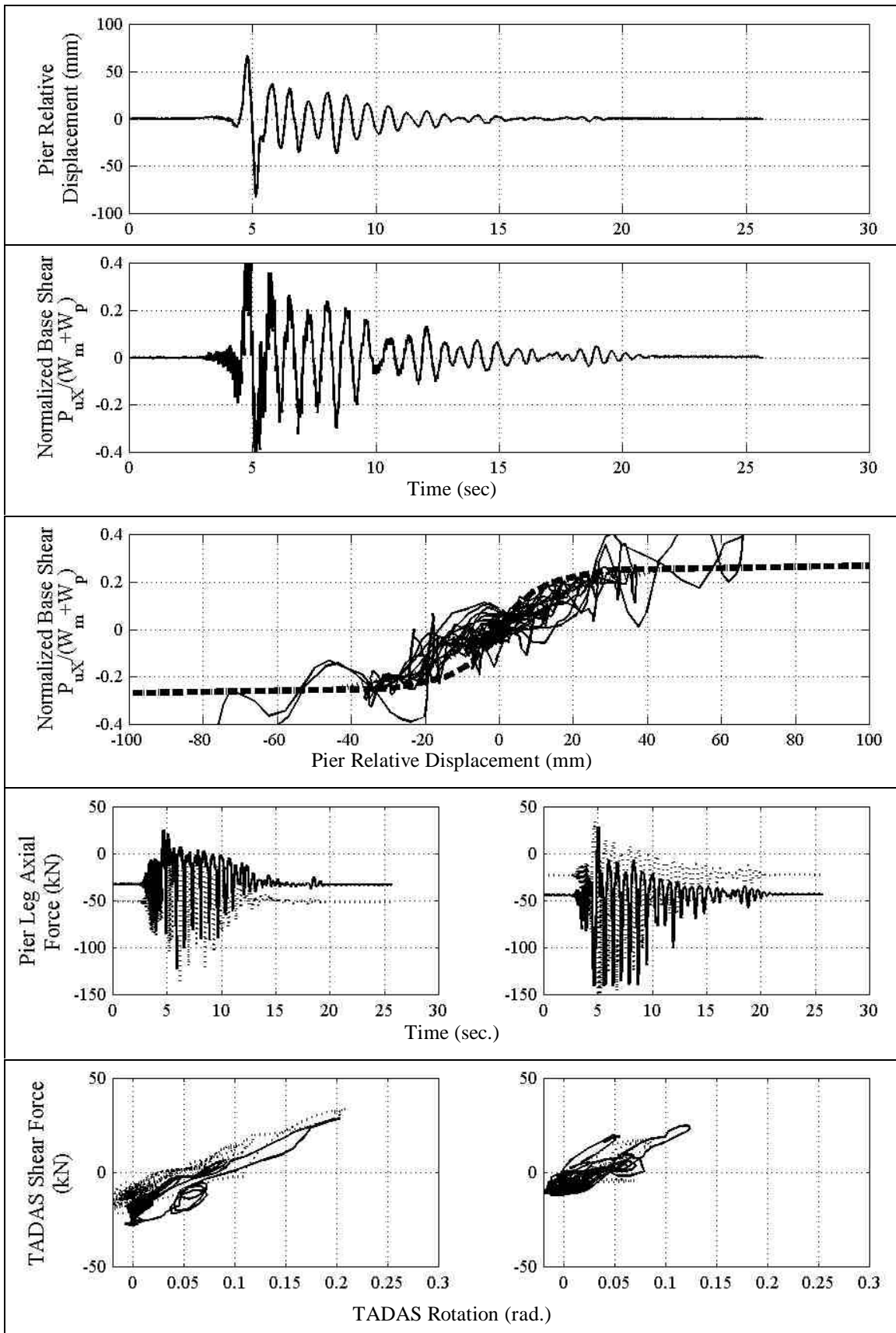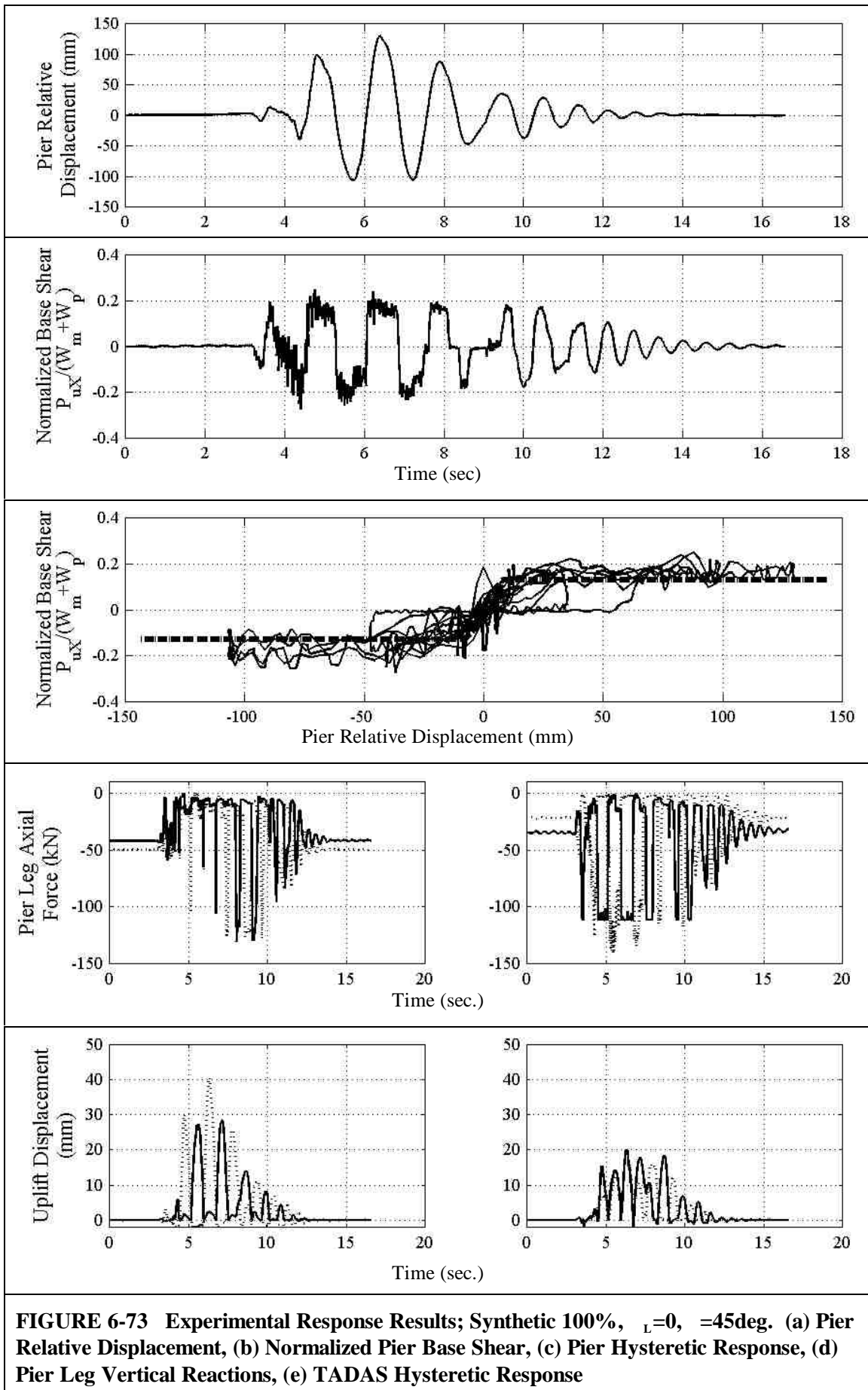
239
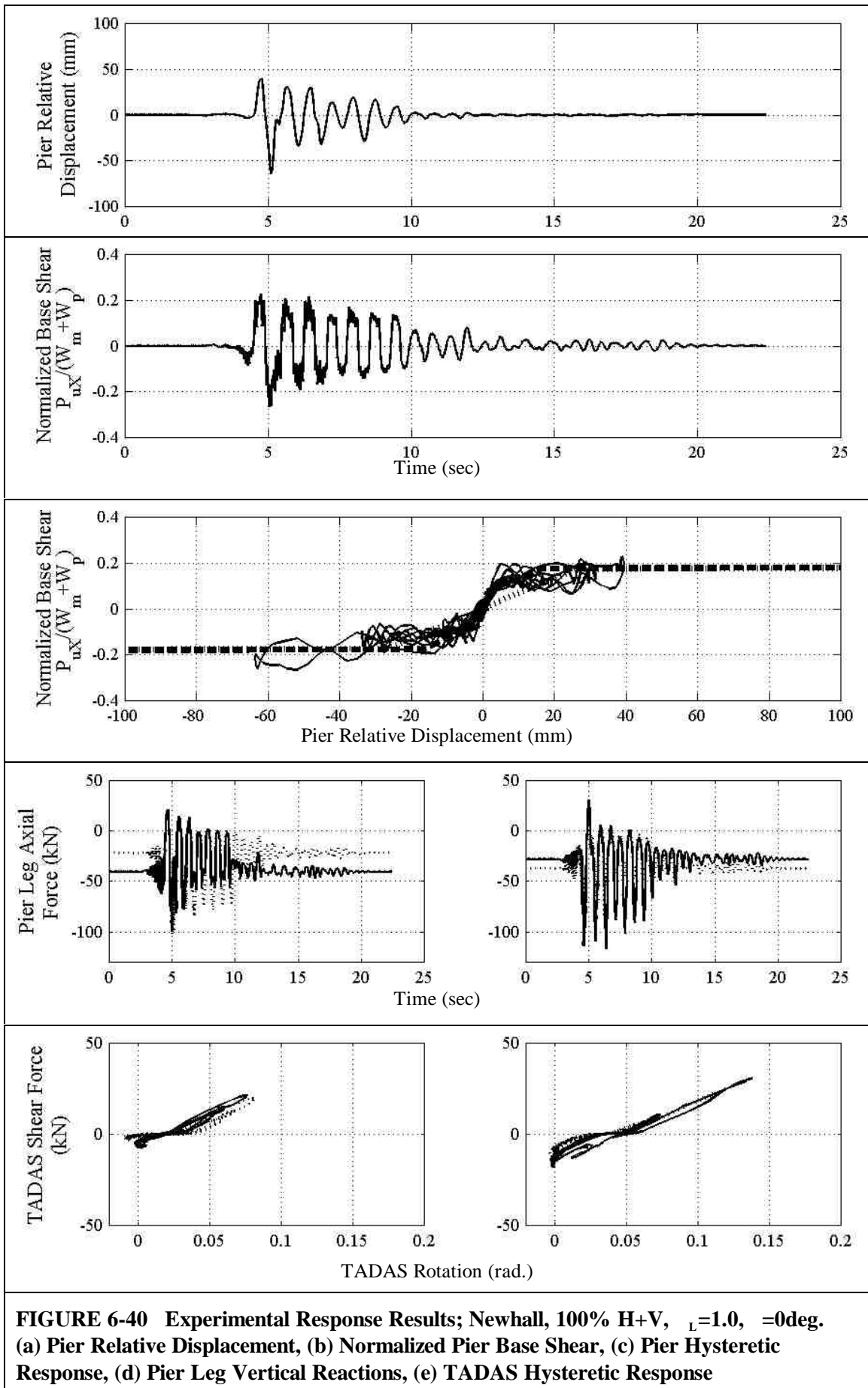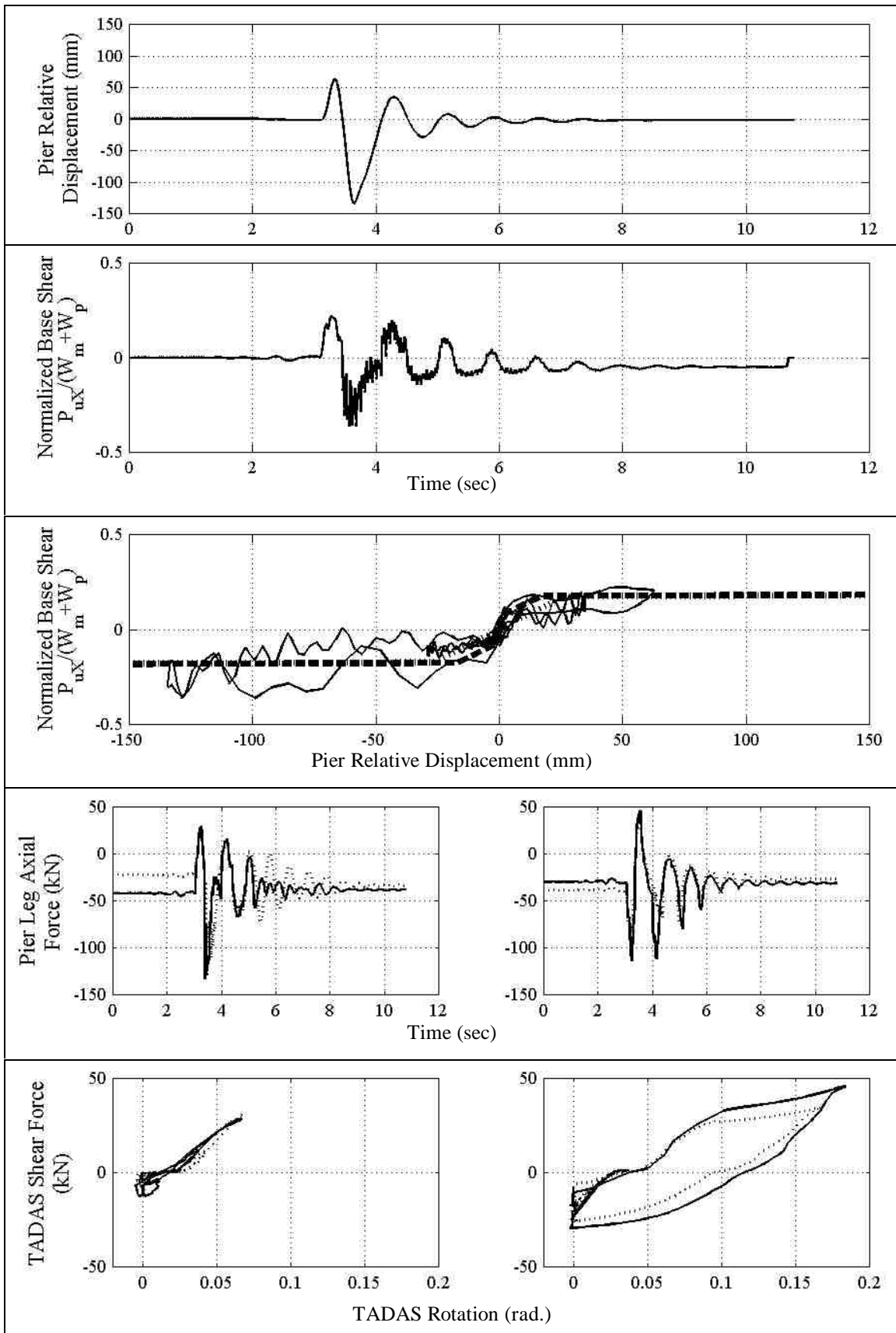
FIGURE 6-41 **Experimental Response Results; Pulse P2, Tp=0.60sec, 100%, ₗ=1.0, =0deg. (a) Pier Relative Displacement, (b) Normalized Pier Base Shear, (c) Pier Hysteretic Response, (d) Pier Leg Vertical Reactions, (e) TADAS Hysteretic Response**

FIGURE 6-42 Experimental Response Results; Synthetic 125%, $_L$=1.0, =0deg. (a) Pier Relative Displacement, (b) Normalized Pier Base Shear, (c) Pier Hysteretic Response, (d) Pier Leg Vertical Reactions, (e) TADAS Hysteretic Response
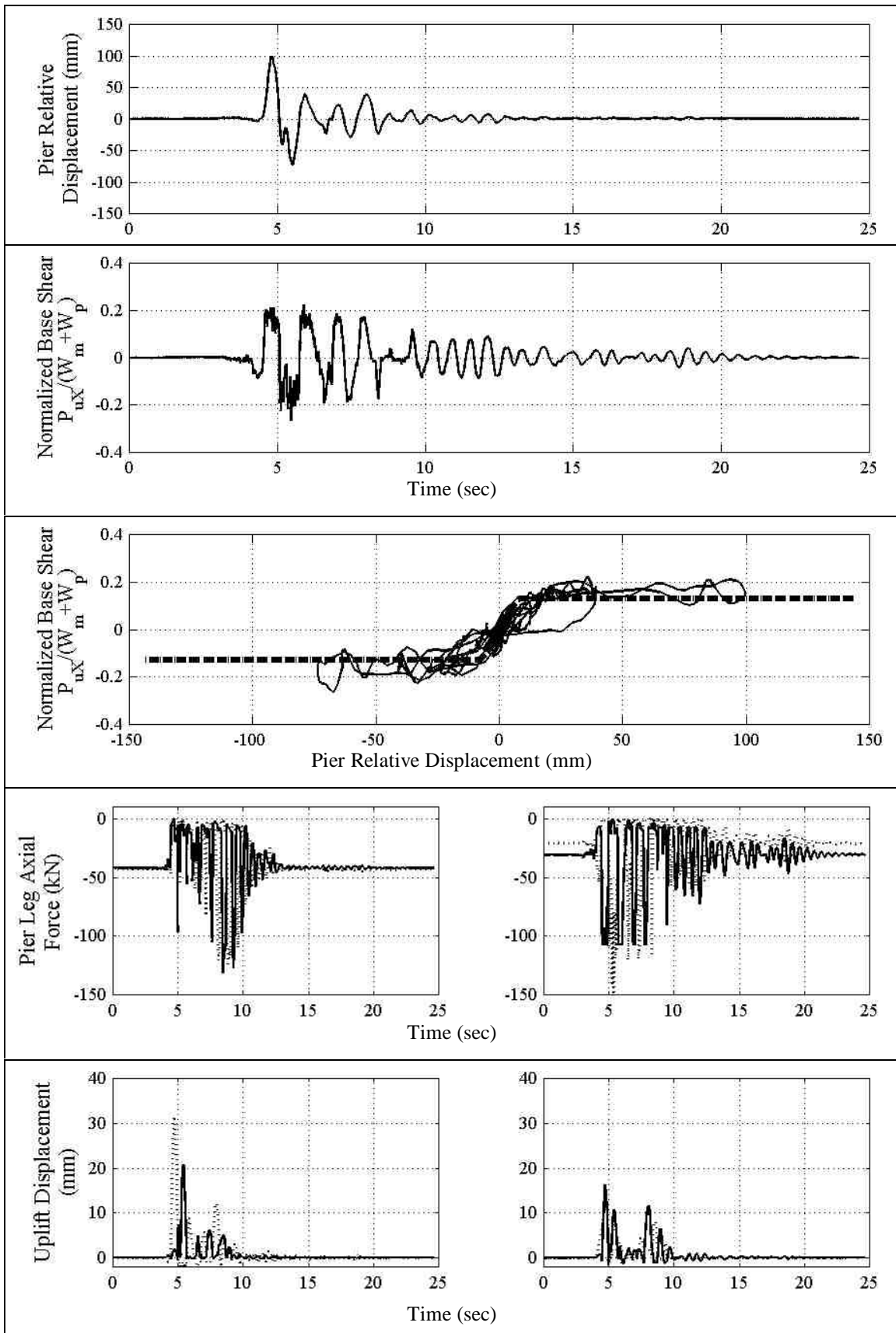
FIGURE 6-43 Experimental Response Results; El Centro 100%, $_L$=0, =0deg. (a) Pier Relative Displacement, (b) Normalized Pier Base Shear, (c) Pier Hysteretic Response, (d) Pier Leg Vertical Reactions, (e) TADAS Hysteretic Response
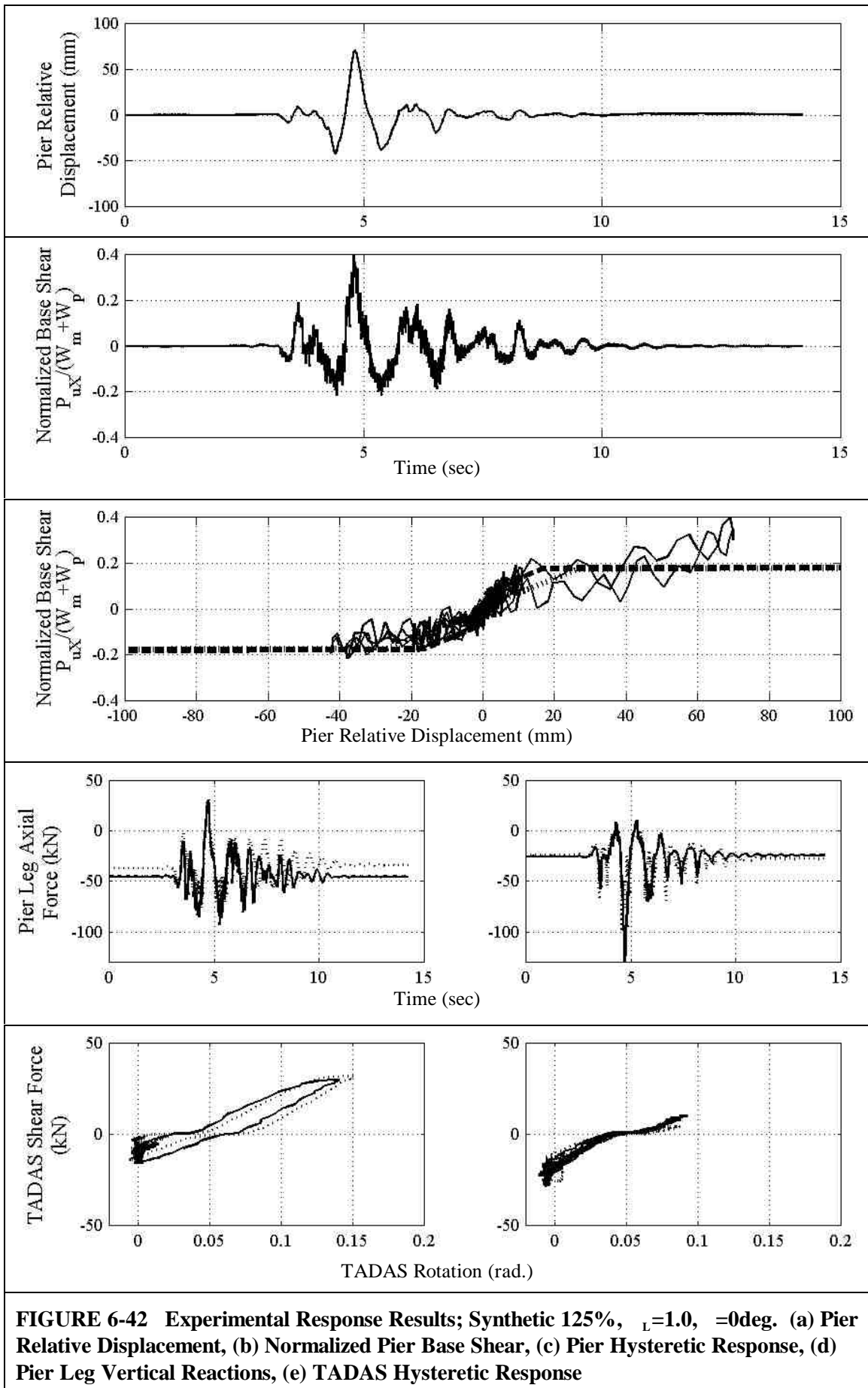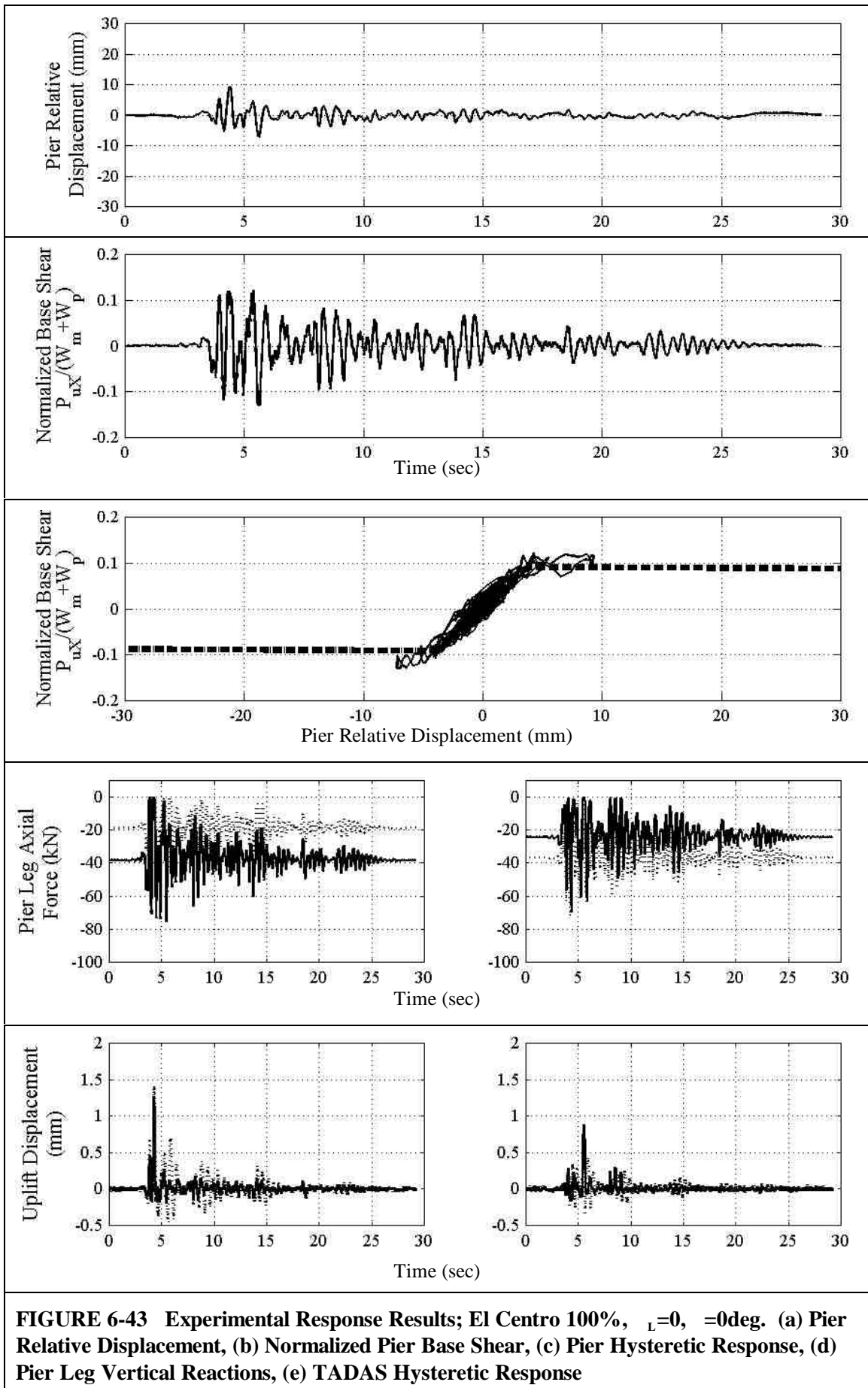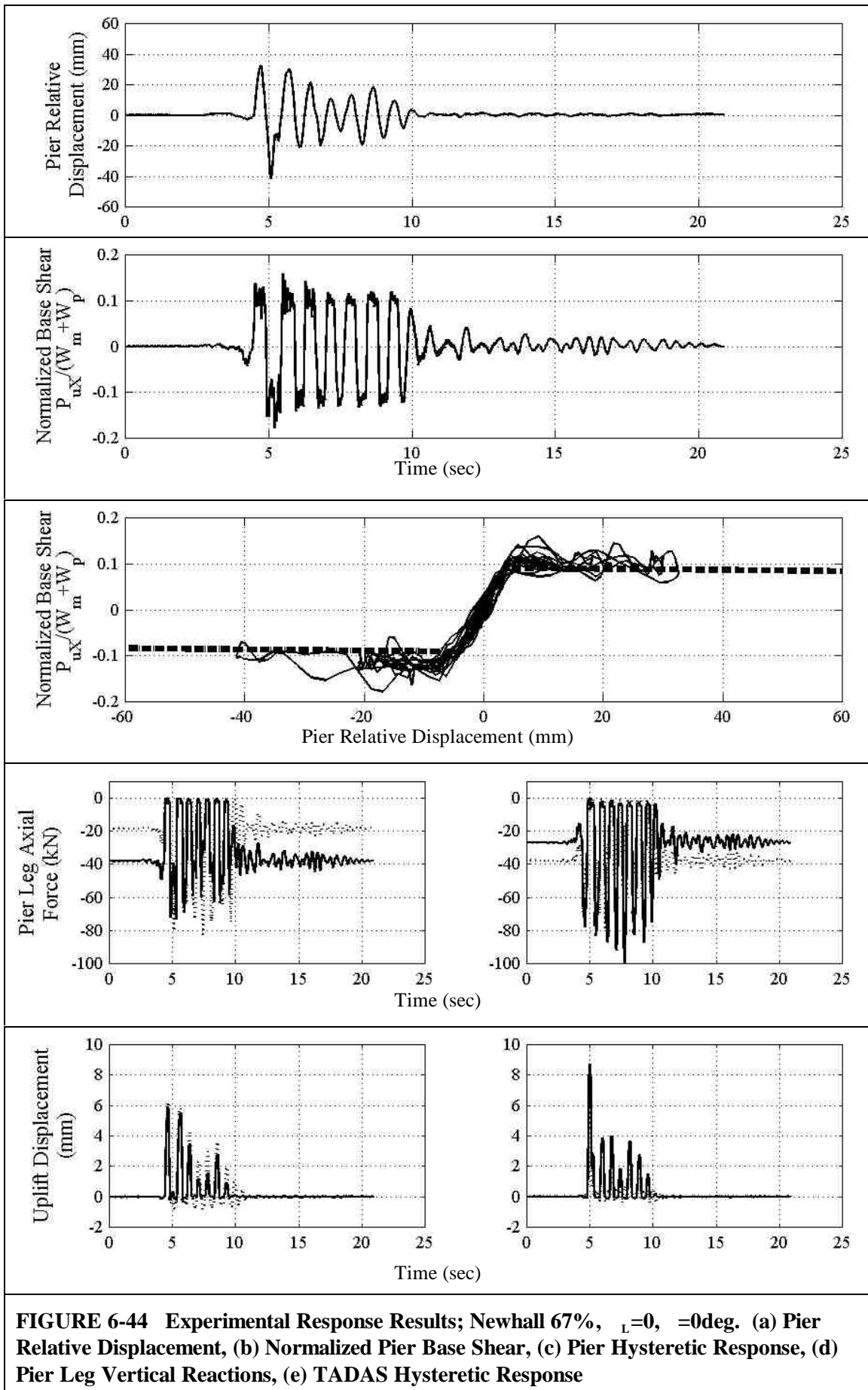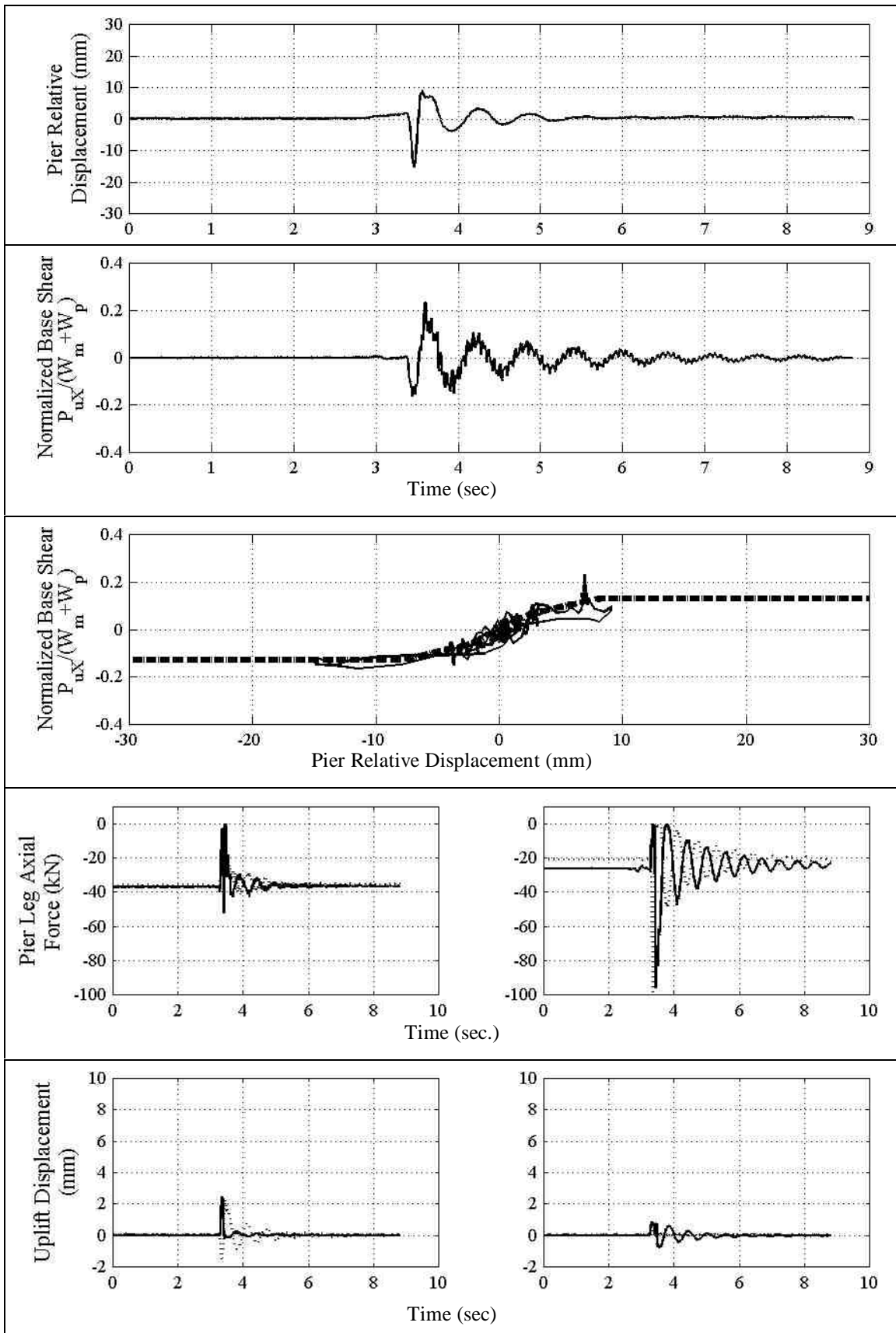
FIGURE 6-44   Experimental Response Results; Newhall 67%, $_L$=0, =0deg. (a) Pier Relative Displacement, (b) Normalized Pier Base Shear, (c) Pier Hysteretic Response, (d) Pier Leg Vertical Reactions, (e) TADAS Hysteretic Response

243

FIGURE 6-45 Experimental Response Results; Synthetic 100%, $_L$=0, =0deg. (a) Pier Relative Displacement, (b) Normalized Pier Base Shear, (c) Pier Hysteretic Response, (d) Pier Leg Vertical Reactions, (e) TADAS Hysteretic Response

244
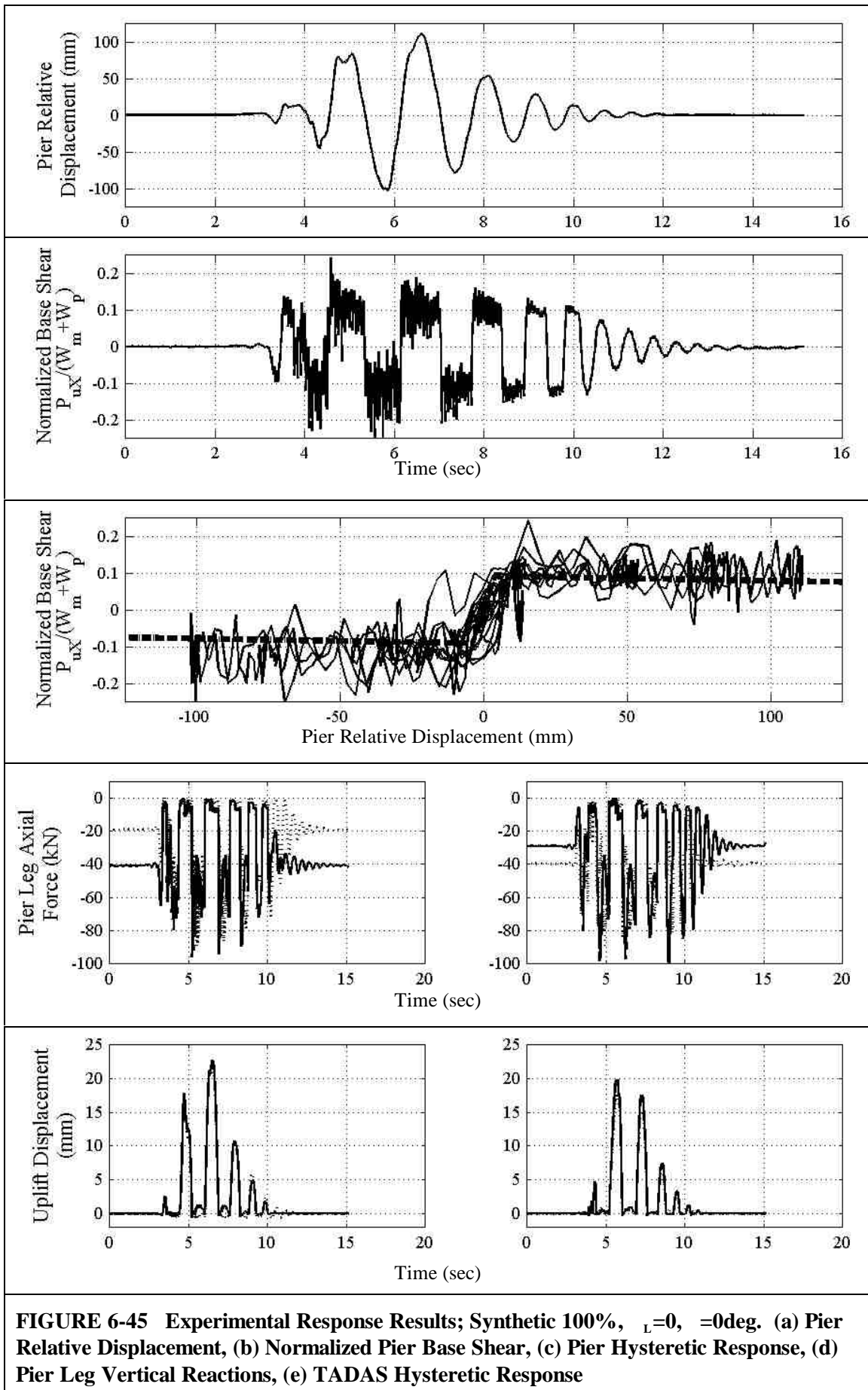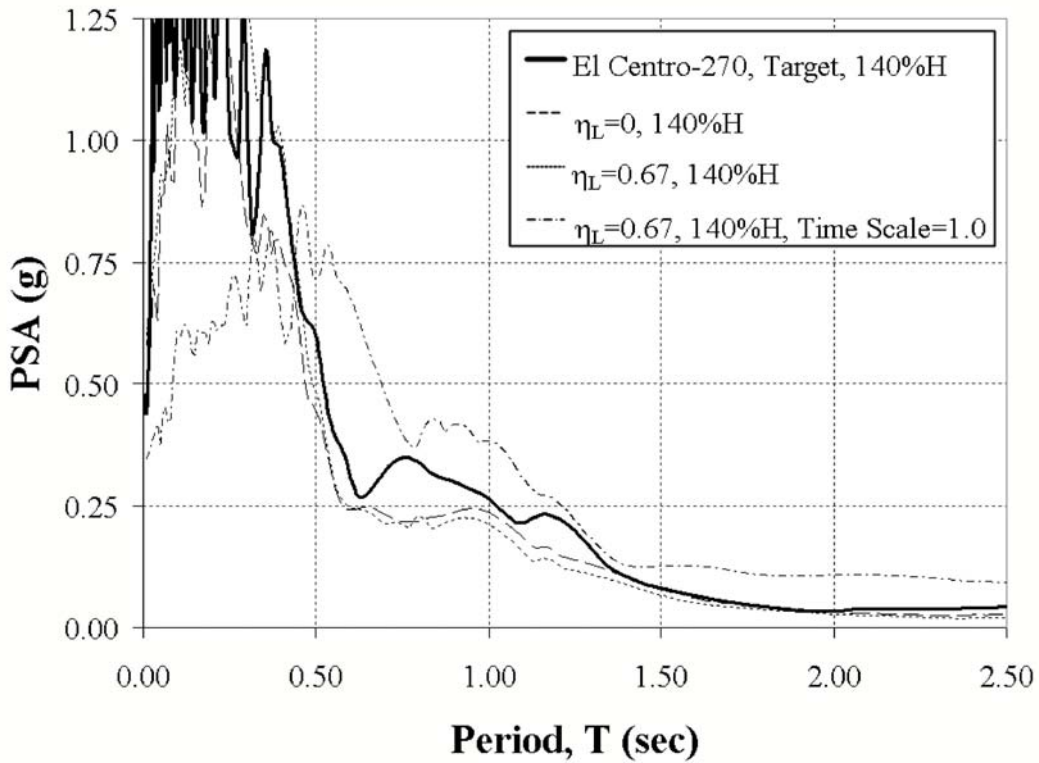
FIGURE 6-46 Actual Table Spectra for El Centro - 140%, 5% Damping (=45deg.)
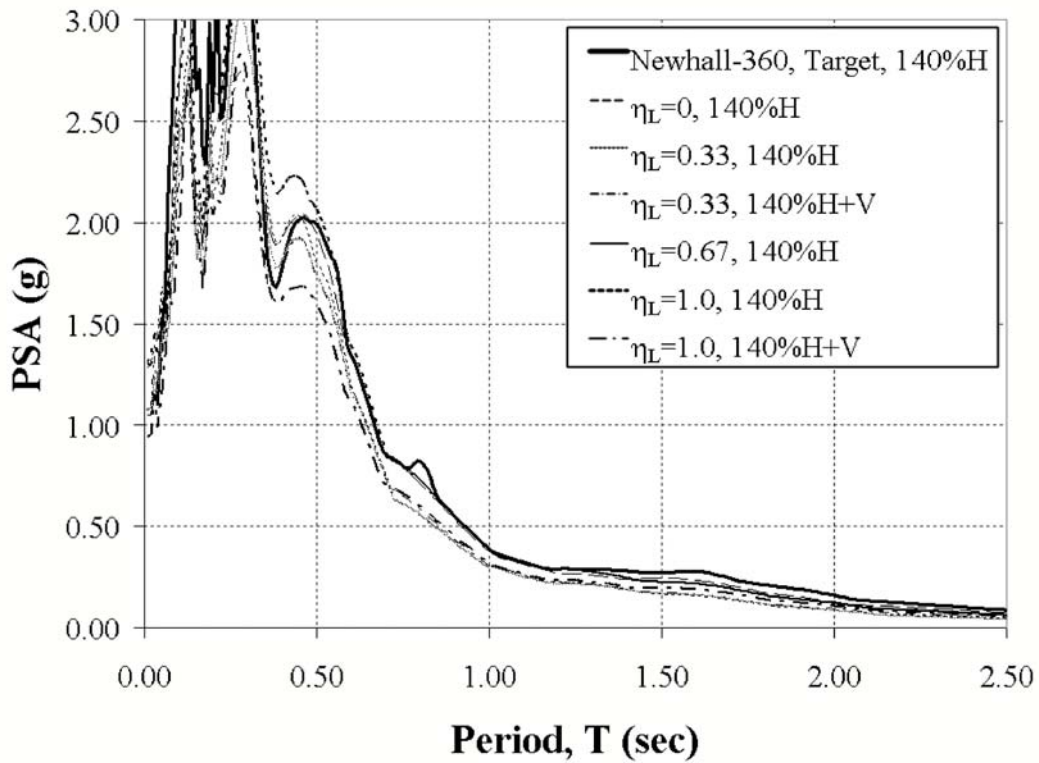
FIGURE 6-47 Actual Table Spectra for Newhall - 140%, 5% Damping (=45deg.)
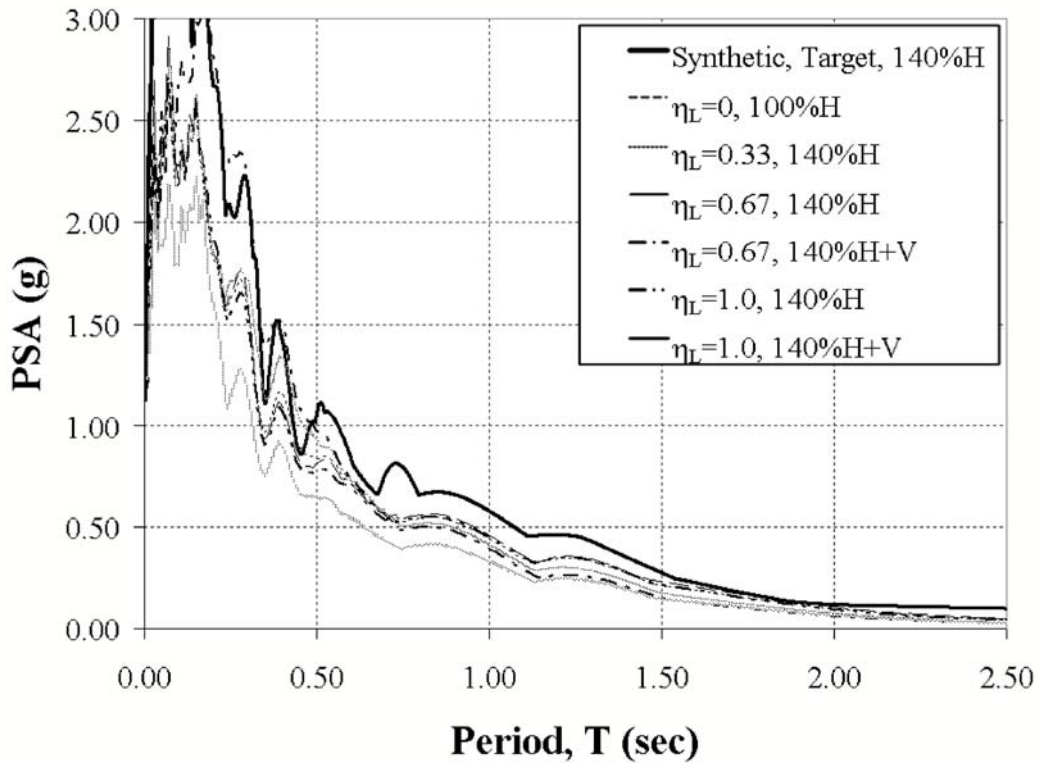
FIGURE 6-48 Actual Table Spectra for Synthetic - 140%, 5% Damping (=45deg.)

FIGURE 6-49 Actual Table Spectra for Pulse P2, T_p=0.20sec - 140%, 5% Damping
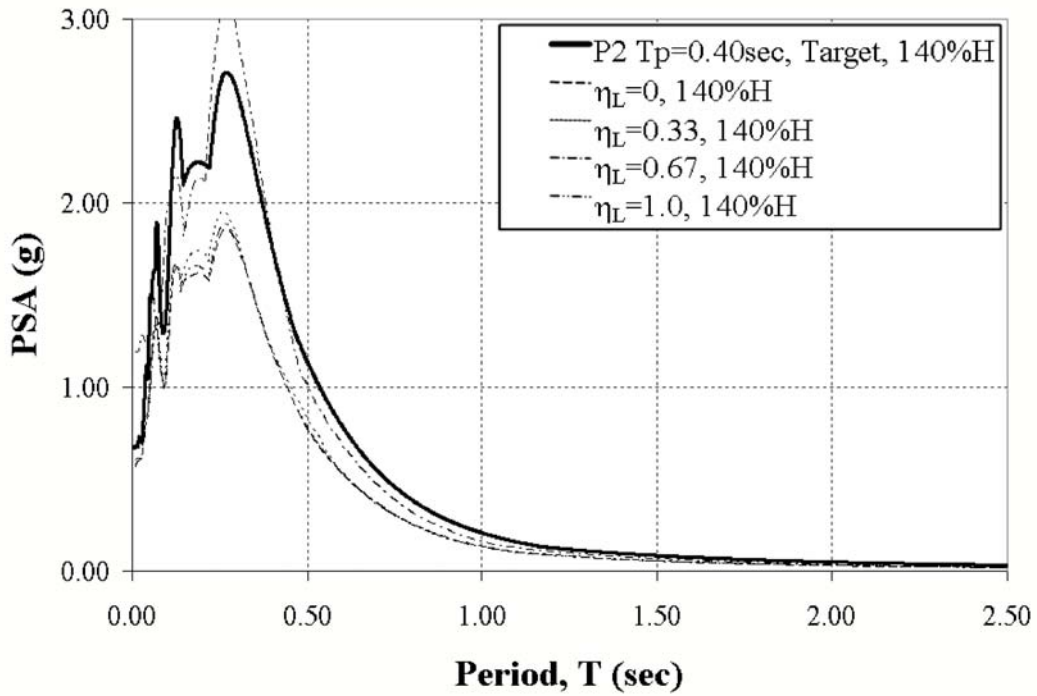
(=45deg.)

FIGURE 6-50 Actual Table Spectra for Pulse P2, T$_p$=0.40sec - 140%, 5% Damping (=45deg.)
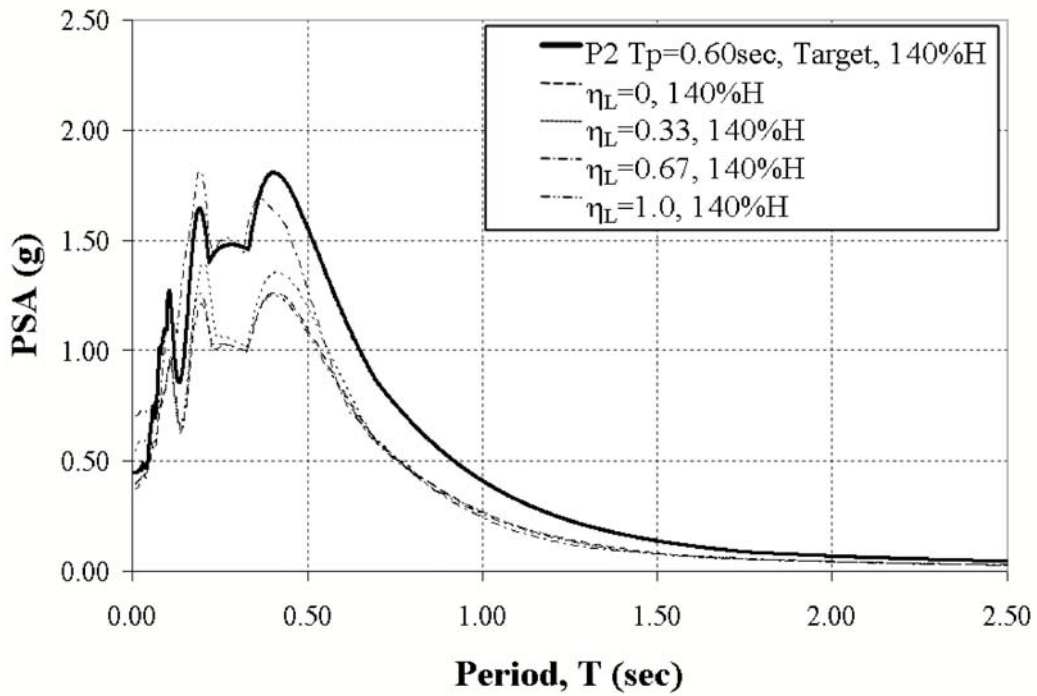
FIGURE 6-51 Actual Table Spectra for Pulse P2, T$_p$=0.60sec - 140%, 5% Damping (=45deg.)

FIGURE 6-52 Experimental Response Results; El Centro** 67%, $_L$=0.67, =45deg. (a) Pier Relative Displacement, (b) Normalized Pier Base Shear, (c) Pier Hysteretic Response, (d) Pier Leg Vertical Reactions, (e) TADAS Hysteretic Response
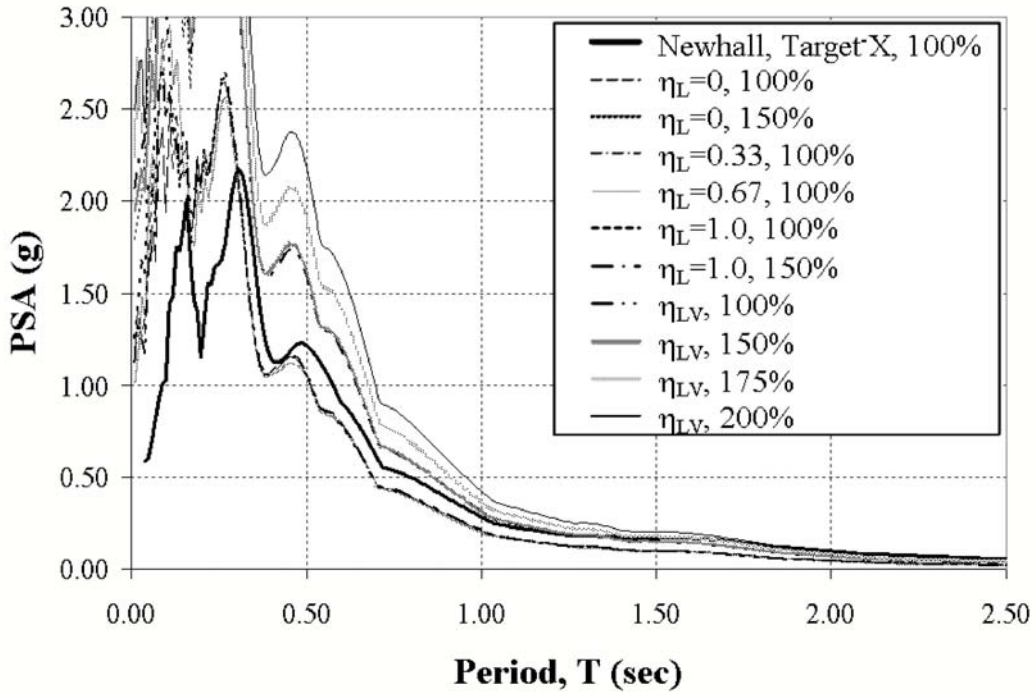
248

FIGURE 6-53 Experimental Response Results; El Centro 100%, $_L$=0.67, =45deg. (a) Pier Relative Displacement, (b) Normalized Pier Base Shear, (c) Pier Hysteretic Response, (d) Pier Leg Vertical Reactions, (e) TADAS Hysteretic Response

249

FIGURE 6-54 Experimental Response Results; Newhall 100%, $_L$=0.67, =45deg. (a) Pier Relative Displacement, (b) Normalized Pier Base Shear, (c) Pier Hysteretic Response, (d) Pier Leg Vertical Reactions, (e) TADAS Hysteretic Response

FIGURE 6-55 Experimental Response Results; Synthetic 100%, $_L$=0.67, =45deg. (a) Pier Relative Displacement, (b) Normalized Pier Base Shear, (c) Pier Hysteretic Response, (d) Pier Leg Vertical Reactions, (e) TADAS Hysteretic Response

251

**FIGURE 6-56   Experimental Response Results; Synthetic 100% H+V, $_L$=0.67,   =45deg.
(a) Pier Relative Displacement, (b) Normalized Pier Base Shear, (c) Pier Hysteretic
Response, (d) Pier Leg Vertical Reactions, (e) TADAS Hysteretic Response**

FIGURE 6-57 Experimental Response Results; Pulse P2 Tp=0.20sec 100%, $_L$=0.67, =45deg. (a) Pier Relative Displacement, (b) Normalized Pier Base Shear, (c) Pier Hysteretic Response, (d) Pier Leg Vertical Reactions, (e) TADAS Hysteretic Response

FIGURE 6-58   Experimental Response Results; Pulse P2 Tp=0.40sec 100%, ₗ=0.67, =45deg. (a) Pier Relative Displacement, (b) Normalized Pier Base Shear, (c) Pier Hysteretic Response, (d) Pier Leg Vertical Reactions, (e) TADAS Hysteretic Response

FIGURE 6-59   Experimental Response Results; Pulse P2 Tp=0.60sec 100%, $_L$=0.67,
 =45deg. (a) Pier Relative Displacement, (b) Normalized Pier Base Shear, (c) Pier
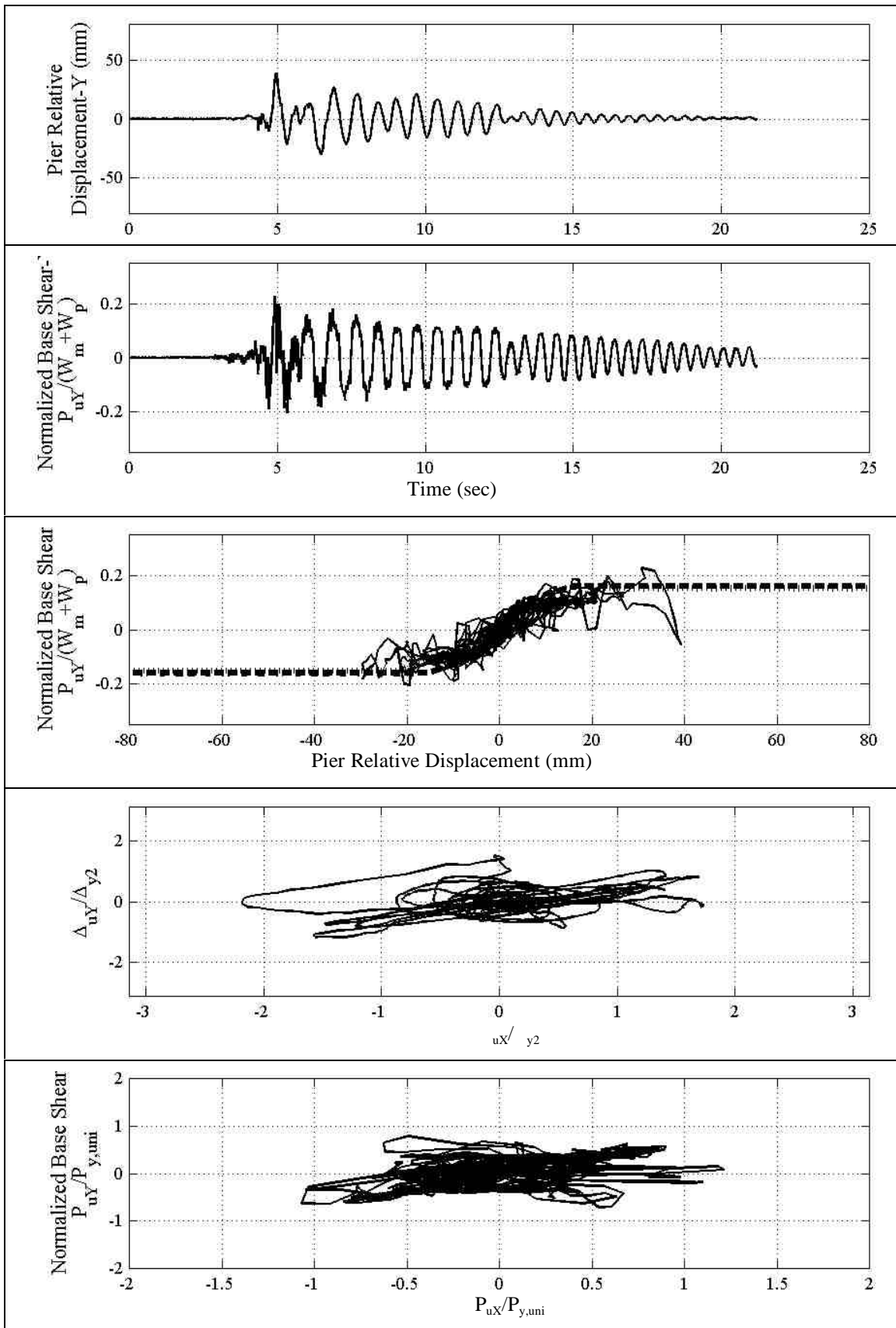Hysteretic Response, (d) Pier Leg Vertical Reactions, (e) TADAS Hysteretic Response

FIGURE 6-60 Experimental Response Results; Newhall 100%, $_L$=0.33, =45deg. (a) Pier Relative Displacement, (b) Normalized Pier Base Shear, (c) Pier Hysteretic Response, (d) Pier Leg Vertical Reactions, (e) TADAS Hysteretic Response

FIGURE 6-61 Experimental Response Results; Newhall 100% H+V, $_L$=0.33, =45deg. (a) Pier Relative Displacement, (b) Normalized Pier Base Shear, (c) Pier Hysteretic Response, (d) Pier Leg Vertical Reactions, (e) TADAS Hysteretic Response

FIGURE 6-62 **Experimental Response Results; Synthetic 100%,** $_L$=0.33, =45deg. **(a) Pier Relative Displacement, (b) Normalized Pier Base Shear, (c) Pier Hysteretic Response, (d) Pier Leg Vertical Reactions, (e) TADAS Hysteretic Response**

258
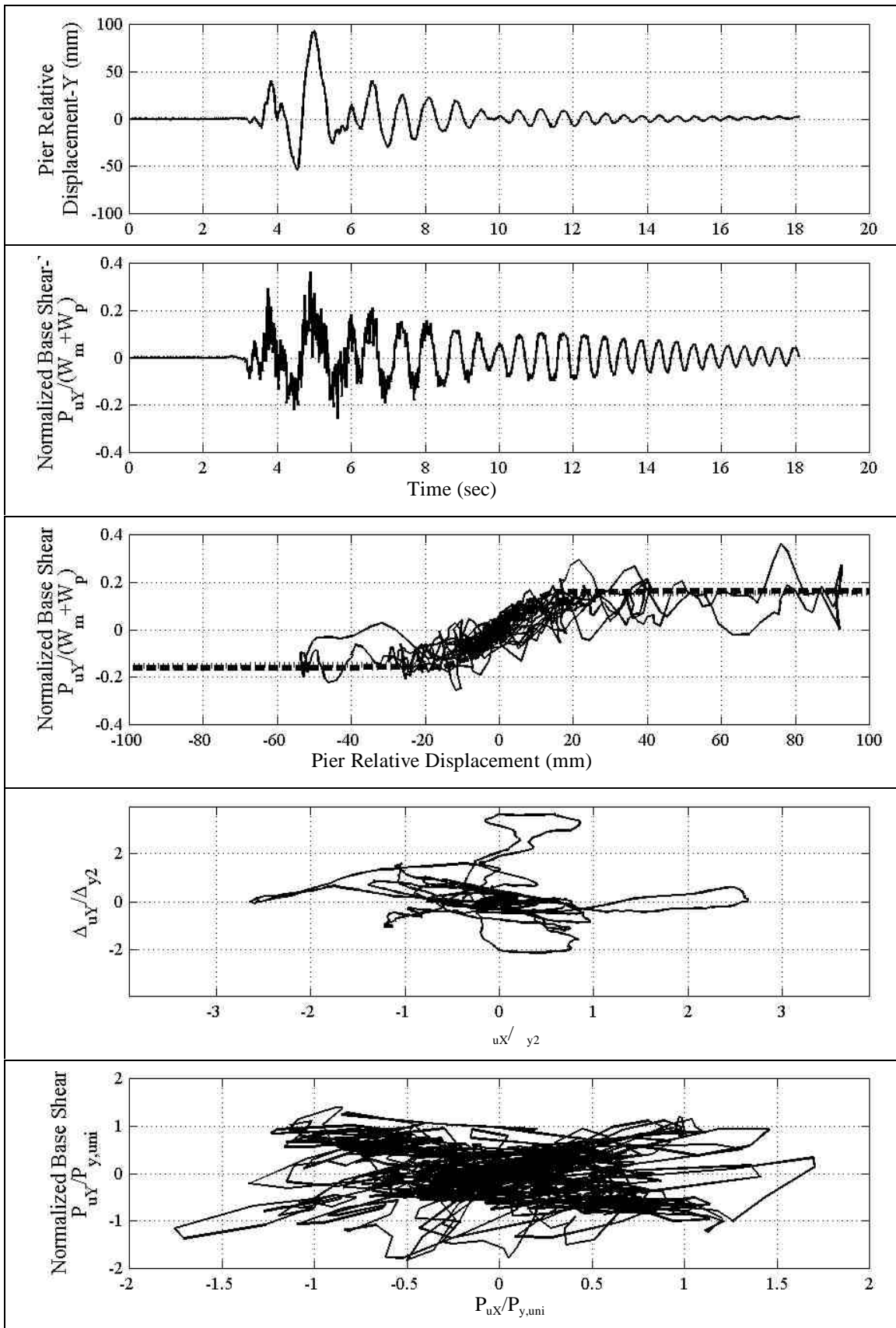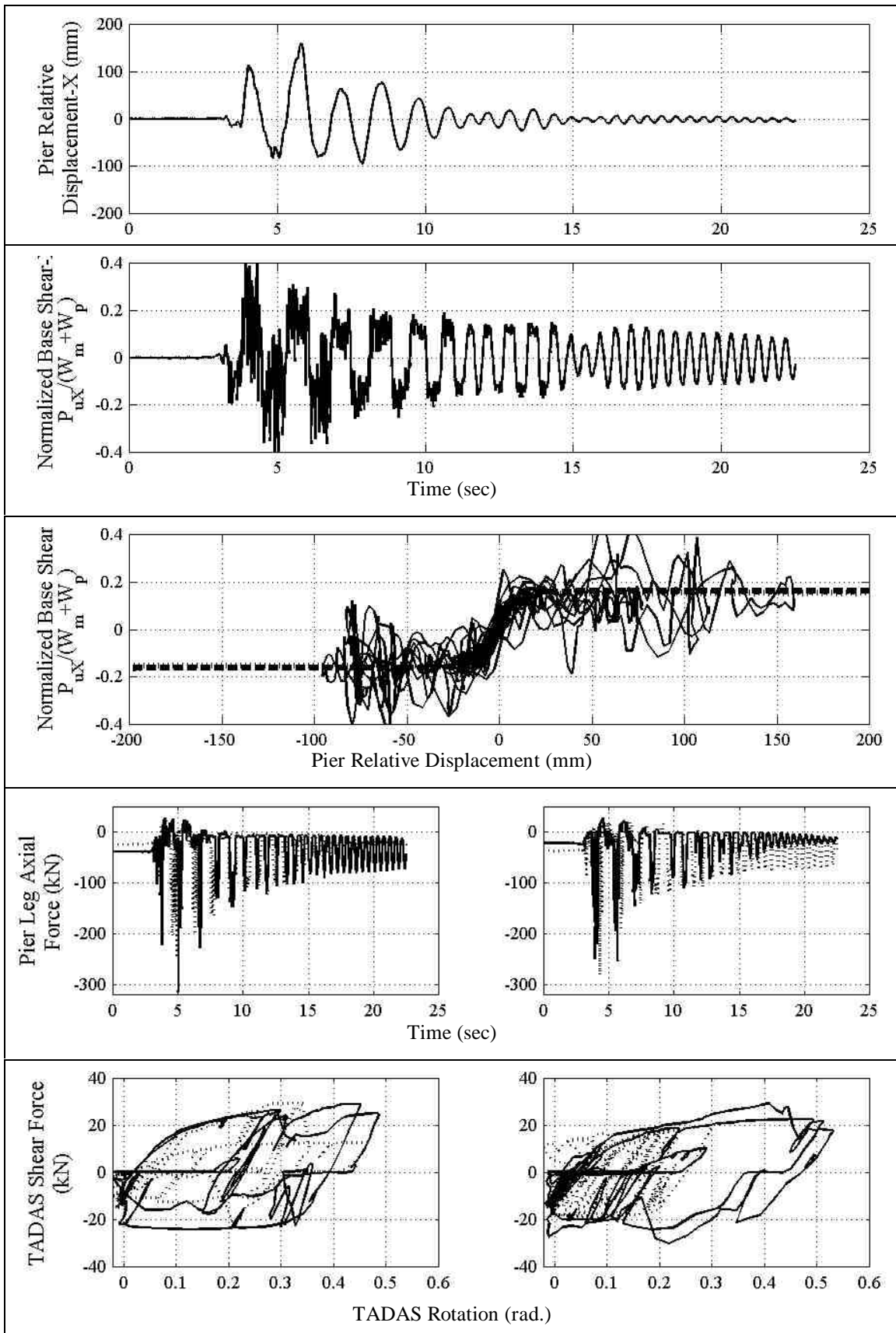
FIGURE 6-63 Experimental Response Results; Pulse P2, Tp=0.20sec. 100%, _L=0.33, =45deg. (a) Pier Relative Displacement, (b) Normalized Pier Base Shear, (c) Pier Hysteretic Response, (d) Pier Leg Vertical Reactions, (e) TADAS Hysteretic Response

FIGURE 6-64 Experimental Response Results; Pulse P2, Tp=0.40sec. 100%, $_L$=0.33, =45deg. (a) Pier Relative Displacement, (b) Normalized Pier Base Shear, (c) Pier Hysteretic Response, (d) Pier Leg Vertical Reactions, (e) TADAS Hysteretic Response

FIGURE 6-65 Experimental Response Results; Pulse P2, Tp=0.60sec. 100%, $_L$=0.33, =45deg. (a) Pier Relative Displacement, (b) Normalized Pier Base Shear, (c) Pier Hysteretic Response, (d) Pier Leg Vertical Reactions, (e) TADAS Hysteretic Response
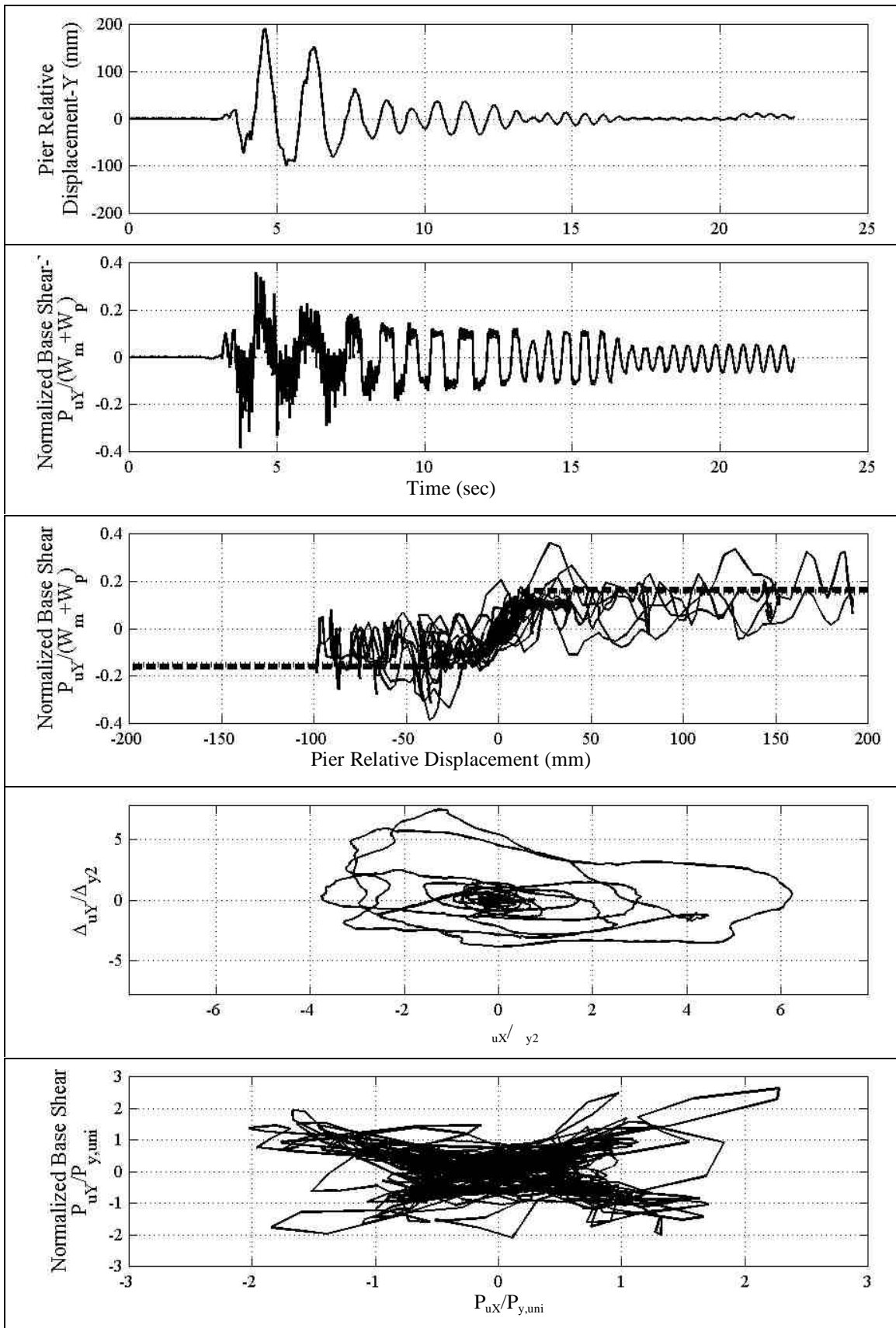
261
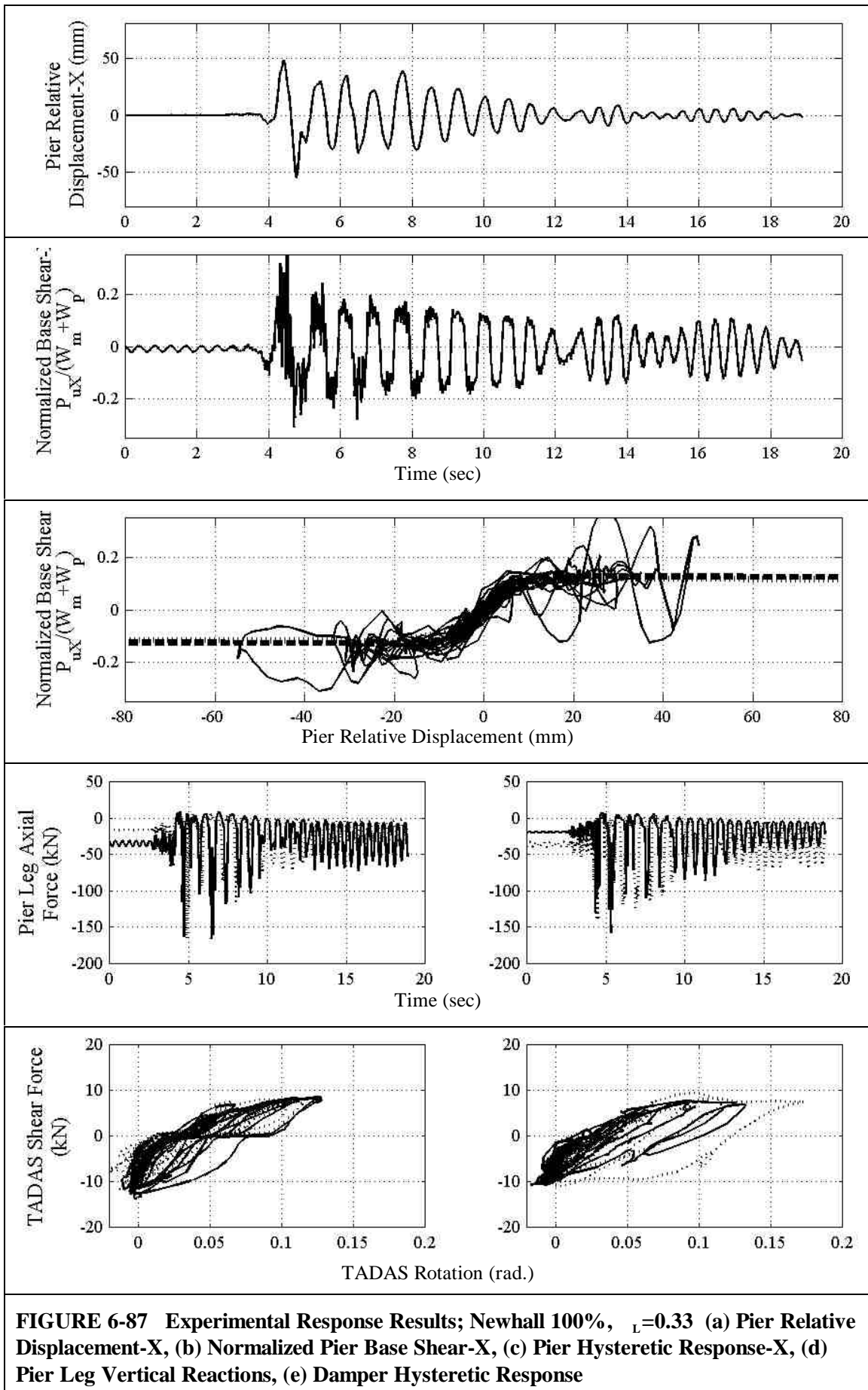
FIGURE 6-66 Experimental Response Results; Newhall 100%, $_L$=1.0, =45deg. (a) Pier Relative Displacement, (b) Normalized Pier Base Shear, (c) Pier Hysteretic Response, (d) Pier Leg Vertical Reactions, (e) TADAS Hysteretic Response

262

FIGURE 6-67 Experimental Response Results; Synthetic 100%, $_L$=1.0, =45deg. (a) Pier Relative Displacement, (b) Normalized Pier Base Shear, (c) Pier Hysteretic Response, (d) Pier Leg Vertical Reactions, (e) TADAS Hysteretic Response
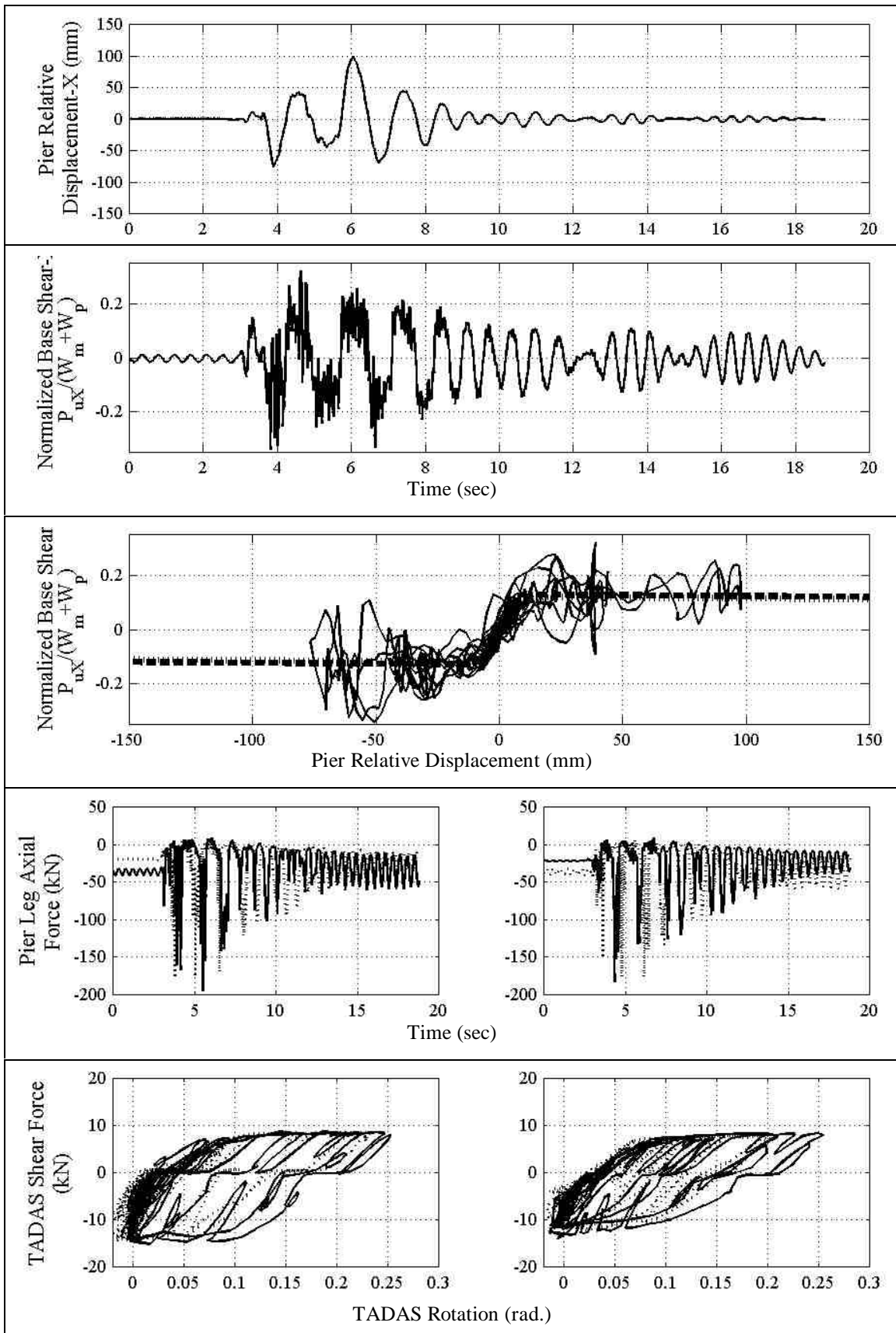
FIGURE 6-68   Experimental Response Results; Synthetic 100% H+V, $_L$=1.0, =45deg. (a) Pier Relative Displacement, (b) Normalized Pier Base Shear, (c) Pier Hysteretic Response, (d) Pier Leg Vertical Reactions, (e) TADAS Hysteretic Response

FIGURE 6-69 **Experimental Response Results; Pulse P2 Tp=0.20sec 100%, ₗ=1.0, =45deg. (a) Pier Relative Displacement, (b) Normalized Pier Base Shear, (c) Pier Hysteretic Response, (d) Pier Leg Vertical Reactions, (e) TADAS Hysteretic Response**

FIGURE 6-70 Experimental Response Results; Pulse P2 Tp=0.40sec 100%, ₗ=1.0, =45deg. (a) Pier Relative Displacement, (b) Normalized Pier Base Shear, (c) Pier Hysteretic Response, (d) Pier Leg Vertical Reactions, (e) TADAS Hysteretic Response
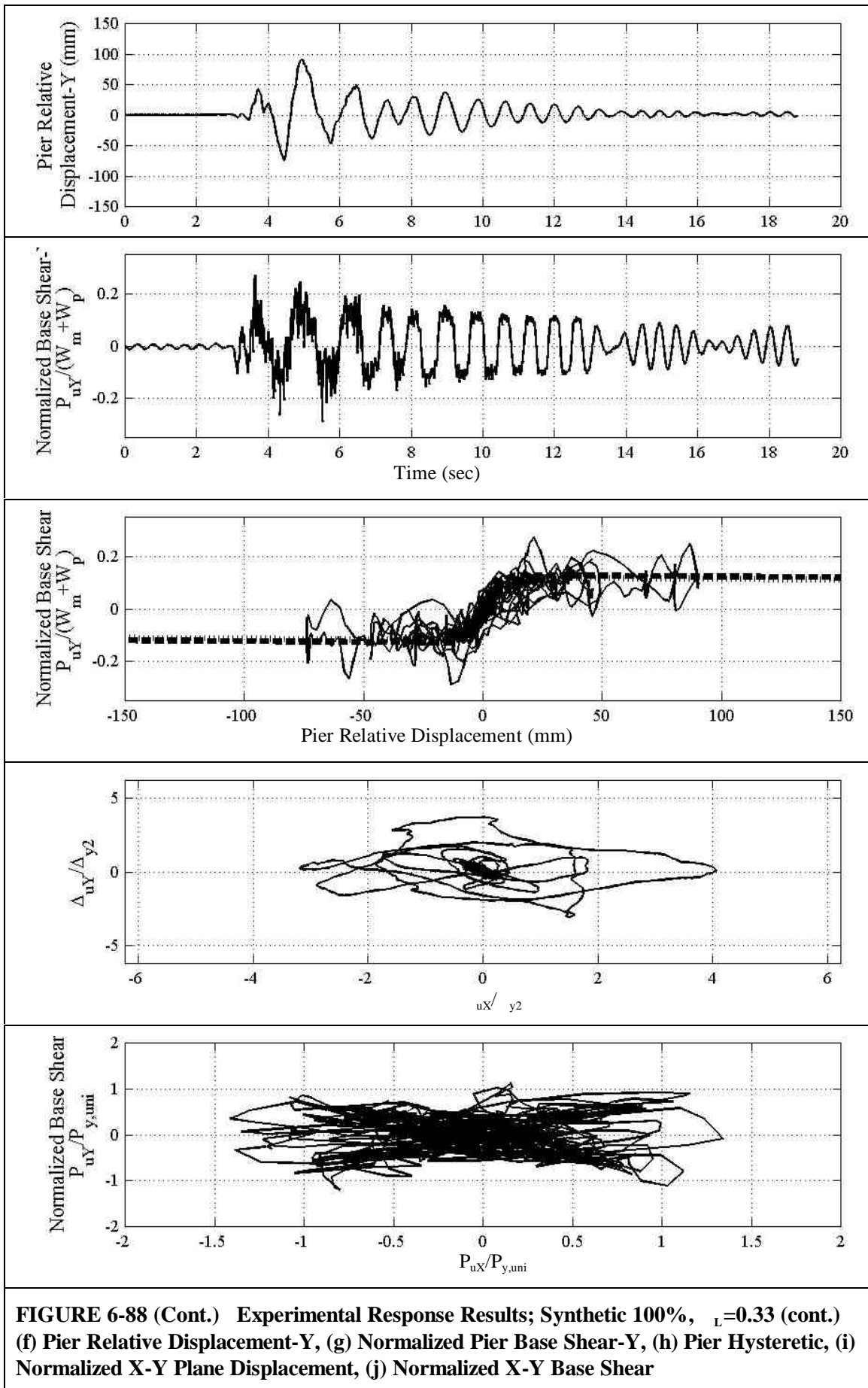
**FIGURE 6-71   Experimental Response Results; Pulse P2 Tp=0.60sec 100%, L=1.0,
 =45deg. (a) Pier Relative Displacement, (b) Normalized Pier Base Shear, (c) Pier
Hysteretic Response, (d) Pier Leg Vertical Reactions, (e) TADAS Hysteretic Response**

**FIGURE 6-72   Experimental Response Results; Newhall 100% H+V, $_L$=1.0, =45deg.
(a) Pier Relative Displacement, (b) Normalized Pier Base Shear, (c) Pier Hysteretic
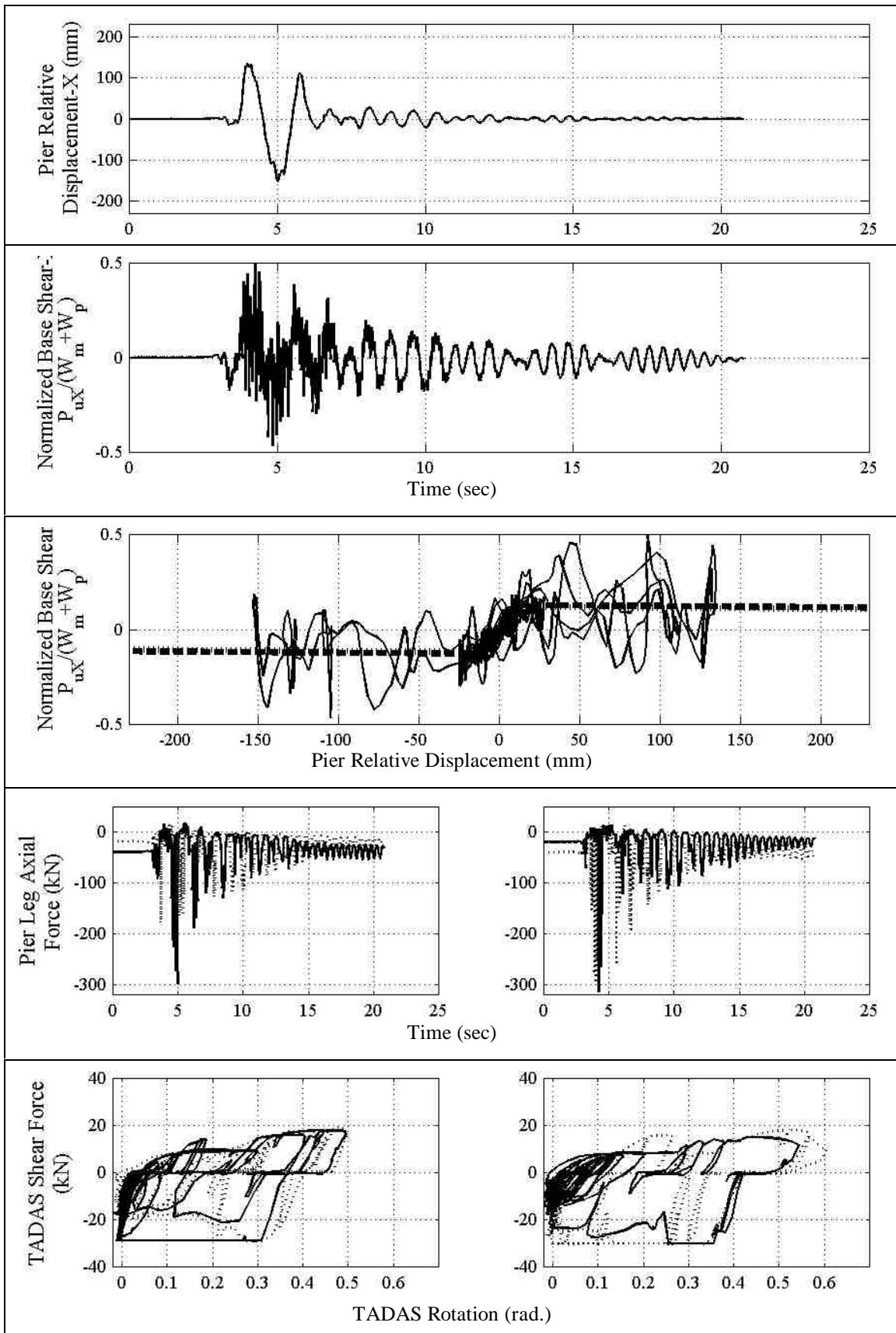Response, (d) Pier Leg Vertical Reactions, (e) TADAS Hysteretic Response**

FIGURE 6-73 **Experimental Response Results; Synthetic 100%, $_L$=0, =45deg. (a) Pier Relative Displacement, (b) Normalized Pier Base Shear, (c) Pier Hysteretic Response, (d) Pier Leg Vertical Reactions, (e) TADAS Hysteretic Response**
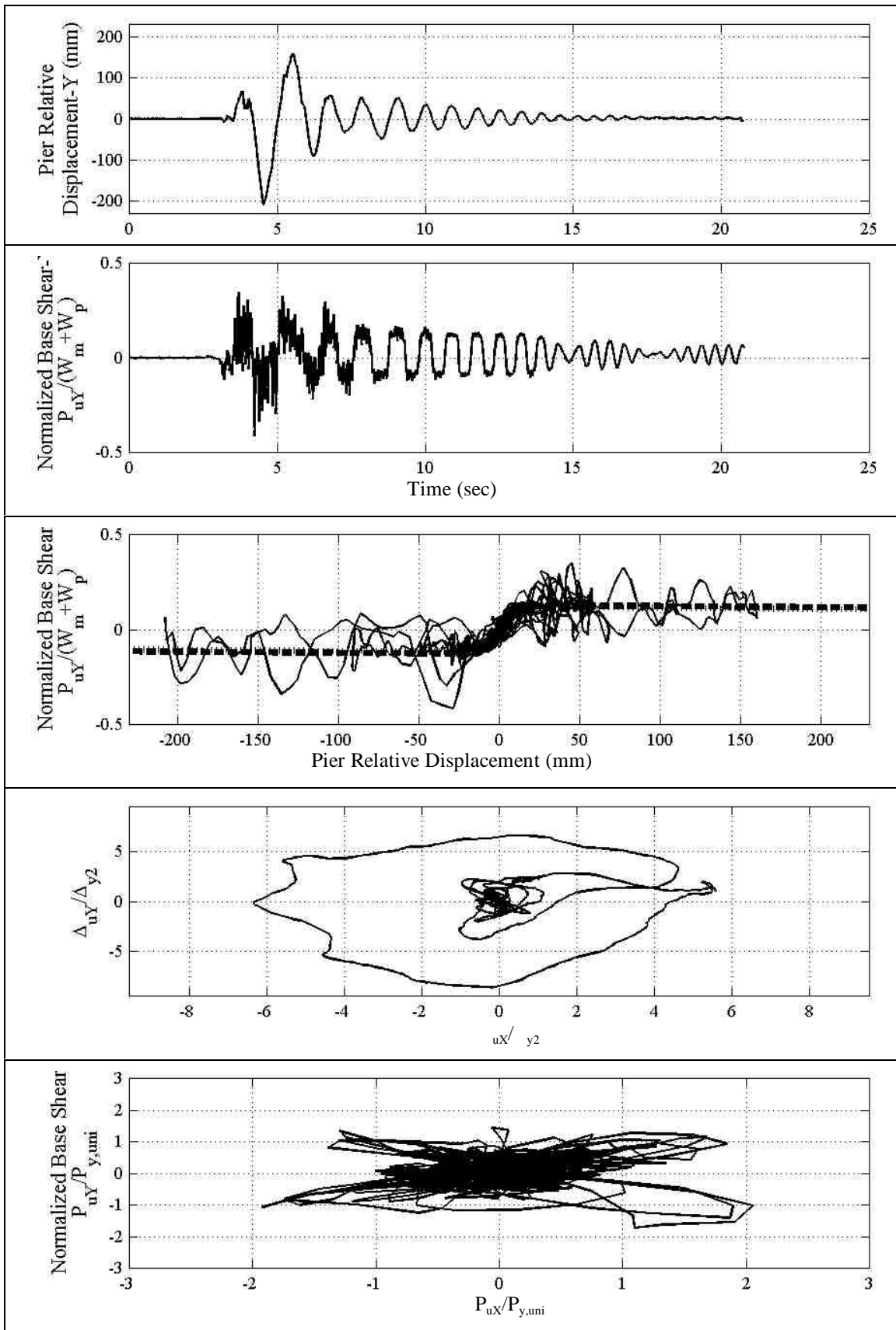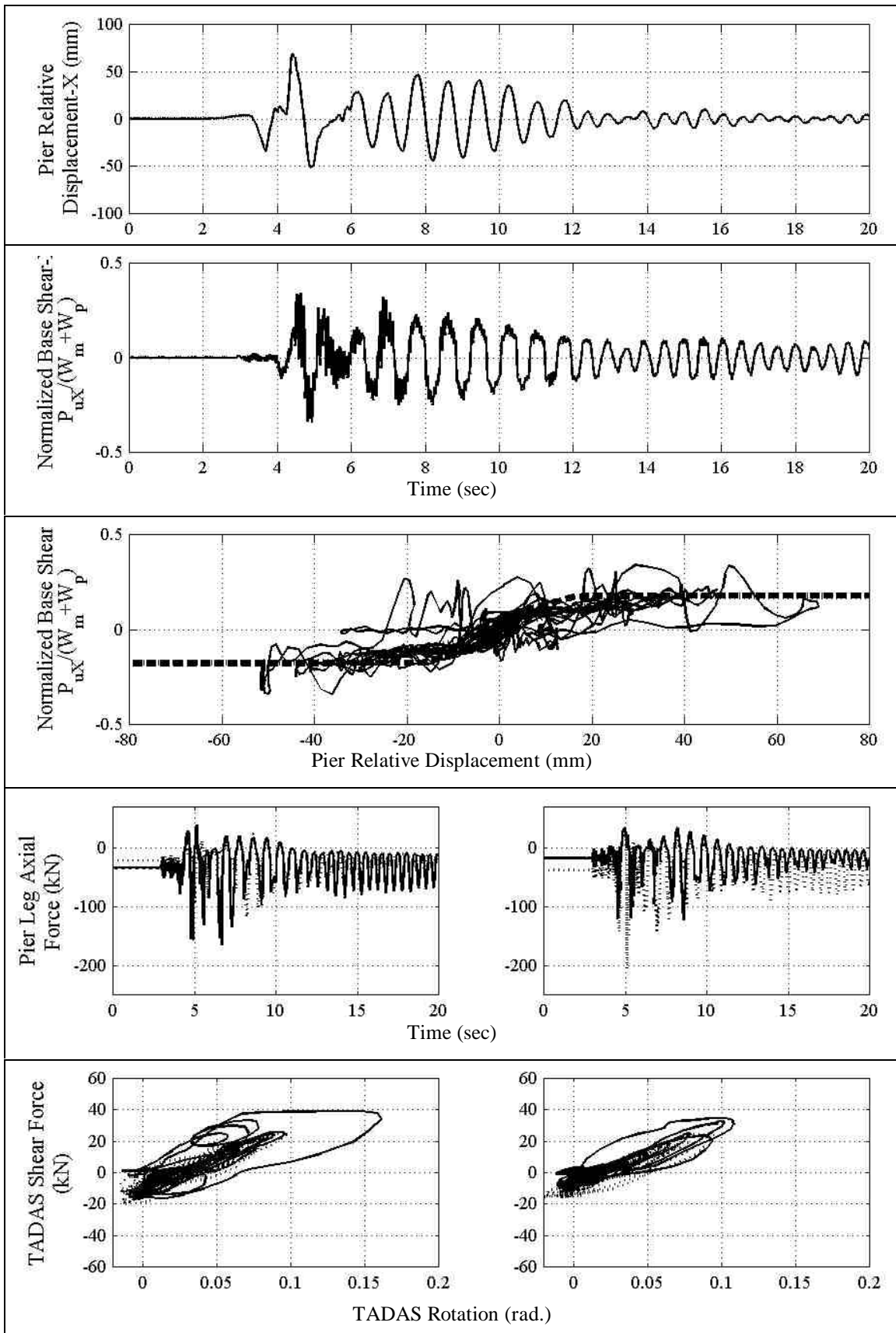
FIGURE 6-74 Experimental Response Results; Newhall 100%, $_L$=0, =45deg. (a) Pier Relative Displacement, (b) Normalized Pier Base Shear, (c) Pier Hysteretic Response, (d) Pier Leg Vertical Reactions, (e) TADAS Hysteretic Response

270

FIGURE 6-75 Experimental Response Results; Pulse P2, Tp=0.20sec. 100%, _L=0, =45deg. (a) Pier Relative Displacement, (b) Normalized Pier Base Shear, (c) Pier Hysteretic Response, (d) Pier Leg Vertical Reactions, (e) TADAS Hysteretic Response

271
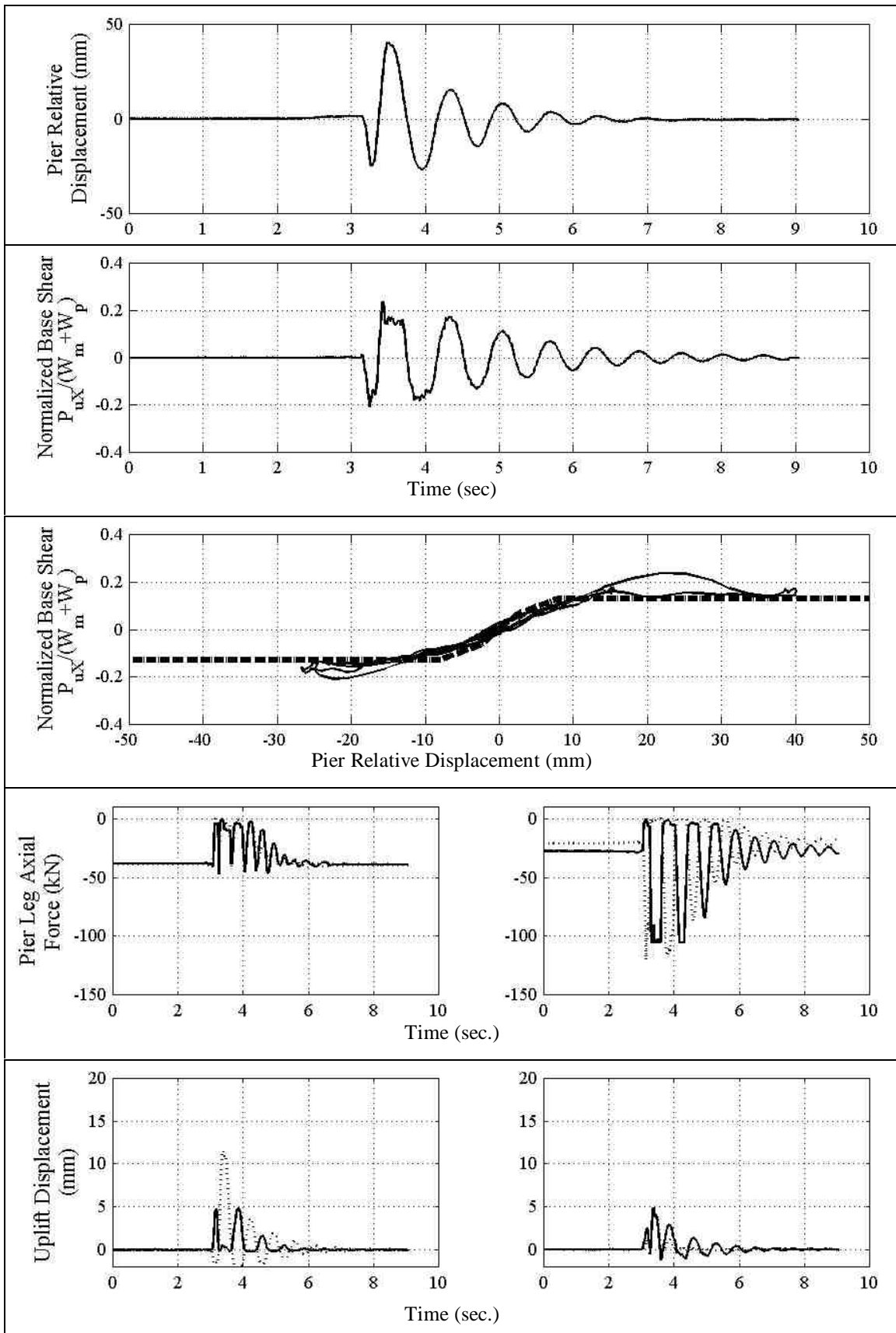
FIGURE 6-76   Experimental Response Results; Pulse P2, Tp=0.40sec. 100%, ₗ=0, =45deg. (a) Pier Relative Displacement, (b) Normalized Pier Base Shear, (c) Pier Hysteretic Response, (d) Pier Leg Vertical Reactions, (e) TADAS Hysteretic Response
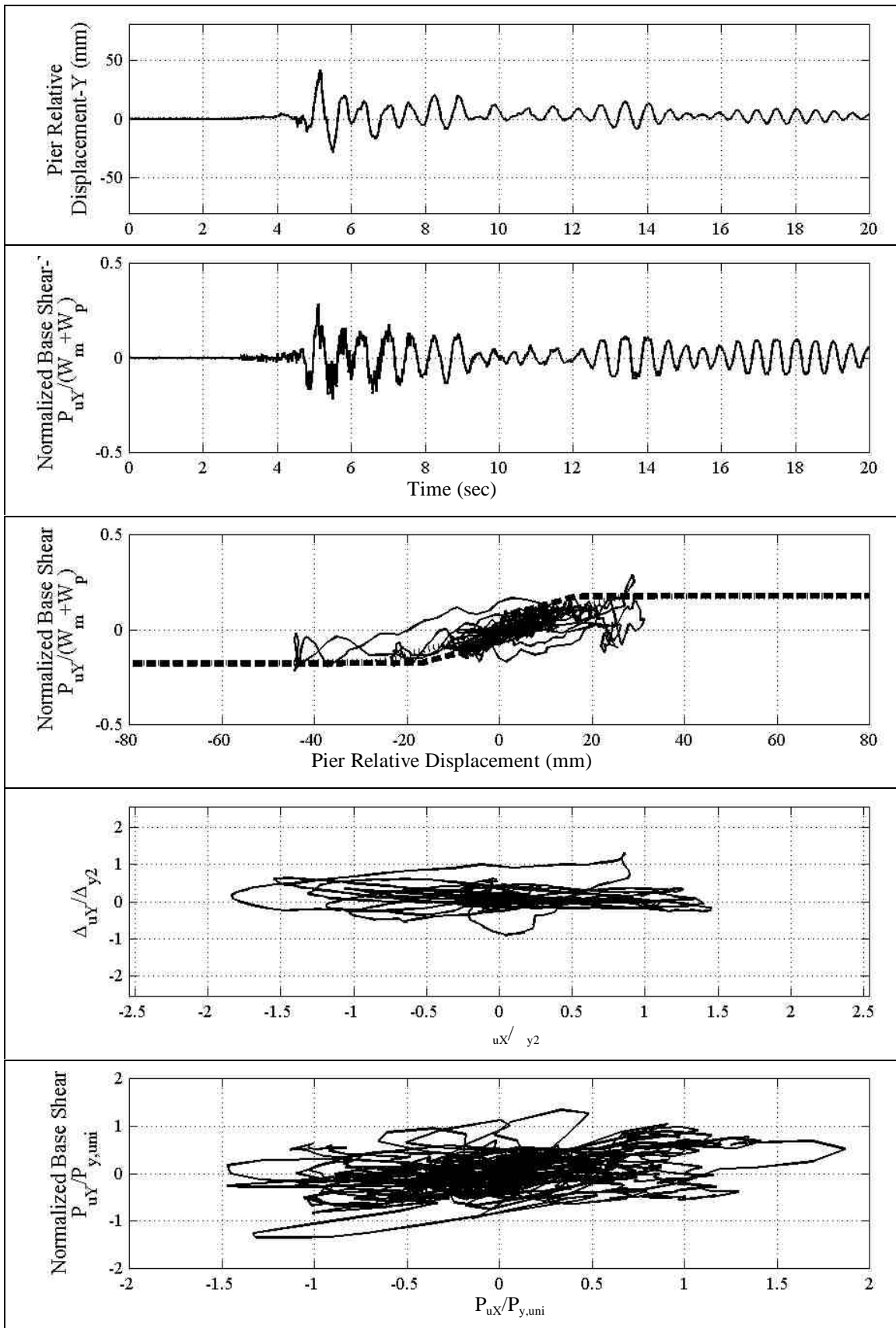
272
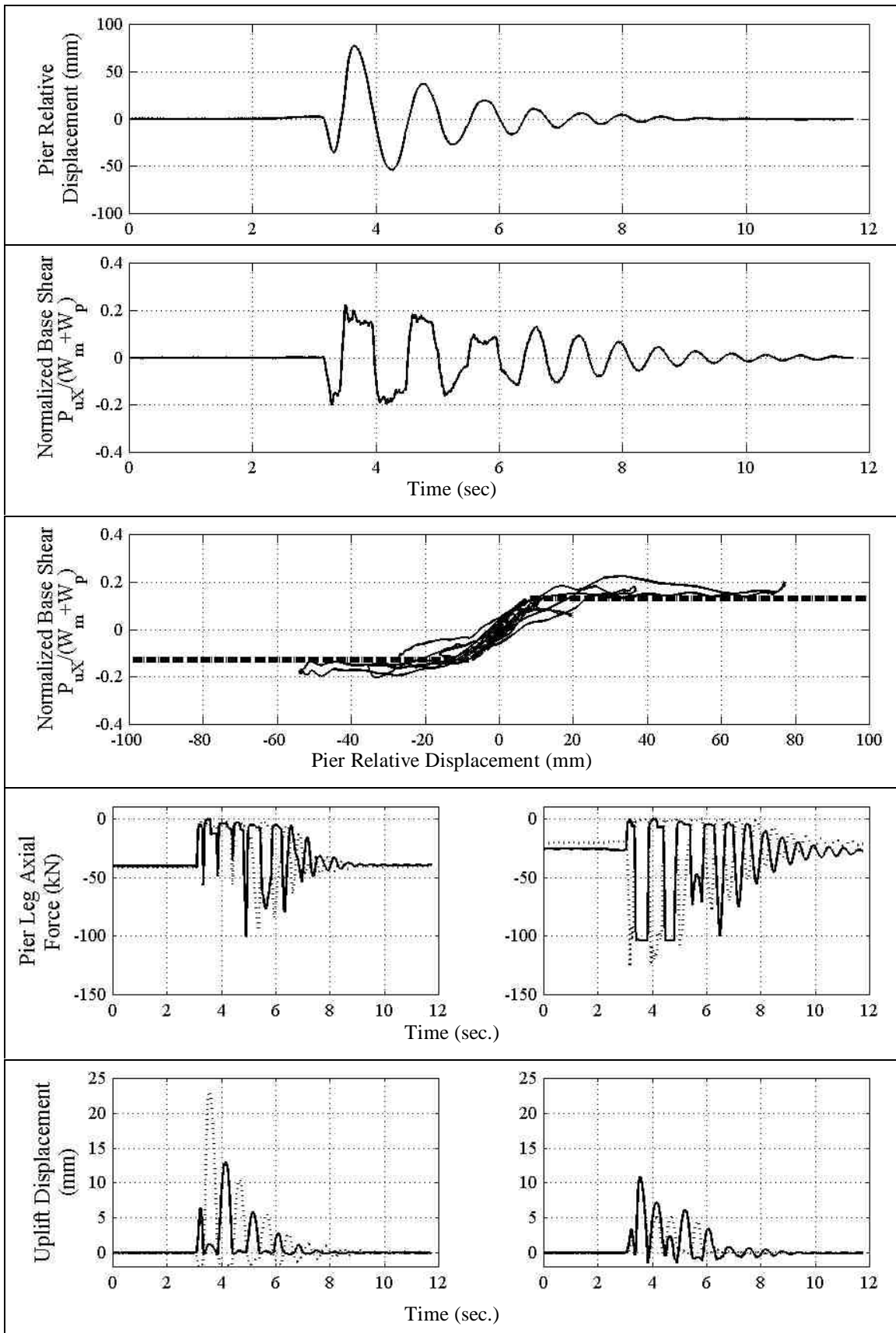
FIGURE 6-77   Experimental Response Results; Pulse P2, Tp=0.60sec. 100%, ₗ=0, =45deg. (a) Pier Relative Displacement, (b) Normalized Pier Base Shear, (c) Pier Hysteretic Response, (d) Pier Leg Vertical Reactions, (e) TADAS Hysteretic Response

273

FIGURE 6-78 Actual Table Spectra for Newhall-X , 5% Damping, Phase II
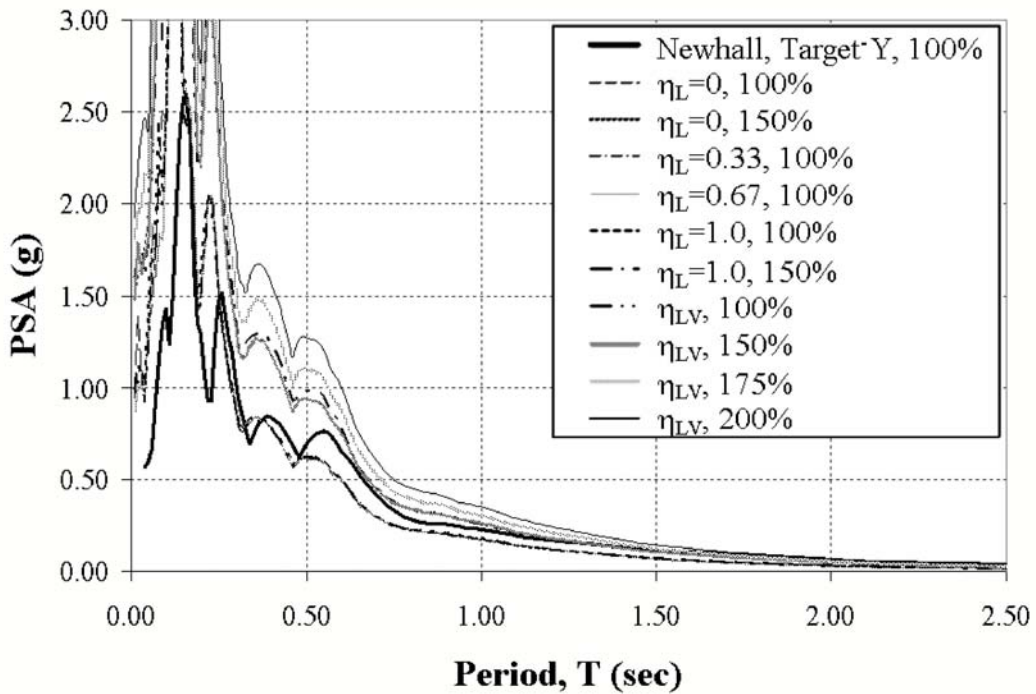
FIGURE 6-79 Actual Table Spectra for Newhall-Y , 5% Damping, Phase II
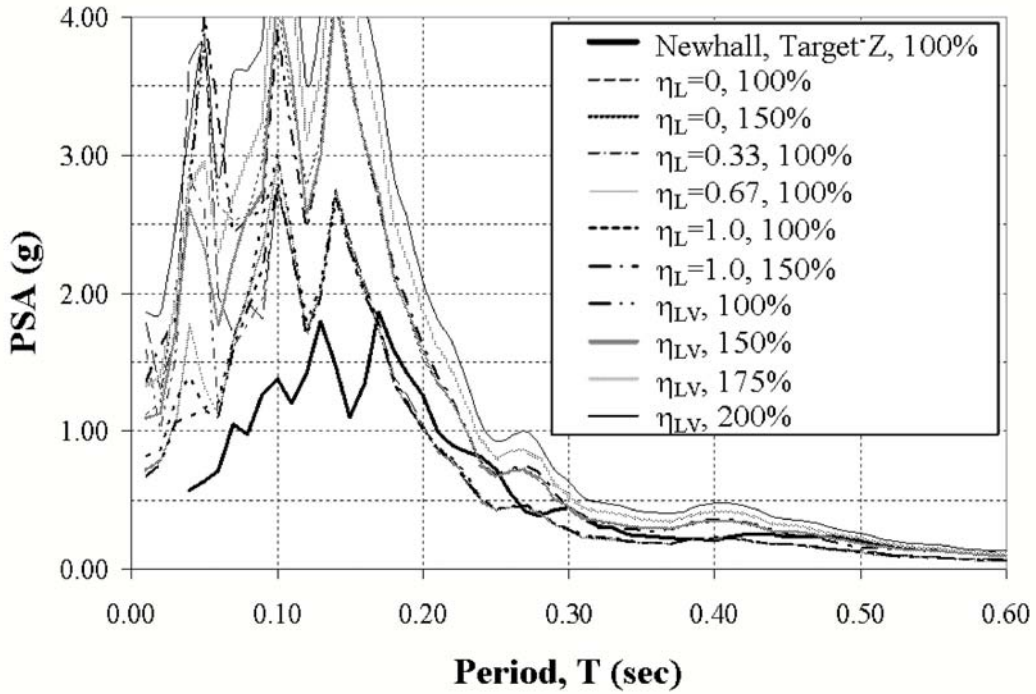
FIGURE 6-80 Actual Table Spectra for Newhall-Z , 5% Damping, Phase II
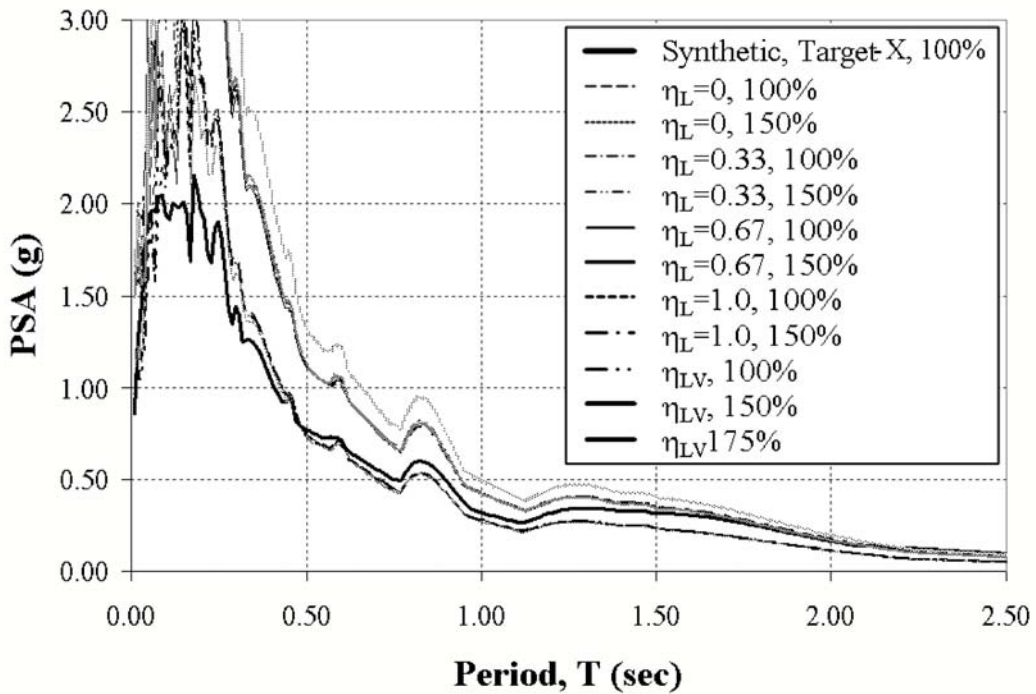
FIGURE 6-81 Actual Table Spectra for Synthetic-X , 5% Damping, Phase II
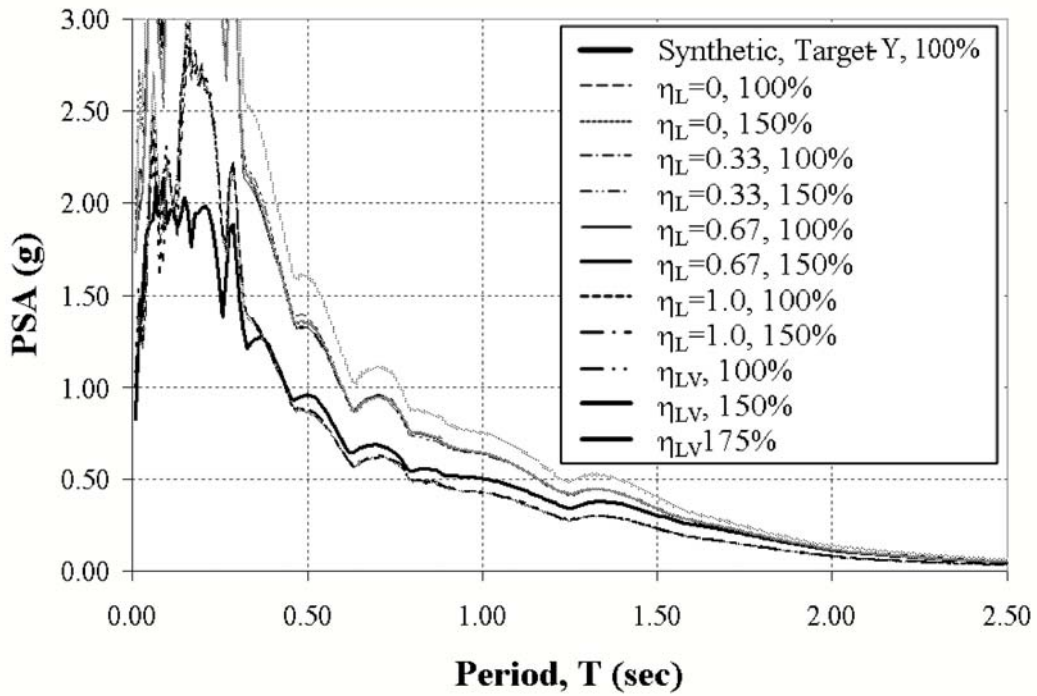
FIGURE 6-82 Actual Table Spectra for Synthetic-Y , 5% Damping, Phase II
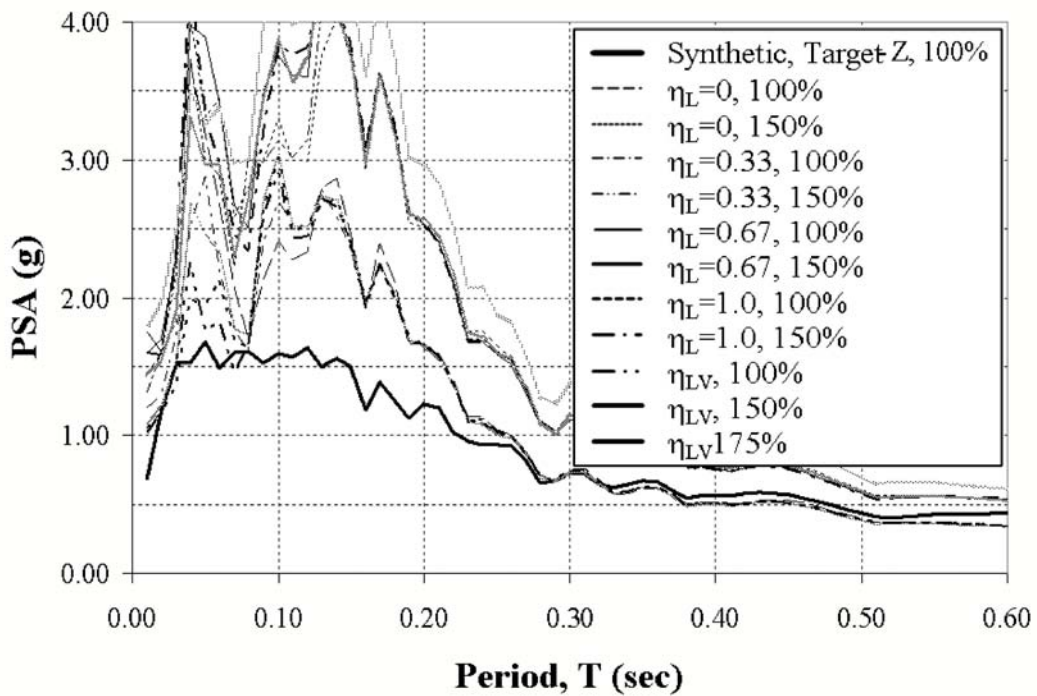
FIGURE 6-83 Actual Table Spectra for Synthetic-Z , 5% Damping, Phase II
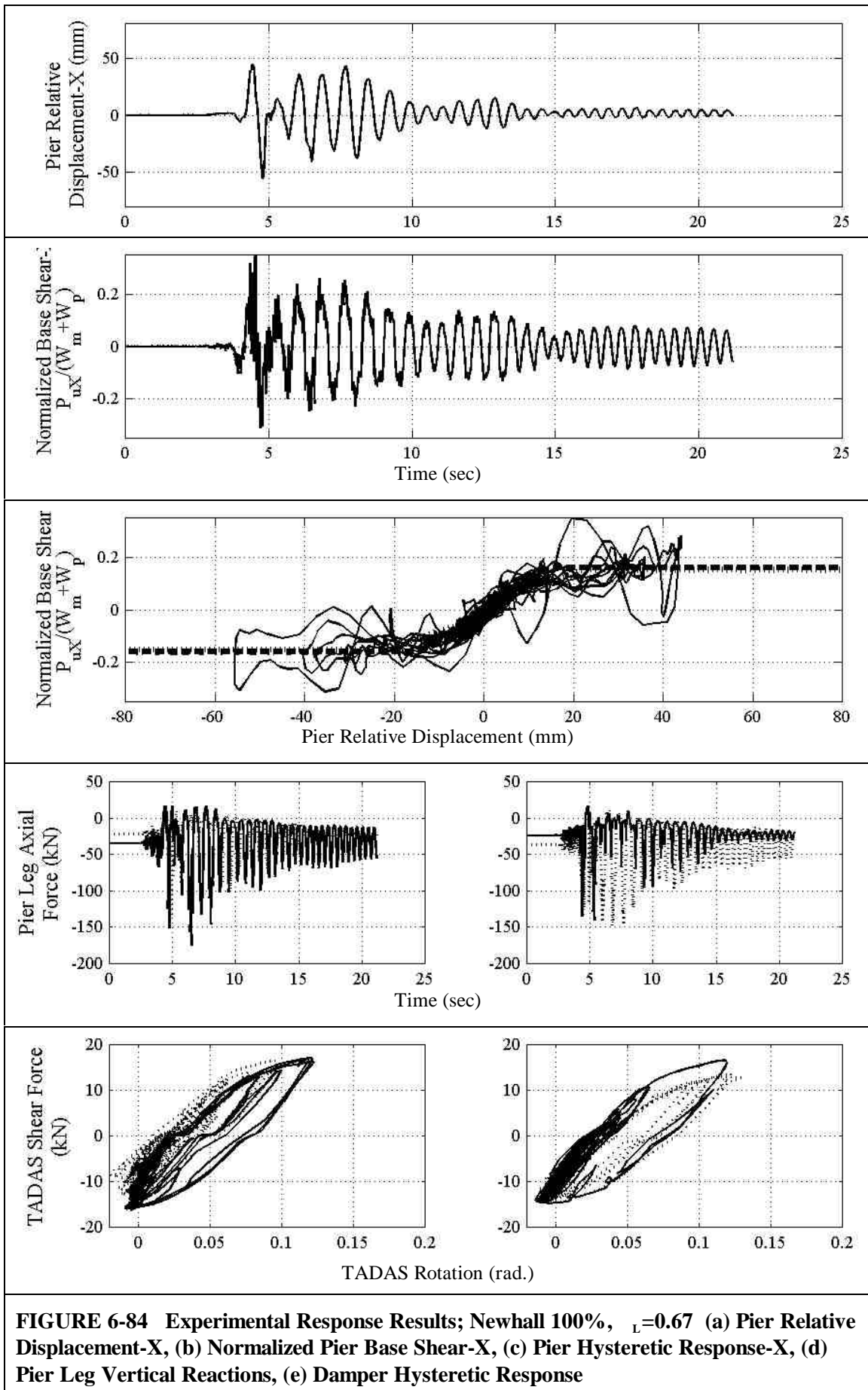
FIGURE 6-84 Experimental Response Results; Newhall 100%, $_L$=0.67 (a) Pier Relative Displacement-X, (b) Normalized Pier Base Shear-X, (c) Pier Hysteretic Response-X, (d) Pier Leg Vertical Reactions, (e) Damper Hysteretic Response
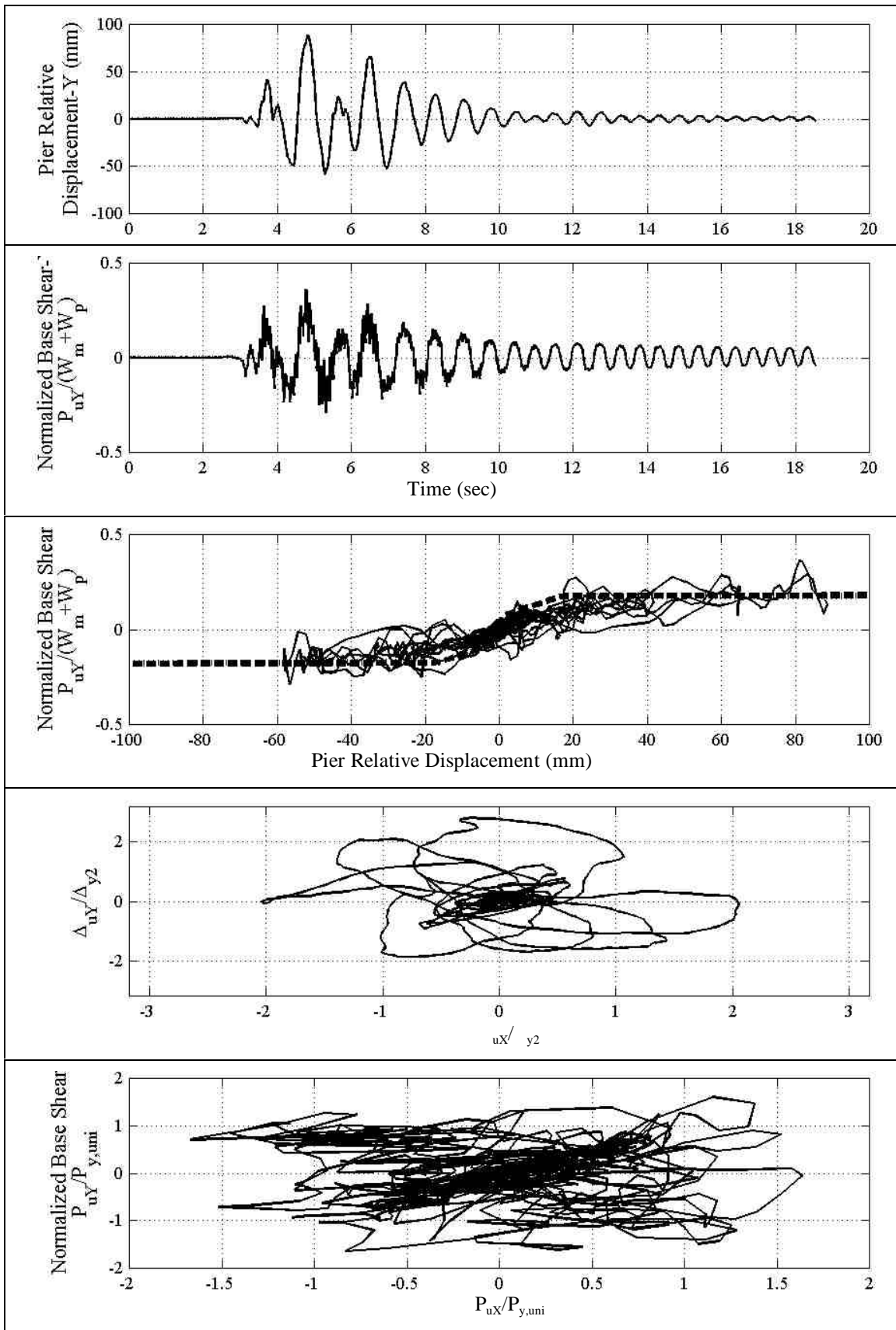
277

FIGURE 6-84 (Cont.) Experimental Response Results; Newhall 100%, $_L$=0.67 (cont.) (f) Pier Relative Displacement-Y, (g) Normalized Pier Base Shear-Y, (h) Pier Hysteretic, (i) Normalized X-Y Plane Displacement, (j) Normalized X-Y Base Shear
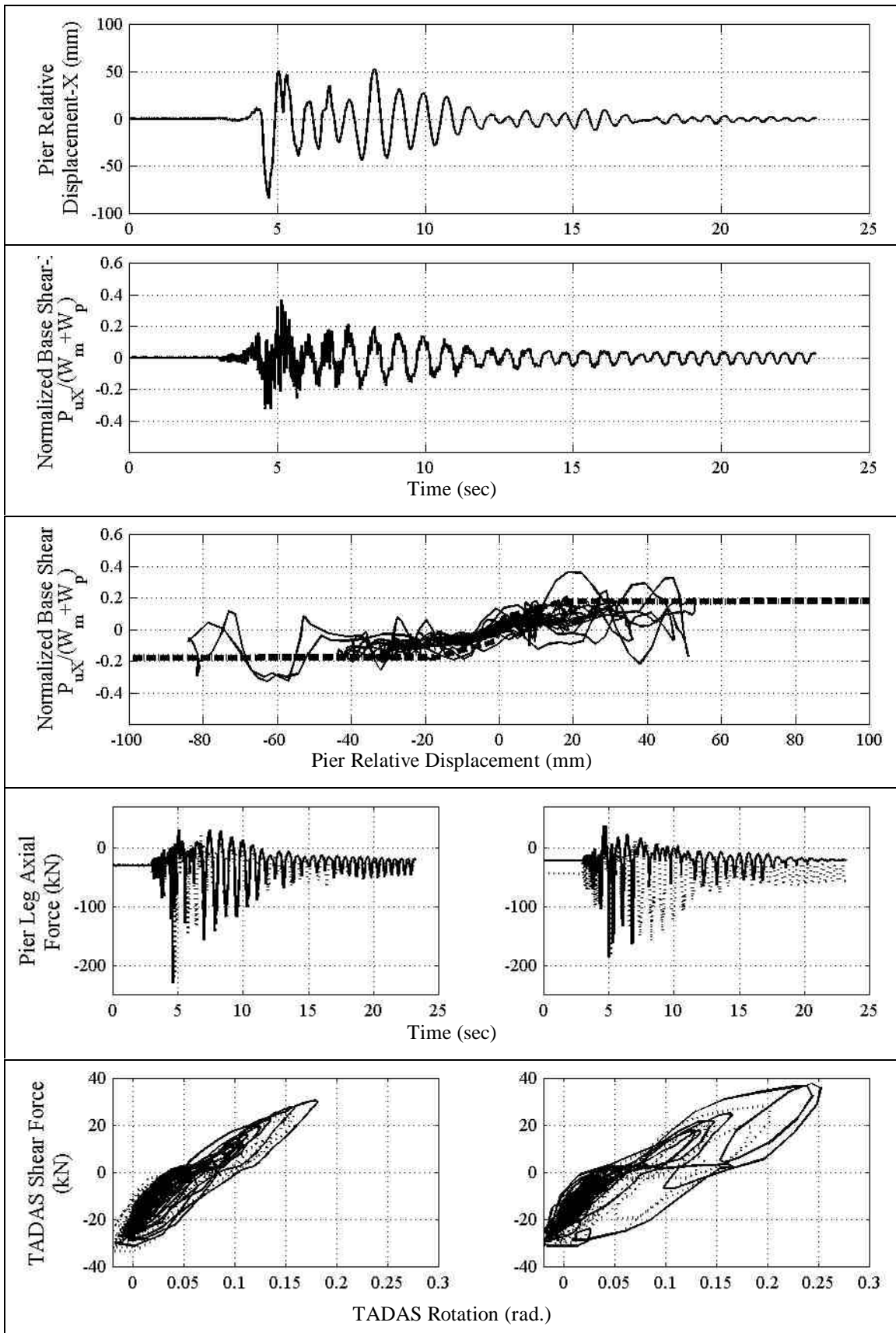
278
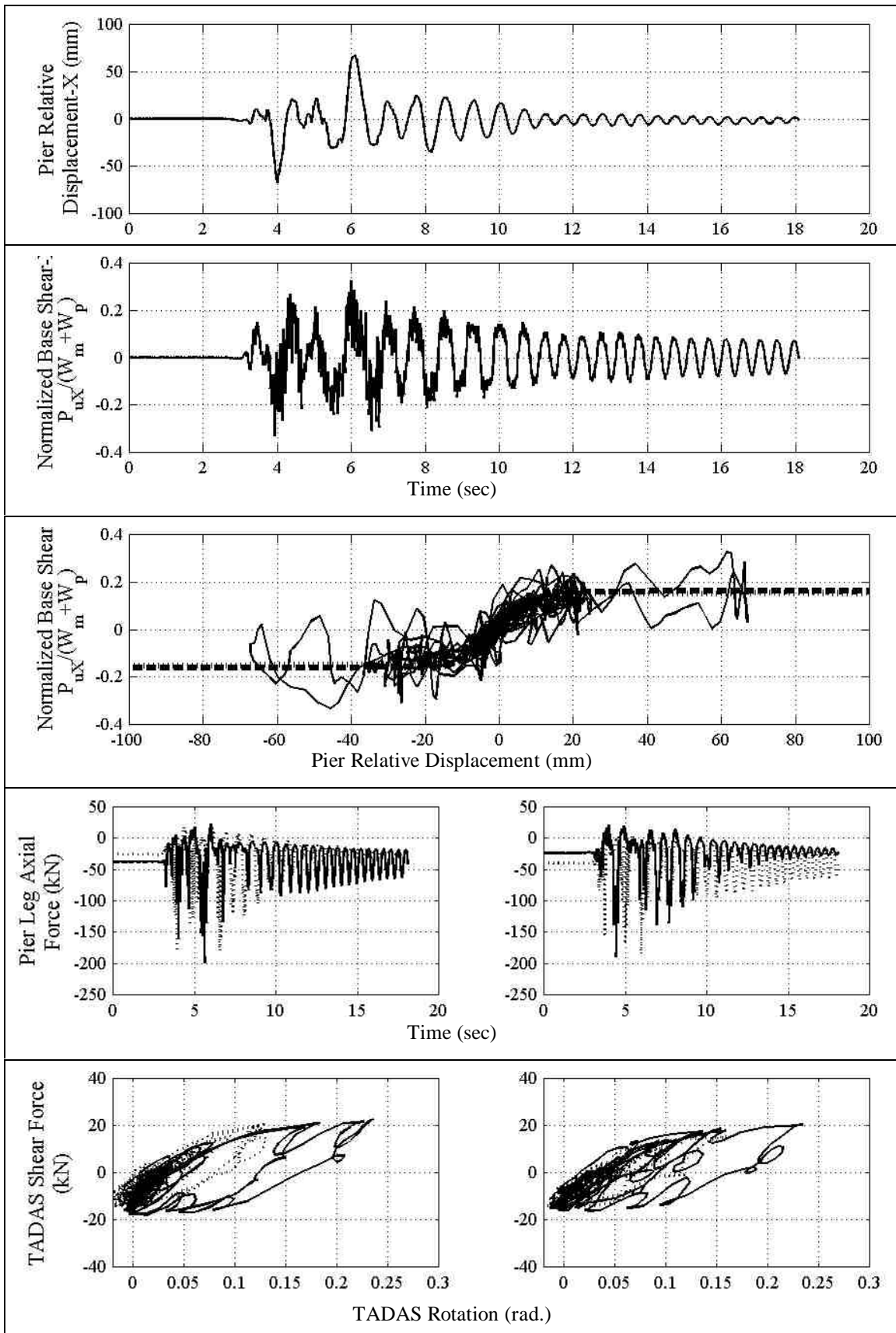
FIGURE 6-85 Experimental Response Results; Synthetic 100%, _L=0.67 (a) Pier Relative Displacement-X, (b) Normalized Pier Base Shear-X, (c) Pier Hysteretic Response-X, (d) Pier Leg Vertical Reactions, (e) Damper Hysteretic Response
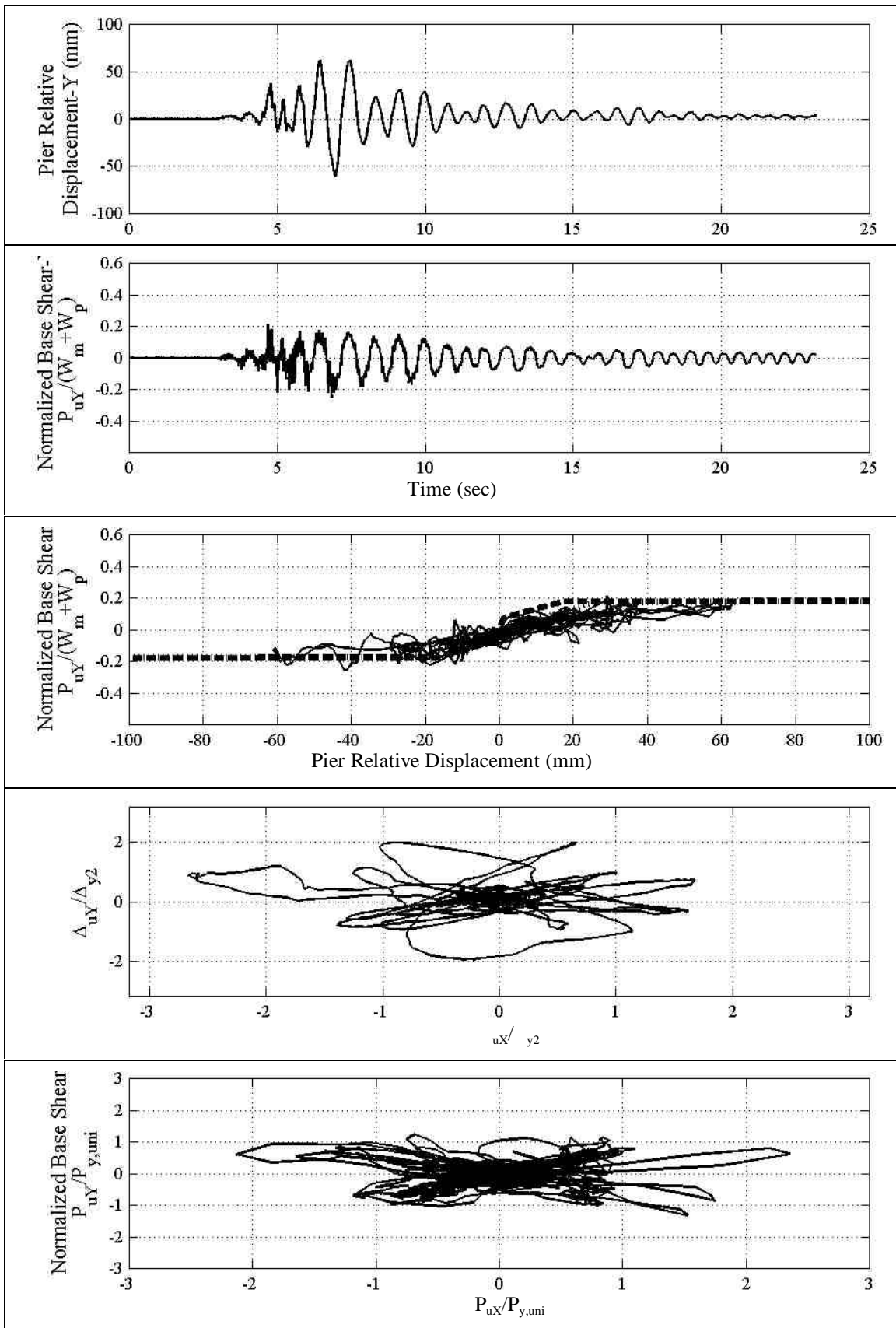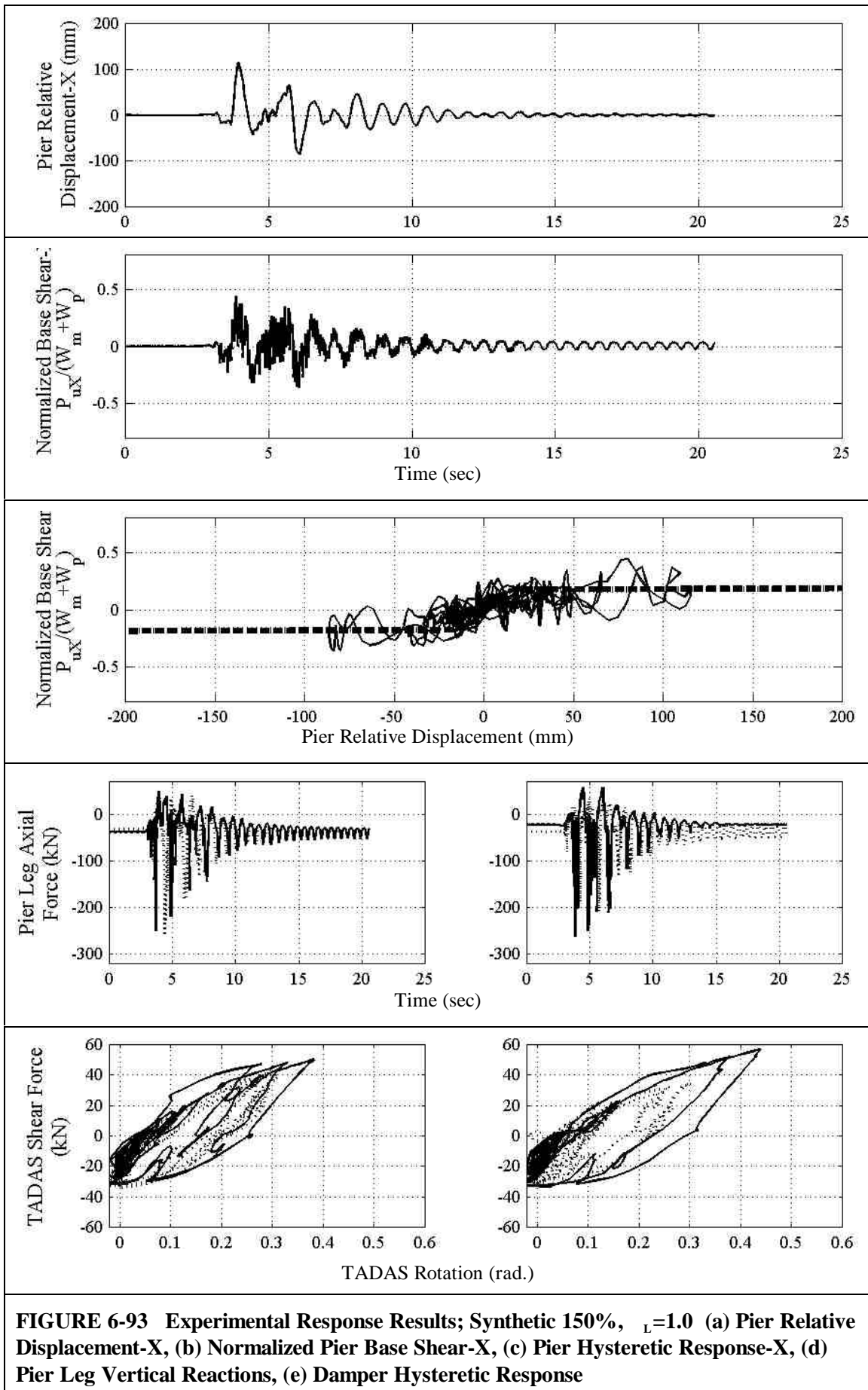
279

FIGURE 6-85 (Cont.) Experimental Response Results; Synthetic 100%, $_L$=0.67 (cont.) (f) Pier Relative Displacement-Y, (g) Normalized Pier Base Shear-Y, (h) Pier Hysteretic, (i) Normalized X-Y Plane Displacement, (j) Normalized X-Y Base Shear

FIGURE 6-86   Experimental Response Results; Synthetic 150%, $_L$=0.67 (a) Pier Relative Displacement-X, (b) Normalized Pier Base Shear-X, (c) Pier Hysteretic Response-X, (d) Pier Leg Vertical Reactions, (e) Damper Hysteretic Response

281

FIGURE 6-86 (Cont.) Experimental Response Results; Synthetic 150%, ᴸ=0.67 (cont.) (f) Pier Relative Displacement-Y, (g) Normalized Pier Base Shear-Y, (h) Pier Hysteretic, (i) Normalized X-Y Plane Displacement, (j) Normalized X-Y Base Shear
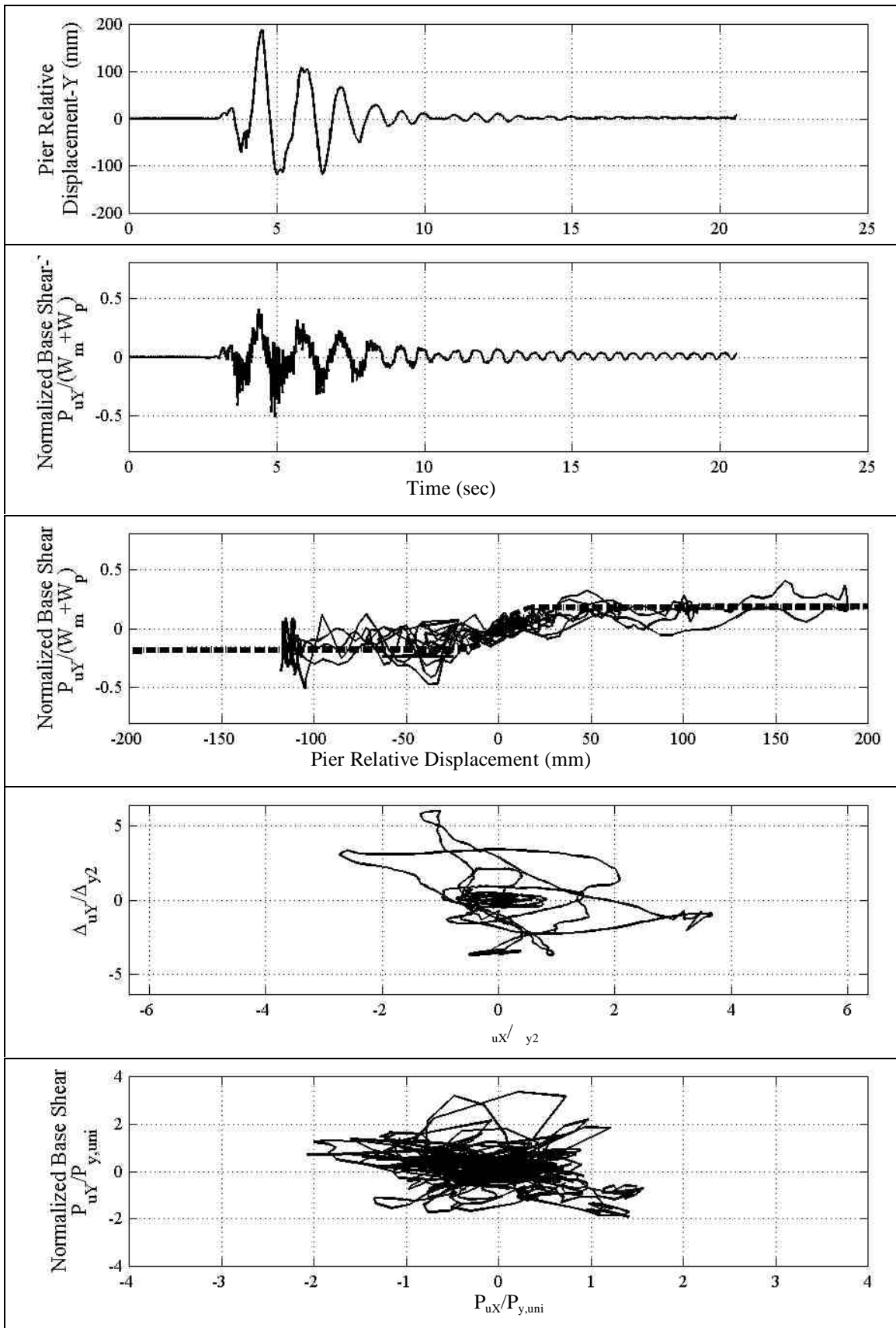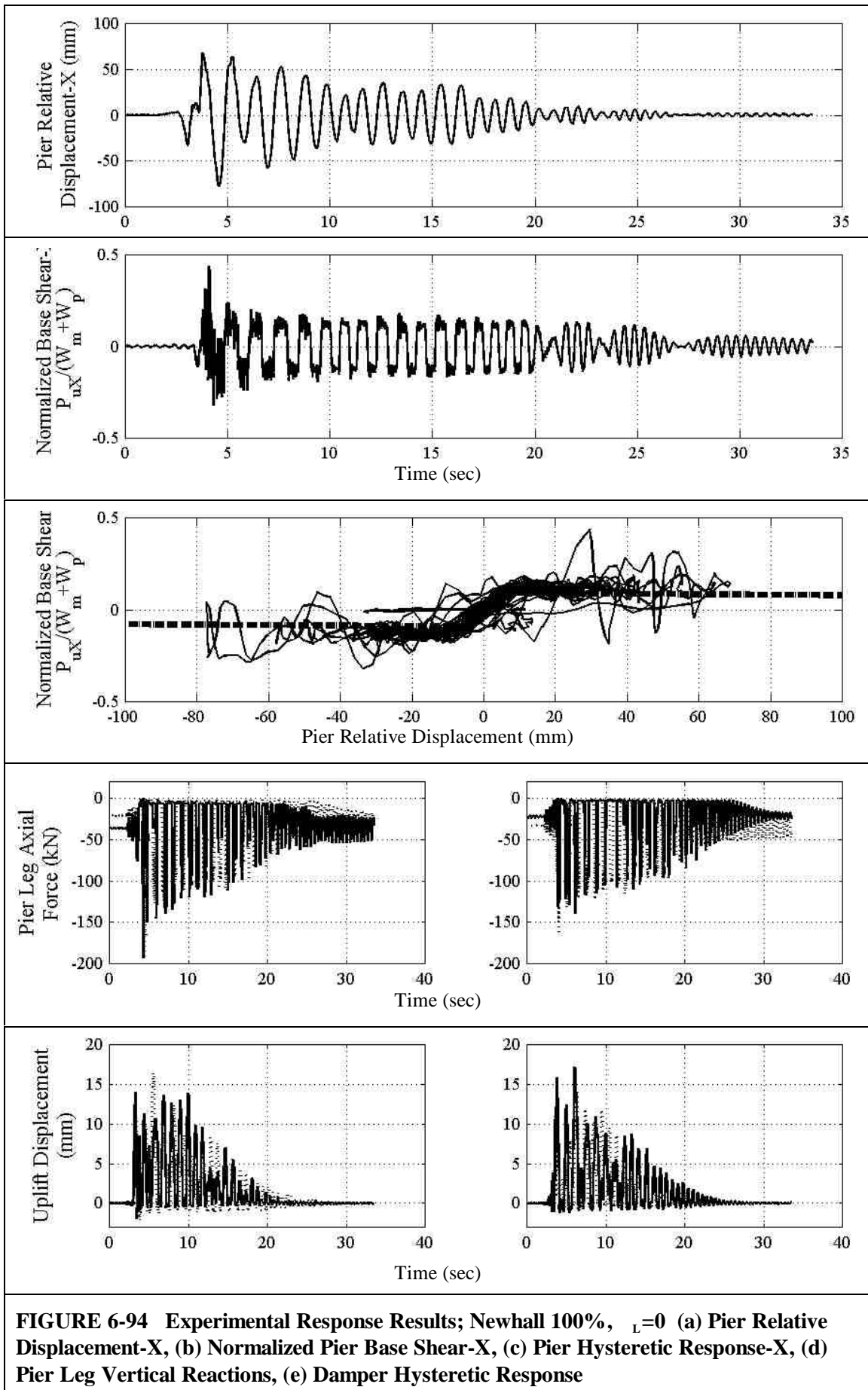
FIGURE 6-87   Experimental Response Results; Newhall 100%, _L=0.33 (a) Pier Relative Displacement-X, (b) Normalized Pier Base Shear-X, (c) Pier Hysteretic Response-X, (d) Pier Leg Vertical Reactions, (e) Damper Hysteretic Response

283
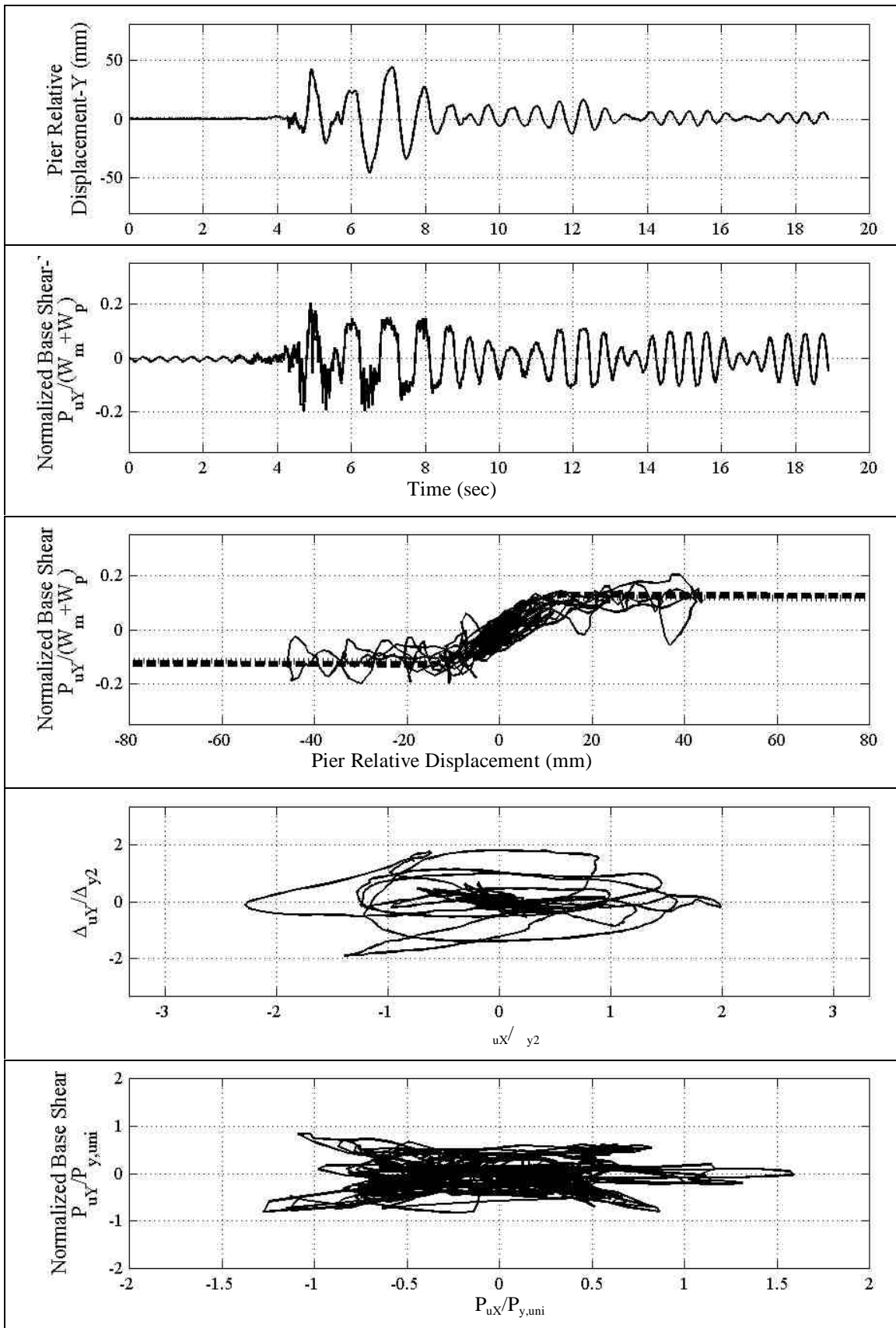
**FIGURE 6-87 (Cont.)   Experimental Response Results; Newhall 100%, γ_L=0.33 (cont.)
(f) Pier Relative Displacement-Y, (g) Normalized Pier Base Shear-Y, (h) Pier Hysteretic, (i)
Normalized X-Y Plane Displacement, (j) Normalized X-Y Base Shear**

FIGURE 6-88   Experimental Response Results; Synthetic 100%, ₗ=0.33 (a) Pier Relative Displacement-X, (b) Normalized Pier Base Shear-X, (c) Pier Hysteretic Response-X, (d) Pier Leg Vertical Reactions, (e) Damper Hysteretic Response
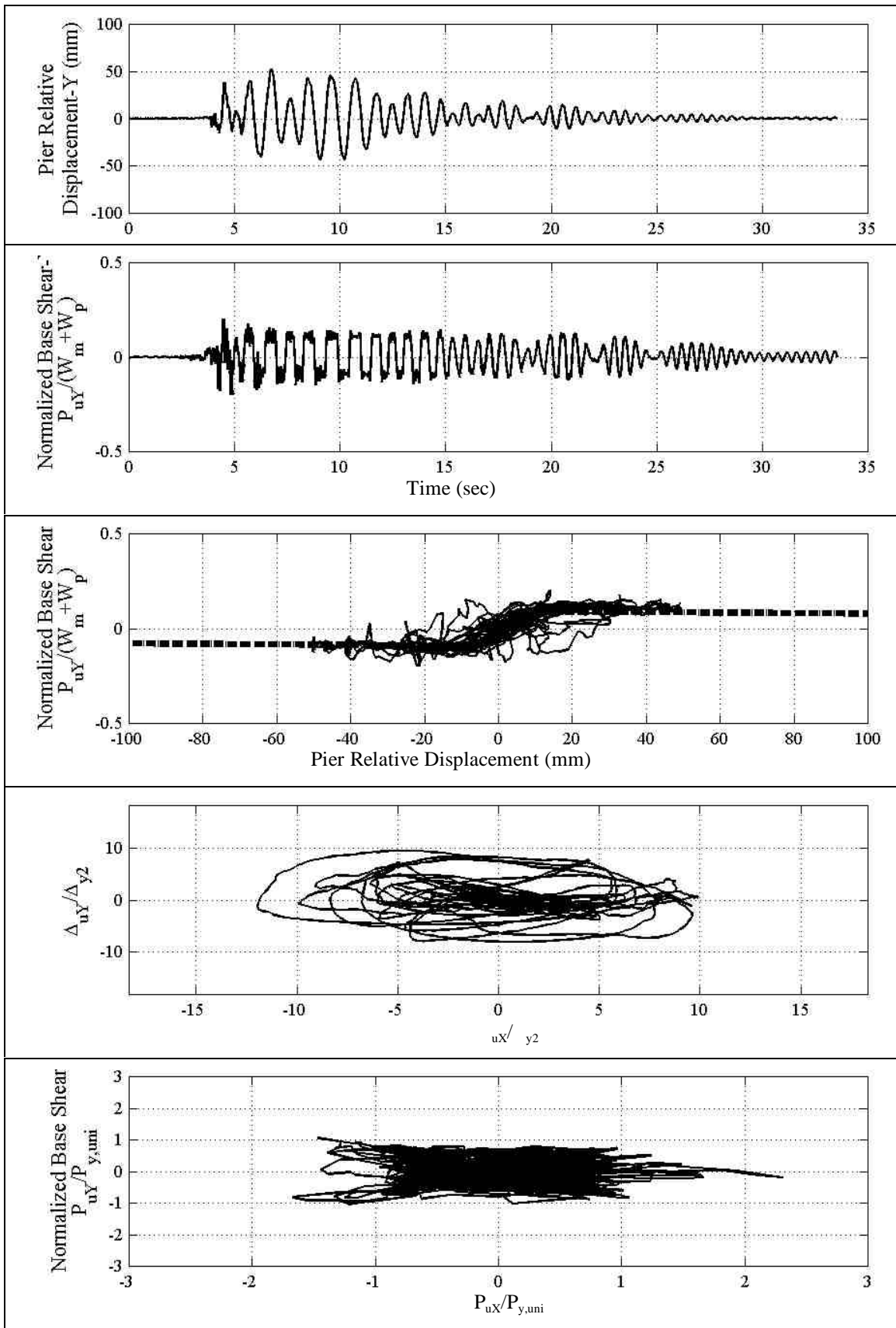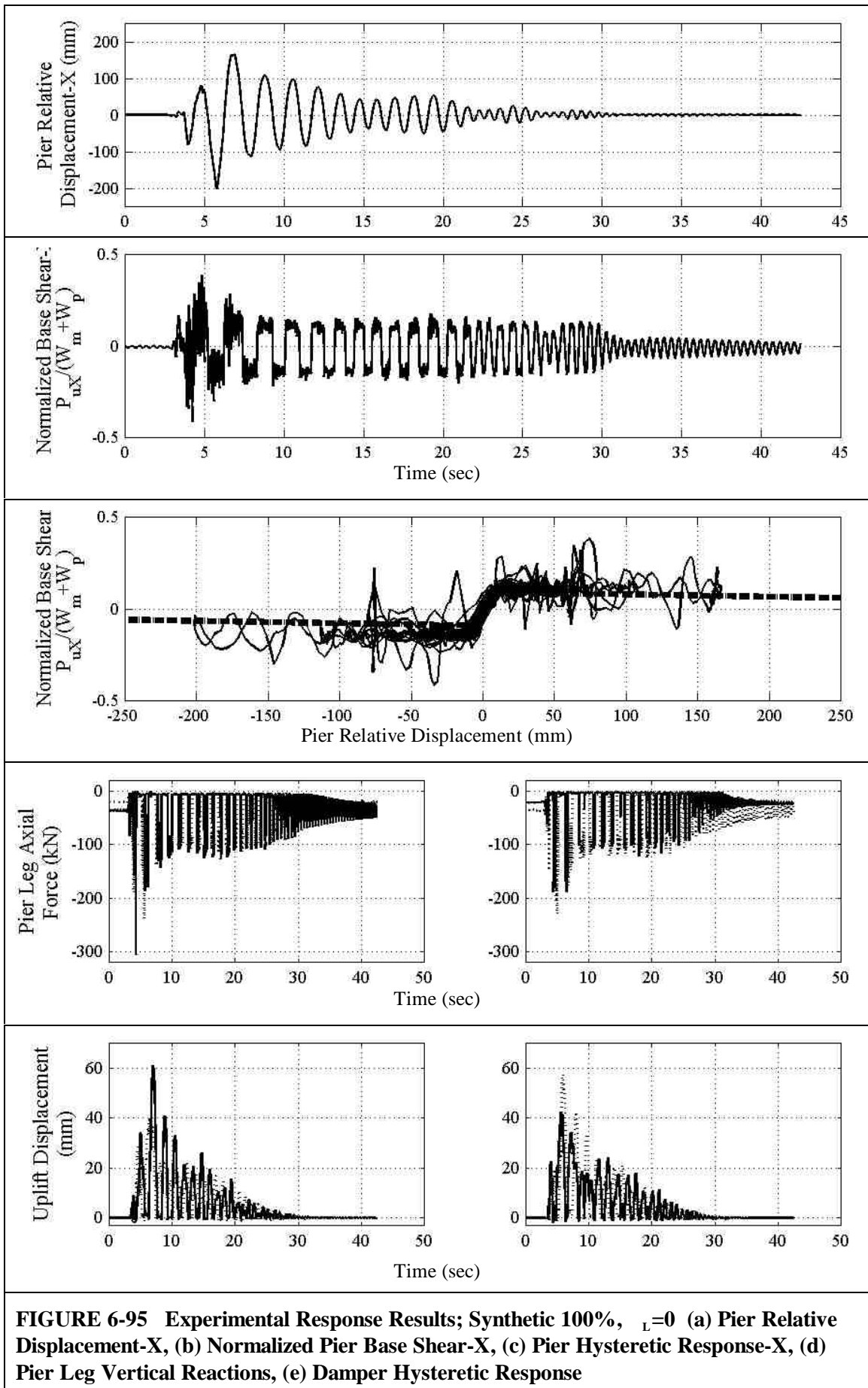
FIGURE 6-88 (Cont.)   Experimental Response Results; Synthetic 100%, ζ_L=0.33 (cont.) (f) Pier Relative Displacement-Y, (g) Normalized Pier Base Shear-Y, (h) Pier Hysteretic, (i) Normalized X-Y Plane Displacement, (j) Normalized X-Y Base Shear
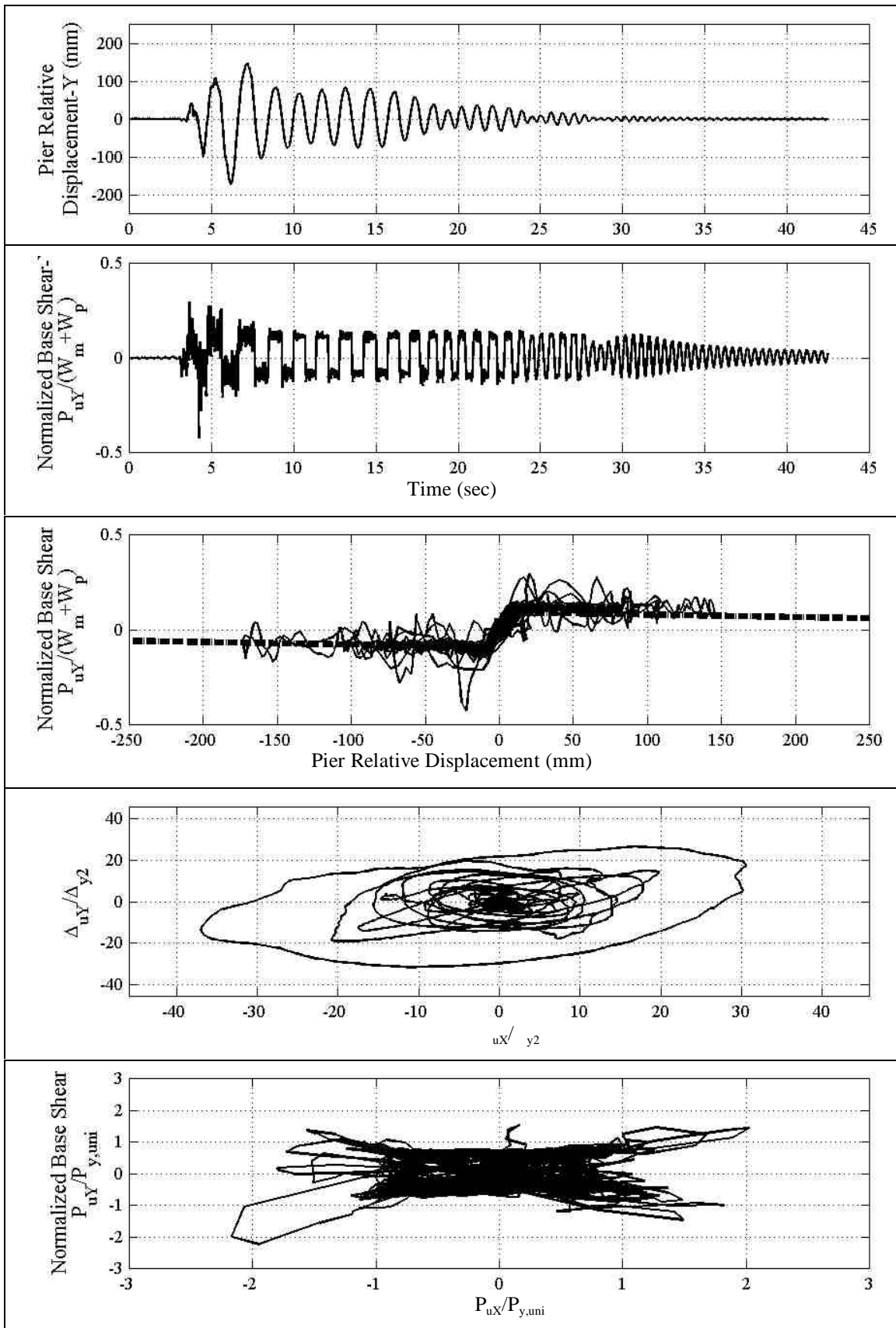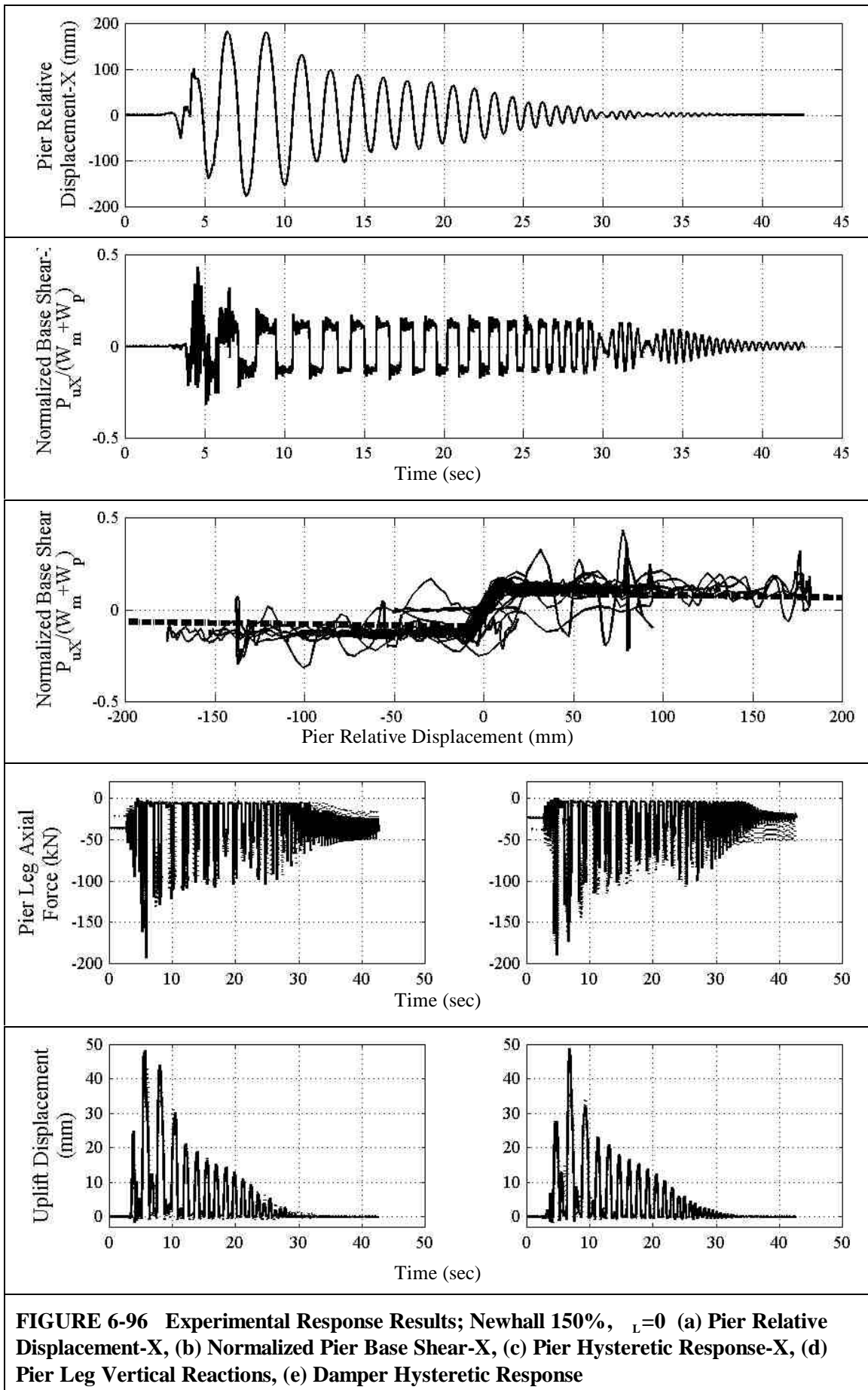
286

FIGURE 6-89 Experimental Response Results; Synthetic 150%, $_L$=0.33 (a) Pier Relative Displacement-X, (b) Normalized Pier Base Shear-X, (c) Pier Hysteretic Response-X, (d) Pier Leg Vertical Reactions, (e) Damper Hysteretic Response

287

FIGURE 6-89 (Cont.) Experimental Response Results; Synthetic 150%, ζ_L=0.33 (cont.) (f) Pier Relative Displacement-Y, (g) Normalized Pier Base Shear-Y, (h) Pier Hysteretic, (i) Normalized X-Y Plane Displacement, (j) Normalized X-Y Base Shear
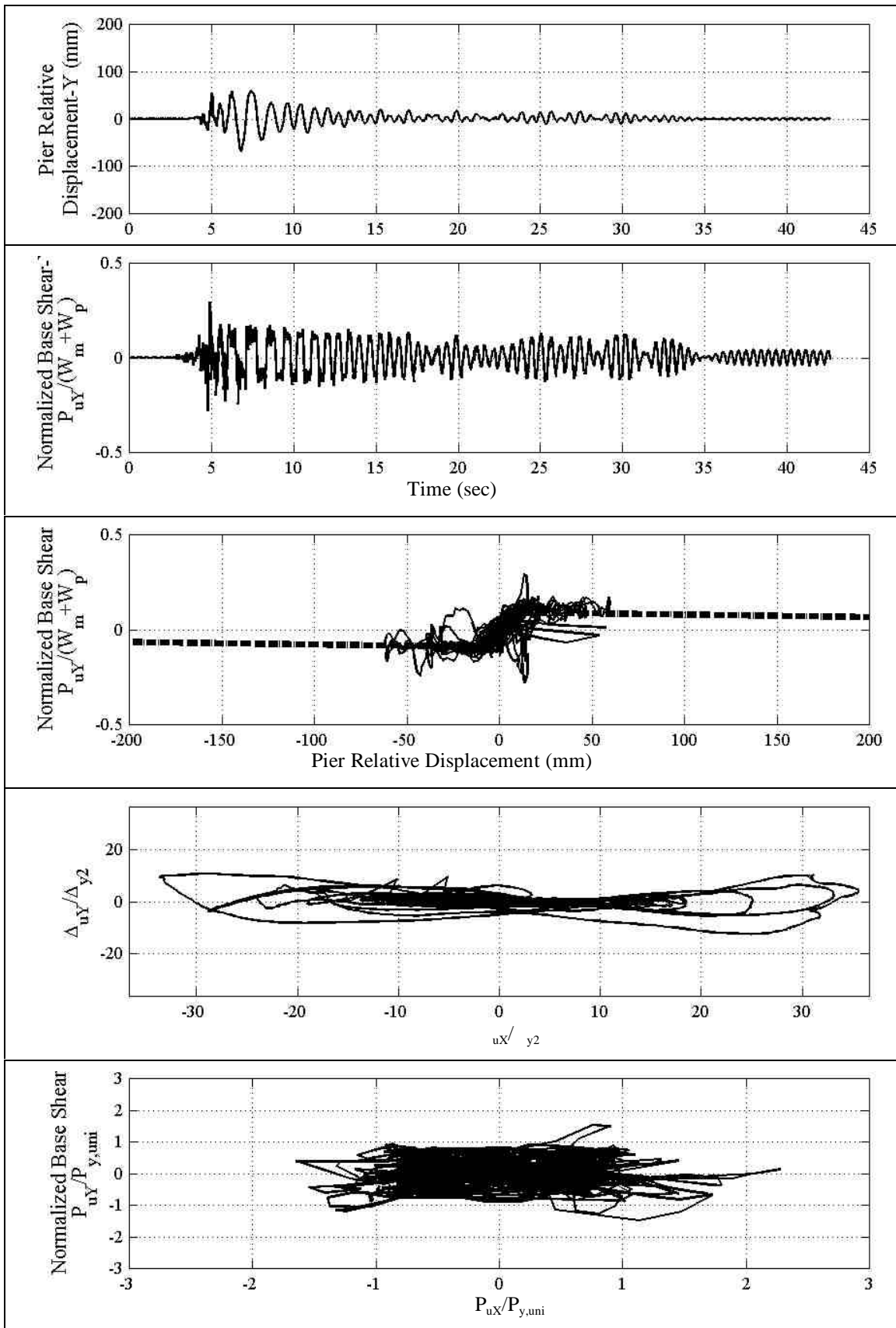
288

FIGURE 6-90 Experimental Response Results; Newhall 100%, $_L$=1.0 (a) Pier Relative Displacement-X, (b) Normalized Pier Base Shear-X, (c) Pier Hysteretic Response-X, (d) Pier Leg Vertical Reactions, (e) Damper Hysteretic Response

289

FIGURE 6-90 (Cont.)   Experimental Response Results; Newhall 100%, $_L$=1.0 (cont.) (f) Pier Relative Displacement-Y, (g) Normalized Pier Base Shear-Y, (h) Pier Hysteretic, (i) Normalized X-Y Plane Displacement, (j) Normalized X-Y Base Shear
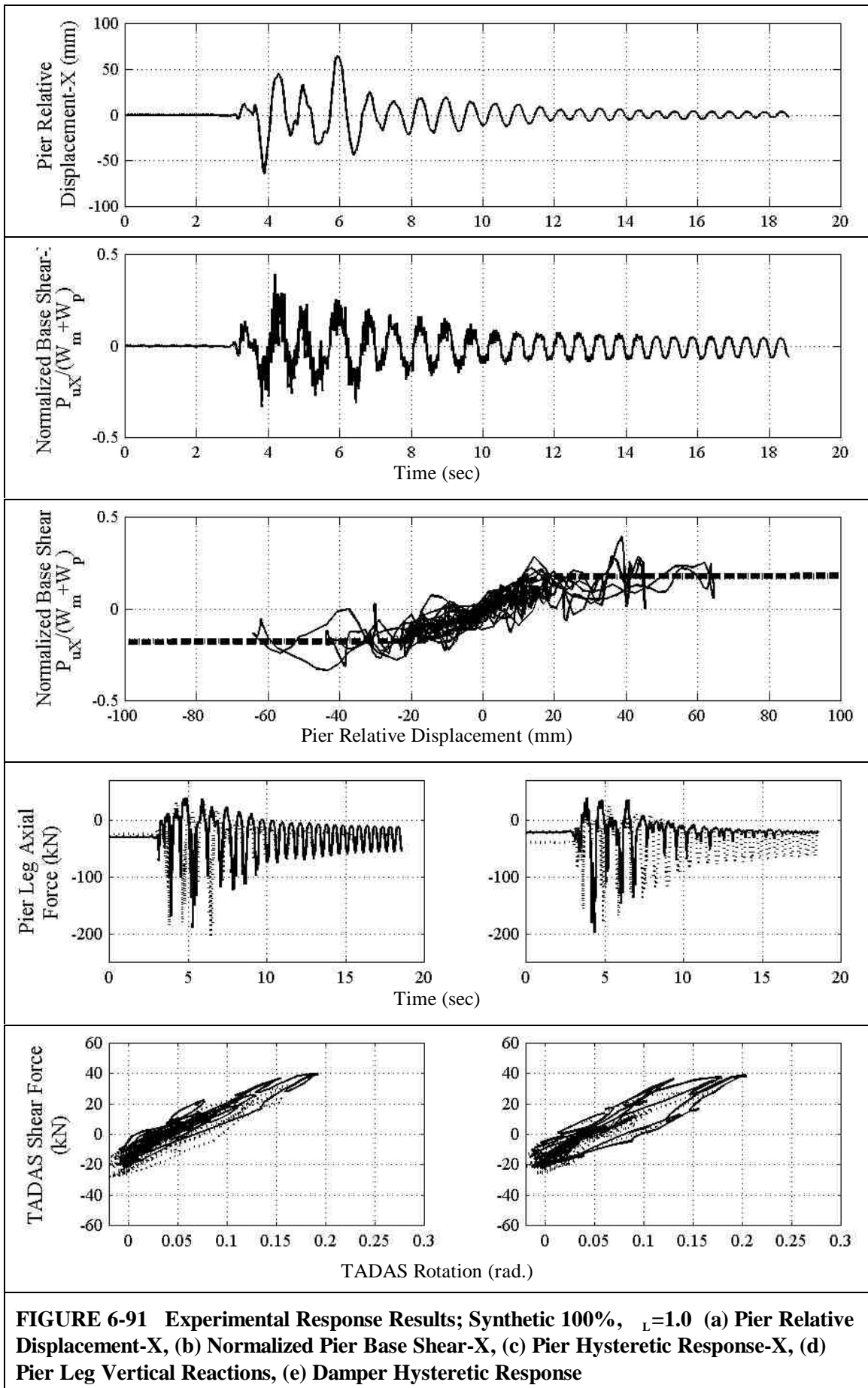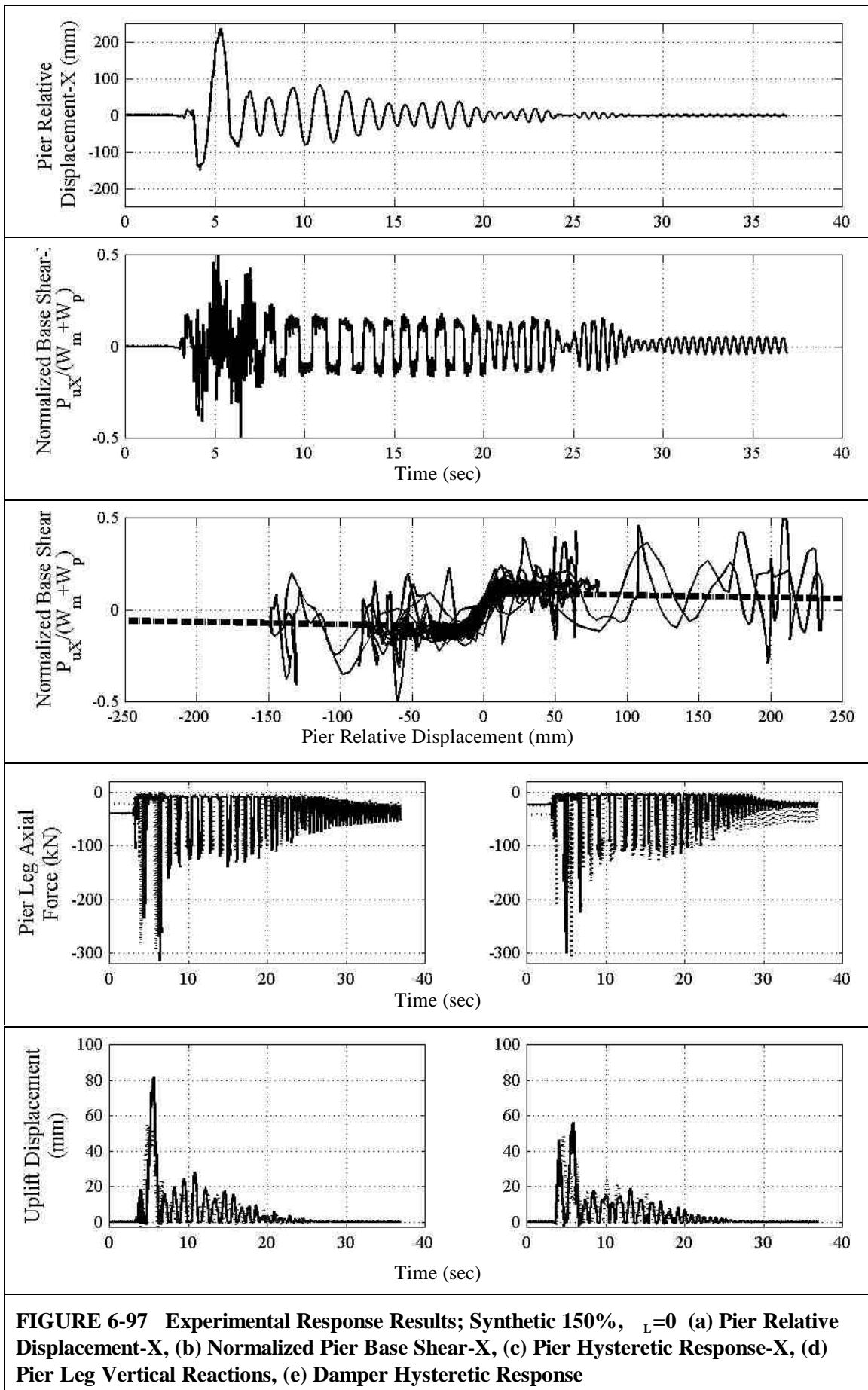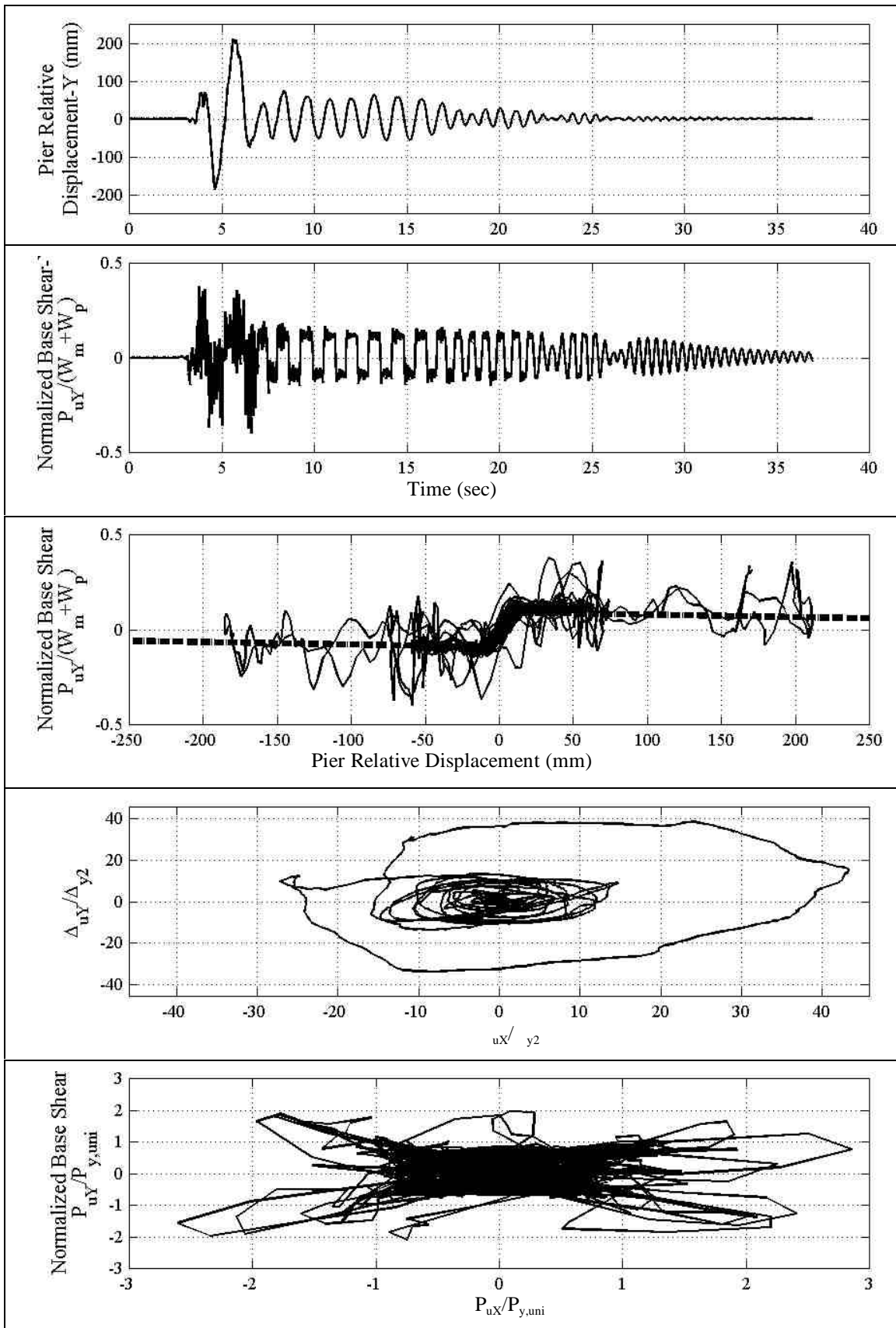
FIGURE 6-91 Experimental Response Results; Synthetic 100%, μ_L=1.0 (a) Pier Relative Displacement-X, (b) Normalized Pier Base Shear-X, (c) Pier Hysteretic Response-X, (d) Pier Leg Vertical Reactions, (e) Damper Hysteretic Response

291

FIGURE 6-91 (Cont.)   Experimental Response Results; Synthetic 100%, $_L$**=1.0 (cont.)
(f) Pier Relative Displacement-Y, (g) Normalized Pier Base Shear-Y, (h) Pier Hysteretic, (i)
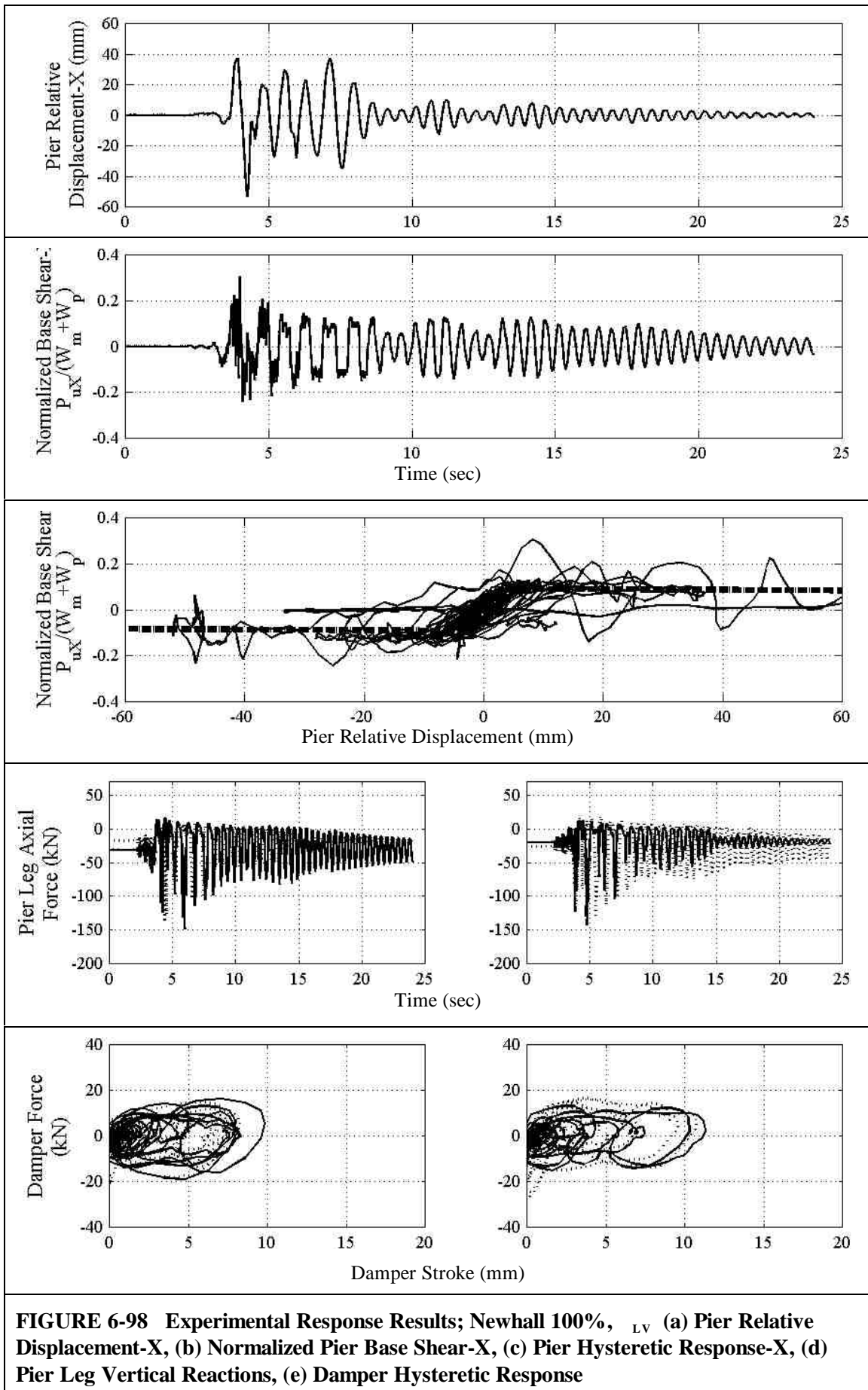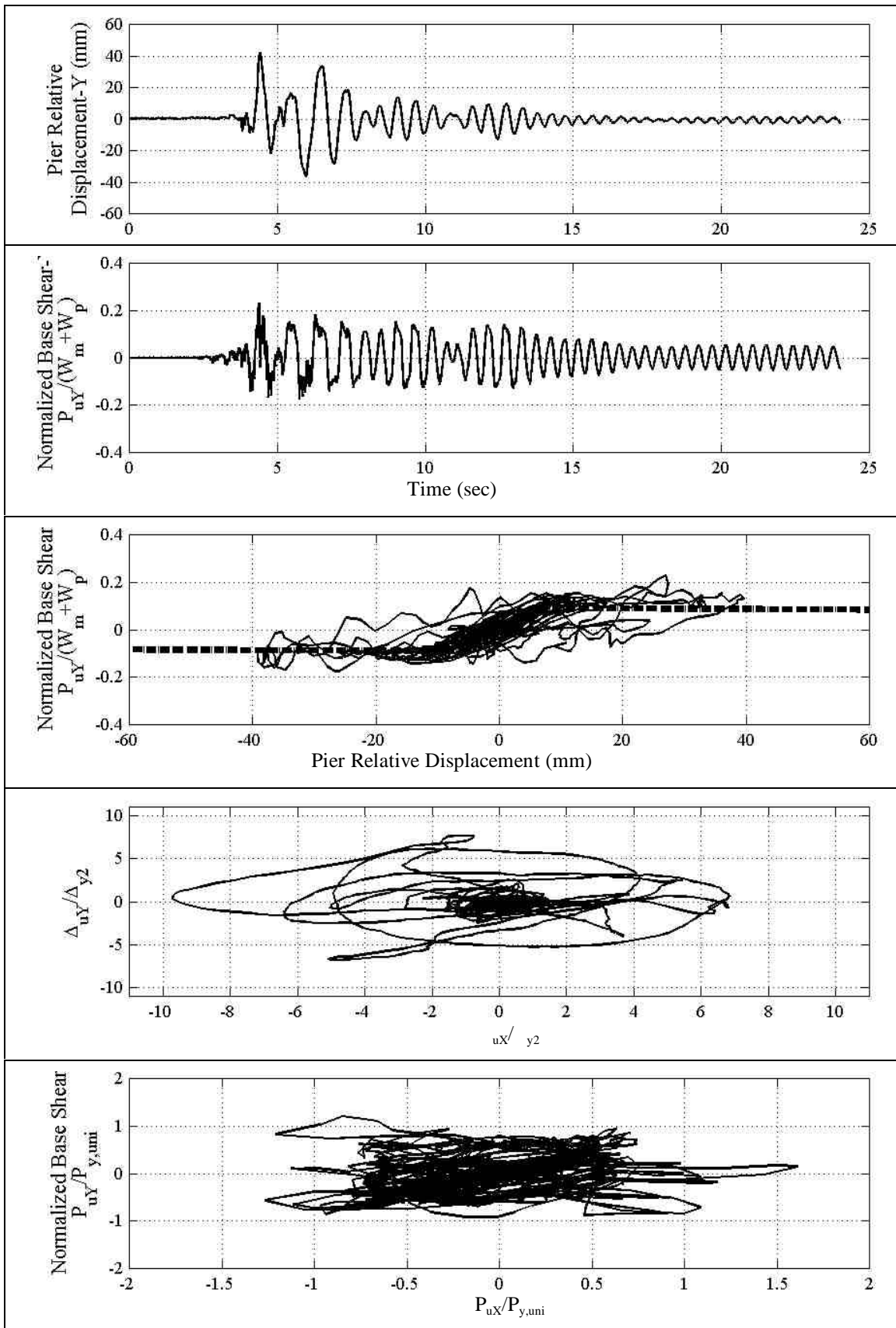Normalized X-Y Plane Displacement, (j) Normalized X-Y Base Shear**

FIGURE 6-92 Experimental Response Results; Newhall 150%, $_L$=1.0 (a) Pier Relative Displacement-X, (b) Normalized Pier Base Shear-X, (c) Pier Hysteretic Response-X, (d) Pier Leg Vertical Reactions, (e) Damper Hysteretic Response

293

FIGURE 6-92 (Cont.)   Experimental Response Results; Newhall 150%, $_L$=1.0 (cont.) (f) Pier Relative Displacement-Y, (g) Normalized Pier Base Shear-Y, (h) Pier Hysteretic, (i) Normalized X-Y Plane Displacement, (j) Normalized X-Y Base Shear
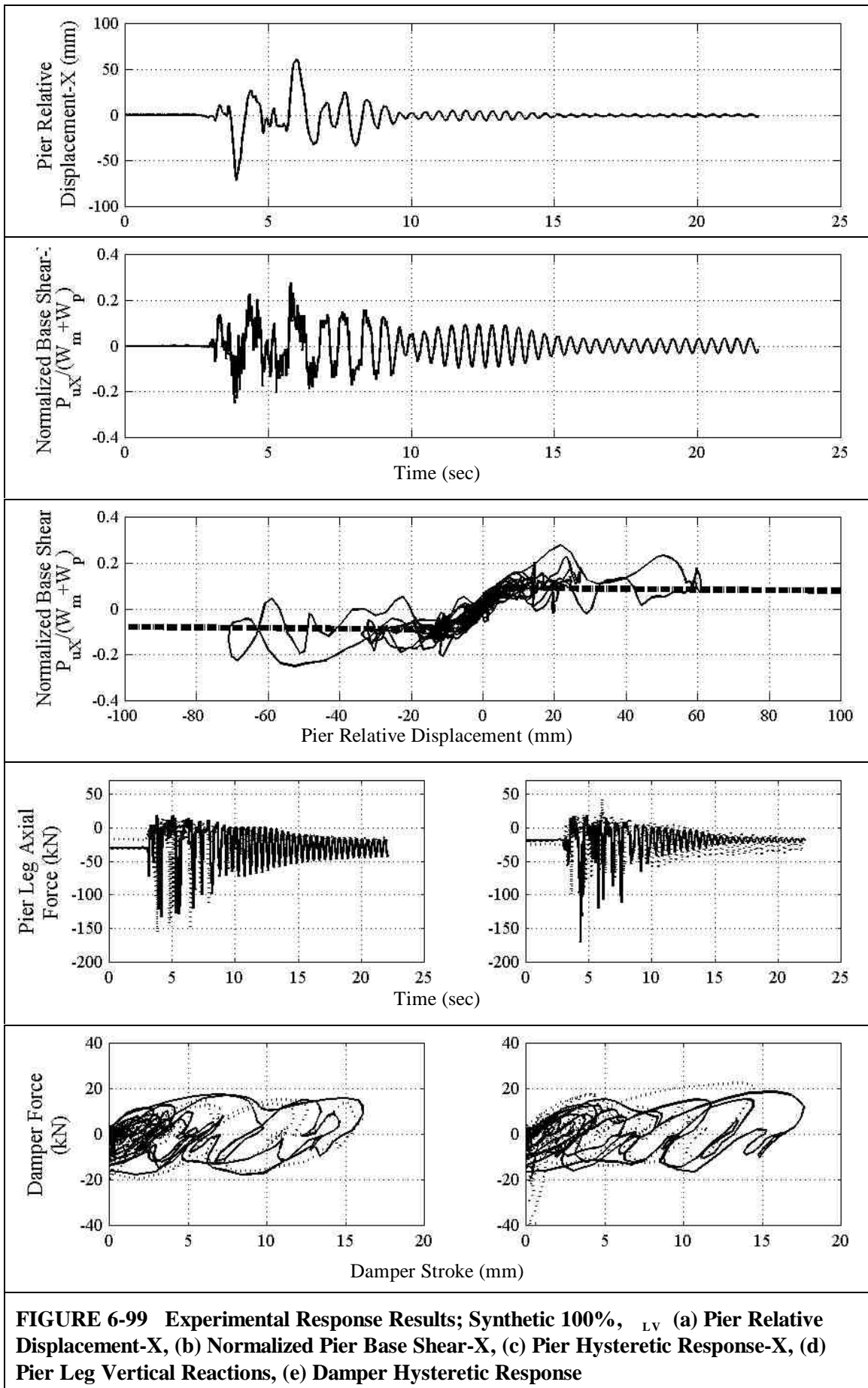
FIGURE 6-93 Experimental Response Results; Synthetic 150%, β_L=1.0 (a) Pier Relative Displacement-X, (b) Normalized Pier Base Shear-X, (c) Pier Hysteretic Response-X, (d) Pier Leg Vertical Reactions, (e) Damper Hysteretic Response
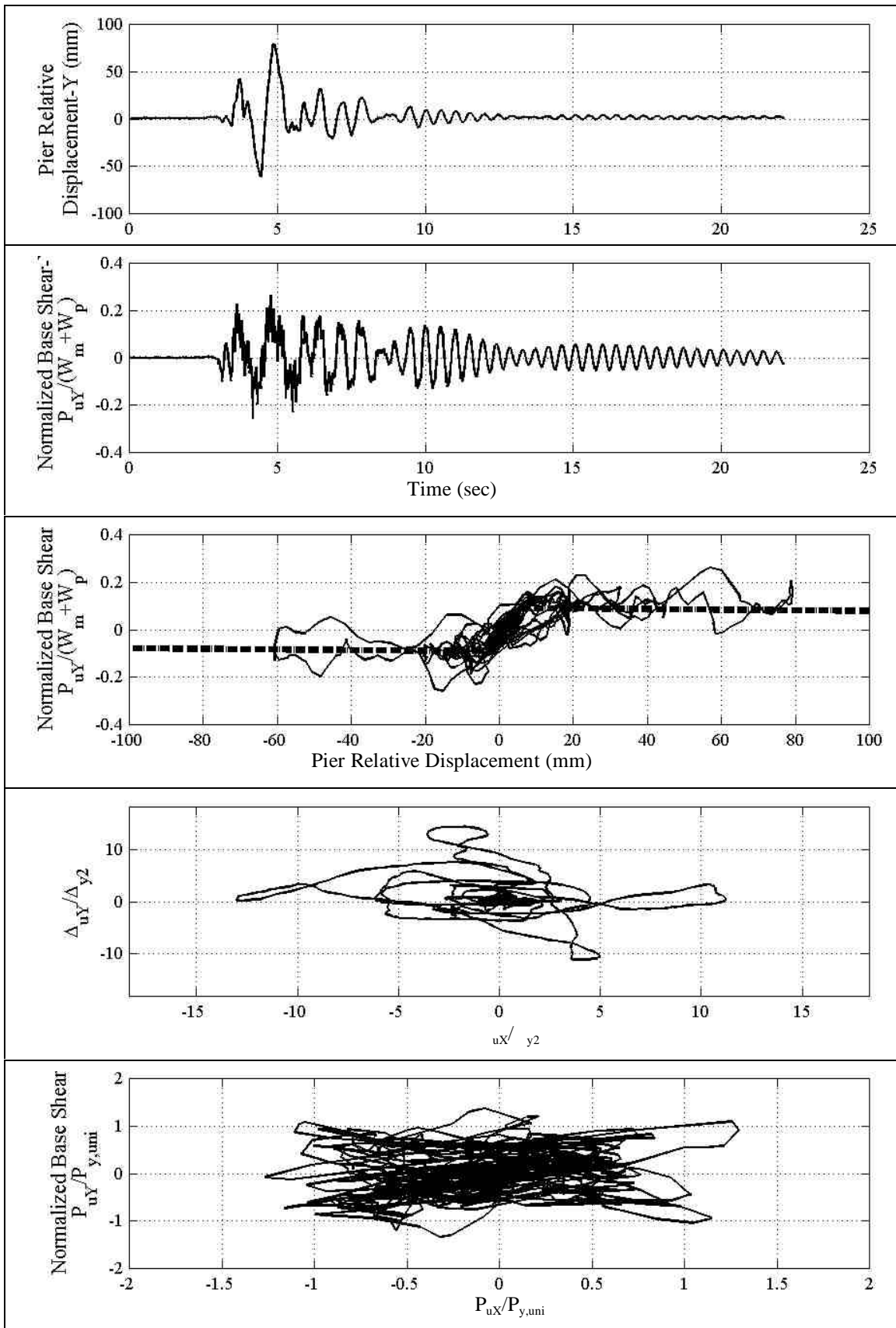
295

FIGURE 6-93 (Cont.)   Experimental Response Results; Synthetic 150%, $_L$=1.0 (cont.) (f) Pier Relative Displacement-Y, (g) Normalized Pier Base Shear-Y, (h) Pier Hysteretic, (i) Normalized X-Y Plane Displacement, (j) Normalized X-Y Base Shear

FIGURE 6-94   Experimental Response Results; Newhall 100%, $\zeta_L=0$ (a) Pier Relative Displacement-X, (b) Normalized Pier Base Shear-X, (c) Pier Hysteretic Response-X, (d) Pier Leg Vertical Reactions, (e) Damper Hysteretic Response

297

FIGURE 6-94 (Cont.)   Experimental Response Results; Newhall 100%, ζ_L=0 (cont.) (f) Pier Relative Displacement-Y, (g) Normalized Pier Base Shear-Y, (h) Pier Hysteretic, (i) Normalized X-Y Plane Displacement, (j) Normalized X-Y Base Shear
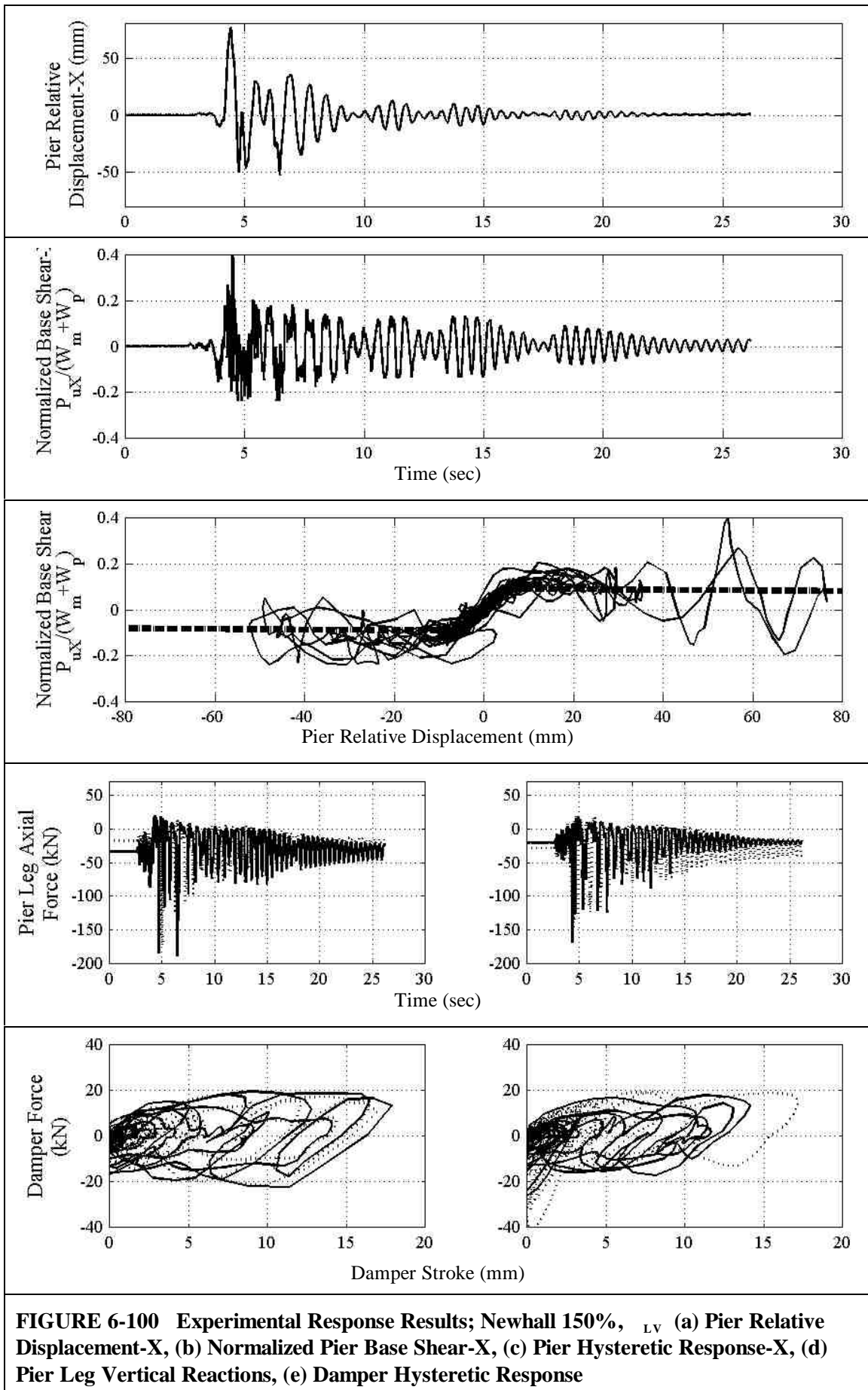
FIGURE 6-95   Experimental Response Results; Synthetic 100%, $_L$=0 (a) Pier Relative Displacement-X, (b) Normalized Pier Base Shear-X, (c) Pier Hysteretic Response-X, (d) Pier Leg Vertical Reactions, (e) Damper Hysteretic Response
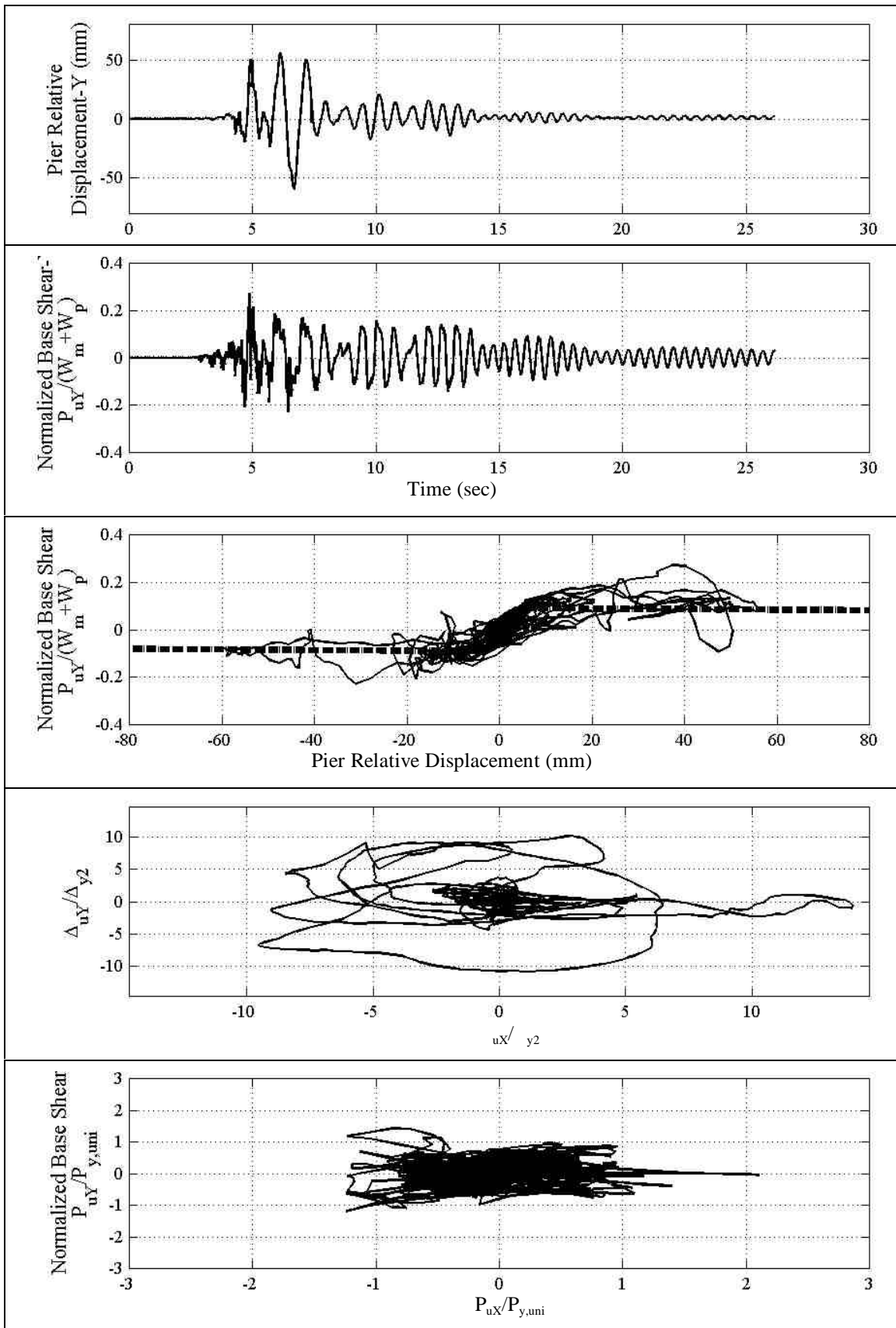
299

FIGURE 6-95 (Cont.)   Experimental Response Results; Synthetic 100%, ξ_L=0 (cont.) (f) Pier Relative Displacement-Y, (g) Normalized Pier Base Shear-Y, (h) Pier Hysteretic, (i) Normalized X-Y Plane Displacement, (j) Normalized X-Y Base Shear
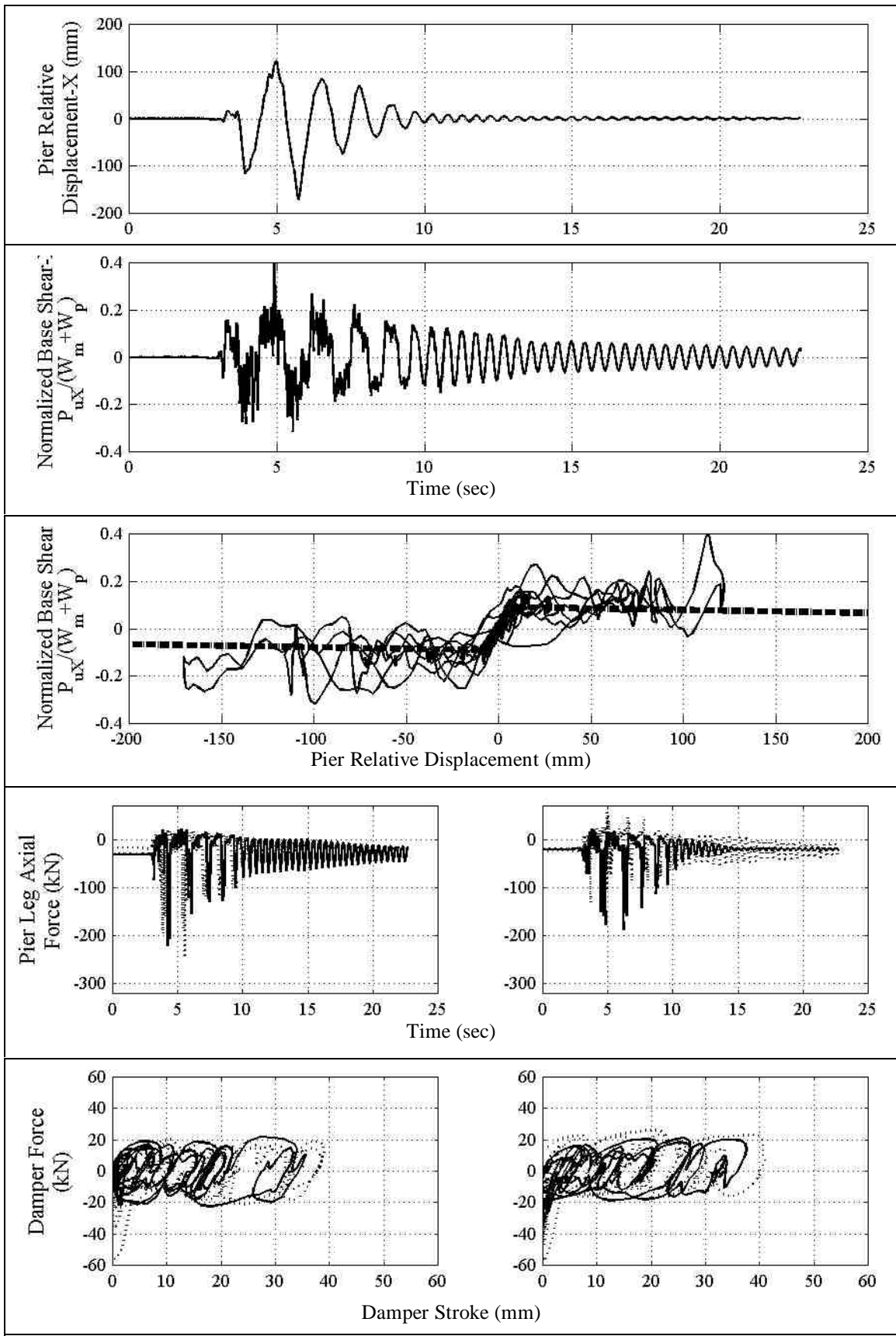
FIGURE 6-96   Experimental Response Results; Newhall 150%, $_L$=0 (a) Pier Relative Displacement-X, (b) Normalized Pier Base Shear-X, (c) Pier Hysteretic Response-X, (d) Pier Leg Vertical Reactions, (e) Damper Hysteretic Response
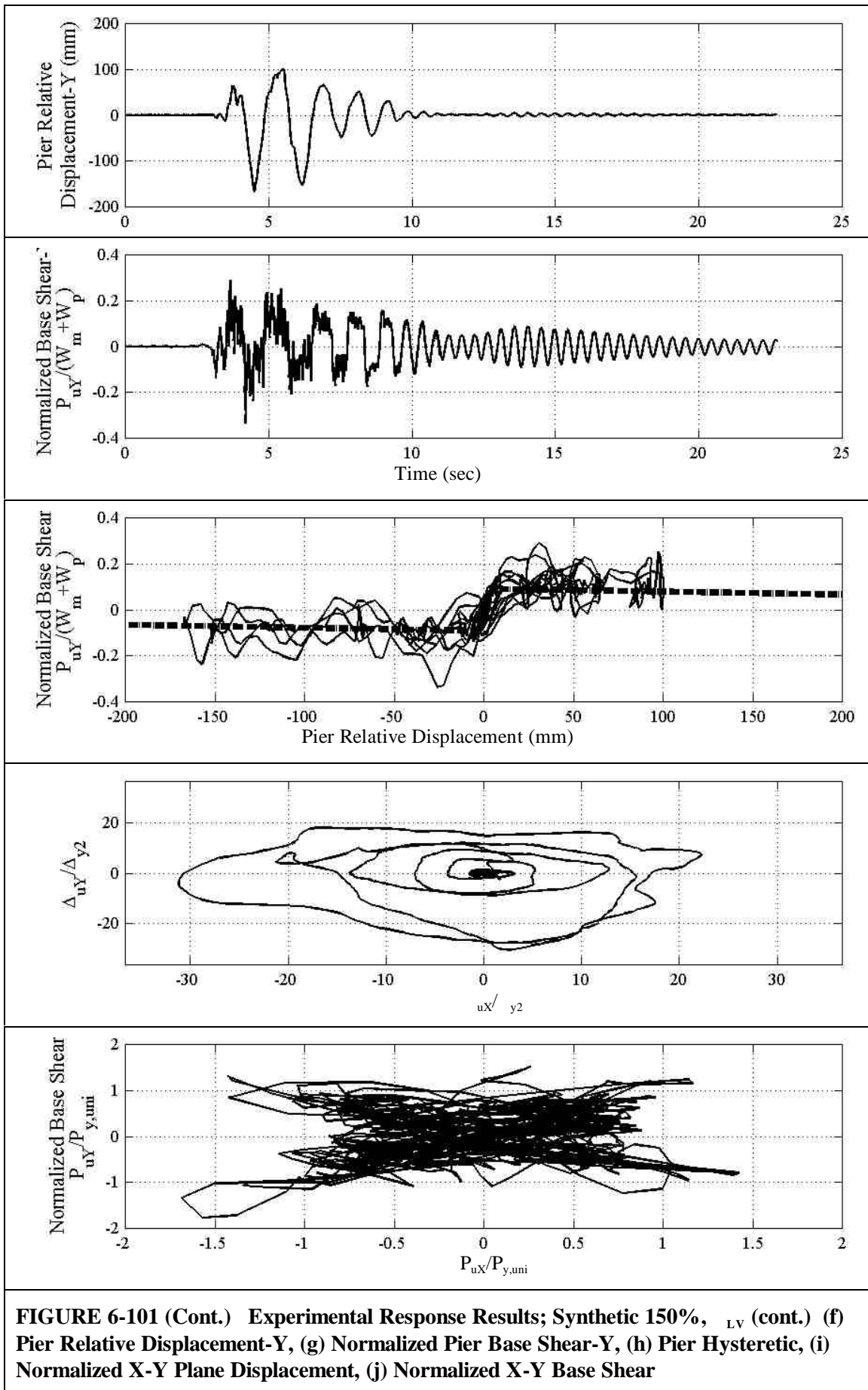
FIGURE 6-96 (Cont.)   Experimental Response Results; Newhall 150%, $_L$=0 (cont.) (f) Pier Relative Displacement-Y, (g) Normalized Pier Base Shear-Y, (h) Pier Hysteretic, (i) Normalized X-Y Plane Displacement, (j) Normalized X-Y Base Shear

FIGURE 6-97   Experimental Response Results; Synthetic 150%, $_L$=0 (a) Pier Relative Displacement-X, (b) Normalized Pier Base Shear-X, (c) Pier Hysteretic Response-X, (d) Pier Leg Vertical Reactions, (e) Damper Hysteretic Response

303

FIGURE 6-97 (Cont.)   Experimental Response Results; Synthetic 150%, ζ_L=0 (cont.) (f) Pier Relative Displacement-Y, (g) Normalized Pier Base Shear-Y, (h) Pier Hysteretic, (i) Normalized X-Y Plane Displacement, (j) Normalized X-Y Base Shear
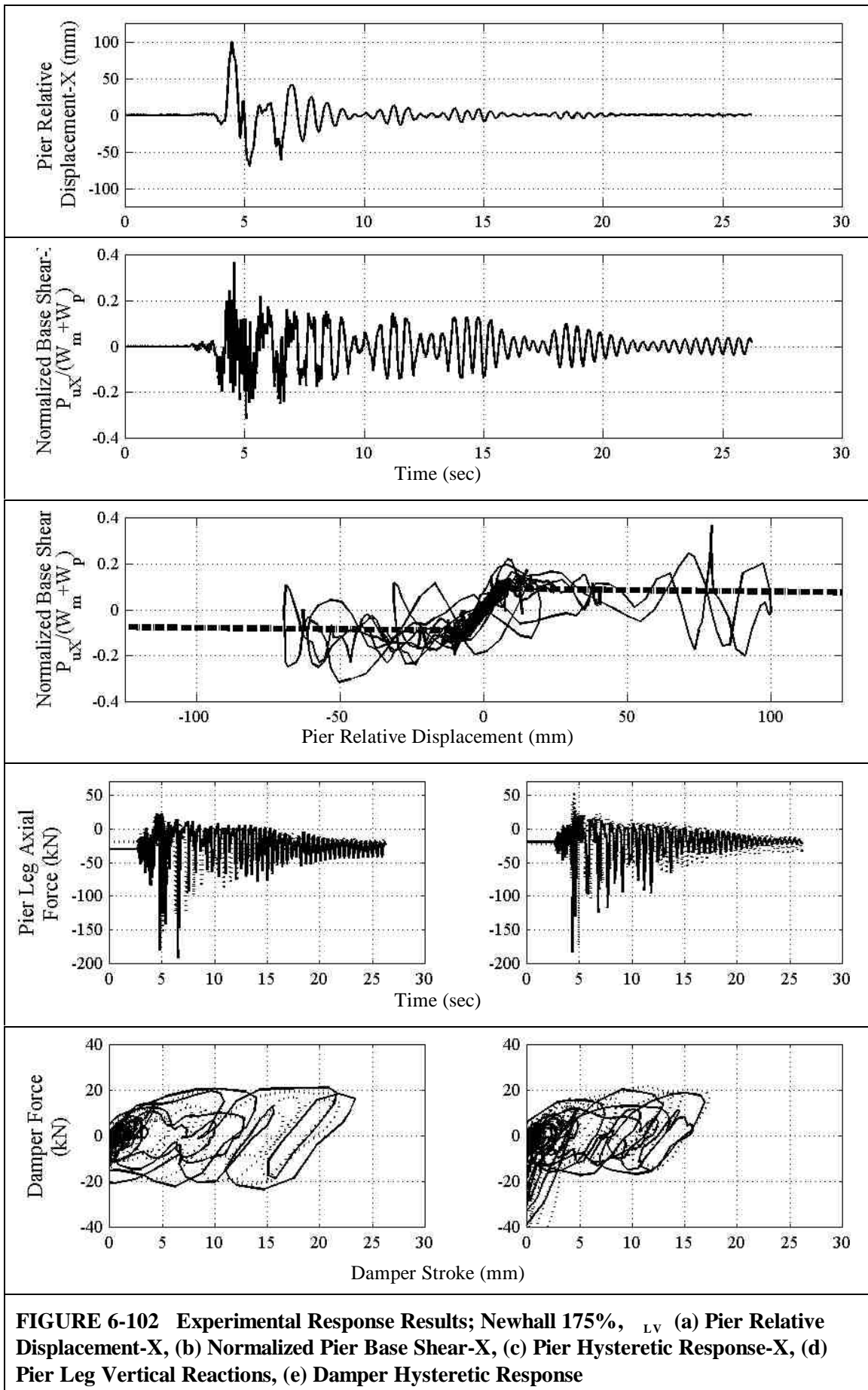
FIGURE 6-98   Experimental Response Results; Newhall 100%, LV (a) Pier Relative Displacement-X, (b) Normalized Pier Base Shear-X, (c) Pier Hysteretic Response-X, (d) Pier Leg Vertical Reactions, (e) Damper Hysteretic Response
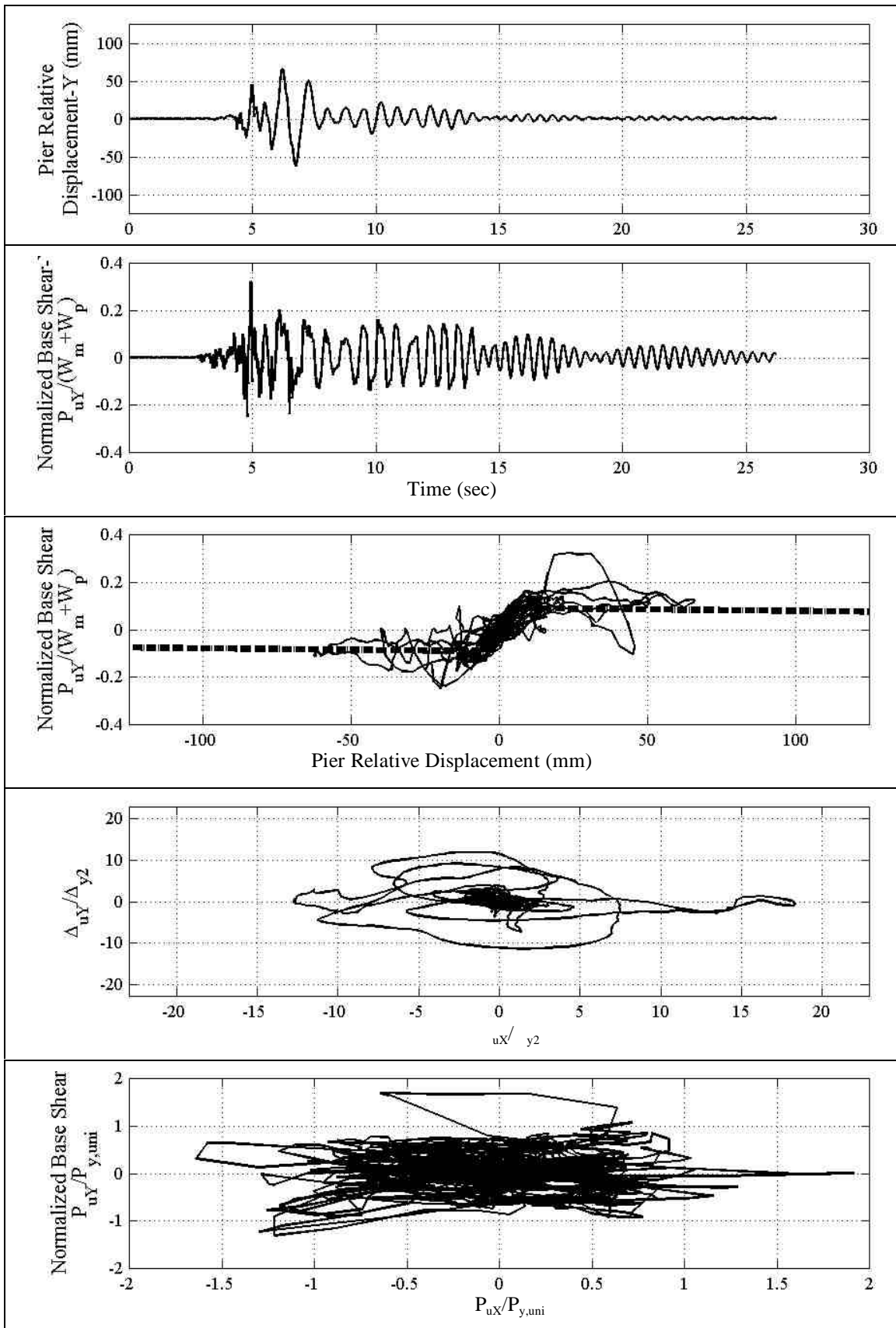
305

FIGURE 6-98 (Cont.)   Experimental Response Results; Newhall 100%, $_{LV}$ (cont.) (f) Pier Relative Displacement-Y, (g) Normalized Pier Base Shear-Y, (h) Pier Hysteretic, (i) Normalized X-Y Plane Displacement, (j) Normalized X-Y Base Shear
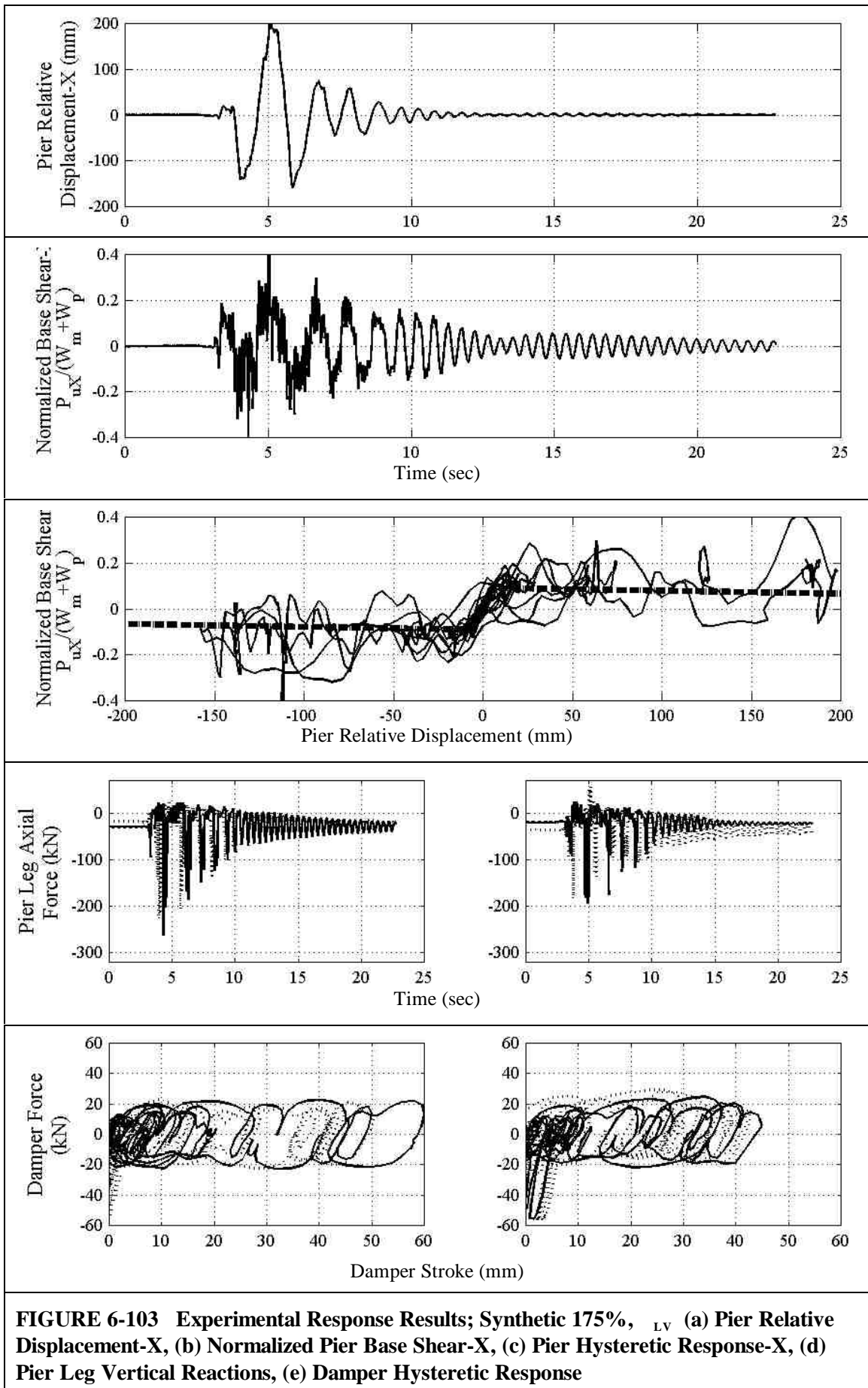
FIGURE 6-99 Experimental Response Results; Synthetic 100%, LV (a) Pier Relative Displacement-X, (b) Normalized Pier Base Shear-X, (c) Pier Hysteretic Response-X, (d) Pier Leg Vertical Reactions, (e) Damper Hysteretic Response
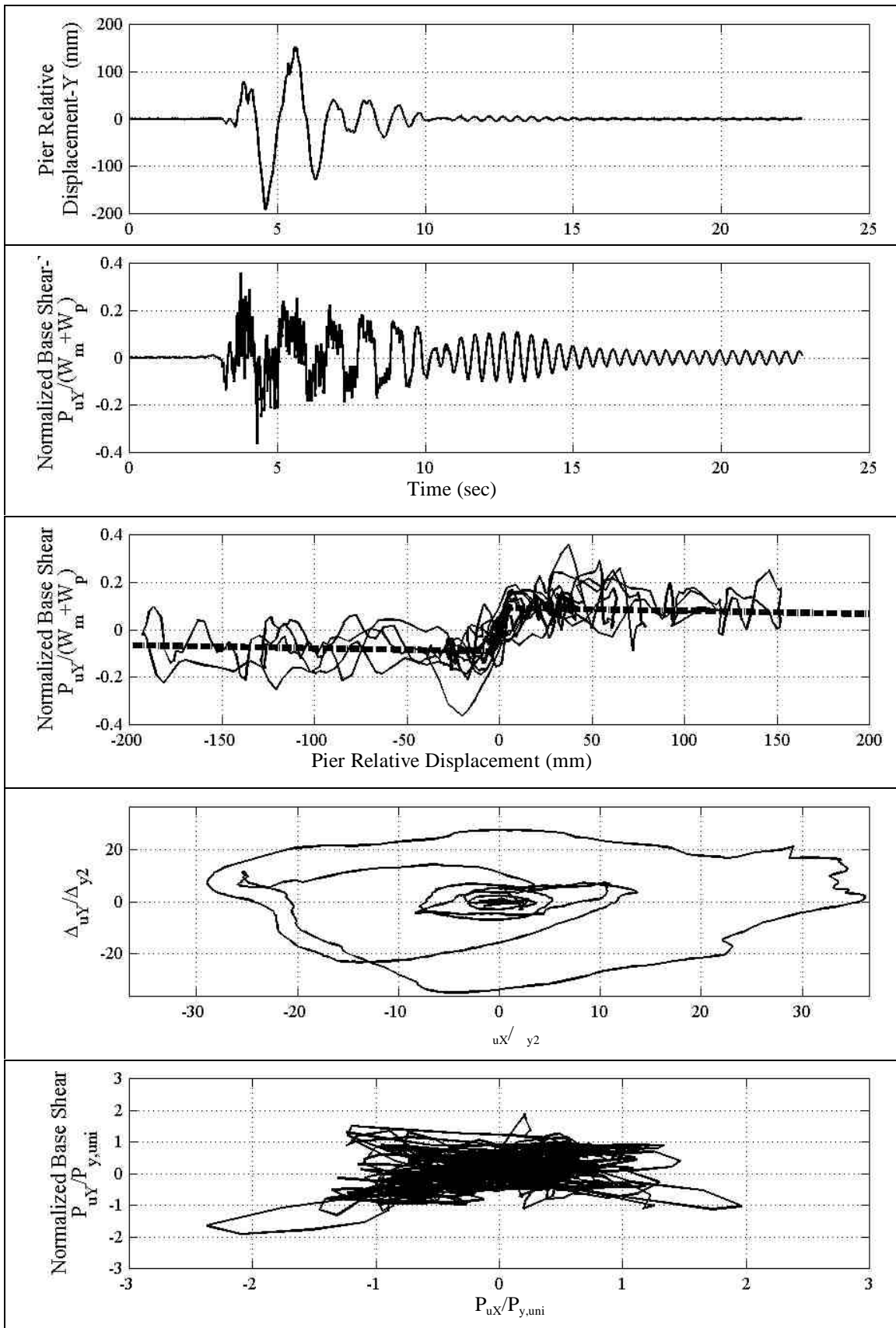
FIGURE 6-99 (Cont.)   Experimental Response Results; Synthetic 100%, $_{LV}$ (cont.) (f) Pier Relative Displacement-Y, (g) Normalized Pier Base Shear-Y, (h) Pier Hysteretic, (i) Normalized X-Y Plane Displacement, (j) Normalized X-Y Base Shear

FIGURE 6-100 Experimental Response Results; Newhall 150%, $_{LV}$ (a) Pier Relative Displacement-X, (b) Normalized Pier Base Shear-X, (c) Pier Hysteretic Response-X, (d) Pier Leg Vertical Reactions, (e) Damper Hysteretic Response

FIGURE 6-100 (Cont.)   Experimental Response Results; Newhall 150%, $_{LV}$ (cont.) (f) Pier Relative Displacement-Y, (g) Normalized Pier Base Shear-Y, (h) Pier Hysteretic, (i) Normalized X-Y Plane Displacement, (j) Normalized X-Y Base Shear
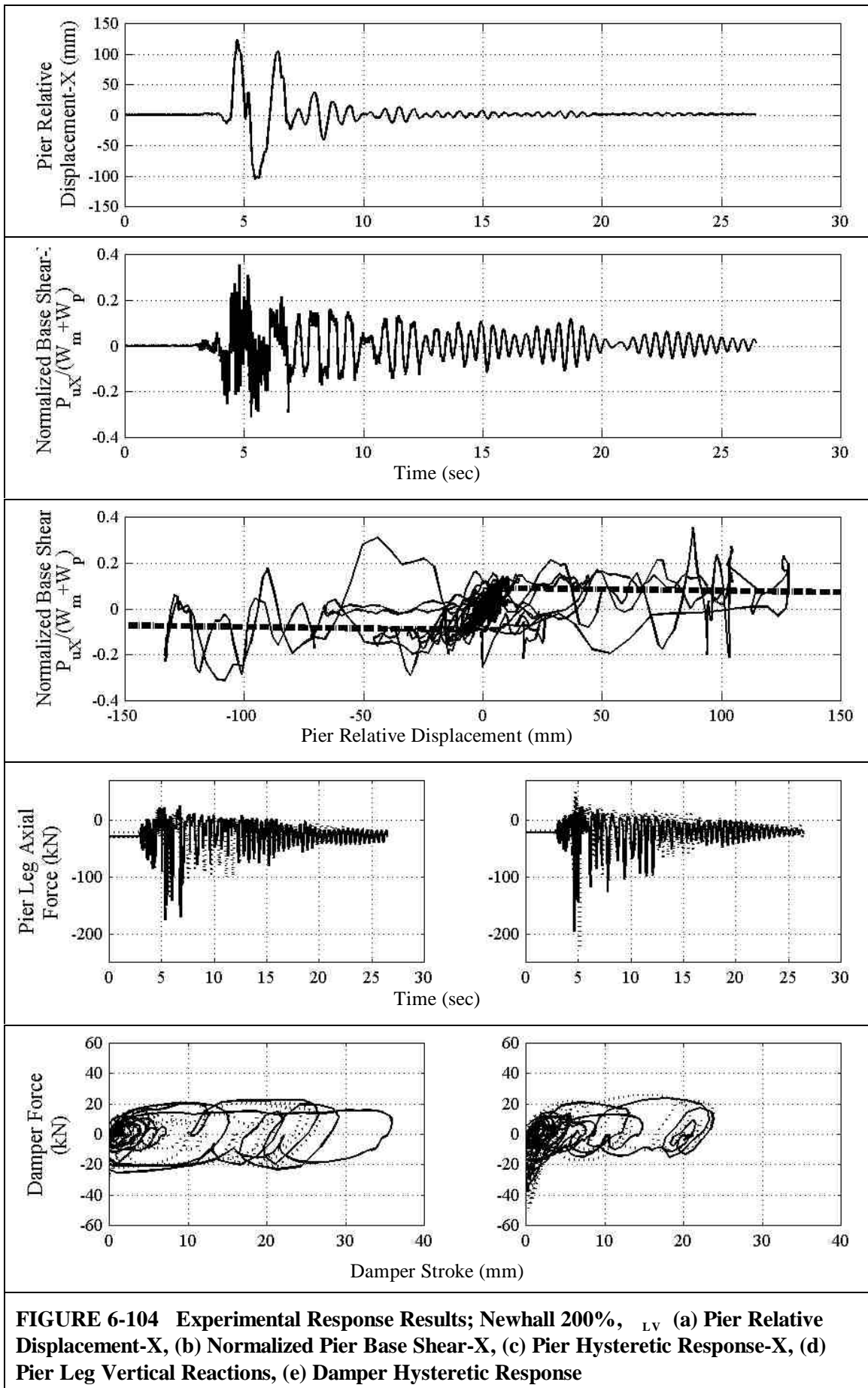
310

FIGURE 6-101 Experimental Response Results; Synthetic 150%, $_{LV}$ (a) Pier Relative Displacement-X, (b) Normalized Pier Base Shear-X, (c) Pier Hysteretic Response-X, (d) Pier Leg Vertical Reactions, (e) Damper Hysteretic Response
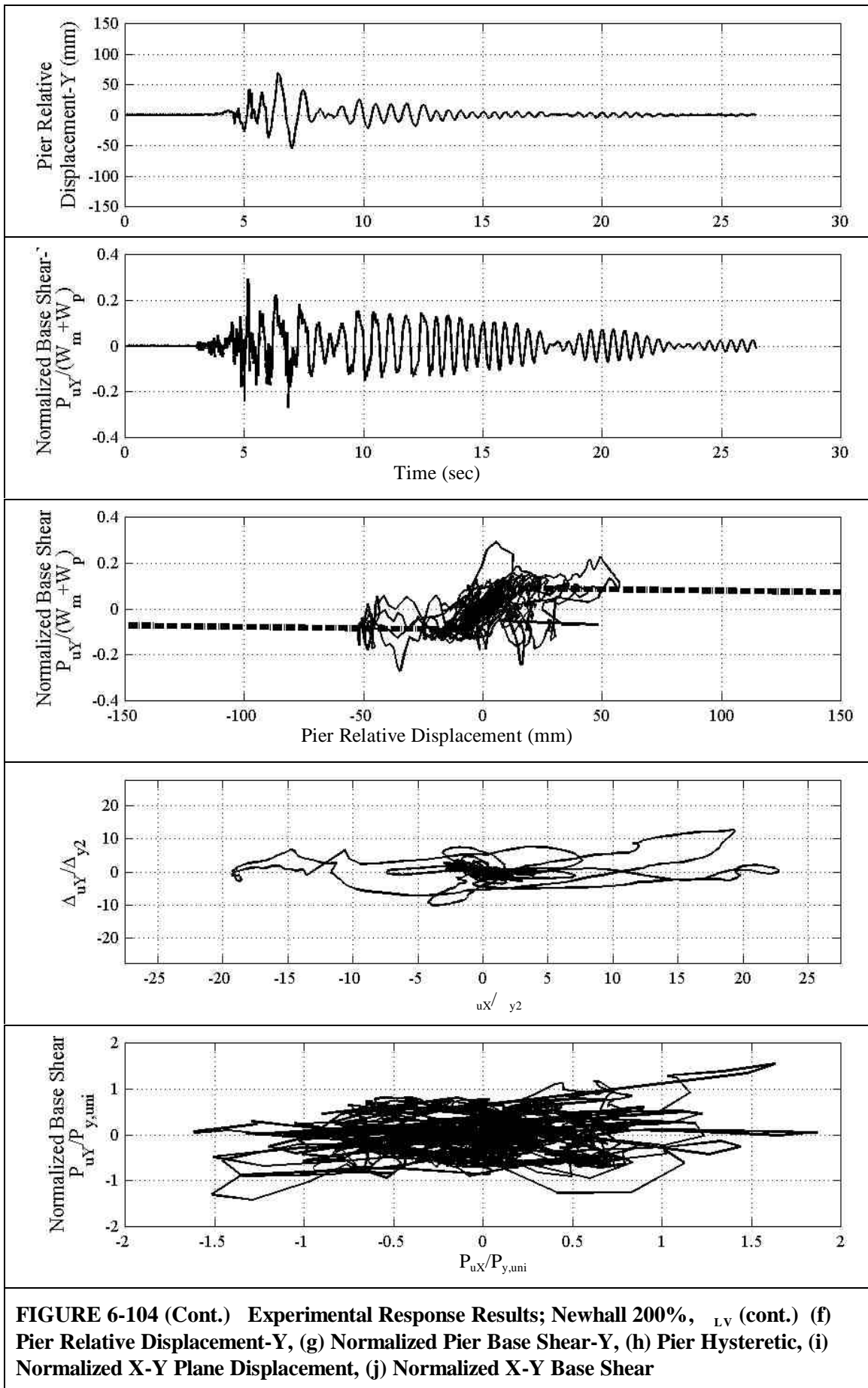
311

FIGURE 6-101 (Cont.)   Experimental Response Results; Synthetic 150%, ₗᵥ (cont.) (f) Pier Relative Displacement-Y, (g) Normalized Pier Base Shear-Y, (h) Pier Hysteretic, (i) Normalized X-Y Plane Displacement, (j) Normalized X-Y Base Shear

FIGURE 6-102 Experimental Response Results; Newhall 175%, _LV_ **(a) Pier Relative Displacement-X, (b) Normalized Pier Base Shear-X, (c) Pier Hysteretic Response-X, (d) Pier Leg Vertical Reactions, (e) Damper Hysteretic Response**

313

FIGURE 6-102 (Cont.) Experimental Response Results; Newhall 175%, LV (cont.) (f) Pier Relative Displacement-Y, (g) Normalized Pier Base Shear-Y, (h) Pier Hysteretic, (i) Normalized X-Y Plane Displacement, (j) Normalized X-Y Base Shear

FIGURE 6-103 Experimental Response Results; Synthetic 175%, $_{LV}$ (a) Pier Relative Displacement-X, (b) Normalized Pier Base Shear-X, (c) Pier Hysteretic Response-X, (d) Pier Leg Vertical Reactions, (e) Damper Hysteretic Response

315

FIGURE 6-103 (Cont.)   Experimental Response Results; Synthetic 175%, $_{LV}$ (cont.) (f) Pier Relative Displacement-Y, (g) Normalized Pier Base Shear-Y, (h) Pier Hysteretic, (i) Normalized X-Y Plane Displacement, (j) Normalized X-Y Base Shear

FIGURE 6-104   Experimental Response Results; Newhall 200%, $_{LV}$ (a) Pier Relative Displacement-X, (b) Normalized Pier Base Shear-X, (c) Pier Hysteretic Response-X, (d) Pier Leg Vertical Reactions, (e) Damper Hysteretic Response

317

FIGURE 6-104 (Cont.)   Experimental Response Results; Newhall 200%, $_{LV}$ (cont.) (f) Pier Relative Displacement-Y, (g) Normalized Pier Base Shear-Y, (h) Pier Hysteretic, (i) Normalized X-Y Plane Displacement, (j) Normalized X-Y Base Shear
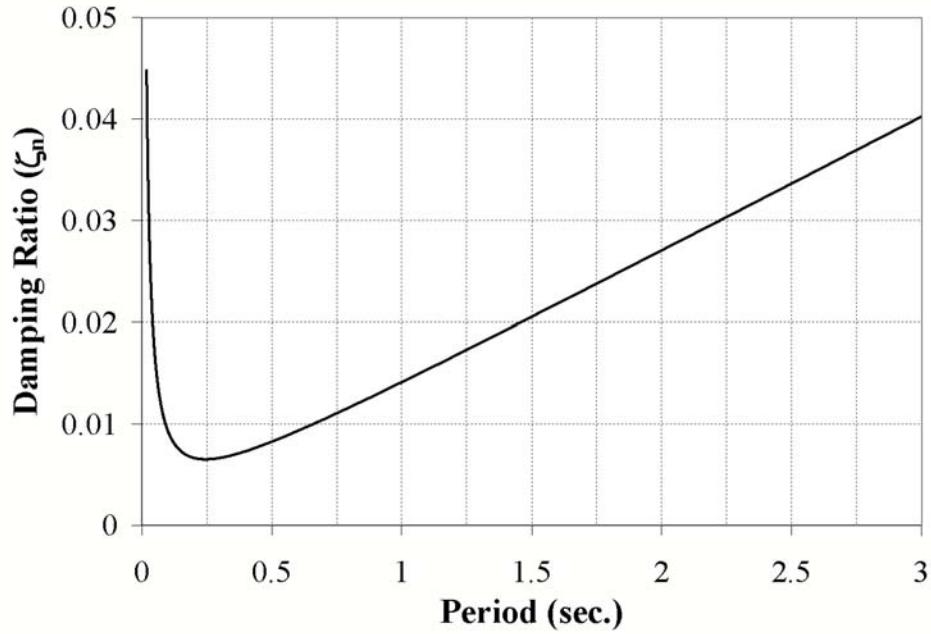
**FIGURE 6-105 Variation of Modal Damping Ratio Assigned through Rayleigh Damping Matrix in Analytical Model**
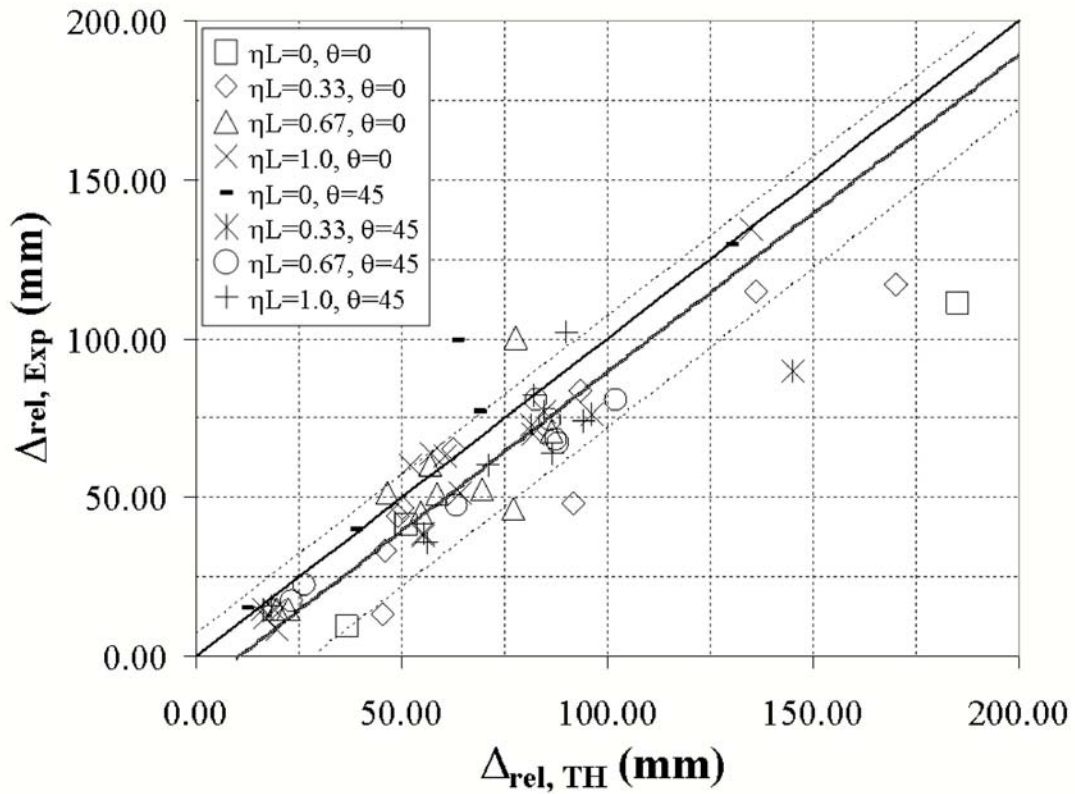
FIGURE 6-106 Experimental-Time History Comparison of Peak Response, Relative Pier Displacement (Δ_{rel}), Phase I
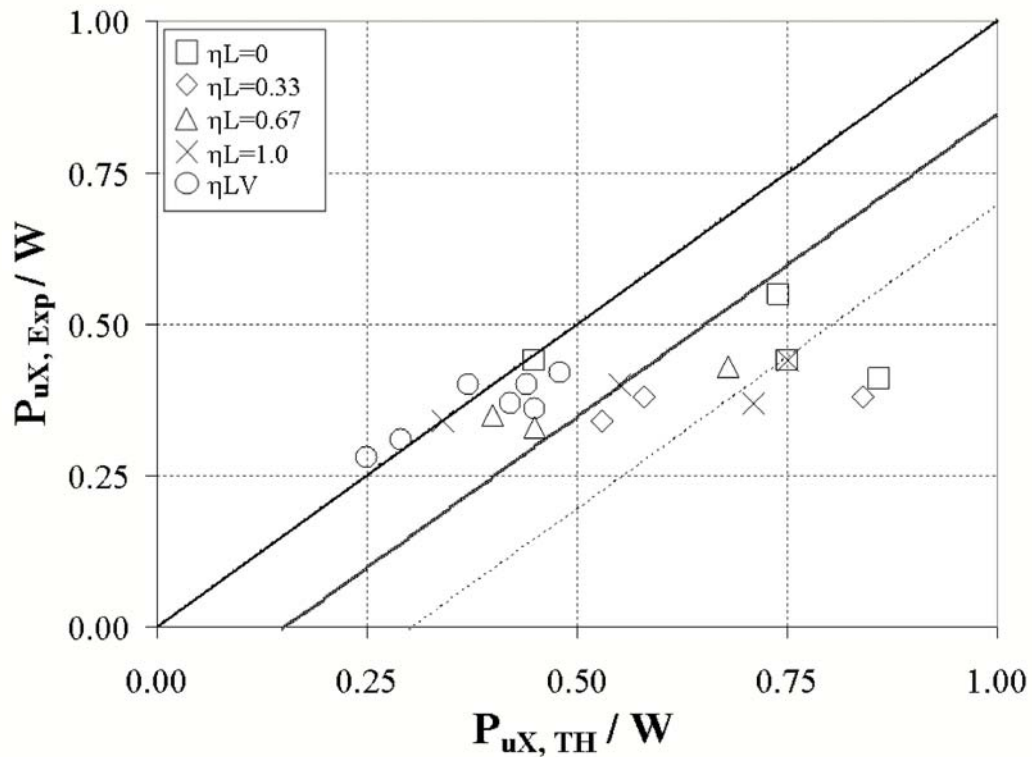
319
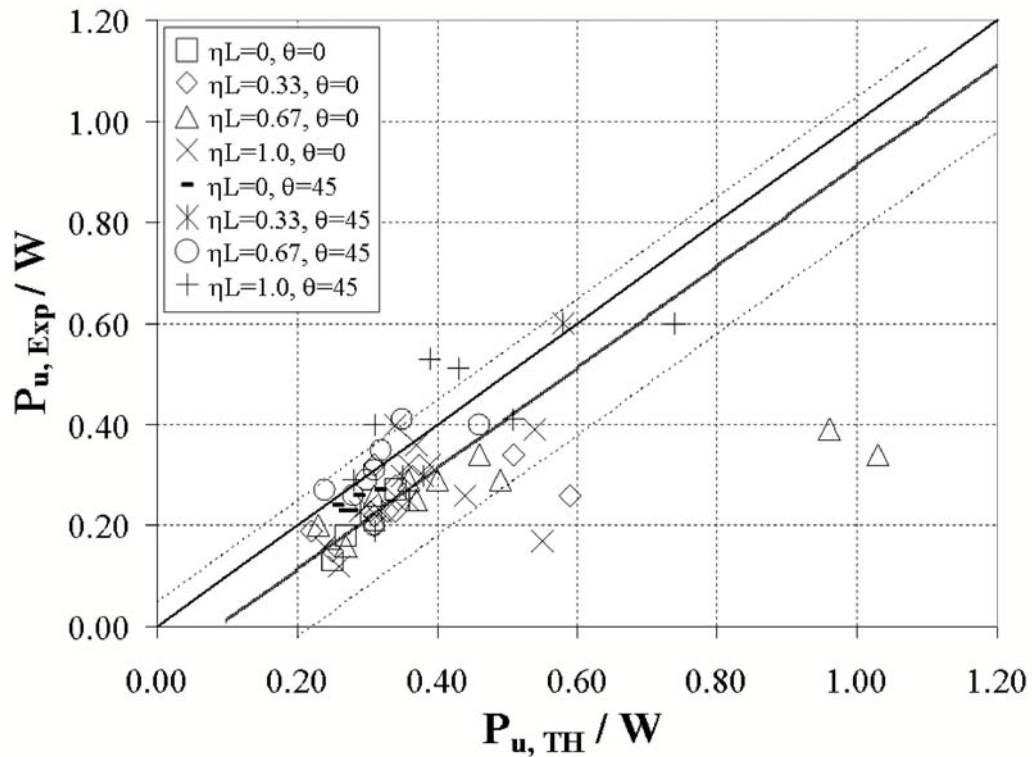
FIGURE 6-107 Experimental-Time History Comparison of Peak Response, Base Shear Force (P$_u$), Phase I
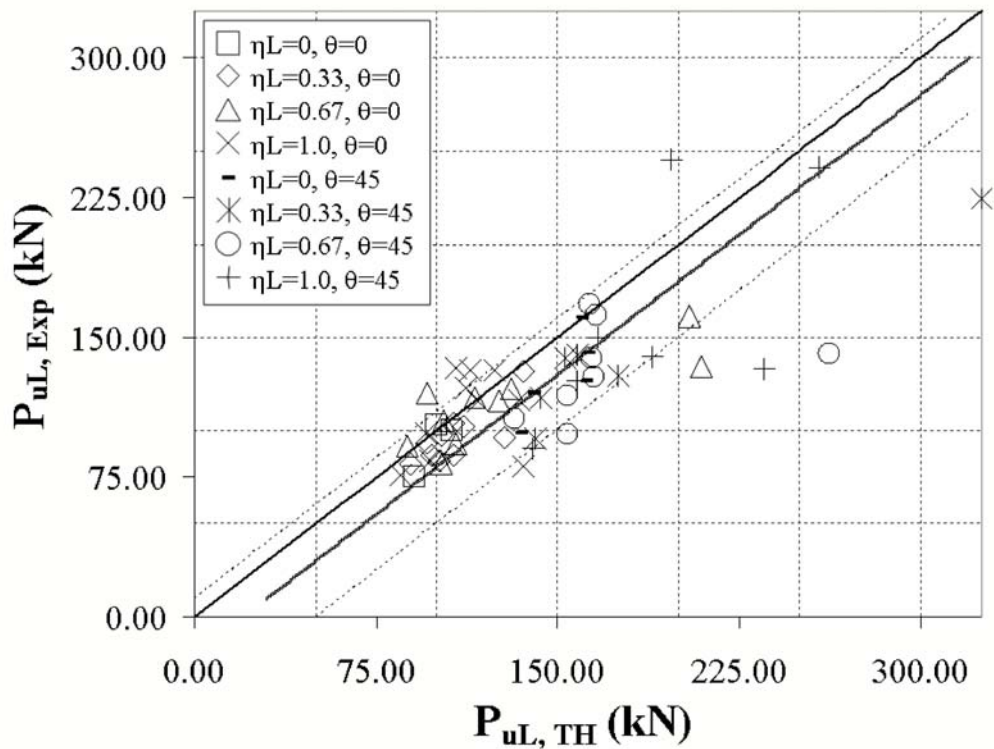
FIGURE 6-108 Experimental-Time History Comparison of Peak Response, Pier Leg Axial Force (P$_{uL}$), Phase I
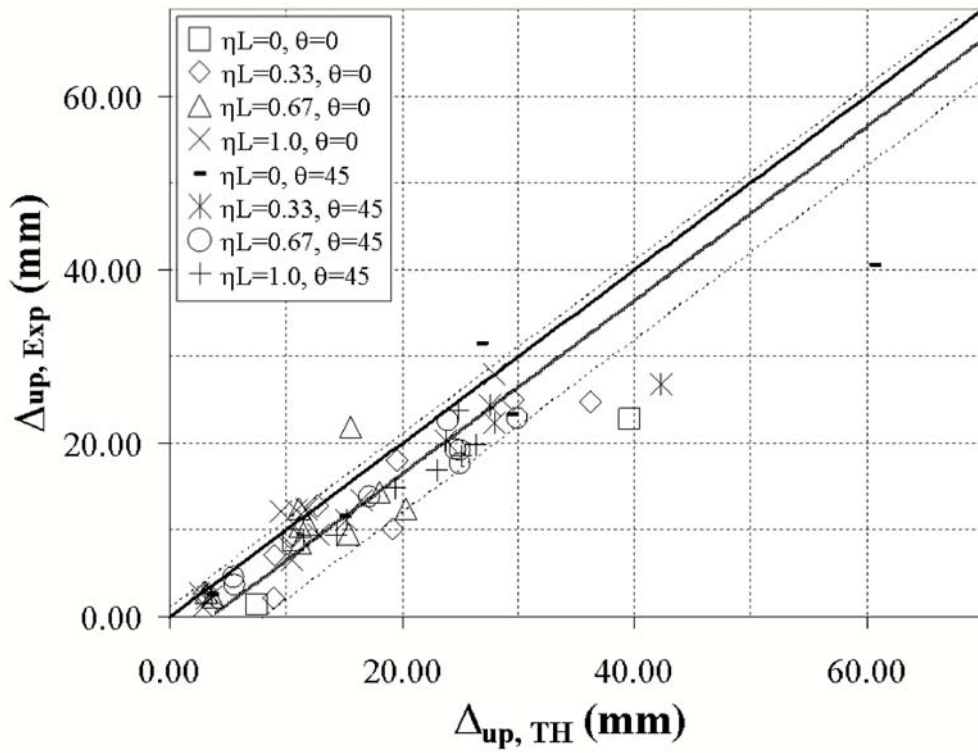
FIGURE 6-109 Experimental-Time History Comparison of Peak Response, Uplift Displacement (Δ_{up}), Phase I
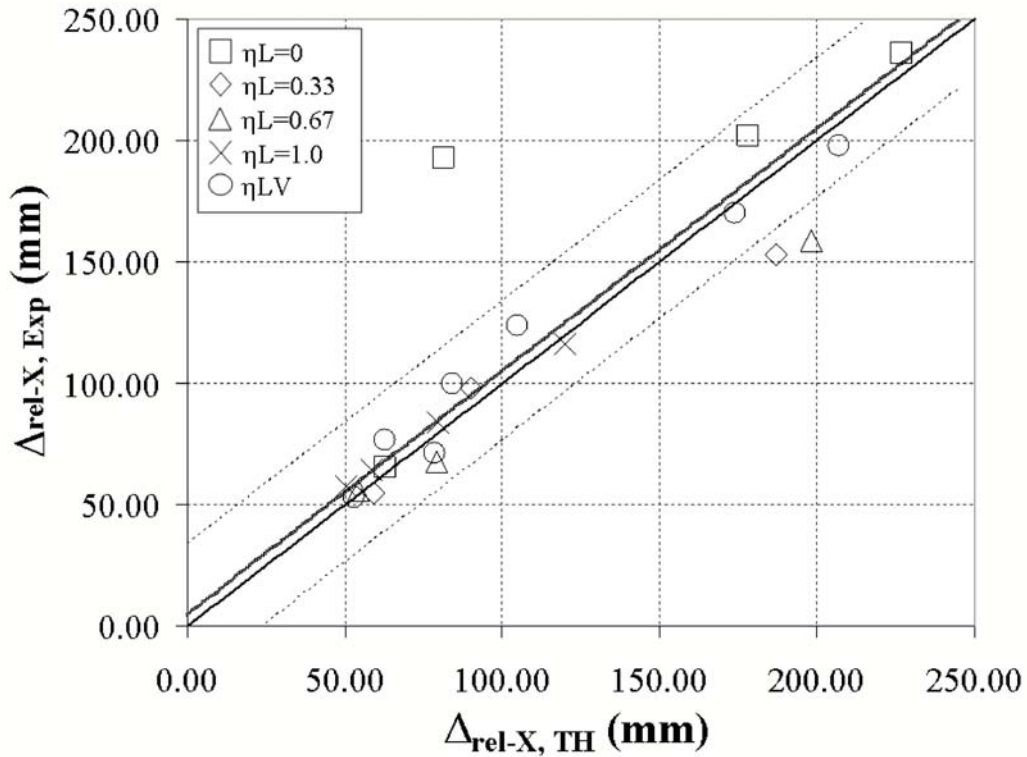
FIGURE 6-110 Experimental-Time History Comparison of Peak Response, Relative Pier Displacement X-direction ($\Delta_{rel,X}$), Phase II
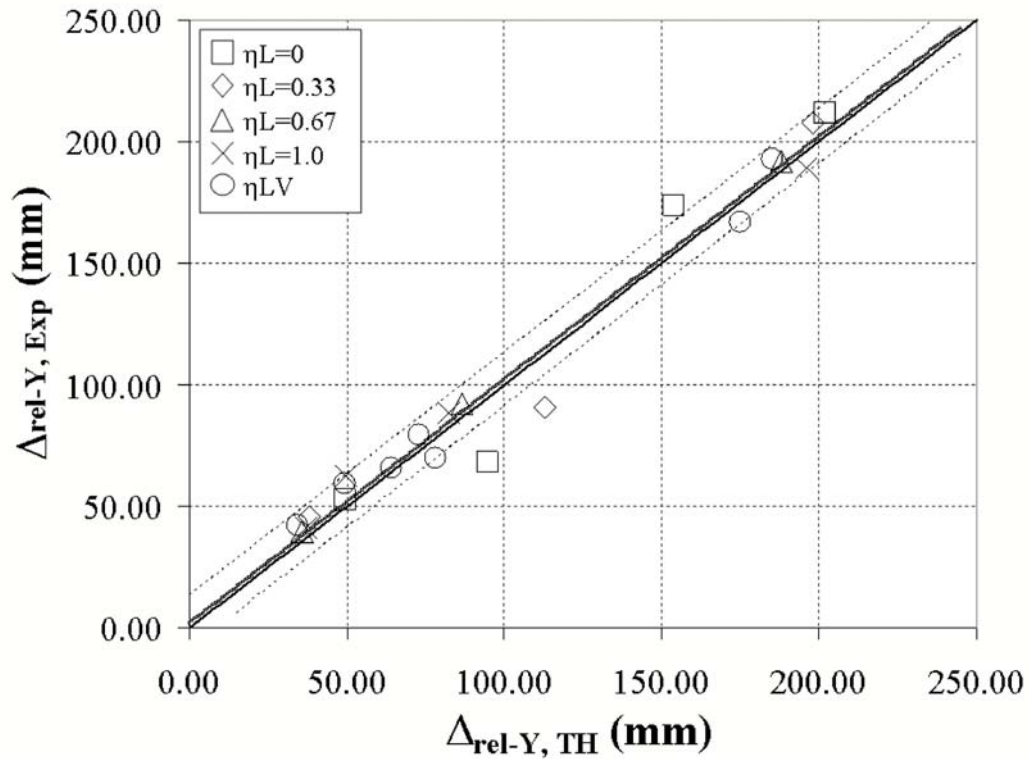
FIGURE 6-111 Experimental-Time History Comparison of Peak Response, Relative

Pier Displacement Y-direction ($\Delta_{rel,Y}$), Phase II

FIGURE 6-112 Experimental-Time History Comparison of Peak Response, Base

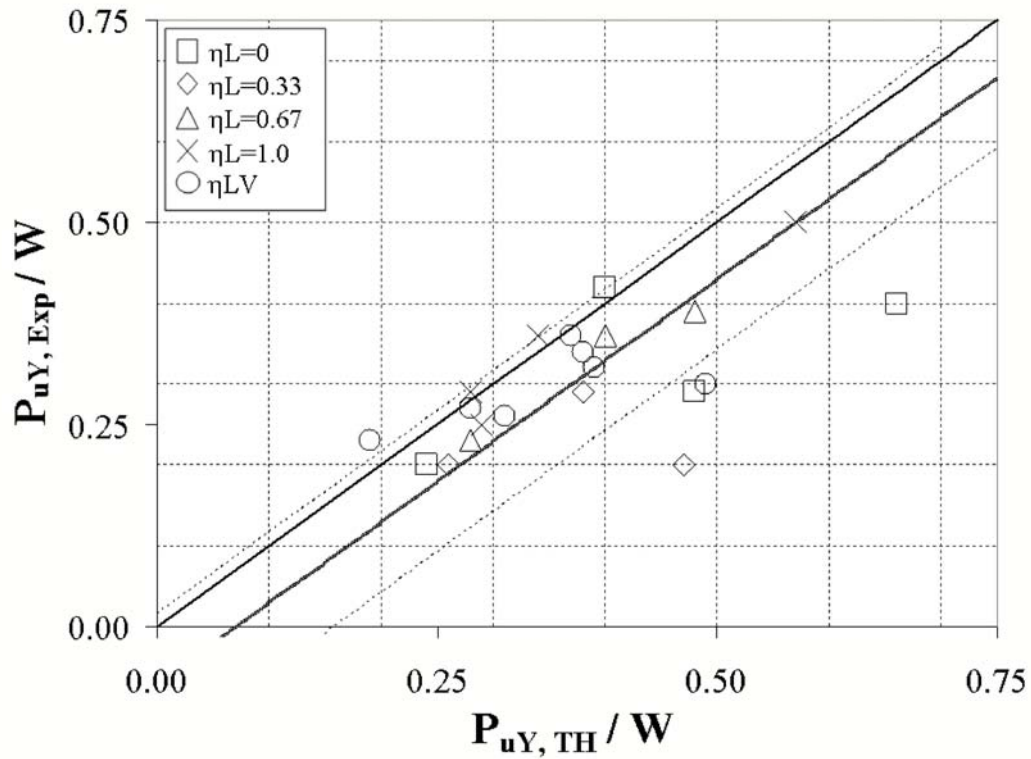Shear Force X-direction (P_{uX}), Phase II

322

FIGURE 6-113 Experimental-Time History Comparison of Peak Response, Base Shear Force Y-direction (P$_{uY}$), Phase II
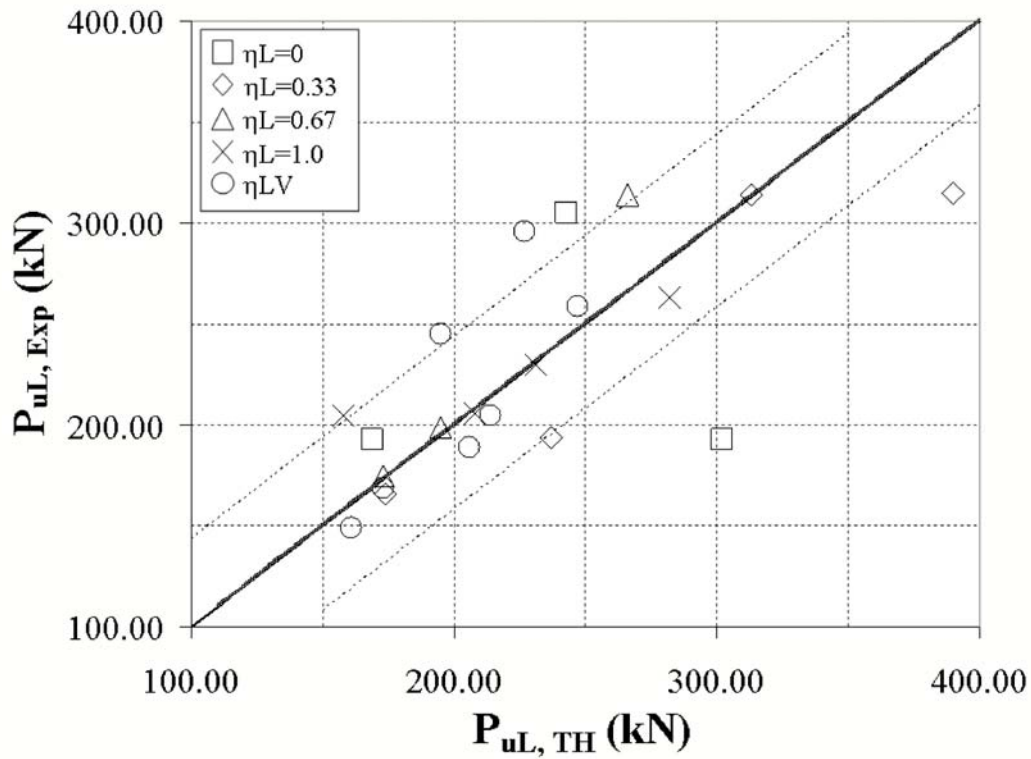

FIGURE 6-114 Experimental-Time History Comparison of Peak Response, Pier Leg Axial Force (P$_{uL}$), Phase II
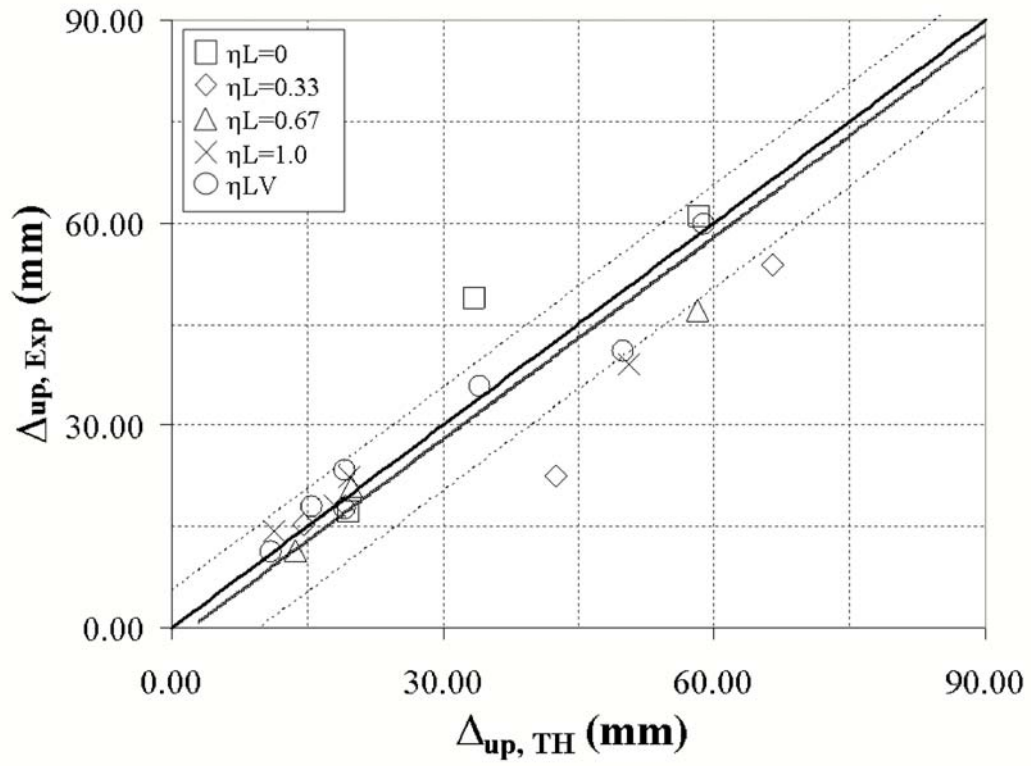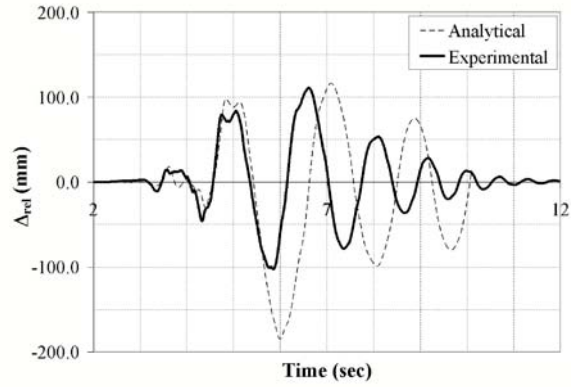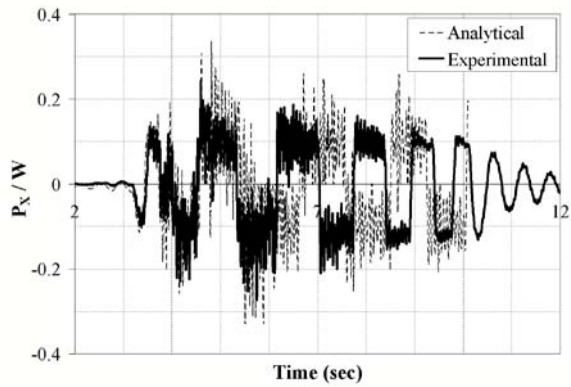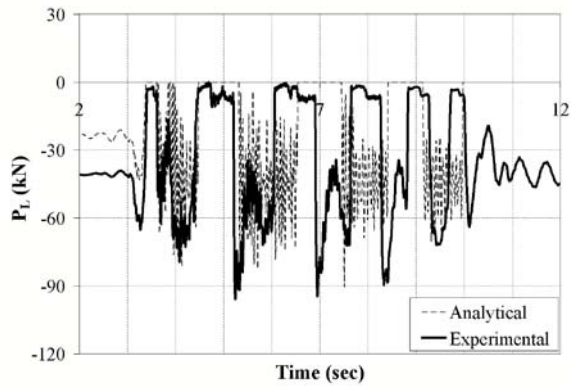
323

FIGURE 6-115 Experimental-Time History Comparison of Peak Response, Uplift Displacement (Δ_{up}), Phase II

FIGURE 6-116 Experimental-Time History Response Quantity Trace Comparison; Synthetic 100%, $_L$=0, PI (a) Pier Relative Displacement, (b) Normalized Pier Base Shear, and (c) Pier Leg Force (Leg 1)

325

**FIGURE 6-117 Experimental-Time History Response Quantity Trace Comparison;
Newhall 125%, $_L$=0.33, PI (a) Pier Relative Displacement, (b) Normalized Pier Base
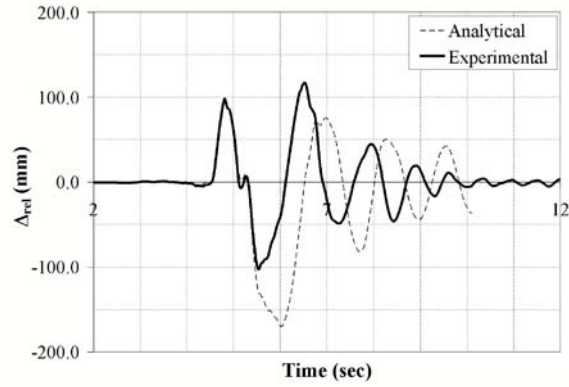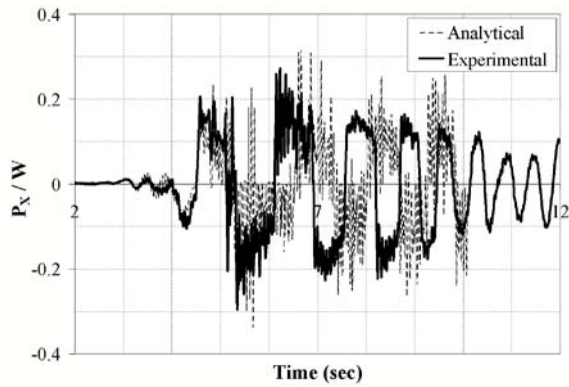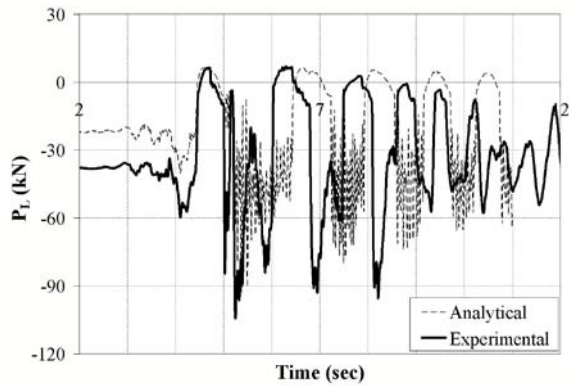Shear, and (c) Pier Leg Force (Leg 1)**

FIGURE 6-118 Experimental-Time History Response Quantity Trace Comparison; Synthetic 150%, μ_L=0.67, PI (a) Pier Relative Displacement, (b) Normalized Pier Base Shear, and (c) Pier Leg Force (Leg 1)

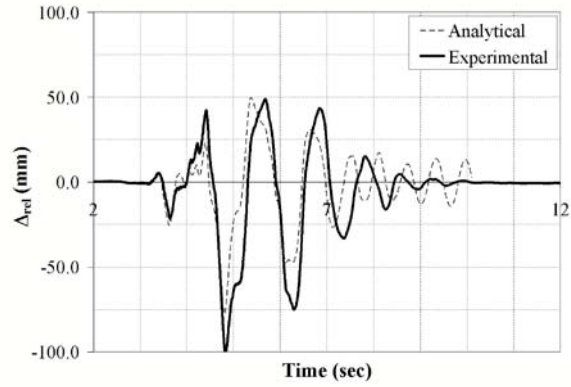**(a)**

(b)

(c)

FIGURE 6-119 Experimental-Time History Response Quantity Trace Comparison; Pulse P2, T_p=0.60sec, 100%, $_L$=1.0, PI (a) Pier Relative Displacement, (b) Normalized Pier Base Shear, and (c) Pier Leg Force (Leg 1)

FIGURE 6-120 Experimental-Time History Response Quantity Trace Comparison; Synthetic 150%, $_L$=0, PII (a) Pier Relative Displacement X, (b) Pier Relative Displacement Y, (c) Normalized Pier Base Shear X, (d) Normalized Pier Base Shear Y, (e) Pier Leg Force (Leg 1)
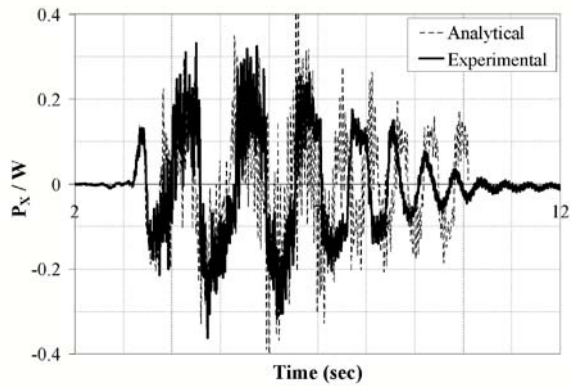
FIGURE 6-121 Experimental-Time History Response Quantity Trace Comparison; Synthetic 100%, μ_L=0.33, PII (a) Pier Relative Displacement X, (b) Pier Relative Displacement Y, (c) Normalized Pier Base Shear X, (d) Normalized Pier Base Shear Y, (e) Pier Leg Force (Leg 1)
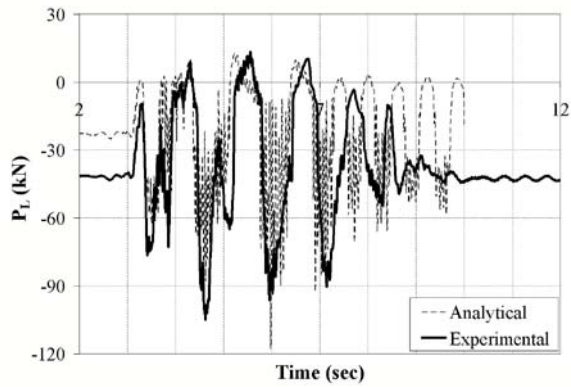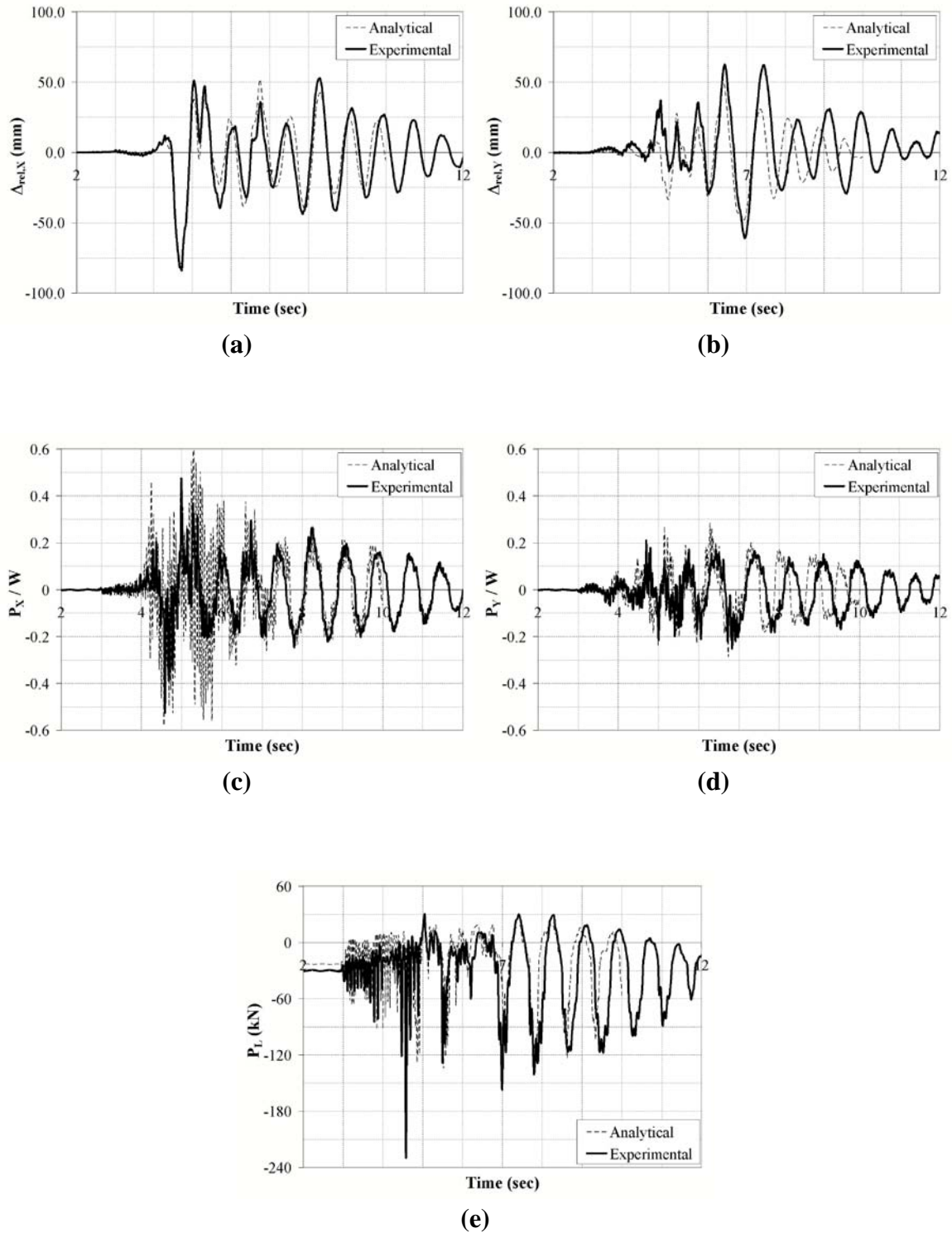
FIGURE 6-122 Experimental-Time History Response Quantity Trace Comparison;
Newhall 150%, μ_L=1.0, PII (a) Pier Relative Displacement X, (b) Pier Relative
Displacement Y, (c) Normalized Pier Base Shear X, (d) Normalized Pier Base Shear
Y, (e) Pier Leg Force (Leg 1)

FIGURE 6-123 Experimental-Time History Response Quantity Trace Comparison; Newhall 200%, $_{LV}$, PII (a) Pier Relative Displacement X, (b) Pier Relative Displacement Y, (c) Normalized Pier Base Shear X, (d) Normalized Pier Base Shear Y, (e) Pier Leg Force (Leg 1)
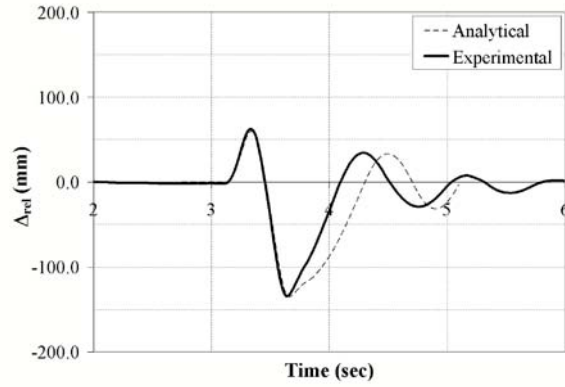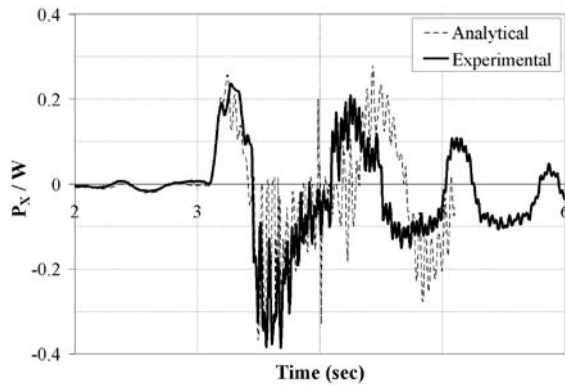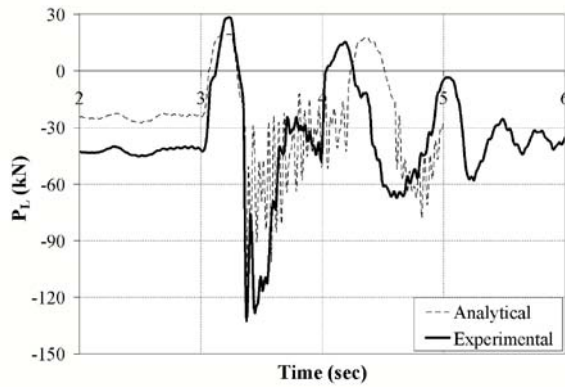
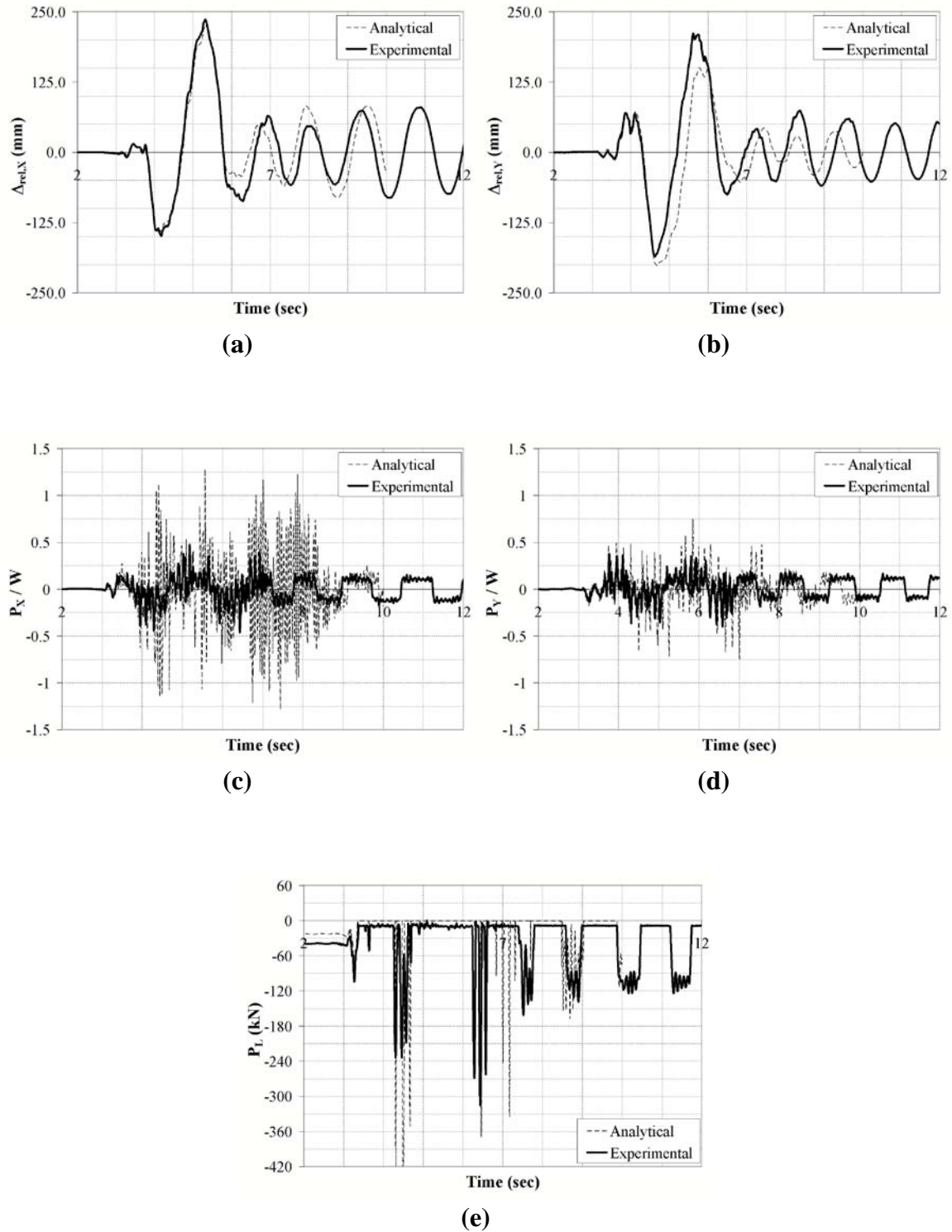**FIGURE 6-124 Experimental-Time History Response Quantity Trace Comparison; Synthetic 175%, $_{LV}$, PII (a) Pier Relative Displacement X, (b) Pier Relative Displacement Y, (c) Normalized Pier Base Shear X, (d) Normalized Pier Base Shear Y, (e) Pier Leg Force (Leg 1)**

333
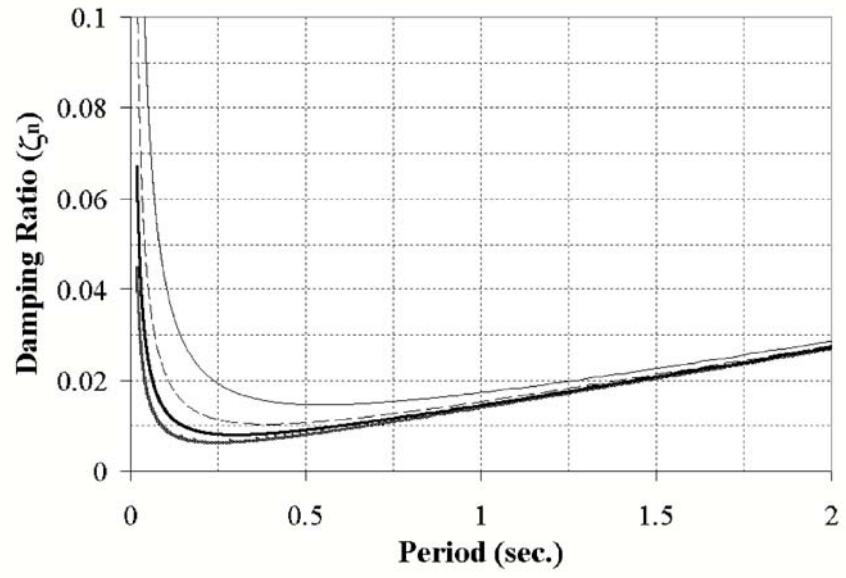
**FIGURE 6-125 Variation of Modal Damping Ratio with Increasing Stiffness
Proportional Damping**
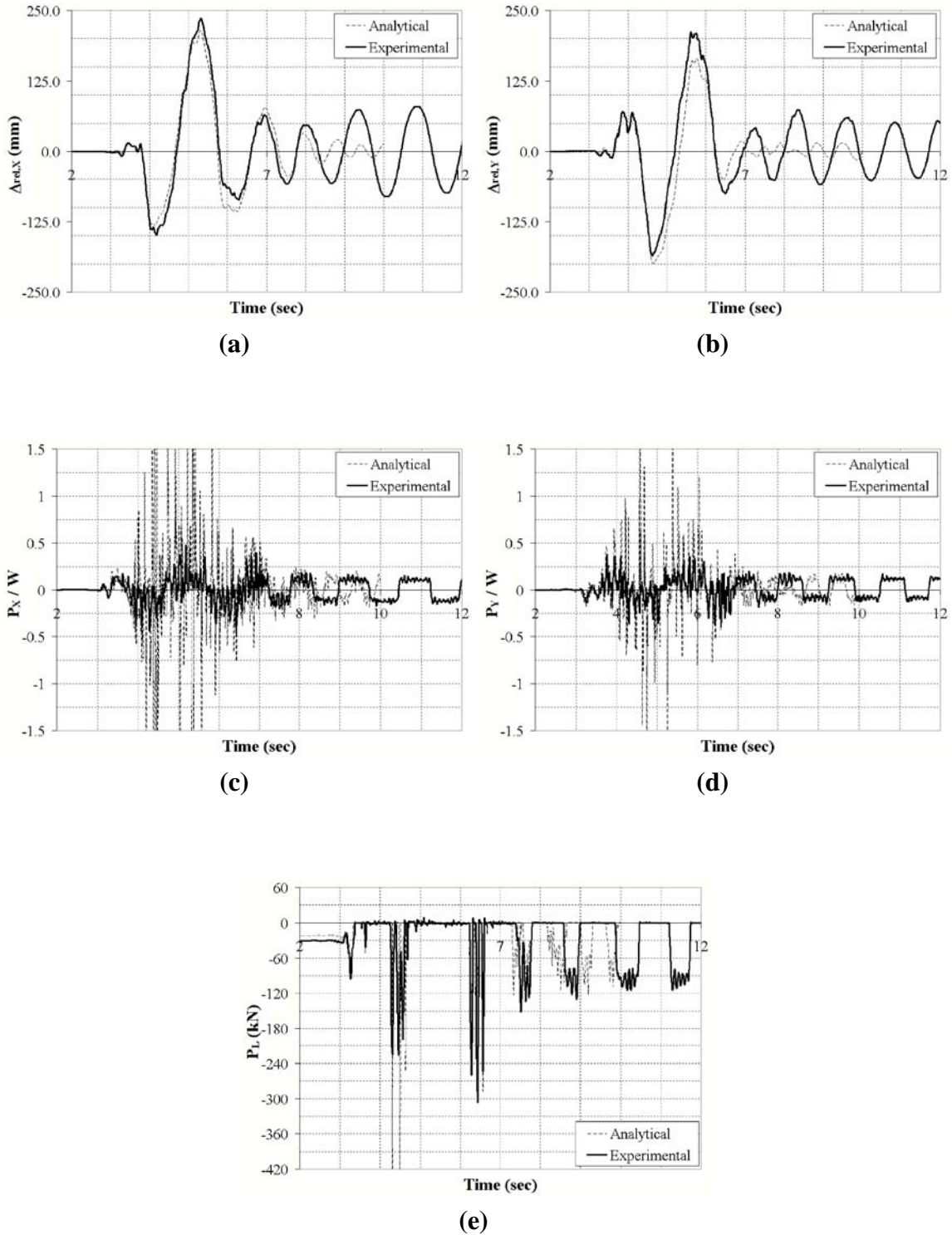
FIGURE 6-126 Experimental-Time History Response Quantity Trace Comparison; Synthetic 150%, $_L$=0, PII, Stiffness Proportional Damping (3%) (a) Pier Relative Displacement X, (b) Pier Relative Displacement Y, (c) Normalized Pier Base Shear X, (d) Normalized Pier Base Shear Y, (e) Pier Leg Force (Leg 1)
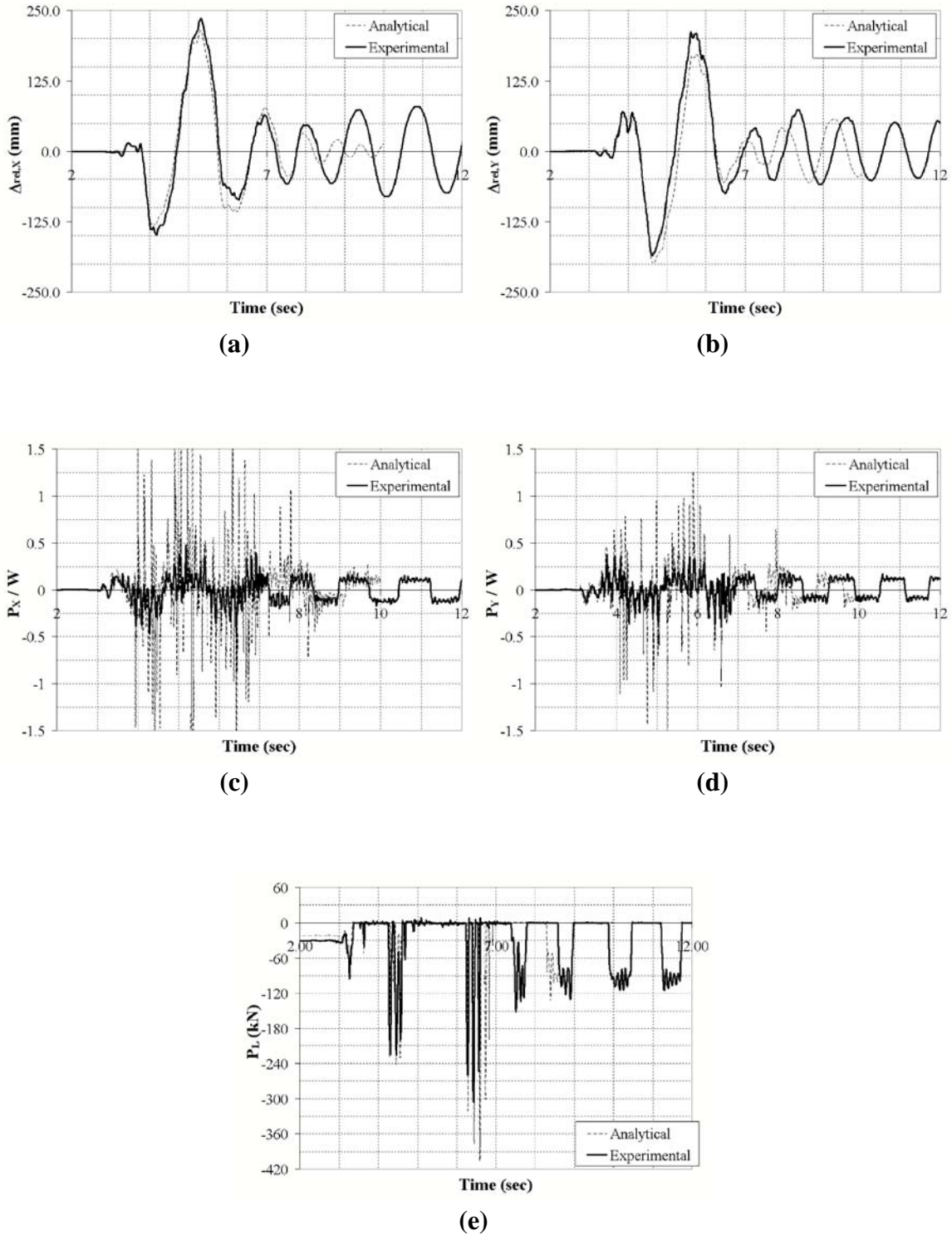
FIGURE 6-127 Experimental-Time History Response Quantity Trace Comparison; Synthetic 150%, $_L$=0, PII, Stiffness Proportional Damping (5%) (a) Pier Relative Displacement X, (b) Pier Relative Displacement Y, (c) Normalized Pier Base Shear X, (d) Normalized Pier Base Shear Y, (e) Pier Leg Force (Leg 1)
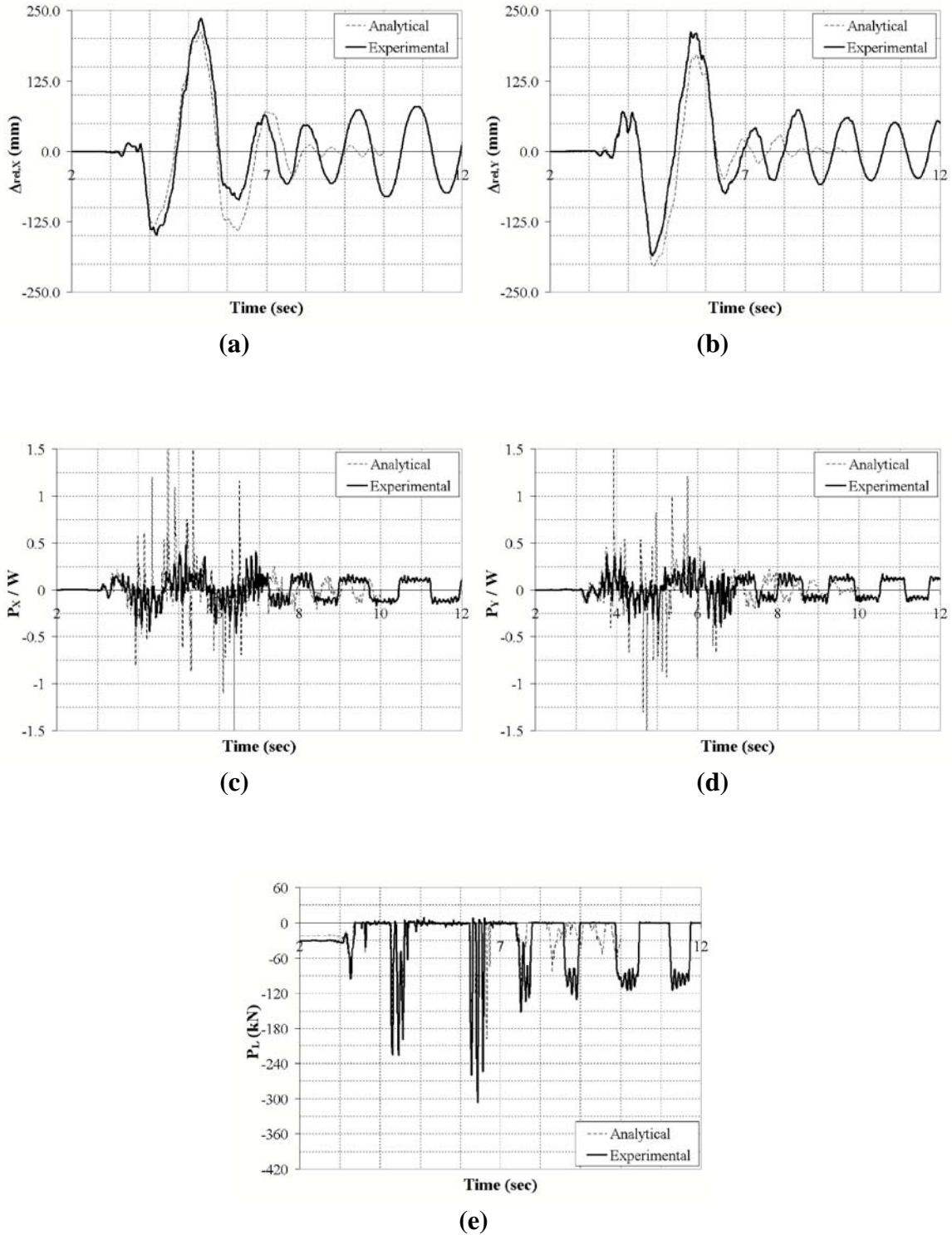
FIGURE 6-128 Experimental-Time History Response Quantity Trace Comparison; Synthetic 150%, ζ_L=0, PII, Stiffness Proportional Damping (10%) (a) Pier Relative Displacement X, (b) Pier Relative Displacement Y, (c) Normalized Pier Base Shear X, (d) Normalized Pier Base Shear Y, (e) Pier Leg Force (Leg 1)
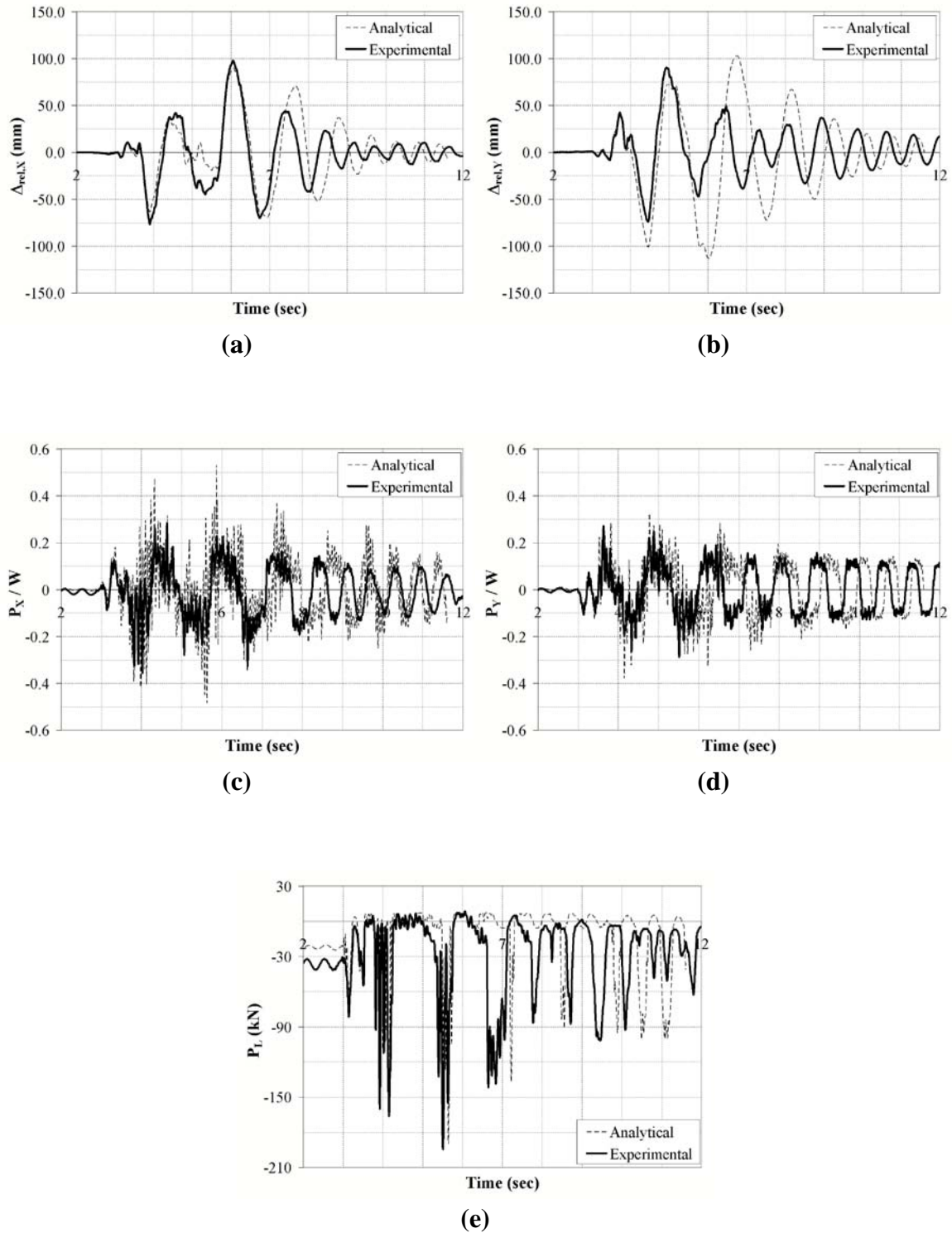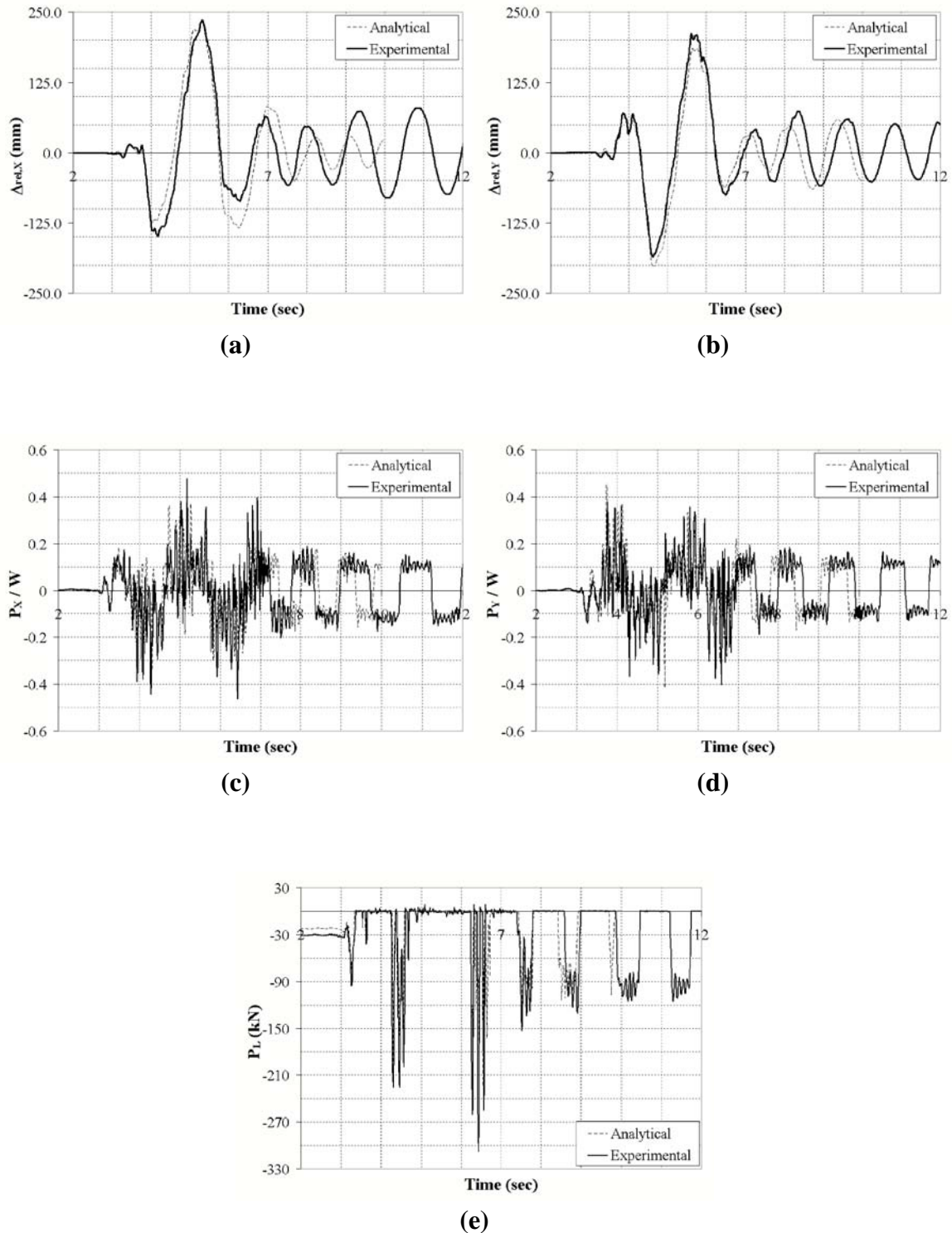
FIGURE 6-129 Experimental-Time History Response Quantity Trace Comparison; Synthetic 150%, $_L$=0, PII, Stiffness Proportional Damping (10%), Specimen Mass Removed (a) Pier Relative Displacement X, (b) Pier Relative Displacement Y, (c) Normalized Pier Base Shear X, (d) Normalized Pier Base Shear Y, (e) Pier Leg Force (Leg 1)

FIGURE 6-130 Modified Boundary Elements at Base of Structure
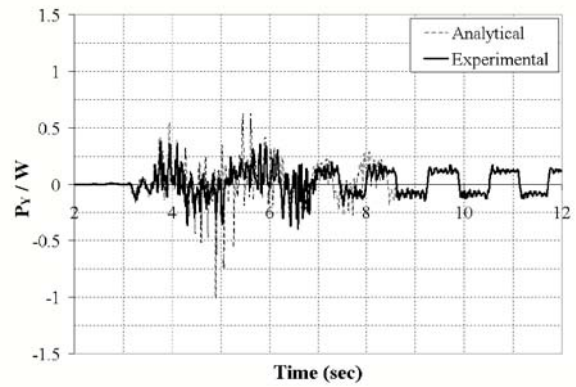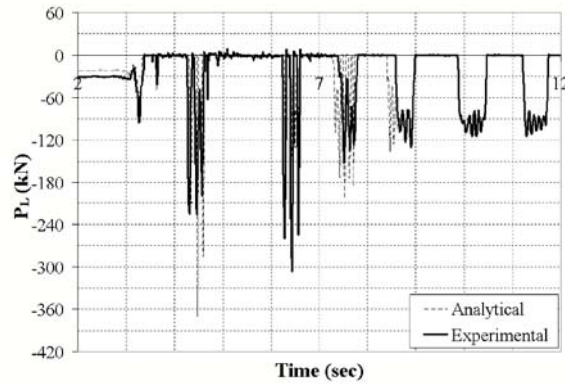
FIGURE 6-131 Experimental-Time History Response Quantity Trace Comparison; Synthetic 150%, μ_L=0, PII, Modified Boundary Elements (a) Pier Relative Displacement X, (b) Pier Relative Displacement Y, (c) Normalized Pier Base Shear X, (d) Normalized Pier Base Shear Y, (e) Pier Leg Force (Leg 1)
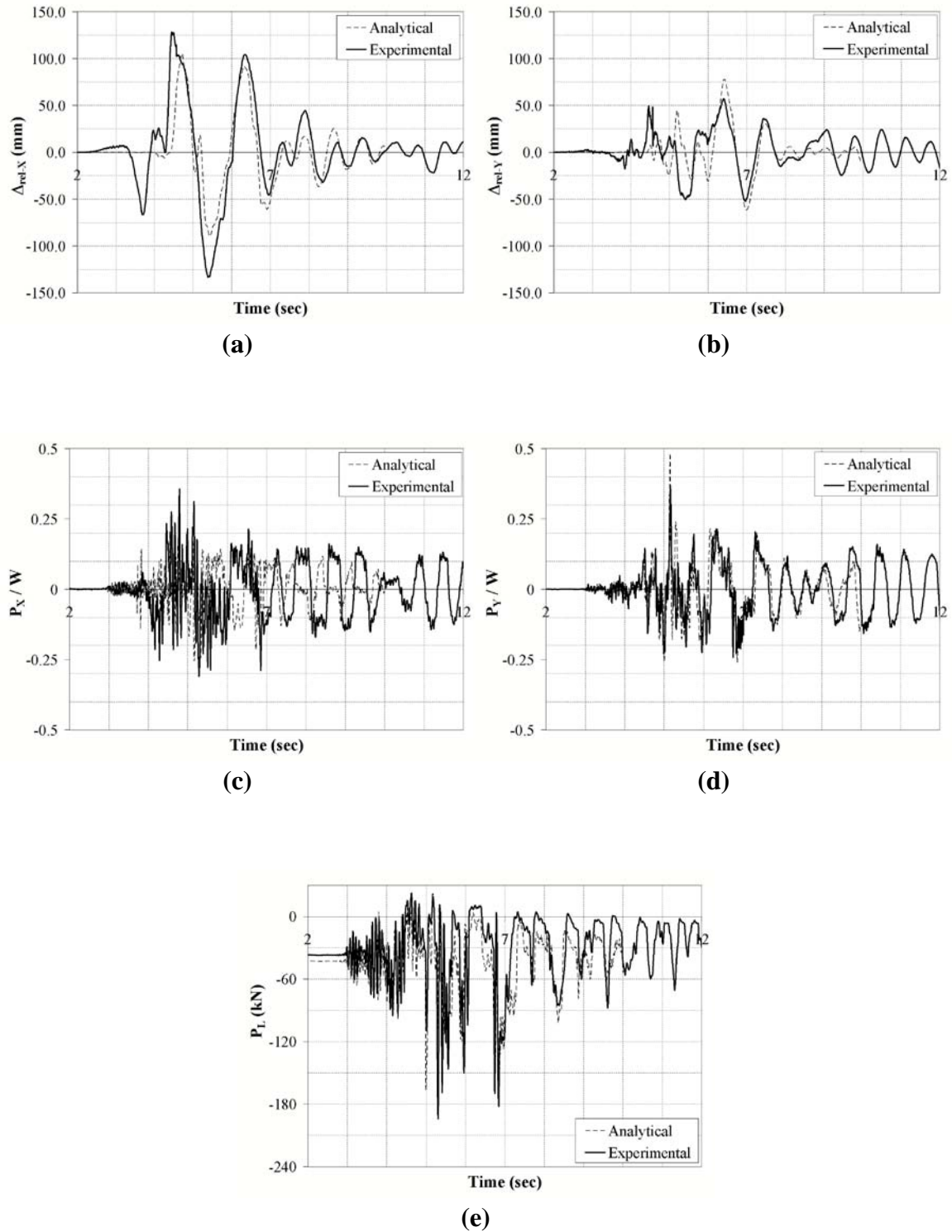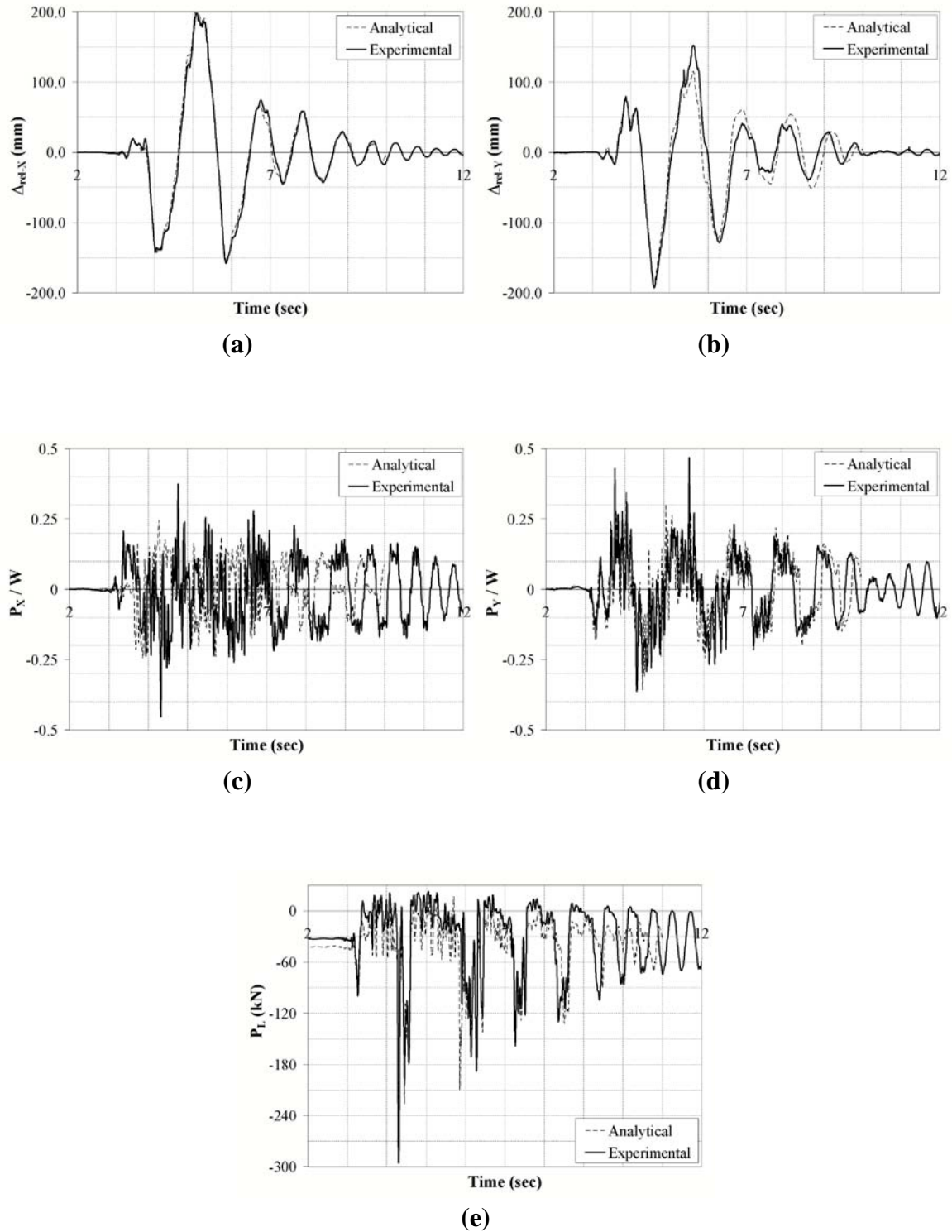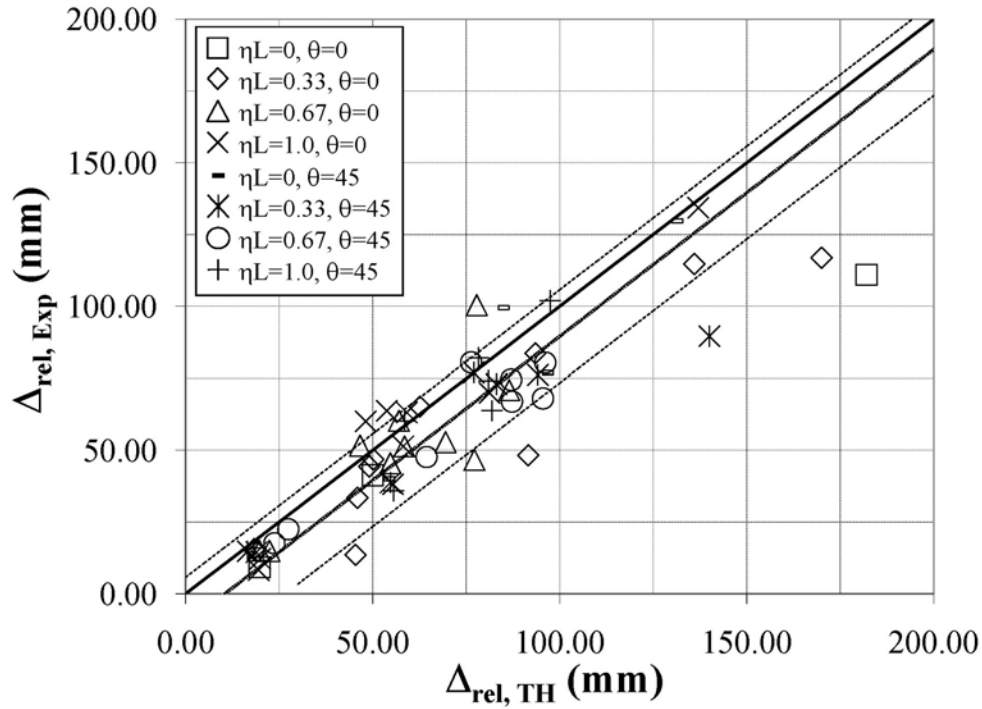
FIGURE 6-132 Experimental-Time History Comparison of Peak Response (Revised Damping Model), Relative Pier Displacement (Δ_{rel}), Phase I
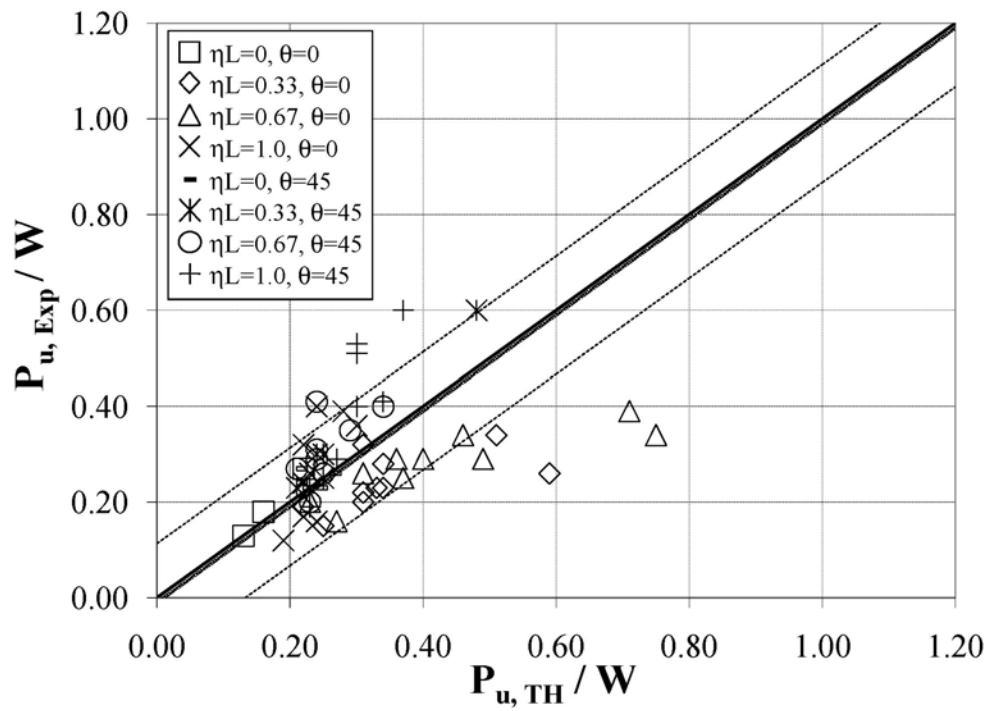
FIGURE 6-133 Experimental-Time History Comparison of Peak Response (Revised Damping Model), Base Shear Force (P_u), Phase I
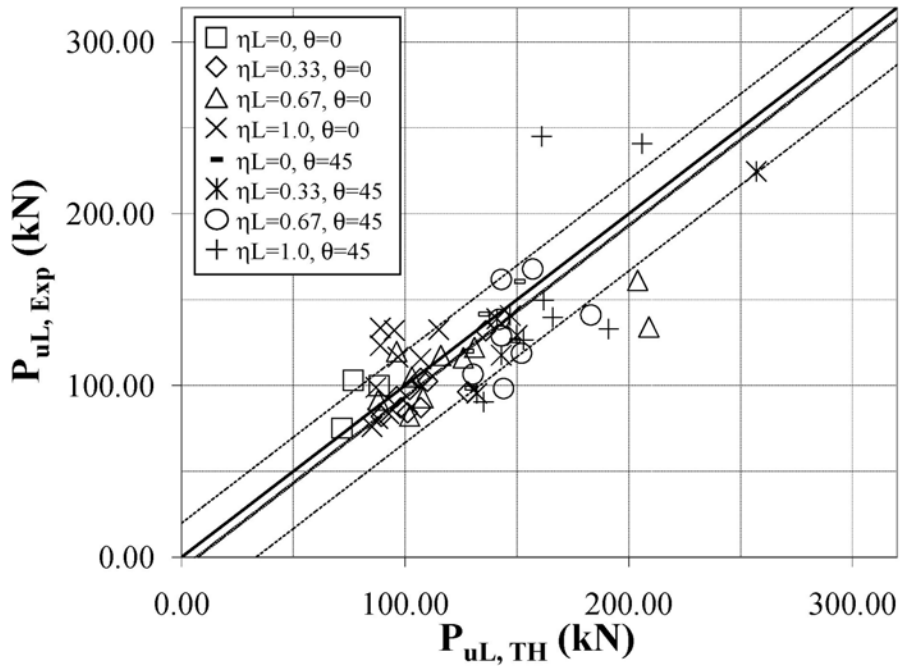
FIGURE 6-134 Experimental-Time History Comparison of Peak Response (Revised Damping Model), Pier Leg Axial Force (P_{uL}), Phase I
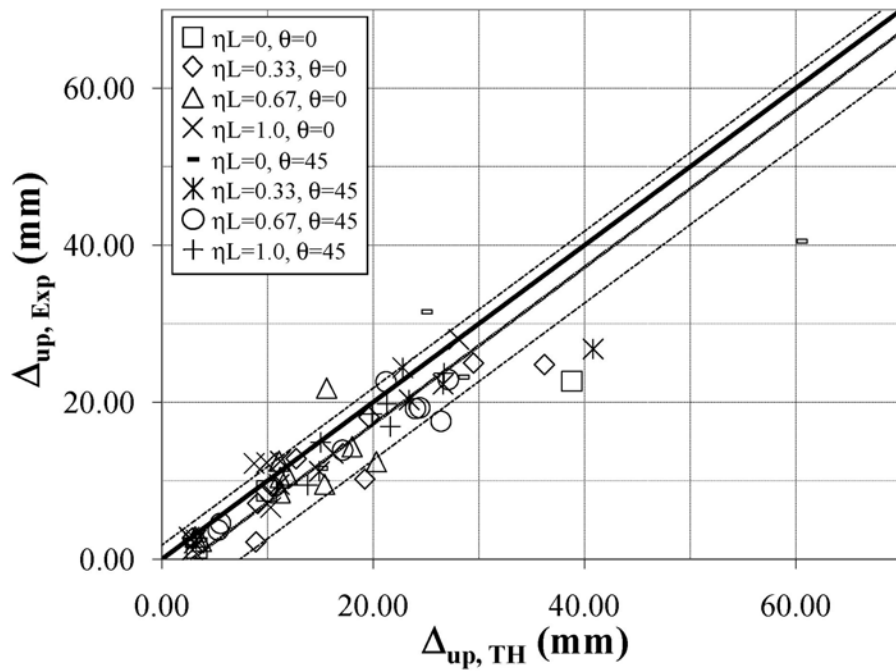
FIGURE 6-135 Experimental-Time History Comparison of Peak Response (Revised Damping Model), Uplift Displacement (Δ_{up}), Phase I
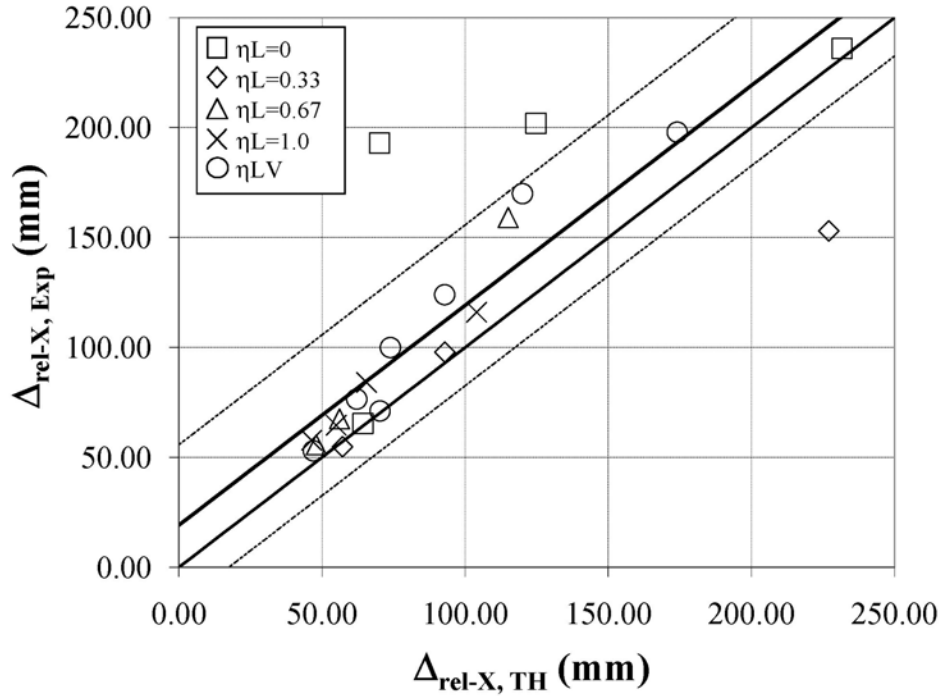
FIGURE 6-136 Experimental-Time History Comparison of Peak Response (Revised Damping Model), Relative Pier Displacement X-direction ($\Delta_{rel,X}$), Phase II
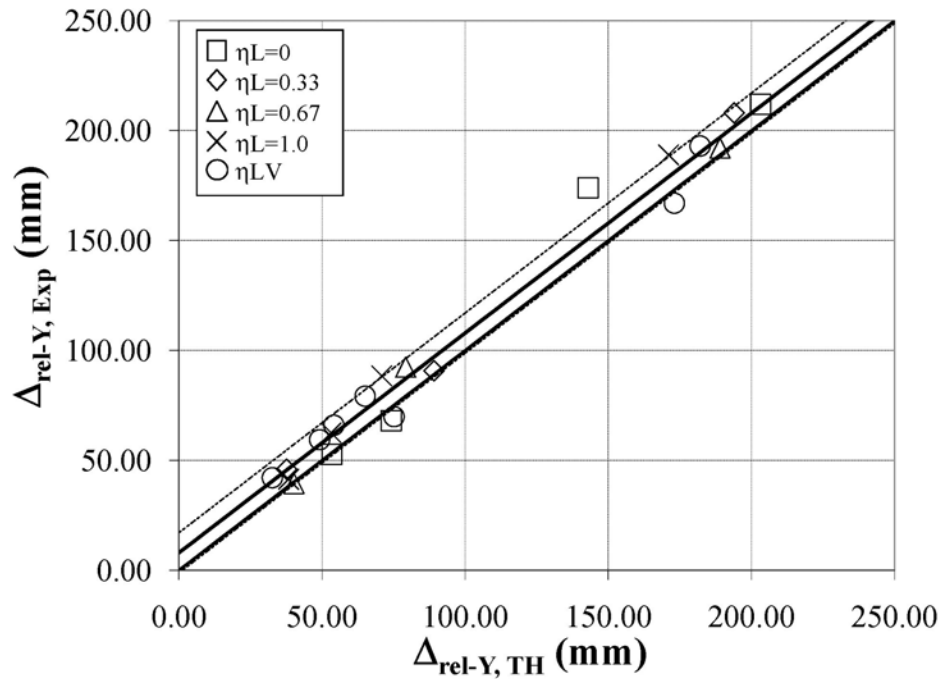
FIGURE 6-137 Experimental-Time History Comparison of Peak Response (Revised Damping Model), Relative Pier Displacement Y-direction ($\Delta_{rel,Y}$), Phase II
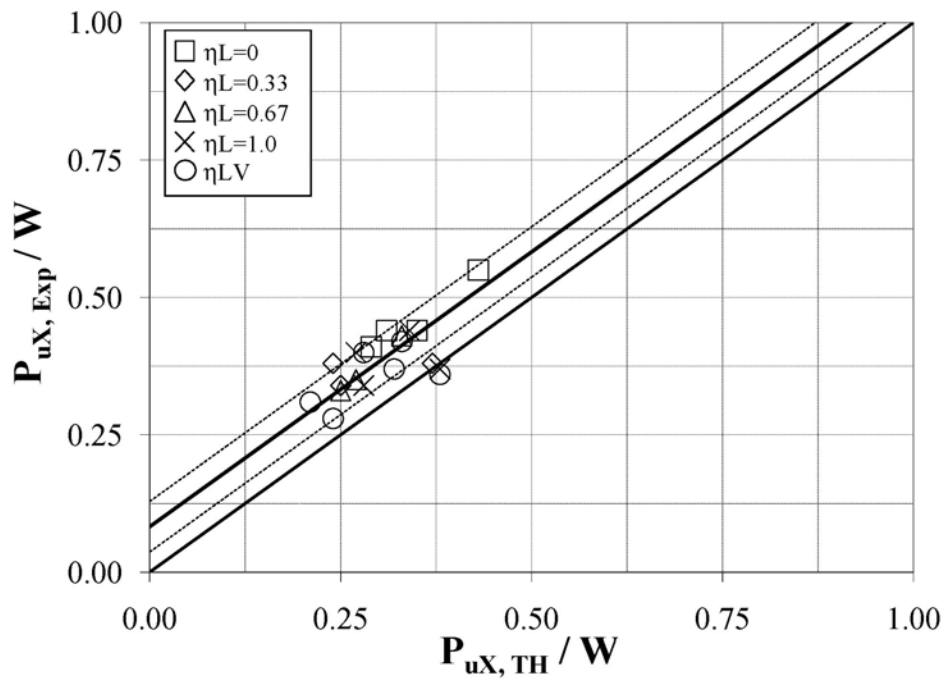
FIGURE 6-138 Experimental-Time History Comparison of Peak Response (Revised Damping Model), Base Shear Force X-direction (P_{uX}), Phase II
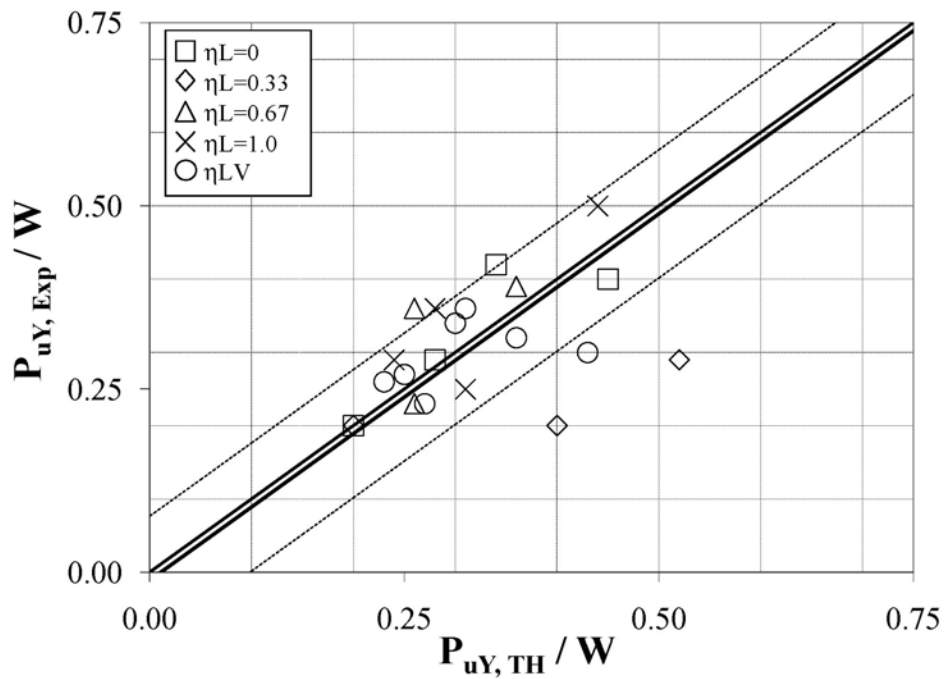
FIGURE 6-139 Experimental-Time History Comparison of Peak Response (Revised Damping Model), Base Shear Force Y-direction (P_{uY}), Phase II
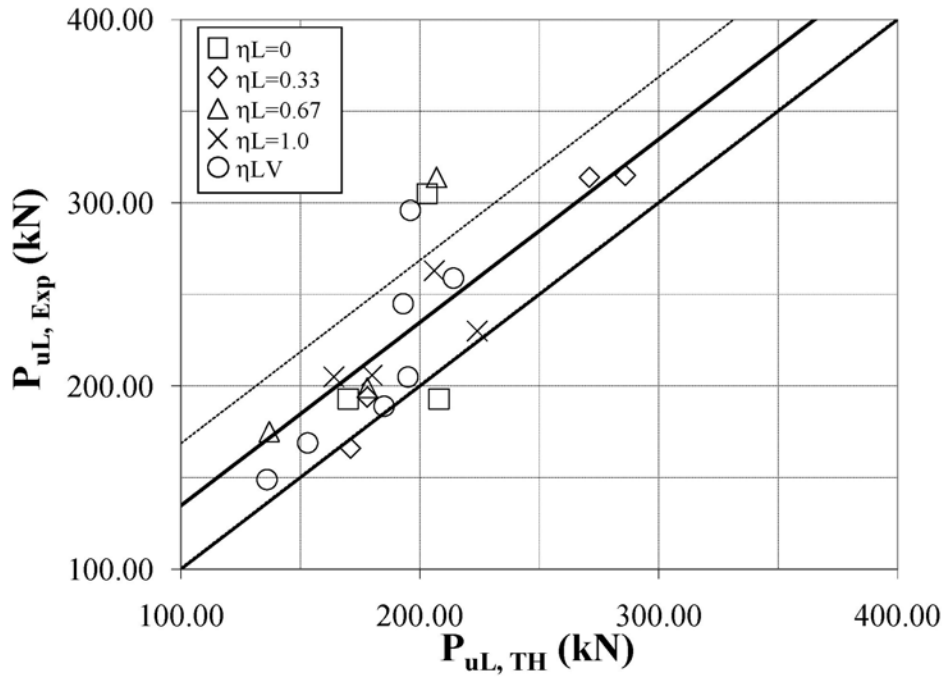
FIGURE 6-140 Experimental-Time History Comparison of Peak Response (Revised Damping Model), Pier Leg Axial Force (P_{uL}), Phase II
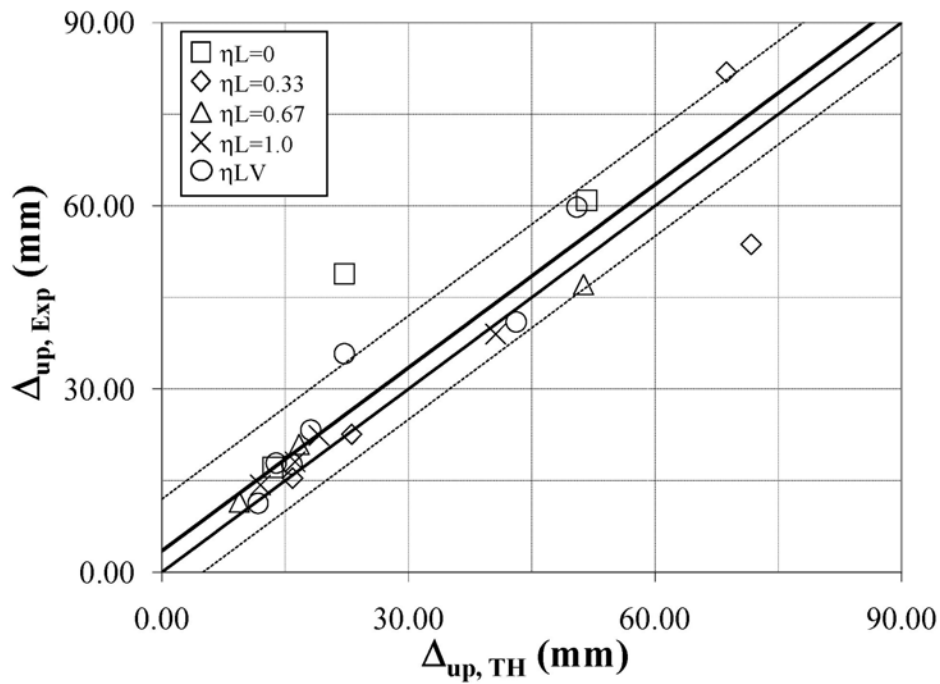
FIGURE 6-141 Experimental-Time History Comparison of Peak Response (Revised Damping Model), Uplift Displacement (Δ_{up}), Phase II

345
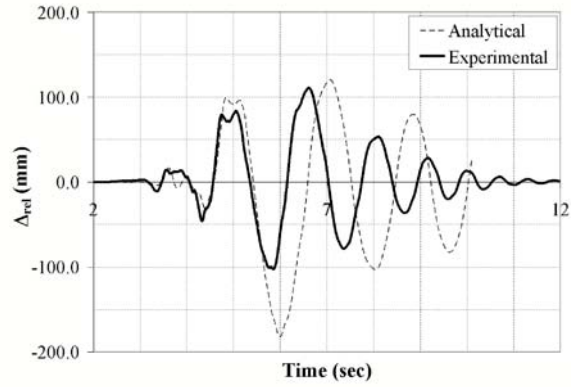
(a)
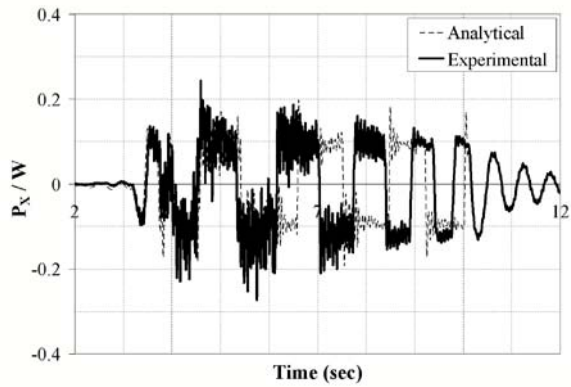
(b)
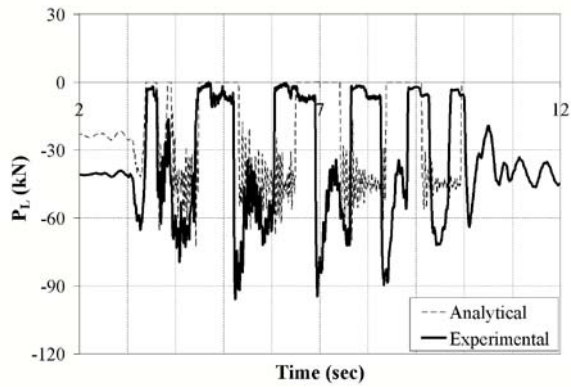
(c)

FIGURE 6-142 Experimental-Time History Response Quantity Trace Comparison; Synthetic 100%, $_L$=0, PI (Revised Damping Model) (a) Pier Relative Displacement, (b) Normalized Pier Base Shear, and (c) Pier Leg Force (Leg 1)
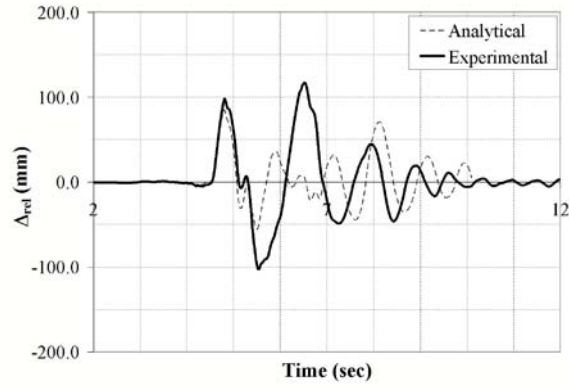
(a)
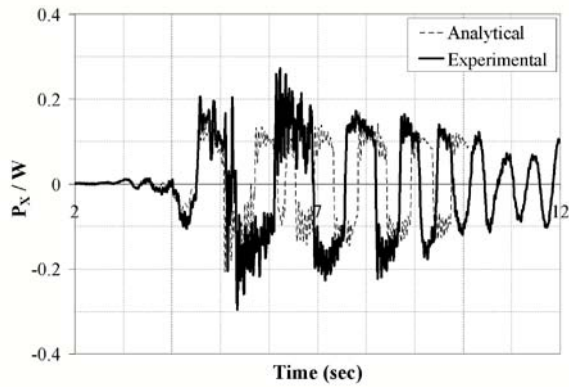
(b)
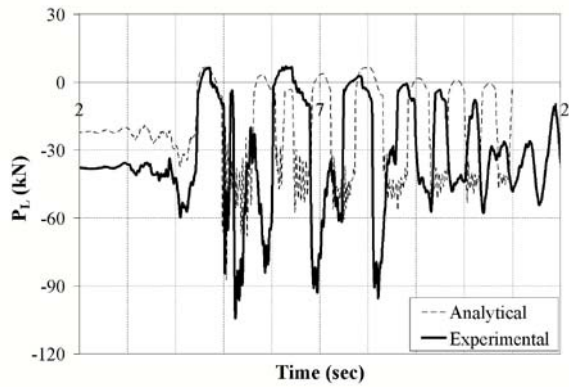
(c)

FIGURE 6-143 Experimental-Time History Response Quantity Trace Comparison; Newhall 125%, $_L$=0.33, PI (Revised Damping Model) (a) Pier Relative Displacement, (b) Normalized Pier Base Shear, and (c) Pier Leg Force (Leg 1)

347
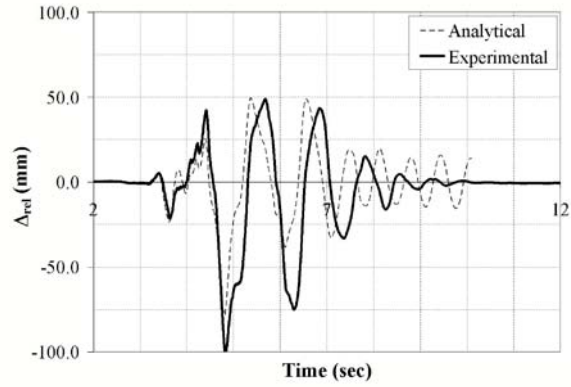
(a)
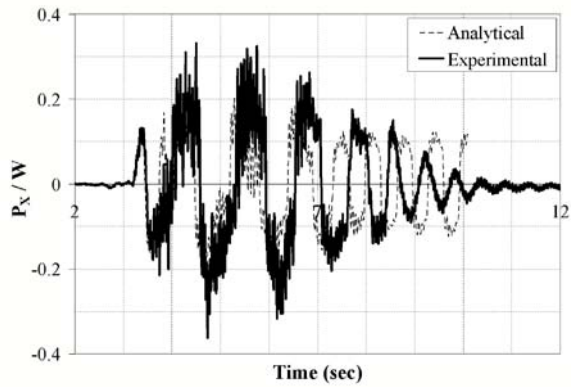
(b)
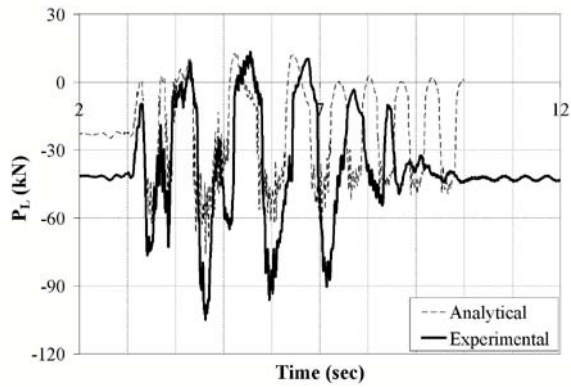
(c)

**FIGURE 6-144 Experimental-Time History Response Quantity Trace Comparison;
Synthetic 150%, ₗ=0.67, PI (Revised Damping Model) (a) Pier Relative
Displacement, (b) Normalized Pier Base Shear, and (c) Pier Leg Force (Leg 1)**

348
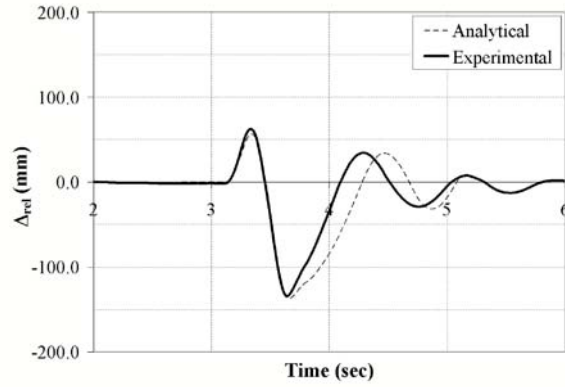
(a)
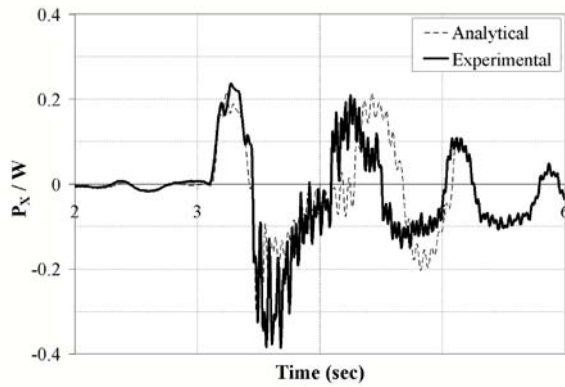
(b)
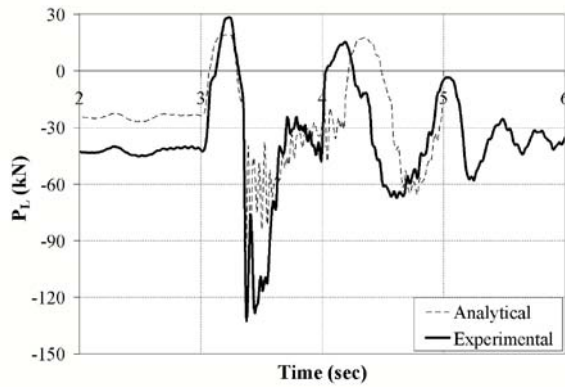
(c)

FIGURE 6-145 Experimental-Time History Response Quantity Trace Comparison; Pulse P2, T_p=0.60sec, 100%, $_L$=1.0, PI (Revised Damping Model) (a) Pier Relative Displacement, (b) Normalized Pier Base Shear, and (c) Pier Leg Force (Leg 1)
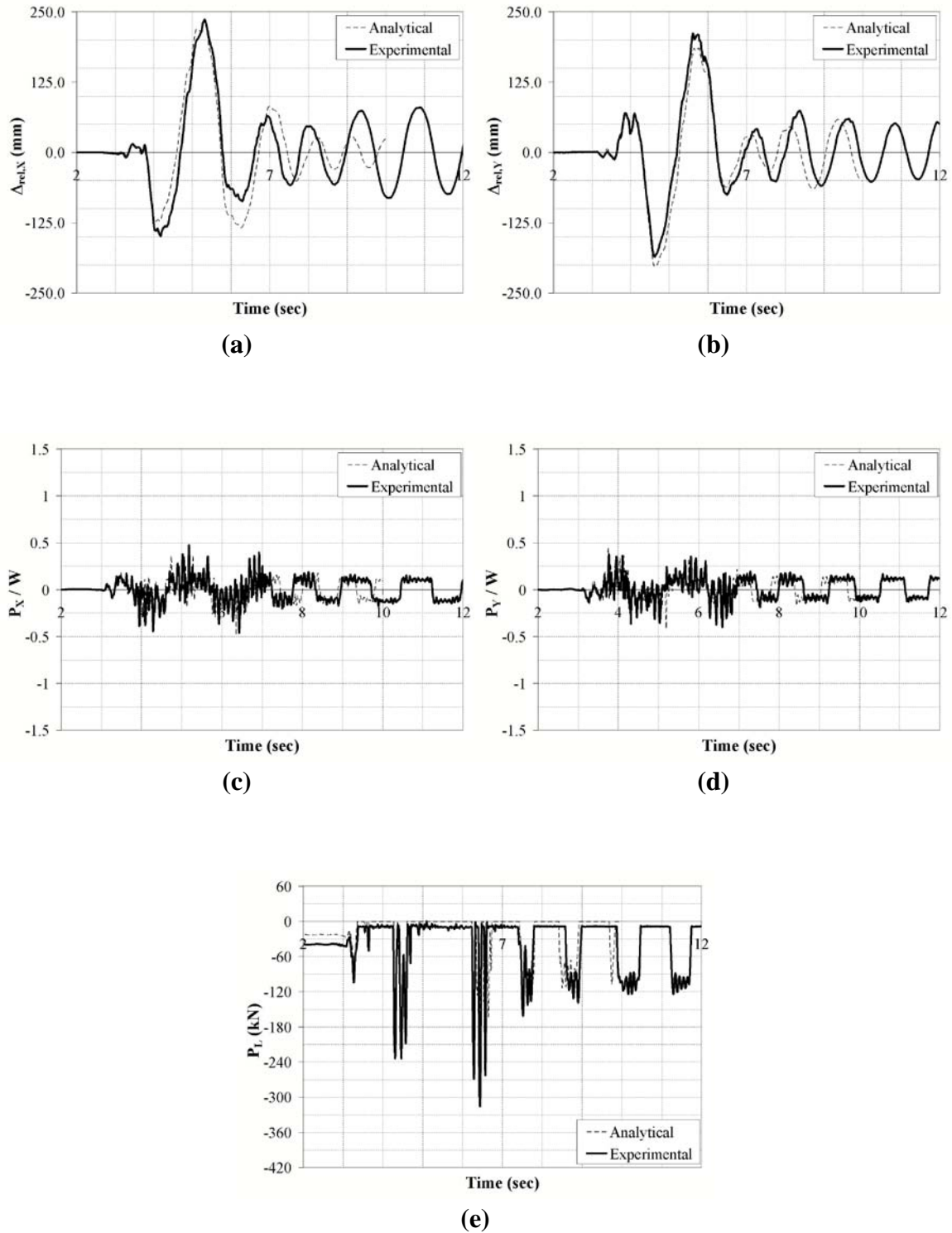
FIGURE 6-146 Experimental-Time History Response Quantity Trace Comparison; Synthetic 150%, $_L$=0, PII (Revised Damping Model) (a) Pier Relative Displacement X, (b) Pier Relative Displacement Y, (c) Normalized Pier Base Shear X, (d) Normalized Pier Base Shear Y, (e) Pier Leg Force (Leg 1)
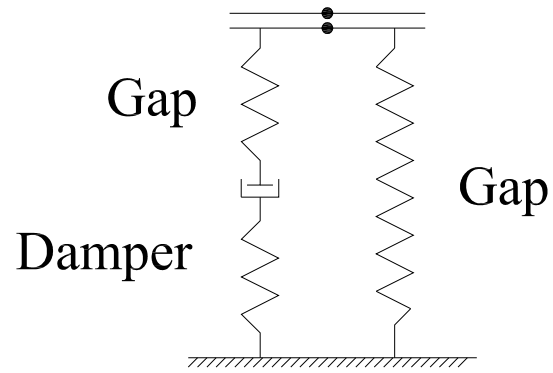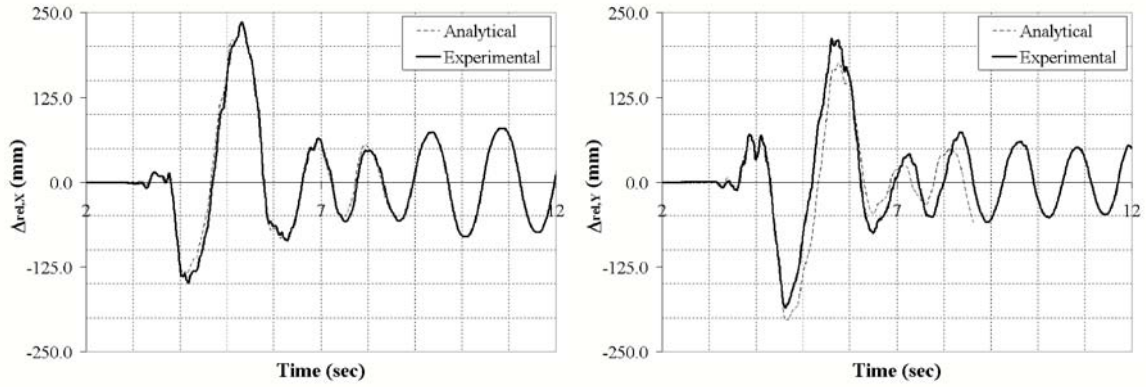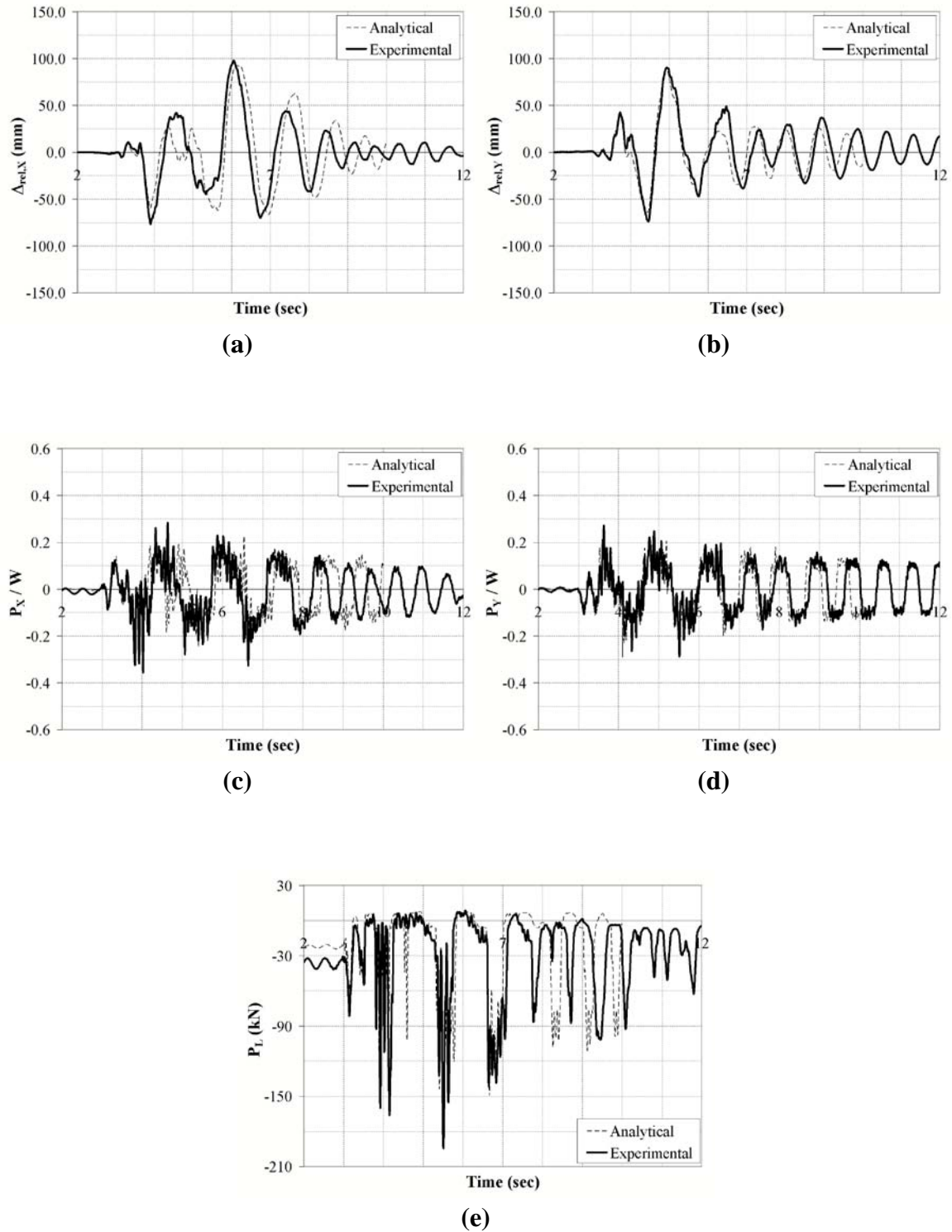
FIGURE 6-147 Experimental-Time History Response Quantity Trace Comparison; Synthetic 100%, μ_L=0.33, PII (Revised Damping Model) (a) Pier Relative Displacement X, (b) Pier Relative Displacement Y, (c) Normalized Pier Base Shear X, (d) Normalized Pier Base Shear Y, (e) Pier Leg Force (Leg 1)
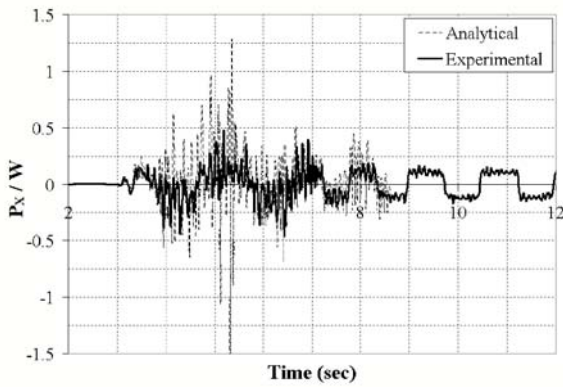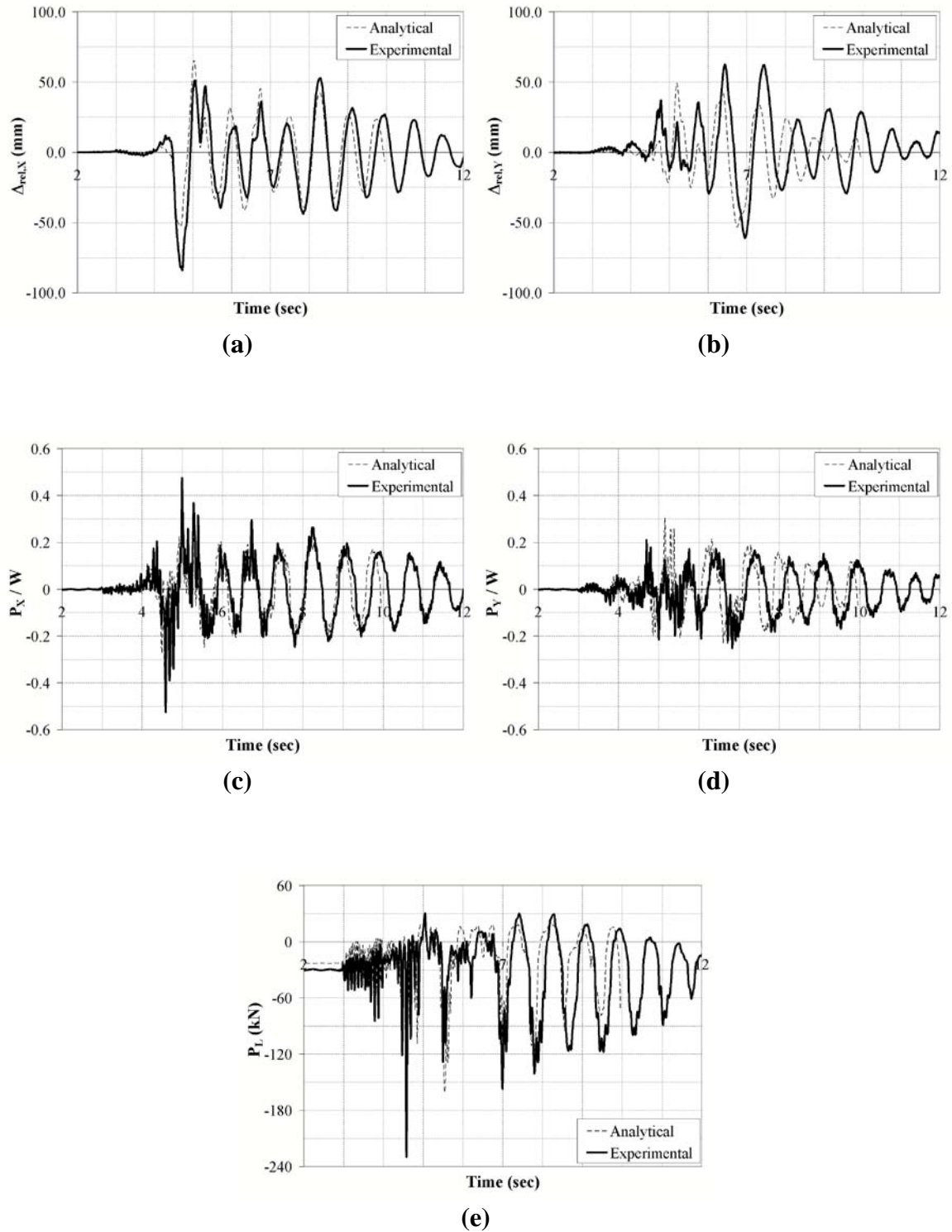
FIGURE 6-148 Experimental-Time History Response Quantity Trace Comparison; Newhall 150%, ∟=1.0, PII (Revised Damping Model) (a) Pier Relative Displacement X, (b) Pier Relative Displacement Y, (c) Normalized Pier Base Shear X, (d) Normalized Pier Base Shear Y, (e) Pier Leg Force (Leg 1)
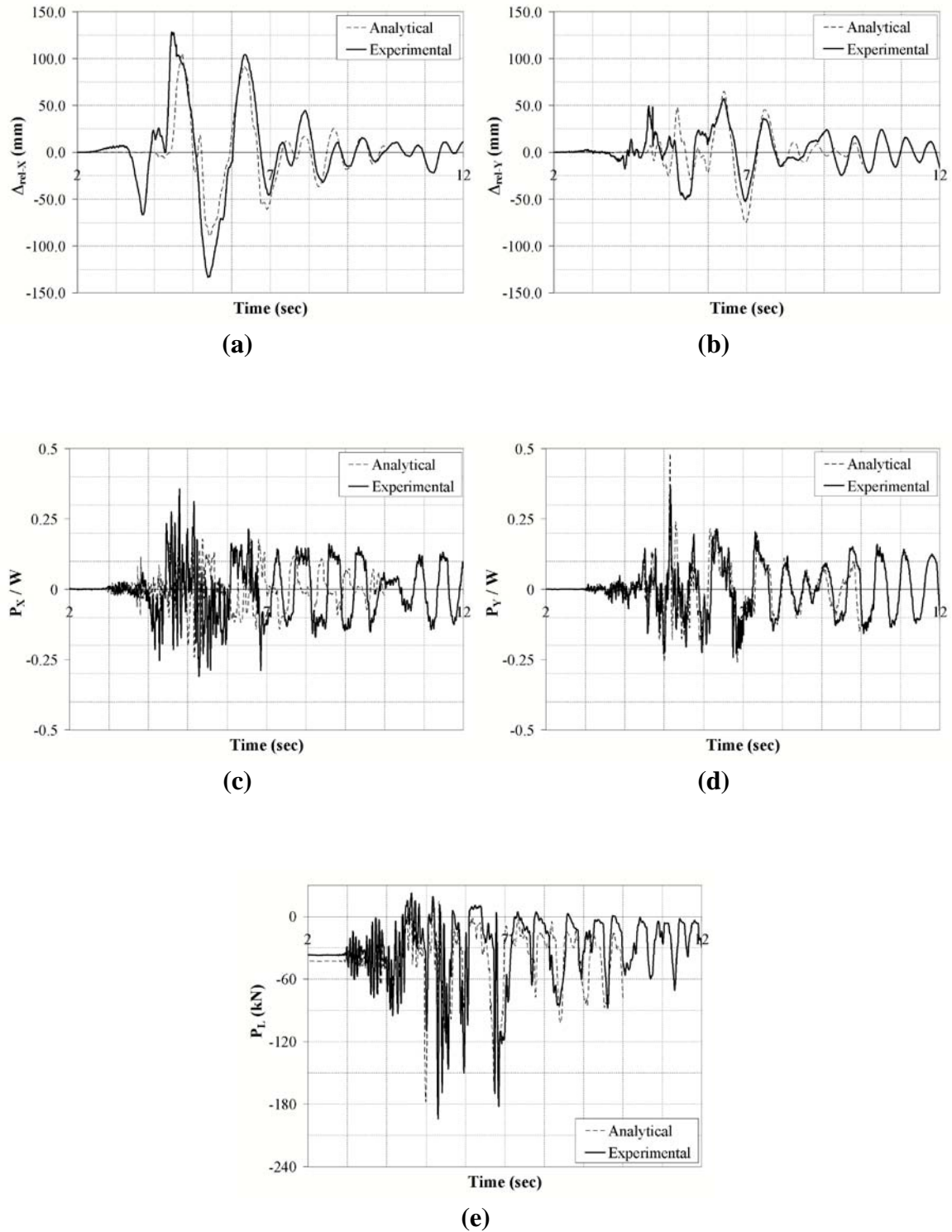
FIGURE 6-149 Experimental-Time History Response Quantity Trace Comparison; Newhall 200%, ₗᵥ, PII (Revised Damping Model) (a) Pier Relative Displacement X, (b) Pier Relative Displacement Y, (c) Normalized Pier Base Shear X, (d) Normalized Pier Base Shear Y, (e) Pier Leg Force (Leg 1)
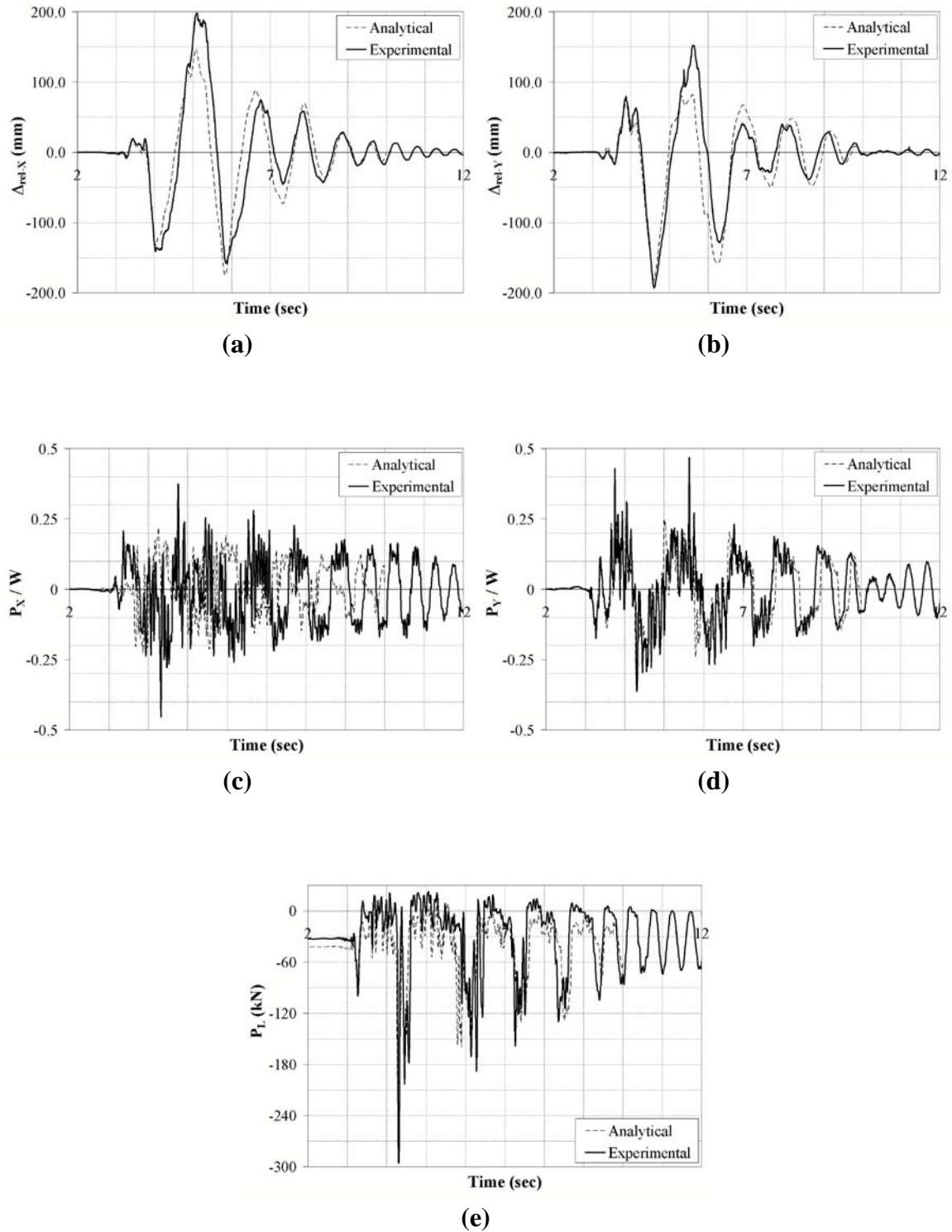
FIGURE 6-150 Experimental-Time History Response Quantity Trace Comparison; Synthetic 175%, LV, PII (Revised Damping Model) (a) Pier Relative Displacement X, (b) Pier Relative Displacement Y, (c) Normalized Pier Base Shear X, (d) Normalized Pier Base Shear Y, (e) Pier Leg Force (Leg 1)

(a)

(b)

(c)
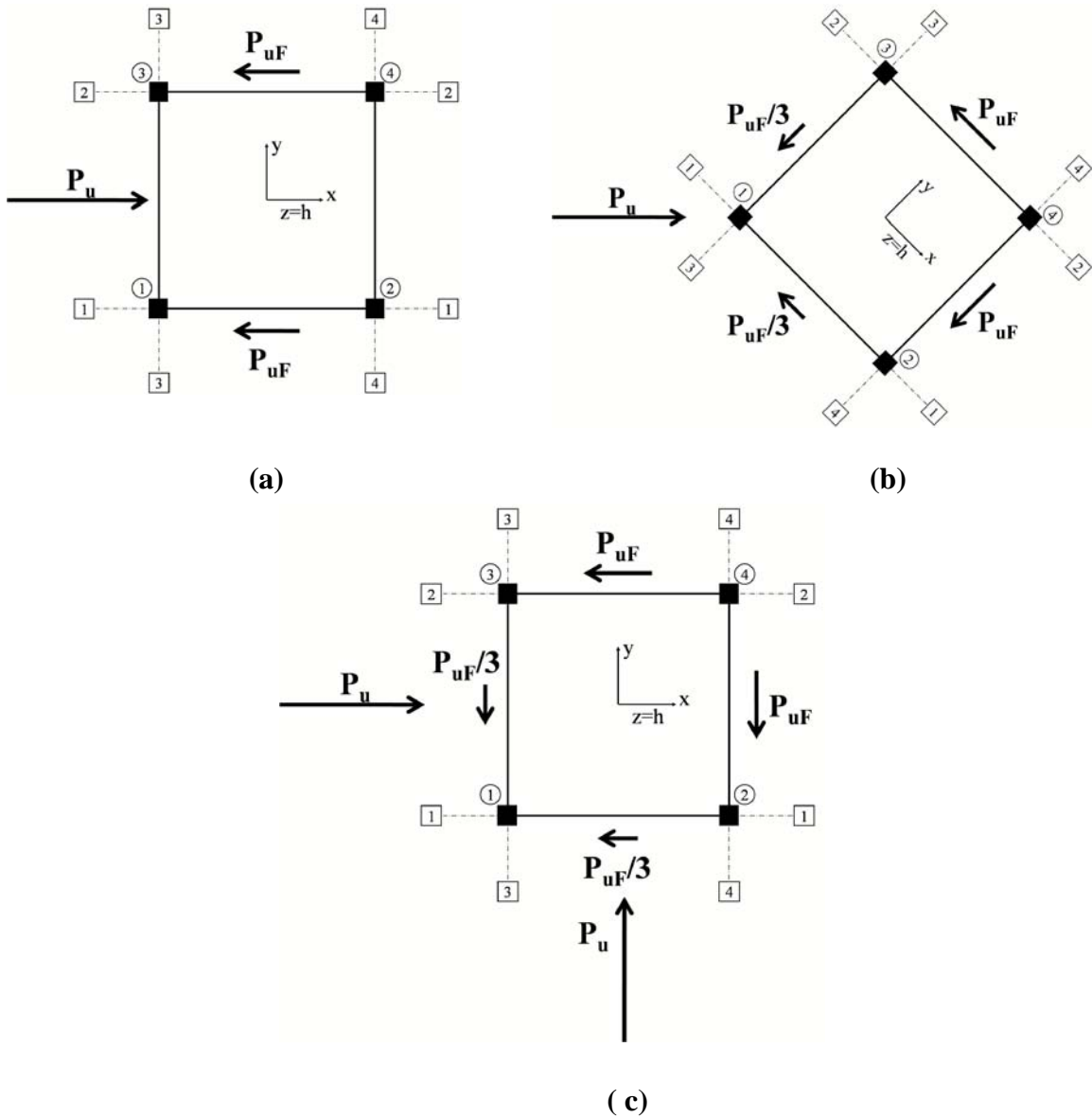
FIGURE 6-151 Assumed Base Shear Force Distribution for (a) Phase I, =0deg., (b) Phase I, =45deg., and (c) Phase II
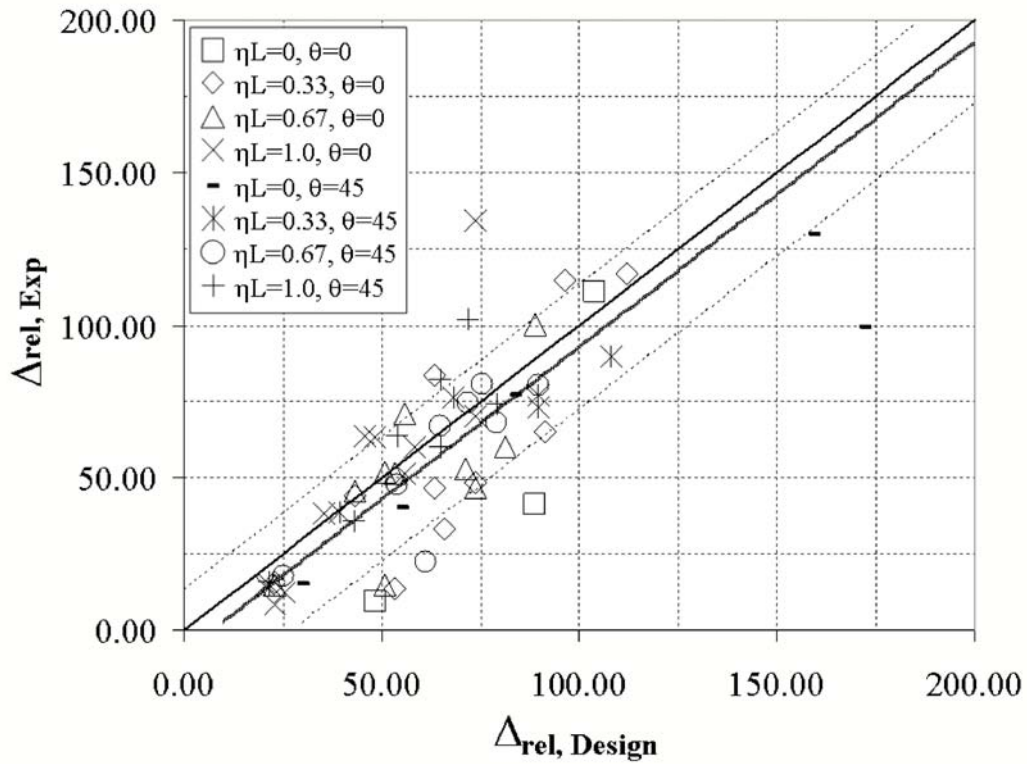
FIGURE 6-152 Experimental-Design Comparison of Peak Response, Relative Pier Displacement (Δ_{rel}), Phase I
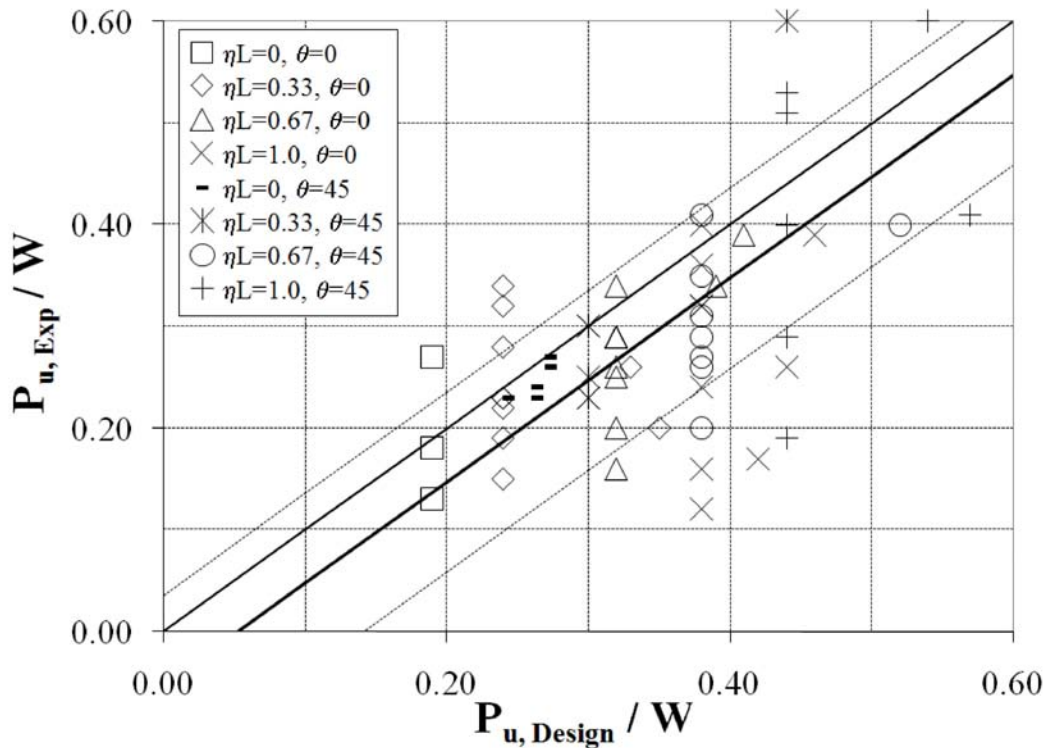
FIGURE 6-153 Experimental-Design Comparison of Peak Response, Base Shear Force (P_u), Phase I
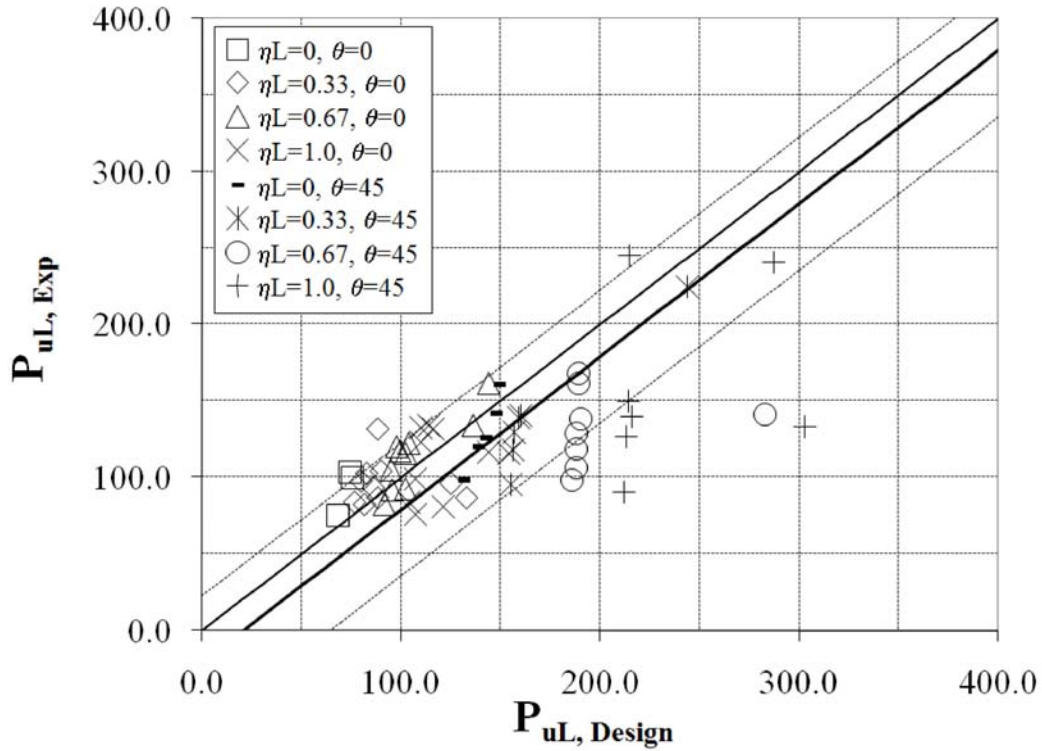
FIGURE 6-154 Experimental-Design Comparison of Peak Response, Pier Leg Axial Force (P_{uL}), Phase I
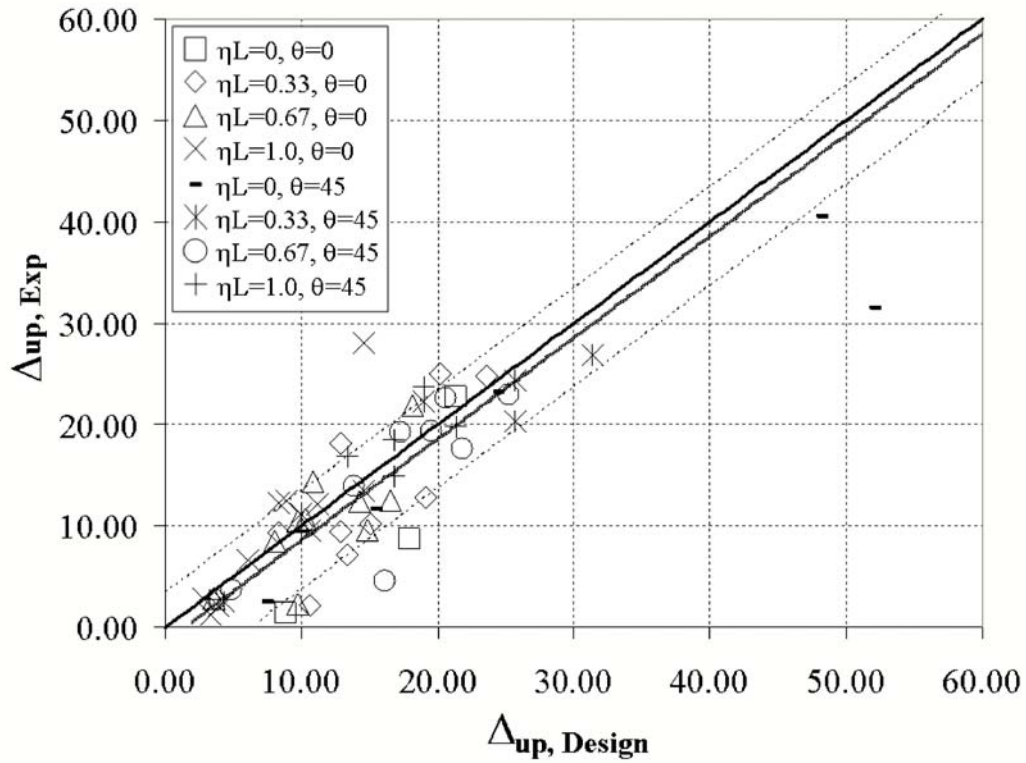
FIGURE 6-155 Experimental-Design Comparison of Peak Response, Uplift Displacement (Δ_{up}), Phase I
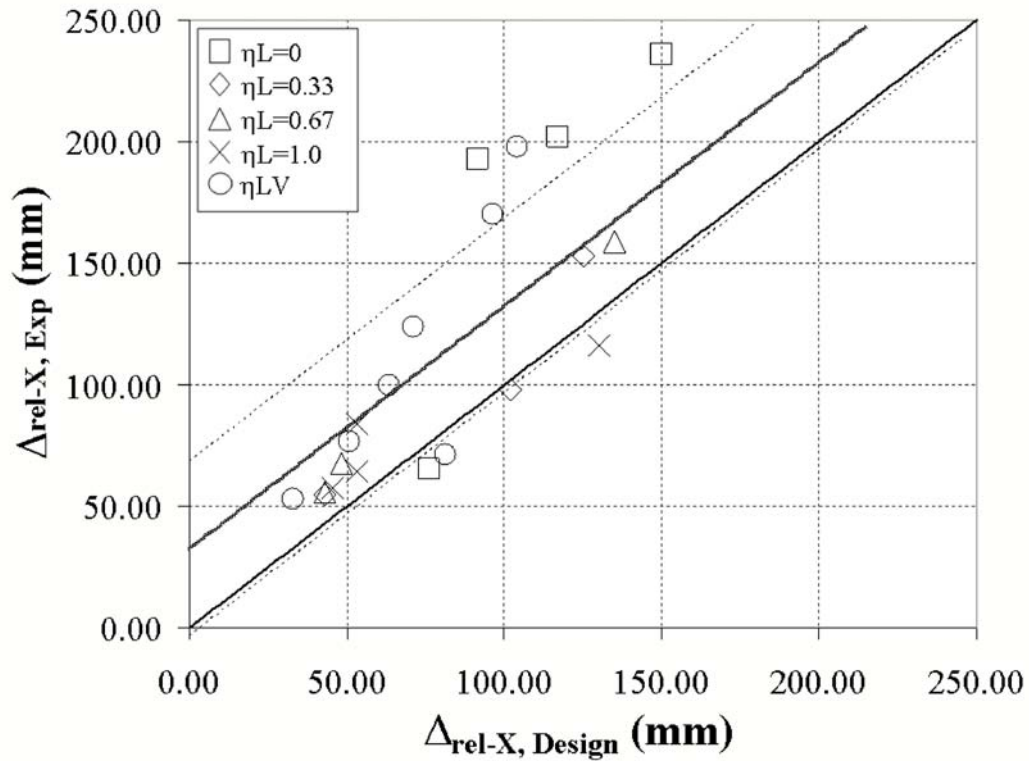
FIGURE 6-156 Experimental-Design Comparison of Peak Response, Relative Pier Displacement X-direction ($\Delta_{rel,X}$), Phase II
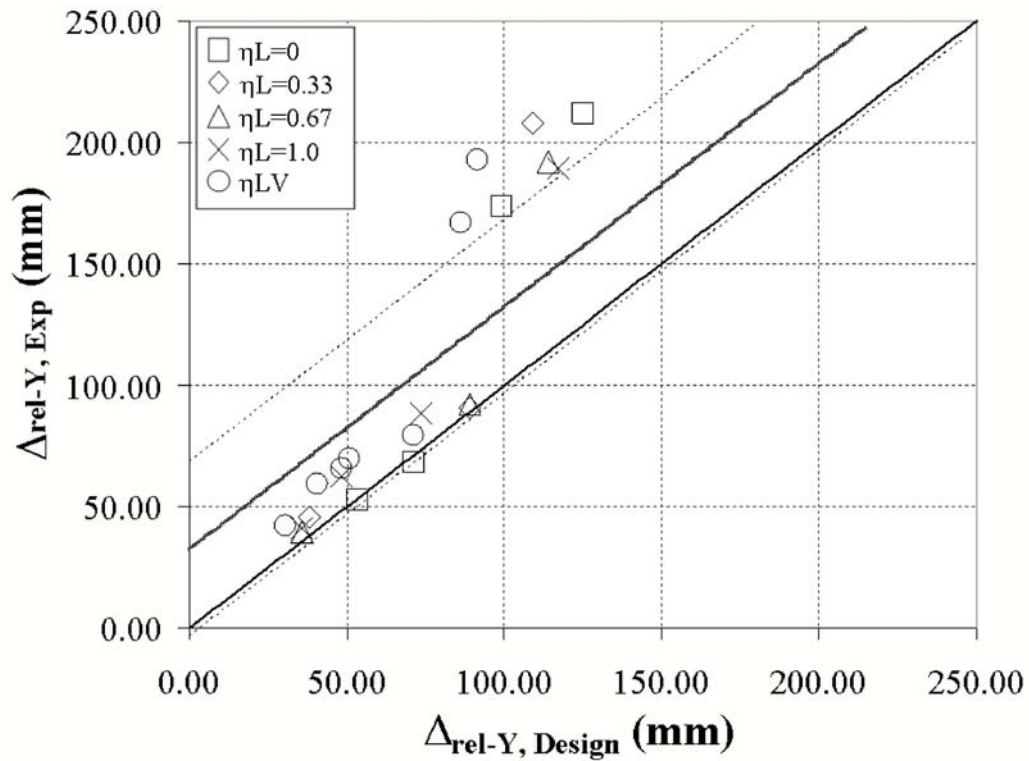
FIGURE 6-157 Experimental-Design Comparison of Peak Response, Relative Pier Displacement Y-direction ($\Delta_{rel,Y}$), Phase II
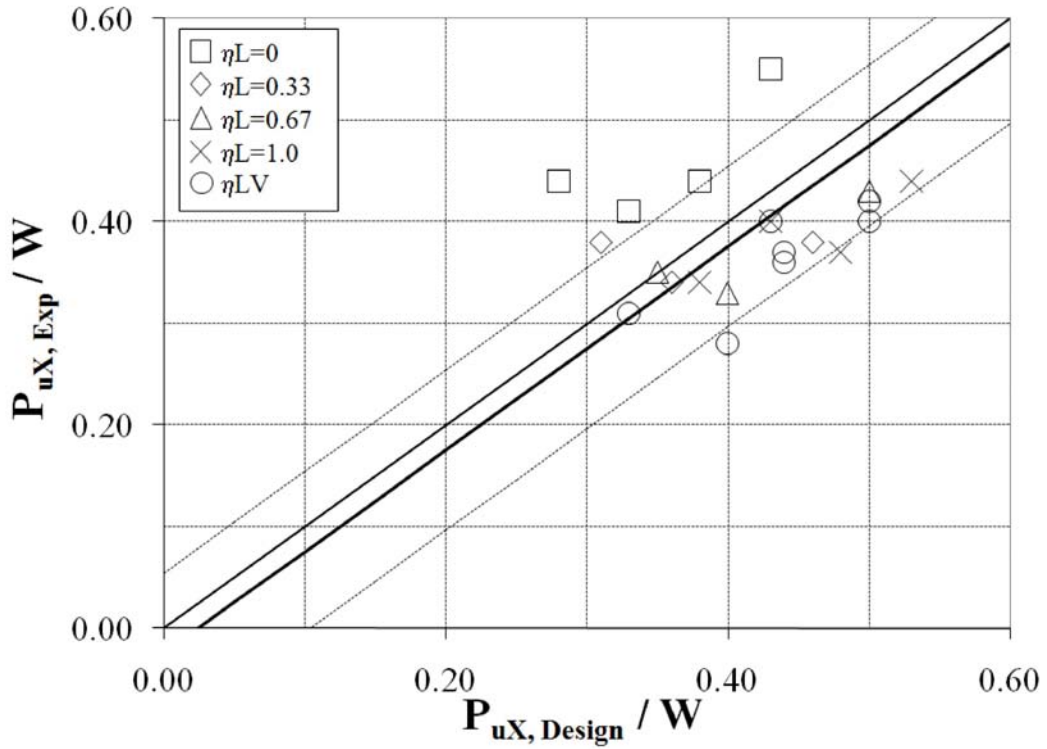
FIGURE 6-158 Experimental-Design Comparison of Peak Response, Base Shear Force X-direction (P$_{uX}$), Phase II
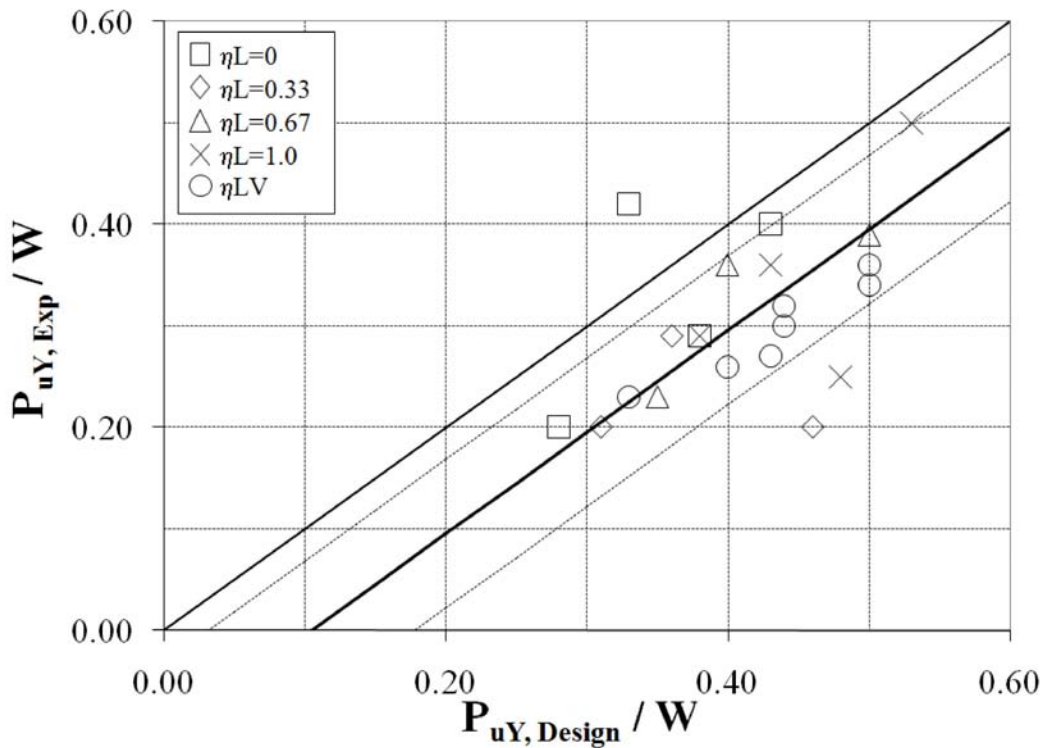
FIGURE 6-159 Experimental-Design Comparison of Peak Response, Base Shear Force Y-direction (P$_{uY}$), Phase II

359
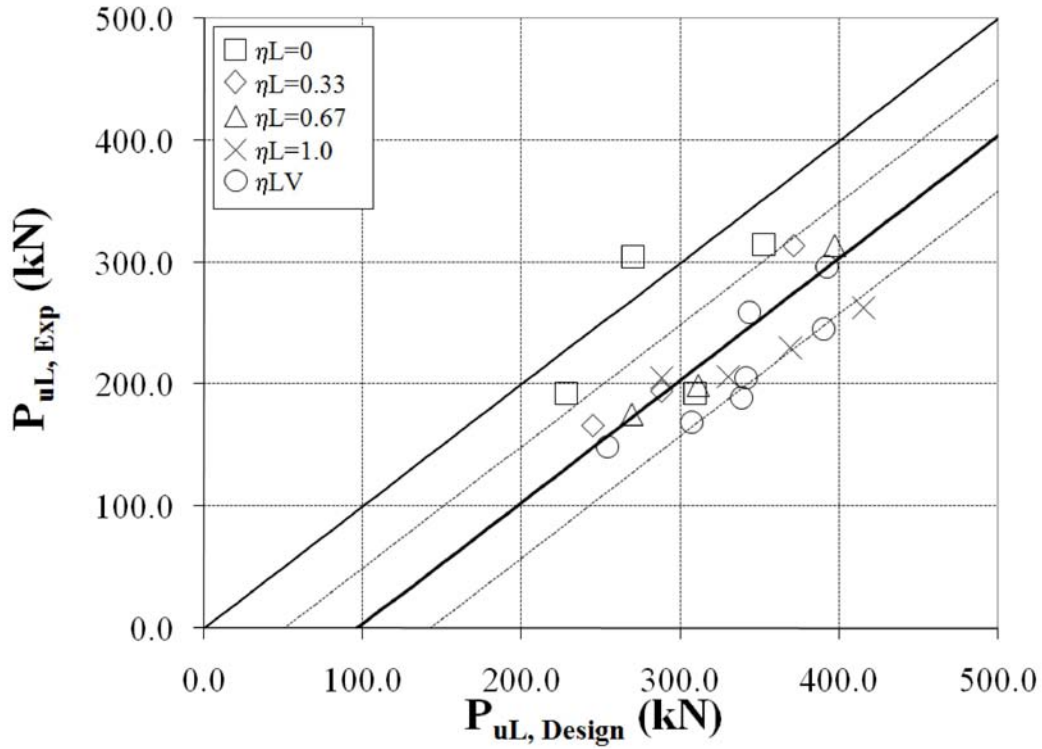
FIGURE 6-160 Experimental-Design Comparison of Peak Response, Pier Leg Axial Force (P_{uL}), Phase II
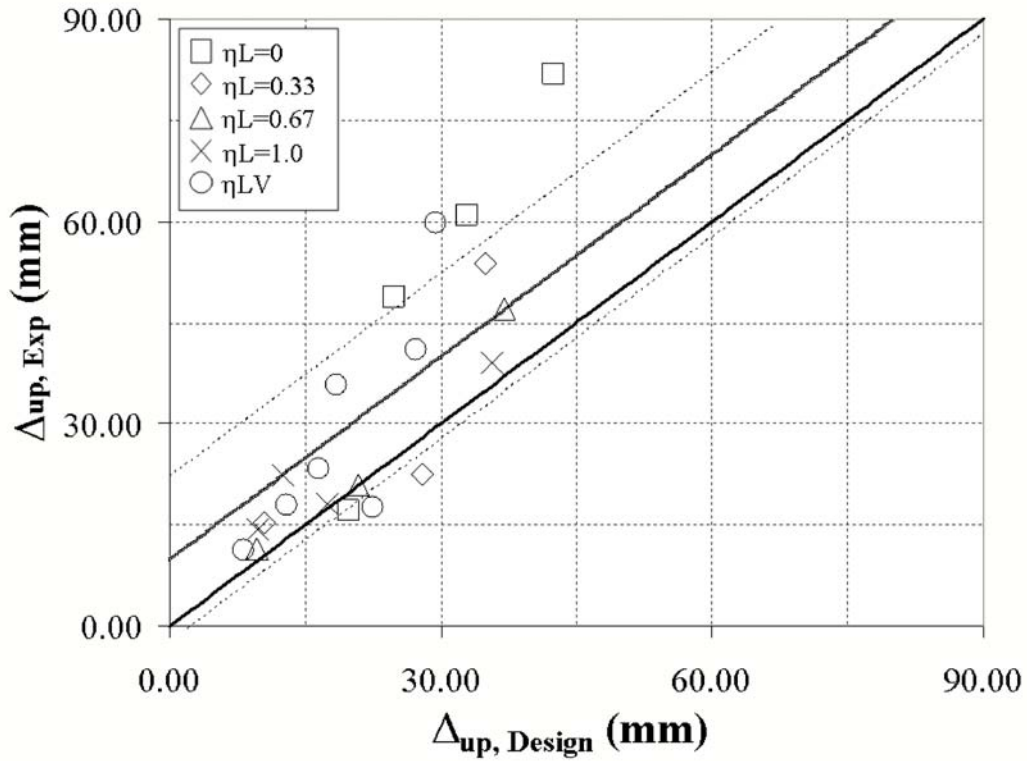
FIGURE 6-161 Experimental-Design Comparison of Peak Response, Uplift Displacement (Δ_{up}), Phase II

SECTION 7

SUMMARY, CONCLUSIONS, AND RECOMMENDATIONS FOR FUTURE RESEARCH

7.1 Summary

This research has investigated, using analytical and experimental methods, an approach for the seismic protection of bridge steel truss piers that relies on controlled rocking. The approach allows these piers to uplift from their foundation and uses passive energy dissipation devices implemented at the uplifting location to control response. Proper design of a controlled rocking pier can allow the structure to remain elastic while providing a self-centering mechanism using the inherent restoring force provided by its gravitational weight. Many aspects of the behavior and design of controlled rocking 2-legged and 4-legged piers are addressed.

This study was based from earlier work (Pollino 2004) that introduced and developed some basic concepts of the controlled rocking approach. The key parameters that define the cyclic hysteretic curve of a 2-legged controlled rocking pier are provided in Section 2 and are used in parts of this report. Also, an important effect of rocking response is described in that work that characterizes and quantifies higher vertical mode participation during rocking response that occurs even when piers are subjected to solely horizontal excitation. The dynamic force effects resulting from the vertical mode participation is captured in the dynamic amplification factors, R_{dv} and R_{dL}, which are used throughout this document.

The response of controlled rocking 2-legged piers to simultaneous horizontal and vertical excitation is investigated in Section 3 to further develop the controlled rocking approach from that done in Pollino (2004). First, methods of response prediction were developed that combined the effects of multiple components of seismic excitation (X+Z) and the demands due to dynamic forces that developed. Based on the current state of practice, a 100%-40% combination rule was applied to effects resulting from multiple components of excitation while an SRSS modal combination rule was applied to effects resulting from multiple modes excited due to a single component of motion. Nonlinear time history analysis was conducted to evaluate the response predictions. The ground motions were synthetically generated,

361

characteristic of a site founded on rock, and the vertical pseudo-acceleration spectrum was simply taken as 2/3 of the horizontal.

It was then desired to investigate the response of controlled rocking 2-legged piers to seismic excitation typical of the fault-normal component of shaking at a site close to a fault (<15km). Nonlinear time history analysis was conducted using earthquake records that were synthetically generated considering a number of scenarios for a site located in Northridge, CA at a distance ranging from 4.6 to 7.5km from the fault. The adequacy of the prediction of key response parameters was then investigated to ensure that the seismic response was not significantly influenced by this "pulse" or "fling" type of input. Following this, the influence on displacement response of controlled rocking piers to simple pulse-type input was examined. The correlation between pulse period and structural period on maximum displacement response was investigated to determine the range to which this type of input would significantly affect response.

The majority of this research considers the use of steel yielding devices as the passive control device, but the use of fluid viscous dampers is also discussed. In each case, the energy dissipated per cycle for uni-directional motion of a controlled rocking is defined and design equations are formulated for each set of devices.

The behavior of a 4-legged controlled rocking pier, undergoing bi-directional horizontal motion, was developed at a fundamental level by defining the kinematic and hysteretic variables relevant to its design. These properties were verified using nonlinear static pushover analysis. The application of the simplified analysis procedure and design equations were discussed and re-formulated to apply to the response of 4-legged controlled rocking piers subjected to three components of ground motion. The design response predictions were then verified using nonlinear time history analysis using a 3-dimensional finite element model.

An experimental program was performed for a one-fifth length scale, 4-legged bridge pier specimen. The testing was conducted in two phases (using 5- and 6-DOF shake tables),

implemented both steel yielding devices (TADAS) and fluid viscous dampers, and the specimen was subjected to different forms of table input. Response was investigated for solely horizontal (X), horizontal and vertical (X+Z), and all three components of motion (X+Y+Z). White noise testing was performed to determine the "fixed-base" periods and damping ratios of the model structure. The horizontal period in each direction was 0.40sec and the structure had an inherent damping of approximately 2.8% of critical. Many seismic tests were performed that generated a maximum relative pier displacement of 236mm (3.9% drift) and 82mm of uplift. The specimen was not damaged during the testing program and re-centered following each test. The results of the testing program were used to assess the adequacy of the design predictions and overall dynamic behavior. Analytical methods were assessed in terms of peak response and response history traces (in the case of time history analysis).

7.2 Conclusions

An approach for the seismic protection of bridge steel truss piers that relies on rocking response with added passive energy dissipation devices has been investigated using analytical and experimental techniques. The key conclusions from this study are as follows:

1. The simplified method of analysis was shown to provide adequate results for the prediction of maximum displacements. This included prediction of maximum relative pier displacement of 2-legged piers, whether subjected to base excitation typical of far-fault or near-fault seismic sources. For the case of bi-directional horizontal rocking (discussed in Section 4), it was recommended to simply consider the uni-directional pier properties using this analysis method. The uni-directional properties provide a lower-bound on the structural capacity and an upper-bound on the seismic demand (after accounting for the equivalent damping). There were a few instances in the prediction of the maximum displacement of the experimental specimen in which the simplified analysis approach provided displacements 30%-50% below that observed in experiments. Also, the maximum uplifting displacements may be influenced by the vertical ground displacements which is not

accounted for in the prediction of displacements and would primarily influence deformations of the passive energy dissipation devices.

2.	The bi-directional behavior developed for 4-legged piers showed that uplifting and yield of three steel yielding devices would result for a global displacement ductility, considering uni-directional behavior, greater than 2.5 ($\mu_{G,uni}$>2.5) using a 100%-40% directional combination rule. This was an important conclusion for the design of controlled rocking 4-legged piers.

3.	Design equations for combination of multi-component, multi-modal force effects were found to provide conservative, yet reasonably accurate, prediction of response. The derivation of maximum forces assumes development of the controlled rocking pier's yield mechanism (either uni-directional or bi-directional mechanism). Some results of experimental tests for systems that underwent bi-directional response showed significant deviation in force response from that predicted by the design equations, however this was mostly for cases in which the pier was not subjected to the design level of excitation. In general, the response of systems that achieved a global displacement ductility ($\mu_{G,uni}$) greater than approximately 3 matched reasonably accurately with the predicted force response.

4.	The development of the bi-directional yield mechanism and support of the pier on a single leg along with the effects of vertical excitation can cause significant axial forces in the pier legs such that they may likely require strengthening. However, a conventional seismically designed pier undergoing bi-directional yielding may subject the leg to similar levels of axial force and would also require design of a significant uplift force at the anchorage connection.

5.	It was found that the analytical model is sensitive to the damping (or energy loss) assigned. Different methods of damping were considered for calibration of the analytical model to the experimental results. It was found that large damping values in the high frequency range of a Rayleigh damping matrix along with removal of pier

member mass artificially removed the participation of many spurious higher modes not present during experimental testing.

7.3 Recommendations for Further Research

The following recommendations for further research are provided based on the observations and results of this research and for the continued development of the controlled rocking approach for seismic resistance of structures:

1. The influence of boundary conditions at the base of the structure and damping model in the finite element analysis modeling should to be addressed. As was evident in the modeling of the experimental specimen, the mechanism for energy loss in addition to that provided by the energy dissipation devices can significantly influence the maximum forces developed.

2. The influence of using controlled rocking piers on system response of an entire bridge should be investigated. Interaction between piers due to flexibility of the superstructure, although believed to be of limited influence, would be also integrated in such studies. It is likely that different retrofit strategies would need to be applied to different piers based on their aspect ratios, stiffness, and connection details (among other factors); and the impact on the overall response should be of primary interest. The developments on the behavior of single controlled rocking piers in this study have provided a basis for the inclusion into complete bridge systems.

3. The inclusion of the controlled rocking approach into building structures should be investigated. Buildings provide additional flexibility in the design variables such as rocking frame aspect ratio and different vertical and horizontal tributary weights. These are variables that can significantly influence the rocking behavior. However, large accelerations in the building near the rocking frame may be detrimental to non-structural equipment.

SECTION 8
REFERENCES

AASHTO (1998). *LRFD Bridge Design Specifications*, American Association of State Highway and Transportation Officials, Washington, D.C.

Abrahamson and Silva (1997). "Empirical Response Spectral Attenuation Relations for Shallow Crustal Earthquakes", *Seismological Research Letters* 68, 94-127.

AISC (2005). Seismic Provisions for Structural Steel Buildings. American Institute of Steel Construction, Chicago, IL.

Ajrab, J., Pekcan, G., Mander, J. (2004). "Rocking Wall-Frame Structures with Supplemental Tendon Systems." J. Struct. Div. ASCE, 130(6), 895-903.

Alavi and Krawinkler (2004). "Behavior of Moment-resisting Frame Structures Subjected to Near-fault Ground Motions", *Earthquake Engineering and Structural Dynamics*, Vol. 33, No.6, pp.687-706.

ATC/MCEER (2004). NCHRP 12-49 *Recommended LRFD Guidelines for the Seismic Design of Highway Bridges, Part I: Specifications*, ATC/MCEER Joint Venture.

Bathe, K. (1996). *Finite Element Procedures*, Prentice-Hall, Upper Saddle River, N.J.

Bendat, J.S. and Piersol, A.G. (1980). *Engineering Applications of Correlation and Spectral Analysis*, John Wiley and Sons, New York, NY.

Berman, J.W. and Bruneau, M. (2005). *Approaches for the Seismic Retrofit of Braced Steel Bridge Piers and Proof-of-Concept Testing of an Eccentrically Braced Frame with Tubular Link. Technical Report MCEER-05-0004, Multidisciplinary Center for Earthquake Engineering Research,* The State University of New York at Buffalo, Buffalo, NY.

Black, C., Makris, N. and Aiken, I. (2002). "Component Testing, Stability Analysis and Characterization of Buckling-Restrained Unbonded Braces", *Report No. EERC 2002-08, Earthquake Engineering Research Center*, College of Engineering, University of California, Berkeley, September 2002.

Bracci, J.M., Reinhorn, A.M., and Mander, J.B. (1992). "Seismic Resistance of Reinforced Concrete Frame Structures Designed Only for Gravity Loads: Part I - Design and Properties of a One-Third Scale Model Structure", *Technical Report NCEER-92-0027, National Center for Earthquake Engineering Research*, The State University of New York at Buffalo, Buffalo, NY.

Christopoulos, C., Filiatrault, A., Uang, C.M., and Folz, B. (2002a). "Posttensioned Energy Dissipating Connections for Moment-resisting Steel Frames", *Journal of Structural Engineering*, ASCE, Vol. 128, No. 9, pp. 1111-1120.

Christopoulos, C., Filiatrault, A., and Folz, B. (2002b). "Seismic Response of Self-centering Hysteretic SDOF Systems", *Earthquake Engineering and Structural Dynamics*, Vol. 31, No. 5, pp. 1131-1150.

Clough, R.W. and Penzien, J. (1975). *Dynamics of Structures*, McGraw-Hill, Inc., New York.

Constantinou, M.C., Soong, T.T., and Dargush, G.F. (1998). "Passive Energy Dissipation Systems for Structural Design and Retrofit", Monograph Series No. 1, Multidisciplinary Center for Earthquake Engineering Research, University at Buffalo, The State University of New York at Buffalo, Buffalo, N.Y.

Constantinou, M.C. and Symans, M.D. (1992). "Experimental and Analytical Investigation of Structures with Supplemental Fluid Viscous Dampers", *Technical Report NCEER-92-0032, National Center for Earthquake Engineering Research,* The State University of New York at Buffalo, Buffalo, NY.

Dowdell, D. and Hamersley, B. (2001) "Lions' Gate Bridge North Approach: Seismic Retrofit", Behaviour Steel Structures in Seismic Areas: Proceedings of the Third International Conference: STESSA 2000; Montreal, Canada, August 21-24, 2000, pp. 319-326.

FEMA (1997). *FEMA 274 NEHRP Commentary on the Guidelines for the Seismic Rehabilitation of Buildings*, Building Seismic Safety Council for the Federal Emergency Management Agency, Washington, D.C.

FEMA (2004). *FEMA 450 NEHRP Recommended Provisions for Seismic Regulations for New Buildings and Other Structures*, Building Seismic Safety Council for the Federal Emergency Management Agency, Washington, D.C.

Harris, H. and Sabnis, G. (1999). *Structural Modeling and Experimental Techniques* (2nd Edition), CRC Press LLC, Boca Raton, FL.

Hasegawa, H., Takeuchi, T., Nakata, Y., Iwata, M., Yamada, S., and Akiyama, H. (1999). "Experimental Study on Dynamic Behavior of Unbonded Braces", *AIJ J. Technol. Des.* No. 9, pp. 103-106.

Hibbeler, R. (1999). *Structural Analysis*, Prentice-Hall Inc., Upper Saddle River, NJ.

Holden, T., Restrepo, J.I., and Mander, J.B. (2003). "Seismic Response of Precast Reinforced and Prestressed Concrete Walls", *Journal of Structural Engineering*, ASCE, Vol. 129, No. 3, pp. 286-296.

Housner, G. (1963). "The Behavior of Inverted Pendulum Structures During Earthquakes", Bulletin of the Seismological Society of America, Vol. 53, No. 2, February 1963, pp. 403-417.

Housner, G., Chairman, The Governor's Board of Inquiry on the 1989 Loma Prieta Earthquake. *Competing Against Time*. State of California, Office of Planning and Research, May 31, 1990.

Ingham, T., Rodriguez, S., Nadar, M., Taucer, F. and Seim, C. (1997). "Seismic Retrofit of the Golden Gate Bridge", Proceedings of the National Seismic Conference on Bridges and Highways: Progress in Research and Practice, December 10-13, San Diego, CA.

Iwata, M., Kato, T., Wada, A. (2000). "Buckling-restrained braces as hysteretic dampers", Behaviour of Steel Structures in Seismic Areas, STESSA 2000, pp. 33-38.

Jones, M., Holloway, L., Toan, V. and Hinman, J. (1997). "Seismic Retrofit of the 1927 Carquinez Bridge by a Displacement Capacity Approach", Proceedings of the Second National Seismic Conference on Bridges and Highways: Progress in Research and Practice, July 8-11, Sacramento, CA.

Kelley, J. and Tsztoo, D. (1977). "Earthquake Simulation Testing of a Stepping Frame with Energy-Absorbing Devices", *Report No. EERC 77-17, Earthquake Engineering Research Center*, College of Engineering, University of California, Berkeley, August 1977.

Konstantinidis, D. and Makris, N. (2005). "Seismic Response Analysis of Multidrum Classical Columns", *Earthquake Engineering and Structural Dynamics*, Vol. 34, No.10, pp.1243-1270.

Lee, K., and Bruneau, M. (2004). "Seismic Vulnerability Evaluation of Axially Loaded Steel Built-Up Laced Members." *Technical Report MCEER-04-0007*, Multidisciplinary Center for Earthquake Engineering Research, State University of New York at Buffalo, Buffalo, NY.

Makris, N. and Black, C.J. (2004). "Dimensional Analysis of Rigid-plastic and Elastoplastic Structures under Pulse-type Excitations", *Journal of Engineering Mechanics*, ASCE, Vol. 130, No. 9, pp. 1006-1018.

Makris, N. and Konstantinidis, D. (2002). "The rocking spectrum and the limitations of practical design methodologies", *Earthquake Engineering and Structural Dynamics*, Vol. 32, pp. 265-289.

Malvern, L.E. (1969). *Introduction to the Mechanics of a Continuous Medium*, Prentice-Hall, Englewood Cliffs, N.J.

Mander, J. and Cheng, C. (1997). "Seismic Resistance of Bridge Piers Based on Damage Avoidance Design", *Technical Report NCEER-97-0014, National Center for Earthquake Engineering Research*, The State University of New York at Buffalo, Buffalo, NY.

Marriott, D., Palermo, A., and Pampanin, S. (2006). "Quasi-static and Pseudo-dynamic Testing of Damage-resistant Bridge Piers with Hybrid Connections", Proceedings of the 1st ECEES, Sept. 3-8, Geneva, Switzerland.

Meek, J.W. (1975). "Effects of Foundation Tipping on Dynamic Response", *Journal of the Structural Division*, ASCE, Vol. 101, No. ST7, pp. 1297-1311.

Midorikawa, M., Azuhata, T., Ishihara, T. and Wada, A. (2003). "Shaking table tests on rocking structural systems installed yielding base plates in steel frames", Behaviour of Steel Structures in Seismic Areas, STESSA 2003, pp. 449-454.

Newmark, N. M. (1959). "A Method of Computation for Structural Dynamics", *Journal of Engineering Mechanics Division*, ASCE, Vol. 85, pp. 67-94.

Newmark, N., and Hall, W. (1982). *Earthquake Spectra and Design*, Earthquake Engineering Research Institute, Oakland, CA.

Palermo, A., Pampanin, S., and Calvi, G.M. (2005). "Concept and Development of Hybrid Solutions for Seismic Resistant Bridge Systems", *Journal of Earthquake Engineering*, Imperial College Press, Vol. 9, No. 6, pp. 899-921.

Perez, F.J., Pessiki, S., and Sause, R. (2004). "Lateral Load Behavior of Unbonded Post-tensioned Precast Walls with Vertical Joints", *PCI Journal*, Vol. 49, No. 2, pp. 48-63.

Pollino, M. (2004). "Seismic Retrofit of Bridge Steel Truss Piers Using a Controlled Rocking Approach", M.S. Thesis. The State University of New York at Buffalo.

Priestley, M.J.N., Evison, R.J. and Carr, A.J. (1978). "Seismic Response of Structures Free to Rock on Their Foundations", Bulletin of the New Zealand National Society for Earthquake Engineering, Vol. 11, No. 3, Sep. 1978.

Priestley, M.J.N. and Kowalsky, M.J. (2000). "Direct displacement-based seismic design of concrete buildings", Bulletin of the New Zealand Society for Earthquake Engineering, Vol. 33, No. 4, pp. 421-444.

Priestley, M.J.N., Seible, F. and Calvi, G.M. (1996). *Seismic Design and Retrofit of Bridges*, John Wiley & Sons, New York.

Prucz, Z., Conway, W.B., Schade, J.E., and Ouyang, Y. (1997). "Seismic Retrofit Concepts and Details for Long-span Steel Bridges", Proceedings of the 2nd National Seismic Conference on Bridges and Highways: Progress in Research and Practice, Sacramento, CA, U.S.A., July 8-11, 1997.

Psycharis, I.N. (1982). "Dynamic Behavior of Rocking Structures Allowed to Uplift," Ph.D. Dissertation, California Institute of Technology, Pasadena, CA.

Ramirez, O., Constantinou, M., Kircher, C., Whittaker, A., Johnson, M. and Gomez, J. (2000). "Development and Evaluation of Simplified Procedures for Analysis and Design of

Buildings with Passive Energy Dissipation Systems", *Technical Report MCEER-00-0010, Multidisciplinary Center for Earthquake Engineering Research*, The State University of New York at Buffalo, Buffalo, NY.

Reinhorn, A.M., Li, C., and Constantinou, M.C. (1995). "Experimental and Analytical Investigation of Seismic Retrofit of Structures with Supplemental Damping Part I: Fluid Viscous Damping Devices", *Technical Report NCEER-95-0001, National Center for Earthquake Engineering Research*, The State University of New York at Buffalo, Buffalo, NY.

Ricles, J.M., Sause, R., Garlock, M.M., and Zhao, C. (2001). "Posttensioned Seismic-resistant Connections for Steel Frames", *Journal of Structural Engineering*, ASCE, Vol. 127, No. 2, pp. 113-121.

Ritchie, P., Kauhl, N. and Kulicki, J. (1999). "Critical Seismic Issues for Existing Steel Bridges", *Technical Report MCEER-99-0013, Multidisciplinary Center for Earthquake Engineering Research*, The State University of New York at Buffalo, Buffalo, NY.

Roh, H.S. and Reinhorn, A.M. (2006). "Nonlinear Behavior of Rocking Beam-columns with Confined Ends", Proceedings, 8th U.S. National Seismic Conference on Earthquake Engineering, Paper No. 1627, April 18-22, San Francisco, CA.

Sabnis, G. M. (1983). *Structural modeling and experimental techniques*, Prentice-Hall, Englewood Cliffs, N.J.

Seleemah, A.A. and Constantinou, M.C. (1997). "Investigation of Seismic Response of Buildings with Linear and Nonlinear Fluid Viscous Dampers", *Technical Report NCEER-97-0004, National Center for Earthquake Engineering Research,* The State University of New York at Buffalo, Buffalo, NY.

Somerville, P. (1997). "Development of Ground Motion Time Histories for Phase 2 of the FEMA/SAC Steel Project", Report No. SAC/BD-97/04, SAC Joint Venture, Sacramento, CA.

Soong, T.T. and Spencer, B.F. (2002). "Supplemental Energy Dissipation: State-of-the-art and State-of-practice." Engineering Structures, Elsevier Science Ltd., Vol. 24, No. 3, pp. 243-259.

Stone, W.C, Cheok, G.S., and Stanton, J.F. (1995). "Performance of Hybrid Moment-resisting Precast Beam-column Concrete Connections Subjected to Cyclic Loading", *Structural Journal*, ACI, Vol. 91, No. 2, pp. 229-249.

Toranzo, L.A., Carr, A.J. and Restrepo, J.I. (2001). "Displacement Based Design of Rocking Walls Incorporating Hysteretic Energy Dissipators", 7th International Seminar on Seismic Isolation, Passive Energy Dissipation and Active Control of Vibrations of Structures, Assisi, Italy, October 2-5, 2001.

Tsai, K.C., Chen, H.W., Hong, C.P., and Su, Y.F. (1993). "Design of Steel Triangular Plate Energy Absorbers for Seismic-Resistant Construction", *Earthquake Spectra*, EERI, Vol. 9, No. 3, pp. 505-528.

Vargas, R. (2006). "Analytical and Experimental Investigation of the Structural Fuse Concept", Ph.D. Dissertation. The State University of New York at Buffalo.

Wada, A., Saeki, E., Takeuch, T., and Watanabe, A. (1989). "Development of unbonded brace", Column (A Nippon Steel Publication), No. 115 1989.12.

Watanabe, A., Hitomoi, Y., Saeki, E., Wada, A., and Fujimoto, M. (1988). "Properties of brace encased in buckling-restraining concrete and steel tube", Proceedings of Ninth World Conference on Earthquake Engineering, Tokyo-Kyoto, Japan, Vol. IV, pp. 719-724.

Watanabe, A. and Nakamura, H. (1992). "Study on the behavior of buildings using steel with low yield point", Proceedings of Tenth World Conference on Earthquake Engineering, Balkema, Rotterdam, pp. 4465-4468.

Wen, Y. K. (1976). "Method for Random Vibration of Hysteretic Systems," *Journal of the Engineering Mechanics Division*, ASCE, Vol. 102, No. EM2.

Whittaker, A.S., Aiken, I., Bergman, D., Clark, P., Kelly, J., and Scholl, R. (1993). "Code Requirements for the Design and Implementation of Passive Energy Dissipation Systems". Proceedings, ATC-17-1, Seminar on Seismic Isolation, Passive Energy Dissipation, and Active Control, Applied Technology Council, Redwood City, California.

Wilson, E. (2000). *Three Dimensional Static and Dynamic Analysis of Structures*. Computers and Structures, Inc., Berkeley, CA.

Wolf, J.P. (1991). "Consistent lumped-parameter models for unbounded soil: physical representation", *Earthquake Engineering and Structural Dynamics*, Vol. 20, No.1, pp.11-32.

Yao, G. (1991). "Diagnostic Studies of Steel Structures Through Vibrational Signature Analysis", Ph.D. Dissertation. The State University of New York at Buffalo.

Zahrai, S.M. and Bruneau, M. (1998). "Seismic Retrofit of Steel Slab-on-Girder Bridges using Ductile End-Diaphragms", *Report OCEERC 98-20, Ottawa Carleton Earthquake Engineering Research Centre*, Ottawa, Canada.

APPENDIX A

REPRESENTATIVE PIER PROPERTIES

Calculations of the "fixed-based" stiffness and period of vibration for the adopted "representative" pier properties used in Sections 3 and 4 are shown in this appendix. The properties for piers having aspect ratios of 3 and 4 are presented.

Representative Pier Properties:

constants:

$$g := 9.81 \frac{m}{\sec^2}$$

$$E := 200\text{GPa}$$

General Pier

$P_v=1^*$ $\frac{m}{2}$ $\frac{m}{2}$

m: bridge mass tributary to pier

h

Tower Diagonal (A_d, L_d)

A_d: cross-sectional area of tower diagonals

L_d: length of tower diagonals

Tower Leg (A_L)

d

A_L: cross-sectional area of tower legs
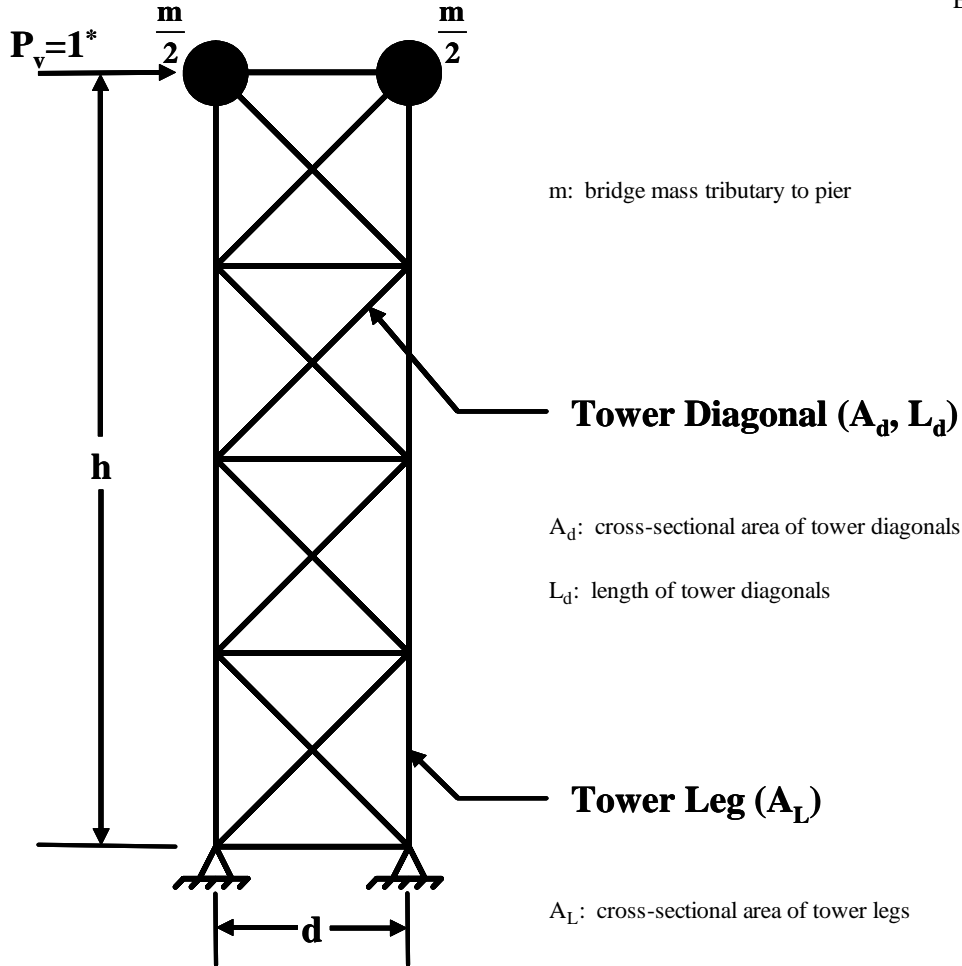
$$m := \frac{1730\text{kN}}{g}$$

$$A_d := 7097\text{mm}^2$$

(properties of piers assumed representative,
as discussed in section 3.4.2)

$$L_d := 10389\text{mm}$$

$$A_L := 31100\text{mm}^2$$

-pier moment of inertia

$$I := \frac{1}{2} A_L \cdot d^2 \quad I = 0.832\,\text{m}^4$$

$\dfrac{h}{d} = 4$ $\quad\quad\quad$ $d := 7315\,mm$

$h := 29260\,mm$

-pier stiffness k_o:

$P_v := 1\,kN \quad$ (virtual unit load)

$n_b := 4 \quad$ (number of x-braced bays)

bending: $\quad\quad\quad\quad\quad\quad$ shear:

$\Delta_b := \dfrac{P_v \cdot h^3}{3 \cdot E \cdot I}$ $\quad\quad\quad\quad$ $\Delta_v := \dfrac{P_v \cdot L_d^{\,3}}{2 \cdot E \cdot d^2 \cdot A_d} \cdot n_b$

$k_b := \dfrac{P_v}{\Delta_b}$ $\quad\quad\quad\quad\quad$ $k_v := \dfrac{P_v}{\Delta_v}$

$k_o := \left(\dfrac{1}{k_b} + \dfrac{1}{k_v} \right)^{-1}$

$k_o = 12.5\,\dfrac{kN}{mm}$

-natural period of vibration of fixed-base pier:

$T_o := 2 \cdot \pi \cdot \sqrt{\dfrac{m}{k_o}}$

$T_o = 0.74\,sec$

$$\frac{h}{d} = 3$$

$d := 7315 \text{mm}$

$h := 21946 \text{mm}$

-pier stiffness k_o:

$P_v := 1 \text{kN}$ (virtual unit load)

$n_b := 3$ (number of x-braced bays)

bending: shear:

$$\Delta_b := \frac{P_v \cdot h^3}{3 \cdot E \cdot I} \qquad\qquad \Delta_v := \frac{P_v \cdot L_d^{\ 3}}{2 \cdot E \cdot d^2 \cdot A_d} \cdot n_b$$

$$k_b := \frac{P_v}{\Delta_b} \qquad\qquad k_v := \frac{P_v}{\Delta_v}$$

$$k_o := \left(\frac{1}{k_b} + \frac{1}{k_v}\right)^{-1}$$

$$k_o = 23.1 \frac{\text{kN}}{\text{mm}}$$

-natural period of vibration of fixed-base pier:

$$T_o := 2 \cdot \pi \cdot \sqrt{\frac{m}{k_o}}$$

$$T_o = 0.55 \text{ sec}$$

APPENDIX B

HYSTERETIC VARIABLES FOR CONTROLLED ROCKING 4-LEGGED PIER

The hysteretic variables for a 4-legged controlled rocking pier with general steel yielding devices implemented at the base are provided in this appendix. The variables defining the cyclic hysteretic behavior of 2-legged controlled rocking piers were developed in Section 2.6.1. The primary difference is due to the use of four steel yielding devices (one attached at the base of each leg) as opposed to two. The changes are quite subtle however are provided here for reference since these variable will be used in Section 4 and also for description of properties of the experimental specimen, which had four legs. The variables for 4-legged piers are displayed in table B-1 along with the variables for 2-legged piers (derived in Section 2) for comparison.

TABLE B-1 Variables Defining Uni-directional Cyclic Hysteretic Behavior

Variable Description	4-legged (Uni-directional)	2-legged
Base Shear at Point of Uplift During 1st Cycle	$P_{up1} = \dfrac{w_v}{2}\left(\dfrac{d}{h}\right)$	$P_{up1} = \dfrac{w_v}{2}\left(\dfrac{d}{h}\right)$
Top of Pier Displacement at Point of Uplift During 1st Cycle	$\Delta_{up1} = \dfrac{P_{up1}}{k_o}$	$\Delta_{up1} = \dfrac{P_{up1}}{k_o}$
Rocking Stiffness (Post-Uplift Global Stiffness)	$k_r = \left(\dfrac{1}{k_o} + \dfrac{1}{2\,k_d\left(\dfrac{d}{h}\right)^2}\right)^{-1}$	$k_r = \left(\dfrac{1}{k_o} + \dfrac{1}{k_d\left(\dfrac{d}{h}\right)^2}\right)^{-1}$
Base Shear at Point of Yielding of Devices	$P_y = \left(\dfrac{w_v}{2} + 2\cdot F_{yd}\right)\dfrac{d}{h}$	$P_y = \left(\dfrac{w_v}{2} + F_{yd}\right)\dfrac{d}{h}$
Top of Pier Displacement at Point of Device Yielding During 1st Cycle	$\Delta_{y1} = \left(\dfrac{w_v}{2k_o} + \dfrac{2F_{yd}}{k_r}\right)\dfrac{d}{h}$	$\Delta_{y1} = \left(\dfrac{w_v}{2k_o} + \dfrac{F_{yd}}{k_r}\right)\dfrac{d}{h}$
Base Shear at Point of Compressive Yielding of Devices	$P_c = \left(\dfrac{w_v}{2} - 2F_{yd}\right)\left(\dfrac{d}{h}\right)$	$P_c = \left(\dfrac{w_v}{2} - F_{yd}\right)\left(\dfrac{d}{h}\right)$
Top of Pier Displacement at Point of Compressive Yielding of Devices	$\Delta_c = \Delta_u - \dfrac{4F_{yd}\dfrac{d}{h}}{k_o} - 2\Delta_{yd}\dfrac{h}{d}$	$\Delta_c = \Delta_u - \dfrac{2F_{yd}\dfrac{d}{h}}{k_o} - 2\Delta_{yd}\dfrac{h}{d}$
Local Strength Ratio (η_L)	$\eta_L = \dfrac{F_{yd}}{w_v/4}$	$\eta_L = \dfrac{F_{yd}}{w_v/2}$
Base Shear at Point of Uplift During 2nd Cycle	$P_{up2} = P_c = (1-\eta_L)\dfrac{w_v}{2}\dfrac{d}{h}$	$P_{up2} = P_c = (1-\eta_L)\dfrac{w_v}{2}\dfrac{d}{h}$
Top of Pier Displacement at Point of Uplift During 2nd Cycle	$\Delta_{up2} = \dfrac{P_{up2}}{k_o}$	$\Delta_{up2} = \dfrac{P_{up2}}{k_o}$
Top of Pier Displacement at Point of Device Yielding During 2nd Cycle	$\Delta_{y2} = \dfrac{(1-\eta_L)\dfrac{w_v}{2}\dfrac{d}{h}}{k_o} + \dfrac{4F_{yd}\dfrac{d}{h}}{k_r}$	$\Delta_{y2} = \dfrac{(1-\eta_L)\dfrac{w_v}{2}\dfrac{d}{h}}{k_o} + \dfrac{2F_{yd}\dfrac{d}{h}}{k_r}$

APPENDIX C

CALIBRATION OF LARGE CAPACITY LOAD CELLS

C.1 General

This appendix discusses the procedure and data obtained for the calibration of the set of four, five-channel large capacity (black) load cells (LC). These load cells were used during the experimental testing to measure reactions at the base of the pier specimen. The five-channel reaction load cells described here were designed and constructed for the Structural Engineering and Earthquake Simulation Laboratory (SEESL) by a faculty member of the Department of Civil, Structural, and Environmental Engineering at the University at Buffalo.

C.2 Load Cell Description

The load cells are identical, to within fabrication tolerances, in terms of construction, geometry and instrumentation. Each LC consists of a thick wall cylindrical steel tube machined to a specified thickness, two square steel end-plates, connection hardware, four strain rosettes, twelve uniaxial stain gages, connective wiring, and a protective cover. A LC elevation and plan view, including dimensions, is shown in figure C-1.

The machined portion of the thick wall cylindrical steel tube forms the instrument portion of the LC and governs its capacity. Since inelastic (permanent) deformations are undesirable, the stress limit of the LC is restricted to the elastic limit of the material and dependent on its cross-section geometry. The capacity of one LC, in terms of first yield, to resist simultaneous axial (normal) force, shear force, and bending moment is plotted in figure C-2. In this figure, the axial force capacity is plotted as a function of the applied moment for various, arbitrarily chosen, levels of applied shear force. Each line corresponds to a specific shear force magnitude as indicated by the two numerical values plotted atop the line. The first numerical value is in units of kilo-newton and the second, in parenthesis, in units of kips. The lines plotted in figure C-2 were calculated using Von Mises criterion:

$$\sigma^2 + 3\tau^2 = \sigma_y^2 \tag{C-1}$$

where σ =normal stress; τ =shear stress; and σ_y=yield stress set equal to 250MPa (36ksi).

Each LC is instrumented with four strain rosettes and twelve uniaxial strain gages positioned around the circumference of the machined portion of the cylindrical steel tube. The position, orientation, and connectivity of these gages facilitates the measurement of applied: (N) normal force in the z-direction; (Sx) shear force in the x-direction; (Sy) shear force in the y-direction; (Mx) moment in the x-direction (about the y-axis); and (My) moment in the y-direction (about the x-axis). Individual gages and rosettes are grouped around the circumference of the LC. The position and orientation of each gage within a particular group is shown by the schematic presented in figure C-3a. In this figure, gage numbers 1, 2, and 3 compose a strain rosette while numbers 4, 5, and 6 are individual uniaxial strain gages. Group location around the circumference of the cross-section is shown. Specific gages around the circumference are connected to form Wheatstone bridge circuits (Sabnis, 1983). The connectivity of each gage and the resulting five Wheatstone bridge circuits are presented diagrammatically in figure C-3b.

Each circuit diagram shown in figure C-3b is denoted by an abbreviation of the measured action, for example, N, represents the normal force circuit. In this figure strain gages are denoted using a two digit alpha-numeric sequence representing the group and gage number. The normal circuit is composed of gages measuring normal strain (A2, B2, C2 and D2) and thermal compensation gages oriented perpendicular to the normal strain (A6, B6, C6 and D6). The shear and moment circuits are designed such that no additional gages are required for thermal compensation.

C.3 Load Cell Calibration

The LCs were calibrated against a NIST (National Institute of Standards and Technology) traceable reference load cell (Calibration Certificate: UB-2006-03-02) using the Tinius Olsen tension-compression machine, manufactured by the Tinius Olsen Testing Machine Co. formerly of Willow Grove Pennsylvania, and a Pacific Instruments 6000 Acquisition and Control system.

Two configurations were required to calibrate all five channels of each LC. The normal force channels were calibrated simultaneously by stacking the LCs in series with the

reference load cell, then compressing the reference and reaction LCs using the Tinius Olsen machine (see figure C-4a). The shear and moment channels were calibrated using a two-point loading scheme (as shown in figure C-4b). The reference load cell and a W310x67 (W12x45) "two-point" loading beam were used to apply two-point loading to the reaction LC assembly. Steel 12.7mm(1/2in) diameter rods were used to simulate point loading and to support each end of the reaction LCs. The steel rods supporting the two-point loading beam were approximately located at the center of the inner end-plate of the outer two load cells then tack welded to the two-point loading beam. The steel rods supporting the LCs were approximately located at the center of the outer end-plates of the outer load cells. The actual location of the rods was measured each time the orientation (or arrangement) of the load cells was changed to ensure consistent set-up dimensions for calculation of applied moments to the load cells. During two-point loading, a shear channel of the outer load cells and a moment channel of the inner two load cells were calibrated. The remaining shear and moment channels were calibrated through a series of rotating and rearranging the LC assembly.

A Pacific Instruments 6000 Series Acquisition and Control System was used to calibrate each channel and to record calibration data-sets. Each channel was calibrated according to the following procedure:

1. balance channels (circuits)
2. zero reference load cell
3. apply load via the Tinius Olsen machine
4. initiate a two-point engineering unit (EU) calibration
5. enter first EU calibration point (at full-scale)
6. remove load
7. enter second EU calibration point (zero load)
8. determine EU slope for channel under calibration (CUC)
9. balance circuits again
10. zero reference load cell
11. initiate calibration data-set

12. apply a single sided cycle of loading to full-scale EU value

13. terminate calibration data-set

A summary of calibration information is presented in table C-1. For each channel the following information is provided: Data Acquisition (DAQ) channel; Engineering Unit (EU); Gain; Unamplified Full-Scale Output in milli-volts; Amplified Full-Scale Output in volts; EU slope in Engineering Unit per milli-volt; Full-Scale EU; and the Amplified Output per EU.

Calibration curves (data-sets) for each load cell are presented in figure C-5 through figure C-8. Each plot presents the output of all five channels of a particular LC as a function of the reference signal for a particular channel under calibration (CUC) as identified by the sub-caption. Each scale is then normalized by the maximum reference cell recording (P_{max}) for the data set taken. In some instances data-sets were recorded prior to the calibration of all the LC channels. In this case, the signals recorded prior to calibration were adjusted according to the results of calibrating those particular channels. Moment signals in the normal calibration are unaltered, therefore the values read off the y-axis (on the $1/P_{max}$ scale) are correct however the units are inches. Lastly, moment signals in plots where moment and shear were under calibration are also normalized by the Arm value (276mm or 10.875in.) for the purpose of presentation. For completeness, the measured Arm value is presented in these plots. In many plots a significant signal from channels other than the CUC are observed. This can be attributed to either the calibration setup, gage location, and/or slight gage misalignment. This is especially apparent in the normal calibration data sets.

TABLE C-1 Calibration Data Summary

Load Cell No.	Load Cell Channel	DAQ Channel	Eng. Unit	Gain	Unamp. Full-Scale Output (mV)	Amp. Full-Scale Output (V)	EU Slope (EU/mV)	Full-Scale EU	Amp. Output/EU
1	N	2	kips	1000	10	10	10.21	102.1	0.098
1	Sx	3	kips	1000	10	10	6.32	63.2	0.158
1	Sy	4	kips	1000	10	10	6.56	65.6	0.152
1	Mx	5	kip-in	500	20	10	19.10	382.0	0.026
1	My	6	kip-in	500	20	10	18.76	375.2	0.027
2	N	7	kips	1000	10	10	10.62	106.2	0.094
2	Sx	8	kips	1000	10	10	6.33	63.3	0.158
2	Sy	9	kips	1000	10	10	6.16	61.6	0.162
2	Mx	10	kip-in	500	20	10	20.09	401.8	0.025
2	My	11	kip-in	500	20	10	19.37	387.4	0.026
3	N	12	kips	1000	10	10	10.09	100.9	0.099
3	Sx	13	kips	1000	10	10	7.12	71.2	0.140
3	Sy	14	kips	1000	10	10	7.21	72.1	0.139
3	Mx	15	kip-in	500	20	10	19.85	397.0	0.025
3	My	16	kip-in	500	20	10	20.00	400.0	0.025
4	N	17	kips	1000	10	10	10.67	106.7	0.094
4	Sx	18	kips	1000	10	10	6.56	65.6	0.152
4	Sy	19	kips	1000	10	10	6.58	65.8	0.152
4	Mx	20	kip-in	500	20	10	18.73	374.6	0.027
4	My	21	kip-in	500	20	10	17.99	359.8	0.028
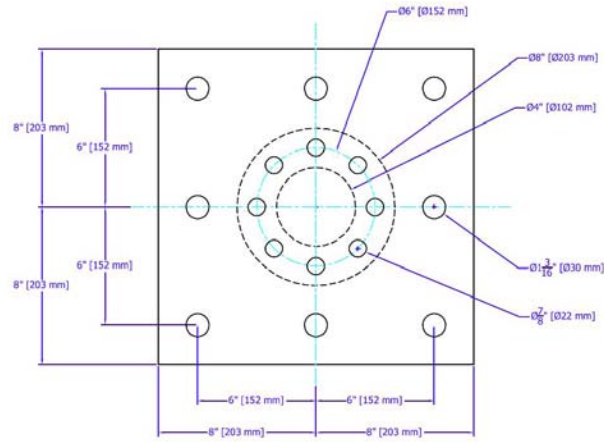
(a) Plan View
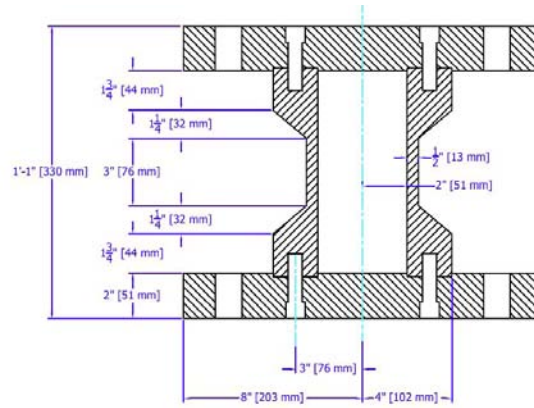
(b) Elevation Cross-section View

FIGURE C-1   Large Load Cell Dimensions
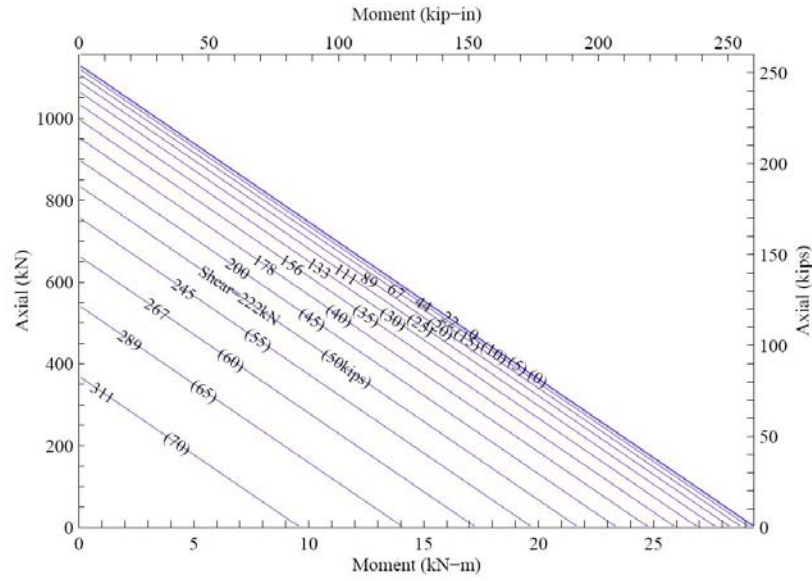
FIGURE C-2   LC Capacity based on Von Mises Yield Criterion
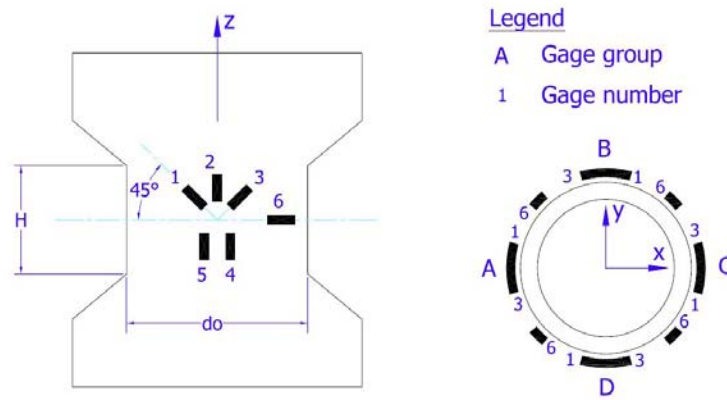
(a)
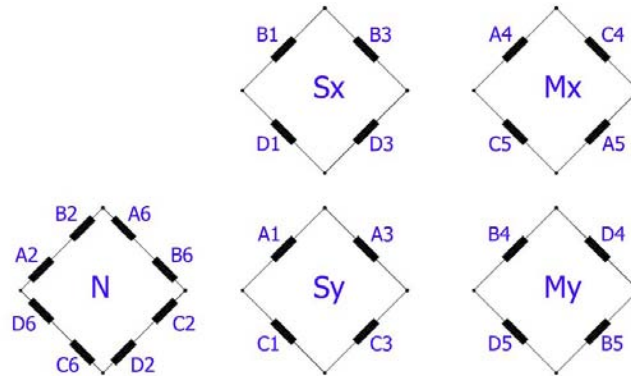
(b)

FIGURE C-3   Internal Strain Gage Layout and Circuitry of Load Cells (a) Strain Gage Layout on LC Cylinder and (b) Wheatstone Bride Circuits (adapted from Bracci et. al. 1992)
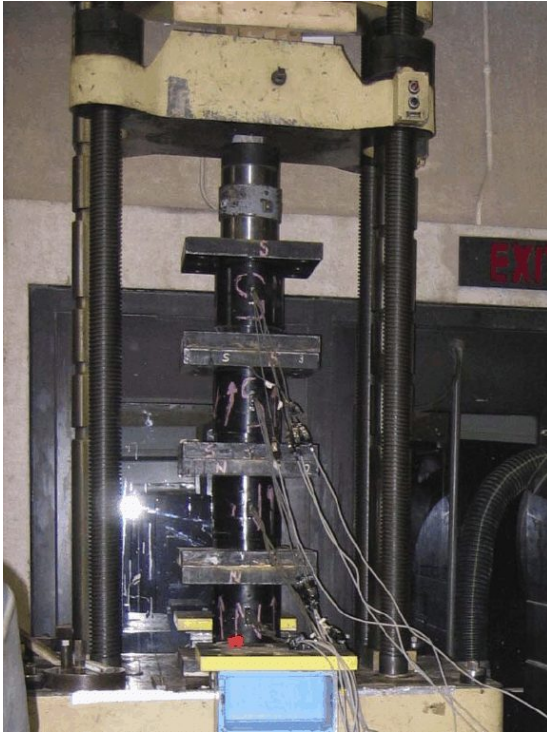
(a)
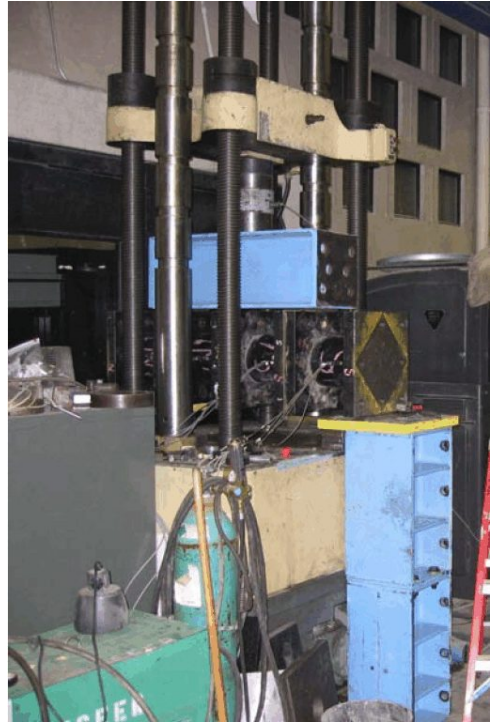
(b)

FIGURE C-4   Load Cell Calibration Set-up Photographs (a) Normal Calibration and (b) Shear and Moment Calibration

(a) Sx

(b) Sy
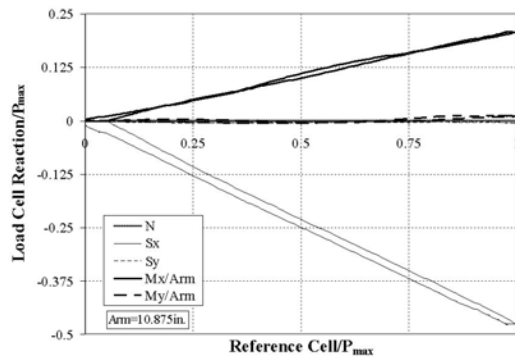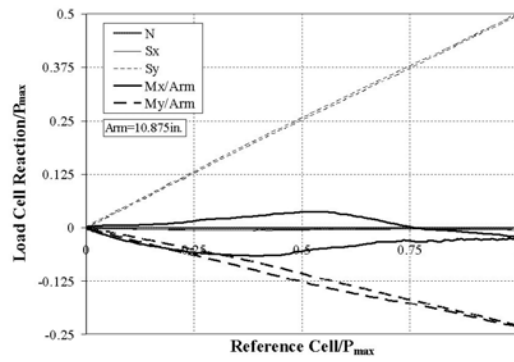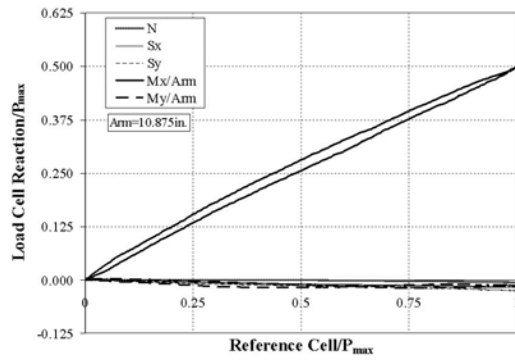
(c) Mx
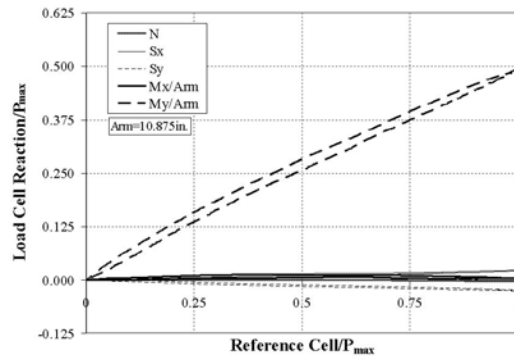
(d) My
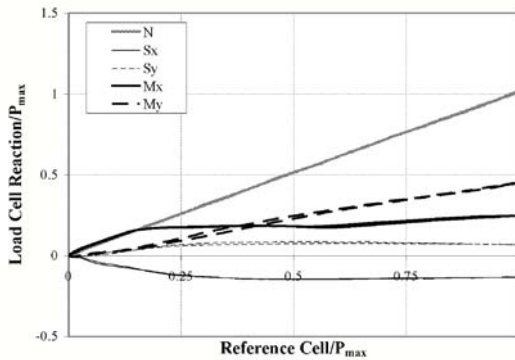
(e) N

FIGURE C-5   Calibration Data Sets For LC1

(a) Sx

(b) Sy
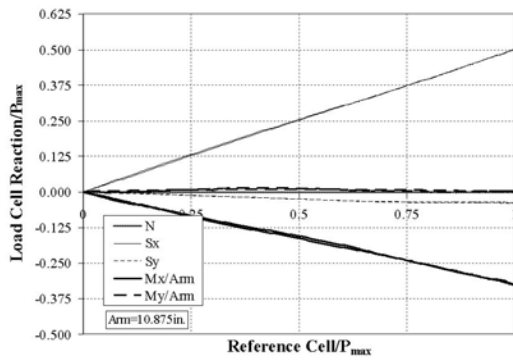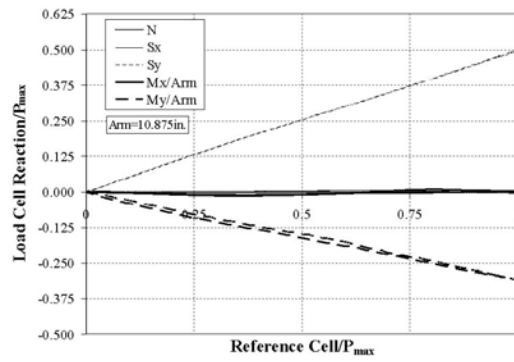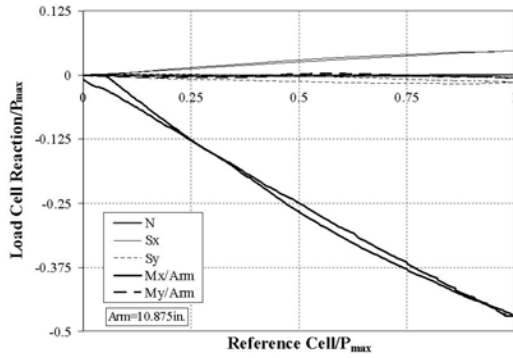
(c) Mx
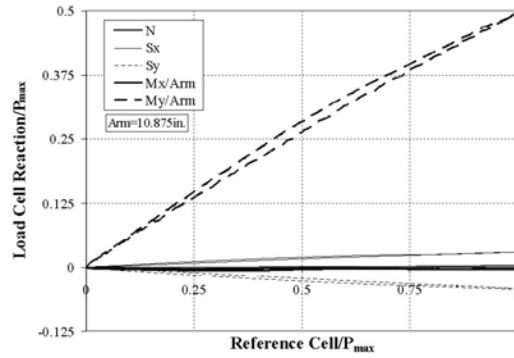
(d) My
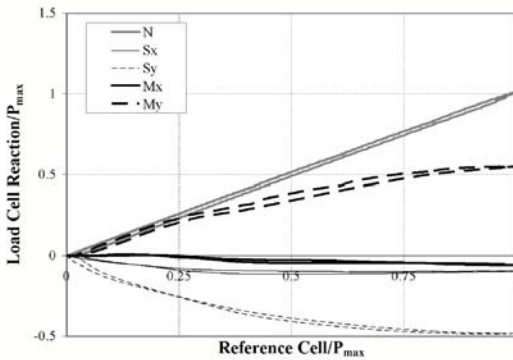
(e) N

FIGURE C-6   Calibration Data Sets For LC2

(a) Sx

(b) Sy
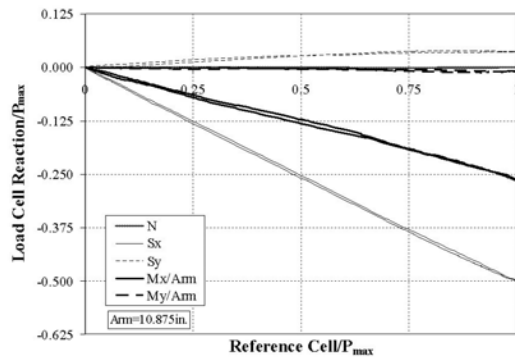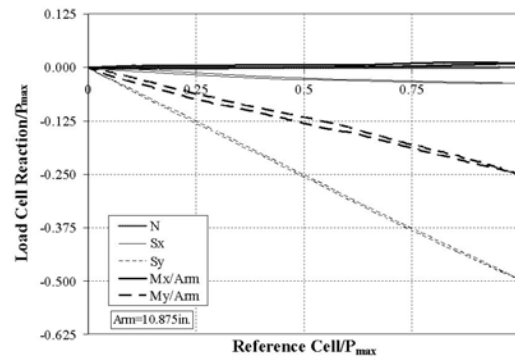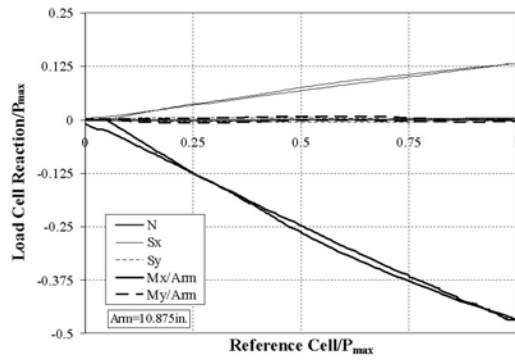
(c) Mx
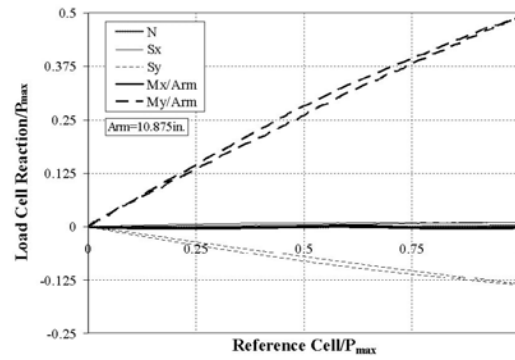
(d) My
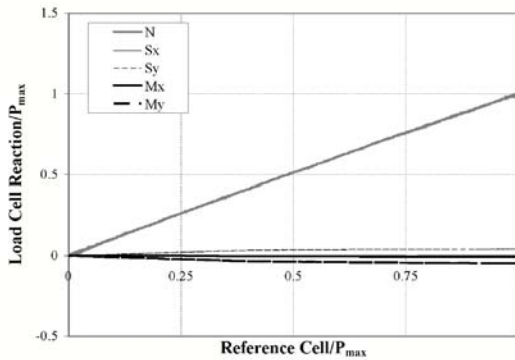
(e) N

FIGURE C-7   Calibration Data Sets For LC3

394

(a) Sx

(b) Sy
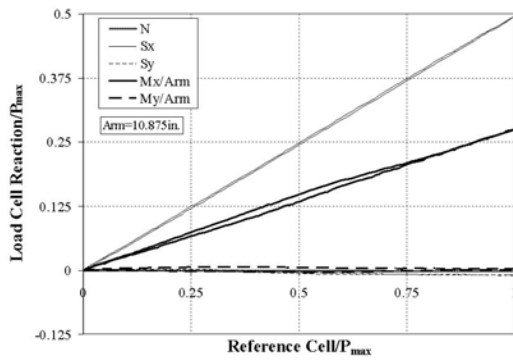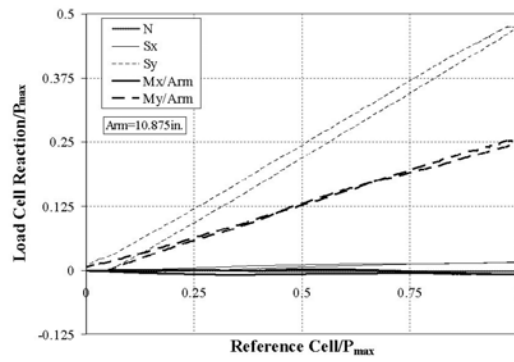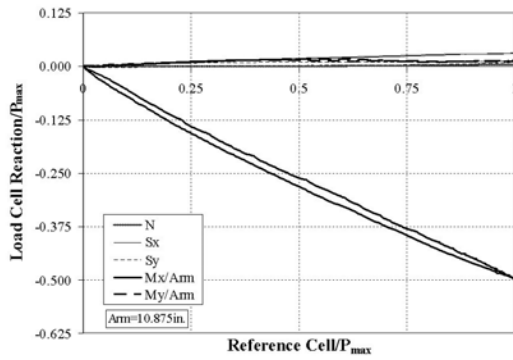
(c) Mx
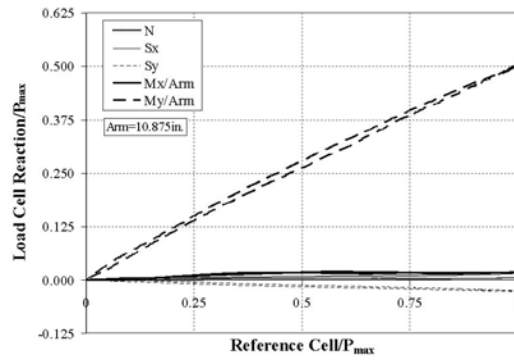
(d) My
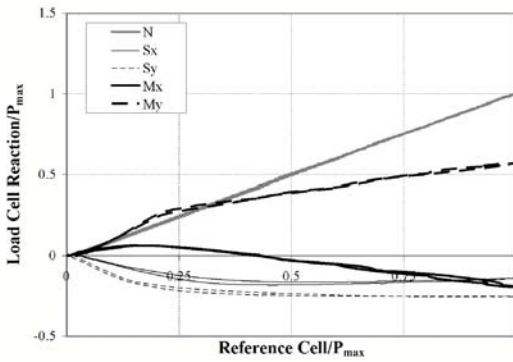
(e) N

FIGURE C-8   Calibration Data Sets For LC4

395

APPENDIX D

RESPONSE PREDICTION CALCULATIONS

A sample set of calculations of response using the simplified method of analysis and design equations for the experimental specimen with steel yielding devices and viscous dampers are provided in this appendix. The calculations presented are based on developments from Sections 2, 3, and 4 and discussion of the experimental model properties in Sections 5 and 6.

Model Pier Properties

$h_m := 6.09m$

$d_m := 1.52m$ (rocking width)

$d_{clm} := 1.32m$ (column centerline width)

$\dfrac{h_m}{d_m} = 4$

$W_{xm} := 80.1kN$

$W_{zm} := 80.1kN$

$W_{pm} := 11.1kN$

$m_{xm} := \dfrac{W_{xm}}{g}$

$m_{zm} := \dfrac{W_{zm}}{g}$

Mass Dimensions and Mass Moment of Inertia of Added Mass (steel plates):

$w_{sp} := 3073mm$

$d_{sp} := 178mm$

$I_{oxm} := \dfrac{1}{12} \dfrac{W_{xm}}{g} \cdot \left(w_{sp}^2 + d_{sp}^2\right)$

$I_{oxm} = 63.2 \dfrac{kN}{g} \cdot m^2$

$E_m := 200GPa$ (modulus of elasticity of steel)

Column Properties   Beam Properties   Diagonal Properties

$\theta_{1m} := 34deg$

$A_{Lm} := 15.55cm^2$ $I_{bm} := 137cm^4$ $d_{rod} := 9.53mm$

$\theta_{25m} := 42deg$

$I_{cmXX} := 429cm^4$ $L_b := 88.9cm$

$I_{cmYY} := 91.6cm^4$ $n_b := 5$ $A_{dm} := 0.70 \dfrac{\pi \cdot d_{rod}^2}{4}$ $A_{dm} = 49.931\ mm^2$

$h_{Lm} := 5.97m$

$L_{dYYm} := 102cm$
      (effective length of diagonals)

$L_{dXXm} := 122cm$

$P_{preD} := 17.8kN$ (pre-tension force applied to diagonals)

Pier Stiffness in X-X Direction   Stiffness of Single Frame in X-X Direction

$$k_{oxm} := 2.0\,\frac{kN}{mm}$$

$$k_{xfm} := \frac{k_{oxm}}{2}$$

Modes of Interest:

$$k_{Lm} := \frac{E_m \cdot A_{Lm}}{h_m} \quad \text{(axial stiffness of single pier leg)}$$

$$k_{vm} := 42.5\,\frac{kN}{mm} \quad \text{(vertical "shearing" stiffness of pier)}$$

Horizontal Vibration of Pier:

$$T_{oxm} := 2\cdot\pi\cdot\sqrt{\frac{m_{xm}}{k_{oxm}}} \quad \boxed{T_{oxm} = 0.4\,\sec}$$

Axial Vibration of Pier Leg:

$$k_{Lm} = 51.067\,\frac{kN}{mm}$$

$$T_{Lm} := 2\cdot\pi\cdot\sqrt{\frac{m_{zm}}{4\cdot k_{Lm}}} \quad \boxed{T_{Lm} = 0.04\,\sec}$$

Vertical Shearing Vibration of Pier:

$$T_{vm} := 2\cdot\pi\cdot\sqrt{\frac{m_{zm}}{2k_{vm}}} \quad \boxed{T_{vm} = 0.062\,\sec}$$

$$\lambda_{tprov} := \frac{T_{oxp}}{T_{oxm}} \quad \text{(time scale factor}$$
$$\text{provided based on}$$
$$\text{fixed-base period of}$$
$$\lambda_{tprov} = 1.843 \quad \text{pier)}$$

Steel Yielding Device Properties (TADAS)

$\eta_L := 0.67$ (system local strength ratio)

$L := 88.9\,mm$

$b := 54.0\,mm$

$t := 11.1\,mm$

$F_y := 50\,ksi$ $\dfrac{L}{t} = 8.01$ $\gamma_{max} := 0.30$

$N := 2$

$\alpha_{TADAS} := 0.02$ (post-elastic stiffness ratio)

$k_{eTADAS} := \dfrac{E_m \cdot b \cdot N}{6} \cdot \left(\dfrac{t}{L}\right)^3$ $k_{eTADAS} = 7.0\,\dfrac{kN}{mm}$

$V_{yTADAS} := \dfrac{F_y \cdot b \cdot t^2 \cdot N}{6 \cdot L}$ $V_{yTADAS} = 8.60\,kN$

$\Delta_{pTADAS} := \dfrac{3}{2} \dfrac{F_y \cdot L^2}{E_m \cdot t}$ $\Delta_{pTADAS} = 1.841\,mm$

$V_{pTADAS} := \eta_L \cdot \dfrac{W_{zm}}{4}$ $V_{pTADAS} = 13.42\,kN$

$\mu_{TADAS} := \dfrac{\gamma_{max} \cdot L}{\Delta_{pTADAS}}$ $\mu_{TADAS} = 14.5$ (maximum device ductility based on limiting rotation to γ_{max})

$\Omega := 1.5$ (device overstrength factor)

$\phi_v := 0.75$

$\dfrac{\Omega\, \eta_L \cdot W_{zm}}{4} = 20.1\,kN$ (maximum device output shear force)

$M_p := \Omega \cdot N \cdot b \cdot \left(\dfrac{t}{2}\right)^2 \cdot F_y$ (maximum device output bending moment)

$M_p = 1720\,kN \cdot mm$

Development of Uni-directional Pushover Curve

-2nd cycle properties used
-Used for approximate analysis method (cap. spec.)

Uni-directional Yield Properties of System:

$$P_{up1} := \frac{W_{zm}}{2} \cdot \frac{d_m}{h_m} \qquad P_{up1} = 10.00 \, kN$$

$$P_{up2} := (1 - \eta_L) \cdot \frac{W_{zm}}{2} \cdot \frac{d_m}{h_m}$$

$$P_{up2} = 3.30 \, kN$$

$$\Delta_{up2} := \frac{P_{up2}}{k_{oxm}}$$

$$\Delta_{up1} := \frac{P_{up1}}{k_{oxm}}$$

$$\Delta_{up2} = 1.65 \, mm$$

$$k_r := \frac{1}{\dfrac{1}{k_{oxm}} + \dfrac{1}{(2 \cdot k_{eTADAS}) \cdot \left(\dfrac{d_m}{h_m}\right)^2}} \quad \text{(rocking stiffness)}$$

$$k_r = 0.608 \, \frac{kN}{mm}$$

$$P_{y2} := \frac{W_{zm}}{2} \cdot \frac{d_m}{h_m} + 2 \cdot V_{pTADAS} \cdot \frac{d_m}{h_m}$$

$$P_{y2} = 16.69 \, kN$$

$$\Delta_{y2} := \frac{(1 - \eta_L) \cdot \dfrac{W_{zm}}{2} \cdot \dfrac{d_m}{h_m}}{k_{oxm}} + \frac{4 \cdot V_{pTADAS} \cdot \dfrac{d_m}{h_m}}{k_r}$$

$$\Delta_{y2} = 23.69 \, mm$$

$$\Delta_{y1} := \frac{\dfrac{W_{zm}}{2} \cdot \dfrac{d_m}{h_m}}{k_{oxm}} + \frac{2 \cdot V_{pTADAS} \cdot \dfrac{d_m}{h_m}}{k_r}$$

$\Delta := 0\text{in}, 0.05\text{in} .. 30\text{in}$

$$
P(\Delta) := \left\| \begin{array}{l}
\left[\left(k_{oxm} - \dfrac{W_{zm}}{h_m}\right)\cdot\Delta\right] \quad \text{if} \ \Delta \le \Delta_{up2} \\[3mm]
\left(k_{oxm} - \dfrac{W_{zm}}{h_m}\right)\cdot\Delta_{up2} + \left(k_r - \dfrac{W_{zm}}{h_m}\right)\cdot\left(\Delta - \Delta_{up2}\right) \quad \text{if} \ \Delta_{up2} < \Delta \le \Delta_{y2} \\[3mm]
\left(k_{oxm} - \dfrac{W_{zm}}{h_m}\right)\cdot\Delta_{up2} + \left(k_r - \dfrac{W_{zm}}{h_m}\right)\cdot\left(\Delta_{y2} - \Delta_{up2}\right) ... \qquad\qquad \text{if} \ \Delta > \Delta_{y2} \\[3mm]
+ \left[\left[\dfrac{1}{k_{oxm}} + \dfrac{1}{\alpha_{TADAS}\cdot\left(2\cdot k_{eTADAS}\right)\cdot\left(\dfrac{d_m}{h_m}\right)^2}\right]^{-1} - \dfrac{W_{zm}}{h_m}\right]\cdot\left(\Delta - \Delta_{y2}\right)
\end{array} \right.
$$

$$
\left[\dfrac{1}{k_{oxm}} + \dfrac{1}{\alpha_{TADAS}\cdot\left(2\cdot k_{eTADAS}\right)\cdot\left(\dfrac{d_m}{h_m}\right)^2}\right]^{-1} - \dfrac{W_{zm}}{h_m} = 4.158 \times 10^{-3} \ \dfrac{kN}{mm} \quad \text{(post-yield stiffness)}
$$

Idealized Bi-linear, Uni-directional Pushover Curve:

Pier at Target Maximum Uni-directional Displacement:

$\Delta_u := 135\text{mm}$ (maximum pier displacement, iterated to determine effective damping of system)
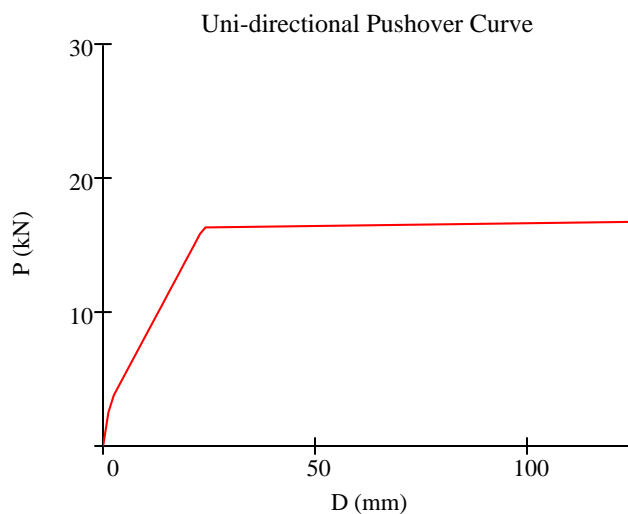
Uni-directional Pushover Curve

Converstion to Spectral Capacity Curve:

$$S_{ac}(\Delta) := \frac{P(\Delta)}{W_{M1}} \cdot \frac{g}{g} \qquad \phi := 1$$

$$\Gamma := 1$$

(conversion to spectral ordinates, piers idealized as SDOF system for horizontal response)

$$S_{dc}(\Delta) := \frac{\Delta}{\phi \cdot \Gamma}$$

Spectral Capacity Curve

Spectral Acceleration (g) vs Displacement (mm)
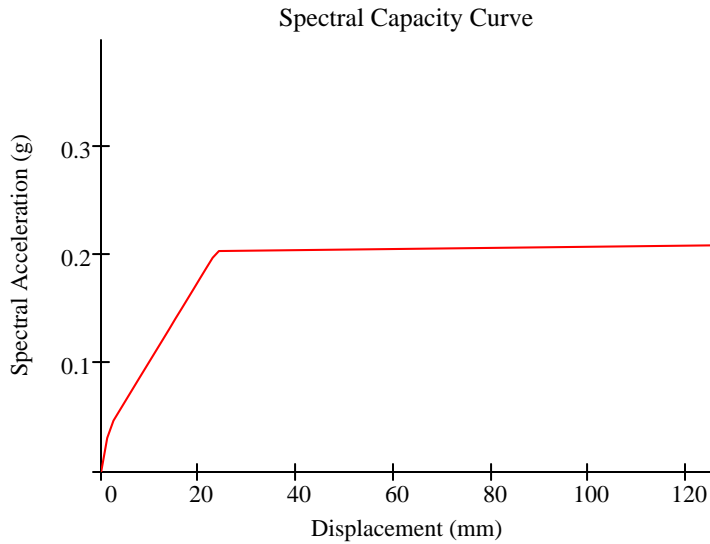
Spectral Demand Curve:

$$W_k := \frac{1}{2} \cdot P_{y2} \cdot \Delta_u \qquad \text{(stored strain energy at displacement, } D_u)$$

$$W_D := 4 \cdot P_{y2} \cdot (\Delta_u - \Delta_{y2}) \qquad \text{(energy dissipation of bi-linear system at displacement, } \Delta_u)$$

$\beta_o := 0.02$ (assumed inherent structural damping)

$$\beta_b := \begin{cases} \dfrac{W_D}{4 \cdot \pi \cdot W_k} & \text{if } \dfrac{W_D}{4 \cdot \pi \cdot W_k} > 0 \\ 0 & \text{otherwise} \end{cases} \qquad \beta_b = 0.505$$

$$q := \frac{\eta_L}{1 + \eta_L} \qquad q = 0.401 \qquad \begin{array}{l}\text{(factor accounting for flag-shaped hysteresis} \\ \text{deviation from bi-linear response)}\end{array}$$

$$\beta_{eff} := q \cdot \beta_b + \beta_o$$

$\beta_{eff} = 0.22$ (equivalent viscous damping for inelastic system)

$$B_s := \begin{cases} 0.8 & \text{if } \beta_{eff} \le 0.02 \\ x_1 & \text{if } 0.02 < \beta_{eff} \le 0.05 \\ x_2 & \text{if } 0.05 < \beta_{eff} \le 0.10 \\ x_3 & \text{if } 0.10 < \beta_{eff} \le 0.20 \\ x_4 & \text{if } 0.20 < \beta_{eff} \le 0.30 \\ x_5 & \text{if } 0.30 < \beta_{eff} \le 0.40 \\ x_6 & \text{if } 0.40 < \beta_{eff} \le 0.50 \\ 3.0 & \text{if } \beta_{eff} > 0.50 \end{cases} \qquad B_1 := \begin{cases} 0.8 & \text{if } \beta_{eff} \le 0.02 \\ y_1 & \text{if } 0.02 < \beta_{eff} \le 0.05 \\ y_2 & \text{if } 0.05 < \beta_{eff} \le 0.10 \\ y_3 & \text{if } 0.10 < \beta_{eff} \le 0.20 \\ y_4 & \text{if } 0.20 < \beta_{eff} \le 0.30 \\ y_5 & \text{if } 0.30 < \beta_{eff} \le 0.40 \\ y_6 & \text{if } 0.40 < \beta_{eff} \le 0.50 \\ 2.0 & \text{if } \beta_{eff} > 0.50 \end{cases}$$

$B_s = 1.914$ Damping Modification Factors
(FEMA 273 Table 2-15)
$B_1 = 1.546$

$PSA_{Syn} :=$

C:\..\hl067syn150_SpecX.TXT

(read in file containing spectra data for actual acceleration history recorded on shake table)

$TT_{Syn} :=$

C:\..\TT-ActualMotions.TXT

$S_{aX} := PSA_{Syn} \cdot g$

$TT := TT_{Syn} \cdot sec$

$T_o := \dfrac{0.4sec}{\lambda_{tprov}}$

$S_{av} := 2.75g$ (vertical spectral acceleration value at vertical period of pier)

Demand Spectrum

4.933

PSA_{Syn}

0.03

0.01 $\dfrac{TT_{Syn}}{sec}$ 2

Reduction of Spectral Demand Curve for Equivalent Damping:

$$S_{aXr_j} := \begin{vmatrix} \dfrac{S_{aX_j}}{B_s} & \text{if } TT_j < T_o \\[3mm] \dfrac{S_{aX_j}}{B_1} & \text{if } TT_j \geq T_o \end{vmatrix}$$

Conversion to Spectral Demand Curve:

$$S_{ddx_j} := \left(\dfrac{TT_j}{2 \cdot \pi} \right)^2 \cdot S_{aX_j}$$

$$S_{ddxr_j} := \left(\dfrac{TT_j}{2 \cdot \pi} \right)^2 \cdot S_{aXr_j}$$

$T_{plot} := 0.5\sec, 1.0\sec .. 2\sec$

$x := 0in, 1in .. 30in$

$y(T_{plot}, x) := \dfrac{4 \cdot \pi^2}{T_{plot}^2} x$

Capacity Spectrum Plot

Base Shear/Weight and Spectral Acc.

$S_{ac}(\Delta)$

$\dfrac{y(T_{plot}, x)}{g}$

$\dfrac{S_{aX_j}}{g}$

$\dfrac{S_{aXr_j}}{g}$

1

0

0

200

$\dfrac{S_{dc}(\Delta)}{mm}, \dfrac{x}{mm}, \dfrac{S_{ddx_j}}{mm}, \dfrac{S_{ddxr_j}}{mm}$

Deformation and Spectral Displacement-in

$\Delta_{uf} := 135mm$ (displacement at intersection of reduced spectral demand and spectral capacity curves, iterative with initially guessed max displacement, Δu)

Design Displacements and Forces:

Maximum Pier Displacements:

$$\Delta_{ux} := 135mm \qquad \Delta_{uy} := 114mm$$

$$\Delta_{ux} = 135.0\ mm \qquad \Delta_{uy} = 114\ mm$$

$$\Delta_{u10040} := \sqrt{\left(1.0 \cdot max\left(\Delta_{ux}, \Delta_{uy}\right)\right)^2 + \left(0.4 \cdot min\left(\Delta_{ux}, \Delta_{uy}\right)\right)^2}$$

$$\Delta_{u10040} = 142.5\ mm \qquad \text{(100\% - 40\% Combination Rule for Orthogonal Ground Motion Components)}$$

Maximum Uplifting Displacment:

$$\Delta_{upbi} := \frac{d_m}{h_m} \cdot \left[1.0 \cdot max\left(\Delta_{ux}, \Delta_{uy}\right) + 0.4 \cdot min\left(\Delta_{ux}, \Delta_{uy}\right) - \frac{\dfrac{W_{zm}}{2}\left(1 + \eta_L\right) \cdot \dfrac{d_m}{h_m}}{k_{xfm}} \right]$$

$$\Delta_{upbi} = 37.0\ mm$$

Maximum Device Rotation:

$$\gamma_{TADAS} := \frac{\Delta_{upbi}}{L} \qquad \gamma_{TADAS} = 0.42$$

Maximum Device Force:

$$P_{ud} := \Omega \cdot V_{pTADAS} + \alpha_{TADAS} \cdot k_{eTADAS} \cdot \left(\Delta_{upbi} - \Delta_{pTADAS}\right)$$

$$P_{ud} = 24.3\ kN$$

Maximum Impact Velocity:

$$v_{ox} := \sqrt{g \cdot \left[\frac{1}{\dfrac{1}{4} \cdot \left(\dfrac{h_m}{d_m}\right)^2 + \dfrac{1}{2}}\right] \cdot \left[\frac{W_{xm}}{2} \cdot \frac{\left(\eta_L{}^2 - 1\right)}{k_{oxm}} \cdot \left(\frac{d_m}{h_m}\right)^2 + 2 \cdot \eta_L \cdot \Delta_{pTADAS} + \Delta_{ux} \cdot \frac{d_m}{h_m} \cdot \left(1 - \eta_L\right)\right]}$$

$$v_{ox} = 148.1\ \frac{mm}{sec}$$

$$v_{oy} := \sqrt{g \cdot \left[\frac{1}{\frac{1}{4} \cdot \left(\frac{h_m}{d_m}\right)^2 + \frac{1}{2}}\right] \cdot \left[\frac{W_{xm}}{2} \cdot \frac{\left(\eta_L^2 - 1\right)}{k_{oxm}} \cdot \left(\frac{d_m}{h_m}\right)^2 + 2\eta_L \cdot \Delta_{pTADAS} + 0.40\Delta_{uy} \cdot \frac{d_m}{h_m} \cdot \left(1 - \eta_L\right)\right]}$$

$$v_{oy} = 98.5 \frac{mm}{sec}$$

$$v_o := v_{ox} + v_{oy}$$

$$v_o = 246.6 \frac{mm}{sec}$$

Dynamic Amplification Factors During Rocking Response:

$$T_{vm} = 0.062 \ sec \qquad\qquad\qquad\qquad T_{Lm} = 0.04 \ sec$$

$$P_{uxst} := P_{y2} + \left[\left[\frac{1}{k_{oxm}} + \frac{1}{\alpha_{TADAS} \cdot \left(2 \cdot k_{eTADAS}\right) \cdot \left(\frac{d_m}{h_m}\right)^2}\right]^{-1}\right] \cdot \left(\Delta_{ux} - \Delta_{y2}\right)$$

$$\Delta_{y1} := \left(\frac{W_{xm}}{2 \cdot k_{oxm}} + \frac{2 \cdot V_{pTADAS}}{k_r}\right) \cdot \frac{d_m}{h_m} \qquad\qquad \Delta_{up1} := \frac{\frac{W_{xm}}{2} \cdot \frac{d_m}{h_m}}{k_{oxm}}$$

$$T_{sec} := 2 \cdot \pi \cdot \sqrt{\frac{m_{zm} \cdot \Delta_{ux}}{P_{uxst}}} \qquad T_{sec} = 1.55 \ sec \qquad\qquad t_{rL} := \frac{T_{sec}}{2 \cdot \pi} \cdot asin\left(\frac{\Delta_{up1}}{\Delta_{ux}}\right) \qquad t_{rL} = 0.0083 \ sec$$

$$t_{rv} := \frac{T_{sec}}{2 \cdot \pi} \cdot asin\left(\frac{\frac{1}{2} \cdot \Delta_{y1}}{\Delta_{ux}}\right) \qquad t_{rv} = 0.013 \ sec \qquad R_{dL} := \left\| \begin{array}{l} \left(1 + \dfrac{\sin\left(\dfrac{\pi \cdot t_{rL}}{T_{Lm}}\right)}{\dfrac{\pi \cdot t_{rL}}{T_{Lm}}}\right) \ \text{if} \ t_{rL} > 3 \cdot T_{Lm} \\[20pt] \max\left[1.67, \left(1 + \dfrac{\sin\left(\dfrac{\pi \cdot t_{rL}}{T_{Lm}}\right)}{\dfrac{\pi \cdot t_{rL}}{T_{Lm}}}\right)\right] \ \text{if} \ t_{rL} \le 3 \cdot T_{Lm} \end{array} \right.$$

$$R_{dv} := \left\| \begin{array}{l} \left(1 + \dfrac{\left|\sin\left(\dfrac{\pi \cdot t_{rv}}{T_{vm}}\right)\right|}{\dfrac{\pi \cdot t_{rv}}{T_{vm}}}\right) \ \text{if} \ t_{rv} > 3 \cdot T_{vm} \\[20pt] \max\left[1.67, \left(1 + \dfrac{\left|\sin\left(\dfrac{\pi \cdot t_{rv}}{T_{vm}}\right)\right|}{\dfrac{\pi \cdot t_{rv}}{T_{vm}}}\right)\right] \ \text{if} \ t_{rv} \le 3 \cdot T_{vm} \end{array} \right.$$

$$R_{dv} = 1.92 \qquad\qquad R_{dL} = 1.93$$

Maximum Base Shear Force:

$S_{av} = 2.75\,g$ (vertical spectral acceleration response at vertical period of pier, 2% damp)

$$P_{uFst} := \left(\frac{3 \cdot W_{zm}}{8} + \frac{3}{2} \cdot V_{pTADAS}\right) \cdot \frac{d_m}{h_m}$$

100-40 Combination Rule:

$$P_{u100401} := 1.33\left[P_{uFst} + 1.0 \cdot \left[P_{uFst} \cdot (R_{dv} - 1)\right] + 0.4 \cdot \left(\frac{3 \cdot m_{zm}}{8} \cdot S_{av} \cdot \frac{d_m}{h_m}\right)\right]$$

$$P_{u100402} := 1.33\left[P_{uFst} + 0.4 \cdot \left[P_{uFst} \cdot (R_{dv} - 1)\right] + \left(\frac{3 \cdot m_{zm}}{8} \cdot S_{av} \cdot \frac{d_m}{h_m}\right)\right]$$

$$P_{u10040} := \max\left(P_{u100401}, P_{u100402}\right)$$

$P_{u10040} = 45.6\,kN$ $\dfrac{P_{u10040}}{W_{zm} + W_{pm}} = 0.50$

Maximum Diagonal Member Axial Force

$$P_{dEQ} := \frac{\dfrac{P_{u10040}}{1.33}}{2 \cdot \cos(\theta_{1m})} \qquad P_{dEQ} = 20.687\,kN$$

$P_{ud} := P_{dEQ} + P_{preD}$ $P_{preD} = 17.8\,kN$

$P_{ud} = 38.49\,kN$

Maximum Pier Leg Axial Force:

Absolute Sum Rule:

$$P_{uLabs} := \left(W_{zm} + 3 \cdot V_{pTADAS}\right) + m_{zm} \cdot S_{av} + v_o \cdot \sqrt{\frac{m_{zm} \cdot k_{Lm}}{4}} + \left(R_{dL} - 1\right) \cdot \frac{W_{zm}}{4} \ldots$$
$$+ \left(\frac{3 W_{zm}}{4} + 3 \cdot V_{pTADAS}\right) \cdot \left(R_{dv} - 1\right)$$

$P_{uLabs} = 531.7\,kN$

100-40 Directional and SRSS Modal Combination Rules:

$$P_{uL1} := \left(W_{zm} + 3 \cdot V_{pTADAS}\right) + 0.4 \cdot m_{zm} \cdot S_{av} \; ...$$
$$+ 1.0 \sqrt{\left(v_o \cdot \sqrt{\frac{m_{zm} \cdot k_{Lm}}{4}}\right)^2 + \left[\left(R_{dL} - 1\right) \cdot \frac{W_{zm}}{4}\right]^2 + \left[\left(\frac{3 \cdot W_{zm}}{4} + 3 \cdot V_{pTADAS}\right) \cdot \left(R_{dv} - 1\right)\right]^2}$$

$$P_{uL1} = 349.1 \text{ kN}$$

$$P_{uL2} := \left(W_{zm} + 3 \cdot V_{pTADAS}\right) + 1.0 \cdot m_{zm} \cdot S_{av} \; ...$$
$$+ 0.4 \sqrt{\left(v_o \cdot \sqrt{\frac{m_{zm} \cdot k_{Lm}}{4}}\right)^2 + \left[\left(R_{dL} - 1\right) \cdot \frac{W_{zm}}{4}\right]^2 + \left[\left(\frac{3 \cdot W_{zm}}{4} + 3 \cdot V_{pTADAS}\right) \cdot \left(R_{dv} - 1\right)\right]^2}$$

$$P_{uL2} = 396.9 \text{ kN}$$

$$P_{uL} := \max\left(P_{uL1}, P_{uL2}\right)$$

$$P_{uL} = 396.9 \text{ kN}$$

Model Pier Properties

$h_m := 6.09m$

$d_m := 1.52m$ (rocking width)

$d_{clm} := 1.32m$ (column centerline width)

$\dfrac{h_m}{d_m} = 4$

$W_{xm} := 80.1kN$

$W_{zm} := 80.1kN$

$W_{pm} := 11.1kN$

$m_{xm} := \dfrac{W_{xm}}{g}$

$m_{zm} := \dfrac{W_{zm}}{g}$

Mass Dimensions and Mass Moment of Inertia of Added Mass (steel plates):

$w_{sp} := 3073mm$

$d_{sp} := 178mm$

$I_{oxm} := \dfrac{1}{12} \dfrac{W_{xm}}{g} \cdot \left(w_{sp}^2 + d_{sp}^2\right)$

$I_{oxm} = 63.2 \dfrac{kN}{g} \cdot m^2$

$E_m := 200GPa$ (modulus of elasticity of steel)

Column Properties	Beam Properties	Diagonal Properties	
			$\theta_{1m} := 34deg$
$A_{Lm} := 15.55cm^2$	$I_{bm} := 137cm^4$	$d_{rod} := 9.53mm$	
			$\theta_{25m} := 42deg$
$I_{cmXX} := 429cm^4$	$L_b := 88.9cm$		
$I_{cmYY} := 91.6cm^4$	$n_b := 5$	$A_{dm} := 0.70 \dfrac{\pi \cdot d_{rod}^2}{4}$ $A_{dm} = 49.931 \, mm^2$	
$h_{Lm} := 5.97m$		$L_{dYYm} := 102cm$ (effective length of diagonals)	
		$L_{dXXm} := 122cm$	
		$P_{preD} := 17.8kN$ (pre-tension force applied to diagonals)	

Pier Stiffness in X-X Direction   Stiffness of Single Frame in X-X Direction

$$k_{oxm} := 2.0 \frac{kN}{mm}$$

$$k_{xfm} := \frac{k_{oxm}}{2}$$

Modes of Interest:

$$k_{Lm} := \frac{E_m \cdot A_{Lm}}{h_m} \quad \text{(axial stiffness of single pier leg)}$$

$$k_{vm} := 42.5 \frac{kN}{mm} \quad \text{(vertical "shearing" stiffness of pier)}$$

Horizontal Vibration of Pier:

$$T_{oxm} := 2 \cdot \pi \cdot \sqrt{\frac{m_{xm}}{k_{oxm}}} \quad \boxed{T_{oxm} = 0.4 \, sec}$$

Axial Vibration of Pier Leg:

$$T_{Lm} := 2 \cdot \pi \cdot \sqrt{\frac{m_{zm}}{4 \cdot k_{Lm}}} \quad \boxed{T_{Lm} = 0.04 \, sec}$$

$$k_{Lm} = 51.067 \frac{kN}{mm}$$

Vertical Shearing Vibration of Pier:

$$T_{vm} := 2 \cdot \pi \cdot \sqrt{\frac{m_{zm}}{2 k_{vm}}} \quad \boxed{T_{vm} = 0.062 \, sec}$$

$$\lambda_{tprov} := \frac{T_{oxp}}{T_{oxm}} \quad \text{(time scale factor provided based on fixed-base period of pier)}$$

$$\lambda_{tprov} = 1.843$$

Viscous Damper Properties

$\alpha := 0.5$ (damping exponent)

$c := 1.500 \text{kips} \cdot \left(\dfrac{\sec}{\text{in}} \right)^{\alpha}$ (damping coefficient)

$\Delta_u := 96.5 \text{mm}$ (maximum pier displacement, iterated to determine effective damping of system)

$\Delta_{upL} := \left(\Delta_u - \dfrac{\dfrac{W_{zm}}{2} \cdot \dfrac{d_m}{h_m}}{k_{oxm}} \right) \dfrac{d_m}{h_m}$

$\Delta_{upL} = 0.806 \text{ in}$

Development of Uni-directional Pushover Curve

-2nd cycle properties used
-Used for approximate analysis method (cap. spec.)

Uni-directional Yield Properties of System:

$P_{up1} := \dfrac{W_{zm}}{2} \cdot \dfrac{d_m}{h_m}$ $P_{up1} = 8.88 \text{ kN}$

$\Delta_{up1} := \dfrac{P_{up1}}{k_{oxm}}$

$P_{y2} := P_{up1}$

$P_{y2} = 8.88 \text{ kN}$

$\Delta_{y1} := \Delta_{up1}$

$\Delta_{y1} = 4.23 \text{ mm}$

$\Delta := 0\text{in}, 0.05\text{in} .. 30\text{in}$

$$P(\Delta) := \left[\left|\begin{array}{l} \left(k_{oxm} - \dfrac{W_{zm}}{h_m}\right) \cdot \Delta \quad \text{if} \ \ \Delta \le \Delta_{up1} \\[4mm] \left(k_{oxm} - \dfrac{W_{zm}}{h_m}\right) \cdot \Delta_{up1} - \dfrac{W_{zm}}{h_m} \cdot \left(\Delta - \Delta_{up1}\right) \quad \text{if} \ \ \Delta > \Delta_{up1} \end{array}\right.\right]$$

$\dfrac{-W_{zm}}{h_m} = -0.013 \, \dfrac{\text{kN}}{\text{mm}}$

(post-yield stiffness)

Idealized Bi-linear, Uni-directional Pushover Curve:

Pier at Target Maximum Uni-directional Displacement:

Uni-directional Pushover Curve
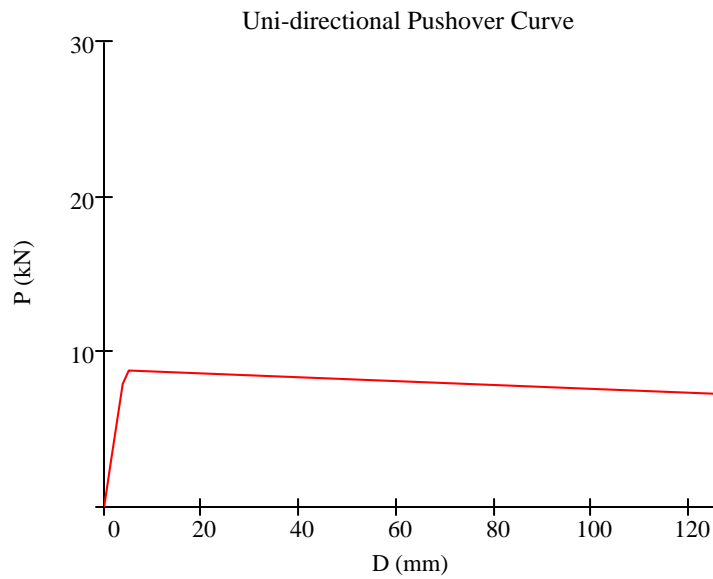
Converstion to Spectral Capacity Curve:

$S_{ac}(\Delta) := \dfrac{P(\Delta)}{W_{M1}} \cdot \dfrac{g}{g}$ $\qquad \phi := 1$ $\qquad$ (conversion to spectral ordinates, piers idealized as SDOF system for horizontal response)

$\Gamma_1 := 1$

$S_{dc}(\Delta) := \dfrac{\Delta}{\phi \cdot \Gamma_1}$

Spectral Capacity Curve

Spectral Demand Curve:

$$W_k := \frac{1}{2} \cdot P_{y2} \cdot \Delta_u \qquad \text{(stored strain energy at displacement, } D_u\text{)}$$

$$T_{sec} := 2 \cdot \pi \cdot \sqrt{\frac{W_{xm} \cdot \Delta_u}{g \cdot P_{y2}}} \qquad T_{sec} = 1.87 \text{ sec}$$

$$W_D := 2 \left(\frac{2 \cdot \pi}{T_{sec}}\right)^{\alpha} \cdot c \cdot \left[4 \cdot 2^{\alpha} \cdot \frac{\left(\Gamma\left(1 + \frac{\alpha}{2}\right)\right)^2}{\Gamma(2 + \alpha)} \right] \cdot \left(\Delta_{upL}\right)^{1+\alpha} \qquad \text{(energy dissipated by 2 dampers in 1cycle at displacement, } \Delta_u\text{)}$$

$\beta_o := 0.02 \qquad$ (assumed inherent structural damping)

$$\beta_b := \begin{vmatrix} \dfrac{W_D}{4 \cdot \pi \cdot W_k} & \text{if} & \dfrac{W_D}{4 \cdot \pi \cdot W_k} > 0 \qquad\qquad \beta_b = 0.292 \\ 0 & \text{otherwise} \end{vmatrix}$$

$$\beta_{eff} := \beta_b + \beta_o$$

$\beta_{eff} = 0.31 \qquad$ (equivalent viscous damping for inelastic system)

$$B_s := \begin{array}{ll} 0.8 & \text{if } \beta_{eff} \le 0.02 \\ x_1 & \text{if } 0.02 < \beta_{eff} \le 0.05 \\ x_2 & \text{if } 0.05 < \beta_{eff} \le 0.10 \\ x_3 & \text{if } 0.10 < \beta_{eff} \le 0.20 \\ x_4 & \text{if } 0.20 < \beta_{eff} \le 0.30 \\ x_5 & \text{if } 0.30 < \beta_{eff} \le 0.40 \\ x_6 & \text{if } 0.40 < \beta_{eff} \le 0.50 \\ 3.0 & \text{if } \beta_{eff} > 0.50 \end{array}$$

$$B_1 := \begin{array}{ll} 0.8 & \text{if } \beta_{eff} \le 0.02 \\ y_1 & \text{if } 0.02 < \beta_{eff} \le 0.05 \\ y_2 & \text{if } 0.05 < \beta_{eff} \le 0.10 \\ y_3 & \text{if } 0.10 < \beta_{eff} \le 0.20 \\ y_4 & \text{if } 0.20 < \beta_{eff} \le 0.30 \\ y_5 & \text{if } 0.30 < \beta_{eff} \le 0.40 \\ y_6 & \text{if } 0.40 < \beta_{eff} \le 0.50 \\ 2.0 & \text{if } \beta_{eff} > 0.50 \end{array}$$

$B_s = 2.346$ Damping Modification Factors
(FEMA 273 Table 2-15)
$B_1 = 1.723$

$PSA_{Syn} :=$

C:\..\hlvsyn150_SpecX.TXT   (read in file containing spectra data for actual acceleration history recorded on shake table)

$TT_{Syn} :=$

C:\..\TT-ActualMotions.TXT

$S_{aX} := PSA_{Syn} \cdot g$

$TT := TT_{Syn} \cdot sec$

$T_o := \dfrac{0.4sec}{\lambda_{tprov}}$

$S_{av} := 2.75g$ (vertical spectral acceleration value at vertical period of pier)

Demand Spectrum

4.928

PSA_{Syn}

0.032

0.01 $\dfrac{TT_{Syn}}{sec}$ 2
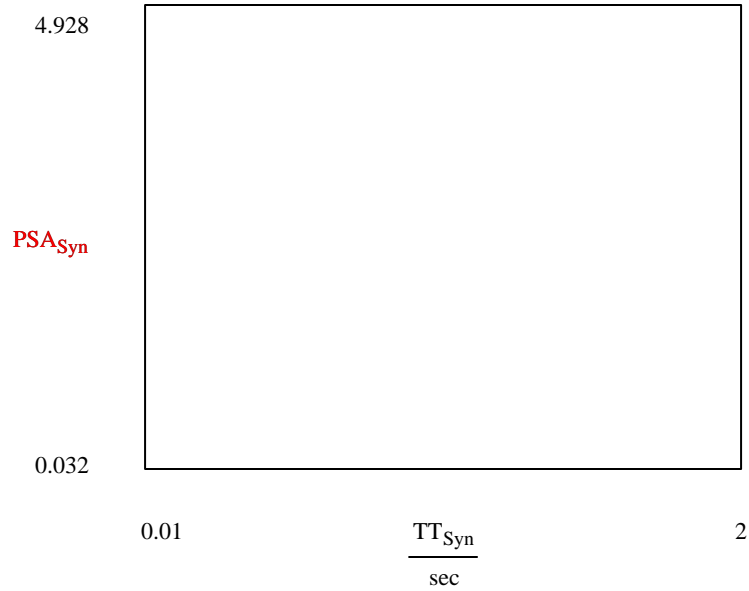
Reduction of Spectral Demand Curve for Equivalent Damping:

$$S_{aXr_j} := \begin{cases} \dfrac{S_{aX_j}}{B_s} & \text{if } TT_j < T_o \\[3mm] \dfrac{S_{aX_j}}{B_1} & \text{if } TT_j \geq T_o \end{cases}$$

Conversion to Spectral Demand Curve:

$$S_{ddx_j} := \left(\dfrac{TT_j}{2 \cdot \pi}\right)^2 \cdot S_{aX_j}$$

$$S_{ddxr_j} := \left(\dfrac{TT_j}{2 \cdot \pi}\right)^2 \cdot S_{aXr_j}$$

$T_{plot} := 0.5sec, 1.0sec .. 2sec$

$x := 0in, 1in .. 30in$

$$y(T_{plot}, x) := \frac{4 \cdot \pi^2}{T_{plot}^2} x$$

Capacity Spectrum Plot

Base Shear/Weight and Spectral Acc.

$S_{ac}(\Delta)$

$\dfrac{y(T_{plot}, x)}{g}$

$\dfrac{S_{aX_j}}{g}$

$\dfrac{S_{aXr_j}}{g}$

1

0

0

$\dfrac{S_{dc}(\Delta)}{mm}, \dfrac{x}{mm}, \dfrac{S_{ddx_j}}{mm}, \dfrac{S_{ddxr_j}}{mm}$

150

Deformation and Spectral Displacement-in
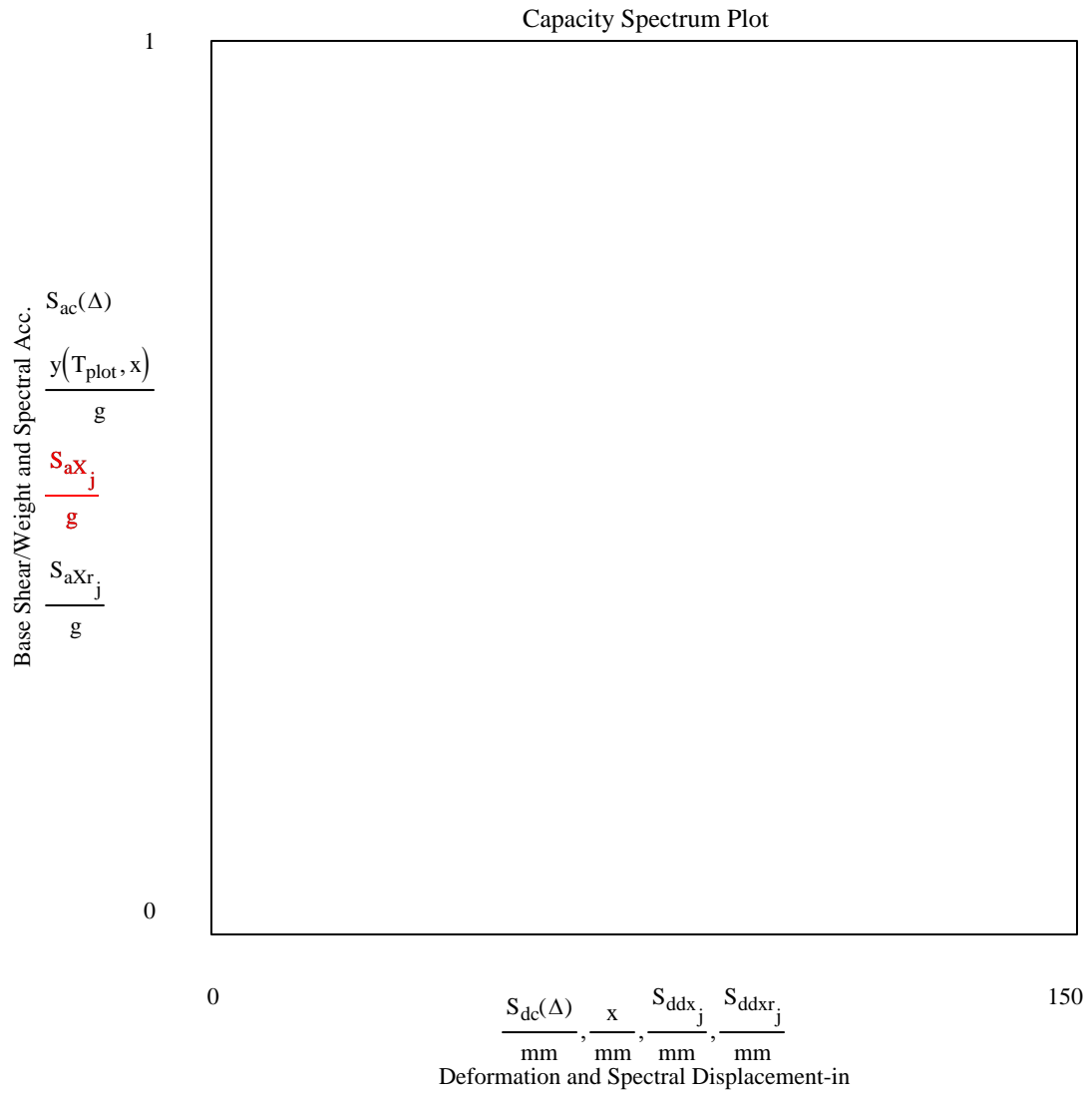
$\Delta_{uf} := 96.5mm$

(displacement at intersection of reduced spectral demand and spectral capacity curves, iterative with initially guessed max displacement, Δu)

Design Displacements and Forces:

Maximum Pier Displacements:

$\Delta_{ux} := 96.5mm$ $\Delta_{uy} := 86.4mm$

$\Delta_{ux} = 96.5\ mm$ $\Delta_{uy} = 86.4\ mm$

$$\Delta_{u10040} := \sqrt{\left(1.0 \cdot \max\left(\Delta_{ux}, \Delta_{uy}\right)\right)^2 + \left(0.4 \cdot \min\left(\Delta_{ux}, \Delta_{uy}\right)\right)^2}$$

$\Delta_{u10040} = 102.5\ mm$ (100% - 40% Combination Rule for Orthogonal Ground Motion Components)

Maximum Uplifting Displacment:

$$\Delta_{upbi} := \frac{d_m}{h_m} \cdot \left(1.0 \cdot \max\left(\Delta_{ux}, \Delta_{uy}\right) + 0.4 \cdot \min\left(\Delta_{ux}, \Delta_{uy}\right) - \frac{\dfrac{W_{zm}}{2} \dfrac{d_m}{h_m}}{k_{xfm}}\right)$$

$\Delta_{upbi} = 27.2\ mm$

Maximum Impact Velocity:

-maximum impact velocity in x-direction, where "x" is considered the larger displaced direction here

$$\Delta_{upLx} := 1.0 \cdot \max\left(\Delta_{ux}, \Delta_{uy}\right) \cdot \frac{d_m}{h_m} - \frac{\dfrac{W_{zm}}{2} \cdot \left(\dfrac{d_m}{h_m}\right)^2}{k_{oxm}}$$

$$T_{secx} := 2 \cdot \pi \cdot \sqrt{\frac{W_{xm} \cdot \Delta_{ux}}{g \cdot P_{y2}}}$$

$$W_{vdx} := 2 \cdot \left[\frac{1}{4} \cdot \left(\frac{2 \cdot \pi}{T_{secx}}\right)^{\alpha} \cdot c \cdot \left[4 \cdot 2^{\alpha} \cdot \frac{\left(\Gamma\left(1 + \dfrac{\alpha}{2}\right)\right)^2}{\Gamma(2 + \alpha)}\right] \cdot \left(\Delta_{upLx}\right)^{1+\alpha}\right]$$

$$v_{ox} := \sqrt{\frac{2}{m_{xm} \cdot \left[\left(\dfrac{h_m}{d_m}\right)^2 + \dfrac{1}{2}\right]} \cdot \left(\Delta_{upLx} \cdot \frac{W_{zm}}{2} - W_{vdx}\right)}$$

$v_{ox} = 73.3\ \dfrac{mm}{sec}$

$$\Delta_{upLy} := 0.4 \cdot \min(\Delta_{ux}, \Delta_{uy}) \cdot \frac{d_m}{h_m} - \frac{\frac{W_{zm}}{2} \cdot \left(\frac{d_m}{h_m}\right)^2}{k_{oxm}}$$

$$T_{secy} := 2 \cdot \pi \cdot \sqrt{\frac{W_{xm} \cdot \Delta_{uy}}{g \cdot P_{y2}}}$$

$$W_{vdy} := 2 \cdot \left[\frac{1}{4} \cdot \left(\frac{2 \cdot \pi}{T_{secy}}\right)^{\alpha} \cdot c \cdot \left[4 \cdot 2^{\alpha} \cdot \frac{\left(\Gamma\left(1 + \frac{\alpha}{2}\right)\right)^2}{\Gamma(2 + \alpha)}\right] \cdot \left(\Delta_{upLy}\right)^{1+\alpha}\right]$$

$$v_{oy} := \sqrt{\frac{2}{m_{xm} \cdot \left[\left(\frac{h_m}{d_m}\right)^2 + \frac{1}{2}\right]} \cdot \left(\Delta_{upLy} \cdot \frac{W_{zm}}{2} - W_{vdy}\right)}$$

$$v_{oy} = 48.788 \frac{mm}{sec}$$

$$v_o := v_{ox} + v_{oy}$$

$$v_o = 122.1 \frac{mm}{sec}$$

Maximum Device Force:

$$P_{ud} := c \cdot v_o{}^{\alpha}$$

$$P_{ud} = 14.6 \, kN$$

$$\eta_{Lv} := \frac{P_{ud}}{\frac{W_{zm}}{4}} \qquad \eta_{Lv} = 0.705$$

Dynamic Amplification Factors During Rocking Response:

$T_{vm} = 0.062 \text{ sec}$ $\qquad\qquad\qquad\qquad$ $T_{Lm} = 0.04 \text{ sec}$

$T_{sec} := 2 \cdot \pi \cdot \sqrt{\dfrac{m_{zm} \cdot \Delta_{ux}}{P_{y2}}}$ $\quad$ $T_{sec} = 1.87 \text{ sec}$

$t_{rv} := \dfrac{T_{sec}}{2 \cdot \pi} \cdot asin\left(\dfrac{\Delta_{up1}}{\Delta_{ux}}\right)$ $\qquad$ $t_{rv} = 0.013 \text{ sec}$ $\qquad$ $t_{rL} := \dfrac{T_{sec}}{2 \cdot \pi} \cdot asin\left(\dfrac{\Delta_{up1}}{\Delta_{ux}}\right)$ $\quad$ $t_{rL} = 0.013 \text{ sec}$

$$R_{dL} := \left\| \begin{array}{ll} \left(1 + \dfrac{\sin\left(\dfrac{\pi \cdot t_{rL}}{T_{Lm}}\right)}{\dfrac{\pi \cdot t_{rL}}{T_{Lm}}}\right) & \text{if } t_{rL} > 3 \cdot T_{Lm} \\[2em] \max\left[1.67, \left(1 + \dfrac{\sin\left(\dfrac{\pi \cdot t_{rL}}{T_{Lm}}\right)}{\dfrac{\pi \cdot t_{rL}}{T_{Lm}}}\right)\right] & \text{if } t_{rL} \leq 3 \cdot T_{Lm} \end{array} \right.$$

$$R_{dv} := \left\| \begin{array}{ll} \left(1 + \dfrac{\left|\sin\left(\dfrac{\pi \cdot t_{rv}}{T_{vm}}\right)\right|}{\dfrac{\pi \cdot t_{rv}}{T_{vm}}}\right) & \text{if } t_{rv} > 3 \cdot T_{vm} \\[2em] \max\left[1.67, \left(1 + \dfrac{\left|\sin\left(\dfrac{\pi \cdot t_{rv}}{T_{vm}}\right)\right|}{\dfrac{\pi \cdot t_{rv}}{T_{vm}}}\right)\right] & \text{if } t_{rv} \leq 3 \cdot T_{vm} \end{array} \right.$$

$R_{dv} = 1.93$ $\qquad\qquad\qquad\qquad\qquad\qquad$ $R_{dL} = 1.83$

Maximum Base Shear Force:

$S_{av} = 2.75 \text{ g}$ $\qquad$ (vertical spectral acceleration response at vertical period of pier, 2% damp)

$P_{uFst} := \left(\dfrac{3 \cdot W_{zm}}{8} + \dfrac{1}{2} \cdot c \cdot v_o{}^{\alpha} + c \cdot v_{ox}{}^{\alpha}\right) \cdot \dfrac{d_m}{h_m}$

100-40 Combination Rule:

$P_{u100401} := 1.33\left[P_{uFst} + 1.0 \cdot \left[P_{uFst} \cdot (R_{dv} - 1)\right] + 0.4 \cdot \left(\dfrac{3 \cdot m_{zm}}{8} \cdot S_{av} \cdot \dfrac{d_m}{h_m}\right)\right]$

$P_{u100402} := 1.33\left[P_{uFst} + 0.4 \cdot \left[P_{uFst} \cdot (R_{dv} - 1)\right] + \left(\dfrac{3 \cdot m_{zm}}{8} \cdot S_{av} \cdot \dfrac{d_m}{h_m}\right)\right]$

$P_{u10040} := \max\left(P_{u100401}, P_{u100402}\right)$

$P_{u10040} = 45.4 \text{ kN}$ $\qquad$ $\dfrac{P_{u10040}}{W_{zm} + W_{pm}} = 0.50$

Maximum Diagonal Member Axial Force

$$P_{dEQ} := \frac{\dfrac{P_{u10040}}{1.33}}{2 \cdot \cos(\theta_{1m})} \qquad P_{dEQ} = 20.586 \, kN$$

$$P_{udiag} := P_{dEQ} + P_{preD} \quad P_{preD} = 17.8 \, kN$$

$$\boxed{P_{udiag} = 38.39 \, kN}$$

Maximum Pier Leg Axial Force:

100-40 Directional and SRSS Modal Combination Rules:

$$P_{uL1} := \left(W_{zm} + c \cdot v_o{}^\alpha + c \cdot v_{ox}{}^\alpha + c \cdot v_{oy}{}^\alpha \right) + 0.4 \cdot m_{zm} \cdot S_{av} \, ...$$
$$+ 1.0 \sqrt{ \left(v_o \cdot \sqrt{\frac{m_{zm} \cdot k_{Lm}}{4}} \right)^2 + \left[(R_{dL} - 1) \cdot \frac{W_{zm}}{4} \right]^2 \, ... } $$
$$+ \left[\left[\frac{3 \cdot W_{zm}}{4} + \left(c \cdot v_o{}^\alpha + c \cdot v_{ox}{}^\alpha + c \cdot v_{oy}{}^\alpha \right) \right] \cdot (R_{dv} - 1) \right]^2$$

$$P_{uL1} = 313.5 \, kN$$

$$P_{uL2} := \left(W_{zm} + c \cdot v_o{}^\alpha + c \cdot v_{ox}{}^\alpha + c \cdot v_{oy}{}^\alpha \right) + 1.0 \cdot m_{zm} \cdot S_{av} \, ...$$
$$+ 0.4 \cdot \sqrt{ \left(v_o \cdot \sqrt{\frac{m_{zm} \cdot k_{Lm}}{4}} \right)^2 + \left[(R_{dL} - 1) \cdot \frac{W_{zm}}{4} \right]^2 \, ... } $$
$$+ \left[\left[\frac{3 \cdot W_{zm}}{4} + \left(c \cdot v_o{}^\alpha + c \cdot v_{ox}{}^\alpha + c \cdot v_{oy}{}^\alpha \right) \right] \cdot (R_{dv} - 1) \right]^2$$

$$P_{uL2} = 389.7 \, kN$$

$$P_{uL} := \max(P_{uL1}, P_{uL2})$$

$$\boxed{P_{uL} = 389.7 \, kN}$$

MCEER Technical Reports

MCEER publishes technical reports on a variety of subjects written by authors funded through MCEER. These reports are available from both MCEER Publications and the National Technical Information Service (NTIS). Requests for reports should be directed to MCEER Publications, MCEER, University at Buffalo, State University of New York, Red Jacket Quadrangle, Buffalo, New York 14261. Reports can also be requested through NTIS, 5285 Port Royal Road, Springfield, Virginia 22161. NTIS accession numbers are shown in parenthesis, if available.

NCEER-87-0001   "First-Year Program in Research, Education and Technology Transfer," 3/5/87, (PB88-134275, A04, MF-A01).

NCEER-87-0002   "Experimental Evaluation of Instantaneous Optimal Algorithms for Structural Control," by R.C. Lin, T.T. Soong and A.M. Reinhorn, 4/20/87, (PB88-134341, A04, MF-A01).

NCEER-87-0003   "Experimentation Using the Earthquake Simulation Facilities at University at Buffalo," by A.M. Reinhorn and R.L. Ketter, to be published.

NCEER-87-0004   "The System Characteristics and Performance of a Shaking Table," by J.S. Hwang, K.C. Chang and G.C. Lee, 6/1/87, (PB88-134259, A03, MF-A01). This report is available only through NTIS (see address given above).

NCEER-87-0005   "A Finite Element Formulation for Nonlinear Viscoplastic Material Using a Q Model," by O. Gyebi and G. Dasgupta, 11/2/87, (PB88-213764, A08, MF-A01).

NCEER-87-0006   "Symbolic Manipulation Program (SMP) - Algebraic Codes for Two and Three Dimensional Finite Element Formulations," by X. Lee and G. Dasgupta, 11/9/87, (PB88-218522, A05, MF-A01).

NCEER-87-0007   "Instantaneous Optimal Control Laws for Tall Buildings Under Seismic Excitations," by J.N. Yang, A. Akbarpour and P. Ghaemmaghami, 6/10/87, (PB88-134333, A06, MF-A01). This report is only available through NTIS (see address given above).

NCEER-87-0008   "IDARC: Inelastic Damage Analysis of Reinforced Concrete Frame - Shear-Wall Structures," by Y.J. Park, A.M. Reinhorn and S.K. Kunnath, 7/20/87, (PB88-134325, A09, MF-A01). This report is only available through NTIS (see address given above).

NCEER-87-0009   "Liquefaction Potential for New York State: A Preliminary Report on Sites in Manhattan and Buffalo," by M. Budhu, V. Vijayakumar, R.F. Giese and L. Baumgras, 8/31/87, (PB88-163704, A03, MF-A01). This report is available only through NTIS (see address given above).

NCEER-87-0010   "Vertical and Torsional Vibration of Foundations in Inhomogeneous Media," by A.S. Veletsos and K.W. Dotson, 6/1/87, (PB88-134291, A03, MF-A01). This report is only available through NTIS (see address given above).

NCEER-87-0011   "Seismic Probabilistic Risk Assessment and Seismic Margins Studies for Nuclear Power Plants," by Howard H.M. Hwang, 6/15/87, (PB88-134267, A03, MF-A01). This report is only available through NTIS (see address given above).

NCEER-87-0012   "Parametric Studies of Frequency Response of Secondary Systems Under Ground-Acceleration Excitations," by Y. Yong and Y.K. Lin, 6/10/87, (PB88-134309, A03, MF-A01). This report is only available through NTIS (see address given above).

NCEER-87-0013   "Frequency Response of Secondary Systems Under Seismic Excitation," by J.A. HoLung, J. Cai and Y.K. Lin, 7/31/87, (PB88-134317, A05, MF-A01). This report is only available through NTIS (see address given above).

NCEER-87-0014   "Modelling Earthquake Ground Motions in Seismically Active Regions Using Parametric Time Series Methods," by G.W. Ellis and A.S. Cakmak, 8/25/87, (PB88-134283, A08, MF-A01). This report is only available through NTIS (see address given above).

NCEER-87-0015   "Detection and Assessment of Seismic Structural Damage," by E. DiPasquale and A.S. Cakmak, 8/25/87, (PB88-163712, A05, MF-A01). This report is only available through NTIS (see address given above).

NCEER-87-0016   "Pipeline Experiment at Parkfield, California," by J. Isenberg and E. Richardson, 9/15/87, (PB88-163720, A03, MF-A01). This report is available only through NTIS (see address given above).

NCEER-87-0017   "Digital Simulation of Seismic Ground Motion," by M. Shinozuka, G. Deodatis and T. Harada, 8/31/87, (PB88-155197, A04, MF-A01). This report is available only through NTIS (see address given above).

NCEER-87-0018   "Practical Considerations for Structural Control: System Uncertainty, System Time Delay and Truncation of Small Control Forces," J.N. Yang and A. Akbarpour, 8/10/87, (PB88-163738, A08, MF-A01). This report is only available through NTIS (see address given above).

NCEER-87-0019   "Modal Analysis of Nonclassically Damped Structural Systems Using Canonical Transformation," by J.N. Yang, S. Sarkani and F.X. Long, 9/27/87, (PB88-187851, A04, MF-A01).

NCEER-87-0020   "A Nonstationary Solution in Random Vibration Theory," by J.R. Red-Horse and P.D. Spanos, 11/3/87, (PB88-163746, A03, MF-A01).

NCEER-87-0021   "Horizontal Impedances for Radially Inhomogeneous Viscoelastic Soil Layers," by A.S. Veletsos and K.W. Dotson, 10/15/87, (PB88-150859, A04, MF-A01).

NCEER-87-0022   "Seismic Damage Assessment of Reinforced Concrete Members," by Y.S. Chung, C. Meyer and M. Shinozuka, 10/9/87, (PB88-150867, A05, MF-A01). This report is available only through NTIS (see address given above).

NCEER-87-0023   "Active Structural Control in Civil Engineering," by T.T. Soong, 11/11/87, (PB88-187778, A03, MF-A01).

NCEER-87-0024   "Vertical and Torsional Impedances for Radially Inhomogeneous Viscoelastic Soil Layers," by K.W. Dotson and A.S. Veletsos, 12/87, (PB88-187786, A03, MF-A01).

NCEER-87-0025   "Proceedings from the Symposium on Seismic Hazards, Ground Motions, Soil-Liquefaction and Engineering Practice in Eastern North America," October 20-22, 1987, edited by K.H. Jacob, 12/87, (PB88-188115, A23, MF-A01). This report is available only through NTIS (see address given above).

NCEER-87-0026   "Report on the Whittier-Narrows, California, Earthquake of October 1, 1987," by J. Pantelic and A. Reinhorn, 11/87, (PB88-187752, A03, MF-A01). This report is available only through NTIS (see address given above).

NCEER-87-0027   "Design of a Modular Program for Transient Nonlinear Analysis of Large 3-D Building Structures," by S. Srivastav and J.F. Abel, 12/30/87, (PB88-187950, A05, MF-A01). This report is only available through NTIS (see address given above).

NCEER-87-0028   "Second-Year Program in Research, Education and Technology Transfer," 3/8/88, (PB88-219480, A04, MF-A01).

NCEER-88-0001   "Workshop on Seismic Computer Analysis and Design of Buildings With Interactive Graphics," by W. McGuire, J.F. Abel and C.H. Conley, 1/18/88, (PB88-187760, A03, MF-A01). This report is only available through NTIS (see address given above).

NCEER-88-0002   "Optimal Control of Nonlinear Flexible Structures," by J.N. Yang, F.X. Long and D. Wong, 1/22/88, (PB88-213772, A06, MF-A01).

NCEER-88-0003   "Substructuring Techniques in the Time Domain for Primary-Secondary Structural Systems," by G.D. Manolis and G. Juhn, 2/10/88, (PB88-213780, A04, MF-A01).

NCEER-88-0004   "Iterative Seismic Analysis of Primary-Secondary Systems," by A. Singhal, L.D. Lutes and P.D. Spanos, 2/23/88, (PB88-213798, A04, MF-A01).

NCEER-88-0005   "Stochastic Finite Element Expansion for Random Media," by P.D. Spanos and R. Ghanem, 3/14/88, (PB88-213806, A03, MF-A01).

NCEER-88-0006   "Combining Structural Optimization and Structural Control," by F.Y. Cheng and C.P. Pantelides, 1/10/88, (PB88-213814, A05, MF-A01).

NCEER-88-0007   "Seismic Performance Assessment of Code-Designed Structures," by H.H-M. Hwang, J-W. Jaw and H-J. Shau, 3/20/88, (PB88-219423, A04, MF-A01). This report is only available through NTIS (see address given above).

NCEER-88-0008   "Reliability Analysis of Code-Designed Structures Under Natural Hazards," by H.H-M. Hwang, H. Ushiba and M. Shinozuka, 2/29/88, (PB88-229471, A07, MF-A01). This report is only available through NTIS (see address given above).

NCEER-88-0009   "Seismic Fragility Analysis of Shear Wall Structures," by J-W Jaw and H.H-M. Hwang, 4/30/88, (PB89-102867, A04, MF-A01).

NCEER-88-0010   "Base Isolation of a Multi-Story Building Under a Harmonic Ground Motion - A Comparison of Performances of Various Systems," by F-G Fan, G. Ahmadi and I.G. Tadjbakhsh, 5/18/88, (PB89-122238, A06, MF-A01). This report is only available through NTIS (see address given above).

NCEER-88-0011   "Seismic Floor Response Spectra for a Combined System by Green's Functions," by F.M. Lavelle, L.A. Bergman and P.D. Spanos, 5/1/88, (PB89-102875, A03, MF-A01).

NCEER-88-0012   "A New Solution Technique for Randomly Excited Hysteretic Structures," by G.Q. Cai and Y.K. Lin, 5/16/88, (PB89-102883, A03, MF-A01).

NCEER-88-0013   "A Study of Radiation Damping and Soil-Structure Interaction Effects in the Centrifuge," by K. Weissman, supervised by J.H. Prevost, 5/24/88, (PB89-144703, A06, MF-A01).

NCEER-88-0014   "Parameter Identification and Implementation of a Kinematic Plasticity Model for Frictional Soils," by J.H. Prevost and D.V. Griffiths, to be published.

NCEER-88-0015   "Two- and Three- Dimensional Dynamic Finite Element Analyses of the Long Valley Dam," by D.V. Griffiths and J.H. Prevost, 6/17/88, (PB89-144711, A04, MF-A01).

NCEER-88-0016   "Damage Assessment of Reinforced Concrete Structures in Eastern United States," by A.M. Reinhorn, M.J. Seidel, S.K. Kunnath and Y.J. Park, 6/15/88, (PB89-122220, A04, MF-A01). This report is only available through NTIS (see address given above).

NCEER-88-0017   "Dynamic Compliance of Vertically Loaded Strip Foundations in Multilayered Viscoelastic Soils," by S. Ahmad and A.S.M. Israil, 6/17/88, (PB89-102891, A04, MF-A01).

NCEER-88-0018   "An Experimental Study of Seismic Structural Response With Added Viscoelastic Dampers," by R.C. Lin, Z. Liang, T.T. Soong and R.H. Zhang, 6/30/88, (PB89-122212, A05, MF-A01). This report is available only through NTIS (see address given above).

NCEER-88-0019   "Experimental Investigation of Primary - Secondary System Interaction," by G.D. Manolis, G. Juhn and A.M. Reinhorn, 5/27/88, (PB89-122204, A04, MF-A01).

NCEER-88-0020   "A Response Spectrum Approach For Analysis of Nonclassically Damped Structures," by J.N. Yang, S. Sarkani and F.X. Long, 4/22/88, (PB89-102909, A04, MF-A01).

NCEER-88-0021   "Seismic Interaction of Structures and Soils: Stochastic Approach," by A.S. Veletsos and A.M. Prasad, 7/21/88, (PB89-122196, A04, MF-A01). This report is only available through NTIS (see address given above).

NCEER-88-0022   "Identification of the Serviceability Limit State and Detection of Seismic Structural Damage," by E. DiPasquale and A.S. Cakmak, 6/15/88, (PB89-122188, A05, MF-A01). This report is available only through NTIS (see address given above).

NCEER-88-0023   "Multi-Hazard Risk Analysis: Case of a Simple Offshore Structure," by B.K. Bhartia and E.H. Vanmarcke, 7/21/88, (PB89-145213, A05, MF-A01).

NCEER-88-0024   "Automated Seismic Design of Reinforced Concrete Buildings," by Y.S. Chung, C. Meyer and M. Shinozuka, 7/5/88, (PB89-122170, A06, MF-A01). This report is available only through NTIS (see address given above).

NCEER-88-0025   "Experimental Study of Active Control of MDOF Structures Under Seismic Excitations," by L.L. Chung, R.C. Lin, T.T. Soong and A.M. Reinhorn, 7/10/88, (PB89-122600, A04, MF-A01).

NCEER-88-0026   "Earthquake Simulation Tests of a Low-Rise Metal Structure," by J.S. Hwang, K.C. Chang, G.C. Lee and R.L. Ketter, 8/1/88, (PB89-102917, A04, MF-A01).

NCEER-88-0027   "Systems Study of Urban Response and Reconstruction Due to Catastrophic Earthquakes," by F. Kozin and H.K. Zhou, 9/22/88, (PB90-162348, A04, MF-A01).

NCEER-88-0028   "Seismic Fragility Analysis of Plane Frame Structures," by H.H-M. Hwang and Y.K. Low, 7/31/88, (PB89-131445, A06, MF-A01).

NCEER-88-0029   "Response Analysis of Stochastic Structures," by A. Kardara, C. Bucher and M. Shinozuka, 9/22/88, (PB89-174429, A04, MF-A01).

NCEER-88-0030   "Nonnormal Accelerations Due to Yielding in a Primary Structure," by D.C.K. Chen and L.D. Lutes, 9/19/88, (PB89-131437, A04, MF-A01).

NCEER-88-0031   "Design Approaches for Soil-Structure Interaction," by A.S. Veletsos, A.M. Prasad and Y. Tang, 12/30/88, (PB89-174437, A03, MF-A01). This report is available only through NTIS (see address given above).

NCEER-88-0032   "A Re-evaluation of Design Spectra for Seismic Damage Control," by C.J. Turkstra and A.G. Tallin, 11/7/88, (PB89-145221, A05, MF-A01).

NCEER-88-0033   "The Behavior and Design of Noncontact Lap Splices Subjected to Repeated Inelastic Tensile Loading," by V.E. Sagan, P. Gergely and R.N. White, 12/8/88, (PB89-163737, A08, MF-A01).

NCEER-88-0034   "Seismic Response of Pile Foundations," by S.M. Mamoon, P.K. Banerjee and S. Ahmad, 11/1/88, (PB89-145239, A04, MF-A01).

NCEER-88-0035   "Modeling of R/C Building Structures With Flexible Floor Diaphragms (IDARC2)," by A.M. Reinhorn, S.K. Kunnath and N. Panahshahi, 9/7/88, (PB89-207153, A07, MF-A01).

NCEER-88-0036   "Solution of the Dam-Reservoir Interaction Problem Using a Combination of FEM, BEM with Particular Integrals, Modal Analysis, and Substructuring," by C-S. Tsai, G.C. Lee and R.L. Ketter, 12/31/88, (PB89-207146, A04, MF-A01).

NCEER-88-0037   "Optimal Placement of Actuators for Structural Control," by F.Y. Cheng and C.P. Pantelides, 8/15/88, (PB89-162846, A05, MF-A01).

NCEER-88-0038   "Teflon Bearings in Aseismic Base Isolation: Experimental Studies and Mathematical Modeling," by A. Mokha, M.C. Constantinou and A.M. Reinhorn, 12/5/88, (PB89-218457, A10, MF-A01). This report is available only through NTIS (see address given above).

NCEER-88-0039   "Seismic Behavior of Flat Slab High-Rise Buildings in the New York City Area," by P. Weidlinger and M. Ettouney, 10/15/88, (PB90-145681, A04, MF-A01).

NCEER-88-0040   "Evaluation of the Earthquake Resistance of Existing Buildings in New York City," by P. Weidlinger and M. Ettouney, 10/15/88, to be published.

NCEER-88-0041   "Small-Scale Modeling Techniques for Reinforced Concrete Structures Subjected to Seismic Loads," by W. Kim, A. El-Attar and R.N. White, 11/22/88, (PB89-189625, A05, MF-A01).

NCEER-88-0042   "Modeling Strong Ground Motion from Multiple Event Earthquakes," by G.W. Ellis and A.S. Cakmak, 10/15/88, (PB89-174445, A03, MF-A01).

NCEER-88-0043   "Nonstationary Models of Seismic Ground Acceleration," by M. Grigoriu, S.E. Ruiz and E. Rosenblueth, 7/15/88, (PB89-189617, A04, MF-A01).

NCEER-88-0044   "SARCF User's Guide: Seismic Analysis of Reinforced Concrete Frames," by Y.S. Chung, C. Meyer and M. Shinozuka, 11/9/88, (PB89-174452, A08, MF-A01).

NCEER-88-0045   "First Expert Panel Meeting on Disaster Research and Planning," edited by J. Pantelic and J. Stoyle, 9/15/88, (PB89-174460, A05, MF-A01).

NCEER-88-0046   "Preliminary Studies of the Effect of Degrading Infill Walls on the Nonlinear Seismic Response of Steel Frames," by C.Z. Chrysostomou, P. Gergely and J.F. Abel, 12/19/88, (PB89-208383, A05, MF-A01).

NCEER-88-0047   "Reinforced Concrete Frame Component Testing Facility - Design, Construction, Instrumentation and Operation," by S.P. Pessiki, C. Conley, T. Bond, P. Gergely and R.N. White, 12/16/88, (PB89-174478, A04, MF-A01).

NCEER-89-0001   "Effects of Protective Cushion and Soil Compliancy on the Response of Equipment Within a Seismically Excited Building," by J.A. HoLung, 2/16/89, (PB89-207179, A04, MF-A01).

NCEER-89-0002   "Statistical Evaluation of Response Modification Factors for Reinforced Concrete Structures," by H.H-M. Hwang and J-W. Jaw, 2/17/89, (PB89-207187, A05, MF-A01).

NCEER-89-0003   "Hysteretic Columns Under Random Excitation," by G-Q. Cai and Y.K. Lin, 1/9/89, (PB89-196513, A03, MF-A01).

NCEER-89-0004   "Experimental Study of `Elephant Foot Bulge' Instability of Thin-Walled Metal Tanks," by Z-H. Jia and R.L. Ketter, 2/22/89, (PB89-207195, A03, MF-A01).

NCEER-89-0005   "Experiment on Performance of Buried Pipelines Across San Andreas Fault," by J. Isenberg, E. Richardson and T.D. O'Rourke, 3/10/89, (PB89-218440, A04, MF-A01). This report is available only through NTIS (see address given above).

NCEER-89-0006   "A Knowledge-Based Approach to Structural Design of Earthquake-Resistant Buildings," by M. Subramani, P. Gergely, C.H. Conley, J.F. Abel and A.H. Zaghw, 1/15/89, (PB89-218465, A06, MF-A01).

NCEER-89-0007   "Liquefaction Hazards and Their Effects on Buried Pipelines," by T.D. O'Rourke and P.A. Lane, 2/1/89, (PB89-218481, A09, MF-A01).

NCEER-89-0008   "Fundamentals of System Identification in Structural Dynamics," by H. Imai, C-B. Yun, O. Maruyama and M. Shinozuka, 1/26/89, (PB89-207211, A04, MF-A01).

NCEER-89-0009   "Effects of the 1985 Michoacan Earthquake on Water Systems and Other Buried Lifelines in Mexico," by A.G. Ayala and M.J. O'Rourke, 3/8/89, (PB89-207229, A06, MF-A01).

NCEER-89-R010   "NCEER Bibliography of Earthquake Education Materials," by K.E.K. Ross, Second Revision, 9/1/89, (PB90-125352, A05, MF-A01). This report is replaced by NCEER-92-0018.

NCEER-89-0011   "Inelastic Three-Dimensional Response Analysis of Reinforced Concrete Building Structures (IDARC-3D), Part I - Modeling," by S.K. Kunnath and A.M. Reinhorn, 4/17/89, (PB90-114612, A07, MF-A01). This report is available only through NTIS (see address given above).

NCEER-89-0012   "Recommended Modifications to ATC-14," by C.D. Poland and J.O. Malley, 4/12/89, (PB90-108648, A15, MF-A01).

NCEER-89-0013   "Repair and Strengthening of Beam-to-Column Connections Subjected to Earthquake Loading," by M. Corazao and A.J. Durrani, 2/28/89, (PB90-109885, A06, MF-A01).

NCEER-89-0014   "Program EXKAL2 for Identification of Structural Dynamic Systems," by O. Maruyama, C-B. Yun, M. Hoshiya and M. Shinozuka, 5/19/89, (PB90-109877, A09, MF-A01).

NCEER-89-0015   "Response of Frames With Bolted Semi-Rigid Connections, Part I - Experimental Study and Analytical Predictions," by P.J. DiCorso, A.M. Reinhorn, J.R. Dickerson, J.B. Radziminski and W.L. Harper, 6/1/89, to be published.

NCEER-89-0016   "ARMA Monte Carlo Simulation in Probabilistic Structural Analysis," by P.D. Spanos and M.P. Mignolet, 7/10/89, (PB90-109893, A03, MF-A01).

NCEER-89-P017   "Preliminary Proceedings from the Conference on Disaster Preparedness - The Place of Earthquake Education in Our Schools," Edited by K.E.K. Ross, 6/23/89, (PB90-108606, A03, MF-A01).

NCEER-89-0017   "Proceedings from the Conference on Disaster Preparedness - The Place of Earthquake Education in Our Schools," Edited by K.E.K. Ross, 12/31/89, (PB90-207895, A012, MF-A02). This report is available only through NTIS (see address given above).

NCEER-89-0018   "Multidimensional Models of Hysteretic Material Behavior for Vibration Analysis of Shape Memory Energy Absorbing Devices, by E.J. Graesser and F.A. Cozzarelli, 6/7/89, (PB90-164146, A04, MF-A01).

NCEER-89-0019   "Nonlinear Dynamic Analysis of Three-Dimensional Base Isolated Structures (3D-BASIS)," by S. Nagarajaiah, A.M. Reinhorn and M.C. Constantinou, 8/3/89, (PB90-161936, A06, MF-A01). This report has been replaced by NCEER-93-0011.

NCEER-89-0020   "Structural Control Considering Time-Rate of Control Forces and Control Rate Constraints," by F.Y. Cheng and C.P. Pantelides, 8/3/89, (PB90-120445, A04, MF-A01).

NCEER-89-0021   "Subsurface Conditions of Memphis and Shelby County," by K.W. Ng, T-S. Chang and H-H.M. Hwang, 7/26/89, (PB90-120437, A03, MF-A01).

NCEER-89-0022   "Seismic Wave Propagation Effects on Straight Jointed Buried Pipelines," by K. Elhmadi and M.J. O'Rourke, 8/24/89, (PB90-162322, A10, MF-A02).

NCEER-89-0023   "Workshop on Serviceability Analysis of Water Delivery Systems," edited by M. Grigoriu, 3/6/89, (PB90-127424, A03, MF-A01).

NCEER-89-0024   "Shaking Table Study of a 1/5 Scale Steel Frame Composed of Tapered Members," by K.C. Chang, J.S. Hwang and G.C. Lee, 9/18/89, (PB90-160169, A04, MF-A01).

NCEER-89-0025   "DYNA1D: A Computer Program for Nonlinear Seismic Site Response Analysis - Technical Documentation," by Jean H. Prevost, 9/14/89, (PB90-161944, A07, MF-A01). This report is available only through NTIS (see address given above).

NCEER-89-0026   "1:4 Scale Model Studies of Active Tendon Systems and Active Mass Dampers for Aseismic Protection," by A.M. Reinhorn, T.T. Soong, R.C. Lin, Y.P. Yang, Y. Fukao, H. Abe and M. Nakai, 9/15/89, (PB90-173246, A10, MF-A02). This report is available only through NTIS (see address given above).

NCEER-89-0027   "Scattering of Waves by Inclusions in a Nonhomogeneous Elastic Half Space Solved by Boundary Element Methods," by P.K. Hadley, A. Askar and A.S. Cakmak, 6/15/89, (PB90-145699, A07, MF-A01).

NCEER-89-0028   "Statistical Evaluation of Deflection Amplification Factors for Reinforced Concrete Structures," by H.H.M. Hwang, J-W. Jaw and A.L. Ch'ng, 8/31/89, (PB90-164633, A05, MF-A01).

NCEER-89-0029   "Bedrock Accelerations in Memphis Area Due to Large New Madrid Earthquakes," by H.H.M. Hwang, C.H.S. Chen and G. Yu, 11/7/89, (PB90-162330, A04, MF-A01).

NCEER-89-0030   "Seismic Behavior and Response Sensitivity of Secondary Structural Systems," by Y.Q. Chen and T.T. Soong, 10/23/89, (PB90-164658, A08, MF-A01).

NCEER-89-0031   "Random Vibration and Reliability Analysis of Primary-Secondary Structural Systems," by Y. Ibrahim, M. Grigoriu and T.T. Soong, 11/10/89, (PB90-161951, A04, MF-A01).

NCEER-89-0032   "Proceedings from the Second U.S. - Japan Workshop on Liquefaction, Large Ground Deformation and Their Effects on Lifelines, September 26-29, 1989," Edited by T.D. O'Rourke and M. Hamada, 12/1/89, (PB90-209388, A22, MF-A03).

NCEER-89-0033   "Deterministic Model for Seismic Damage Evaluation of Reinforced Concrete Structures," by J.M. Bracci, A.M. Reinhorn, J.B. Mander and S.K. Kunnath, 9/27/89, (PB91-108803, A06, MF-A01).

NCEER-89-0034   "On the Relation Between Local and Global Damage Indices," by E. DiPasquale and A.S. Cakmak, 8/15/89, (PB90-173865, A05, MF-A01).

NCEER-89-0035   "Cyclic Undrained Behavior of Nonplastic and Low Plasticity Silts," by A.J. Walker and H.E. Stewart, 7/26/89, (PB90-183518, A10, MF-A01).

NCEER-89-0036   "Liquefaction Potential of Surficial Deposits in the City of Buffalo, New York," by M. Budhu, R. Giese and L. Baumgrass, 1/17/89, (PB90-208455, A04, MF-A01).

NCEER-89-0037   "A Deterministic Assessment of Effects of Ground Motion Incoherence," by A.S. Veletsos and Y. Tang, 7/15/89, (PB90-164294, A03, MF-A01).

NCEER-89-0038   "Workshop on Ground Motion Parameters for Seismic Hazard Mapping," July 17-18, 1989, edited by R.V. Whitman, 12/1/89, (PB90-173923, A04, MF-A01).

NCEER-89-0039   "Seismic Effects on Elevated Transit Lines of the New York City Transit Authority," by C.J. Costantino, C.A. Miller and E. Heymsfield, 12/26/89, (PB90-207887, A06, MF-A01).

NCEER-89-0040   "Centrifugal Modeling of Dynamic Soil-Structure Interaction," by K. Weissman, Supervised by J.H. Prevost, 5/10/89, (PB90-207879, A07, MF-A01).

NCEER-89-0041   "Linearized Identification of Buildings With Cores for Seismic Vulnerability Assessment," by I-K. Ho and A.E. Aktan, 11/1/89, (PB90-251943, A07, MF-A01).

NCEER-90-0001   "Geotechnical and Lifeline Aspects of the October 17, 1989 Loma Prieta Earthquake in San Francisco," by T.D. O'Rourke, H.E. Stewart, F.T. Blackburn and T.S. Dickerman, 1/90, (PB90-208596, A05, MF-A01).

NCEER-90-0002   "Nonnormal Secondary Response Due to Yielding in a Primary Structure," by D.C.K. Chen and L.D. Lutes, 2/28/90, (PB90-251976, A07, MF-A01).

NCEER-90-0003   "Earthquake Education Materials for Grades K-12," by K.E.K. Ross, 4/16/90, (PB91-251984, A05, MF-A05). This report has been replaced by NCEER-92-0018.

NCEER-90-0004   "Catalog of Strong Motion Stations in Eastern North America," by R.W. Busby, 4/3/90, (PB90-251984, A05, MF-A01).

NCEER-90-0005   "NCEER Strong-Motion Data Base: A User Manual for the GeoBase Release (Version 1.0 for the Sun3)," by P. Friberg and K. Jacob, 3/31/90 (PB90-258062, A04, MF-A01).

NCEER-90-0006   "Seismic Hazard Along a Crude Oil Pipeline in the Event of an 1811-1812 Type New Madrid Earthquake," by H.H.M. Hwang and C-H.S. Chen, 4/16/90, (PB90-258054, A04, MF-A01).

NCEER-90-0007   "Site-Specific Response Spectra for Memphis Sheahan Pumping Station," by H.H.M. Hwang and C.S. Lee, 5/15/90, (PB91-108811, A05, MF-A01).

NCEER-90-0008   "Pilot Study on Seismic Vulnerability of Crude Oil Transmission Systems," by T. Ariman, R. Dobry, M. Grigoriu, F. Kozin, M. O'Rourke, T. O'Rourke and M. Shinozuka, 5/25/90, (PB91-108837, A06, MF-A01).

NCEER-90-0009   "A Program to Generate Site Dependent Time Histories: EQGEN," by G.W. Ellis, M. Srinivasan and A.S. Cakmak, 1/30/90, (PB91-108829, A04, MF-A01).

NCEER-90-0010   "Active Isolation for Seismic Protection of Operating Rooms," by M.E. Talbott, Supervised by M. Shinozuka, 6/8/9, (PB91-110205, A05, MF-A01).

NCEER-90-0011   "Program LINEARID for Identification of Linear Structural Dynamic Systems," by C-B. Yun and M. Shinozuka, 6/25/90, (PB91-110312, A08, MF-A01).

NCEER-90-0012   "Two-Dimensional Two-Phase Elasto-Plastic Seismic Response of Earth Dams," by A.N. Yiagos, Supervised by J.H. Prevost, 6/20/90, (PB91-110197, A13, MF-A02).

NCEER-90-0013   "Secondary Systems in Base-Isolated Structures: Experimental Investigation, Stochastic Response and Stochastic Sensitivity," by G.D. Manolis, G. Juhn, M.C. Constantinou and A.M. Reinhorn, 7/1/90, (PB91-110320, A08, MF-A01).

NCEER-90-0014   "Seismic Behavior of Lightly-Reinforced Concrete Column and Beam-Column Joint Details," by S.P. Pessiki, C.H. Conley, P. Gergely and R.N. White, 8/22/90, (PB91-108795, A11, MF-A02).

NCEER-90-0015   "Two Hybrid Control Systems for Building Structures Under Strong Earthquakes," by J.N. Yang and A. Danielians, 6/29/90, (PB91-125393, A04, MF-A01).

NCEER-90-0016   "Instantaneous Optimal Control with Acceleration and Velocity Feedback," by J.N. Yang and Z. Li, 6/29/90, (PB91-125401, A03, MF-A01).

NCEER-90-0017   "Reconnaissance Report on the Northern Iran Earthquake of June 21, 1990," by M. Mehrain, 10/4/90, (PB91-125377, A03, MF-A01).

NCEER-90-0018   "Evaluation of Liquefaction Potential in Memphis and Shelby County," by T.S. Chang, P.S. Tang, C.S. Lee and H. Hwang, 8/10/90, (PB91-125427, A09, MF-A01).

NCEER-90-0019   "Experimental and Analytical Study of a Combined Sliding Disc Bearing and Helical Steel Spring Isolation System," by M.C. Constantinou, A.S. Mokha and A.M. Reinhorn, 10/4/90, (PB91-125385, A06, MF-A01). This report is available only through NTIS (see address given above).

NCEER-90-0020   "Experimental Study and Analytical Prediction of Earthquake Response of a Sliding Isolation System with a Spherical Surface," by A.S. Mokha, M.C. Constantinou and A.M. Reinhorn, 10/11/90, (PB91-125419, A05, MF-A01).

NCEER-90-0021   "Dynamic Interaction Factors for Floating Pile Groups," by G. Gazetas, K. Fan, A. Kaynia and E. Kausel, 9/10/90, (PB91-170381, A05, MF-A01).

NCEER-90-0022   "Evaluation of Seismic Damage Indices for Reinforced Concrete Structures," by S. Rodriguez-Gomez and A.S. Cakmak, 9/30/90, PB91-171322, A06, MF-A01).

NCEER-90-0023   "Study of Site Response at a Selected Memphis Site," by H. Desai, S. Ahmad, E.S. Gazetas and M.R. Oh, 10/11/90, (PB91-196857, A03, MF-A01).

NCEER-90-0024   "A User's Guide to Strongmo: Version 1.0 of NCEER's Strong-Motion Data Access Tool for PCs and Terminals," by P.A. Friberg and C.A.T. Susch, 11/15/90, (PB91-171272, A03, MF-A01).

NCEER-90-0025   "A Three-Dimensional Analytical Study of Spatial Variability of Seismic Ground Motions," by L-L. Hong and A.H.-S. Ang, 10/30/90, (PB91-170399, A09, MF-A01).

NCEER-90-0026   "MUMOID User's Guide - A Program for the Identification of Modal Parameters," by S. Rodriguez-Gomez and E. DiPasquale, 9/30/90, (PB91-171298, A04, MF-A01).

NCEER-90-0027   "SARCF-II User's Guide - Seismic Analysis of Reinforced Concrete Frames," by S. Rodriguez-Gomez, Y.S. Chung and C. Meyer, 9/30/90, (PB91-171280, A05, MF-A01).

NCEER-90-0028   "Viscous Dampers: Testing, Modeling and Application in Vibration and Seismic Isolation," by N. Makris and M.C. Constantinou, 12/20/90 (PB91-190561, A06, MF-A01).

NCEER-90-0029   "Soil Effects on Earthquake Ground Motions in the Memphis Area," by H. Hwang, C.S. Lee, K.W. Ng and T.S. Chang, 8/2/90, (PB91-190751, A05, MF-A01).

NCEER-91-0001   "Proceedings from the Third Japan-U.S. Workshop on Earthquake Resistant Design of Lifeline Facilities and Countermeasures for Soil Liquefaction, December 17-19, 1990," edited by T.D. O'Rourke and M. Hamada, 2/1/91, (PB91-179259, A99, MF-A04).

NCEER-91-0002   "Physical Space Solutions of Non-Proportionally Damped Systems," by M. Tong, Z. Liang and G.C. Lee, 1/15/91, (PB91-179242, A04, MF-A01).

NCEER-91-0003   "Seismic Response of Single Piles and Pile Groups," by K. Fan and G. Gazetas, 1/10/91, (PB92-174994, A04, MF-A01).

NCEER-91-0004   "Damping of Structures: Part 1 - Theory of Complex Damping," by Z. Liang and G. Lee, 10/10/91, (PB92-197235, A12, MF-A03).

NCEER-91-0005   "3D-BASIS - Nonlinear Dynamic Analysis of Three Dimensional Base Isolated Structures: Part II," by S. Nagarajaiah, A.M. Reinhorn and M.C. Constantinou, 2/28/91, (PB91-190553, A07, MF-A01). This report has been replaced by NCEER-93-0011.

NCEER-91-0006   "A Multidimensional Hysteretic Model for Plasticity Deforming Metals in Energy Absorbing Devices," by E.J. Graesser and F.A. Cozzarelli, 4/9/91, (PB92-108364, A04, MF-A01).

NCEER-91-0007   "A Framework for Customizable Knowledge-Based Expert Systems with an Application to a KBES for Evaluating the Seismic Resistance of Existing Buildings," by E.G. Ibarra-Anaya and S.J. Fenves, 4/9/91, (PB91-210930, A08, MF-A01).

NCEER-91-0008   "Nonlinear Analysis of Steel Frames with Semi-Rigid Connections Using the Capacity Spectrum Method," by G.G. Deierlein, S-H. Hsieh, Y-J. Shen and J.F. Abel, 7/2/91, (PB92-113828, A05, MF-A01).

NCEER-91-0009   "Earthquake Education Materials for Grades K-12," by K.E.K. Ross, 4/30/91, (PB91-212142, A06, MF-A01). This report has been replaced by NCEER-92-0018.

NCEER-91-0010   "Phase Wave Velocities and Displacement Phase Differences in a Harmonically Oscillating Pile," by N. Makris and G. Gazetas, 7/8/91, (PB92-108356, A04, MF-A01).

NCEER-91-0011   "Dynamic Characteristics of a Full-Size Five-Story Steel Structure and a 2/5 Scale Model," by K.C. Chang, G.C. Yao, G.C. Lee, D.S. Hao and Y.C. Yeh," 7/2/91, (PB93-116648, A06, MF-A02).

NCEER-91-0012   "Seismic Response of a 2/5 Scale Steel Structure with Added Viscoelastic Dampers," by K.C. Chang, T.T. Soong, S-T. Oh and M.L. Lai, 5/17/91, (PB92-110816, A05, MF-A01).

NCEER-91-0013   "Earthquake Response of Retaining Walls; Full-Scale Testing and Computational Modeling," by S. Alampalli and A-W.M. Elgamal, 6/20/91, to be published.

NCEER-91-0014   "3D-BASIS-M: Nonlinear Dynamic Analysis of Multiple Building Base Isolated Structures," by P.C. Tsopelas, S. Nagarajaiah, M.C. Constantinou and A.M. Reinhorn, 5/28/91, (PB92-113885, A09, MF-A02).

NCEER-91-0015   "Evaluation of SEAOC Design Requirements for Sliding Isolated Structures," by D. Theodossiou and M.C. Constantinou, 6/10/91, (PB92-114602, A11, MF-A03).

NCEER-91-0016   "Closed-Loop Modal Testing of a 27-Story Reinforced Concrete Flat Plate-Core Building," by H.R. Somaprasad, T. Toksoy, H. Yoshiyuki and A.E. Aktan, 7/15/91, (PB92-129980, A07, MF-A02).

NCEER-91-0017   "Shake Table Test of a 1/6 Scale Two-Story Lightly Reinforced Concrete Building," by A.G. El-Attar, R.N. White and P. Gergely, 2/28/91, (PB92-222447, A06, MF-A02).

NCEER-91-0018   "Shake Table Test of a 1/8 Scale Three-Story Lightly Reinforced Concrete Building," by A.G. El-Attar, R.N. White and P. Gergely, 2/28/91, (PB93-116630, A08, MF-A02).

NCEER-91-0019   "Transfer Functions for Rigid Rectangular Foundations," by A.S. Veletsos, A.M. Prasad and W.H. Wu, 7/31/91, to be published.

NCEER-91-0020   "Hybrid Control of Seismic-Excited Nonlinear and Inelastic Structural Systems," by J.N. Yang, Z. Li and A. Danielians, 8/1/91, (PB92-143171, A06, MF-A02).

NCEER-91-0021   "The NCEER-91 Earthquake Catalog: Improved Intensity-Based Magnitudes and Recurrence Relations for U.S. Earthquakes East of New Madrid," by L. Seeber and J.G. Armbruster, 8/28/91, (PB92-176742, A06, MF-A02).

NCEER-91-0022   "Proceedings from the Implementation of Earthquake Planning and Education in Schools: The Need for Change - The Roles of the Changemakers," by K.E.K. Ross and F. Winslow, 7/23/91, (PB92-129998, A12, MF-A03).

NCEER-91-0023   "A Study of Reliability-Based Criteria for Seismic Design of Reinforced Concrete Frame Buildings," by H.H.M. Hwang and H-M. Hsu, 8/10/91, (PB92-140235, A09, MF-A02).

NCEER-91-0024   "Experimental Verification of a Number of Structural System Identification Algorithms," by R.G. Ghanem, H. Gavin and M. Shinozuka, 9/18/91, (PB92-176577, A18, MF-A04).

NCEER-91-0025   "Probabilistic Evaluation of Liquefaction Potential," by H.H.M. Hwang and C.S. Lee," 11/25/91, (PB92-143429, A05, MF-A01).

NCEER-91-0026   "Instantaneous Optimal Control for Linear, Nonlinear and Hysteretic Structures - Stable Controllers," by J.N. Yang and Z. Li, 11/15/91, (PB92-163807, A04, MF-A01).

NCEER-91-0027   "Experimental and Theoretical Study of a Sliding Isolation System for Bridges," by M.C. Constantinou, A. Kartoum, A.M. Reinhorn and P. Bradford, 11/15/91, (PB92-176973, A10, MF-A03).

NCEER-92-0001   "Case Studies of Liquefaction and Lifeline Performance During Past Earthquakes, Volume 1: Japanese Case Studies," Edited by M. Hamada and T. O'Rourke, 2/17/92, (PB92-197243, A18, MF-A04).

NCEER-92-0002   "Case Studies of Liquefaction and Lifeline Performance During Past Earthquakes, Volume 2: United States Case Studies," Edited by T. O'Rourke and M. Hamada, 2/17/92, (PB92-197250, A20, MF-A04).

NCEER-92-0003   "Issues in Earthquake Education," Edited by K. Ross, 2/3/92, (PB92-222389, A07, MF-A02).

NCEER-92-0004   "Proceedings from the First U.S. - Japan Workshop on Earthquake Protective Systems for Bridges," Edited by I.G. Buckle, 2/4/92, (PB94-142239, A99, MF-A06).

NCEER-92-0005   "Seismic Ground Motion from a Haskell-Type Source in a Multiple-Layered Half-Space," A.P. Theoharis, G. Deodatis and M. Shinozuka, 1/2/92, to be published.

NCEER-92-0006   "Proceedings from the Site Effects Workshop," Edited by R. Whitman, 2/29/92, (PB92-197201, A04, MF-A01).

NCEER-92-0007   "Engineering Evaluation of Permanent Ground Deformations Due to Seismically-Induced Liquefaction," by M.H. Baziar, R. Dobry and A-W.M. Elgamal, 3/24/92, (PB92-222421, A13, MF-A03).

NCEER-92-0008   "A Procedure for the Seismic Evaluation of Buildings in the Central and Eastern United States," by C.D. Poland and J.O. Malley, 4/2/92, (PB92-222439, A20, MF-A04).

NCEER-92-0009   "Experimental and Analytical Study of a Hybrid Isolation System Using Friction Controllable Sliding Bearings," by M.Q. Feng, S. Fujii and M. Shinozuka, 5/15/92, (PB93-150282, A06, MF-A02).

NCEER-92-0010   "Seismic Resistance of Slab-Column Connections in Existing Non-Ductile Flat-Plate Buildings," by A.J. Durrani and Y. Du, 5/18/92, (PB93-116812, A06, MF-A02).

NCEER-92-0011   "The Hysteretic and Dynamic Behavior of Brick Masonry Walls Upgraded by Ferrocement Coatings Under Cyclic Loading and Strong Simulated Ground Motion," by H. Lee and S.P. Prawel, 5/11/92, to be published.

NCEER-92-0012   "Study of Wire Rope Systems for Seismic Protection of Equipment in Buildings," by G.F. Demetriades, M.C. Constantinou and A.M. Reinhorn, 5/20/92, (PB93-116655, A08, MF-A02).

NCEER-92-0013   "Shape Memory Structural Dampers: Material Properties, Design and Seismic Testing," by P.R. Witting and F.A. Cozzarelli, 5/26/92, (PB93-116663, A05, MF-A01).

NCEER-92-0014   "Longitudinal Permanent Ground Deformation Effects on Buried Continuous Pipelines," by M.J. O'Rourke, and C. Nordberg, 6/15/92, (PB93-116671, A08, MF-A02).

NCEER-92-0015   "A Simulation Method for Stationary Gaussian Random Functions Based on the Sampling Theorem," by M. Grigoriu and S. Balopoulou, 6/11/92, (PB93-127496, A05, MF-A01).

NCEER-92-0016   "Gravity-Load-Designed Reinforced Concrete Buildings: Seismic Evaluation of Existing Construction and Detailing Strategies for Improved Seismic Resistance," by G.W. Hoffmann, S.K. Kunnath, A.M. Reinhorn and J.B. Mander, 7/15/92, (PB94-142007, A08, MF-A02).

NCEER-92-0017   "Observations on Water System and Pipeline Performance in the Limón Area of Costa Rica Due to the April 22, 1991 Earthquake," by M. O'Rourke and D. Ballantyne, 6/30/92, (PB93-126811, A06, MF-A02).

NCEER-92-0018   "Fourth Edition of Earthquake Education Materials for Grades K-12," Edited by K.E.K. Ross, 8/10/92, (PB93-114023, A07, MF-A02).

NCEER-92-0019   "Proceedings from the Fourth Japan-U.S. Workshop on Earthquake Resistant Design of Lifeline Facilities and Countermeasures for Soil Liquefaction," Edited by M. Hamada and T.D. O'Rourke, 8/12/92, (PB93-163939, A99, MF-E11).

NCEER-92-0020   "Active Bracing System: A Full Scale Implementation of Active Control," by A.M. Reinhorn, T.T. Soong, R.C. Lin, M.A. Riley, Y.P. Wang, S. Aizawa and M. Higashino, 8/14/92, (PB93-127512, A06, MF-A02).

NCEER-92-0021   "Empirical Analysis of Horizontal Ground Displacement Generated by Liquefaction-Induced Lateral Spreads," by S.F. Bartlett and T.L. Youd, 8/17/92, (PB93-188241, A06, MF-A02).

NCEER-92-0022   "IDARC Version 3.0: Inelastic Damage Analysis of Reinforced Concrete Structures," by S.K. Kunnath, A.M. Reinhorn and R.F. Lobo, 8/31/92, (PB93-227502, A07, MF-A02).

NCEER-92-0023   "A Semi-Empirical Analysis of Strong-Motion Peaks in Terms of Seismic Source, Propagation Path and Local Site Conditions, by M. Kamiyama, M.J. O'Rourke and R. Flores-Berrones, 9/9/92, (PB93-150266, A08, MF-A02).

NCEER-92-0024   "Seismic Behavior of Reinforced Concrete Frame Structures with Nonductile Details, Part I: Summary of Experimental Findings of Full Scale Beam-Column Joint Tests," by A. Beres, R.N. White and P. Gergely, 9/30/92, (PB93-227783, A05, MF-A01).

NCEER-92-0025   "Experimental Results of Repaired and Retrofitted Beam-Column Joint Tests in Lightly Reinforced Concrete Frame Buildings," by A. Beres, S. El-Borgi, R.N. White and P. Gergely, 10/29/92, (PB93-227791, A05, MF-A01).

NCEER-92-0026   "A Generalization of Optimal Control Theory: Linear and Nonlinear Structures," by J.N. Yang, Z. Li and S. Vongchavalitkul, 11/2/92, (PB93-188621, A05, MF-A01).

NCEER-92-0027   "Seismic Resistance of Reinforced Concrete Frame Structures Designed Only for Gravity Loads: Part I - Design and Properties of a One-Third Scale Model Structure," by J.M. Bracci, A.M. Reinhorn and J.B. Mander, 12/1/92, (PB94-104502, A08, MF-A02).

NCEER-92-0028   "Seismic Resistance of Reinforced Concrete Frame Structures Designed Only for Gravity Loads: Part II - Experimental Performance of Subassemblages," by L.E. Aycardi, J.B. Mander and A.M. Reinhorn, 12/1/92, (PB94-104510, A08, MF-A02).

NCEER-92-0029   "Seismic Resistance of Reinforced Concrete Frame Structures Designed Only for Gravity Loads: Part III - Experimental Performance and Analytical Study of a Structural Model," by J.M. Bracci, A.M. Reinhorn and J.B. Mander, 12/1/92, (PB93-227528, A09, MF-A01).

NCEER-92-0030   "Evaluation of Seismic Retrofit of Reinforced Concrete Frame Structures: Part I - Experimental Performance of Retrofitted Subassemblages," by D. Choudhuri, J.B. Mander and A.M. Reinhorn, 12/8/92, (PB93-198307, A07, MF-A02).

NCEER-92-0031   "Evaluation of Seismic Retrofit of Reinforced Concrete Frame Structures: Part II - Experimental Performance and Analytical Study of a Retrofitted Structural Model," by J.M. Bracci, A.M. Reinhorn and J.B. Mander, 12/8/92, (PB93-198315, A09, MF-A03).

NCEER-92-0032   "Experimental and Analytical Investigation of Seismic Response of Structures with Supplemental Fluid Viscous Dampers," by M.C. Constantinou and M.D. Symans, 12/21/92, (PB93-191435, A10, MF-A03). This report is available only through NTIS (see address given above).

NCEER-92-0033   "Reconnaissance Report on the Cairo, Egypt Earthquake of October 12, 1992," by M. Khater, 12/23/92, (PB93-188621, A03, MF-A01).

NCEER-92-0034   "Low-Level Dynamic Characteristics of Four Tall Flat-Plate Buildings in New York City," by H. Gavin, S. Yuan, J. Grossman, E. Pekelis and K. Jacob, 12/28/92, (PB93-188217, A07, MF-A02).

NCEER-93-0001   "An Experimental Study on the Seismic Performance of Brick-Infilled Steel Frames With and Without Retrofit," by J.B. Mander, B. Nair, K. Wojtkowski and J. Ma, 1/29/93, (PB93-227510, A07, MF-A02).

NCEER-93-0002   "Social Accounting for Disaster Preparedness and Recovery Planning," by S. Cole, E. Pantoja and V. Razak, 2/22/93, (PB94-142114, A12, MF-A03).

NCEER-93-0003   "Assessment of 1991 NEHRP Provisions for Nonstructural Components and Recommended Revisions," by T.T. Soong, G. Chen, Z. Wu, R-H. Zhang and M. Grigoriu, 3/1/93, (PB93-188639, A06, MF-A02).

NCEER-93-0004   "Evaluation of Static and Response Spectrum Analysis Procedures of SEAOC/UBC for Seismic Isolated Structures," by C.W. Winters and M.C. Constantinou, 3/23/93, (PB93-198299, A10, MF-A03).

NCEER-93-0005   "Earthquakes in the Northeast - Are We Ignoring the Hazard? A Workshop on Earthquake Science and Safety for Educators," edited by K.E.K. Ross, 4/2/93, (PB94-103066, A09, MF-A02).

NCEER-93-0006   "Inelastic Response of Reinforced Concrete Structures with Viscoelastic Braces," by R.F. Lobo, J.M. Bracci, K.L. Shen, A.M. Reinhorn and T.T. Soong, 4/5/93, (PB93-227486, A05, MF-A02).

NCEER-93-0007   "Seismic Testing of Installation Methods for Computers and Data Processing Equipment," by K. Kosar, T.T. Soong, K.L. Shen, J.A. HoLung and Y.K. Lin, 4/12/93, (PB93-198299, A07, MF-A02).

NCEER-93-0008   "Retrofit of Reinforced Concrete Frames Using Added Dampers," by A. Reinhorn, M. Constantinou and C. Li, to be published.

NCEER-93-0009   "Seismic Behavior and Design Guidelines for Steel Frame Structures with Added Viscoelastic Dampers," by K.C. Chang, M.L. Lai, T.T. Soong, D.S. Hao and Y.C. Yeh, 5/1/93, (PB94-141959, A07, MF-A02).

NCEER-93-0010   "Seismic Performance of Shear-Critical Reinforced Concrete Bridge Piers," by J.B. Mander, S.M. Waheed, M.T.A. Chaudhary and S.S. Chen, 5/12/93, (PB93-227494, A08, MF-A02).

NCEER-93-0011   "3D-BASIS-TABS: Computer Program for Nonlinear Dynamic Analysis of Three Dimensional Base Isolated Structures," by S. Nagarajaiah, C. Li, A.M. Reinhorn and M.C. Constantinou, 8/2/93, (PB94-141819, A09, MF-A02).

NCEER-93-0012   "Effects of Hydrocarbon Spills from an Oil Pipeline Break on Ground Water," by O.J. Helweg and H.H.M. Hwang, 8/3/93, (PB94-141942, A06, MF-A02).

NCEER-93-0013   "Simplified Procedures for Seismic Design of Nonstructural Components and Assessment of Current Code Provisions," by M.P. Singh, L.E. Suarez, E.E. Matheu and G.O. Maldonado, 8/4/93, (PB94-141827, A09, MF-A02).

NCEER-93-0014   "An Energy Approach to Seismic Analysis and Design of Secondary Systems," by G. Chen and T.T. Soong, 8/6/93, (PB94-142767, A11, MF-A03).

NCEER-93-0015   "Proceedings from School Sites: Becoming Prepared for Earthquakes - Commemorating the Third Anniversary of the Loma Prieta Earthquake," Edited by F.E. Winslow and K.E.K. Ross, 8/16/93, (PB94-154275, A16, MF-A02).

NCEER-93-0016   "Reconnaissance Report of Damage to Historic Monuments in Cairo, Egypt Following the October 12, 1992 Dahshur Earthquake," by D. Sykora, D. Look, G. Croci, E. Karaesmen and E. Karaesmen, 8/19/93, (PB94-142221, A08, MF-A02).

NCEER-93-0017   "The Island of Guam Earthquake of August 8, 1993," by S.W. Swan and S.K. Harris, 9/30/93, (PB94-141843, A04, MF-A01).

NCEER-93-0018   "Engineering Aspects of the October 12, 1992 Egyptian Earthquake," by A.W. Elgamal, M. Amer, K. Adalier and A. Abul-Fadl, 10/7/93, (PB94-141983, A05, MF-A01).

NCEER-93-0019   "Development of an Earthquake Motion Simulator and its Application in Dynamic Centrifuge Testing," by I. Krstelj, Supervised by J.H. Prevost, 10/23/93, (PB94-181773, A-10, MF-A03).

NCEER-93-0020   "NCEER-Taisei Corporation Research Program on Sliding Seismic Isolation Systems for Bridges: Experimental and Analytical Study of a Friction Pendulum System (FPS)," by M.C. Constantinou, P. Tsopelas, Y-S. Kim and S. Okamoto, 11/1/93, (PB94-142775, A08, MF-A02).

NCEER-93-0021   "Finite Element Modeling of Elastomeric Seismic Isolation Bearings," by L.J. Billings, Supervised by R. Shepherd, 11/8/93, to be published.

NCEER-93-0022   "Seismic Vulnerability of Equipment in Critical Facilities: Life-Safety and Operational Consequences," by K. Porter, G.S. Johnson, M.M. Zadeh, C. Scawthorn and S. Eder, 11/24/93, (PB94-181765, A16, MF-A03).

NCEER-93-0023   "Hokkaido Nansei-oki, Japan Earthquake of July 12, 1993, by P.I. Yanev and C.R. Scawthorn, 12/23/93, (PB94-181500, A07, MF-A01).

NCEER-94-0001   "An Evaluation of Seismic Serviceability of Water Supply Networks with Application to the San Francisco Auxiliary Water Supply System," by I. Markov, Supervised by M. Grigoriu and T. O'Rourke, 1/21/94, (PB94-204013, A07, MF-A02).

NCEER-94-0002   "NCEER-Taisei Corporation Research Program on Sliding Seismic Isolation Systems for Bridges: Experimental and Analytical Study of Systems Consisting of Sliding Bearings, Rubber Restoring Force Devices and Fluid Dampers," Volumes I and II, by P. Tsopelas, S. Okamoto, M.C. Constantinou, D. Ozaki and S. Fujii, 2/4/94, (PB94-181740, A09, MF-A02 and PB94-181757, A12, MF-A03).

NCEER-94-0003   "A Markov Model for Local and Global Damage Indices in Seismic Analysis," by S. Rahman and M. Grigoriu, 2/18/94, (PB94-206000, A12, MF-A03).

NCEER-94-0004   "Proceedings from the NCEER Workshop on Seismic Response of Masonry Infills," edited by D.P. Abrams, 3/1/94, (PB94-180783, A07, MF-A02).

NCEER-94-0005   "The Northridge, California Earthquake of January 17, 1994: General Reconnaissance Report," edited by J.D. Goltz, 3/11/94, (PB94-193943, A10, MF-A03).

NCEER-94-0006   "Seismic Energy Based Fatigue Damage Analysis of Bridge Columns: Part I - Evaluation of Seismic Capacity," by G.A. Chang and J.B. Mander, 3/14/94, (PB94-219185, A11, MF-A03).

NCEER-94-0007   "Seismic Isolation of Multi-Story Frame Structures Using Spherical Sliding Isolation Systems," by T.M. Al-Hussaini, V.A. Zayas and M.C. Constantinou, 3/17/94, (PB94-193745, A09, MF-A02).

NCEER-94-0008   "The Northridge, California Earthquake of January 17, 1994: Performance of Highway Bridges," edited by I.G. Buckle, 3/24/94, (PB94-193851, A06, MF-A02).

NCEER-94-0009   "Proceedings of the Third U.S.-Japan Workshop on Earthquake Protective Systems for Bridges," edited by I.G. Buckle and I. Friedland, 3/31/94, (PB94-195815, A99, MF-A06).

435

NCEER-94-0010   "3D-BASIS-ME: Computer Program for Nonlinear Dynamic Analysis of Seismically Isolated Single and Multiple Structures and Liquid Storage Tanks," by P.C. Tsopelas, M.C. Constantinou and A.M. Reinhorn, 4/12/94, (PB94-204922, A09, MF-A02).

NCEER-94-0011   "The Northridge, California Earthquake of January 17, 1994: Performance of Gas Transmission Pipelines," by T.D. O'Rourke and M.C. Palmer, 5/16/94, (PB94-204989, A05, MF-A01).

NCEER-94-0012   "Feasibility Study of Replacement Procedures and Earthquake Performance Related to Gas Transmission Pipelines," by T.D. O'Rourke and M.C. Palmer, 5/25/94, (PB94-206638, A09, MF-A02).

NCEER-94-0013   "Seismic Energy Based Fatigue Damage Analysis of Bridge Columns: Part II - Evaluation of Seismic Demand," by G.A. Chang and J.B. Mander, 6/1/94, (PB95-18106, A08, MF-A02).

NCEER-94-0014   "NCEER-Taisei Corporation Research Program on Sliding Seismic Isolation Systems for Bridges: Experimental and Analytical Study of a System Consisting of Sliding Bearings and Fluid Restoring Force/Damping Devices," by P. Tsopelas and M.C. Constantinou, 6/13/94, (PB94-219144, A10, MF-A03).

NCEER-94-0015   "Generation of Hazard-Consistent Fragility Curves for Seismic Loss Estimation Studies," by H. Hwang and J-R. Huo, 6/14/94, (PB95-181996, A09, MF-A02).

NCEER-94-0016   "Seismic Study of Building Frames with Added Energy-Absorbing Devices," by W.S. Pong, C.S. Tsai and G.C. Lee, 6/20/94, (PB94-219136, A10, A03).

NCEER-94-0017   "Sliding Mode Control for Seismic-Excited Linear and Nonlinear Civil Engineering Structures," by J. Yang, J. Wu, A. Agrawal and Z. Li, 6/21/94, (PB95-138483, A06, MF-A02).

NCEER-94-0018   "3D-BASIS-TABS Version 2.0: Computer Program for Nonlinear Dynamic Analysis of Three Dimensional Base Isolated Structures," by A.M. Reinhorn, S. Nagarajaiah, M.C. Constantinou, P. Tsopelas and R. Li, 6/22/94, (PB95-182176, A08, MF-A02).

NCEER-94-0019   "Proceedings of the International Workshop on Civil Infrastructure Systems: Application of Intelligent Systems and Advanced Materials on Bridge Systems," Edited by G.C. Lee and K.C. Chang, 7/18/94, (PB95-252474, A20, MF-A04).

NCEER-94-0020   "Study of Seismic Isolation Systems for Computer Floors," by V. Lambrou and M.C. Constantinou, 7/19/94, (PB95-138533, A10, MF-A03).

NCEER-94-0021   "Proceedings of the U.S.-Italian Workshop on Guidelines for Seismic Evaluation and Rehabilitation of Unreinforced Masonry Buildings," Edited by D.P. Abrams and G.M. Calvi, 7/20/94, (PB95-138749, A13, MF-A03).

NCEER-94-0022   "NCEER-Taisei Corporation Research Program on Sliding Seismic Isolation Systems for Bridges: Experimental and Analytical Study of a System Consisting of Lubricated PTFE Sliding Bearings and Mild Steel Dampers," by P. Tsopelas and M.C. Constantinou, 7/22/94, (PB95-182184, A08, MF-A02).

NCEER-94-0023   "Development of Reliability-Based Design Criteria for Buildings Under Seismic Load," by Y.K. Wen, H. Hwang and M. Shinozuka, 8/1/94, (PB95-211934, A08, MF-A02).

NCEER-94-0024   "Experimental Verification of Acceleration Feedback Control Strategies for an Active Tendon System," by S.J. Dyke, B.F. Spencer, Jr., P. Quast, M.K. Sain, D.C. Kaspari, Jr. and T.T. Soong, 8/29/94, (PB95-212320, A05, MF-A01).

NCEER-94-0025   "Seismic Retrofitting Manual for Highway Bridges," Edited by I.G. Buckle and I.F. Friedland, published by the Federal Highway Administration (PB95-212676, A15, MF-A03).

NCEER-94-0026   "Proceedings from the Fifth U.S.-Japan Workshop on Earthquake Resistant Design of Lifeline Facilities and Countermeasures Against Soil Liquefaction," Edited by T.D. O'Rourke and M. Hamada, 11/7/94, (PB95-220802, A99, MF-E08).

NCEER-95-0001 "Experimental and Analytical Investigation of Seismic Retrofit of Structures with Supplemental Damping: Part 1 - Fluid Viscous Damping Devices," by A.M. Reinhorn, C. Li and M.C. Constantinou, 1/3/95, (PB95-266599, A09, MF-A02).

NCEER-95-0002 "Experimental and Analytical Study of Low-Cycle Fatigue Behavior of Semi-Rigid Top-And-Seat Angle Connections," by G. Pekcan, J.B. Mander and S.S. Chen, 1/5/95, (PB95-220042, A07, MF-A02).

NCEER-95-0003 "NCEER-ATC Joint Study on Fragility of Buildings," by T. Anagnos, C. Rojahn and A.S. Kiremidjian, 1/20/95, (PB95-220026, A06, MF-A02).

NCEER-95-0004 "Nonlinear Control Algorithms for Peak Response Reduction," by Z. Wu, T.T. Soong, V. Gattulli and R.C. Lin, 2/16/95, (PB95-220349, A05, MF-A01).

NCEER-95-0005 "Pipeline Replacement Feasibility Study: A Methodology for Minimizing Seismic and Corrosion Risks to Underground Natural Gas Pipelines," by R.T. Eguchi, H.A. Seligson and D.G. Honegger, 3/2/95, (PB95-252326, A06, MF-A02).

NCEER-95-0006 "Evaluation of Seismic Performance of an 11-Story Frame Building During the 1994 Northridge Earthquake," by F. Naeim, R. DiSulio, K. Benuska, A. Reinhorn and C. Li, to be published.

NCEER-95-0007 "Prioritization of Bridges for Seismic Retrofitting," by N. Basöz and A.S. Kiremidjian, 4/24/95, (PB95-252300, A08, MF-A02).

NCEER-95-0008 "Method for Developing Motion Damage Relationships for Reinforced Concrete Frames," by A. Singhal and A.S. Kiremidjian, 5/11/95, (PB95-266607, A06, MF-A02).

NCEER-95-0009 "Experimental and Analytical Investigation of Seismic Retrofit of Structures with Supplemental Damping: Part II - Friction Devices," by C. Li and A.M. Reinhorn, 7/6/95, (PB96-128087, A11, MF-A03).

NCEER-95-0010 "Experimental Performance and Analytical Study of a Non-Ductile Reinforced Concrete Frame Structure Retrofitted with Elastomeric Spring Dampers," by G. Pekcan, J.B. Mander and S.S. Chen, 7/14/95, (PB96-137161, A08, MF-A02).

NCEER-95-0011 "Development and Experimental Study of Semi-Active Fluid Damping Devices for Seismic Protection of Structures," by M.D. Symans and M.C. Constantinou, 8/3/95, (PB96-136940, A23, MF-A04).

NCEER-95-0012 "Real-Time Structural Parameter Modification (RSPM): Development of Innervated Structures," by Z. Liang, M. Tong and G.C. Lee, 4/11/95, (PB96-137153, A06, MF-A01).

NCEER-95-0013 "Experimental and Analytical Investigation of Seismic Retrofit of Structures with Supplemental Damping: Part III - Viscous Damping Walls," by A.M. Reinhorn and C. Li, 10/1/95, (PB96-176409, A11, MF-A03).

NCEER-95-0014 "Seismic Fragility Analysis of Equipment and Structures in a Memphis Electric Substation," by J-R. Huo and H.H.M. Hwang, 8/10/95, (PB96-128087, A09, MF-A02).

NCEER-95-0015 "The Hanshin-Awaji Earthquake of January 17, 1995: Performance of Lifelines," Edited by M. Shinozuka, 11/3/95, (PB96-176383, A15, MF-A03).

NCEER-95-0016 "Highway Culvert Performance During Earthquakes," by T.L. Youd and C.J. Beckman, available as NCEER-96-0015.

NCEER-95-0017 "The Hanshin-Awaji Earthquake of January 17, 1995: Performance of Highway Bridges," Edited by I.G. Buckle, 12/1/95, to be published.

NCEER-95-0018 "Modeling of Masonry Infill Panels for Structural Analysis," by A.M. Reinhorn, A. Madan, R.E. Valles, Y. Reichmann and J.B. Mander, 12/8/95, (PB97-110886, MF-A01, A06).

NCEER-95-0019 "Optimal Polynomial Control for Linear and Nonlinear Structures," by A.K. Agrawal and J.N. Yang, 12/11/95, (PB96-168737, A07, MF-A02).

NCEER-95-0020 "Retrofit of Non-Ductile Reinforced Concrete Frames Using Friction Dampers," by R.S. Rao, P. Gergely and R.N. White, 12/22/95, (PB97-133508, A10, MF-A02).

NCEER-95-0021 "Parametric Results for Seismic Response of Pile-Supported Bridge Bents," by G. Mylonakis, A. Nikolaou and G. Gazetas, 12/22/95, (PB97-100242, A12, MF-A03).

NCEER-95-0022 "Kinematic Bending Moments in Seismically Stressed Piles," by A. Nikolaou, G. Mylonakis and G. Gazetas, 12/23/95, (PB97-113914, MF-A03, A13).

NCEER-96-0001 "Dynamic Response of Unreinforced Masonry Buildings with Flexible Diaphragms," by A.C. Costley and D.P. Abrams," 10/10/96, (PB97-133573, MF-A03, A15).

NCEER-96-0002 "State of the Art Review: Foundations and Retaining Structures," by I. Po Lam, to be published.

NCEER-96-0003 "Ductility of Rectangular Reinforced Concrete Bridge Columns with Moderate Confinement," by N. Wehbe, M. Saiidi, D. Sanders and B. Douglas, 11/7/96, (PB97-133557, A06, MF-A02).

NCEER-96-0004 "Proceedings of the Long-Span Bridge Seismic Research Workshop," edited by I.G. Buckle and I.M. Friedland, to be published.

NCEER-96-0005 "Establish Representative Pier Types for Comprehensive Study: Eastern United States," by J. Kulicki and Z. Prucz, 5/28/96, (PB98-119217, A07, MF-A02).

NCEER-96-0006 "Establish Representative Pier Types for Comprehensive Study: Western United States," by R. Imbsen, R.A. Schamber and T.A. Osterkamp, 5/28/96, (PB98-118607, A07, MF-A02).

NCEER-96-0007 "Nonlinear Control Techniques for Dynamical Systems with Uncertain Parameters," by R.G. Ghanem and M.I. Bujakov, 5/27/96, (PB97-100259, A17, MF-A03).

NCEER-96-0008 "Seismic Evaluation of a 30-Year Old Non-Ductile Highway Bridge Pier and Its Retrofit," by J.B. Mander, B. Mahmoodzadegan, S. Bhadra and S.S. Chen, 5/31/96, (PB97-110902, MF-A03, A10).

NCEER-96-0009 "Seismic Performance of a Model Reinforced Concrete Bridge Pier Before and After Retrofit," by J.B. Mander, J.H. Kim and C.A. Ligozio, 5/31/96, (PB97-110910, MF-A02, A10).

NCEER-96-0010 "IDARC2D Version 4.0: A Computer Program for the Inelastic Damage Analysis of Buildings," by R.E. Valles, A.M. Reinhorn, S.K. Kunnath, C. Li and A. Madan, 6/3/96, (PB97-100234, A17, MF-A03).

NCEER-96-0011 "Estimation of the Economic Impact of Multiple Lifeline Disruption: Memphis Light, Gas and Water Division Case Study," by S.E. Chang, H.A. Seligson and R.T. Eguchi, 8/16/96, (PB97-133490, A11, MF-A03).

NCEER-96-0012 "Proceedings from the Sixth Japan-U.S. Workshop on Earthquake Resistant Design of Lifeline Facilities and Countermeasures Against Soil Liquefaction, Edited by M. Hamada and T. O'Rourke, 9/11/96, (PB97-133581, A99, MF-A06).

NCEER-96-0013 "Chemical Hazards, Mitigation and Preparedness in Areas of High Seismic Risk: A Methodology for Estimating the Risk of Post-Earthquake Hazardous Materials Release," by H.A. Seligson, R.T. Eguchi, K.J. Tierney and K. Richmond, 11/7/96, (PB97-133565, MF-A02, A08).

NCEER-96-0014 "Response of Steel Bridge Bearings to Reversed Cyclic Loading," by J.B. Mander, D-K. Kim, S.S. Chen and G.J. Premus, 11/13/96, (PB97-140735, A12, MF-A03).

NCEER-96-0015 "Highway Culvert Performance During Past Earthquakes," by T.L. Youd and C.J. Beckman, 11/25/96, (PB97-133532, A06, MF-A01).

NCEER-97-0001 "Evaluation, Prevention and Mitigation of Pounding Effects in Building Structures," by R.E. Valles and A.M. Reinhorn, 2/20/97, (PB97-159552, A14, MF-A03).

NCEER-97-0002 "Seismic Design Criteria for Bridges and Other Highway Structures," by C. Rojahn, R. Mayes, D.G. Anderson, J. Clark, J.H. Hom, R.V. Nutt and M.J. O'Rourke, 4/30/97, (PB97-194658, A06, MF-A03).

NCEER-97-0003   "Proceedings of the U.S.-Italian Workshop on Seismic Evaluation and Retrofit," Edited by D.P. Abrams and G.M. Calvi, 3/19/97, (PB97-194666, A13, MF-A03).

NCEER-97-0004   "Investigation of Seismic Response of Buildings with Linear and Nonlinear Fluid Viscous Dampers," by A.A. Seleemah and M.C. Constantinou, 5/21/97, (PB98-109002, A15, MF-A03).

NCEER-97-0005   "Proceedings of the Workshop on Earthquake Engineering Frontiers in Transportation Facilities," edited by G.C. Lee and I.M. Friedland, 8/29/97, (PB98-128911, A25, MR-A04).

NCEER-97-0006   "Cumulative Seismic Damage of Reinforced Concrete Bridge Piers," by S.K. Kunnath, A. El-Bahy, A. Taylor and W. Stone, 9/2/97, (PB98-108814, A11, MF-A03).

NCEER-97-0007   "Structural Details to Accommodate Seismic Movements of Highway Bridges and Retaining Walls," by R.A. Imbsen, R.A. Schamber, E. Thorkildsen, A. Kartoum, B.T. Martin, T.N. Rosser and J.M. Kulicki, 9/3/97, (PB98-108996, A09, MF-A02).

NCEER-97-0008   "A Method for Earthquake Motion-Damage Relationships with Application to Reinforced Concrete Frames," by A. Singhal and A.S. Kiremidjian, 9/10/97, (PB98-108988, A13, MF-A03).

NCEER-97-0009   "Seismic Analysis and Design of Bridge Abutments Considering Sliding and Rotation," by K. Fishman and R. Richards, Jr., 9/15/97, (PB98-108897, A06, MF-A02).

NCEER-97-0010   "Proceedings of the FHWA/NCEER Workshop on the National Representation of Seismic Ground Motion for New and Existing Highway Facilities," edited by I.M. Friedland, M.S. Power and R.L. Mayes, 9/22/97, (PB98-128903, A21, MF-A04).

NCEER-97-0011   "Seismic Analysis for Design or Retrofit of Gravity Bridge Abutments," by K.L. Fishman, R. Richards, Jr. and R.C. Divito, 10/2/97, (PB98-128937, A08, MF-A02).

NCEER-97-0012   "Evaluation of Simplified Methods of Analysis for Yielding Structures," by P. Tsopelas, M.C. Constantinou, C.A. Kircher and A.S. Whittaker, 10/31/97, (PB98-128929, A10, MF-A03).

NCEER-97-0013   "Seismic Design of Bridge Columns Based on Control and Repairability of Damage," by C-T. Cheng and J.B. Mander, 12/8/97, (PB98-144249, A11, MF-A03).

NCEER-97-0014   "Seismic Resistance of Bridge Piers Based on Damage Avoidance Design," by J.B. Mander and C-T. Cheng, 12/10/97, (PB98-144223, A09, MF-A02).

NCEER-97-0015   "Seismic Response of Nominally Symmetric Systems with Strength Uncertainty," by S. Balopoulou and M. Grigoriu, 12/23/97, (PB98-153422, A11, MF-A03).

NCEER-97-0016   "Evaluation of Seismic Retrofit Methods for Reinforced Concrete Bridge Columns," by T.J. Wipf, F.W. Klaiber and F.M. Russo, 12/28/97, (PB98-144215, A12, MF-A03).

NCEER-97-0017   "Seismic Fragility of Existing Conventional Reinforced Concrete Highway Bridges," by C.L. Mullen and A.S. Cakmak, 12/30/97, (PB98-153406, A08, MF-A02).

NCEER-97-0018   "Loss Asssessment of Memphis Buildings," edited by D.P. Abrams and M. Shinozuka, 12/31/97, (PB98-144231, A13, MF-A03).

NCEER-97-0019   "Seismic Evaluation of Frames with Infill Walls Using Quasi-static Experiments," by K.M. Mosalam, R.N. White and P. Gergely, 12/31/97, (PB98-153455, A07, MF-A02).

NCEER-97-0020   "Seismic Evaluation of Frames with Infill Walls Using Pseudo-dynamic Experiments," by K.M. Mosalam, R.N. White and P. Gergely, 12/31/97, (PB98-153430, A07, MF-A02).

NCEER-97-0021   "Computational Strategies for Frames with Infill Walls: Discrete and Smeared Crack Analyses and Seismic Fragility," by K.M. Mosalam, R.N. White and P. Gergely, 12/31/97, (PB98-153414, A10, MF-A02).

NCEER-97-0022   "Proceedings of the NCEER Workshop on Evaluation of Liquefaction Resistance of Soils," edited by T.L. Youd and I.M. Idriss, 12/31/97, (PB98-155617, A15, MF-A03).

MCEER-98-0001   "Extraction of Nonlinear Hysteretic Properties of Seismically Isolated Bridges from Quick-Release Field Tests," by Q. Chen, B.M. Douglas, E.M. Maragakis and I.G. Buckle, 5/26/98, (PB99-118838, A06, MF-A01).

MCEER-98-0002   "Methodologies for Evaluating the Importance of Highway Bridges," by A. Thomas, S. Eshenaur and J. Kulicki, 5/29/98, (PB99-118846, A10, MF-A02).

MCEER-98-0003   "Capacity Design of Bridge Piers and the Analysis of Overstrength," by J.B. Mander, A. Dutta and P. Goel, 6/1/98, (PB99-118853, A09, MF-A02).

MCEER-98-0004   "Evaluation of Bridge Damage Data from the Loma Prieta and Northridge, California Earthquakes," by N. Basoz and A. Kiremidjian, 6/2/98, (PB99-118861, A15, MF-A03).

MCEER-98-0005   "Screening Guide for Rapid Assessment of Liquefaction Hazard at Highway Bridge Sites," by T. L. Youd, 6/16/98, (PB99-118879, A06, not available on microfiche).

MCEER-98-0006   "Structural Steel and Steel/Concrete Interface Details for Bridges," by P. Ritchie, N. Kauhl and J. Kulicki, 7/13/98, (PB99-118945, A06, MF-A01).

MCEER-98-0007   "Capacity Design and Fatigue Analysis of Confined Concrete Columns," by A. Dutta and J.B. Mander, 7/14/98, (PB99-118960, A14, MF-A03).

MCEER-98-0008   "Proceedings of the Workshop on Performance Criteria for Telecommunication Services Under Earthquake Conditions," edited by A.J. Schiff, 7/15/98, (PB99-118952, A08, MF-A02).

MCEER-98-0009   "Fatigue Analysis of Unconfined Concrete Columns," by J.B. Mander, A. Dutta and J.H. Kim, 9/12/98, (PB99-123655, A10, MF-A02).

MCEER-98-0010   "Centrifuge Modeling of Cyclic Lateral Response of Pile-Cap Systems and Seat-Type Abutments in Dry Sands," by A.D. Gadre and R. Dobry, 10/2/98, (PB99-123606, A13, MF-A03).

MCEER-98-0011   "IDARC-BRIDGE: A Computational Platform for Seismic Damage Assessment of Bridge Structures," by A.M. Reinhorn, V. Simeonov, G. Mylonakis and Y. Reichman, 10/2/98, (PB99-162919, A15, MF-A03).

MCEER-98-0012   "Experimental Investigation of the Dynamic Response of Two Bridges Before and After Retrofitting with Elastomeric Bearings," by D.A. Wendichansky, S.S. Chen and J.B. Mander, 10/2/98, (PB99-162927, A15, MF-A03).

MCEER-98-0013   "Design Procedures for Hinge Restrainers and Hinge Sear Width for Multiple-Frame Bridges," by R. Des Roches and G.L. Fenves, 11/3/98, (PB99-140477, A13, MF-A03).

MCEER-98-0014   "Response Modification Factors for Seismically Isolated Bridges," by M.C. Constantinou and J.K. Quarshie, 11/3/98, (PB99-140485, A14, MF-A03).

MCEER-98-0015   "Proceedings of the U.S.-Italy Workshop on Seismic Protective Systems for Bridges," edited by I.M. Friedland and M.C. Constantinou, 11/3/98, (PB2000-101711, A22, MF-A04).

MCEER-98-0016   "Appropriate Seismic Reliability for Critical Equipment Systems: Recommendations Based on Regional Analysis of Financial and Life Loss," by K. Porter, C. Scawthorn, C. Taylor and N. Blais, 11/10/98, (PB99-157265, A08, MF-A02).

MCEER-98-0017   "Proceedings of the U.S. Japan Joint Seminar on Civil Infrastructure Systems Research," edited by M. Shinozuka and A. Rose, 11/12/98, (PB99-156713, A16, MF-A03).

MCEER-98-0018   "Modeling of Pile Footings and Drilled Shafts for Seismic Design," by I. PoLam, M. Kapuskar and D. Chaudhuri, 12/21/98, (PB99-157257, A09, MF-A02).

MCEER-99-0001 "Seismic Evaluation of a Masonry Infilled Reinforced Concrete Frame by Pseudodynamic Testing," by S.G. Buonopane and R.N. White, 2/16/99, (PB99-162851, A09, MF-A02).

MCEER-99-0002 "Response History Analysis of Structures with Seismic Isolation and Energy Dissipation Systems: Verification Examples for Program SAP2000," by J. Scheller and M.C. Constantinou, 2/22/99, (PB99-162869, A08, MF-A02).

MCEER-99-0003 "Experimental Study on the Seismic Design and Retrofit of Bridge Columns Including Axial Load Effects," by A. Dutta, T. Kokorina and J.B. Mander, 2/22/99, (PB99-162877, A09, MF-A02).

MCEER-99-0004 "Experimental Study of Bridge Elastomeric and Other Isolation and Energy Dissipation Systems with Emphasis on Uplift Prevention and High Velocity Near-source Seismic Excitation," by A. Kasalanati and M. C. Constantinou, 2/26/99, (PB99-162885, A12, MF-A03).

MCEER-99-0005 "Truss Modeling of Reinforced Concrete Shear-flexure Behavior," by J.H. Kim and J.B. Mander, 3/8/99, (PB99-163693, A12, MF-A03).

MCEER-99-0006 "Experimental Investigation and Computational Modeling of Seismic Response of a 1:4 Scale Model Steel Structure with a Load Balancing Supplemental Damping System," by G. Pekcan, J.B. Mander and S.S. Chen, 4/2/99, (PB99-162893, A11, MF-A03).

MCEER-99-0007 "Effect of Vertical Ground Motions on the Structural Response of Highway Bridges," by M.R. Button, C.J. Cronin and R.L. Mayes, 4/10/99, (PB2000-101411, A10, MF-A03).

MCEER-99-0008 "Seismic Reliability Assessment of Critical Facilities: A Handbook, Supporting Documentation, and Model Code Provisions," by G.S. Johnson, R.E. Sheppard, M.D. Quilici, S.J. Eder and C.R. Scawthorn, 4/12/99, (PB2000-101701, A18, MF-A04).

MCEER-99-0009 "Impact Assessment of Selected MCEER Highway Project Research on the Seismic Design of Highway Structures," by C. Rojahn, R. Mayes, D.G. Anderson, J.H. Clark, D'Appolonia Engineering, S. Gloyd and R.V. Nutt, 4/14/99, (PB99-162901, A10, MF-A02).

MCEER-99-0010 "Site Factors and Site Categories in Seismic Codes," by R. Dobry, R. Ramos and M.S. Power, 7/19/99, (PB2000-101705, A08, MF-A02).

MCEER-99-0011 "Restrainer Design Procedures for Multi-Span Simply-Supported Bridges," by M.J. Randall, M. Saiidi, E. Maragakis and T. Isakovic, 7/20/99, (PB2000-101702, A10, MF-A02).

MCEER-99-0012 "Property Modification Factors for Seismic Isolation Bearings," by M.C. Constantinou, P. Tsopelas, A. Kasalanati and E. Wolff, 7/20/99, (PB2000-103387, A11, MF-A03).

MCEER-99-0013 "Critical Seismic Issues for Existing Steel Bridges," by P. Ritchie, N. Kauhl and J. Kulicki, 7/20/99, (PB2000-101697, A09, MF-A02).

MCEER-99-0014 "Nonstructural Damage Database," by A. Kao, T.T. Soong and A. Vender, 7/24/99, (PB2000-101407, A06, MF-A01).

MCEER-99-0015 "Guide to Remedial Measures for Liquefaction Mitigation at Existing Highway Bridge Sites," by H.G. Cooke and J. K. Mitchell, 7/26/99, (PB2000-101703, A11, MF-A03).

MCEER-99-0016 "Proceedings of the MCEER Workshop on Ground Motion Methodologies for the Eastern United States," edited by N. Abrahamson and A. Becker, 8/11/99, (PB2000-103385, A07, MF-A02).

MCEER-99-0017 "Quindío, Colombia Earthquake of January 25, 1999: Reconnaissance Report," by A.P. Asfura and P.J. Flores, 10/4/99, (PB2000-106893, A06, MF-A01).

MCEER-99-0018 "Hysteretic Models for Cyclic Behavior of Deteriorating Inelastic Structures," by M.V. Sivaselvan and A.M. Reinhorn, 11/5/99, (PB2000-103386, A08, MF-A02).

MCEER-99-0019   "Proceedings of the 7th U.S.- Japan Workshop on Earthquake Resistant Design of Lifeline Facilities and Countermeasures Against Soil Liquefaction," edited by T.D. O'Rourke, J.P. Bardet and M. Hamada, 11/19/99, (PB2000-103354, A99, MF-A06).

MCEER-99-0020   "Development of Measurement Capability for Micro-Vibration Evaluations with Application to Chip Fabrication Facilities," by G.C. Lee, Z. Liang, J.W. Song, J.D. Shen and W.C. Liu, 12/1/99, (PB2000-105993, A08, MF-A02).

MCEER-99-0021   "Design and Retrofit Methodology for Building Structures with Supplemental Energy Dissipating Systems," by G. Pekcan, J.B. Mander and S.S. Chen, 12/31/99, (PB2000-105994, A11, MF-A03).

MCEER-00-0001   "The Marmara, Turkey Earthquake of August 17, 1999: Reconnaissance Report," edited by C. Scawthorn; with major contributions by M. Bruneau, R. Eguchi, T. Holzer, G. Johnson, J. Mander, J. Mitchell, W. Mitchell, A. Papageorgiou, C. Scaethorn, and G. Webb, 3/23/00, (PB2000-106200, A11, MF-A03).

MCEER-00-0002   "Proceedings of the MCEER Workshop for Seismic Hazard Mitigation of Health Care Facilities," edited by G.C. Lee, M. Ettouney, M. Grigoriu, J. Hauer and J. Nigg, 3/29/00, (PB2000-106892, A08, MF-A02).

MCEER-00-0003   "The Chi-Chi, Taiwan Earthquake of September 21, 1999: Reconnaissance Report," edited by G.C. Lee and C.H. Loh, with major contributions by G.C. Lee, M. Bruneau, I.G. Buckle, S.E. Chang, P.J. Flores, T.D. O'Rourke, M. Shinozuka, T.T. Soong, C-H. Loh, K-C. Chang, Z-J. Chen, J-S. Hwang, M-L. Lin, G-Y. Liu, K-C. Tsai, G.C. Yao and C-L. Yen, 4/30/00, (PB2001-100980, A10, MF-A02).

MCEER-00-0004   "Seismic Retrofit of End-Sway Frames of Steel Deck-Truss Bridges with a Supplemental Tendon System: Experimental and Analytical Investigation," by G. Pekcan, J.B. Mander and S.S. Chen, 7/1/00, (PB2001-100982, A10, MF-A02).

MCEER-00-0005   "Sliding Fragility of Unrestrained Equipment in Critical Facilities," by W.H. Chong and T.T. Soong, 7/5/00, (PB2001-100983, A08, MF-A02).

MCEER-00-0006   "Seismic Response of Reinforced Concrete Bridge Pier Walls in the Weak Direction," by N. Abo-Shadi, M. Saiidi and D. Sanders, 7/17/00, (PB2001-100981, A17, MF-A03).

MCEER-00-0007   "Low-Cycle Fatigue Behavior of Longitudinal Reinforcement in Reinforced Concrete Bridge Columns," by J. Brown and S.K. Kunnath, 7/23/00, (PB2001-104392, A08, MF-A02).

MCEER-00-0008   "Soil Structure Interaction of Bridges for Seismic Analysis," I. PoLam and H. Law, 9/25/00, (PB2001-105397, A08, MF-A02).

MCEER-00-0009   "Proceedings of the First MCEER Workshop on Mitigation of Earthquake Disaster by Advanced Technologies (MEDAT-1), edited by M. Shinozuka, D.J. Inman and T.D. O'Rourke, 11/10/00, (PB2001-105399, A14, MF-A03).

MCEER-00-0010   "Development and Evaluation of Simplified Procedures for Analysis and Design of Buildings with Passive Energy Dissipation Systems, Revision 01," by O.M. Ramirez, M.C. Constantinou, C.A. Kircher, A.S. Whittaker, M.W. Johnson, J.D. Gomez and C. Chrysostomou, 11/16/01, (PB2001-105523, A23, MF-A04).

MCEER-00-0011   "Dynamic Soil-Foundation-Structure Interaction Analyses of Large Caissons," by C-Y. Chang, C-M. Mok, Z-L. Wang, R. Settgast, F. Waggoner, M.A. Ketchum, H.M. Gonnermann and C-C. Chin, 12/30/00, (PB2001-104373, A07, MF-A02).

MCEER-00-0012   "Experimental Evaluation of Seismic Performance of Bridge Restrainers," by A.G. Vlassis, E.M. Maragakis and M. Saiid Saiidi, 12/30/00, (PB2001-104354, A09, MF-A02).

MCEER-00-0013   "Effect of Spatial Variation of Ground Motion on Highway Structures," by M. Shinozuka, V. Saxena and G. Deodatis, 12/31/00, (PB2001-108755, A13, MF-A03).

MCEER-00-0014   "A Risk-Based Methodology for Assessing the Seismic Performance of Highway Systems," by S.D. Werner, C.E. Taylor, J.E. Moore, II, J.S. Walton and S. Cho, 12/31/00, (PB2001-108756, A14, MF-A03).

MCEER-01-0001 "Experimental Investigation of P-Delta Effects to Collapse During Earthquakes," by D. Vian and M. Bruneau, 6/25/01, (PB2002-100534, A17, MF-A03).

MCEER-01-0002 "Proceedings of the Second MCEER Workshop on Mitigation of Earthquake Disaster by Advanced Technologies (MEDAT-2)," edited by M. Bruneau and D.J. Inman, 7/23/01, (PB2002-100434, A16, MF-A03).

MCEER-01-0003 "Sensitivity Analysis of Dynamic Systems Subjected to Seismic Loads," by C. Roth and M. Grigoriu, 9/18/01, (PB2003-100884, A12, MF-A03).

MCEER-01-0004 "Overcoming Obstacles to Implementing Earthquake Hazard Mitigation Policies: Stage 1 Report," by D.J. Alesch and W.J. Petak, 12/17/01, (PB2002-107949, A07, MF-A02).

MCEER-01-0005 "Updating Real-Time Earthquake Loss Estimates: Methods, Problems and Insights," by C.E. Taylor, S.E. Chang and R.T. Eguchi, 12/17/01, (PB2002-107948, A05, MF-A01).

MCEER-01-0006 "Experimental Investigation and Retrofit of Steel Pile Foundations and Pile Bents Under Cyclic Lateral Loadings," by A. Shama, J. Mander, B. Blabac and S. Chen, 12/31/01, (PB2002-107950, A13, MF-A03).

MCEER-02-0001 "Assessment of Performance of Bolu Viaduct in the 1999 Duzce Earthquake in Turkey" by P.C. Roussis, M.C. Constantinou, M. Erdik, E. Durukal and M. Dicleli, 5/8/02, (PB2003-100883, A08, MF-A02).

MCEER-02-0002 "Seismic Behavior of Rail Counterweight Systems of Elevators in Buildings," by M.P. Singh, Rildova and L.E. Suarez, 5/27/02. (PB2003-100882, A11, MF-A03).

MCEER-02-0003 "Development of Analysis and Design Procedures for Spread Footings," by G. Mylonakis, G. Gazetas, S. Nikolaou and A. Chauncey, 10/02/02, (PB2004-101636, A13, MF-A03, CD-A13).

MCEER-02-0004 "Bare-Earth Algorithms for Use with SAR and LIDAR Digital Elevation Models," by C.K. Huyck, R.T. Eguchi and B. Houshmand, 10/16/02, (PB2004-101637, A07, CD-A07).

MCEER-02-0005 "Review of Energy Dissipation of Compression Members in Concentrically Braced Frames," by K.Lee and M. Bruneau, 10/18/02, (PB2004-101638, A10, CD-A10).

MCEER-03-0001 "Experimental Investigation of Light-Gauge Steel Plate Shear Walls for the Seismic Retrofit of Buildings" by J. Berman and M. Bruneau, 5/2/03, (PB2004-101622, A10, MF-A03, CD-A10).

MCEER-03-0002 "Statistical Analysis of Fragility Curves," by M. Shinozuka, M.Q. Feng, H. Kim, T. Uzawa and T. Ueda, 6/16/03, (PB2004-101849, A09, CD-A09).

MCEER-03-0003 "Proceedings of the Eighth U.S.-Japan Workshop on Earthquake Resistant Design f Lifeline Facilities and Countermeasures Against Liquefaction," edited by M. Hamada, J.P. Bardet and T.D. O'Rourke, 6/30/03, (PB2004-104386, A99, CD-A99).

MCEER-03-0004 "Proceedings of the PRC-US Workshop on Seismic Analysis and Design of Special Bridges," edited by L.C. Fan and G.C. Lee, 7/15/03, (PB2004-104387, A14, CD-A14).

MCEER-03-0005 "Urban Disaster Recovery: A Framework and Simulation Model," by S.B. Miles and S.E. Chang, 7/25/03, (PB2004-104388, A07, CD-A07).

MCEER-03-0006 "Behavior of Underground Piping Joints Due to Static and Dynamic Loading," by R.D. Meis, M. Maragakis and R. Siddharthan, 11/17/03, (PB2005-102194, A13, MF-A03, CD-A00).

MCEER-03-0007 "Seismic Vulnerability of Timber Bridges and Timber Substructures," by A.A. Shama, J.B. Mander, I.M. Friedland and D.R. Allicock, 12/15/03.

MCEER-04-0001 "Experimental Study of Seismic Isolation Systems with Emphasis on Secondary System Response and Verification of Accuracy of Dynamic Response History Analysis Methods," by E. Wolff and M. Constantinou, 1/16/04 (PB2005-102195, A99, MF-E08, CD-A00).

MCEER-04-0002   "Tension, Compression and Cyclic Testing of Engineered Cementitious Composite Materials," by K. Kesner and S.L. Billington, 3/1/04, (PB2005-102196, A08, CD-A08).

MCEER-04-0003   "Cyclic Testing of Braces Laterally Restrained by Steel Studs to Enhance Performance During Earthquakes," by O.C. Celik, J.W. Berman and M. Bruneau, 3/16/04, (PB2005-102197, A13, MF-A03, CD-A00).

MCEER-04-0004   "Methodologies for Post Earthquake Building Damage Detection Using SAR and Optical Remote Sensing: Application to the August 17, 1999 Marmara, Turkey Earthquake," by C.K. Huyck, B.J. Adams, S. Cho, R.T. Eguchi, B. Mansouri and B. Houshmand, 6/15/04, (PB2005-104888, A10, CD-A00).

MCEER-04-0005   "Nonlinear Structural Analysis Towards Collapse Simulation: A Dynamical Systems Approach," by M.V. Sivaselvan and A.M. Reinhorn, 6/16/04, (PB2005-104889, A11, MF-A03, CD-A00).

MCEER-04-0006   "Proceedings of the Second PRC-US Workshop on Seismic Analysis and Design of Special Bridges," edited by G.C. Lee and L.C. Fan, 6/25/04, (PB2005-104890, A16, CD-A00).

MCEER-04-0007   "Seismic Vulnerability Evaluation of Axially Loaded Steel Built-up Laced Members," by K. Lee and M. Bruneau, 6/30/04, (PB2005-104891, A16, CD-A00).

MCEER-04-0008   "Evaluation of Accuracy of Simplified Methods of Analysis and Design of Buildings with Damping Systems for Near-Fault and for Soft-Soil Seismic Motions," by E.A. Pavlou and M.C. Constantinou, 8/16/04, (PB2005-104892, A08, MF-A02, CD-A00).

MCEER-04-0009   "Assessment of Geotechnical Issues in Acute Care Facilities in California," by M. Lew, T.D. O'Rourke, R. Dobry and M. Koch, 9/15/04, (PB2005-104893, A08, CD-A00).

MCEER-04-0010   "Scissor-Jack-Damper Energy Dissipation System," by A.N. Sigaher-Boyle and M.C. Constantinou, 12/1/04 (PB2005-108221).

MCEER-04-0011   "Seismic Retrofit of Bridge Steel Truss Piers Using a Controlled Rocking Approach," by M. Pollino and M. Bruneau, 12/20/04 (PB2006-105795).

MCEER-05-0001   "Experimental and Analytical Studies of Structures Seismically Isolated with an Uplift-Restraint Isolation System," by P.C. Roussis and M.C. Constantinou, 1/10/05 (PB2005-108222).

MCEER-05-0002   "A Versatile Experimentation Model for Study of Structures Near Collapse Applied to Seismic Evaluation of Irregular Structures," by D. Kusumastuti, A.M. Reinhorn and A. Rutenberg, 3/31/05 (PB2006-101523).

MCEER-05-0003   "Proceedings of the Third PRC-US Workshop on Seismic Analysis and Design of Special Bridges," edited by L.C. Fan and G.C. Lee, 4/20/05, (PB2006-105796).

MCEER-05-0004   "Approaches for the Seismic Retrofit of Braced Steel Bridge Piers and Proof-of-Concept Testing of an Eccentrically Braced Frame with Tubular Link," by J.W. Berman and M. Bruneau, 4/21/05 (PB2006-101524).

MCEER-05-0005   "Simulation of Strong Ground Motions for Seismic Fragility Evaluation of Nonstructural Components in Hospitals," by A. Wanitkorkul and A. Filiatrault, 5/26/05 (PB2006-500027).

MCEER-05-0006   "Seismic Safety in California Hospitals: Assessing an Attempt to Accelerate the Replacement or Seismic Retrofit of Older Hospital Facilities," by D.J. Alesch, L.A. Arendt and W.J. Petak, 6/6/05 (PB2006-105794).

MCEER-05-0007   "Development of Seismic Strengthening and Retrofit Strategies for Critical Facilities Using Engineered Cementitious Composite Materials," by K. Kesner and S.L. Billington, 8/29/05 (PB2006-111701).

MCEER-05-0008   "Experimental and Analytical Studies of Base Isolation Systems for Seismic Protection of Power Transformers," by N. Murota, M.Q. Feng and G-Y. Liu, 9/30/05 (PB2006-111702).

MCEER-05-0009   "3D-BASIS-ME-MB: Computer Program for Nonlinear Dynamic Analysis of Seismically Isolated Structures," by P.C. Tsopelas, P.C. Roussis, M.C. Constantinou, R. Buchanan and A.M. Reinhorn, 10/3/05 (PB2006-111703).

MCEER-05-0010 "Steel Plate Shear Walls for Seismic Design and Retrofit of Building Structures," by D. Vian and M. Bruneau, 12/15/05 (PB2006-111704).

MCEER-05-0011 "The Performance-Based Design Paradigm," by M.J. Astrella and A. Whittaker, 12/15/05 (PB2006-111705).

MCEER-06-0001 "Seismic Fragility of Suspended Ceiling Systems," H. Badillo-Almaraz, A.S. Whittaker, A.M. Reinhorn and G.P. Cimellaro, 2/4/06 (PB2006-111706).

MCEER-06-0002 "Multi-Dimensional Fragility of Structures," by G.P. Cimellaro, A.M. Reinhorn and M. Bruneau, 3/1/06 (PB2007-106974, A09, MF-A02, CD A00).

MCEER-06-0003 "Built-Up Shear Links as Energy Dissipators for Seismic Protection of Bridges," by P. Dusicka, A.M. Itani and I.G. Buckle, 3/15/06 (PB2006-111708).

MCEER-06-0004 "Analytical Investigation of the Structural Fuse Concept," by R.E. Vargas and M. Bruneau, 3/16/06 (PB2006-111709).

MCEER-06-0005 "Experimental Investigation of the Structural Fuse Concept," by R.E. Vargas and M. Bruneau, 3/17/06 (PB2006-111710).

MCEER-06-0006 "Further Development of Tubular Eccentrically Braced Frame Links for the Seismic Retrofit of Braced Steel Truss Bridge Piers," by J.W. Berman and M. Bruneau, 3/27/06 (PB2007-105147).

MCEER-06-0007 "REDARS Validation Report," by S. Cho, C.K. Huyck, S. Ghosh and R.T. Eguchi, 8/8/06 (PB2007-106983).

MCEER-06-0008 "Review of Current NDE Technologies for Post-Earthquake Assessment of Retrofitted Bridge Columns," by J.W. Song, Z. Liang and G.C. Lee, 8/21/06 06 (PB2007-106984).

MCEER-06-0009 "Liquefaction Remediation in Silty Soils Using Dynamic Compaction and Stone Columns," by S. Thevanayagam, G.R. Martin, R. Nashed, T. Shenthan, T. Kanagalingam and N. Ecemis, 8/28/06 06 (PB2007-106985).

MCEER-06-0010 "Conceptual Design and Experimental Investigation of Polymer Matrix Composite Infill Panels for Seismic Retrofitting," by W. Jung, M. Chiewanichakorn and A.J. Aref, 9/21/06 (PB2007-106986).

MCEER-06-0011 "A Study of the Coupled Horizontal-Vertical Behavior of Elastomeric and Lead-Rubber Seismic Isolation Bearings," by G.P. Warn and A.S. Whittaker, 9/22/06 (PB2007-108679).

MCEER-06-0012 "Proceedings of the Fourth PRC-US Workshop on Seismic Analysis and Design of Special Bridges: Advancing Bridge Technologies in Research, Design, Construction and Preservation," Edited by L.C. Fan, G.C. Lee and L. Ziang, 10/12/06 (PB2007-109042).

MCEER-06-0013 "Cyclic Response and Low Cycle Fatigue Characteristics of Plate Steels," by P. Dusicka, A.M. Itani and I.G. Buckle, 11/1/06 06 (PB2007-106987).

MCEER-06-0014 "Proceedings of the Second US-Taiwan Bridge Engineering Workshop," edited by W.P. Yen, J. Shen, J-Y. Chen and M. Wang, 11/15/06.

MCEER-06-0015 "User Manual and Technical Documentation for the REDARS^{TM} Import Wizard," by S. Cho, S. Ghosh, C.K. Huyck and S.D. Werner, 11/30/06 (PB2007-114766).

MCEER-06-0016 "Hazard Mitigation Strategy and Monitoring Technologies for Urban and Infrastructure Public Buildings: Proceedings of the China-US Workshops," edited by X.Y. Zhou, A.L. Zhang, G.C. Lee and M. Tong, 12/12/06 (PB2008-500018).

MCEER-07-0001 "Static and Kinetic Coefficients of Friction for Rigid Blocks," by C. Kafali, S. Fathali, M. Grigoriu and A.S. Whittaker, 3/20/07 (PB2007-114767).

MCEER-07-0002 "Hazard Mitigation Investment Decision Making: Organizational Response to Legislative Mandate," by L.A. Arendt, D.J. Alesch and W.J. Petak, 4/9/07 (PB2007-114768).

MCEER-07-0003   "Seismic Behavior of Bidirectional-Resistant Ductile End Diaphragms with Unbonded Braces in Straight or Skewed Steel Bridges," by O. Celik and M. Bruneau, 4/11/07 (PB2008-105141).

MCEER-07-0004   "Modeling Pile Behavior in Large Pile Groups Under Lateral Loading," by A.M. Dodds and G.R. Martin, 4/16/07(PB2008-105142).

MCEER-07-0005   "Experimental Investigation of Blast Performance of Seismically Resistant Concrete-Filled Steel Tube Bridge Piers," by S. Fujikura, M. Bruneau and D. Lopez-Garcia, 4/20/07 (PB2008-105143).

MCEER-07-0006   "Seismic Analysis of Conventional and Isolated Liquefied Natural Gas Tanks Using Mechanical Analogs," by I.P. Christovasilis and A.S. Whittaker, 5/1/07.

MCEER-07-0007   "Experimental Seismic Performance Evaluation of Isolation/Restraint Systems for Mechanical Equipment – Part 1: Heavy Equipment Study," by S. Fathali and A. Filiatrault, 6/6/07 (PB2008-105144).

MCEER-07-0008   "Seismic Vulnerability of Timber Bridges and Timber Substructures," by A.A. Sharma, J.B. Mander, I.M. Friedland and D.R. Allicock, 6/7/07 (PB2008-105145).

MCEER-07-0009   "Experimental and Analytical Study of the XY-Friction Pendulum (XY-FP) Bearing for Bridge Applications," by C.C. Marin-Artieda, A.S. Whittaker and M.C. Constantinou, 6/7/07 (PB2008-105191).

MCEER-07-0010   "Proceedings of the PRC-US Earthquake Engineering Forum for Young Researchers," Edited by G.C. Lee and X.Z. Qi, 6/8/07.

MCEER-07-0011   "Design Recommendations for Perforated Steel Plate Shear Walls," by R. Purba and M. Bruneau, 6/18/07, (PB2008-105192).

MCEER-07-0012   "Performance of Seismic Isolation Hardware Under Service and Seismic Loading," by M.C. Constantinou, A.S. Whittaker, Y. Kalpakidis, D.M. Fenz and G.P. Warn, 8/27/07, (PB2008-105193).

MCEER-07-0013   "Experimental Evaluation of the Seismic Performance of Hospital Piping Subassemblies," by E.R. Goodwin, E. Maragakis and A.M. Itani, 9/4/07, (PB2008-105194).

MCEER-07-0014   "A Simulation Model of Urban Disaster Recovery and Resilience: Implementation for the 1994 Northridge Earthquake," by S. Miles and S.E. Chang, 9/7/07, (PB2008-106426).

MCEER-07-0015   "Statistical and Mechanistic Fragility Analysis of Concrete Bridges," by M. Shinozuka, S. Banerjee and S-H. Kim, 9/10/07, (PB2008-106427).

MCEER-07-0016   "Three-Dimensional Modeling of Inelastic Buckling in Frame Structures," by M. Schachter and AM. Reinhorn, 9/13/07.

MCEER-07-0017   "Modeling of Seismic Wave Scattering on Pile Groups and Caissons," by I. Po Lam, H. Law and C.T. Yang, 9/17/07.

MCEER-07-0018   "Bridge Foundations: Modeling Large Pile Groups and Caissons for Seismic Design," by I. Po Lam, H. Law and G.R. Martin (Coordinating Author), 12/1/07.

MCEER-07-0019   "Principles and Performance of Roller Seismic Isolation Bearings for Highway Bridges," by G.C. Lee, Y.C. Ou, Z. Liang, T.C. Niu and J. Song, 12/10/07.

MCEER-07-0020   "Centrifuge Modeling of Permeability and Pinning Reinforcement Effects on Pile Response to Lateral Spreading," by L.L Gonzalez-Lagos, T. Abdoun and R. Dobry, 12/10/07.

MCEER-07-0021   "Damage to the Highway System from the Pisco, Perú Earthquake of August 15, 2007," by J.S. O'Connor, L. Mesa and M. Nykamp, 12/10/07.

MCEER-07-0022   "Experimental Seismic Performance Evaluation of Isolation/Restraint Systems for Mechanical Equipment – Part 2: Light Equipment Study," by S. Fathali and A. Filiatrault, 12/13/07.

MCEER-07-0023 "Fragility Considerations in Highway Bridge Design," by M. Shinozuka, S. Banerjee and S.H. Kim, 12/14/07.

MCEER-07-0024 "Performance Estimates for Seismically Isolated Bridges," by G.P. Warn and A.S. Whittaker, 12/30/07.

MCEER-08-0001 "Seismic Performance of Steel Girder Bridge Superstructures with Conventional Cross Frames," by L.P. Carden, A.M. Itani and I.G. Buckle, 1/7/08.

MCEER-08-0002 "Seismic Performance of Steel Girder Bridge Superstructures with Ductile End Cross Frames with Seismic Isolators," by L.P. Carden, A.M. Itani and I.G. Buckle, 1/7/08.

MCEER-08-0003 "Analytical and Experimental Investigation of a Controlled Rocking Approach for Seismic Protection of Bridge Steel Truss Piers," by M. Pollino and M. Bruneau, 1/21/08.